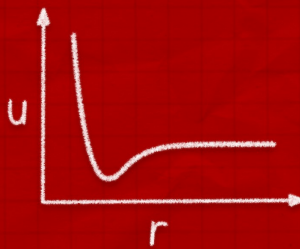


Measuring interactions between colloidal (nano)particles



Maarten Bransen

Measuring interactions between colloidal (nano)particles

PhD thesis, Utrecht University
Measuring interactions between colloidal (nano)particles
Maarten Bransen, May 2024


ISBN: 978-90-393-7683-6

doi: <https://doi.org/10.33540/2252>

Printed by Gildeprint B.V., Enschede

Fonts: Libertinus Serif (body), Libertinus Sans (figures, captions), Liberation Sans (cover)

Cover: colloidal nanoparticles exploring their local free energy landscape through Brownian motion as they interact with one another. Digital composite with digitally drawn elements and textures of crumpled and torn paper. © 2024 Maarten Bransen

The contents of this work, with the exception of reprinted figures (as indicated in captions) and artwork on cover & part pages, are published under *CC BY 4.0*. To view a copy of this licence, visit <https://creativecommons.org/licenses/by/4.0/> 

Measuring interactions between colloidal (nano)particles

Het meten van interacties tussen colloïdale (nano)deeltjes
(met een samenvatting in het Nederlands)

Proefschrift

ter verkrijging van de graad van doctor aan de Universiteit Utrecht
op gezag van de rector magnificus, prof. dr. H. R. B. M. Kummeling,
ingevolge het besluit van het college voor promoties in het
openbaar te verdedigen op

maandag 27 mei 2024
des middags te 2.15 uur

door

Maarten Bransen

geboren op 5 januari 1994
te Vleuten-De Meern

Promotor:

Prof. dr. A. van Blaaderen

Beoordelingscommissie:

Prof. dr. M. Dijkstra

Prof. dr. D. G. Grier

Prof. dr. W. K. Kegel

Prof. dr. J. Lipfert

Prof. dr. R. H. H. G. van Roij

Dit onderzoek werd financieel ondersteund door het *Netherlands Center for Multiscale Catalytic Energy Conversion* (MCEC), een NWO Zwaartekrachtprogramma gefinancierd door het Nederlandse ministerie van Onderwijs, Cultuur en Wetenschap.

Contents

1	Introduction	1
I Status Quo		
2	Experimental techniques for measuring (N)P interactions	17
3	Synthesis & characterisation of colloidal model systems	53
II Interactions from Distribution Functions		
4	Using solvent-arresting to probe interactions in 3D	97
5	Measuring ligand-dependent AuNP interactions using cryo-TEM	129
III Interactions from Trajectories		
6	Measuring interaction forces from multi-particle trajectories	165
7	Measuring anisotropic interaction forces from particle trajectories	205
8	Conclusions and outlook	235
	References	241
	Summary for the general public	265
	Samenvatting voor een breed publiek	275
	Acknowledgements	289
	List of publications	293
	About the author	295

CHAPTER 1

Introduction

SETTING THE STAGE

Nature, in all of its beauty and complexity, has evolved over eons of time a near-infinite number of materials with properties that rival the best of what our own intelligent design has been able to produce. From the strength and stretching of spider silk to the critical components of our cells, evolution invented it all. Creating complexity, molecule by molecule, protein by protein, bit by bit, from the bottom up. Yet a chemist, staring at the long list of elements on the periodic table on their wall, might realise that nature pulls most of its tricks from a remarkably small hat. A mere handful of elements –carbon, hydrogen, nitrogen and oxygen– make up the vast majority of all living things. Nature achieves this not just by mastering the *covalent* bonds between these elements, but by ordering molecules and materials in a hierarchical manner using a myriad of *non-covalent* interactions. From the hydrogen bonding and π - π stacking that can give a protein its shape from within, to the complex intermolecular interactions *between* proteins, these comparatively weak non-covalent bonds form the bridge between the molecular and the macroscopic. Chemistry as a discipline has devoted itself to and mastered the art of making and breaking ‘chemical’* bonds, of not just that handful of elements abundant in organic matter, but across most of the periodic table. But for all our mastery of materials synthesis, much remains to be learned from nature when it comes to those weaker interactions and our ability to manipulate and structure materials at the nanometer scale.

It is precisely there, at the *nano*-scale, where some of the most fascinating fundamental processes occur. For many processes and properties the nano-scale forms a sort of transition regime between two extremes: the *microscopic* world –or more aptly *nanoscopic*–, dominated by quantum-mechanical principles, and the *macroscopic* world more familiar to us. Take for example gold, a material famous for its golden colour and lack of chemical reactivity. Cutting a piece of gold in two would not do anything to change this, and why would it? After all, changing its size does nothing to change the materials’ fundamental properties. Yet when the size of our piece of gold is decreased until its diameter is best expressed in *nanometers*, one-billionths of a meter, something remarkable happens: its colour changes to a deep red and its chemical reactivity increases. Not only that, but it starts to move, erratically yet consistently, driven by collisions with the molecules around it. Even a slight change in the size or shape of our particle now continually changes how it interacts with the world around it. This variability, this ability to precisely tune how materials interact –be that optically, chemically, magnetically, kinetically, ... – is not unique to gold. It is something nearly any material does when one of its dimensions is on the order of nanometers. It is *this* what makes nanoparticles so interesting to scientists. Now imagine doing with *our* perfectly tailored nanoparticles what nature does best with *its* nanoparticles, and master the process of assembling them with microscopic order into mesoscopic and macroscopic materials that we can study and use, particle by particle, bit by bit, from the bottom up. To understand those non-covalent interactions between nanoparticles, to develop the techniques to learn more about them, *that* is what this thesis is about.

“There is plenty of room at the bottom” – Richard Feynman, 1959^[1]

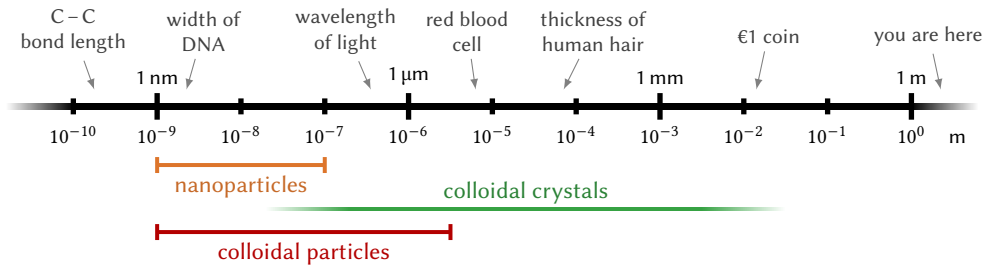


Figure 1.1: the size of colloidal particles. The sizes of the particles in this thesis are indicated on a logarithmic scale relating the macroscopic (right hand side) to the microscopic (left hand side). For context, the relevant units of length and the typical sizes of some common objects/phenomena are indicated.

1.1 Colloidal particles: from micro to nano

In this thesis we will explore the interactions of *colloidal particles*, also commonly called *colloids*. Colloids are microscopic particles with a size between one nanometer and at most ten micrometers, dispersed and suspended in some medium in which they are insoluble. Examples of this include the emulsion droplets in milk (liquid particles in a liquid medium), pigment particles in paints (solid particles in a liquid medium) and soot particles in smoke (solid particles in a gaseous medium). Particles in the colloidal size range have been used in applications such as paints, glues, inks and ceramics for centuries, but are also ubiquitous in nature. This work specifically concerns colloidal suspensions, that is solid particles in a liquid dispersing medium. Colloids possess some unique properties owing to their size range: sitting inbetween atomic/molecular matter on the one hand and the bulk properties we observe in our macroscopic world on the other, there are similarities and differences with respect to either. Like molecules, colloids undergo Brownian motion due to constant collisions with molecules of the surrounding dispersion. This random motion allows the particles to explore their local environment with an energy on the order of the thermal energy, $k_B T$, where $k_B \approx 1.38 \cdot 10^{-23}$ J/K is the Boltzmann constant and T the absolute temperature. The interplay between Brownian diffusion and gravity means that rather than immediately ‘falling’ or sedimenting to the bottom, colloids form a density gradient with a typical decay length dependent on their size and density, much like the density of air molecules in our atmosphere. But unlike most of the world of the molecular, colloids are large enough to be observed directly in real-space and real-time using microscopy techniques.^[2-5] **Figure 1.1** places the particles discussed in this thesis on a logarithmic ‘ruler’ ranging from the typical length scale of atoms (~ 1 Ångstrom, which is 10^{-10} m), to the typical length scale of humans.

The properties and stability of colloidal particles in their dispersing medium, typically water, depend crucially on the *interaction forces* between the particles. One can imagine that when colloids have attractive interactions—that is they can minimize their free energy by being close to one another—they will start to stick together in clusters and eventually precipitate out or form jammed glassy networks. On the other hand, when there is an energy barrier preventing the particles from getting near one another, colloidal dispersions may remain colloiddally stable practically indefinitely. Considerable attention has been devoted

* usually meaning covalent, ionic or metallic

to understanding and tuning inter-particle interaction forces for the purpose of colloidal *self-assembly* (SA), by which complicated structures with novel properties can be created using a bottom-up approach.^[6–11] While self-assembled materials of colloidal *microparticles* (μPs) possess interesting optical properties such as the ability to form a photonic band gap,^[12,13] more recently, considerable attention has been devoted to self-assembly of colloidal *nanoparticles* (NPs). We make an explicit distinction between colloidal *microparticles* (μPs), with a size (diameter) of >100 nm, and *nanoparticles*, which we define as particles having a diameter between 1–100 nm. As alluded to previously, when the particle size is decreased to below 100 nm and increasingly so as the particle size approaches only a few nanometers, the properties of NPs drastically change when compared to their larger μP counterparts, because of effects such as the high surface-to-volume ratio of NPs, the discrete nature of atoms and molecules and quantum confinement.^[8,14] Examples of these effects are the increased per-mass catalytic activity of NPs in heterogeneous catalysis, the non-metallic nature of sufficiently small ‘metal’ NPs, and the size-dependent band gap in semiconductor NPs respectively. Self-assembly of NPs can lead to materials with emergent properties not found in conventional bulk materials, which is of great interest for many applications such as energy conversion, nano-scale sensing and quantum matter.^[15–17] In order to rationally design and effectively fine-tune these materials, the interaction forces between NPs *must* be understood.^[14,18]

While the enormous progress in synthesis of (colloidal) nanoparticles has gone hand in hand with improved theoretical understanding of the underlying processes and mechanisms, progress in nanoparticle self-assembly can be largely attributed to empirical discovery^[14]. Accurate and reasonably general theoretical descriptions of the most important interaction forces between colloidal particles have been derived but are predominantly applied to μPs . This is in part because the properties of these larger colloids can be observed in real-space using optical microscopy, but perhaps more so because NPs exhibit particularly complex interaction forces.^[19,20] The difficulty herein lies in the fact that NPs, consisting of hundreds up to tens of millions of atoms, are generally too large and complex to be understood using methods designed for interactions between atoms or molecules (such as density functional theory). On the other hand, a 10 nm NP is within two orders of magnitude of the typical size of atomic bond-lengths and solvated ions. Therefore, theories based on continuum descriptions of NPs and their environment do not accurately predict their interactions, and properties like the dielectric constant, density and surface charge deviate from bulk values. Rather than developing theoretical descriptions of inter-particle interactions, in this thesis we instead explore methods for measuring interactions between colloidal particles *experimentally*.

1.2 Outline of this thesis

The aim of this work is thus to develop and evaluate methods for experimentally measuring interaction forces between colloidal particles, in the context of colloidal stability and self-assembly. Firstly, in this introductory chapter we have introduced the subject of colloids and their relevance, and we will go on to provide an introduction into the most common types of interaction forces, how these have been described theoretically, and how these change when the particle size and/or inter-particle distance are reduced to the nanometer scale. This thesis is structured around three parts of two chapters each. In **Part I**, we focus on existing work. In **Chapter 2** we will review the different methods with which inter-particle forces have been measured in the last several decades of colloid science. This involves both the

experimental techniques, be that atomic force microscopy, optical microscopy or in-situ electron microscopy, as well as the basic theoretical concepts required to infer the interaction forces from these techniques. In particular, we will focus on methods which have been or can be advanced towards measurement of interactions between nanoparticles. In **Chapter 3**, we will explore the synthesis of colloidal particles as model systems for interaction measurement. A number of different protocols for the synthesis of silica and gold based particle syntheses are reproduced to prepare the particles which were used throughout this work as well as in in-situ studies elsewhere.

In **Part II**, we focus on extracting interactions from static coordinates obtained using real-space microscopy through analysis of the radial distribution function using a method called test-particle insertion (TPI). In **Chapter 4** the TPI method is introduced and we explore a novel solvent-polymerization procedure with which colloidal dispersions may be rapidly arrested, preserving their real-space structure. This solvent arresting is used in combination with TPI and 3D confocal laser scanning microscopy (CLSM) or focussed ion-beam scanning electron microscopy (FIB-SEM) to measure interactions in arrested colloidal dispersions, as well as to study sedimentation and crystallisation in binary particle systems. In **Chapter 5** we demonstrate that interactions between nanoparticles may be similarly obtained by rapid cryogenic vitrification of nanoparticle dispersions and subsequent analysis using transmission electron microscopy (TEM). This in combination with TPI is used to measure inter-particle interactions in quasi 2-dimensional liquid films. Using a novel sample preparation technique based on cryogenically frozen graphene liquid cells, we show that it is possible to measure the 3-dimensional real-space particle distribution of NPs during self-assembly in evaporating emulsion droplets.

In **Part III**, we explore a method for extracting interaction forces of colloidal μPs from *dynamic* data, *i.e.* multi-particle trajectories, and explore how it can be used to measure anisotropic interactions and interactions of colloids out of equilibrium. We refer to this as trajectory analysis (TA). In **Chapter 6** the TA method is introduced and benchmarked using simulated trajectories. Then, we use fast fluorescence microscopy to obtain 2D and 3D trajectories of colloidal microparticles and evaluate the performance of TA, and show that this approach may be used to measure interaction forces out of equilibrium. Finally, in **Chapter 7** the trajectory analysis method is theoretically extended to enable measurement of *anisotropic* interactions from multi-particle trajectories. Using simulated data and preliminary experiments, we show that it is in principle possible to measure the anisotropic dipolar interactions of colloidal particles in external alternating current electric fields, although the extremely high measurement rates required make it particularly challenging to achieve this in practise.

1.3 Inter-particle interactions

Much of the widely known theories on colloidal particles have been developed for or predominantly applied to what we call the ‘classical colloid’. As shown in **Figure 1.2**, the classical colloid is a smooth spherical particle of homogeneous composition with a solid surface and a modest surface charge, dispersed stably in a liquid dispersing medium containing some background concentration of point-like ions. This picture, ignorant of the complexity of real materials as it may be, is very useful in its simplicity as it turns out to be a good model for many colloidal materials in the μP range. When considering the depiction of what a nanoparticle might look like, it is clear that such a description only has limited use when

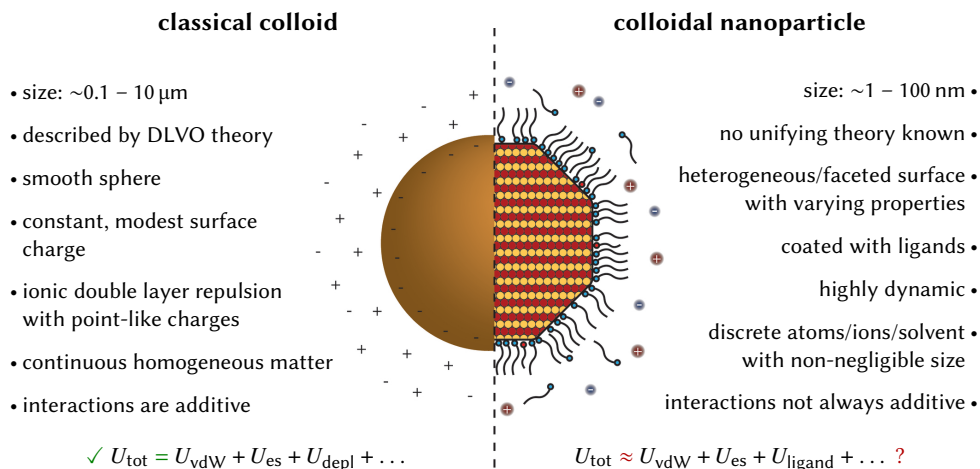


Figure 1.2: nanoparticles versus the ‘classic colloid’. The reality for nanoparticles is contrasted with the assumptions typically made for colloidal particles in theories describing inter-particle interactions, which we dub the classical colloid.

considering real NPs. Below, we will briefly discuss the concept of the pairwise interaction potential and the idea of additivity of interactions. Then, we give a short overview of some commonly encountered types of colloid-colloid interactions, their microscopic origins, and in when applicable we give analytical models which may be used to predict these interactions. Finally, we discuss how this picture may change when going from the ‘classic colloid’ to nanoparticles. However, the subject of interactions between colloids and colloidal NPs specifically has been written about extensively, and for more detailed discussions we refer readers to some of the many reviews of interaction forces.^[7,14,16–26]

1.3.1 The pairwise interaction potential

There are many ways in which interaction forces between colloidal particles may be expressed. In this work, we will predominantly express the interactions in terms of the *pairwise interaction potential*, $U(r)$, which is defined as the change in free energy for a pair of particles brought to some inter-particle distance r , where the energy at infinite separation is set to 0. One can also think of the interaction in terms of forces between particles, analogously given as the pairwise interaction force $F(r)$: the force exerted on a particle by a neighbouring particle as a function of the inter-particle distance r . The force is given by the change in free energy with respect to the particles’ relative positions:

$$F(r) = -\frac{\partial}{\partial r}U(r) \quad (1.1)$$

where a repulsive force is positive by convention. The pairwise potential and pairwise force are, as their names imply, strictly defined for a particle *pair* in isolation. In reality any one particle typically interacts with multiple neighbouring particles. This can be dealt with by assuming *pairwise additivity*: that the total change in the free energy of a particle is given by the sum of the pairwise interactions with each neighbour. While this is a reasonable assumption in many cases, there are cases where three-body or higher order

effects are significant such as depletion interactions with certain depletant-particle size ratios,^[27] long ranged repulsive interactions where the second nearest neighbour shell is within interaction range,^[28–31] and binary hard-sphere systems when confined to a quasi 2-dimensional layer.^[32]

1.3.2 Additivity of interactions and the DLVO potential

Let us turn again to the image of the ‘classic colloid’. It is often well described by arguably the most widely used theory / model potential for colloidal particles: DLVO potential, named after Derjaguin & Landau and Verweij & Overbeek who independently arrived at the theory for describing the combination of van der Waals and screened electrostatic interactions between colloids.^[33,34] In its original form the DLVO potential is given only as the sum of (attractive) van der Waals forces, and the (attractive or repulsive*) electrostatic forces that arise from overlapping of clouds of counter ions –the electric double layers– surrounding charged particles in salt solutions. The total interaction potential is then:^[23,35]

$$U_{\text{DLVO}}(r) = U_{\text{vdW}}(r) + U_{\text{es}}(r) \quad (1.2)$$

with U_{vdW} and U_{es} the pair potentials due to van der Waals and electrostatic forces respectively. The important assumption here is that the individual contributions are assumed to be independent from one another, and thus *additive*. This idea of evaluating the different contributions separately greatly simplifies the theory and allows for various different types of interaction to be included when necessary. Over the years, the DLVO potential has been extended by adding other terms for additional types of interactions with varying degrees of rigour and success,^[35] and some of these extension will be discussed below.

1.3.3 Overview of common inter-particle forces

Let us now give a short overview and go through some of the most common types of inter-particle interactions, what their microscopic origins are, and, where applicable, how these may be described using straightforward analytical functions.

Van der Waals / dispersion forces:

Van der Waals (VdW) forces arise from the intrinsic (non-covalent) interactions between the constituent atoms of particles and those in nearby particles and/or (solvent) molecules. The most important contribution to VdW forces is formed by London dispersion forces, which arise from spontaneous fluctuations in electron density in atomic orbitals that create a dipole moment, which in turn induce dipoles moments in nearby atoms, leading to a net attractive force due to their coupling.^[36] Similarly, the presence of molecules with a (thermally/rotationally averaged) permanent dipole may interact with other such permanent dipoles (Keesom forces) or induce a dipole moment in polarizable materials (Debye forces). All three of these effects are short ranged ($u \propto -1/r^6$) and relatively weak. Nonetheless, they are significant because they are always present and often the *only* relevant attractive component.^[18,24,37] Additionally, when taking the combined (integrated) effects of all VdW interaction between larger bodies such as colloidal particles, the net (total) forces can be much more long ranged (up to $u \propto -1/r$ over short distances), although at long range dipole-coupling is weaker due to retardation effects as a result of the finite speed of light.^[38] The most common method to calculate VdW forces between colloids is based on the work of Hamaker and Derjaguin, which works by integrating over all pairs of volume elements

* depending on whether the particles are like-charged or oppositely charged

between two particles under the assumption that matter is continuous and that the constituent dipole-dipole interactions are pairwise additive.^[2,36,39,40] Unfortunately, neither is an exact approximation when considering nanoparticles, and more advanced methods for calculating vdW interactions have been developed to address these issues.^[37,41–43] Nonetheless, the Hamaker approach is useful in its simplicity. The net magnitude of the interaction of materials in some medium can then be expressed by the Hamaker constant A_H , and analytical equations have been derived for a number of common geometries. A simplified approximation for the vdW attraction energy of two spherical particles with radii R_i and R_j is given as:^[39]

$$U_{\text{vdW}} = -\frac{A_H}{6} \left[\frac{2R_i R_j}{r^2 - (R_i + R_j)^2} + \frac{2R_i R_j}{r^2 - (R_i - R_j)^2} + \ln \left(\frac{r^2 - (R_i + R_j)^2}{r^2 - (R_i - R_j)^2} \right) \right] \quad (1.3)$$

where r is the centre-to-centre distance, and hamaker constant A_H depends on particle and solvent properties.

Electrostatic forces:

Surfaces are rarely uncharged even in low polarity solvents and can acquire surface charges in multiple ways, such as by dissociation of chemical groups at the surface or adsorption of onto the surface. Charged particles interact through Coulomb interactions, but (counter) ions in the solution will form an electric double layer around the charged particles to increase their entropy in response to the field created by the charges on the surface. The net result is that the surface charges will be partially screened from the environment, giving rise to a screened electrostatic interaction between colloids due to overlap between their double layers. This interaction decays exponentially and for two particles i and j with radii R_i and R_j is given by:^[33,34,44]

$$U_{\text{es}}(r) = k_B T Z_i Z_j \lambda_B \frac{e^{\kappa(R_i+R_j)}}{(1 + \kappa R_i)(1 + \kappa R_j)} \frac{e^{-\kappa r}}{r} \quad (1.4)$$

where k_B is the Boltzmann constant, T the absolute temperature, Z_i, Z_j the effective colloid charges, λ_B the Bjerrum length and κ the inverse Debye length. The Bjerrum length is the distance at which the interaction energy of two elementary charges is equal to the thermal energy $k_B T$, and is given by:

$$\lambda_B = \frac{q_e^2}{4\pi\epsilon_r\epsilon_0 k_B T} \quad (1.5)$$

with $q_e \approx 1.60 \cdot 10^{-19}$ C the elementary charge, ϵ_r the relative dielectric constant of the solvent and $\epsilon_0 \approx 8.85 \cdot 10^{-12}$ F/m the dielectric permittivity of vacuum. The Debye length κ^{-1} gives the characteristic length scale of the electrostatic double layer, and is given by:

$$\kappa^{-1} = \frac{1}{\sqrt{8\pi\lambda_B c_s z^2}} \quad (1.6)$$

for a $z:z$ electrolyte, where c_s is the bulk number concentration* of salt. For some context, this means that for a monovalent salt in water at 25 °C, $\kappa^{-1} \approx (0.304/\sqrt{c_s^M})$ nm (with c_s^M the salt concentration in mol/L), giving a double layer sizes of 30, 9.6 and 3.0 nm for 0.1, 1 and 10 mM respectively. Eq. 1.6 is valid for particles with surface potentials <50 mV and c_s^M up to 10 mM (in case of monovalent ions) or 0.1 mM (for ions with high ion charge), and for distances $r > \kappa^{-1}$.^[18] For more advanced solutions see e.g. Sader & Chan *et al.*^[45]

* 'bulk' meaning far from any charged surfaces, 'number' meaning in units of dissociated molecules/m³

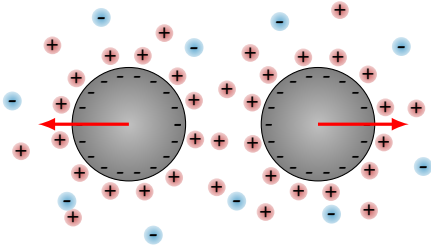


Figure 1.3: electrostatic repulsion

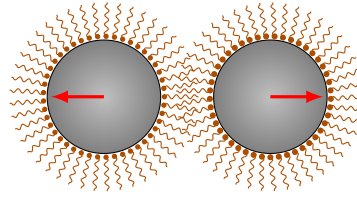


Figure 1.4: steric repulsion

Steric repulsions:

One of the most common ways in which colloids are stabilized is through steric repulsion. In principle, the term ‘steric repulsion’ is used to refer to the restoring force that prevents complete overlap between the electron clouds of atoms, *i.e.* the force that stops objects from passing through one another. Ultimately this is a quantum-mechanical effect that affects all matter, but in the context of colloids ‘steric stabilization’ specifically refers to the coating of particles with organic ligands or polymers to prevent coagulation. These molecules ‘block’ the NP cores from getting in close contact, such that the van der Waals attractions between the cores of two particles are small at the range at which their ligand shells start to overlap. Because the Hamaker constant for most organic molecules is low and often similar to that of the solvents used to disperse colloids in, van der Waals attractions between the ligand shells of two particles are usually negligible. Entropic effects due to interdigitation (mixing of the ligand shells) may also contribute to steric interactions, as in good solvents it may be unfavourable for ligand shells to mix.^[16] While steric stabilisation is common and extremely important for colloidal stability in many industrial processes, its strength depends on many parameters such as ligand size, density, binding strength, solubility in the solvent, etc., and no comprehensive theory has been developed to describe steric forces between colloids.^[23,46,47]

Depletion interactions:

Depletion interactions between colloids can occur when a second population of significantly smaller particles is present with a size intermediate between the colloids and the solvent molecules.^[48] Around each colloidal particle there is an excluded region into which the depletants cannot go (or rather their centres of mass), as that would require overlap between the colloid and the depletant. When two of the large particles approach each other such that their depleted zones overlap, this effectively frees up space for the depletant, thereby increasing its entropy and thus leading to a net attraction between the colloids.* Another way to understand this, is that when the two colloids approach closely the depletant cannot go in the region between the colloids. As a result there is a difference in osmotic pressure between the ‘inside’ (in-between the colloids) and the ‘outside’ which pushes the particles together. Depletion forces are highly tunable, as the range and magnitude of the force depend on the depletants’ size and concentration respectively. Furthermore, the interaction energy is typically on the order of several $K_B T$ and in principle reversible. Depletion interactions between hard particles and (ideal) polymer depletants are commonly modelled using the

* we note that for hard depletants and high volume fractions, the presence of ‘depletants’ can actually lead to an energy barrier at larger distance than the primary minimum, and stabilise colloids^[49,50]

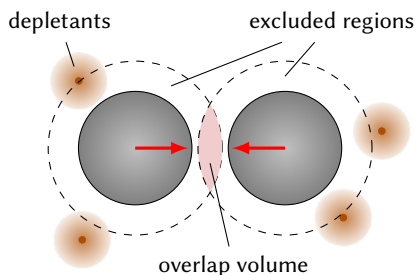


Figure 1.5: depletion attraction

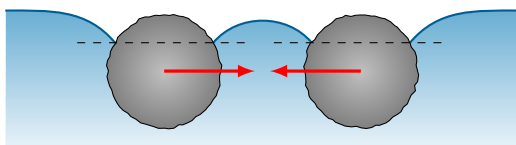


Figure 1.6: capillary attraction

theory by Asakura & Oosawa^[51] (later independently derived by Vrij^[52]), where the depletion attraction between two spheres of radius R given as:^[7,51]

$$U_{\text{depl}} = \begin{cases} -k_B T c_d \pi R \left[2a^2 - 2a(r - 2R) + \frac{1}{2}(r - 2R)^2 \right] & r < 2(a + R) \\ 0 & r \geq 2(a + R) \end{cases} \quad (1.7)$$

where a is the depletant radius and c_d the depletant number concentration. This theory treats the depletants as ideal polymers, and considers only the osmotic pressure and size of an ideal solution of the depletants. In reality many different materials may be used that may interact with each other and the primary colloids through e.g. charge and soft steric interactions. Of course, being a geometric effect also the monodispersity and shape of the primary particles and depletants strongly affect the interactions.^[11,24,53] For such cases more advanced theoretical models have been developed.^[11,54–57] For μPs , as mentioned commonly used depletants are polymers and smaller colloidal particles of e.g. silica, although for these hard depletant particles the Oosawa-Asakura-Vrij theory is less valid because hard colloids are less well approximated by an ideal gas as their excluded volume interaction is significantly more important than for ideal polymer chains.^[55,56] In case of nanoparticles, surfactant micelles, other nanoparticles and short chain polymers can be used to induce depletion.^[11,58]

Capillary forces:

Capillary forces occur when (nano)particles are adsorbed to liquid–air or liquid–liquid interfaces, through deformation of the interface as a result of the contact angle where the interfaces meet the particles.^[20,59] When the interfacial tension of such interfaces is higher than the respective colloid–liquid or colloid–air interfaces, the net interfacial tension may be reduced by adsorbing the colloids to the interface.^[60] This is for example the underlying mechanism for Pickering emulsions, but also occurs when particles are assembled onto substrates by evaporation of the solvent. In (nano)particle powders, absorption of ambient moisture may also significantly alter the interactions between particles. When colloids at interfaces deform/curve the interface, the total surface energy may be reduced (or increased) by overlapping the menisci of neighbouring colloids, analogously to depletion interactions leading to a net attraction (or repulsion). Capillary forces depend on the wetting and surface roughness of the particles, and may be extremely strong (as much as $\sim 100 k_B T$) and relatively long-ranged.^[17,20,59,61] Other effects, such as deformation of the ligand shell and ionic double

layer at/near interfaces can also significantly alter the interactions of colloids when compared to particles in the bulk of the fluid.^[60–62]

Solvation and hydration forces:

Solvation forces occur due to local structuring of the dispersing medium near the surface of particles or interfaces, and it thus a direct consequence of the discreteness of matter. The presence of an interface can induce layering of solvent molecules leading to repulsive or oscillating forces with a length scale on the order of the size of the solvent molecules.^[40,63,64] The presence of a hydration layer, a layer of solvent molecules directly adsorbed onto the particle surface—especially if this surface is close to being atomically smooth—, can prevent the surfaces from approaching closer than the thickness of two solvent layers as this would require full desorption of the liquid, thereby stabilizing the particles.^[20,65,66]

Solvophobic forces:

Solvophobic interactions occur due to insufficient wetting of the particle surface by the dispersing medium when the solvent interact more favourably with itself than with the particles.^[7,67] Analogous to the phase separation of oil and water, particles with hydrophobic surface coatings may interact less favourably with dispersing water molecules than the water would when hydrogen bonding with itself. Similarly, this may be further aided by van der Waals attractions between the particles. As a result, the free energy of the system may be lowered by minimizing the interfacial area between the particles and the medium, causing the particles to be aggregated.

Supramolecular forces:

Supramolecular interactions, which are particularly common in biological materials, are not truly fundamental forces in that they are typically caused by a combination of effects such as van der Waals, electrostatic, dipolar (hydrogen bonding) steric and solvophobic forces. Uniquely though, these interactions consist of a large number of interacting groups and differ from the constituent effects in isolation, in that they are typically highly specific—such as the interaction between strands of complementary DNA or the binding of antibodies to proteins—, highly complex due to the combination of different effects underlying the net interaction, as well as generally anisotropic and not pairwise additive.^[7,14,21,68–70] As the name implies these interactions are predominantly found in biological systems, although e.g. DNA mediated interactions of colloidal (nano)particles have been widely explored for targeted and tunable colloid-colloid interactions.^[71–73]

Hydrodynamic interactions:

Hydrodynamic interactions are the result of the displacement of solvent molecules due to the presence of particles. Consider for example a charged diffusing particle: the ionic double layer around the particle moves with it, encountering drag due to the surrounding solvent and inducing a local flow. When another particle is near, the induced flow from one particle may affect the hydrodynamic drag experienced by the other, thus exerting a force through the fluid medium. In equilibrium hydrodynamic forces are fully reversible and do not contribute to interaction potential between colloids (although they may affect their dynamics),^[74,75] but in case systems are not in equilibrium, they can contribute.^[76] Hydrodynamic forces are complex to simulate and generally non-additive, and modelling them in a general manner has become possible only in the last ~10 years using e.g. lattice-Boltzmann like approaches.^[25,77]

1.3.4 Interactions at the nano-scale

As we have discussed before, many of the models discussed above are less exact or require additional care when talking about nanoparticles, and in particular NPs where the interaction distance is <100 nm. The first, and perhaps most problematic, is the assumption of *additivity* which states that the total potential is the sum of different attractive and repulsive components. This additivity of the different interaction forces* unfortunately breaks down for many nano-scale systems due to the increasing interplay between different processes: *e.g.* the presence of ions near the particle may induce a slight restructuring of the ligand shell which in turn affects the van der Waals forces or the presence of a hydration layer. In other words, all of the physical mechanisms responsible for the different forces are interconnected and cannot be considered separately. These effects are particularly problematic in materials with a high polarisability.^[19] It is also good to consider that typical range of surface forces is ~ 10 – 100 nm.^[26] While for μ Ps the interaction range is often small with respect to the particle size, for NPs the interaction range of a neighbouring particle may cover the particle in its entirety, making a description of interactions as ‘surface forces’ problematic. Considering a critical concentration above which the interaction of a particle on average overlaps with that of multiple neighbours, the system can be considered ‘dilute’ —meaning most particles interact with only a single neighbour— when it is below this critical particle concentration. As the volume in which neighbouring particles interact with a NP is large compared to their size, the critical volume fraction of NPs is much lower than that of μ Ps.^[26] Above the critical concentration each particle interacts with many neighbours and many body effects are more likely to occur. Aside from additivity of interactions, nanoparticles have several properties that are not captured in theories such as the ones discussed in the preceding overview of interaction forces, schematically shown in the right hand side of **Figure 1.2**. To name a few of the most important ones:

NPs are small:

Or to be more specific: NPs are small enough that the size of atoms cannot be neglected and it is not valid to assume that matter is continuous. For example, something like the classical continuous dielectric function is not a good description at the scale of nanometers, instead this must be replaced with the local polarizabilities of the individual atoms.^[19,37] As we have seen, this is for example important in predicting van der Waals forces. A similar argument can be made for the solvent surrounding the particles: solvent molecules have a finite and often non-negligible size, resulting in *e.g.* short range forces due to layering/ordering of solvent molecules when confined between two surfaces, even in cases where there is no formation of a more classical hydration layer.^[64] The size of an ion with its hydration shells in water are typically in the range of 0.5 nm to 1 nm, which is clearly not ‘point-like’ from the perspective of a 10 nm NP.^[78] A common example of this is the occurrence of ion specific effects like the Hofmeister series^[79]

NPs are heterogeneous and anisotropic:

Simple geometric shapes such as spheres, cylinders and ellipsoids yield mathematically elegant theories, but real NPs are rarely perfectly spherical. Crystalline materials generally form NPs with strongly faceted shapes, and most ‘spherical’ particles of these materials in reality more closely resemble regular polyhedra with distinct faces, vertices and corners that all have different chemistries affecting charging and ligand binding. Specific control of facets

* not to be confused with whether or not inter-particle interactions are *pairwise additive*

has given rise to an ever expanding library of anisotropic nanoparticle synthesis methods in the literature.^[8,16] But even when the cores are reasonably spherically symmetrical, ligands may interact in such a way that the overall particle shape is anisotropic.^[80] In some semiconductors, charged facets may result in particles with a significant dipole moment.^[81] Amorphous materials such as silica may display considerable surface roughness and chemical inhomogeneity on the nanometer scale depending on the method of synthesis. Surface roughness in particular strongly affects interactions through *e.g.* depletion and hydration. Polymer NPs are generally globular shapes with a ‘random’ continually changing arrangement of the backbone.^[82] Adding to all of this, in almost all cases the NPs in a dispersion all vary slightly from one another—a concept referred to as the ‘polydispersity’—, meaning that even a model which perfectly captures a nanoparticle’s structure may not be able to capture the properties of a real NP ensemble.

Forces between NPs fluctuate:

NPs are in constant interaction with their environment, and driven by stochastic processes, continually change. While charged groups on the surface of a μP may repeatedly gain and lose charge through dissociation and association of ions on the surface, there are generally enough of these groups that the average surface charge stays more or less constant. For a NP on the other hand, the loss or of a single charged group may represent a considerable alteration of the interaction forces.^[19] Ligands are often only loosely bound, in equilibrium with some background concentration of free surfactant molecules.^[83–85] Polymeric NPs or NPs with polymeric ligands are flexible and can reconfigure depending on the local environment.^[82,86] Even the ‘surface’ of NPs with an inorganic core may dynamically restructure due to the comparatively high reactivity and solubility of surfaces with a high radius of curvature.

1.4 Concluding remarks

Colloidal NPs thus form an exciting class of materials that over the last few decades have proven to be incredibly versatile, and continue to be widely studied because of their potential in a seemingly never-ending list of purported applications. Their assembly, governed by the inter-particle interactions, in many aspects mimics the behaviour of colloidal μPs , for which accurate theories have long been developed. Despite this, many questions remain unanswered for NPs, in part due to the very complexity that leads to many of their interesting properties. With this work we hope to contribute to ongoing work in extending the tools and theories of traditional colloid science towards new directions, be that interaction measurements of nanoparticles, or be that interaction measurement in systems of μPs under conditions which have not been widely studied such as colloids out of equilibrium. We hope that the techniques explored here may be used to provide the experimental evidence necessary to validate the theories and computer simulations that are increasingly common, in order to explore, understand, and predict these interactions.

Part I

Status Quo



CHAPTER 2

A review of experimental techniques for measuring interaction forces between colloidal (nano)particles

ABSTRACT

In the last four decades of soft matter research a wide variety of methods for experimental measurements of colloidal interactions have been reported, starting with the first true measurements of surface forces over nanometer length scales using the surface force apparatus (SFA) and later followed by atomic force microscopy (AFM) and a host of different methods based on optical microscopy. In more recent years there has been a push towards performing these force measurements over ever smaller length- and time-scales, and force measurements between nanoparticles are now within reach. Advances in *in-situ* electron microscopy as well as in simulations & computing power have similarly opened new pathways for studying nanoparticle interactions. In this chapter, we provide an overview of different experimental techniques that have been used to measure interaction forces between colloidal particles and, where appropriate, discuss some of the associated theory needed to extract the pairwise interactions from the measurement data. The different methods are discussed in terms of their main strengths and weaknesses, placed in the context of measuring interactions of colloidal *nanoparticles*, and examples where these techniques were successfully applied are highlighted. Finally, we discuss some of the open questions and where we believe the greatest opportunities lie for the immediate future.

2.1 Introduction

In this chapter we review the experimental techniques used to measure interactions between colloidal particles directly. Many different methods have been already applied to measure interactions between a colloidal particle and a wall, *e.g.* by atomic force microscopy (AFM),^[23] or between multiple colloids in solution such as through the analysis of real-space data obtained with light or electron microscopy.^[87,88] As discussed in **Chapter 1**, predicting interaction forces between colloidal particles is far from trivial, although a large number of methods have been developed, most notably DLVO theory and its many extensions. Those theoretical models were revolutionary in their ability to replicate and explain the behaviour of colloidal dispersions indirectly though *e.g.* colloidal stability, but owe their success in no insignificant part also to the fact that they were experimentally proven to be accurate by direct measurements of interaction forces between colloidal particles. At the same time, interaction measurements are arguable more valuable in revealing when and where theory and reality deviate, and many examples of non-DLVO behaviour have been found. Despite the now almost four decades of interaction measurements, much remains to be learned even on the micrometer scale when it comes to the interactions between colloids, in particular when it comes to the more complex cases of particles which are *e.g.* anisotropic, made out of materials with not yet fully understood surface structures (such as some microgels), or systems which are not in thermodynamic equilibrium, such as in the case of the complex (often attractive) interactions between active particles.^[76] This is even more the case for nanoparticles, where complexity and deviation from ‘simpler’ theories are increasingly likely to occur as the particle size enters the nanoparticle regime.

At the same time, the smaller size makes nanoparticles much more challenging to image and manipulate, and it is far from trivial to take the interaction measurement techniques developed for μPs ($>100\text{ nm}$) and apply them to NPs. There are several reasons for this, such as the fact that the observed signal in many techniques scales with the volume of the particles, *i.e.* with the third power of the diameter.* Meanwhile, the diffusion coefficient scales with $1/D$ and the self-diffusion time—the average time it takes a particle to diffuse over a distance of its own size—scales with D^3 . The smaller size also means that the spatial resolution must be better, which is particularly problematic with optical microscopy methods due to the diffraction limit. Nonetheless, recent years have seen an increasing number of articles where established techniques are improved upon and applied to nanoparticle systems, as well as the emergence of new methods such as the use of *in situ* electron microscopy techniques, which includes both new possibilities to apply it to NPs dispersed in a liquid, but also electron microscopy tomography which allows for coordinate determination in 3D with significant higher accuracy than optical microscopy. Because we expect this trend to continue over the coming years, we will attempt to provide an extensive overview of the different means by which interaction forces have been measured and how these approaches may be used for nanoparticle systems. We place a particular focus on those techniques capable of measuring interaction forces on time, length and energy scales relevant for self-assembly processes, and which do not rely on *a priori* assumptions on the form of the pair potential. Additionally, we discuss what we believe are the key challenges to overcome and where opportunities lie for

* this is the case for *e.g.* the number of fluorescent molecules in fluorescently labelled particles, mass-thickness contrast in transmission electron microscopy and the scattering signal in x-ray scattering. Methods relying on (Mie) scattering of light may even scale as poorly as $I \propto D^6$ (where D is the diameter), meaning that a fivefold reduction in particle size would give a signal reduced by more than *fifteen thousand* times!

nanoparticle science to be pushed forward when it comes to measuring and understanding the surface forces that govern their stability and assembly.

2.2 Surface Force Apparatus

Interaction forces between colloidal particles are, in basis (but less and less so for nanoparticles), surface forces, much like the interaction forces found between macroscopic surfaces when separated by microscopic distances. Some of the first experimental measurements on nanoscale surface interactions, such as the DLVO potential, were reported by Tabor & Winterton^[89] and Israelachvili & Adams^[90,91] after development of the surface force apparatus (SFA) in combination with atomically smooth mica surfaces.* The SFA can directly measure forces between surfaces separated by distances as small as 1 Å by carefully approaching two crossed atomically flat cylinders, one of which is attached to a calibrated spring and which can be moved in precise increments using a piezo element. When the spacing between two cylinders is decreased by some known distance, the true distance between the surfaces can be measured using *e.g.* multiple beam interferometry, and the deflection of the spring can be used to determine the force exerted on the cylinders. As mentioned, the surface of the cylinders is generally made of mica, as it can be peeled into layers which are optically transparent and atomically flat over macroscopic surface areas (mm²), and which can be coated with other materials and submersed in liquids to study a wide range of systems.^[40,64,91,94] The perpendicularly crossed-cylinder geometry is favourable as the actual contact area is comparatively small such that it does not require precise alignment over large distances as flat plates would. Furthermore, using the Derjaguin approximation one can generalize these results to other geometries such as two flat plates, a sphere and a flat plate or two spheres.^[40,95]

The SFA has been key in the early measurement of surface forces, giving the first direct experimental verification of DLVO theory,^[96] as well as many other forces such as depletion interactions and oscillatory solvation forces, the latter of which arises due to structuring of solvent molecules when confined between two surfaces. Such forces are a direct consequence of the discreteness of the solvent and are by definition not accounted for in continuum descriptions of the solvent. Solvation forces can alter interactions significantly when the surface separation is within an order of magnitude of the typical size of solvent molecules or other small solvated species,^[64] and even in the most simple case of a single component system with approximately spherical solvent molecules, the force profile demonstrates a complex oscillatory behaviour which decays exponentially with increasing surface separation.^[40,97] But while the SFA has been tremendously successful in measuring surface forces at the nanoscale, it can only do such measurements between surfaces with radii of curvature many orders of magnitude larger than the surface-to-surface separation and with a contact area that is much wider. Thus while it may be tempting to assume these nano-scale force measurements must hold for nanoscale objects, this is not necessarily the case. Taking for example the effects of solvent layering near the solid-liquid interface, it is not hard to imagine that the solvent molecules will be significantly differently ordered near a surface with nanoscale curvature and/or roughness (especially on a molecular level), than between flat plate-like surfaces. Furthermore, these measurements only give time-averaged forces at

* we note that long range van der Waals forces were already measured directly well over a decade prior by Overbeek & Sparnaay^[92] and Derjaguin & Lifshitz *et al.*,^[93] but surface irregularities had before only allowed for measurements in the retarded regime of van der Waals forces (roughly at distances >5 nm).

fixed separation and subject to thermal noise, and do not capture dynamic effects like the reorientation of nanoparticles and hydrodynamic interactions.^[98] Nonetheless, to this day it remains an important tool in the measurement of forces at nano- and micrometer distances, having aided in the discovery of a wide range of interactions and phenomena relevant for colloidal systems.

2.3 Atomic force microscopy

Force-distance curves between microscopic objects can be obtained using atomic force microscopy (AFM), where a (often atomically sharp) tip is moved with respect to a surface/substrate either laterally (for mapping surface topology) or perpendicularly (for force-distance curves). The AFM-tip is attached to a cantilever with known spring constant, whose deflection can be measured by means of reflecting a laser off of the cantilever and detecting the deflection with a split photodiode. The measured cantilever deflection can be directly converted to a force profile as a function of the spatial position of the tip^[26], although the spring constant of the cantilever must be known and the contact point, the point of zero distance, can be nontrivial to determine in particular for deformable substrates.^[99] With a sufficiently sharp tip resolutions well below 1 Å can be achieved both laterally and perpendicular to the substrate. AFM has thus become a widely adopted technique for imaging surface topology as well as for a wide variety of microscopic force measurements, such as measurement of the local hardness or elasticity of materials, of adhesion forces and of tensile strengths of individual polymer chains.^[23,26,99,100]

2.3.1 Colloidal-probe AFM

Colloidal-probe atomic force microscopy (CP-AFM) is a variant of AFM where a colloidal particle is “glued” to the cantilever of an atomic force microscope and used as probe to directly measure local (surface) forces between colloids and substrates. Colloidal-probe AFM was developed independently by Butt^[102] and Ducker & Pashley *et al.*,^[103] and has since been applied to a wide range of colloidal systems.^[23,96,99,100,104–110] Major advantages of CP-AFM are the high spatial resolution ($< 1 \text{ \AA}$) and the wide range of forces that can be measured. Furthermore, heterogeneities on the single particle level can be probed since it does not intrinsically rely on any ensemble averaging. This is somewhat of a blessing and a curse however, as a major limitation has been that only a single particle can be sampled with any given AFM tip since the particles are typically permanently glued or sintered on. In order to sample a statistically significant number of particles, a large number of AFM tips must therefore be prepared. Similarly, the force resolution is subject to thermal (Brownian) noise and typically several tens of piconewtons, but averaging of multiple force-curves can bring the force resolution down to $< 1 \text{ pN}$. CP-AFM experiments were initially also limited to the use of relatively large μPs , due to the difficulty involved in attaching particles $< 1 \mu\text{m}$ to the AFM cantilever because of the attachment process relying on the use of widefield optical microscopy, although nowadays many methods for CP-AFM tip preparation have been developed.^[104,111] While measuring the force between two particles is possible (with one attached to the cantilever and the other to the substrate), the particle–plane geometry is more common in the literature, and a truly symmetric geometry is not possible.^[109] This may affect the interactions through *e.g.* asymmetry in the ionic double layer near an interface

New techniques have since been developed that no longer require probe particles to be permanently affixed to the tip.^[104] One of these techniques utilizes AFM tips which

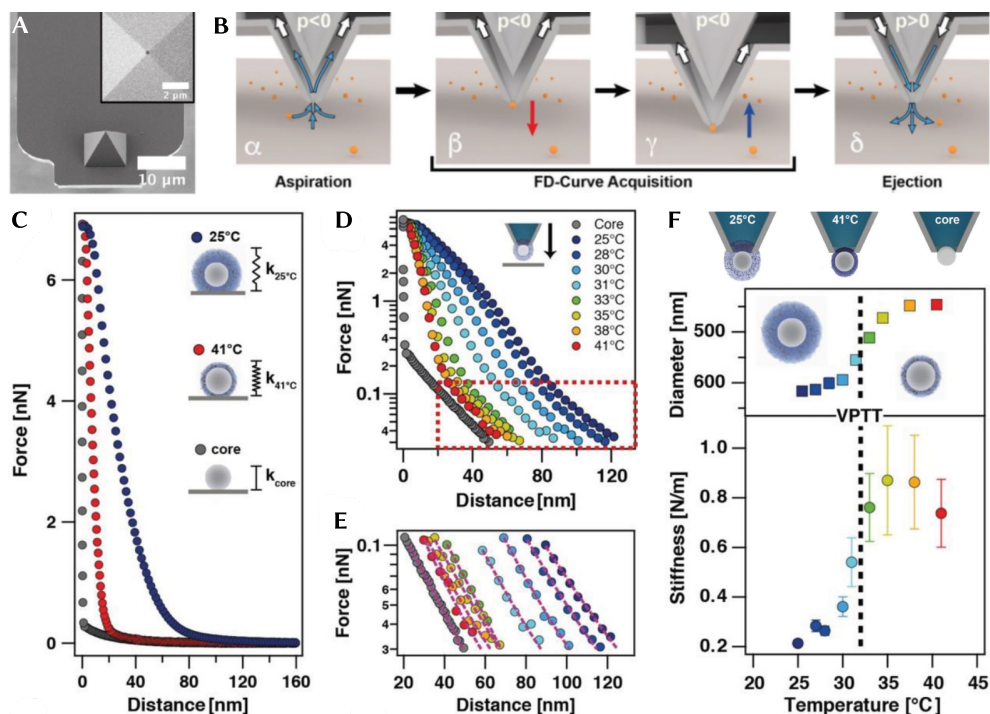


Figure 2.1: microfluidic AFM-tips for reversible attachment of colloidal probes. Silica@PNIPAM core-shell particles were attached using aspiration (suction) after which force-distance (FD) curves could be measured against a glass substrate in H₂O (ion conc.: 0.1 mM). **A:** SEM micrograph of the tip terminating in a 300 nm aperture. **B:** schematic diagram of the attachment, measurement and detachment steps. **C:** Long range (approach) FD-curves of the cores and the core-shell particles above and below the volume phase transition temperature (VPTT). **D,E:** temperature dependent (approach) FD-curves on a log-scale, the long-range low-force regime (<1 nN) is shown in detail (**E**) and corresponds to purely electrostatic repulsion. **F:** the temperature-dependent particle size from dynamic light scattering (DLS) is compared with the stiffness of the PNIPAM shell obtained from the high-force regime in **D**. Reprinted under CC BY-NC-ND 4.0 licence from Mark & Papastavrou *et al.*^[101] Copyright the authors 2019.

have a microfluidic channel terminating at the tip which makes it possible to reversibly attach particles by ‘sucking’ them onto the tip. By decreasing or increasing the pressure in the channel, particles as small as 300 nm can be selectively picked up released again. Unfortunately, as of now this technique cannot be used for nanoparticles due to limitations in the fabrication of sufficiently small microfluidic aperture.^[26,101,112,113] Mark *et al.*^[101] used such an approach to measure the deformability of core-shell particles consisting of a hard silica core and a shell of the thermo-responsive polymer poly-N-isopropylacrylamide (PNIPAM), see **Figure 2.1**. PNIPAM undergoes a volume phase transition at a critical solution temperature (the VPTT) around 32 °C, above which the polymer collapses onto itself leading to a decrease in the particle volume. After adhering the particles onto a microfluidic AFM tip, the mechanical properties of the PNIPAM shell as well as that of a bare silica core could be

determined as a function of temperature by measuring force profiles when in contact with a bare glass substrate. The decreasing size and increasing stiffness with increasing temperature were found to be consistent with the collapsing polymer model, while electrostatic repulsion accounted for the smaller repulsive forces at larger separation.

2.3.2 Nanoparticle–probe AFM

While the conventional method for attaching colloids directly to cantilevers using glue is not well-suited to small particles, it has long been shown that it is possible to attach NPs directly to commercial AFM tips,^[104,111] using e.g. selective chemical functionalisation of the tip,^[114–117] in-situ pick-up from a substrate^[118] and dielectrophoresis,^[119] as well as by localised synthesis using microfluidics,^[118] photocatalysis,^[120] e-beam irradiation^[121] or electrochemistry.^[122] Most of these methods were not developed for the purpose of measuring inter-particle interactions, but rather to enable the use of plasmonic nanoparticles in (tip enhanced) scanning near-field optical microscopy. Nonetheless, with the possibility of a nanoparticle-functionalized AFM tip it might seem somewhat trivial to measure force–distance curves between the NPs and a substrate or another NP. Despite this, very few nanoparticle–nanoparticle interaction forces measured with NP–probe AFM have been reported since its conception.^[26] One of the reasons for this may be the challenges in deconvolving the contributions of particle–substrate and tip–substrate interactions, especially if these contributions are nonadditive. The fact that the particles are immobilized and in contact with the tip or the substrate matters more for NPs because e.g. dipolar interactions with the tip or substrate may alter the particles local dielectric properties. This is generally less of a concern for μ Ps, since there the particle is typically large compared to the interaction range. Additionally, the time scale of approach in AFM is typically much lower than the the time scale of Brownian motion, meaning that dynamic properties such as desorption or rearrangement of the ligand shell have more time to ‘respond’ than in the case of freely diffusing particles. Despite these challenges, nanoparticle–probe AFM (NPP–AFM) is able to measure interaction forces under a wide range of conditions and has found some use.

One of the first NPP–AFM interaction force measurements were reported by Vakarelski & Higashitani,^[115] who used a tip-specific chemical modification to attach individual gold nanoparticles (AuNPs) of 10 nm to 40 nm in size to the apex of commercial AFM tips and measured their interactions with a mica substrate. SEM images of the modified tips and FD-curves measured against a mica substrate are shown in **Figure 2.2**. Clear differences can be seen in the interaction forces, with the reference tip showing short range attraction due to van der Waals forces but no appreciable electrostatic repulsion, while the AuNP functionalised tips showed repulsive interactions up to distances comparable to the particle size. Fitting the FD-curves with DLVO theory –assuming the surface potentials of the AuNP and the mica substrate to be equal– resulted in similar surface potentials of -75 and -80 mV for 20 and 40 nm AuNPs respectively. Conversely, the apparent size of the ionic double layer was found to increase with decreasing particle size, with values of $\kappa^{-1} = 14.0$ nm and $\kappa^{-1} = 11.5$ nm for the 20 and 40 nm AuNPs respectively, while the theoretical value for κ^{-1} using **Eq. 1.6** gives 9.6 nm for 1 mM monovalent salt. Additionally, a significant decrease in the repulsive force compared to the DLVO result was seen at short distances (<5 nm surface separation), which the authors speculated could be a result of the breakdown of the Derjaguin approximation at smaller κD .

Rather than attaching a single NP to an AFM tip, some groups have instead used AFM

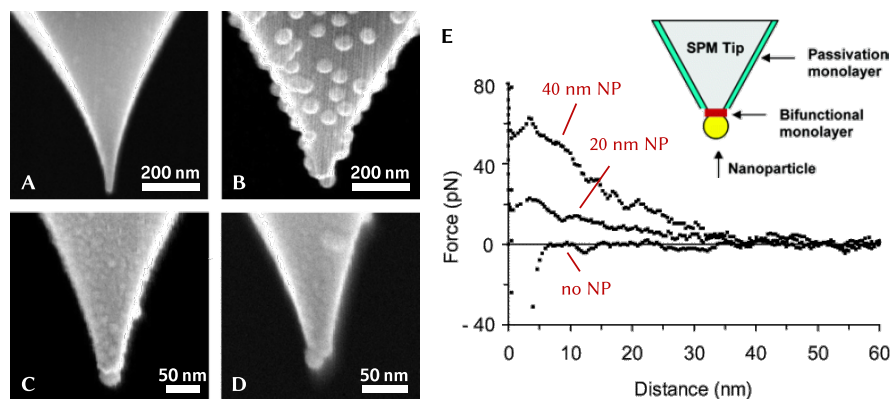


Figure 2.2: nanoparticle–probe AFM measurement of interaction forces. A–D: SEM micrographs of silicon nitride AFM tips after (A) no modification, (B) coating with 40 nm AuNPs, (C) attachment of a single 25 nm AuNP, and (D) attachment of a single 14 nm AuNP. All were sputter-coated with ~2 nm gold for improved SEM imaging. E: FD-curves measured against a flat mica substrate in 1 mM aqueous NaCl solution for AFM tips coated with a single 40 nm or 20 nm AuNP and a reference tip coated entirely with the phenethyltrichlorosilane passivation layer (no AuNP). The inset shows the coating procedure of the AuNP modified tips schematically. Adapted with permission from Vakarelski & Higashitani.^[115] Copyright 2006 American Chemical Society.

tips with many NPs. Ong & Sokolov^[123] used epoxy glue to attach a large number of NPs and made use of the fact that generally about half of the tips produced in this manner had a single NP protruding out at the tips apex. In this way, single-particle FD-curves could be measured for commercially available 50 nm nonspherical ceria particles against a mica substrate and compared to those of ceria μ P particles attached in a similar manner, revealing differences in the pH-dependent interactions due to differences in the chemical structure of the NPs and μ P particles. Similarly, Liu^[117] synthesised silver nanoparticles (AgNPs) directly on an AFM tip using a polydopamine coating and found AgNPs protruding from the apex. These were used to measure the interaction forces between lipid bilayers (a cell membrane model system) and AgNPs before and after protein coating, finding a significant increase in the penetration force required to break-through the lipid bilayer after protein coating. Salameh & Madler *et al.*^[124] used a combined AFM-TEM approach to ‘pull apart’ agglomerates of titania NPs and determined the distribution NP-NP adhesion forces from the breaking of NP strings. They found in combination with molecular dynamics that capillary interactions due to adsorbed ambient moisture were the primary mechanism for the adhesion between the particles.

2.4 Optical microscopy

Real-space (optical) microscopy techniques are a staple in the analysis of colloids.^[4,5,125] With the advent of super-resolution techniques it has become possible to achieve resolutions well below 1 μ m and well below the optical diffraction limit that was once considered a fundamental limit, thus entering the domain of optical *nanoscopy* and enabling microscopy of nanoparticle systems.^[126,127] While not a direct force measurement technique such as AFM *per se*, real-space microscopy can provide insight into the statistical mechanics of a colloidal system through the spatial distribution and dynamics of the particles, and

generally achieves this in a nonintrusive way.^[128] It can do so, because colloidal particles are governed by Boltzmann statistics and probe their local environment through Brownian motion, exploring the potential energy landscape with an energy on the order of $k_B T$. While this is a stochastic process on the scale of individual particles, the ensemble-averaged and/or time-average properties of the system are *not* in that they ‘encode’ information about the energetics of the system. There are generally two ways in which the information on the local energy landscape, set by the interaction forces with nearby interfaces and other particles, can be accessed from data obtained with real-space microscopy:

1. Static methods, based on the analysis of the spatial distribution of particles in equilibrium —*i.e.* particle coordinates— as a probability density function, dependent on the potential energy landscape. This makes use of the fact that under Boltzmann statistics, the probability to find a particle in a given position is linked to the potential energy in that position through the Boltzmann exponent $P \propto \exp(-U/k_B T)$.
2. Dynamic methods, based on the analysis of the motion of particles as a function of their position —*i.e.* particle velocity—, generally treated through overdamped Langevin dynamics where a particle’s motion is given by two terms: a term due to the balance of hydrodynamic drag and the forces acting on the particle, and a stochastic term due to Brownian motion.^[74]

If the spatial positions of the particles in a colloidal dispersion are known, it is thus possible to extract interaction forces from these positions. As an aside, the ‘position’ in the context of interaction measurements does not necessarily refer to the absolute position of the particle (within the microscope’s reference frame), but rather is often expressed as the position relative to the thing it is interacting with, be that a nearby surface or other particles. Optical microscopy is of course a broad term, referring to a wide range of techniques many of which are well-suited to determine particle positions in 2D, like widefield transmission or fluorescence microscopy and total internal reflection microscopy, or 3D, such as confocal laser scanning microscopy (CLSM) and holographic microscopy.^[125] We also note that what we refer to as ‘static methods’ are static in the sense that the analysis does not rely on the time-dimension of the experiments; in principle a single snap-shot of a sufficient number of particles is all that is needed. That being said, in the context of determining the equilibrium probability density distribution there is no difference to ensemble averaging and time averaging,* provided that these time steps are sufficiently far apart that the coordinates from subsequent time steps are uncorrelated. As a result, the recording of microscopy time-series is common even for analysis methods in which no time dependency is used in the analysis. Conversely in dynamic methods, the time dimension is inherent to the analysis and the interactions are extracted from the particle displacements between frames, *i.e.* the dynamic information.

An important limitation of most of these microscopy based methods, is that the particle positions and energy/force ranges that are sampled are thus not chosen by the user, unlike a tool such as atomic force microscopy where one can set predefined inter-particle separations and probe, within experimental limitations, any part of the force profile. In the absence of such a ‘set distance’, colloidal particles only probe the parts of the local potential

* an ensemble average here is the average over many interacting particles at one particular point in time, while the time average is the average of a few interacting particles over many independent points in time.

energy landscape that have energies on the order of the thermal energy of the particles, $k_B T$ while energy barriers which are $\gg k_B T$ above a (local) minimum are exceedingly unlikely to be crossed. While this limits the scope of what interactions can be measured, we note that the interactions with energies of several $k_B T$ are arguably those most relevant to colloidal stability and during equilibrium self-assembly.^[128] As we will see, there are also cases where external manipulation can be used to probe a wider range of forces, such as when using optical tweezers or by analysing interactions out of equilibrium.

2.4.1 Total internal reflection microscopy

One of the first microscopy techniques used to measure interaction potentials of colloidal particles is total internal reflection microscopy (TIRM)^[129], and since then TIRM has been extensively used to measure interactions of colloids with flat substrates.^[75,130,131] In TIRM, a light beam is directed through a prism or objective lens towards a dielectric interface, typically a solid-liquid interface such as glass-water (but also liquid-liquid and liquid-gas interfaces are possible), from the side with the higher refractive index and at a sufficiently high incident angle such that total internal reflection of the incident light beam occurs. While no light propagates into the low index medium when this happens, the reflected incident beam gives rise to an evanescent wave: a near-field effect with an electric field intensity that decays exponentially with distance from the surface, with a decay length typically on the order of 100 nm. As a result, TIRM is only sensitive to the part of the sample near the interface (typically within <200 nm).^[75,130] Because the intensity varies exponentially with distance from the interface, the signal of particles —be that scattering/reflection in TIRM or fluorescence in TIRFM— is extremely sensitive to the ‘height’ h of particles above the interface, allowing for h to be determined with nanometer precision. Initially, signal collection was achieved using an iris and photomultiplier tube to study a single spot in the sample. Nowadays, it is more common to combine TIRM with video microscopy for detection because many single-particle signals may be recorded simultaneously for faster data collection. This has also been used to compare single-particle and ensemble properties^[132] and to study particle-substrate and particle-particle interactions simultaneously.^[133]

In TIRM, the probability $P(h)$ of observing a particle as function of height can be found by calculating a histogram of a statistically large number of particle height observations. This probability distribution then relates to the potential energy $U(h)$ through Boltzmann statistics as follows:

$$\frac{P(h)}{P(h_0)} = \exp\left(-\frac{U(h) - U(h_0)}{k_B T}\right) \quad (2.1)$$

where h_0 is some reference height which is taken as the 0 for the potential energy. Typically, h_0 is chosen as the height corresponding to the minimum in $U(h)$.^[130] For μ Ps, $U(h)$ is typically made up of a combination of particle-substrate interactions and the gravitational energy of the particles, but since the particle’s buoyant mass is usually known, the ‘pure’ particle-substrate interaction potential may be extracted. Since the first measurements of colloid-plate DLVO potentials,^[129] TIRM has been used to measure a wide variety of microparticle-wall interactions such as depletion,^[56,134,135] steric,^[136] magnetic,^[137] surfactant-mediated^[138,139] and Casimir-like forces.^[140] In addition to solid-liquid interfaces, TIRM measurements on interactions of both μ Ps and emulsion droplets with liquid-liquid interfaces have been reported.^[141] The high time and spatial resolutions of TIRM make it a promising technique for elucidating interaction forces of nanoparticles. Indeed, some interaction measurements

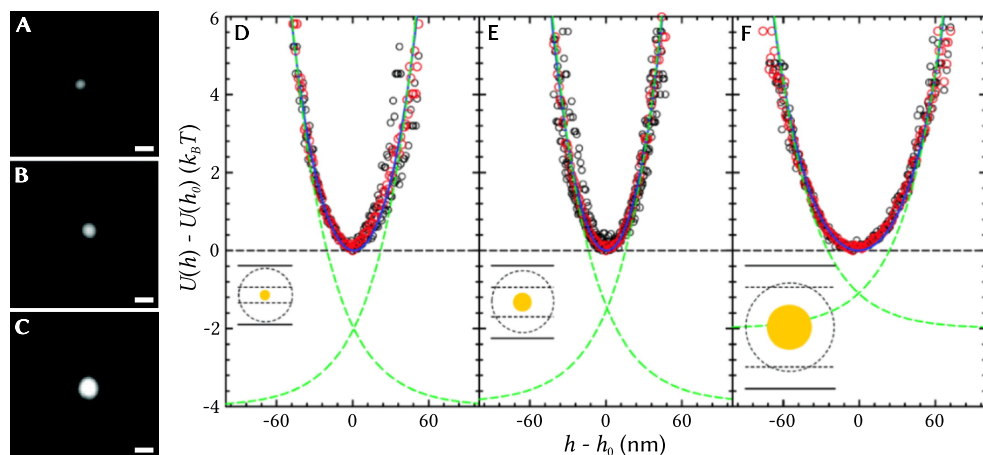


Figure 2.3: AuNP-glass interactions measured with TIRM. AuNPs dispersed in ultra-pure water containing 0.1 mM sodium dodecyl sulfate interacted through electrostatic repulsion with two parallel glass substrates. **A–C** TIRM micrographs of resp. 50, 100 and 250 nm AuNPs adsorbed onto the bottom glass. Scale bars: 2 μm . **D–F**: potential energy profiles of AuNPs with sizes of resp. 57, 123 and 213 nm between walls separated by resp. 342, 342 and 619 nm. Black and red circles indicate single particle and ensemble averaged potentials respectively, solid blue lines are theoretical fits of the ensemble data using a combination of the gravitational potential and the electrostatic interactions with each wall. Only the surface potentials of the NPs and walls were used as fit parameters, where $k^{-1} \approx 30$ nm was determined from the electric conductivity of the sample. Green dashed lines show the interaction with each interface separately. Adapted with permission from Eichmann & Bevan *et al.*^[142] Copyright 2008 American Chemical Society.

of NPs have been reported,^[142–148] but there are significant challenges to be overcome when compared to μPs . The gravitational forces are much smaller for NPs and are not sufficient to keep the particles near the dielectric interface, and their fast diffusion makes that the NPs rapidly leave the field of view. Furthermore, the scattering intensity is proportional to as much as the 6th power of the radius, leading to a poor signal-to-noise ratio (SNR) for smaller particles. While detection of fluorescence can, to some extent, alleviate this problem, it requires strongly fluorescent particles such as quantum dots (QDs) and is therefore not generally applicable. It was recently also found that photon counting statistics (shot noise) can significantly affect the spatial resolution achievable in TIRM in the low-signal limit, leading to a significant blurring of interaction potentials with sharp features such as in the case of DNA-mediated interactions.^[149,150]

Eichmann & Bevan *et al.*^[142] overcame some of these issues by confining strongly scattering gold nanoparticles of 50–200 nm in size between two parallel glass surfaces which were spaced closely enough that their electrostatic double layers overlapped, creating a well-defined energy minimum for the AuNPs in-between. Potential energy curves for AuNPs of different sizes are shown in **Figure 2.3**. By fitting the potential profiles with the electrostatic part of the DLVO potential for a sphere and a flat wall, the surface potentials of AuNPs and the glass substrate were found. In the same way, particle-wall interactions of protein-coated AuNPs^[143] as well as (rotationally averaged) interactions of carbon nanotubes

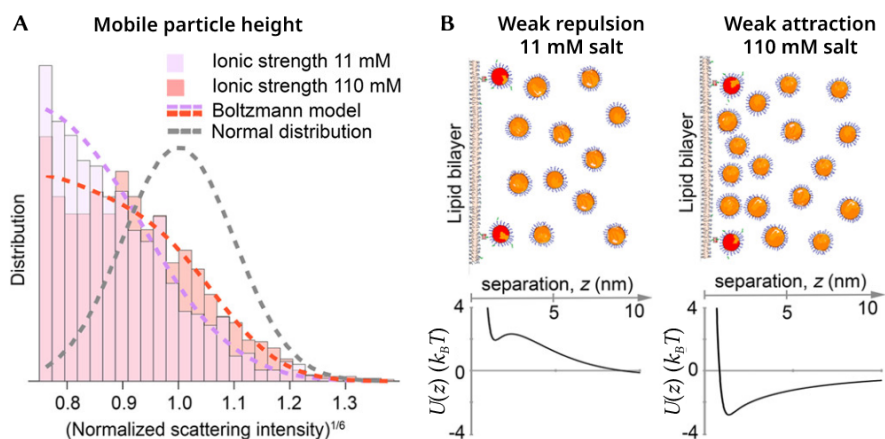


Figure 2.4: AuNP-lipid bilayer interactions measured with waveguide-TIRM. Immobilized and freely diffusing (mobile) 50 nm AuNPs on/near a biotin-functionalised lipid bilayer were imaged simultaneously using waveguide TIRM. **A:** normalised scattering intensity ($\sqrt[6]{I}/\langle\sqrt[6]{I_{\text{TIRM}}}\rangle$) histogram of mobile particles at two different ionic strengths, fitted with expected Boltzmann distributions of DLVO potentials (coloured dashed lines). For comparison a Gaussian fit of the distribution of scattering intensities of the immobilised particles is shown (gray dashed line). **B:** fitted DLVO potentials with schematic depiction of the particle distribution near the substrate. Reprinted with permission from Lundgren & Höök *et al.*^[147] Copyright 2016 American Chemical Society.

were determined.^[144] A different method to assure particles are confined close the interface is to make use of optical gradient forces,^[145,146,148,151,152] similar to the optical trapping used in optical tweezers (see Sec. 2.4.3). Schein & Erickson *et al.*^[146] used photonic crystal resonators to confine light in 3 dimensions (instead of a 1D evanescent wave), thereby confining it much closer to the interface than in conventional TIRM. This provided a higher light intensity, which lead to optical trapping near the substrate and which boosted the SNR. Using this method which the authors referred to as ‘Nanophotonic Force Microscopy’ it was possible to measure interactions of a variety of particles with the resonator with force resolution below 1 pN. This was further extended with the use of waveguides that confine light in 2D and automatically propel particles along the waveguide, which enabled high-throughput of particles during the measurement, allowing for faster data collection as well as particle size determination from single particle diffusion tracking.^[145,151] Using the waveguide particles as small as 50 nm could be measured.^[145] The use of waveguides may also reduce the background signal to the extent that the SNR is good enough that it is not necessary to confine particles near the interface at all.^[153] Lundgren & Höök *et al.*^[147] used TIRM to study the interaction of targeted and untargeted AuNPs with lipid membranes (see Fig. 2.4), to elucidate the mechanism behind the increase in cellular uptake of AuNPs of 50 nm when compared to 20 nm particles. The authors found that van der Waals interactions, which are relatively weak compared to the targeted ligand–receptor binding, significantly increased the residence time of larger AuNPs near the membrane, increasing the probability of bond formation between the targeted ligands and receptors in the membrane by an order of magnitude.

TIRM is thus a widely applicable technique to probe interaction forces between a colloids

and (flat) interfaces, and can under some conditions be extended to include nanoparticle measurements. Due to the near-field nature of the evanescent wave, the distances can be probed with a resolution much higher and over smaller distances than is commonly achieved in more conventional optical microscopy techniques as we will see in [Section 2.4.2](#), while the force range is set by the thermal energy of the particles. Therefore, TIRM is one of the key techniques available for nonintrusive measurement of $k_B T$ scale forces of NP interactions. However, the use of TIRM to measure forces from height distributions in this manner cannot be used to directly probe colloid-colloid interactions. In the Derjaguin approximation it is possible to rescale the results to other geometries, and in that limit a sphere of radius R interacting with a flat wall (such as in TIRM) is equivalent to the interaction of two spheres with a radius of $2R$, however, we do not expect this approximation to hold for nanoparticles and nanoparticle specific interactions, because processes such as solvent ordering and ligand interdigitation for example depend strongly on surface curvature.

2.4.2 Real-space microscopy with particle localisation

Similarly to TIRM, where the distribution of particle-substrate distances is assumed to follow Boltzmann statistics and thereby related to the interaction energy, it is possible to extract particle-particle interactions if the distribution of particle-particle distances is known. This can be determined from a set of particle coordinates obtained using real-space microscopy techniques such as video microscopy (VM) in combination with particle localisation algorithms. A widely used measure to express the relative probabilities of particle-particle distances is the *radial distribution function*, $g(r)$, also known as the *pair correlation function*. The $g(r)$ gives the probability of finding a pair of particles separated by a centre-to-centre distance r , normalized by the probability in an uncorrelated system at the same density, or in other words the $g(r)$ tells you what the particle density a distance r from another particle is, relative to the average particle density. This can be calculated from a set of particle coordinates by calculating a histogram of pairwise particle-particle distances and normalizing it as follows:

$$g(r) = \frac{N(r, r + \Delta r)}{n\rho V(r, r + \Delta r)} \quad (2.2)$$

where $N(r, r + \Delta r)$ is the number of particle pairs with a distance between r and $r + \Delta r$ —*i.e.* the value of one bin in the histogram of pairwise distances—, n is the total number of particles in the system, ρ is the average number density of particles and $V(r, r + \Delta r)$ is the volume of a spherical shell (in 3D) or the area of a circular ring (in 2D). The $g(r)$ thus depends only on the relative positions of the particles in the system and can be calculated directly from a list of particle coordinates obtained from microscopy data.* More information on the calculation of the $g(r)$ is also given in [Chapter 4](#).

Under equilibrium conditions the radial distribution function is related to the interaction forces between the particles through Boltzmann statistics, analogous to the particle-wall separation in [Eq. 2.1](#). This is the basis of *Henderson's theorem*, which states the following:^[156,157]

Given a classical fluid with only pairwise interactions, the pair potential giving rise to a given $g(r)$ is unique up to an additive constant.

In other words, the $g(r)$ in principle contains the necessary information on the interaction potential: if one can find a trial $U(r)$ that correctly reproduces the $g(r)$ of a particular

* we note that video microscopy may also be used to measure particle-substrate interactions^[154,155]

system, it *must* be the real one. Unfortunately, Henderson’s theorem does not tell us *how to find* such a $U(r)$ from the $g(r)$ or how sensitive the $g(r)$ is to changes in the $U(r)$.^{*} The first point, how to extract potentials from the $g(r)$, remains a substantial open question in statistical physics. Fortunately, several different methods for extracting the pair potential from the radial distribution function have been devised and the most common ones are discussed below. The second point is particularly important in the experimental context: for Henderson’s theorem to hold the $g(r)$ must be known exactly and up to large separation (where it asymptotes to 1), which is never true in experiments. Two drastically different pair potentials may give $g(r)$ ’s that differ only slightly such that they appear the same within experimental accuracy.^[158,159] These issues can be alleviated to some extent by careful choice of the combination of analysis method and system parameters and by the incorporation of additional information such as the change in the $g(r)$ upon changes in particle density or temperature, but care must be taken when interpreting pair potentials obtained from structure data to assure that it is in fact the correct solution.

Direct inversion of the radial distribution function:

It may seem that it is possible to directly invert the $g(r)$ using the Boltzmann equation, like was the case in Eq. 2.1 for the distribution of particle-substrate distances. But while the $g(r)$ is calculated as a pair-wise sum, each particle can be part of many pairs with many neighbouring particles, and as a result the $g(r)$ is dependent on the particle density even when $U(r)$ is not. Rather than relating directly to the pair potential, it can be shown that the $g(r)$ relates to the *potential of mean force*, $w(r)$, as

$$g(r) = e^{-w(r)/k_B T} \tag{2.3}$$

where $w(r)$ is defined as the reversible work associated with bringing two particles in a system of given density from infinite separation to a relative separation r , where the interaction energy with all other particles is taken as an average of all possible configurations.^[160] Note that $w(r)$ thus differs from the pair potential $U(r)$ in that it is defined in the presence of other particles, and will therefore depend on the particle density and temperature of the system. However, if the system is sufficiently dilute so that each particle in the system interacts with at most one other particle, one can state that $w(r)$ approaches $U(r)$. As a result Eq. 2.4 can be used to calculate $U(r)$ from the $g(r)$ at sufficiently low concentration using the simple relation:

$$U(r) \approx -k_B T \ln g(r). \tag{2.4}$$

This was first used for interaction measurements of colloids by Vondermassen & Versmold *et al.*^[87] and Kepler & Fraden^[161] who each used 2D wide-field video microscopy in combination with particle detection algorithms to obtain $g(r)$ ’s for polystyrene (PS) colloids with long range electrostatic repulsion.[†] At what particle concentration the system was ‘dilute enough’ for Eq. 2.4 to be valid, was determined by diluting the system until the $g(r)$ no longer depended on the concentration,^[87,88] or by comparing the $g(r)$ at higher concentration with simulations using the measured potential directly^[161] or a model function.^[88] While it was

^{*} strictly speaking it does not even guarantee the existence of such a potential, although of course a ‘real’ $g(r)$ from a physical system can only be the result of *some* kind of interactions

[†] this was also reported around the same time by Crocker & Grier,^[162] but rather than inversion of the (ensemble) $g(r)$ they measured distance distributions for individual (isolated) particle pairs created with the help of optical tweezers, as we will discuss in Section 2.4.3

possible to measure the $g(r)$ at these low but finite particle concentrations, the requirement for low concentration is a major downside of this method of direct inversion of the $g(r)$. The number of particle pairs in a given volume, *i.e.* the statistical sample size, is proportional with the square of the number of particles, and thus in any given time much more data can be collected when the concentration is higher. An alternative strategy used to account for the difference between $w(r)$ and $U(r)$ at finite concentration, was to measure the potential of mean force as a function of particle concentration and use linear regression to extrapolate $w(r, \rho)$ to the pair potential at infinite dilution.^[163] In this case, the particle concentration may be greater although not one but rather multiple $g(r)$'s at varying concentration are required to determine the pairwise potential.

Reverse Monte Carlo simulations:

While calculating the pair potential from the radial distribution function at finite concentration directly remains an open problem, it is possible to do the reverse and calculate the $g(r)$ for a given pair potential, density and temperature in several different ways, one of the more common of such methods is the use of numerical simulations, most notably Monte Carlo simulations (MCS). The ability to solve the *forward* problem, $U(r) \rightarrow g(r)$, can be combined with Henderson's theorem to solve the inverse problem, $g(r) \rightarrow U(r)$: if we make a reasonable guess for the pair potential, use it to determine a $g(r)$, and find that it correctly reproduces the experimental distribution function, we know that, within experimental and numerical accuracy, our trial potential *must* be the correct $U(r)$. When a functional form for the pair potential is known this can be achieved by manually optimizing parameters until good agreement is found, but it is also possible to do this for arbitrary potentials in an iterative scheme such as the following.^[164]

$$U_{j+1}(r) = U_j(r) - k_B T \ln \left(\frac{g_{\text{exp}}(r)}{g_j(r)} \right) \quad (2.5)$$

where $g_{\text{exp}}(r)$ is the experimental distribution function and $U_j(r)$ and $g_j(r)$ are the trial pair potential and the resulting simulated distribution function at the j^{th} iteration step respectively. In this method, also referred to as the *Iterative Boltzmann Inversion* (IBI) method, the difference between simulated and 'real' $g(r)$'s is used to generate a correction to the potential energy function in each iteration step.^[164,165] The potential of mean force is commonly used as initial trial potential. MC simulations were previously used in a similar reverse manner for atomic pair potentials from scattering data,^[166,167] but reverse MCS can be directly applied to real-space data of colloidal systems.^[56,128,133,135,168–170] As infinite dilution is not assumed, this is applicable to a wider range of concentrations provided that interactions are still pairwise additive (or can be otherwise included in the simulations accurately), but each iteration requires a simulation run which is relatively computationally expensive compared to analytical calculations.

Solving the Ornstein-Zernike equation:

In addition to simulations, it is also possible to approximate the $g(r)$ for a given pair potential using liquid state theory, most notably using the Ornstein-Zernike (OZ) equation:^[22,171,172]

$$h(r) = g(r) - 1 = c(r) + \rho \int c(r') h(|r - r'|) dr' \quad (2.6)$$

which considers the total correlation function, $h(r)$, as consisting of two parts: the direct correlation between two particles i and j , given by the direct correlation function $c(r)$,

and the indirect effect of i on j via other nearby particles (at distance r') averaged over all possible positions and weighted by the particle density ρ . As $c(r)$ is unknown, a closure relation is necessary to link $h(r)$, $c(r)$ and $U(r)$. A number of different approximate closure relations have been derived, the most commonly used of which are the Percus Yervick (PY) approximation given by

$$c_{\text{PY}}(r) \approx g(r) \left(1 - e^{U(r)/k_B T}\right) \quad (2.7)$$

which is mostly used for hard spheres, and the hypernetted chain (HNC) approximation given by

$$c_{\text{HNC}}(r) \approx h(r) - \ln g(r) - \frac{U(r)}{k_B T} \quad (2.8)$$

which is commonly used for ‘soft’ particles.^[172,173] Eq. 2.6 in combination with one of these closure relations may be solved in an inverse manner to obtain $U(r)$ directly from the $g(r)$, or in a forward manner to obtain $g(r)$ for a given trial $U(r)$ in an iterative approach similar to e.g. reverse Monte Carlo methods using Eq. 2.5.^[133]

Test-particle insertion:

Another approach to obtain interactions from the $g(r)$ is through Widom’s test-particle insertion (TPI) method, which is an alternative method for calculating the $g(r)$ from a set of particle coordinates through calculation of local chemical potentials based on the inter-particle interactions.^[174,175] In Widom’s method, the $g(r)$ is expressed as a ratio of the local and ensemble probabilities associated with the insertion of a hypothetical test-particle into the existing set of particle coordinates as follows:^[176,177]

$$g(r) = \frac{P(r)}{P_{\text{tot}}} = \frac{\langle \exp(-\psi_i/k_B T) \rangle_{i \in r}}{\langle \exp(-\psi_i/k_B T) \rangle_i} \quad (2.9)$$

where $P(r)$ and P_{tot} are the distant-dependent and average Boltzmann probabilities of insertion, ψ_i is the chemical potential—the change in free energy associated with insertion of a test particle i at some position—, and angled brackets indicate either an average over all test-particles in the dataset ($\langle \dots \rangle_i$) or only over the subset of test-particles inserted at distance r from any of the particle coordinates in the dataset ($\langle \dots \rangle_{i \in r}$). The potential energy of insertion ψ depends only on inter-particle interactions, and can be calculated e.g. as a sum of all pairwise interactions of the test-particle with the real particles in the dataset for a given pair potential $U(r)$. Note that ‘insertion probability’ here refers to the relative equilibrium probability a particle would be in the insertion location based on the potential energy, and *not* to some kind probability associated with the choice of the test-particle insertion locations using e.g. pseudorandom number generation. Similarly to reverse Monte Carlo simulations and the forward Ornstein-Zernike approach, this forward method can be used for measurement of the pair potential by optimizing a trial potential in an iterative manner using Eq. 2.5, where the $g(r)$ measured using the conventional distance histogram method (Eq. 2.2) is used as reference.^[177] TPI has several advantages over the previous methods. In particular, no assumptions or approximations with regards to the pair potential need to be made, and unlike direct $g(r)$ inversion it places no constraints on particle concentration as long as enough pairwise distances can be sampled and the system is fluid-like. Because test-particles are evaluated with respect to the pre-existing (experimental) set of particle coordinates, computational demands are much lower than in e.g. reverse MCS. Interestingly,

test particle insertion in principle does not require interactions to be pairwise, and it may be modified using higher order correlation functions to extract higher order interactions higher order interactions.^[178] Similarly, it may be adapted for multicomponent systems where different species interact with different potentials.

Velocity analysis:

So far we have only discussed what we referred to as ‘static methods’, which rely on the equilibrium particle distribution to extract information about the potential energy landscape. Let us now turn to analysis of the particle dynamics, where we consider the *velocity* of colloidal particles as a function of their position. The motion of colloidal particles is dominated by the stochastic fluctuations of Brownian motion, but when another force is acting on the particles there is an additional systematic component to their motion. Consider for example a colloidal μP which is denser than its surrounding solvent experiencing a force due to gravity. At any given time in any particular location, the particle may be moving up, down, left or right. But if this observation of the particle’s motion is repeated many times it is clear that *on average* the particle is sedimenting down. More generally, it is thus possible to extract force fields by determining the average velocities of colloids as a function of position, be that with respect to external fields, nearby interfaces or relative to neighbouring particles, and a number of articles exploring this idea have been published.^[179-184] More formally, the equation of motion of colloidal particles is well described by the overdamped Langevin equation:^[74]

$$\dot{\mathbf{r}}(t) = \frac{\mathbf{f}(\mathbf{r}, t)}{\gamma} + \sqrt{2D_0} \boldsymbol{\xi}(t). \quad (2.10)$$

where \mathbf{r} is the position, $\dot{\mathbf{r}}$ the velocity (the dot indicating the time derivative), \mathbf{f} the net force exerted on the particle, $\gamma = k_B T / D_0$ the friction due to the solvent, D_0 the diffusion coefficient and $\boldsymbol{\xi}$ is a stochastic variable representing Brownian motion as Gaussian white noise, with zero mean and delta-correlated time dependence, *i.e.* $\langle \boldsymbol{\xi}(t) \rangle = 0$ and $\langle \boldsymbol{\xi}(t) \boldsymbol{\xi}(t') \rangle = \delta(t - t')$. The velocity may be estimated from the particle coordinates in two snapshots using a first order finite difference scheme. Since fluctuations due to Brownian motion are symmetric, averaging many displacements at the same \mathbf{r} should yield \mathbf{f} .

To obtain pairwise inter-particle interactions it is possible to measure the trajectories for isolated particle pairs such that a pairwise force is obtained directly,^[179,181] but a more general approach for particle ensembles is to decompose the force acting on each particle into the relative contributions of all neighbouring particles. This may be done *e.g.* by solving for the linear least squares solution of a discretized (binned) force profile for all particles simultaneously,^[180] or by employing machine learning to find the local properties underlying collective dynamics.^[184] For more details on the least-squares approach of velocity analysis for extracting inter-particle interactions, we refer readers to **Chapter 6** where we apply this methodology to simulated and experimental trajectories. Notably, these velocity analysis methodologies do not rely on the particles forming an equilibrium distribution, and may thus be used to measure (effective) interactions in systems which are not in equilibrium. This could be for example the transient response to changes in external fields or systems with active matter.^[181,183,184] There are several difficulties with velocity analysis however, in particular when it comes to nanoparticles. The Brownian forces experienced by the particles effectively acts as noise on the trajectories, and this becomes more prominent with respect to the particle size as the particle size decreases. The faster diffusion and smaller

size of NPs also require higher time and spatial resolution in the analysis which may make practical implementation of such methods infeasible for the nanoscale except in cases with e.g. extremely high viscosities.

Real space microscopy techniques in combination with particle localisation can thus use particles' intrinsic Brownian motion as a tool provide direct access into $k_B T$ -scale interactions in a variety of ways with varying underlying assumptions. Having discussed the different means through which interactions may be obtained from coordinates, let us now discuss the different methods which have been used to obtain those coordinates. The first and still one of the most important techniques is wide-field transmission microscopy, owing to its widespread use, simple setup, and flexibility with respect to sample requirements. Widefield fluorescence and scattering microscopy are similar, requiring slightly more complicated setups but allowing for imaging with a low background. With use of CCD or CMOS cameras, imaging rates on the order of a kHz or more may be obtained at frame sizes well beyond a Mpx.^[4,185] The in-plane resolution in all of these techniques is set by the diffraction limit and is typically >200 nm, while the axial resolution (perpendicular to the imaging plane) is significantly worse at typically >500 nm. From the perspective of colloidal systems, these techniques are thus mostly effective for measurements in 2D. The 2-dimensional nature of the imaging and analysis in combination with the 3-dimensional nature of colloids may be dealt with in different ways. Perhaps the simplest option is to image a quasi 2-dimensional slice of the sample (with the slice thickness given roughly by the focal depth) and only consider the in-plane particle positions, ignoring displacement along the axial direction of the microscope,^[87] but this can lead to considerable error in the analysis.^[186] Another option is to assure the particles themselves conform to a quasi 2D arrangement, which may be achieved e.g. by sedimenting particles to a solid-liquid interface^[173] or confining the particles between parallel charged surfaces, thus assuring that displacements along the axial direction are negligible.^[161] However, the presence of nearby interfaces is known to be able to affect interaction potentials and care should be taken in interpreting the results.^[187]

Several microscopy techniques exist which can resolve colloidal dispersions in 3 dimensions and image away from interfaces such as confocal laser scanning microscopy (CLSM),^[188,189] holographic video microscopy (HVM)^[190,191] and light-sheet microscopy (LSM).^[192] In particular, CLSM has found widespread use in colloid science. Royall & van Blaaderen *et al.*^[88] reported the first interaction potentials obtained from 3D measurements of the $g(r)$ in the bulk of the fluid (away from interfaces) using CLSM for poly(methyl methacrylate) (PMMA) μ Ps with long ranged electrostatic interactions, and found a good agreement with DLVO theory. As a more recent example, Bergman & Schurtenberger *et al.*^[193,194] used CLSM to measure $g(r)$'s in combination with the OZ equation to determine the applicability of different model potentials to the interactions of microgel particles. It was found that interactions of soft neutral microgel particles were well described using a multi-Hertzian model representing the hard core and outer layers,^[193] while the interactions of charged crosslinked microgel particles additionally featured contributions from charged dangling ends.^[194]

While optical microscopy techniques have seen great use for the measurement of interactions between colloidal μ Ps, very little has been reported on their use for the measurement of interactions between nanoparticles. The likely reasons for this are the limited optical resolution in conventional optical microscopy, the lower SNR associated with the smaller

particles and the higher imaging rates required due to faster diffusion. We however explicitly note that resolution in the conventional sense is defined as minimum distance at which two point-emitters can be resolved from one another, and not as the precision with which a particle may be located, or the minimum size of particle which may be observed. Particles far smaller than the resolution limit (and even single molecules) can be and are routinely imaged, and may be localised with precisions on the order of one or a few tens of nanometers with automated particle tracking algorithms provided they are ‘optically separated’: their signals must have limited overlap. Since the landmark work by Crocker & Grier^[195] on the fast and simple centroiding method, a large number of particle detection algorithms have been devised that vary in computational complexity and accuracy, often balancing generalisability with reliance on assumptions or prior knowledge of the image formation process.^[195–202] The choice of particle detection algorithm requires some care, as different methods introduce different biases, which can have considerable consequences for the determination of interaction potentials.^[203,204] An example of how prior knowledge can be included in particle detection, is the work by Bierbaum & Sethna *et al.*^[201,205] on a method they dubbed ‘parameter extraction from reconstructing images’ (PERI) which is shown in **Figure 2.5**. In PERI, fully modelling the sample and optical train made it possible to reconstruct images based on a set of parameters such as the particle positions and radii and global parameters like the PSF. This resulted in a large parameter space which was optimized to find the least-squares fit to the data, giving in a set of particle radii and coordinates with a localisation error of only 3 nm which was used to determine the interaction potential. For a more complete and detailed discussion on these and other particle localisation algorithms we refer the reader to some of the reviews on this subject.^[4,5,127,205–207]

To image particles at nanoscale inter-particle distances, higher resolution imaging (<100 nm) is possible using super-resolution (nanoscopy) methods such as stimulated emission depletion (STED), photo-activated localization microscopy (PALM), stochastic optical reconstruction microscopy (STORM) and re-scan confocal microscopy (RCM).^[69,126,208] Unfortunately, some of these methods like PALM and STORM are intrinsically more time consuming and therefore not well suited to imaging dynamic systems such as diffusing NPs.^[4] STED is in principle not slower than conventional CLSM (which in itself is slower than video microscopy), but reduces the fluorescent signal and thus longer integration times are typically needed although it has been shown that high-speed STED under some conditions is feasible.^[209] RCM does not suffer from these issues as much but can only improve the resolution by a limited amount ($\sim \sqrt{2}$). The time-resolution limits when imaging NPs may be overcome *e.g.* by the use of solvents with extremely high viscosity, or by completely arresting the dynamics of an equilibrium particle system using a solvent-polymerisation approach such as the one we present in **Chapter 4**.

2.4.3 Optical tweezers

Optical tweezing (OT) —the use of optical tweezers (OTs)— is not an imaging method *per se* but rather a method by which individual colloidal particles may be manipulated *in situ* in a microscopy sample, while simultaneously imaging the system. Similarly to CP-AFM where a particle on a cantilever is moved with respect to a substrate in predefined steps, OT allows one to place individual particles in specific positions. This is achieved using a tightly focussed laser spot, which can act as trap for a colloidal particle due to optical gradient forces: when a particle refracts incoming photons, conservation of momentum dictates that a force must be

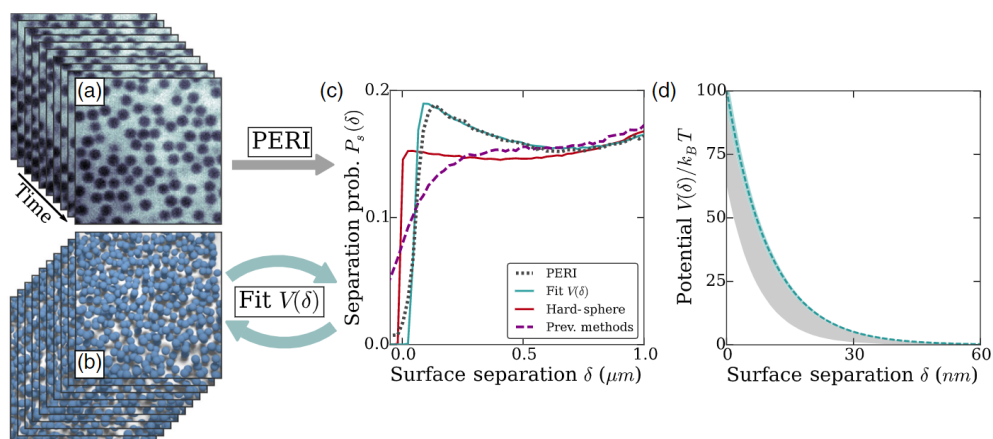


Figure 2.5: interactions of silica μPs measured with CLSM in combination with PERI particle localisation. The particles were $1.3\ \mu\text{m}$ in size and dispersed in a water/glycerol mixture. **A** PERI was used to determine the positions and radii of ~ 1200 particles and used to calculate the $P(\delta)$, the distribution of surface-to-surface spacings shown in C (dotted black line). **B**: a reverse MC approach was used to iteratively optimize a pair potential to fit the experimental distribution (blue line). For comparison, the distribution resulting from a hard core potential and from conventional centroid-based particle tracking are given (red and purple dashed lines respectively). **D**: pair potential obtained from the reverse MC fit. The blue and grey shaded areas represent errors in the fit and systematic errors respectively. Reprinted under CC BY 4.0 licence from Bierbaum & Sethna *et al.*^[201] Copyright 2017 the American Physical Society.

exerted on the particle. For a particle in an optical intensity gradient, this force is asymmetric and the particle is drawn towards the side with higher intensity, thereby confining it in the focus point where the intensity is highest. By splitting or multiplexing (time-sharing) the laser, multiple traps may be formed simultaneously and moved independently using *e.g.* galvanometer-driven mirrors.^[109,210,211] The ability to position or ‘hold’ particles in specific positions allows for a wide variety of interesting experiments in soft matter and elsewhere. In the context of interaction measurements in particular, it provides a practical means by which to create isolated particle pairs—two interacting particles in absence of any other nearby particles—in very dilute suspensions such that *e.g.* Eq. 2.4 may be used. It also means that particle to particle heterogeneities can be measured because it does not rely on ensemble statistics. There are several conceptually different methods by which interaction forces may be measured using OT, which we discuss below.

Optical tweezers as force transducers:

The first method is to use optical traps as force transducers (*i.e.* as a ‘spring’), analogous to the cantilever in CP-AFM, by measuring the displacement of the time-averaged position of the particle with respect to the centre position of the trap.^[212–215] The magnitude of this displacement is the result of the interaction force acting on the particles on the one hand and the restoring force towards the centre of the optical trap on the other. Converting the displacement into a force requires knowledge/calibration of the force profile of the optical trap, which is usually assumed to be well approximated by a harmonic potential well. When

using OT as a force transducer in this manner, a time-averaged interaction potential subject to thermal noise may be obtained with a force resolution similar to CP-AFM.^[128] However, care must be taken when assuming that an optical trap acts as an equilibrium potential well: while optical gradient forces in the classical ray-optics picture of OT are conservative—that is path-independent—, optical forces due to radiation pressure and in the Mie-scattering regime are not.^[182,216–219] For small particles and/or at high trapping power there may thus be significant non-conservative forces acting on the particles, meaning that the view of the trap as a simple potential well is no longer correct. We note that it is possible to reconstruct the full force field including non-conservative forces by analysis of particle dynamics (rather than their equilibrium positions).^[182,219] Aside from this, there is a lower bound on the possible steepness and size of optical traps due to the diffraction limit. Thus, two traps cannot be moved arbitrarily close to one another without overlapping, ultimately lowering the energy barrier between them. As a result, this method can only sample centre-to-centre interparticle distances on the order of several hundreds of nanometers or more, and therefore only useful for measuring interactions between NPs if they are extremely long ranged with respect to the particle size.

The use of OTs as force transducers has one key advantage over other microscopy and OT-based methods, namely that it allows the operator to set the range of positions and forces to be sampled, instead of relying on sampling due to thermal motion. Aside from the ability to reach parts of the force profile that are unlikely to be sampled in (free) equilibrium, this is particularly valuable in cases where there is a large parameter space for the interaction potential such as in anisotropic interactions. As an example of this, Kang & Park *et al.*^[215] used OT to fully characterise the angle-dependent interaction potential $U(r, \phi_1, \phi_2)$ of ellipsoidal particles on an oil-water interface interacting through capillary interactions, where ϕ_1 and ϕ_2 are the angles of the particles with respect to the displacement vector between them. By altering the orientations and separation of two ellipsoidal particles using two optical traps per particle, the authors were able to measure the full capillary field around the particles from the displacements in position and orientation, and found that the interactions were quadrupolar, anisotropic and heterogeneous in nature.

Confined diffusion of a particle pair within an optical trap:

The second method by which interaction forces may be measured, is to measure the time-averaged equilibrium distribution of pairwise distances like in [Section 2.4.2](#), but use a single optical trap to confine two particles, thus providing a restoring force to keep the particles close together. The use of OTs assures that sufficient sampling is possible in very dilute systems, with a single particle pair being kept in each others vicinity while being far from other particles. For these measurements it is common to use line-scanning optical tweezers, where the two particles are diffusing in an elongated trap in which they are effectively fully confined along two dimensions but can diffuse along the trap length. By modulating the trapping power along the trap length, it is possible to tune the potential along the line to *e.g.* be flat in the centre at close contact. This makes the diffusion effectively one-dimensional and aids in measurement of the pairwise distances. In a manner similar to TIRM analysis, inverting the pairwise distance distribution and subtracting out the trap potential if necessary then gives the pair potential between the particles.^[50,220–222] Such an approach with line-scanning OTs was used by Rogers & Crocker^[72] to measure short ranged DNA mediated interactions between pairs of DNA-functionalised μ Ps. Although the particles were relatively large (1 μ m), it was possible to track their positions with high

precision and determine the surface-to-surface spacing with an error of only ~ 3 nm. Particle pairs where both particles were functionalised with the same DNA sequences exhibited purely repulsive steric interactions, while pairs with complementary DNA sequences were found to additionally exhibit attractive interactions with a range of ~ 30 nm and an energy minimum of $\sim 6 k_B T$, which gradually decreased as the temperature was increased from 30.5°C to $>36^\circ\text{C}$.

Free diffusion using blinking optical tweezers:

Both of the preceding methods apply the trapping force to the particles during the force measurement, thereby potentially affecting the interactions. This can be circumvented by utilizing *blinking* optical tweezers, where OTs are used only to bring two particles in a dilute system into each others vicinity and subsequently turned off by blanking the trapping laser, in order to release the particles and measure their trajectories without influence of optical forces. This process is then repeated many times to obtain sufficient statistics.^[162,195,223] Because the initial configuration is set by the tweezers, the system is not ‘initialised’ in equilibrium, and simply histogramming the pairwise distances would result in a biased $g(r)$. Interactions forces are therefore generally extracted using dynamic methods, such as analysis of the time evolution of the probability density function as it relaxes to equilibrium^[162,195] or using direct velocity analysis similar to that in [Section 2.4.2](#), which can obtain information of local hydrodynamic effects in addition to interaction forces.^[31,179,224,225] Naturally, optical tweezers —holographic OTs in particular^[224]— offer the possibility of placing any number of particles in any predefined arrangement, and force measurements with OTs are not limited to pairwise interactions.^[226–229] This was shown by Merrill & Dufresne *et al.*,^[228,229] who used blinking OTs to measure trajectories of three and seven-body systems and found that at low ionic strength, electrostatic repulsion deviated significantly from the results expected based on measured interaction forces between pairs.

Having seen the different methods to use OTs for interaction force measurements, we now briefly place this in the context of measurements using NPs. From the simplified ray-optics picture of optical gradient forces it may seem that trapping small* objects such as NPs is not possible without resorting to extremely short wavelength lasers or the use of nanostructures like wave-guides to trap using near-field effects,^[230] but the ray-optics picture does not hold in the Rayleigh scattering regime applicable to NPs ($D \ll \lambda$, with λ the wavelength of the trapping radiation), and trapping of strongly scattering nanoparticles is in fact possible.^[231,232] Using infrared lasers with modest laser power, stable 3D trapping of particles as small as 9.5 nm has been reported.^[233] Nonetheless, the use of OTs as force transducers is not well-suited to the measurement of nanoscale inter-particle distances as discussed. Similarly, while the use of blinking OTs for NPs is, in principle, possible, the initial set configuration is subject to the same constraints due to the lower bound on the trap size, although particles may diffuse to smaller separations during the ‘off’-state of the trap. On the other hand, nothing prevents the possibility to confine two particles in a single trap such that small distances ($r \ll \lambda$) are sampled. That being said, since analysis usually relies on tracking of the particle positions from simultaneous video microscopy in many cases the optical resolution is still limiting with regards to the inter-particle separations that may be analysed. One method to circumvent this limitation is to use plasmonic particles, whose localised

* with respect to the optical resolution

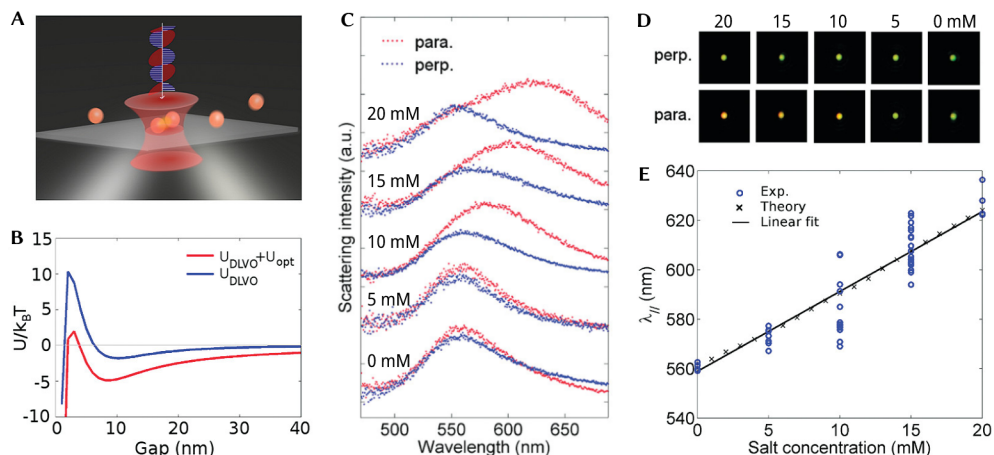


Figure 2.6: scattering spectra of AuNP dimers in an optical trap. **A:** schematic depiction of the experiment. Two 80 nm AuNPs were confined in an optical trap and their scattering spectra were recorded with white light polarised either parallel or perpendicular to the polarization of the trapping radiation. **B:** theoretical interaction potentials based on DLVO including (red) and excluding (blue) the effect of optical forces. **C,D:** scattering spectra and images of NP dimers at varying salt concentration show increased plasmon coupling parallel to the trapping polarisation with increased salt concentration, which corresponds to the long axis of the dimer due to a torque as a result of the optical forces. **E:** experimental and theoretical peak positions as a function of ionic strength, based on Mie theory calculations using inter-particle spacings predicted by DLVO theory. The solid black line is a linear fit of the experimental data. Adapted with permission from Tong & Käll *et al.*^[236] Copyright 2011 American Chemical Society.

surface plasmon resonances couple when the particles are within each others vicinity, thereby allowing the inter-particle distance to be obtained from their optical properties.^[234–238] This was used for example by Tong & Käll *et al.*,^[236] who trapped pairs of 80 nm AuNPs in an optical trap. As shown in **Figure 2.6**, their scattering spectra were dependent on the average inter-particle spacing, which could be compared to the expected inter-particle spacing from theoretical interaction potentials by calculation of the theoretical dimer scattering spectra for a given average spacing. Unfortunately, such analysis methods are highly dependent on properties of the particles and hard to generalize to other NP systems.

2.5 Electron microscopy

In principle, the methods discussed for real-space optical microscopy rely on the determination of the real-space coordinates of particles and therefore apply directly to electron microscopy (EM). Electron microscopy methods can offer a spatial resolution vastly superior to optical microscopy techniques,^[239] and are a staple in the characterisation of nanoparticles. As a result, EM seems the natural choice for interaction measurements of NPs. However, compared to visible light electrons interact much more strongly with all matter. Therefore, electron microscopes are typically operated under high-vacuum conditions meaning that they are not normally suited to look at liquid samples. Nanoparticles are normally dried onto a special conductive substrate to facilitate imaging their morphology *ex situ*. The strong

interaction of the electron beam with samples also means that the beam penetrates only thin samples: tens of nanometers up to at most several micrometers depending on the material and beam energy in the case transmission electron microscopy (TEM), or typically only a few nanometers at most in case of scanning electron microscopy (SEM). To probe properties of nanoparticles *in situ* –in their liquid dispersing media– special techniques have to be employed.^[240] The two most common means to achieve this in the context liquid samples are:

1. cryogenic electron microscopy (cryo-TEM), where a liquid sample is rapidly frozen* to preserve its structure and obtain a static solid sample
2. liquid-cell electron microscopy (LC-EM), where specialised sample cells allow for direct observation of liquid samples by protecting them from the vacuum using thin electron-transparent windows.

Measurement of interaction forces using EM techniques may be conceptually similar to optical microscopy techniques, but in practice they pose different challenges and advantages that are worth discussing separately.

2.5.1 cryo-EM

In cryo electron microscopy a thin film of a liquid sample (such as a nanoparticle dispersion) is vitrified –that is cooled very rapidly to far below its freezing point– *e.g.* by plunge-freezing into liquid nitrogen or liquid ethane. As the timescale of this process can be much shorter than that of diffusion of the NPs in the sample, the structure can be essentially arrested in place, with a typical cooling rate well beyond 10^5 °C/s^[241] depending on the cryogen. These vitrified structures thus represent ‘snapshots’ of the system as it was before freezing commenced, but can be imaged as solid material using transmission electron microscopy (TEM) using specialized holders and equipment that keep the sample at low temperature throughout the sample transfer and imaging procedures to prevent melting or other changes in the sample from occurring. Cryo-EM techniques were pioneered for biological samples, where the presence of water is integral to the structure of cells and cellular components. Nowadays, cryo-EM is has become a routine tool in structural biology and as a result sample preparation techniques focussed on aqueous samples have matured and have been commercialised.^[242] Cryo-EM has also found regular use in materials science,^[243–245] but this has been predominantly focused on aqueous systems while knowledge and procedures for preparation of *non*-aqueous samples are severely lacking behind.^[246] As we will see such samples pose additional challenges. A schematic overview of the typical cryo-TEM sample can be seen in **Figure 2.7A**, where a special sample grid and partial removal (blotting) of the liquid sample result in a quasi 2-dimensional layer of sample that is thin enough for the electron beam to penetrate, typically 20 – 50 nm. This is then plunged into a liquid cryogen –an extremely cold liquid– for maximal heat transfer out of the sample. For aqueous samples, liquid ethane cooled to near its melting temperature (90 K) using liquid nitrogen (LN₂) is generally used. Liquid ethane offers a high heat conductivity because there is little to no formation of gas layers/ bubbles due to boiling when a room-temperature sample is inserted. Liquid ethane cannot be used for many organic (in particular apolar) solvents however, as it can dissolve those samples readily even at temperatures close to its freezing point.^[246,247]

* more precisely it is vitrified by cooling (‘freezing’) a sample so quickly that the solvent molecules do not have the time to rearrange and crystallize

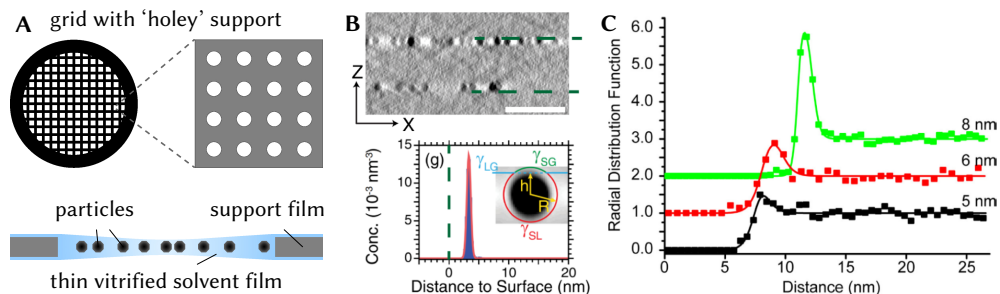


Figure 2.7: Cryo-TEM of NPs. **A:** schematic depiction of conventional cryo-TEM samples: thin free-standing solvent films are created by applying the sample to a support film with holes (typically $\varnothing = 2 \mu\text{m}$), removing the excess liquid by blotting with filter paper and finally plunge-freezing the sample in a liquid cryogen. **B:** TEM tomography cross-section of PbSe NPs in decalin, the green dashed lines indicate the top and bottom liquid-air interfaces. Scale bar: 25 nm. The histogram of particle-interface distances shows that all particles are adsorbed to the interface. Reprinted figure (B) with permission from van Rijssel & Ern  *et al.*^[250] Copyright 2013 by the American Physical Society. **C:** $g(r)$'s of PbSe NPs measured from 2D cryo-TEM, solid lines are fits to the experimental data (squares), the data are shifted vertically for clarity. Reprinted (C) under ACS AuthorChoice from van Rijssel & Philipse *et al.*^[251] Copyright 2014 American Chemical Society.

In those cases LN_2 may be used directly as the cryogen, but this offers significantly lower cooling rates of $<10^4 \text{ }^\circ\text{C/s}$ due to the Leidenfrost effect (the formation of a gas layer, preventing direct contact of the sample with the LN_2). This may be reduced by the use of nitrogen slush—partially solidified N_2 , prepared by temporarily placing LN_2 in a partial vacuum to lower its boiling point—.^[248,249]

While cryo-TEM is used regularly to image the morphology of for example polymer particles,^[243–245] it has found only limited use as a tool for accessing thermodynamic properties of nanoparticle systems through their equilibrium spatial distribution.^[81,250–255] Van Rijssel & Philipse *et al.*^[250,251,255] used cryo-TEM to image PbSe quantum dots in quasi 2-dimensional vitrified decalin films and determine the 2D $g(r)$ as a function of particle size (see Fig. 2.7). The $g(r)$ was used in this case to determine the second virial coefficient of osmotic pressure, a first order correction to the ideal gas law, which was compared with values obtained by small-angle x-ray scattering (SAXS) and analytical ultracentrifugation (AUC).^[251] By controlling the temperature of the particle dispersions just prior to the plunge-freezing, it was also possible to determine the temperature dependent association and dissociation behaviour of such NPs using cryo-TEM.^[255] While the 2-dimensional nature of thin particle films makes imaging and analysis straightforward, it poses challenges in the interpretation of the results as particles are by necessity at or near an interface. NPs are often surface active, and adsorption of particles to the liquid-air or liquid-support interface prior to plunge-freezing is a common issue in cryo-TEM imaging.^[256] Indeed van Rijssel & Ern  *et al.*^[250] found that under the conditions of ref. [251] effectively all particles were adsorbed to the liquid-air interface. In such cases, interfacial effects are thus likely to alter the measured interaction potential when compared to particles in the bulk dispersion.

The influence of interfacial effects may be avoided by imaging particles in the ‘bulk’ of the samples, that is away from any interfaces by more than the typical interaction range.

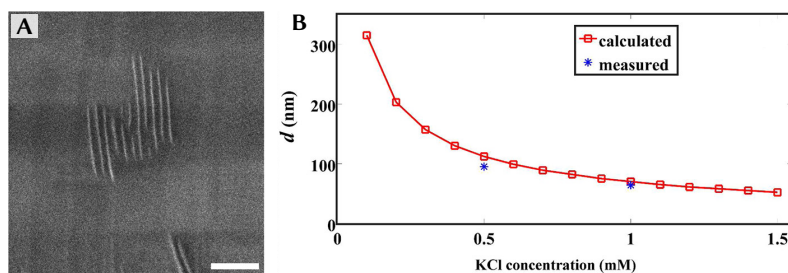


Figure 2.8: Cryo-FIB-SEM of gold nanoplatelets. A cross-section of a cryogenically frozen sample of AuNPLs in a 30 wt.% glycerol/water mixture was exposed by means of focused ion beam milling, and imaged using SEM. **A:** SEM micrograph of a side-on cross-section of a stack of AuNPLs at a KCl concentration of 1 mM, showing the inter-particle spacing. Scale bar: 500 nm. **B:** comparison between measured surface spacing and calculated positions of the secondary minimum of the DLVO potential at varying salt concentration. Reprinted with permission from Vutukuri & van Blaaderen *et al.*^[261] Copyright 2015 American Chemical Society.

Fortunately, performing 3-dimensional imaging of cryo-EM samples it is possible, albeit significantly more challenging and time consuming. Perhaps as a result of this, no interaction measurements between nanoparticles using 3D cryo-EM techniques have been reported to the best of our knowledge, other than the work we will present in **Chapter 5**. In transmission electron microscopy, 3D imaging is achieved using tomography, where TEM micrographs of a sample are taken over a range of different angles and the 3D structure is reconstructed using algorithms. In the context of cryo-TEM, this can be done for a frozen liquid film directly, although it can be challenging to obtain a controllable liquid film thickness: too thin and particles are still within interaction range of the interfaces, but too thick and there may be poor penetration of the electron beam, particularly at high tilt angle, which leads to a poor SNR. Better control over the thickness or shape of the frozen sample may also be achieved using specialised sample substrates^[257] or via the graphene liquid cell approach we introduce in **Chapter 5**. Alternatively, thin sections (lamella) of ‘bulk’ cryo- or otherwise arrested samples may be prepared using *e.g.* ultramicrotomy or focussed ion-beam milling (FIB), and transferred into the TEM for tomographic imaging.^[258–260]

Finally, scanning electron microscopy combined with FIB milling can also be used directly for 3D imaging of cryo- or otherwise arrested samples via serial sectioning,^{*} where imaging and removal of thin slices of material are alternated in order to build a 3-dimensional image.^[249,259,262] The z -resolution of FIB-SEM is set by the minimum slice thickness and resolution of the ion beam, and can be as small as 3 nm.^[262] That (cryo-)FIB-SEM may be used to image equilibrium configurations of interacting particles was shown by Vutukuri & van Blaaderen *et al.*,^[261] who utilised cryo-FIB-SEM to image stacks of gold nanoplates (AuNPLs) as shown in **Figure 2.8**. The authors proposed that the AuNPLs assembled into stacks at low salt concentration due to the presence of a secondary minimum in the DLVO potential, and, using cryo-FIB-SEM, were able to show that the inter-particle spacing within the stacks was consistent with the location of the secondary minimum in DLVO calculations. We note that due to the 1-dimensional geometry of the problem a single cross-sectional

* also known as FIB-SEM tomography, serial block-face imaging, and ‘slice & view’

image was sufficient in this case, and it was not necessary to do a full 3D serial sectioning experiment.

2.5.2 Liquid-cell EM

Recent developments have also made it possible to image liquid samples directly using liquid-cell (scanning) transmission electron microscopy (LC-(S)TEM).^[263–266] Here, special sample cells are used containing a small liquid volume sealed off from the vacuum by thin electron transparent windows, allowing for direct observation of nanoparticle dispersions *in situ*. Whereas cryo-TEM can only provide static data, LCTEM in principle allows for both static and dynamic analysis methods to be used, provided that imaging can be achieved at a sufficient time resolution in case of the latter. The ability to directly image processes such as NP formation and self-assembly at length scales far below those accessible by optical microscopy has led to its rapid adoption in research on colloidal NPs.^[267,268] Nowadays, micro-fabricated chip based liquid cells (LCs) with specialised holders are commercially available which make it possible to study the response of a nanoparticle systems to external stimuli such as electric fields, and changes in pressure, temperature or in the dispersing medium via micro-fluidic flows. Such chips offer lower resolution than conventional (dry) TEM due to electron scattering in the relatively thick windows (10–100 nm) and sample volume (0.1–10 μm). Graphene-based liquid cells (GLCs) on the other hand generally contain fixed liquid pockets and allow for little to no external stimuli, but enable imaging at (near) atomic resolution due to the thinner liquid pockets and atomically thin windows.^[265,266] Chip-based graphene LCs are being developed which combine the advantages of both methods.^[269]

There are two main challenges when it comes to LCTEM for the measurement of *e.g.* interactions between NPs. Firstly, TEM and by extension LCTEM is primarily a 2-dimensional imaging technique. While it is in principle possible to use electron tomography to obtain 3D structures of LCs,^[270] acquisition of tomographic tilt-series cannot at present be achieved at sufficiently fast time resolutions to image diffusing NPs in 3D,* although it may be possible to determine particle heights from the height-dependent point spread function of due to beam broadening in the sample,^[272] via point-spread-function shaping, or through ptychographic imaging.^[273] So far, interaction measurements have thus relied on the 2D projections of 3D NP coordinates. Furthermore, the thickness of the liquid layer may be small enough such that the particles are more or less confined in 2D, and such that interaction with the windows is likely, in particular in GLCs where sample thicknesses tens of nanometers or less are common.^[269] In many cases, even for thicker chip-based LCs, particles are adsorbed to or near the electron-transparent windows due to *e.g.* charge interactions rather than exhibiting truly free diffusion.^[274–277] Thin geometries are also likely to alter the hydrodynamics of the particles when compared to the bulk. Secondly, the interaction of the electron beam with the sample and sample cell can significantly alter the system due to effects such as beam-induced local heating,^[278] bubble formation,^[279] momentum transfer,^[278,280] enhanced dissolution of solid species (*e.g.* NPs),^[281–283] deposition of material or formation of solvated species like ions and radicals due to radiolysis,^[279,281,284] and the build-up of charge within the sample or on the electron transparent windows.^[275,278,281,285] Naturally, all of these effects can considerably alter the NPs interactions or drive the system out of equilibrium depending on the beam dose rate and total accumulated electron dose. While excluding electron

* we note that tomographic analysis of the 3D structure of individual NPs in a LC is possible via *e.g.* the rotational diffusion^[271]

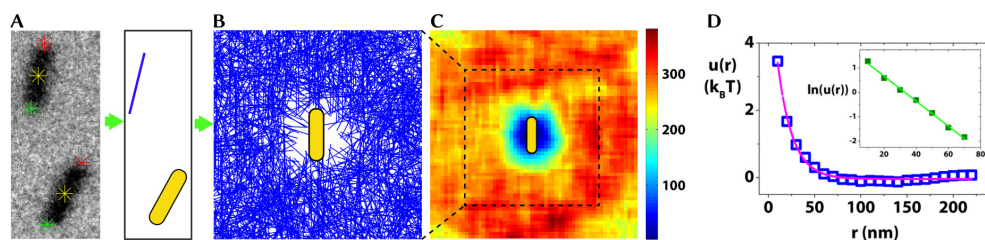


Figure 2.9: LCTEM measurement of gold nanorod interactions Gold nanorod (AuNR) trajectories were sampled using LCTEM. **A,B** pairwise particle positions were automatically determined (yellow star is the centroid, green and red stars indicate particle tips). One of the particles was then arbitrarily chosen as reference (indicated in yellow) and the pair was reoriented with the reference particle in the origin to obtain the distribution of neighbour (blue lines) distances and orientations. **C**: 2D histogram of particle positions (bin size $5 \times 5 \text{ nm}^2$) shows an approximately isotropic distribution of neighbours. **D**: pair potential obtained from direct Boltzmann inversion of the $g(r)$ (blue squares) with an exponential fit (red line), the inset shows the logarithm of the data to indicate the exponential nature of the pair potential. Adapted under ACS AuthorChoice licence from Chen & Alivisatos *et al.*^[288] Copyright 2015 American Chemical Society.

beam effects remains challenging even for well-understood processes such as Brownian diffusion,^[276,286] careful choice of experimental conditions can be used to reduce or avoid such problems.^[272,287] To further exclude influence of beam-induced effects from the results, LCTEM results should be correlated with ex-situ measurements whenever possible, and information on beam-dose and sample preparation should always be reported with the data to aid with reproducibility.

Despite these challenges, LCTEM has emerged as a key technique for investigation of interactions between NPs.^[267,268] So far these studies of NP interactions and NP SA have focused predominantly on (noble) metallic particles, which are particularly well-suited to LCTEM studies due to their high electron contrast and stability against beam damage and/or dissolution.^[268,283] An early example of the use of LCTEM to measure inter-particle interactions was the work by Chen & Alivisatos *et al.*^[288] shown in **Figure 2.9**, who used LCTEM to image the 2D diffusion of gold nanorods (AuNRs) in aqueous solution over the electron transparent window, and obtained the full orientation and distance dependent pair distribution. The authors found the pair distribution function to be approximately isotropic, and used direct Boltzmann inversion of the $g(r)$ to obtain the pair potential, although the authors also demonstrated that the length scale of the (repulsive) charge interactions was altered via e-beam intensity dependent radiolysis of the solvent which led to changes in the ionic strength. This enabled selective tip-to-tip assembly of the AuNRs when the range of the electrostatic interactions was reduced such that it was comparable to the length of the AuNRs. Similar LCTEM studies using various (anisotropic) NPs have since been reported and show that even relatively simple interactions due to *e.g.* charge, when combined with anisotropic particle shape, can lead to complex behaviour.^[268,289–294] That LCTEM may be used to quantitatively determine electrostatic interactions at low-dose conditions where interactions are *not* affected by the e-beam, was shown by Welling & van Blaaderen *et al.*,^[295] who quantified the range of motion of titania and gold (nano)particle cores in rattle-type core@void@shell μ Ps. Rather than tracking and binning the core positions within the shell,

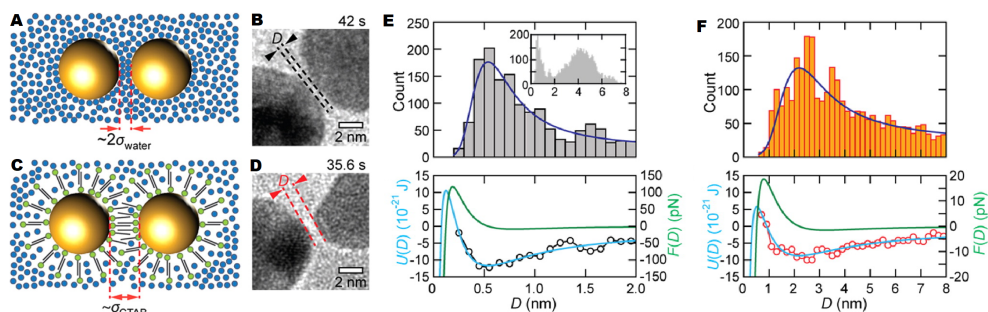


Figure 2.10: LC-TEM measurement of hydration- and ligand-layer mediated interactions of AuNPs. Bare and CTAB coated AuNPs were formed and imaged during aggregation in water using LC-TEM. **A,B:** schematic and LC-TEM video snapshot showing a metastable particle pair separated by a layer of two water molecules. **C,D:** a metastable pair with CTAB ligands separated by a single ligand bilayer. **E,F:** histograms of surface separation distances D for bare and CTAB-coated AuNPs respectively, together with extracted pair potentials and forces obtained by fitting the distance distribution with the direct Boltzmann inversion of a model potential given by $U(D) = W \exp(-D/\delta) - (A_H R/12D)$, where the first term represents steric repulsion of length scale δ and the second term the van der Waals attraction between two spheres of radius R . Adapted with permission from Anand & Mirsaidov *et al.*^[66] Copyright 2016 American Chemical Society.

the authors time-averaged the signal of the moving core and deconvolved the resulting images with the signal of the core to obtain the probability density distributions at varying ionic strengths. In combination with finite element calculations, the core-shell interactions were determined.

Solvent discreteness effects between NPs (such as the formation of hydration layers) are challenging to measure using other methods due to their short range and dynamic nature. Anand & Mirsaidov *et al.*^[66] studied the irreversible coalescence of 2 nm AuNPs synthesised *in situ* with LC-TEM *via* dissolution and subsequent reduction of Au due to e-beam irradiation. By analysis of pairwise trajectories, it was found that the approach of particle pairs typically briefly stalled at a fixed distance, followed by a jump to contact. Binning the surface-to-surface distances revealed a peak at close separation in the distribution as shown in **Figure 2.10**, where the separation was consistent with steric repulsion by two monolayers of water in case of bare AuNPs and interdigitated ligand layers in case of CTAB-coated AuNPs respectively. Zhu & Sun *et al.*^[296] subsequently performed similar experiments and obtained comparable results when studying oriented attachment of citrate-stabilised AuNPs, but additionally looked at the influence of the relative orientations of the atomic lattices using atomic resolution imaging. In both cases the authors fitted pairwise distance distributions obtained from trajectories of coalescing particles with a model interaction potential via direct Boltzmann inversion. However, we note that this is valid only under equilibrium conditions which was likely not satisfied in case of these trajectories, and care should be taken when interpreting potentials obtained in such manner.

As an alternative option to the use of liquid cell samples, it is also possible to use environmental EM methods that are designed to operate at moderate gas pressures such that the use of liquid samples is possible.^[297,298] Nonetheless, these methods retain many of the same challenges when it comes to e-beam effects, and pose constraints on the particle

and solvent systems under study. Alternatively, ionic liquids (ILs) may be used as dispersing medium for use in EM without the need for liquid cells or environmental EM techniques. Over the last several years, ILs have emerged in this application as they are non-volatile even under high vacuum conditions, have relatively high electrical conductivity (preventing charge build up) and they are comparatively stable under influence of electron beams.^[290,299–302] Kim & Russell *et al.*^[300] used SEM to image polymer-grafted silica colloids adsorbed to the surface of a droplet of IL, which allowed them to obtain the pair potential via direct inversion of the $g(r)$ of sufficiently dilute samples. It was found that ligand length affected the interfacial interactions from short ranged repulsive to weakly long ranged attractive due to ligand-induced menisci.

Of all interaction measurement techniques, liquid-phase EM techniques seems most widely used for interaction measurements between NPs, despite their relatively recent development when compared to *e.g.* optical microscopy techniques and AFM. Whereas the practicalities of in-situ imaging with LC-EM methods have undergone rapid development, we believe that the analysis and interpretation of results is an area where improvements may be made. In most cases, data are either interpreted qualitatively —are the particles stable or do they cluster?—, or based on relatively limiting methods such as direct Boltzmann inversion in case of more quantitative determination of interaction forces, where the validity of the underlying assumptions are not always properly verified. As we have seen however, there are many ways to obtain interaction forces from coordinate or trajectory data which should be directly applicable to LC-EM studies. In particular, nonequilibrium effects due to the e-beam can complicate quantitative interpretation of results, and dynamic analysis methods may provide an outcome in those cases. Alternatively, low-dose techniques and STEM imaging may be used to obtain more representative results. Another area where improvements may be made is image analysis and particle tracking. These techniques for EM-based studies will have different requirements and suffer from different artefacts than established methods developed for analysis of optical microscopy due to *e.g.* the complicated contrast mechanism in bright-field TEM, and indeed specialised methods have been developed.^[303,304]

2.6 Scattering methods

Scattering methods (using for example light, x-rays or neutrons) offer the ability to probe local structure in (colloidal) matter in a nonintrusive way with a high spatial resolution and for statistically large amounts of particles such that the ensemble average is obtained. The angle-dependent scattering intensity $I(k)$ (with k the wave vector) can give information on both the internal structure of particles —their shape, size and composition— through the form factor $P(k)$, and their organisation in relation to each other through the structure factor $S(k)$. However, scattering-based methods are indirect techniques in that the data are recorded in reciprocal space. Inversion of reciprocal-space data to obtain real-space data such as the $g(r)$ is, in principle, possible via a (radially averaged) Fourier transform^[160]

$$S(k) = \frac{I(k)}{P(k)} = 1 + \frac{4\pi\rho}{k} \int_0^\infty [g(r) - 1] r \sin(kr) dr, \quad (2.11)$$

which has found some success in elucidating inter-atomic potentials in the past in combination with *e.g.* the Ornstein-Zernike approach and reverse MCS, as well as to a lesser degree in work on colloidal dispersions.^[186,305–309] However, applying this to colloidal (nano)particle

dispersions is challenging in practice as interactions become more complicated due to the finite precision and range of the recorded k -space values. Interactions are typically strongest at short range (large k), whilst the scattering intensity generally decreases with increasing k . While Henderson's theorem applies equally well to $g(r)$ s obtained from $S(k)$ in theory, the effects of finite measurement range and noise make that $g(r)$ s obtained in this manner are generally not very sensitive to changes in $U(r)$, and as a result multiple different potentials may 'fit' the data.^[159] Nonetheless, the broad applicability and high spatial resolution of x-ray and neutron scattering methods make them attractive techniques for studying structural properties in soft matter research, and improved methods for obtaining real-space interaction potentials from scattering data remains the subject of active research.^[159,310,311]

2.7 Advances in theory and simulations

While the focus of this work is on experimental techniques, it would not be complete without briefly discussing the progress which has been made in theory on NP interactions and even more so the advances in computational and simulation techniques which can be used to model interacting NPs and extract interaction potentials. We have already mentioned some of the advances in theory in [Section 1.3](#) of the introduction of this thesis. Some of the equations underlying DLVO theory for example have been re-derived under assumptions more suited to NPs, *e.g.* electrostatic repulsion for all κR instead of only for $\kappa R \ll 1$ ^[45], but ultimately mean-field approaches like the Poisson-Boltzmann equation that form the basis of most theories simply do not apply at nanometer length scales because of multiple-ion correlation effects when charges are separated by less than the Bjerrum length ($\lambda_B \approx 0.7$ nm in water and 28 nm in heptane).^[14,19] Considerable effort has gone into calculation of van der Waals forces in a discrete (atom by atom) manner including the considerable many-body contributions, where atomic polarisabilities are used rather than the continuum dielectric functions.^[37,43,312–314] Similarly for most of the other interaction forces models have been developed which improve predictions of certain interactions between nanoparticles. Still, analytical models are often extremely difficult or impossible to solve for many-particle systems, and no single general and broadly applicable model exist which captures the total interaction potential.^[19,26]

Progress in computational power and simulation techniques have also made it possible to simulate interacting nanoparticles using atomistic and coarse grained molecular dynamics simulations.^[16,25,80,315–319] Here structural details such as the capping ligands are explicitly included, although in most studies their structure is coarse grained in order to be computationally feasible for all but the smallest particles. For the same reason, the solvent is often only included implicitly in the interaction parameters between the (groups of) atoms.^[320] Nonetheless, fully atomistic simulations of small NPs are within reach. However, the interatomic interactions are generally model potentials with tunable parameters, and not calculated from first principles during the simulation. The choice of these atomic interaction parameters / force fields is not trivial and one of the key challenges in order to make accurate predictions for real-world behaviour.^[19] MD simulations do offer many advantages however. With the correct choice of parameters they can provide not just the inter-particle interaction potential, but they can give direct insight into the underlying mechanisms responsible for these interactions while addressing the non-additive nature of the constituent effects and the discreteness of matter. The dynamic nature of things such as ligand dissociation, which occurs on timescales beyond the ability of most experimental techniques, can, in principle, be in-

cluded in the simulation.* The ability to probe specific configurations opens up opportunities for studying anisotropic potentials and things like 3-particle interactions efficiently.^[321,322] The importance of non-pairwise contributions to interactions in particular is an ongoing subject of study.^[316,323,324] To rationalize the choice of force fields multi-scale simulation methods in combination with *e.g.* DFT may be used. Combined simulation and experimental approaches where microscopic details from simulations are directly linked to experimentally observable behaviour are particularly powerful and are indeed being explored.^[80,193,325,326] We therefore expect combined simulation and experimental approaches to be the key for future exploration of nanoscale interactions.

2.8 Future challenges and new horizons

Having seen a wide range of techniques and the progression to interaction measurements involving ever smaller particles, one can ask: “What’s next?” We believe that nanoscale interaction measurements will play a significant role in understanding colloidal assembly processes on the nanometer scale, in combination with theoretical and computational efforts. The examples highlighted in this work show the feasibility of measuring interactions of NPs, thereby providing direct experimental evidence for proposed mechanisms in *e.g.* self-assembly. Still, results must be interpreted with the limitations of the measurement and the assumptions underlying the analysis in mind. In our opinion, there are several challenges (discussed below) which could be addressed in future work in order to make interaction measurements more generally applicable and to measure under conditions which more accurately resemble those during synthesis, SA or in applications.

2.8.1 Smaller, better, faster, stronger

Perhaps the most obvious of all challenges are the practical and technological difficulties in achieving ever-increasing precision and resolution. As it stands, for many of the methods we have discussed, the realm of nanoparticle interactions lies at the limit of their spatial or temporal resolutions. Further improvements to existing technology can push interaction measurements forwards to a considerable degree. Since the advent of super-resolution techniques in optical microscopy in the 90’s, dramatic improvements have been achieved in the ability to image and localize particles, and this trend may well continue. Ultimately though, there are fundamental limits to many aspects which hinder continuous advancement. As an example, detection techniques for light in the visible wavelength range are already close to detecting single photons with a unity quantum yield. In electron microscopy on the other hand, resolution has long been good enough to resolve even detail on the atomic scale, but the difficulties typically lie in the time and electron dose required to achieve such high-resolution results. The recent appearance of direct electron detectors has enabled orders of magnitude improvements in detection sensitivity, and has thereby enabled nonintrusive imaging at much shorter timescales and with reduced beam-damage effects.^[258,327] As these devices become more widespread, in-situ imaging of nanoparticles may well become a more ‘everyday’ task. Furthermore, in-situ EM techniques such as LC-TEM are still in their infancy, and LC-chip/holder technology and standardised procedures are undergoing rapid development and are expected continue improving in the (near) future.^[240,258]

Aside from technological advances in equipment, we expect continuing development in the theory and computational routines used for the analysis of microscopy data in order to

* although this is almost never done so

extract more of the available information from the data, and to aid in processing large datasets. In much of the work that has been published so far, the predominant source of uncertainty was not the intrinsic resolution of the measurement technique, but rather the limited sample sizes that could be measured and processed. Automated procedures for data acquisition can lower the barrier to obtaining a sufficient sampling, while automated data processing can aid in the analysis phase. In particular, most of the methods we have discussed rely on image processing (notable particle localisation) where enormous improvements have been made purely by improved image analysis methods such as deconvolution and specialised particle detection algorithms. Machine learning techniques are seeing rapidly increasing use in this area, and we believe that this trend will continue in the near-future to enable reliable and fast image processing.

2.8.2 Beyond model systems

Despite three decades of work on measuring colloidal interactions, so far a majority of the work has been on well-understood colloidal model systems in the form of ‘proof-of-principle’ experiments or on systems where reasonable assumptions about the form of the pair potential could be made. Verification and ‘benchmarking’ are important steps in the development of new experimental techniques, but rarely lead to new insights about the model systems used for testing them. In order for interaction measurements to become a routine tool in the toolkit of nanoparticle scientists, we must move beyond model systems and show that *new* insights can be gained when applying these techniques to systems with *unknown* properties and to open questions. Good initial candidates for such measurements are NPs whose interactions and SA is of interest for applications and which possess many of the properties of model systems—*isotropic shape and interactions, known and monodisperse size and structure, well-suited to the measurement technique—but for which the interactions are unknown and difficult to predict.* Several reports have focussed on gold nanoparticles, which indeed satisfy many of these criteria. They are of interest for SERS, catalysis and biochemical applications, the physical and chemical properties are well-documented, imaging is helped by their strong interaction with both electrons and photons, and functionalisation with many surface groups can be used to tune interactions.

Unfortunately, NPs are rarely truly monodisperse. Rather than solely their average diameter, NPs are more accurately described by a distribution of sizes. In addition to size-heterogeneity, particles may vary in their shape, chemical composition and surface properties, all of which can affect interactions on a particle-per-particle basis.^[215] Systems with two or three distinct subsets of particles may still be expressed in terms of the unique pair-wise combinations, *e.g.* A-A, A-B and B-B for a two-component system, but such an approach is infeasible as the number of variations increases or the particles no longer fall into a small number of distinct groups.^[188] This is less of an issue for techniques such as CP-AFM, where particles are measured one at a time, although these results are then harder to generalise when significantly different results are obtained from particle to particle. Accounting for the effects of polydispersity in ensemble measurements in a general way remains an open challenge, even though it can have significant consequences for the outcome of interaction measurements. Analysis of (size) polydisperse systems *as if they are monodisperse* can lead to interaction potentials which quantitatively or even qualitatively differ from reality, such as due to blurring of features in the $g(r)$ and $U(r)$.^[132,168,328] In some cases, the size of each individual particle may be obtained together with its position such that the potential can be

expressed in terms of the surface-to-surface separation.^[5,201] This may yield valid interaction potentials, provided that the interaction forces are not otherwise dependent on the particle size, or allow for more complex analysis that takes the size of each individual particle into account.

2.8.3 Interaction measurements under relevant experimental conditions

Often-times, interactions vary significantly under different experimental conditions such as temperature, particle or ion concentration, or in the presence of nearby interfaces. For example, applications may need particles on or near interfaces such as in porous networks. Interactions with the local neighbourhood through e.g. charge or hydrodynamics can alter their behaviour. In an ideal world, one would thus measure interactions in systems that closely resemble the conditions under which one wishes to understand the effects of the interactions, such as the final phases of self-assembly. Conversely, many of the techniques we discussed pose specific constraints on the systems under study or may affect the interactions in other ways. Continuing developments in specialized sample cells and holders and micro-fabricated measurement chips have made it possible to perform microscopy in a wide variety of chemical environments, at both low and high temperatures and pressures, in electric or magnetic fields or under mechanical deformation^[240]. The effects of these properties on inter-particle interaction forces is thereby immediately accessible for measurement, provided that influence on particle positions or dynamics through other effects (convection, electrophoresis, etc.) can be excluded or corrected for. Measuring at high particle concentration on the other hand, may pose considerable challenges for both imaging and analysis. Ultimately though, it is unlikely that interaction measurement can always be achieved under the perfect conditions, or even that every open question will be solved by directly measuring the interaction potential in that specific case. Instead, we expect that measurements under well-defined conditions are used to inform theoretical and computational (simulation) techniques, which can subsequently be used to investigate a wider range of systems and conditions.

2.8.4 Beyond $U(r)$

So far we have predominantly considered interactions which could be, at least to a reasonable degree, described by the practical but perhaps naive constraints of the exclusively pairwise and exclusively r -dependent $U(r)$. This, while undoubtedly useful in its simplicity, has its limitations. One of the more commonly discussed examples of this is that of anisotropy: an interaction potential depending on the relative angle between two particles as well as the interparticle distance. In such cases, important details are lost if their interactions are radially averaged. This case is common, as many NPs possess anisotropy in their interactions due to nonspherical shape, compositional heterogeneity, varying surface properties or magnetic or electric fields.^[329] If the orientation of the particles is known, one can determine the orientationally dependent radial distribution function and many of the previously discussed methods can, in principle, be extended to account for such a distribution function with more degrees of freedom. Analysis of these systems requires much more data to obtain comparably accurate results, but several examples of anisotropic interaction measurements have been reported.^[81,170,215,268,288,294,330,331]

Likewise, virtually all colloidal interaction measurements reported in the literature are on particles which are (assumed to be) in local thermodynamic equilibrium. There are many cases however where equilibrium conditions are not met, such as biological systems and active matter, systems undergoing chemical change such as during synthesis, and due to

external manipulation like magnetic or electric fields. Changes to the system, like in SA procedures based on solvent evaporation, or even fluctuations within the NPs itself such as dissociation creating a charge can continually change interactions. Despite this, the $U(r)$ is normally assumed to be static, that is constant over time. It would be interesting to see how dynamic effects influence SA and how the interactions of a single particle pair evolve over time, but this requires a time resolution not yet feasible in most experimental techniques discussed above. Lastly, there are interactions that are not pair-wise. While for large μ Ps the effect of higher order interactions is generally comparatively small, for NPs higher order effects likely contribute significantly to the overall interactions. Fortunately, contributions from 3-body and higher order interactions may be resolved from real-space coordinates much like the pairwise contribution, but the larger number of dependent variables necessitates a much larger amount of data to resolve from any measurement.

2.9 Concluding remarks

In this review we have attempted to connect the recent advances in nanoparticle science and interaction force measurement between NPs in particular, with the lessons learned in several decades of performing such measurements on surfaces and larger colloidal μ Ps. Since the surface force apparatus first provided experimental evidence of the complicated nature of surface forces on the nanometer scale, a wide variety of methods was developed to measure interactions involving colloidal particles directly. The emergence of super-resolution microscopy techniques and in-situ electron microscopy combined with advanced particle localization algorithms have made it possible to extend real-space imaging of colloidal dispersions to the nanoscale, thereby enabling extraction of inter-particle forces by a variety of methods. An overview of the methods we discussed is given in [Table 2.1](#) with the main advantages and disadvantages in the context of nanoscale interactions of NPs. With this, we hope to have provided a comprehensive overview of interaction force measurements and to have given the context within which the rest of the research in this thesis was performed.

Table 2.1: Overview of different methods for measuring colloidal interaction forces, particularly of nanoparticles, with their main advantages and disadvantages and suggested references for further reading.

Technique	Advantages	Disadvantages	Refs.
atomic force microscopy (AFM)	wide range of distances and forces (up to $\gg k_B T$), high spatial resolution, no equilibrium conditions required, single-particle measurements possible	complicated cantilever preparation, hard to separate isolated NP interactions from those with the surface and cantilever, subject to thermal noise for small forces	[23, 99, 332]
total internal reflection microscopy (TIRM)	widely available setup, high spatial resolution (z), noninvasive measurement, high time resolution, measures $k_B T$ scale interactions, single-particle measurements possible	cannot directly probe colloid-colloid interactions, low signal for small particles, hard to confine nanoparticles to the interface	[75, 131]
wide-field (optical) microscopy (WFM)	simple and widely available setup, very few constraints on sample, noninvasive measurement, high time-resolution, measures $k_B T$ scale interactions	low spatial resolution, only 2D information available, only ensemble measurements possible	[128]
confocal laser scanning microscopy (CLSM)	noninvasive measurement, measures $k_B T$ scale interactions, 3D interactions possible, better spatial resolution than WFM, particularly with super-resolution techniques	low time-resolution, low signal and spatial resolution for nanoparticles, only ensemble measurements possible	[128]
optical tweezing (OT)	straightforward analysis, can measure from $k_B T$ scale up to much stronger interactions depending on operating mode, can probe unlikely configurations and in dilute systems	complicated setup, possible non-conservative effects, low spatial resolution of trapping and imaging, not generally practical for all NPs at close distance	[210, 211]
cryogenic electron microscopy (2D cryo-EM)	high spatial resolution, measures $k_B T$ scale interactions, wide choice of particle size/shape/material	poorly controlled sample preparation, interface effects likely, limited choice of solvents, no dynamic measurements possible	[243–246]
tomographic cryo-EM (3D cryo-EM)	high spatial resolution, wide choice of particle size/shape/material, 3D measurement possible	time consuming, complicated sample preparation, limited choice of solvents, expensive setup, no dynamic measurements possible	[243]
liquid-cell electron microscopy (LC-(T)EM)	high (2D) spatial resolution, high time resolution, can be noninvasive at low dose	beam-induced interactions and changes common, only 2D projection of a usually 3D system (with poor to no z resolution), expensive setup, large contrast from solvent, interface effects likely	[266–268]

CHAPTER 3

Synthesis & characterisation of colloidal model systems for interaction force measurements

ABSTRACT

To measure interactions between colloidal (nano)particles, one first needs to obtain particles. In this chapter we discuss which properties of colloidal (nano)particles are desirable for enabling interaction measurements and how these interactions may be modified through post-synthesis modification of the particles. We provide an account of the synthesis of gold and silica based nanoparticles using a variety of synthesis methods, together with detailed experimental methodology. The resulting particles are characterised using predominantly transmission electron microscopy as well as some other characterization techniques. The syntheses discussed here include the particles used throughout the rest of this thesis, as well as several other particle systems which were used in other work or which may be interesting candidates for studying inter-particle interaction forces in the future.

3.1 Introduction

The ideal measurement techniques for interaction forces between colloidal particles would be able to measure any interaction between any kind of particle. As we have seen however, this perfect technique does not exist. Not only do different methods place restrictions on the length or energy scales which can be observed, there are considerations such as which assumptions are made in the analysis method: a technique relying on a radially averaged ensemble measurement like the $g(r)$ is not suited to measure interaction forces between polydisperse and/or anisotropic particles. Likewise, when relying on particle coordinates from microscopy, the particles must be observable using the type of microscope chosen for the measurement. While this seems like a trivial and easily satisfiable requirement, obtaining a strong enough contrast whilst imaging at the right conditions for the measurement is not an easy achievement for many widely studied (nano)particles. In this chapter we discuss the synthesis of several colloidal model systems that are well-suited to perform the interaction measurements throughout the rest of this work. The aim of this work was not to develop entirely novel synthesis procedures, and as such the focus lies on particle systems that are well understood and have established synthesis procedures. Rather, this chapter should be seen as an account of the synthesis of colloidal particles through the eyes of ‘the reproducer’: a scientist who needs colloidal particles for which established methods exist in the literature, but whose research is not focused on the synthesis *per se*. In practice, attempts to reproduce (nano)particle synthesis are often not directly successful at producing particles with similar size, shape and polydispersity as reported. Despite this, it is not common practice in the field of nanoparticle synthesis to publish attempts to reproduce syntheses.* Such accounts are sometimes, particularly when successful, included in method sections or the supporting info or articles, but more often than not these experiments remain only as part of the researchers’ experience and the institutional knowledge of research groups. In this chapter, we report the synthesis of several particle systems which were used throughout this thesis or elsewhere, or which we consider to be good candidates for future studies on interaction measurement.

For this work, we will focus on particles which are sufficiently monodisperse. This is not only because interaction forces may be size-dependent, but also because the methods discussed in this work rely on ensemble measurement of centre-to-centre distances and many interaction forces originate at the particle’s surfaces. Large variations in particle size convolve the true distance dependency of the interaction forces when analysed in this manner. Of course, there is no fundamental reason why the interactions could not be expressed and measured dependent on the surface-to-surface distance, but it is generally much harder to determine the precise radius of an individual particle than merely its position, especially when contrast or resolution are limiting.† In this context, we set a threshold for “sufficiently monodisperse” at a relative polydispersity of below 5%. Secondly, our focus lies on spherically symmetric particles to limit complexity in the analysis. In almost all practical cases, anisotropic particle shapes also lead to anisotropy in the interaction forces which considerably complicates the analysis and puts more stringent requirements on the data acquisition as we will see in **Chapter 7**. When there is anisotropy in the particle shape and

* There are of course exceptions to this, *e.g.* in cases when a synthesis is particularly important for a field and hard to reproduce, such as was the case for the synthesis of silica-core gold-shell particles^[333] and the synthesis of gold nanorods^[334]

† If enough statistics on the dynamics of the individual particles are available even in concentrated systems the exact size and thus distances between all surfaces can be measured.^[197]

this is not taken into account in the analysis, a radial average of the interaction force is obtained which would likely not describe the behaviour of the particles accurately. For this reason, anisotropic particle shapes as well as magnetic materials and materials which may have charged facets (such as some semiconductor nanocrystals) are avoided. Of course, there are more practical manners to consider: the particles must be colloidally stable and safe to work with, it should be possible to tune the interactions, and to facilitate measurements based on microscopy techniques we focus on materials which can provide a good signal or contrast. We demonstrate here a number of variations on three different materials which satisfy these criteria and cover a broad spectrum of possibilities with regard to length scale and choice of solvent: gold nanoparticles, silica nano- and microparticles and poly(methyl methacrylate) microparticles.

3.2 Gold nanoparticles

Gold nanoparticles (AuNPs) are amongst the most widely studied nanoparticles in literature, with a history of their use as colourants dating back many centuries to the ancient Egyptians and Romans, although the microscopic nature and its relation to their colour were not known or understood until the days of Faraday and Mie.^[335–338] Gold nanoparticles possess several properties that make them advantageous for interaction measurements. Firstly, their ubiquity in nanoparticle literature means that their synthesis has been widely studied and many shapes and sizes may be produced,^[339–342] whilst their properties such as surface chemistry, stability and optical properties are well-understood.^[8] They are non-toxic, stable against oxidation and compatible with water as well as many other polar and apolar solvents. Surface modification is straightforward with amino- or thiol containing ligands for reversible and nearly covalently bound^[343] capping molecules respectively^[8,85,344–347] as well as by means of shell-growth of other materials such as silica, titania or alumina.^[348–352] Gold also has a large contrast in electron microscopy and is relatively resistant against beam-damage. All of these make AuNPs an ideal candidate for EM-based studies of NP interactions and assembly. We describe here three different methods for preparing AuNPs over the full range of colloidal NP sizes and with positively charged, negatively charged and neutral capping molecules: the extremely widely used and highly reproducible citrate reduction method for 16 nm AuNPs, a more recent CTAC-based method for synthesis of spherical AuNPs up to >100 nm and an oleylamine based synthesis of sub-10 nm AuNPs for use in apolar systems.

3.2.1 Citrate stabilized AuNPs (17 nm)

By far the most commonly used method in the synthesis of spherical AuNPs is what is known as the citrate-reduction or Turkevich method, where Au^{3+} is reduced with trisodium citrate (often referred to simply as sodium citrate) in a boiling aqueous solution, which yields AuNPs in the size range of 10 nm to 30 nm.^[338,353] The procedure used here is based on the work by Frens^[354] and is simple and highly reproducible, although it is of note that since then many other variations of the Turkevich method have been reported to give lower PDs.^[355–357] Full experimental details are given in **Section 3.7.2**. In short: an aqueous solution of HAuCl_4 was brought to reflux (boiling) and a solution containing an excess of trisodium citrate solution was rapidly injected. The sodium citrate acted both as reducing agent, ligand (providing charge stabilisation of the resulting AuNPs) and pH-regulator.^[356] We note that the particle size may be varied between ~5–30 nm by varying the ratio of Au^{3+} to citrate (with lower citrate concentration giving larger particles). In this work, the molar ratio was kept constant

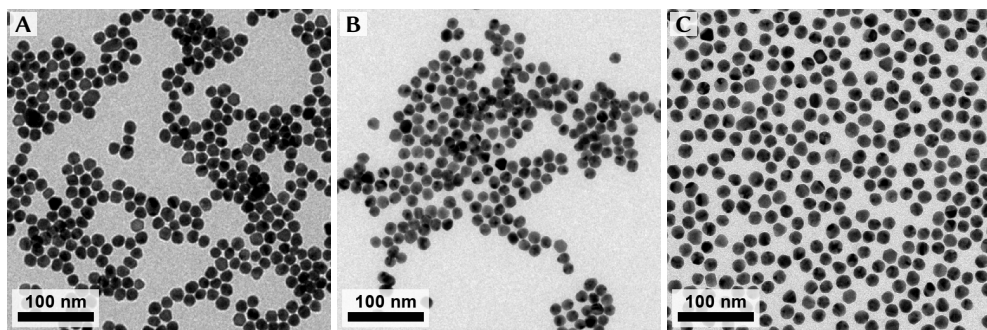


Figure 3.1: AuNPs@citrate. Three representative batches of AuNPs@citrate made using the Turkevich & Frens method are shown, particle sizes and polydispersities for **A–C** were 16.7 ± 1.1 nm (6.3%), 17.5 ± 1.3 nm (7.4%) and 18.1 ± 1.1 nm (6.0%) respectively.

at $[\text{citrate}^-]/[\text{Au}^{3+}] = 4.0$ where the most monodisperse and spherical particles are obtained. This synthesis was performed some 10 times throughout this research and always yielded similar results with a mean size between 15 nm to 18 nm and polydispersity of 5% to 8%, some representative examples of AuNPs@citrate* are given in **Figure 3.1**. Batch to batch variations in size are likely due to variation in the pH of the water used as well as slight variations in reactant concentrations.

Citrate-stabilised particles by themselves were not colloidal stable without the use of excess citrate in the dispersing medium due to the weak attachment of citrate to the surface. But even in the unpurified synthesis mixture with a background concentration of citrate (~ 1 mM), particle precipitates started to form within weeks after the synthesis. The addition of salt or non-aqueous solvent may also cause rapid aggregation. Therefore, the AuNPs@citrate were further modified to alter their surface properties and thereby interactions. Citrate could be replaced by the addition of ligands containing a thiol functionality, which readily binds to the Au surface upon addition without requiring heating or any pre-treatment of the particles, although we note that it is likely that some citrate remains on the surface.^[358] Various thiol-terminated polyethylene glycol (PEG) ligands were used to functionalise the AuNPs@citrate, as PEG is widely used in the literature due to its good solubility in a wide range of solvents and up to high salt concentration and its excellent biocompatibility.^[359–361] An overview of thiolated PEG ligands and their approximate sizes is given in **Table 3.1**, experimental methods and molecular structures are given in **Section 3.7.3**. In short, an excess of ligand (ca. 60 molecules/nm² of particle surface) is added to the as-synthesised particles together with a small amount of NaOH to increase the pH and speed up the reaction by activating the SH-bond. It is of note that PEG may also undergo considerable physisorption onto NPs, and PEG functionalisation is possible even in absence of a thiol-functionality.^[362]

In **Figure 3.2** results of functionalisation with thiolated mPEGs of varying molecular

* on notation: it is common in the literature to use “A@B” as a shorthand for “material A supported/deposited onto (at) material B”. In colloid/nanoparticle science it is, perhaps confusingly, convention that A@B refers to “material B around material A” and not vice versa. AuNPs@citrate thus means AuNPs *coated with* citrate molecules, and not AuNPs *at* some citrate substrate. Similarly, AuNPs@silica@PEG would be a gold core–silica shell particle with PEG coated on the silica shell. To not add to the confusion any further, we will follow this convention throughout this thesis.

Table 3.1: overview of thiol-terminated polyethylene glycol ligands. M_W is the (weight) average molecular mass, n the average number of monomer units, L the average contour length and R_0 the root-mean-squared (RMS) end-to-end distance assuming an ideal chain (*theta*-solvent). Values for the Kuhn monomer size were taken from Rubinstein & Colby.^[363, p. 53] r_{NN} and D_{DLS} are the nearest-neighbour spacing from transmission electron microscopy (TEM) and hydrodynamic diameter from dynamic light scattering (DLS) respectively.

ligand	M_W (g/mol)	n	L (nm)	R_0 (nm)	r_{NN} (nm)	D_{DLS} (nm)
citrate	258	-	-	-	17.9 ± 2.4	16.5 ± 3.9
mPEG2k-SH	2000	43	16.1	4.2	18.5 ± 1.6	19.3 ± 2.5
mPEG5k-SH	5000	112	40.1	6.6	20.7 ± 2.0	26.7 ± 2.0
HS-PEG5k-COOH	5000	112	40.1	6.6	26.4 ± 1.9	-
HS-PEG5k-NH ₂ ·HCl	5000	112	40.1	6.6	23.6 ± 2.4	-
mPEG10k-SH	10 000	225	80.3	9.4	25.5 ± 2.8	32.7 ± 3.7

weight are shown. No colour change could be observed visually or with extinction spectroscopy as would be the case upon aggregation of the particles due to coupling of the localised surface plasmon resonances (LSPR) upon close contact, indicating that the particles remained colloidally stable throughout the ligand exchange process. It is clear from transmission electron microscopy (TEM) images and the increase in particle spacing with respect to the unmodified AuNPs@citrate that functionalisation was successful in all cases. The distribution of centre-to-centre nearest neighbour distances in regions with predominantly hexagonal ordering was determined algorithmically for $\sim 10^4$ particles per sample by determining the intensity weighted centroid position and calculating the distances to each particles' 3 nearest neighbours up to a maximum distance of 35 nm (Fig. 3.2F). It is clear that as the M_W of the ligand increases, so does the minimum inter-particle spacing. In particular for mPEG10k-SH there is also a considerable increase in the width of the distribution which could be explained by the increasing ability of the ligand shell to flex and interdigitate with ligands of neighbouring particles during the drying process or a varying number of PEG chains per particle, such that a wider range of inter-particle distances may be accommodated. Of course, such TEM samples are dried and thus the spacing only represents the final stage after drying. Dynamic light scattering (DLS) was used to measure the hydrodynamic sizes of the particles while in aqueous dispersion (Fig. 3.2G) and shows a similar trend. The grafting density was not determined in this work but known from literature to be typically 1 molecule/nm² for mPEG5K-SH, with lower grafting density for higher M_W and vice versa.^[359,360,364,365]

To demonstrate the enhanced stability of the AuNPs@PEG, the particles' stability in various solvents was verified by centrifugation and redispersion. The particles were fully colloidally stable in a wide range of solvents including H₂O, methanol, dimethylsulfoxide (DMSO), tetrahydrofuran (THF), acetonitrile, *N,N*-dimethylformamide (DMF), chloroform and dichloromethane (DCM), and metastable (stable for several days) in ethanol. Unlike the AuNPs@citrate, aggregation was reversible upon addition of good solvents and particles could be fully redispersed in e.g. water after drying. Two examples are shown in Figure 3.3 where ethanol or a concentrated salt solution was added to AuNPs@PEG and AuNPs@citrate dispersed in water. The addition of ethanol stripped the citrate ligands from the NP surface,

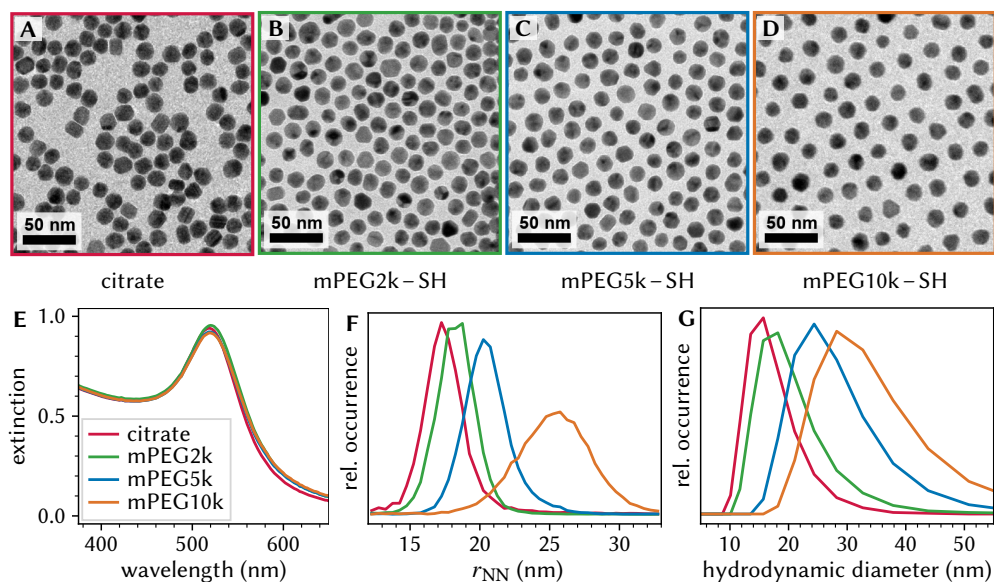


Figure 3.2: Functionalisation of AuNPs@citrate with mPEG-SH of varying M_W . The AuNP cores had a size of 16.10 ± 0.99 nm (6.1 %). **A-D:** TEM micrographs of (dried) AuNPs show an increased spacing between particles with increased ligand M_W , indicative of a thicker/denser organic coating. Note that the organic ligand shell has insufficient electron contrast to be seen directly in these micrographs. **E:** UV-Vis extinction spectra show no shift in the LSPR peak upon functionalisation, indicating no aggregation occurred. **F:** r_{NN} distributions obtained from TEM micrographs. **G:** number-averaged hydrodynamic sizes obtained by DLS of the AuNPs dispersed in water.

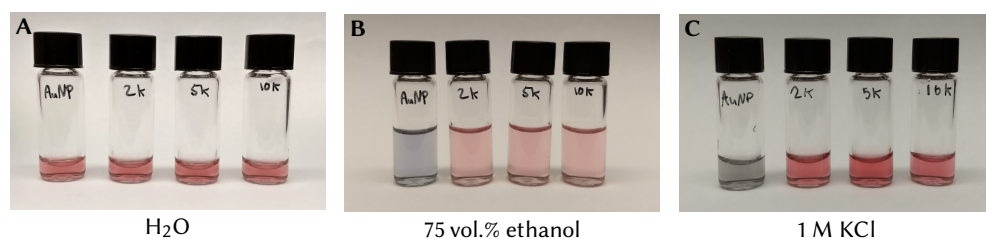


Figure 3.3: enhanced stability of AuNPs@PEG against aggregation. Vials containing from left to right AuNPs@citrate (AuNP), AuNPs@PEG2k (2k), AuNPs@PEG5k (5k) and AuNPs@PEG10k (10k). **A:** dispersed in H₂O as prepared, **B:** after addition of ethanol or **C:** after addition of a concentrated salt solution. The red colour due to the LSPR can be clearly seen, a blue or grey colour indicates aggregation of the particles.

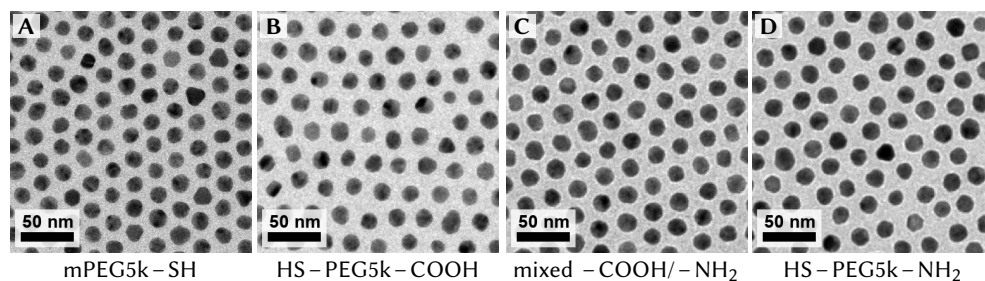


Figure 3.4: Functionalisation of AuNPs@citrate with variously end-functionalized PEG-SH. All particles were made from the same AuNP@citrate cores which had a size of 16.10 ± 0.99 nm (6.1 %).

leading to aggregation of the AuNPs@citrate within seconds, while the more strongly-bound PEG remained on the particles. Since AuNPs@citrate were charge-stabilized, addition of salt also lead to aggregation due to screening of the stabilising surface charges. PEG predominantly provides steric stabilisation, and is therefore compatible with high ion concentrations. That being said, while AuNPs@PEG do not *rely* on charge-stabilisation, some residual charge typically remains on the NP surface after PEG coating. Zeta potentials were measured using DLS and were typically -10 mV to -5 mV for AuNPs@mPEG5k-SH (in 1 mM LiCl in H_2O), compared to typically -50 mV to -40 mV for AuNPs@citrate (in 1 mM trisodium citrate in H_2O).

The ability to alter the surface-charge of the AuNPs without loss of stability due to the strong steric stabilisation of PEG was explored further by ligand exchange using bifunctional PEG molecules –containing a charged end-group opposite the thiol-functionality–. **Figure 3.4** shows that both SH-PEG5k-COOH, containing a (nominally) negatively charged end-group, and HS-PEG5k-NH₂, containing a nominally positively charged end-group, could be grafted onto the particles. Additionally, by adding a 50/50 (mol) mixture both functionalities could be incorporated onto the particles, allowing for some interesting experiments involving *e.g.* a high degree of tunability of the particles' surface charge through tuning of the solvent pH. A clear charge-effect was observed on TEM grids prepared by drop-casting and drying aqueous dispersions of the differently charged AuNPs@PEG onto Formvar/carbon TEM support grids. While mPEG-SH and HS-PEG-COOH capped AuNPs were arranged in typical drying patterns for aqueous systems such as concentrated (multilayer) 'islands' and small coffee-stain rings, the (positively charged) AuNPs@HS-PEG-NH₂ formed a relatively homogeneous monolayer over the entire grid. These differences were attributed to attractive charge-interactions with the carbon support film, which typically had a slight negative surface charge even when not glow-discharged due to the presence of carboxylic acid groups.

In addition to organic ligands, AuNPs may also be coated with a silica-shell. As will be discussed in **Section 3.3** the properties of silica colloids are widely studied and well-understood and hybrid gold-silica particles can thus combine many of the advantageous properties of both materials.^[366,367] This work followed the method by Graf & van Blaaderen *et al.*^[348] where the AuNPs@citrate were first coated with polyvinylpyrrolidone (PVP) by means of physisorption. This facilitated transfer to an ethanol/ammonia/water mixture in which a silica shell could be grown onto the particles under Stöber-synthesis like conditions. Full experimental details are given in **Section 3.7.4**. The shell growth was based on the

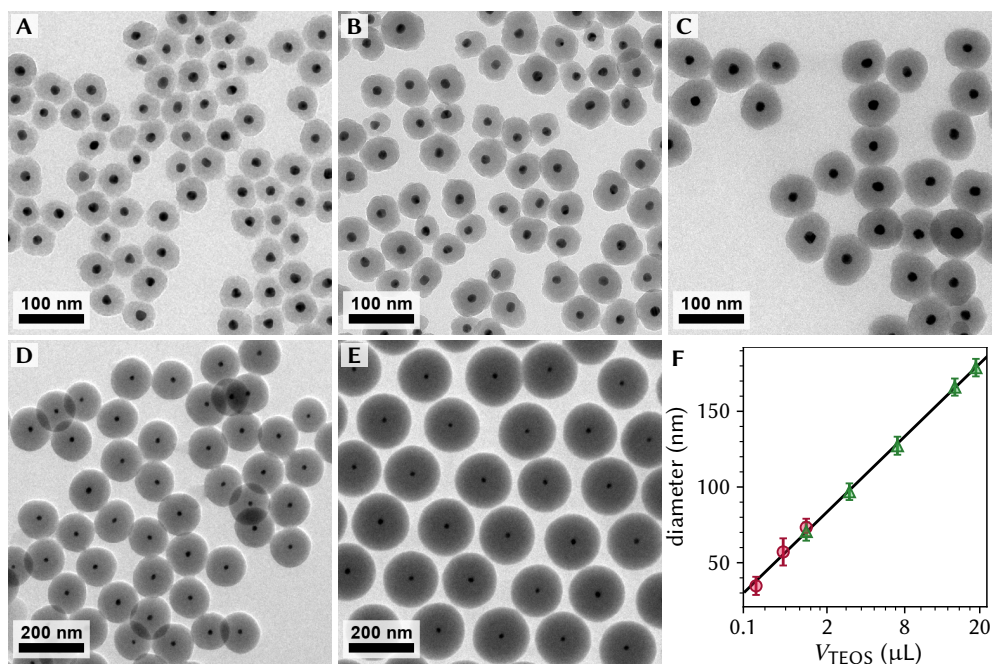


Figure 3.5: silica coating of AuNPs@PVP. A–E: TEM micrographs of AuNPs@SiO₂ with various shell thickness, the total particle diameters were respectively 50.8 ± 6.2 nm (12%), 57.1 ± 9.0 nm (15%), 70.6 ± 6.0 nm (8.6%) 127.0 ± 6.0 nm (4.7%) and 179.0 ± 5.8 nm (3.2%). F: particle diameter as a function of the volume of added TEOS (per mL of AuNP solution), where the x-axis is plotted on a cube-root scale to highlight the linear relationship between the amount of TEOS per particle and the silica shell volume. Error bars indicate the polydispersity; the two colours represent two separate series of stepwise TEOS additions on the same batch of AuNPs@PVP.

reaction of tetraethyl orthosilicate (TEOS)—an organic silicon precursor—with water under alkaline conditions to form silica, SiO₂, in a slow and controlled manner. This was achieved by means of stepwise addition of TEOS with sufficient time in-between steps to allow for all TEOS to react, thus preventing a build-up of unreacted precursor which could have lead to secondary nucleation or an increase in ionic strength and thereby possibly also clustering. Typically, the volume of TEOS added was increased after each addition to account for the increased surface area of the particles as the silica shell grew thicker. The resulting AuNPs@silica after a varying number and/or volume of TEOS addition steps are shown in **Figure 3.5**. It was found that when using AuNPs@PVP from the same batch, the particles could be reproducibly grown to a certain size. However, the trend (indicated with the solid line in **Fig. 3.5F**) varied from batch to batch. Therefore, when specific shell thicknesses are required we recommend to first perform a small scale calibration experiment where a few different shell thicknesses are synthesised to construct such a calibration curve.

The particles synthesised here were used in a recent work of Grau-Carbonell & van Huis *et al.*^[283] (see **Fig. 3.6**) where it was shown *in-situ* using liquid-cell TEM (LC-TEM) that silica closer to the AuNP core can be preferentially etched away due to its more porous nature than the silica near the outer surface. This is a result of the inclusion of PVP close to the gold and

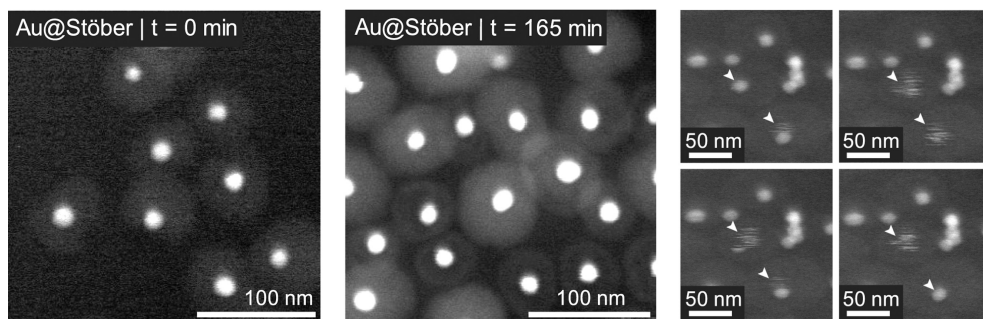


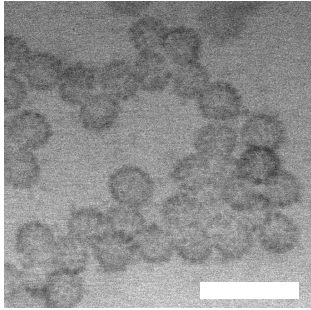
Figure 3.6: LC-TEM observation of the etching of AuNPs@SiO₂ into rattle-type particles. After etching using a 100 mM aqueous NaOH solution at a flow rate of 5 $\mu\text{L}/\text{min}$, silica is removed and hollow shells remain. On the right-hand side movement of some of the AuNP cores (indicated by white arrows) can be seen. The total accumulated electron dose was $1.5 \cdot 10^3 \text{ e}^-/\text{nm}^2$. Reprinted under CC BY-NC-ND 4.0 license from Grau-Carbonell & van Huis *et al.*^[283] Copyright 2021 the authors.

the more condensed nature of the silica near the surface. This etching leaves the core loose within a void surrounded by the remainder of the silica-shell. These rattle-type particles are an interesting model system for studying interactions of NPs in confinement due to the well-defined and highly controllable geometry. Indeed, co-workers Welling & van Blaaderen *et al.*^[295] recently demonstrated such measurements of the interaction potential between an AuNP core and silica shell in similar rattle-like particles using LC-TEM; one of the first examples of measurement of true nano-scale NP interactions using LC-TEM where the interactions were not induced or heavily affected by effects of the e-beam.

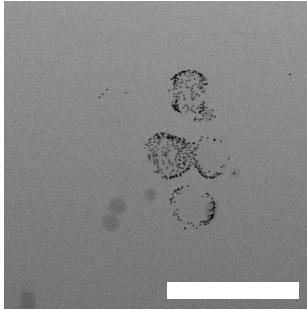
AuNPs here were also used as functionalised markers to enhance the electron contrast in LC-TEM experiments. Poly(*N*-isopropylacrylamide), PNIPAm, is a thermoresponsive polymer which in water (amongst others) can undergo a volume phase transition: PNIPAm dissolves at room temperature—leading to a swollen state—but collapses in on itself above a critical solution temperature (around 32 °C in water). PNIPAm microgel particles, *i.e.* colloidal polymer particles, can thus change their size based on the temperature: a property that has attracted significant attention in the literature.^[82,193,369] Due to the low electron contrast of PNIPAm, particularly in the swollen state where a significant fraction of the particles' volume is occupied by the surrounding solvent, direct observation of the extent of the particle size is challenging. Instead, AuNPs were used to decorate the surface of PNIPAm colloids to act as high-contrast markers in LC-TEM, results are shown in **Figure 3.7**. It was found that differently functionalised AuNPs had a varying tendency to adsorb onto the particle. AuNPs@SiO₂ demonstrated spontaneous adsorption to the surface of the microgel particles without the formation of separate aggregates, making it possible to enhance electron contrast of the PNIPAm particles and observe the volume phase transition. AuNPs@citrate and AuNPs@mPEG-SH, and AuNPs@HS-PEG-COOH only showed beam-induced adsorption. AuNPs@HS-PEG-NH₂ adsorbed selectively to the silicon nitride window due to charge interactions, as the window has a negatively charged surface.

3.2.2 CTAC stabilized AuNPs (30–140 nm)

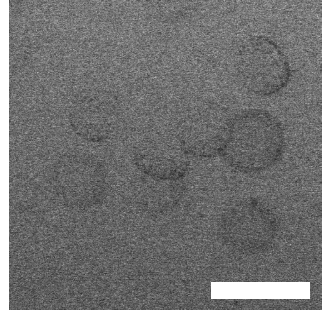
Preparing spherical AuNPs larger than ~30 nm is remarkably challenging. Weakly coordinating ligands such as citrate are increasingly unable to stabilize particles against aggregation

A SiO₂ NPs

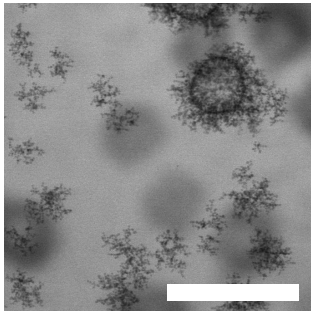
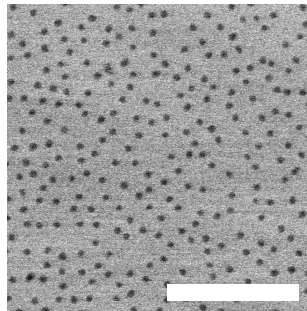
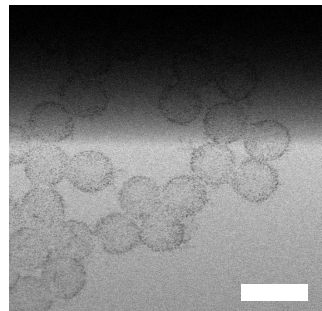
B AuNPs@citrate



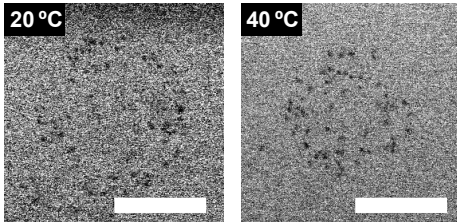
C AuNPs@mPEG-SH



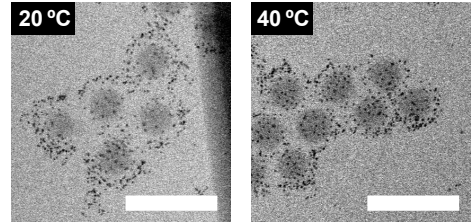
D AuNPs@HS-PEG-COOH

E AuNPs@HS-PEG-NH₂F AuNPs@SiO₂

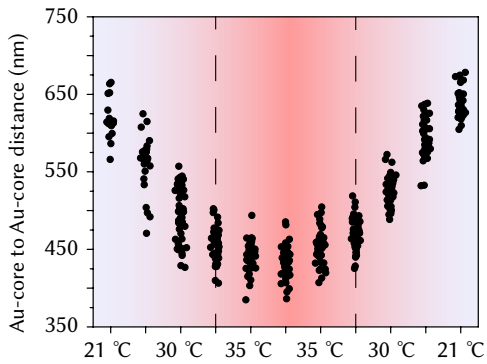
G



H



I



J

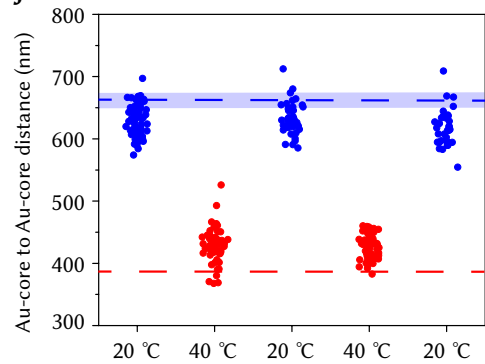


Figure 3.7 (left): AuNPs as high-contrast markers in LC-TEM of PNIPAm microgels. PNIPAm microgels dispersed in water were decorated with AuNPs for enhanced contrast and imaged using a LC-TEM chip with silicon nitride windows. **A–F:** PNIPAm microgels decorated with differently functionalised AuNPs show different adsorption behaviour. Scale bars: 1.5 μm (A–D,F) 0.5 μm (E). **G:** PNIPAm decorated with AuNP@SiO₂ above and below the critical solution temperature. Scale bar: 400 nm. **H:** silica@PNIPAm decorated with AuNPs@silica. Scale bar: 750 nm. **I–J:** detailed evolution and reversible cycling of PNIPAm microgel size measured using the AuNP@silica markers. Dashed lines indicated PNIPAm size obtained from DLS, the shaded blue area is the size obtained from cryo-TEM imaging. Adapted with permission from Grau-Carbonell & van Huis *et al.*^[368]

as the particle size increases, due to the strong Au–Au van der Waals interactions and due to the ability of gold to cold-weld. On the other hand, more strongly stabilizing ligands such as cetyltrimethylammonium bromide (CTAB) and chloride (CTAC) can stabilize larger particles but tend to bind preferably to specific gold facets, leading to faceting / shape control and thus non-spherical particles. To overcome these issues, synthesis procedures for >30 nm spheres tend to rely on stepwise seeded growth where the AuNPs are diluted and used as seeds in each subsequent step^[85,370–372] or on slow growth using soft reducing agents^[364,373] or slow addition of precursors using syringe pumps.^[374,375] Rather than trying to make monodisperse *and* spherical AuNPs directly in a single step, it has also been shown that it is possible to first synthesise monodisperse but strongly faceted polyhedral particles, and convert these faceted particles into smooth spheres in a separate soft etching step^[376–378] or by incorporating etching agents during NP growth.^[342,379] Because of strong passivation of certain facets by ligands (leading to nonspherical faceted particle shapes) and the dependence of growth rate on the degree of coordination of the surface atoms and thus on the radius of curvature, particles can be grown with low polydispersity in the particles' volume under these conditions compared to *e.g.* citrate-based methods.^[341]

Here we used such a seeded growth–etching procedure by Hanske & Liz-Marzán *et al.*^[378] for synthesis of large AuNPs@CTAC. The synthesis steps are schematically outlined in **Figure 3.8A** and detailed experimental methods are given in **Section 3.7.5**. First ~2 nm monocrystalline pre-seeds were synthesised by rapid reduction of aqueous HAuCl₄ using sodium borohydrite (NaBH₄) in the presence of CTAC, which is a widely used method for obtaining high-quality monocrystalline seed particles for a variety of AuNP syntheses.^[380] Because these pre-seeds degrade through Ostwald ripening within hours after synthesis, they were grown further in a second step to the final seed particles of ca. 10 nm, using ascorbic acid as a more gentle reducing agent.^[338] The seed particles were then used in a second seeded growth where they were grown directly to a size slightly larger than the the desired final particle size. The particle size was tuned by varying the volume of seed solution added while keeping [ascorbic acid] and [HAuCl₄] constant. Finally, a small amount of sodium hypochlorite (bleach) was added to selectively etch vertices and edges and smooth the surface of the particles to obtain highly spherical particles. For particles larger than ~50 nm a small amount of HAuCl₄ solution was additionally added to increase the etching rate since a larger amount of material needed to be etched. During the etching procedure, small samples were periodically taken for UV-Vis spectroscopy to monitor the progression of the etching. The etching was found to be self-terminating, at which point the extinction spectrum remained constant and the reaction was assumed to be complete. Finally,

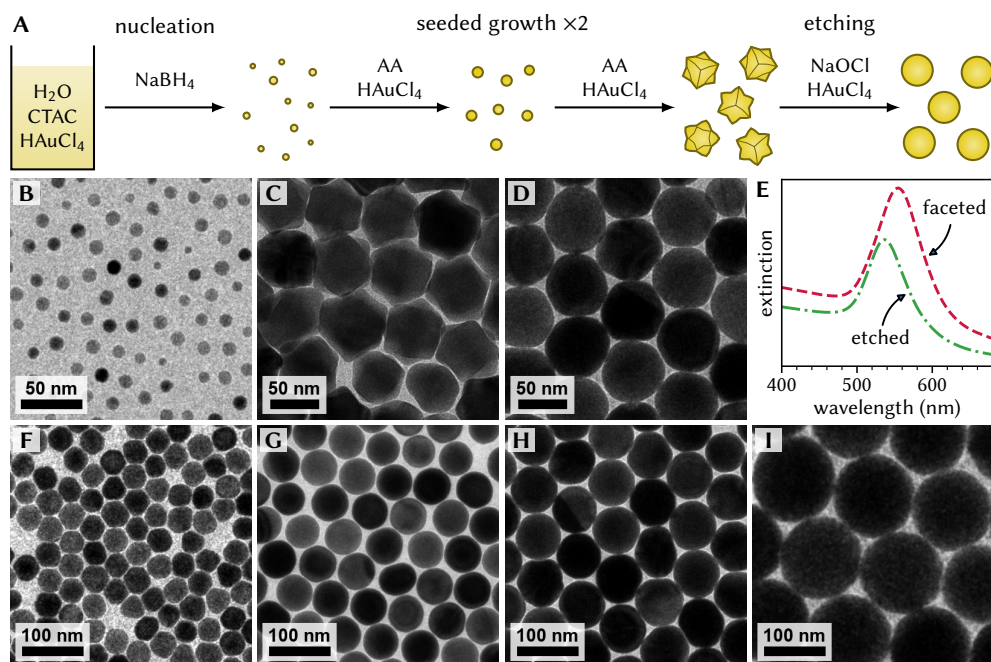


Figure 3.8: synthesis of spherical AuNPs@CTAC. **A:** schematic depiction of the reaction steps. **B:** TEM micrograph of the AuNP seeds used in the synthesis of C–I, the seeds had a mean diameter and polydispersity of 10.6 ± 1.6 nm (15%). **C,D:** TEM micrographs of AuNPs before (C) and after (D) etching. **E:** UV-Vis extinction spectra corresponding to the samples shown in C&D, just before adding the etching agent and at the end of the etching step (prior to washing) respectively, such that the particle concentration was (nearly) the same. **F–I** spherical (etched) AuNPs obtained by varying of the amount of seed particles added in the seeded growth step, scale bars are 100 nm, the sizes and polydispersities for F–I are respectively 41.7 ± 2.5 nm (6.0%), 57.7 ± 4.9 nm (8.4%), 76.9 ± 6.8 nm (8.8%) and 140.0 ± 7.1 nm (5.0%).

the particles were washed with centrifugation to remove leftover reactants and redispersed as concentrated stock dispersion with some added excess CTAC ligand to assure full surface coverage and long-term stability of the particles.

TEM images and optical properties of the resulting particles before and after etching are shown in **Figures 3.8** and **3.9**. The majority of the seed particles were approximately 10 nm in diameter and monocrystalline as evidenced by the homogeneous contrast in BF-TEM images.* After the seeded growth step, strongly faceted particles were obtained which consisted predominantly of concave rhombic dodecahedra and trisoctahedra. Some triangular bipyramids were also observed, which were likely formed due to the presence of a small fraction of seed particles with twinning defects. After the etching step, the particles were highly spherical with a typical average aspect ratio < 1.03 based on a best-fit ellipse of

* bright field TEM contrast of AuNPs is predominantly due to diffraction contrast, which is strongly dependent on the crystal orientation with respect to the electron beam. Different crystal domains thus often show up with different darkneses, see e.g. **Fig. 3.2** where contrast variations due to twinning defects can be seen within the particles.

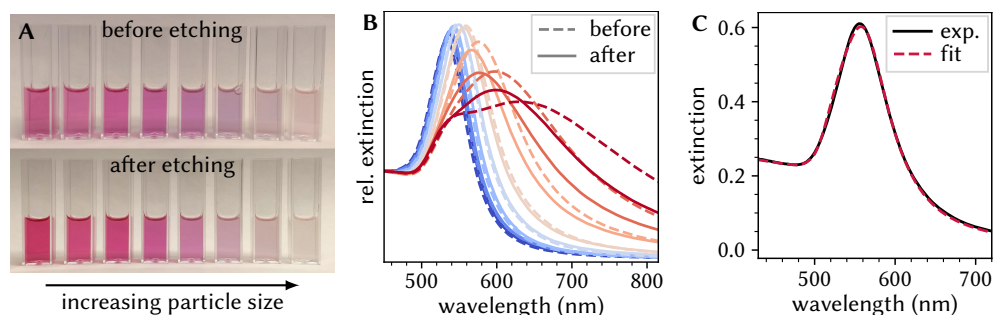


Figure 3.9: optical properties of AuNPs@CTAC. **A,B:** photographs and corresponding UV-Vis extinction spectra before and after etching, for particle sizes see [Table 3.2](#). The spectra were normalized to the extinction at 450 nm, which is proportional to $[\text{Au}^0]$ and mostly shape-independent. **C:** experimental extinction spectrum and corresponding ensemble Mie theory fit for particles of $D_{\text{ext}} = 78.4 \pm 7.6$ nm (after etching).

the particle contours in the TEM images, without any increase in polydispersity. Some ellipsoidal particles (aspect ratio ~ 1.3) were observed which we attribute to the incomplete etching/reshaping of the more elongated triangular bipyramid shape impurities, as well as in some cases a small number of smaller particles due to secondary nucleation in the seeded growth step.

The optical extinction due to the LSPR of the etched particles ([Figure 3.8E](#)) was blue-shifted with respect to the faceted particles due to shape effects, while the lower peak extinction value could be attributed mostly to the slight reduction in volume of the particles. To further verify the optical properties and particle sizes of the AuNPs, we calculated theoretical extinction spectra for spherical AuNPs based on Mie theory,^{[381],[382, pp. 477–482]} further details are given in [Section 3.7.15](#). Experimental data were fitted with ensemble spectra constructed by taking a weighted sum of single-particle spectra for a normally distributed range of particle-sizes, using the mean, standard deviation and area of the normal distribution as fit parameters. Particle sizes obtained from UV-Vis were compared to sizes measured with TEM and are given in [Table 3.2](#). An excellent agreement was found, likely owing to good plasmonic quality of the particles due to their high sphericity and monocrystallinity. Since the final size is limited by the total amount of gold present for each seed particle, a linear relationship is expected between the final particle volume and the inverse of the volume of seed solution, or correspondingly between particle size and the inverse cube root of the amount of added seeds. As can be seen in [Figure 3.10](#), such a trend is indeed observed.

In general, we found typically 1.5 to 2 times higher polydispersity than reported in the original paper,^[378] although it was below 10 % in most cases. With two exceptions the polydispersity was predominantly the result of a secondary population of smaller particles, and not due to a wide distribution of the main population which had a typical polydispersity $< 5\%$. The presence of this secondary population was observed both before and after etching, indicating that they are unlikely to originate from the etching procedure. Rather, we note that a secondary population was also observed in the seed particles (see [Fig. 3.8B](#)) and speculate that poorer quality seed particles are the cause for the higher polydispersity when compared

V_{seed} (μL)	$V_{\text{Au}^{3+}}$ (μL)	C_{Ext} (nM)	$D_{\text{Ext.}}$ (nm)	D_{TEM} (nm)
200	0	72.5	41.9 ± 6.8	41.7 ± 2.5
100	0	36.4	49.9 ± 4.0	48.2 ± 3.0
50.0	1.0	25.2	58.1 ± 3.8	58.3 ± 3.1
25.0	2.5	13.0	69.2 ± 3.7	62.4 ± 5.8
12.5	3.5	6.99	78.4 ± 7.6	78.0 ± 5.1
6.3	4.0	2.80	104.0 ± 6.9	104.0 ± 7.5
3.1	6.0	1.82	129.0 ± 7.2	123.0 ± 11.0
1.6	10.0	1.01	146.0 ± 3.5	140.0 ± 7.0

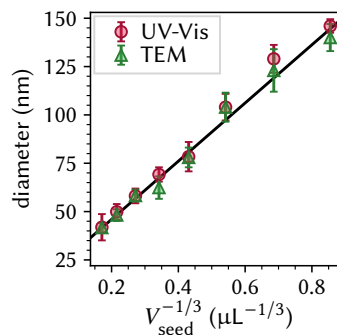


Table 3.2 & Figure 3.10: overview synthesis parameters and resulting sizes for AuNPs@CTAC.

Parameters and results for a series of synthesis batches are given where C_{Ext} is the particle concentration based on fitting of extinction spectra and D_{Ext} and D_{TEM} refer particle sizes obtained from extinction spectroscopy and TEM respectively. The final particle sizes are plotted against the inverse cube root of the amount of seed particles, to highlight the inverse relation of the number of seeds to the final particle volume (the solid black line is added as a guide for the eye). Error bars indicate polydispersities.

to the results by Hanske & Liz-Marzán *et al.*^[378] The relationship between the volume of added seed solution and particle size was consistent when using seeds from the same batch of seed particles (as seen in Fig. 3.10), however the exact relation varied between different seed particle batches, and indeed the particle sizes found in this work vary slightly from those reported in the work of Hanske & Liz-Marzán *et al.*^[378] at comparable synthesis parameters. This can be attributed due to variations in particle concentration in the seed particles and we recommend performing a set of two or three small scale syntheses for calibration purposes for each new batch of seed particles if a specific particle size is desired. Lastly, it was found that the etching was sensitive to the concentration and quality of the NaClO solution as complete etching was not achieved using the standard etching parameters when using a bottle of NaOCl that had been opened more than 6 months prior, and etching rates were found to be more than 2× lower. However, when a freshly opened bottle was used the etching could be reliably reproduced for all particle sizes.

The AuNP@CTAC samples given in Table 3.2 were all synthesised at a 10 mL reaction scale. To obtain a larger quantity of AuNPs, several batches of particles were synthesised after scaling up the synthesis to 250 mL or 400 mL growth solution (seed synthesis was not scaled up). The results were comparable to those of the smaller scale syntheses, confirming the scalability of the method without major alterations. While the CTAC capped particles are highly stable and can be stored long-term in a 5 mM CTAC solution, the CTAC may be removed when the particles are washed repeatedly with pure water or other solvents. To achieve compatibility with a wider range of solvents, the particles could be coated with thiolated PEG molecules in a manner similar to that discussed in Section 3.2.1, although exchange was slower due to the stronger CTAC–Au interactions when compared to citrate. Further details of the PEG coating can be found in Section 3.7.6. The ability to produce larger batches of PEG-coated particles of >30 nm in size was found to be of utility *e.g.* for the work in Chapter 4 where the particle dispersions had to be tens or hundreds of times more concentrated than during synthesis, while still retaining a sufficient sample to be

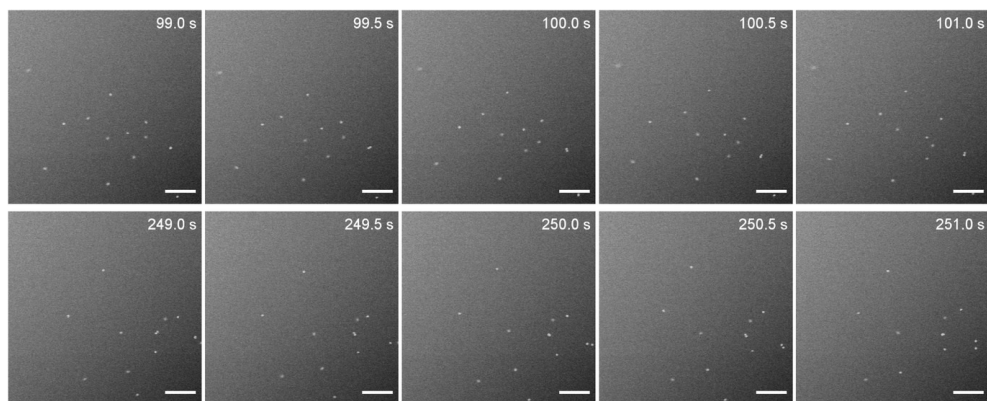


Figure 3.11: Observation of freely diffusing AuNPs using LC-TEM. 77 nm AuNPs were dispersed in 98 vol.% glycerol/water and loaded into a LC-chip with two 50 nm silicon nitride windows, and imaged in HAADF-STEM mode at a frame rate of 2 Hz and a dose rate of $9 \text{ e}^- \text{ nm}^{-2} \text{ s}^{-1}$. Scale bars are 1 μm . From particle tracking an ensemble averaged diffusion constant of $(8.8 \pm 0.1) \cdot 10^3 \mu\text{m}^2/\text{s}$ was found which was in good agreement with theoretical calculations for free diffusion. Adapted from Welling & van Huis *et al.*^[272] (copyright 2020, CC BY-NC 4.0).

handled practically in the lab. The larger size meant that direct observation of the particles' reflection/scattering in confocal laser scanning microscopy (CLSM) was feasible for freely diffusing particles, as well as being well-suited for EM studies. Additionally, one of the batches of AuNPs@PEG synthesised here were also used in work by Welling & van Huis *et al.*^[272] (Fig. 3.11), where the large size and electron contrast made it possible to make in-situ observations using LC-TEM in a liquid-cell chip with a relatively thick liquid layer at low-dose conditions. In this way, un-damped free Brownian diffusion (not affected by e-beam effect) of NPs was observed for the first time using LC-TEM.^[272]

3.2.3 2–10 nm oleylamine stabilised AuNPs

For studying interactions at the smallest scale we utilised a widely used synthesis method originally developed by Peng & Sun *et al.*^[383] (based on the earlier work of Zheng & Stucky *et al.*^[384]) for the synthesis of monodisperse AuNPs below 10 nm, since it is reported to produce highly monodisperse particles in this size range compared to other methods and it is widely used in the literature. The procedure, like the Turkevich & Frens method, works using a single step reduction of HAuCl_4 , but unlike most AuNP syntheses this method is performed in apolar solvents and yields hydrophobic AuNPs using oleylamine (OAm) ligands. These ligands provide strong steric stabilisation which allows for anti-solvent precipitation to be used to wash the particles, as well as for the particles to be fully redispersed after *e.g.* completely drying a sample. Tert-butyl aminoborane complex (TBAB) is used as a reducing agent, as it is compatible with hydrophobic solvents. It is effectively a precursor to the active BH_3 molecule which can donate a total of 6 electrons to fully reduce two Au^{3+} atoms.^[385] The use of TBAB leads to a faster gold reduction rate than *e.g.* citrate but not as fast as NaBH_4 . The high reaction rate leads to the formation of relatively small particles of typically 4 nm, although the exact reaction rate and thus particle size may be tuned by varying the reaction temperature.^[383] Furthermore, the reaction is performed at a 100 \times higher gold concentration

than the Turkevich & Frens method, allowing for larger quantities of particles to be produced without needing to scale up to large (>1 L) reaction volumes.

Full experimental details are given in **Section 3.7.7**, but in short: the reaction was performed by dissolving the gold precursor in a 50/50 mixture (by volume) of tetralin, an organic solvent, and oleylamine, which doubles as solvent and ligand, yielding a dark orange solution. The mixture was placed in a closed flask under light nitrogen flow and a TBAB solution was rapidly injected with a syringe to initiate the reaction. The colour changed within seconds to a brownish or reddish black, depending on the temperature (and thus particle size). The reaction was left to continue for at least 1 hour to ensure complete conversion, after which the particles were washed using repeated anti-solvent precipitation followed by centrifugation and redispersion in hexane. The synthesis was performed at various temperatures between 2 °C to 20 °C by using a water-ice-bath or heated water bath to obtain varying particle sizes. When larger particles were desired, it was also possible to perform a seeded growth of the particles (for details see **Sec. 3.7.8**): gold precursor was dissolved in a mixture of OIAm and 1-octadecene and placed in a closed flask under N₂ flow. Then, a small amount of AuNPs@OIAm was rapidly injected, and the flask was placed in an oil bath at 60 °C and left to react for 2 h.

TEM images and size distributions of AuNPs synthesised at three different temperatures are shown in **Figure 3.12**. As expected, the particle size decreased with increasing temperature consistent with the work of Peng & Sun *et al.*,^[383] although the temperature effect was less strong in our case and we obtained smaller particles than reported at each temperature with sizes of 4.7, 4.3 and 3.2 nm at 30, 21 and 1 °C whereas Peng & Sun *et al.*^[383] reported 9.5, 6.4 and 4.3 nm under similar conditions. This trend of smaller particle size than in the literature was consistent over many experiments, with *e.g.* room temperature synthesis yielding particles with a typical size of 4.0 nm to 4.5 nm where most groups report particles between 5 nm to 6 nm,^[383,386–389] although similarly smaller particles have also been reported by others.^[390–392] In some cases, batches with a mean diameter as small as <3 nm were obtained under similar reaction conditions. The particles we obtained had typically higher PDs than reported in the literature, although it should be noted that below 4 nm the electron contrast of AuNPs significantly dropped off (making accurate size determination from TEM challenging), that smaller particles typically have higher relative PD, and that we report the size and PDs of the Au core only whilst the particles in their totality including ligands are significantly more uniform in size owing to the monodisperse nature of the molecular ligands. The lower relative *total* polydispersity is also evidenced by the tendency of the AuNPs to form ordered hexagonal patterns or even full crystals upon drying.

AuNPs were obtained in all cases, but large differences were seen between different batches of AuNPs that were produced under seemingly similar conditions. **Figure 3.13** shows a number of batches which were all synthesised using the same concentrations and synthesis parameters as the particles in **Figure 3.12B**. Major differences in size and PD are seen, demonstrating the poor reproducibility of the synthesis method in our lab. Peculiarly, in a considerable number of cases the AuNPs@OIAm exhibited bidisperse size distributions, *i.e.* there were two distinct populations with different size. In a majority of samples, there was a minor population of ca. 5 nm particles (comprising typically <10 % of the particles) aside from the major/main population of smaller particles. This can be seen for example in **Figs. 3.12A** and **3.12B**, with extreme cases exhibiting two populations with narrow size distributions with a more than three-fold size difference between them such as seen in **Figs. 3.13E** and **3.13F**.

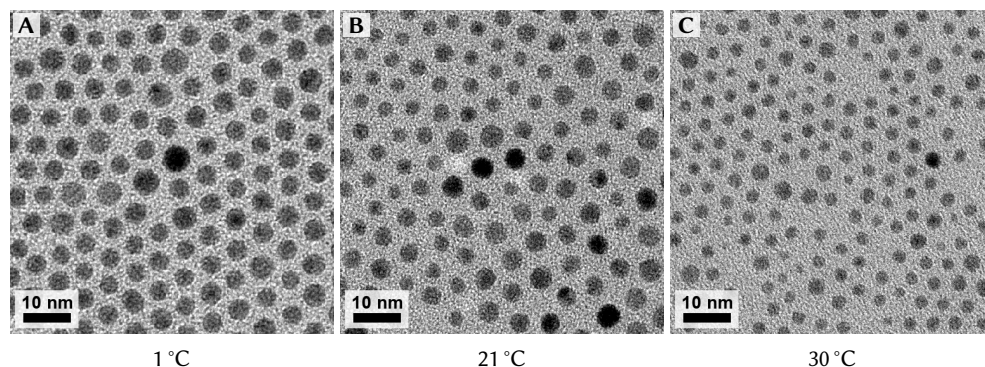


Figure 3.12: effects of reaction temperature on AuNPs@OIAM synthesis. Three batches of AuNPs@OIAM synthesised in identical manner except for the reaction temperature. The particle sizes for **A–C** were respectively 4.7 ± 0.6 nm (12%), 4.3 ± 0.7 nm (16%) and 3.2 ± 0.5 nm (15%). Note that these values refer exclusively to the gold core and do not include the size of ligands.

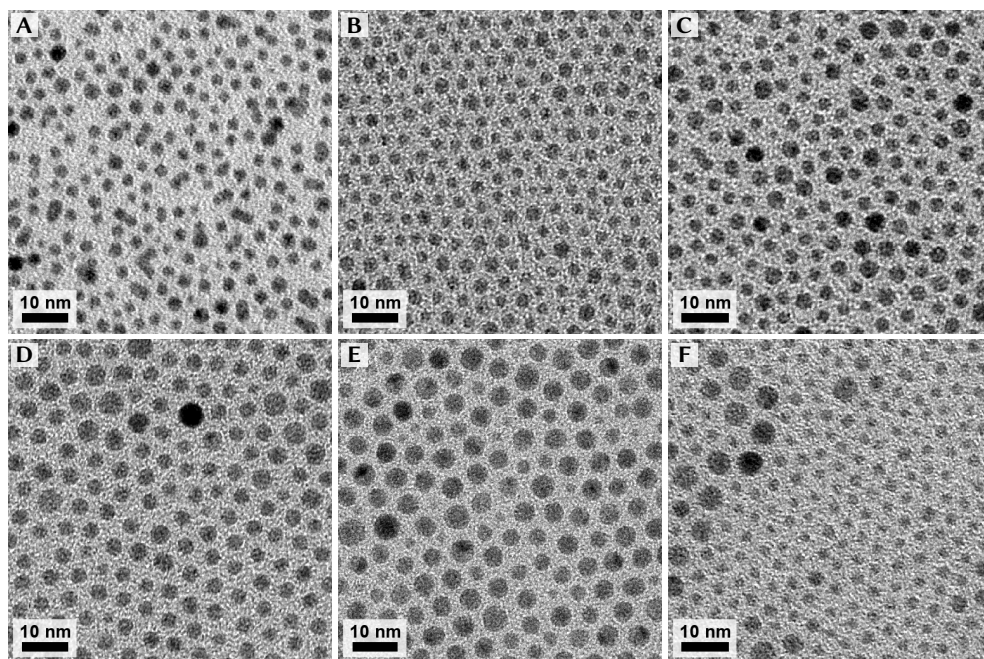


Figure 3.13: batch to batch variations in synthesis of AuNPs@OIAM. All batches were synthesized at room temperature using similar reaction conditions. The mean size and PD were: **A**: 2.3 ± 0.7 nm (31%), **B**: 2.9 ± 0.6 nm (20%), **C**: 3.2 ± 0.6 nm (18%), **D**: 3.9 ± 0.7 nm (7%), **E**: 4.4 ± 1.1 nm (24%) and **F**: 3.2 ± 1.2 nm (36%).

Fortunately, it was possible to further purify particles using size-selective precipitation (SSP). SSP works because particles of different sizes precipitate at different solvent to anti-solvent ratio, it was found that for AuNPs@OLAm the ratio required for precipitation was strongly size dependent, with larger particles precipitating out at lower anti-solvent fraction. **Figure 3.14** shows the results of SSP on a polydisperse batch, demonstrating the ability to improve the monodispersity of the AuNPs. In case of such a large size difference between the populations we achieved a >95 % selectivity in a single step. However, we found SSP to be highly effective even for purification of AuNP batches which had a secondary population with a size difference as low as 0.5 nm, although in such cases it was not possible to split the two populations without some overlap. Instead we optimised the solvent/anti-solvent ratio to obtain one 'pure' fraction with a narrow size distribution, and one 'mixed' one which contained all size-impurities and typically some of the main population. Using SSP it was possible to reliably obtain AuNP batches with an acceptable PD (< 10 %).

When larger particles were desired than could be synthesised directly, SSP-purified batches could be grown further using seeded-growth. In seeded growth, no TBAB reductant was added. Instead, oleylamine was used at elevated temperature as softer reducing agent to gradually convert the gold precursor without inducing secondary nucleation. While it is possible that the octadecene solvent also acts as (co-)reductant, this is not critically important because seeded growth was also successfully achieved in hexadecane (which only contains saturated carbon-carbon bonds). TEM micrographs and particle size histograms for particles after one and two seeded growth steps are shown in **Figure 3.15**. We found that seeded growth on particles of a starting size of at least 4 nm reliably lead to an increase in particle size without the formation of new particles (secondary nucleation) or an increase of the PD. When smaller 3 nm seeds were used the (absolute) PD increased more than twofold during seeded growth. We attribute this to the lower (chemical) stability of smaller particles and increased Ostwald ripening rate at elevated temperature.

The cause of batch to batch variations in the initial synthesis was studied in some detail, and a variety of control experiments was performed in an attempt to elucidate the hidden variables affecting the reaction. The following parameters were investigated:

Manner and rate of TBAB addition:

Rapid burst-nucleation events such as occurs upon TBAB injection in this synthesis are often sensitive to mixing and injection rates, since slow injection may extend the window in which new nuclei are formed whilst earlier nuclei have already undergone significant growth. Two syntheses were performed side-by-side in identical manner and using the same reactant solutions, with the only difference being that in one sample the TBAB solution was injected rapidly (~0.5 s) while in the other the TBAB was added dropwise over the course of ~30 s. The resulting particle dispersions were both strongly bi-disperse with nearly identical sizes and PDs. Other cases where TBAB was added more slowly or in two stages yielded more monodisperse particles, implying that the TBAB addition rate is not a major contributor to batch to batch variations.

Age and purity of reactants:

Gold precursor was of high purity, highly stable over time and purchased in small quantities and sealed under N₂ atmosphere after use to prevent moisture accumulation, and therefore unlikely to vary between syntheses. Oleylamine is well known to vary in purity from batch to batch due it being derived from natural feedstock (beef tallow), which is known to affect

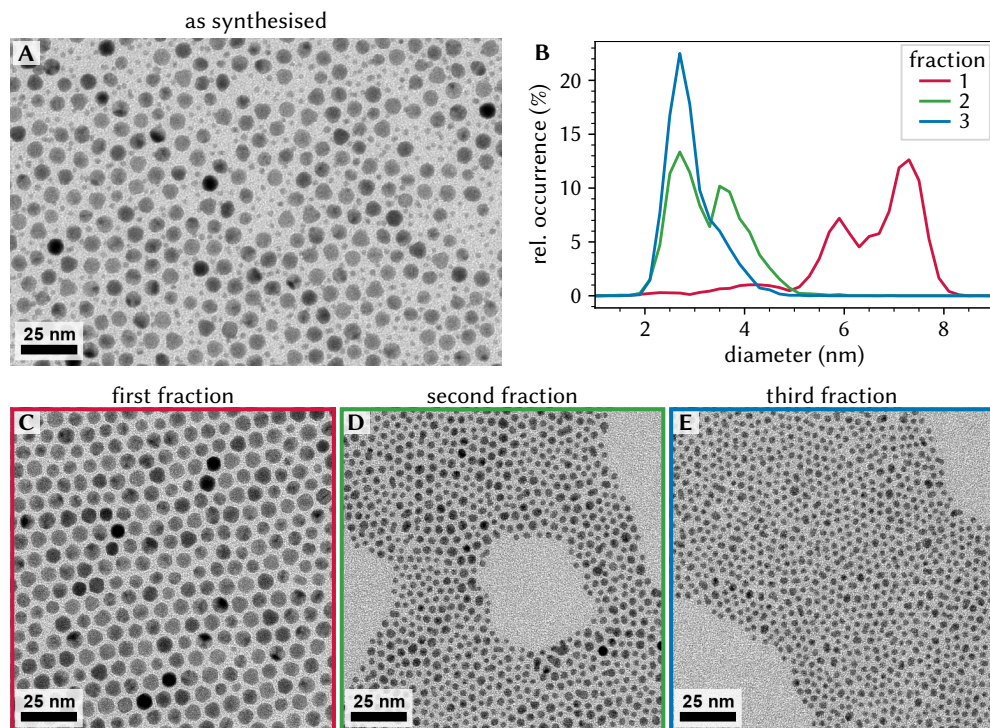


Figure 3.14: size-selective precipitation of polydisperse AuNPs@OIAm. A polydisperse particle batch (as synthesised) was split into three fractions by subsequent SSP steps by removing the sediment and adding additional anti-solvent between each step. **A:** TEM micrograph of the original (as synthesised) particles. **B:** particle size histograms for the three SSP fractions from TEM size measurements. **C–E:** TEM micrographs of the three SSP fractions after separation.

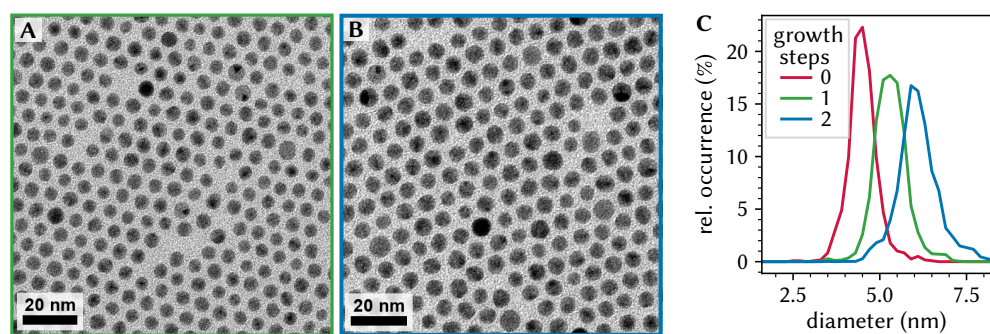


Figure 3.15: sequential seeded growth of AuNPs@OIAm. The original seed particles had a size of 4.5 ± 0.4 nm (9 %) (not shown here). **A:** particle size histograms for the seed particles and the two growth steps. **B:** the particles after one seeded growth step with a size of 5.3 ± 0.5 nm (9 %). **C:** resulting particles after a seeded growth step using the particles in **B** as seeds, the particle size was 6.1 ± 0.6 nm (10 %).

nanocrystal synthesis.^[393-395] Furthermore, the double bond in oleates is known to be able to act as reducing agent in metal NP synthesis,^[396-398] adding another pathway through which its age and purity may affect synthesis results. However, both freshly purchased OLAm and OLAm from bottles which had been opened >1 year ago were used, for both technical grade (70 %) and synthesis grade (80 % to 90 % C₁₈ content) OLAm, and no trend could be observed with regards to particle size or PD. Varying results were seen using OLAm from the same stock mere days apart. TBAB is sensitive to moisture and was found to degrade over time due to oxidation even while stored in a N₂ flow cabinet. However, the effect of older TBAB was found to be consistent with a lower reduction strength comparable to adding a smaller amount of (fresh) TBAB, and did not explain the bi- or poly-dispersity as this was also observed using freshly purchased TBAB.

Reactant concentration:

The reaction was typically performed at 2× higher concentrations of Au³⁺ and TBAB than in the work of Peng & Sun *et al.*^[383] (similar to *e.g.* Elbert & Murray *et al.*^[388]), but it was verified that this twofold increase in the absolute concentration did not affect the particle size and PD, provided the ratio of TBAB to gold was not altered. OLAm is present in large excess in either case, and it is therefore unlikely that the precise concentrations have a profound impact on the resulting particles. Experiments in which the concentration of gold was kept constant but the TBAB concentration was varied between 0.5 to 2× the standard amount (2:1 TBAB:Au³⁺ molar ratio) showed a slight decrease in particle size with increasing [TBAB] but no major influence on the PD or the occurrence of bi-disperse batches. Lowering the TBAB:Au³⁺ ratio below 1 resulted in a drastic increase in PD as well as the formation of larger nonspherical particles.

Reaction duration:

Reaction time varied between 1 h to 3 h, but this did not correlate with size or PD. A series of small samples for TEM imaging taken at regular intervals after TBAB addition revealed that the particles reach their final size within the first 15 min (at room temperature) and no major changes were observed beyond that point.

Degassing time:

The HAuCl₄ solution was always placed in a closed flask under N₂ flow immediately after preparation (which took at most a few minutes), but the time for which it was stirred under N₂ flow prior to injection of the TBAB solution varied, being typically between 15 min and 30 min. Although no clear trend was observed between this degassing time and the resulting particle polydispersity, this was not systematically varied. The manner in which the nitrogen atmosphere was achieved was less well-controlled than full schlenk-line conditions and it is possible that the (varying) presence of residual water or oxygen affects the reaction. Alternatively, it may be that some reactions already take place prior to the addition of TBAB such as the formation of OLAm-Au complexes or the partial reduction of Au³⁺ by OLAm, either of which could be sensitive to the reaction time. That being said, reduction of Au³⁺ to Au⁺ would be accompanied with a disappearance of the bright orange colour of the solution (as this originates from a charge-transfer band of Au³⁺-chloride complexes), but this was not observed. Full reduction of Au³⁺ to metallic gold (Au⁰) is not typically achieved using oleate.

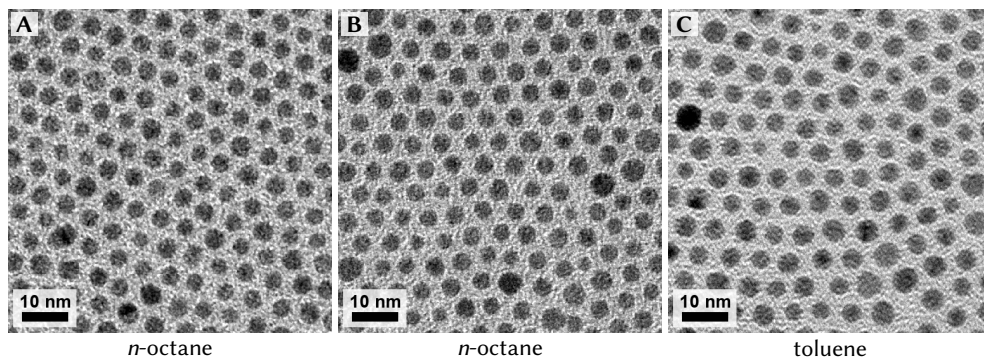


Figure 3.16: AuNP@OIAM synthesis in alternate solvents. All three samples were synthesised at 21 °C. **A:** AuNPs@OIAM synthesised in *n*-octane, the particle size was 4.2 ± 0.4 nm (10 %). **B:** AuNPs@OIAM synthesised in *n*-octane using 0.5 mmol TBAB (1:1 TBAB: Au³⁺, half the normal amount), the particle size was 4.3 ± 0.5 nm (12 %). **C:** AuNPs@OIAM synthesised in toluene using 0.5 mmol TBAB, the particle size was 4.5 ± 0.5 nm (12 %).

Solvent choice:

In their original paper, Peng & Sun *et al.*^[383] did not comment on the reasoning for the choice of tetralin as solvent. It has been suggested that tetralin is actually a rather poor solvent for this reaction, and that more monodisperse particles may be obtained when replacing tetralin with linear alkanes such as hexane or octane.^[385] Furthermore, in that work it was also found that the particle size may be tuned by varying the ratio of TBAB to Au³⁺, with higher [TBAB] giving smaller particles, or by the choice of solvent, with *e.g.* benzene and toluene giving larger particles (>7 nm) than hexane or octane (5 nm). We performed several syntheses at room temperature using *n*-octane instead of tetralin, and with varying TBAB concentrations. TEM images of the resulting particles are shown in **Figure 3.16**. We indeed found that more monodisperse particles were obtained in octane when compared to particles synthesised under similar conditions in tetralin. This is likely because linear alkanes are better solvents for OIAM capped particles, being more able to interpenetrate the ligand shell and solvate the ligands. We also found that the gold precursor and TBAB dissolved much faster in octane than in tetralin. In our experiments, no strong influence of the choice of solvent on the particle size was observed with particles synthesised in toluene only marginally (<10 %) larger than those synthesised in octane. Similar to the results we obtained using tetralin, we found no strong size-effect upon alteration of the TBAB concentration when using octane as solvent.

Ultimately, no clear cause was found for the variability of the AuNP@OIAM synthesis as we were able to rule out most common causes, although likely candidates are the influence of oxygen or moisture on the reaction as well as the influence of some reactions occurring between preparation of the gold solution and the addition of TBAB. As many groups have reported (variations on) this synthesis, a further review into what could be considered ‘typical results’ and under what conditions those were achieved would be of interest, although such a study could be biased due to the tendency of ‘negative’ results not being published. Informal discussions with co-workers from our group as well as researchers at other institutions

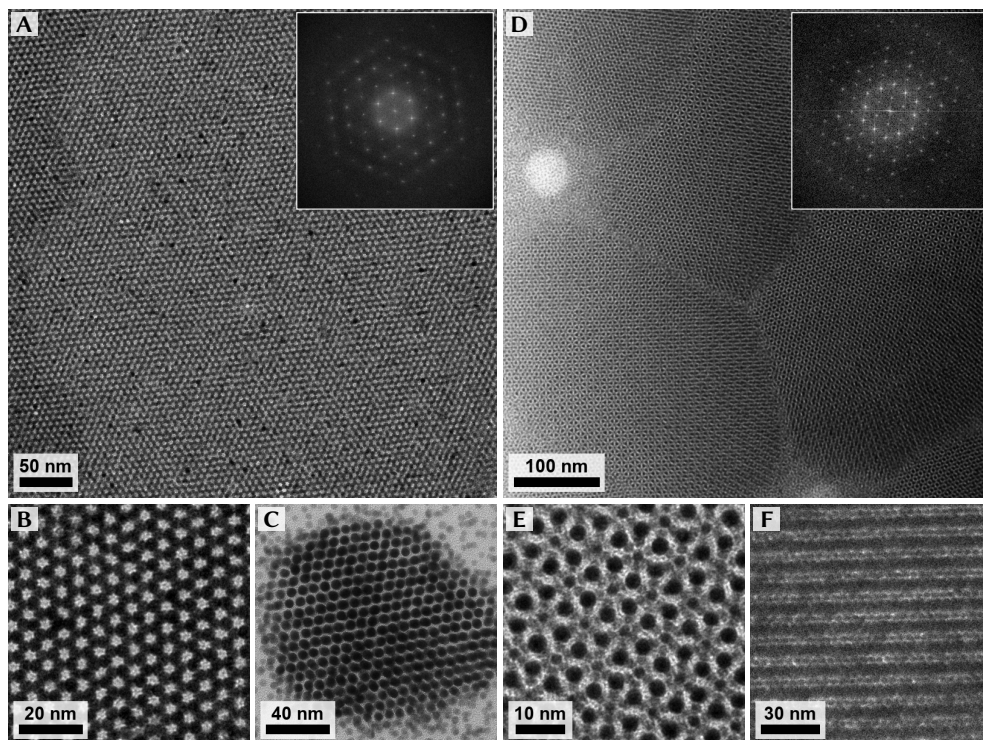


Figure 3.17: spontaneously formed AuNP@OIAm assemblies. All were found on TEM grids prepared by drop-casting AuNP@OIAm dispersions in hexane onto TEM specimen grids. **A–C:** assemblies of monodisperse AuNPs of 4.7 ± 0.5 nm (11 %), the inset in A shows the FFT with the first inner most peaks corresponding to a periodicity of 5.7 nm. **D,E:** overview and zoom-in of binary crystal assemblies of bi-disperse samples, the particle sizes of the two populations were ~ 2.3 and 4.0 nm (excluding ligands) giving a size ratio (including ligands) of ~ 0.71 . The crystal structures were the MgZn_2 Laves phase.^[399] **F:** different region with an AlB_2 binary crystal structure.^[391]

provided some anecdotal evidence that batch-to-batch variations are not uncommon. A more detailed study into the reliance on air-free synthesis conditions and the solvent and manner of preparation of the initial gold solution may provide more clues, but a full study into the exact reaction mechanism may be required to fully elucidate the occasional formation of almost perfectly bi-disperse samples. Despite this, it was possible to rapidly synthesise relatively large quantities of AuNPs of tunable size using temperature control and seeded growth, and performing the synthesis in octane likely gives much more consistent results. This, in combination with the ability for accurate purification using SSP, make the synthesis a worthwhile method to produce small sterically stabilised particles for experiments in self-assembly and interaction measurements.

The tendency of AuNPs@OIAm to rapidly self-assemble was evident from the formation of crystallites in concentrated regions of TEM samples (prepared by drop-casting ca. 3 μL of the AuNP dispersions in hexane, which due to its high vapour pressure at room temperature fully evaporated within seconds). Some examples of such assemblies are shown in **Figure 3.17**.

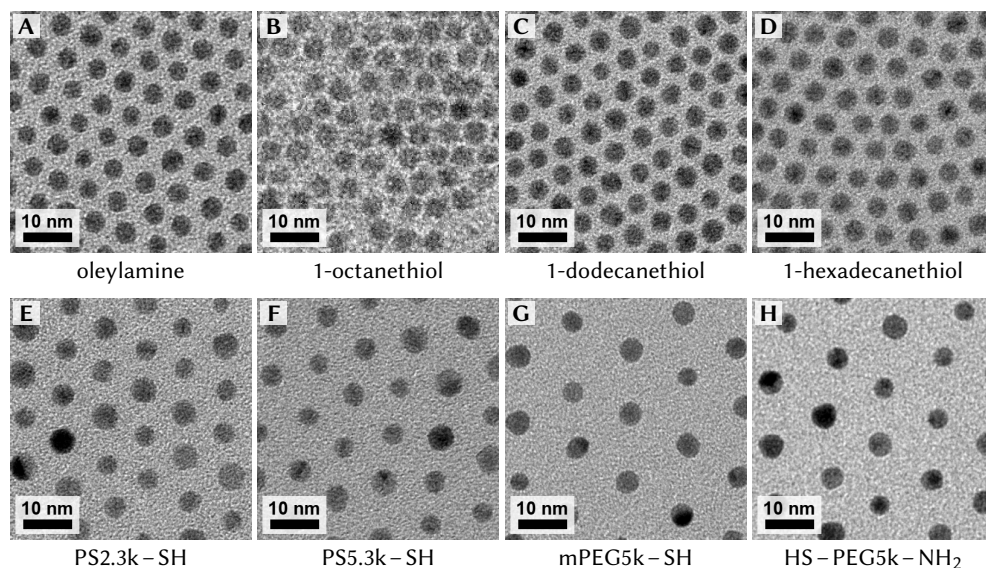


Figure 3.18: ligand exchange of AuNPs@OIAm. The AuNPs had a size of 4.7 ± 0.5 nm (11%) (excluding ligands), successful exchange of the OIAm ligands can be seen from the change in the interparticle spacing due to the size of the ligands.

In most cases, face-centred cubic (FCC) or hexagonal close packed (HCP) crystal structures or random mixtures of the two (random hexagonal, RH) were found. From the fast fourier transform (FFT) of a large crystalline region, an average nearest neighbour distance of 6.6 nm is obtained giving a typical surface-to-surface spacing of 1.9 nm, in good agreement with literature values for partially interdigitated OIAm ligands.^[86,400] Remarkably, in multiple instances bi-disperse samples with narrow size populations spontaneously formed binary crystals when a large excess of the smaller particles was present. To extend the possibilities for self-assembly, the particles could be functionalized further by ligand exchange. Similar to the AuNPs@citrate, it was easily possible to exchange the native OIAm ligands for a wide variety of thiolated molecules. TEM micrographs of AuNPs with various ligands are shown in **Figure 3.18**. AuNPs coated with polystyrene will feature in more detail later in **Chapter 5**.

3.3 Silica particles

Next, we turn our attention to another commonly used material: silica. Silica colloids are widely used in colloid science because of their relative ease of synthesis and functionalisation. Particularly, the ability to fluorescently label silica particles as well as match their refractive index using common solvents have made them one of the primary systems for studies using optical microscopy.^[401,402] Here, we discuss and reproduce three methods for producing silica colloids: direct (single-step) Stöber synthesis, a multi-step Stöber nucleation and growth procedure for synthesis of large, extremely monodisperse spheres, and an amino-acid catalysed silica synthesis and growth process. Together, these methods can be used to produce fluorescently labelled silica particles with a polydispersity below 5% over a wide size range from 30 nm nanoparticles to particles as large as several micrometers.

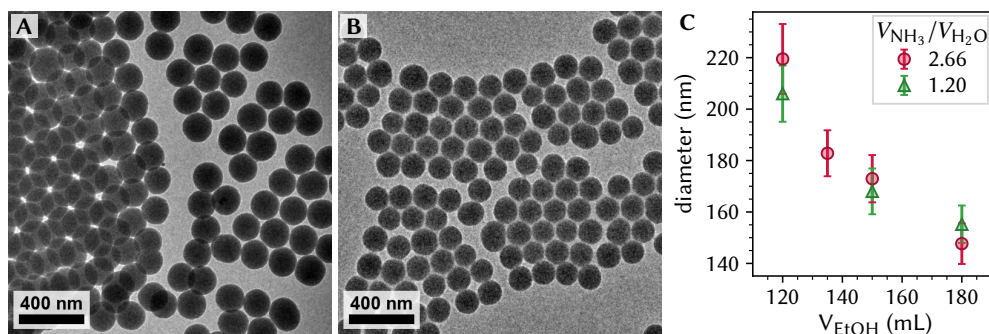


Figure 3.19: results of single-step Stöber silica synthesis without dye. The particles in **A** were synthesised with 135 mL ethanol and were 182.8 ± 9.0 nm (4.9%), the particles in **B** were synthesised with 180 mL ethanol and are 147.7 ± 8.0 nm (5.4%). **C**: particle size as function of ethanol volume for two water/ammonia ratios. Error bars indicate the polydispersity.

3.3.1 Single step synthesis of Stöber silica colloids

By far the most commonly used method in colloid science is what is referred to as the *Stöber* method developed by Stöber & Bohn *et al.*,^[403] which is the reaction of tetraethyl orthosilicate (TEOS) with water under alkaline conditions in an ethanol/ammonia mixture. The reaction allows for tuning of the particle size in the range of 50 nm up to 2 μm through the concentrations of ethanol, ammonia and TEOS as well as through the reaction temperature.^[403] Furthermore, it is possible to include organic functionality, such as fluorescent molecules, into the structure of the silica via silane coupling agents.^[404–406] The exact reaction mechanism remains debated to this day, but sources agree that the early phases are dominated by an aggregative process while the final stages of the reaction are dominated by growth by monomer addition.^[402,407] Here, a simple protocol for direct synthesis of silica colloids is reproduced to produce a set of ‘standard silica’ particles. A number of sizes around 200 nm were prepared by variation of the amount of ethanol with respect to the amounts of water, ammonia and TEOS.^[408] This was done for two different ratios of ammonia to water while keeping the total water concentration ($V_{\text{H}_2\text{O}} + V_{\text{NH}_3}$) constant. TEM micrographs of the resulting particles are shown in **Figure 3.19**. Experimental details and a full overview of parameters and particle sizes are given in **Section 3.7.10**. In all cases spherical silica particles with relative polydispersities around 5% were found. In good agreement with Gao & Owens *et al.*,^[408] a decreasing particle size with increasing ethanol volume was observed regardless of ammonia concentration, with the ammonia concentration having only minor effect on particle size in this range.

3.3.2 Synthesis and growth of fluorescently labelled Stöber silica microparticles

The Stöber method has been ubiquitous as a one-step synthesis method for producing silica colloids, but Stöber-like conditions may also be used for controlled growth onto seed particles. This proceeds through a reaction-limited growth mechanism, which means that all particles (or rather all surfaces) grow by the same absolute amount of silica. When all the diameters D of all particles grow by the same amount the *absolute* polydispersity of the sample remains the same, but the *relative* PD reduces with $1/D$.^[409] As a result extremely low PDs may be achieved through extensive silica growth. For large particles lower PDs are therefore

obtained by initial synthesis of colloids and subsequent seeded growth steps than by direct synthesis of larger colloids. Secondly, while it is possible to tune the size of particles obtained by Stöber nucleation, the reaction is sensitive to slight variations in reactant concentration, temperature, etc. since these affect the exact number of nuclei formed. A seeded growth procedure on the other hand allows for much more accurate tuning of the final particle size because the seed concentration is known and does not change throughout the reaction. In the case of fluorescently labelled particles, a Stöber seeded growth step can be used to add a non-fluorescent shell to prevent leaking of dye from the particles, and to improve imaging by preventing overlap between the fluorescent cores.

For the experiments on 2D interaction measurements we will present in **Chapter 6**, fluorescent silica particles of $>1.5\ \mu\text{m}$ in size were required. For this purpose, a multi-step approach was taken of separate nucleation and growth steps. Detailed experimental methods are given in **Section 3.7.11**. In short: Stöber silica particles of $\sim 400\ \text{nm}$ which were fluorescently labelled with fluorescein isothiocyanate (FITC) were synthesised in a single step in a procedure similar to the ‘standard’ Stöber method, except that FITC was covalently incorporated into the lattice.^[404,410] This was achieved by first reacting FITC with (3-Aminopropyl)triethoxysilane (APTES), a silane coupling agent that has silanol group similar to TEOS which is built into the silica when added during the synthesis. To further increase the volume of fluorescently labelled silica (and thus the number of fluorophores) in order to improve the signal to noise ratio in microscopy, a fluorescent silica shell was grown around the particles to a total size of $\sim 800\ \text{nm}$ (FITC-Stöber@FITC-Stöber*). The seeded growth procedure occurred under Stöber conditions—that is in a mixture of ethanol, ammonia and water—but the formation of new nuclei was avoided by adding the TEOS/FITC-APTES mixture gradually over the course of hours or even days using a syringe pump. Careful tuning of the addition rate assured that unhydrolysed TEOS could not build up over time, taking into account the hydrolysis speed which strongly varies with variables like water and ammonia concentration but is ultimately the limiting step in Stöber growth.^[409] Finally, a non-fluorescent shell was grown around the particles in a similar manner with a syringe pump to increase the particle size to a final target size of $\sim 1.6\ \mu\text{m}$ (FITC-Stöber@FITC-Stöber@Stöber). Between each step, the particle concentration was decreased to avoid the formation of dumbbells.[†]^[411] As the particle size was decreased, it was necessary to also decrease the TEOS addition rate to account for the smaller amount of total silica surface available for the reaction, although the addition rate could be increased throughout the growth phase as the particles increased in size and more surface became available.

TEM micrographs of the particles at each step are shown together with particle size histograms in **Figure 3.20**. In all cases spherical silica colloids close to their target size were obtained. We do note that in case of the final non-fluorescent shell growth, a significant number of smaller particles (100 nm to 400 nm) were present, likely from secondary nucleation. An increase in seed particle concentration or a lower TEOS addition rate would have likely prevented this, however we note that the smaller particles were easily removed from the sample during washing steps with centrifugation due to the large difference in the particles’ volume between the main population and the smaller particles. The (dye-less) size-impurities were removed by repeatedly centrifuging and replacing the supernatant with clean solvent until the supernatant remained clear. After the second round of centrifugation

* for more on this ‘@’ notation see also the footnote on **page 56**

† the term dumbbell is commonly used to refer to a cluster of two particles (irreversibly) stuck together

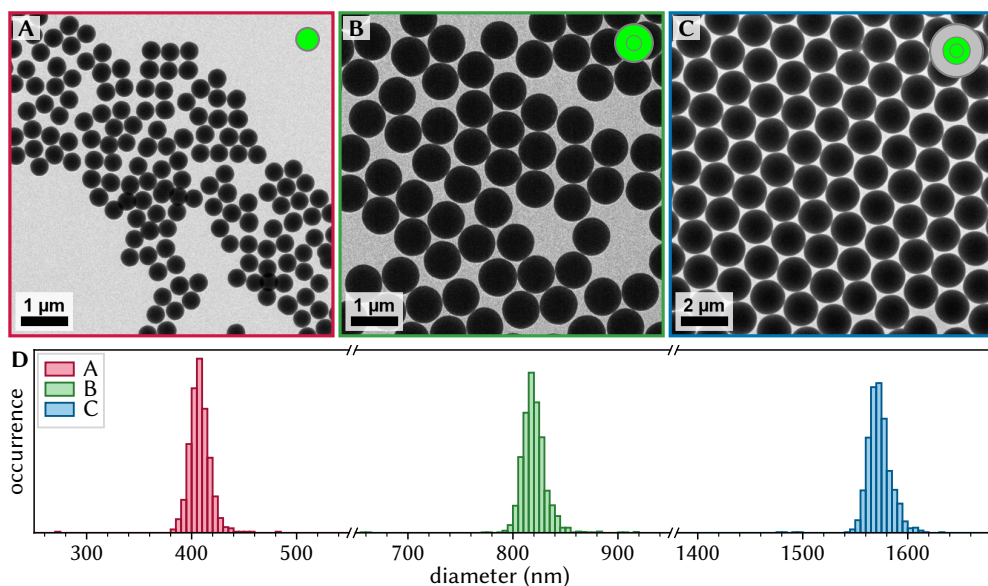


Figure 3.20: multi-step seeded growth of Stöber silica. **A:** FITC-labelled Stöber core particles (FITC-Stöber), $D = 407 \pm 11$ nm (2.8%) **B:** the particles in **A** after growth of an FITC labelled silica shell (FITC-Stöber@FITC-Stöber), $D = 820 \pm 13$ nm (1.6%). **C:** the particles after silica shell growth (FITC-Stöber@FITC-Stöber@Stöber) to the final size of $1.57 \pm 0.01 \mu\text{m}$ ($<1\%$). **D:** particle size histograms for **A–C**, note that breaks were added to the x -axis for clarity.

the supernatant was already nearly clear when the dyed particles had sedimented. A side effect of the formation of secondary nuclei was that less TEOS was available for growth of the main population, and as a result the final particle size was slightly smaller than the target size ($\sim 1.5\%$ smaller by diameter, $\sim 4.4\%$ by volume). When comparing the widths of the size distributions of each step in the synthesis it is immediately clear that during growth under Stöber conditions, as expected, the PD did not significantly increase beyond that introduced in the initial core synthesis. By the final particle size the relative polydispersity had decreased as a result of this to well below the 1% threshold up to which we could reliably determine it from TEM images.

3.3.3 Amino acid catalysed silica synthesis and growth

For experiments on binary crystallisation we will present in **Chapter 4**, a binary system of fluorescent FITC and RITC labelled silica particles of precisely tuned sizes around 300 and 400 nm respectively were needed, as well as a batch of fluorescent silica nanoparticles. While the Stöber method can produce nanoparticles—that is below 100 nm in diameter—the polydispersity and sphericity of these particles is not as good as achievable by more modern methods. As we have seen above, even for those larger particles it is generally best to ‘start small’ and subsequently perform seeded growth to achieve the lowest polydispersity. To produce monodisperse silica nanoparticle seeds, we used a method where TEOS is added to an aqueous solution of alkaline amino acids, which we refer to as the amino acid catalysed silica (AACS) method.^[412–416] Specifically, we used the method reported by Shahabi &

Rezwan *et al.*^[416] based on L-arginine. The AACS synthesis has many similarities with Stöber synthesis: it is a base-catalysed condensation reaction of water and TEOS, although a key difference is that TEOS and water do not mix and instead form a two-phase system. The AACS method produces particles that are typically 10 nm to 30 nm in size depending on the reaction temperature, with a spherical albeit coarse/rough surface and a partially condensed silica structure. It is possible to incorporate fluorescent dye in the synthesis. While the AACS particles at their small size are not directly stable under Stöber-like conditions for further growth,^[407] it is possible to grow the AACS silica further to a size of >50 nm from which Stöber-like growth is possible. This is achieved simply by performing the AACS synthesis again except that a small amount of seed particles from a previous synthesis is added, forcing the growth of existing particles rather than nucleation of new particles.

To produce the 300 and 400 nm binary fluorescent particle system required for **Chapter 4**, we opted to first produce unlabelled silica NP cores using a two-step AACS synthesis and growth approach, and subsequently use Stöber growth of fluorescent and non-fluorescent shells to produce the desired labelling and final size. Not fluorescently labelling the cores meant only a single batch of cores was needed to produce the two different particle batches. Although this theoretically reduces the amount of fluorescence, the cubic relation of diameter and volume means that the cores make up only a fraction of a percent of the total particle volume, thus having a negligible influence on the fluorescence. AACS nanoparticles were prepared at 70 °C and subsequently used in a seeded growth step, detailed experimental methods are given in **Section 3.7.12**. The resulting particles are shown in **Figures 3.21A** and **3.21B** and were around 30 and 70 nm after the synthesis and growth steps respectively. Next, the 70 nm AACS particles were used as seed particles in seeded Stöber growth to produce both FITC and RITC labelled particles of ~240 nm in diameter. Conveniently, it was not necessary to perform any washing steps and the aqueous AACS was added *as is* to an ethanol/ammonia mixture for seeded growth, which was otherwise performed similarly as described before (see **Sec. 3.3.2**). This is important as silica particles below 100 nm generally cannot be fully redispersed after centrifugation. Finally, non-fluorescent shells were grown around these particles to the desired total size to prevent dye-leakage and assure optical separation of the fluorescent cores. TEM micrographs and sizes of the AACS@dye-Stöber core-shell and AACS@dye-Stöber@Stöber core-shell-shell particles are given in **Figures 3.21C** to **F**. We note that in case of the RITC labelled cores it was necessary to reduce the particle and ammonia concentration when compared to the FITC labelled cores. This was needed to prevent dumbbell formation as the positively charged RITC dye reduces the surface charge and thus charge stabilisation of the RITC-silica cores.

For the synthesis of silica nanoparticles, we opted to fluorescently label AACS particles from nucleation in order to incorporate the maximum amount of dye possible. Particles were synthesised in a similar manner to the unlabelled cores described above, except fluorescent rhodamine isothiocyanate (RITC) dye was included in the synthesis mixture in each step. In this case, two seeded growth steps under AAC conditions were used to increase the size of the fluorescent cores further to ~85 nm so that fluorescent Stöber growth was not necessary to increase the fluorescent volume (**Fig. 3.21G**). Due to the lower particle concentration in the second seeded growth step it was necessary to reduce the amount of TEOS to prevent the formation of new particles. Next, the particles were washed using dialysis in order to remove excess dye before the final step of growing a thin non-fluorescent Stöber silica shell as stabilisation layer (**Fig. 3.21H**). This shell was needed as the dye was not covalently bound

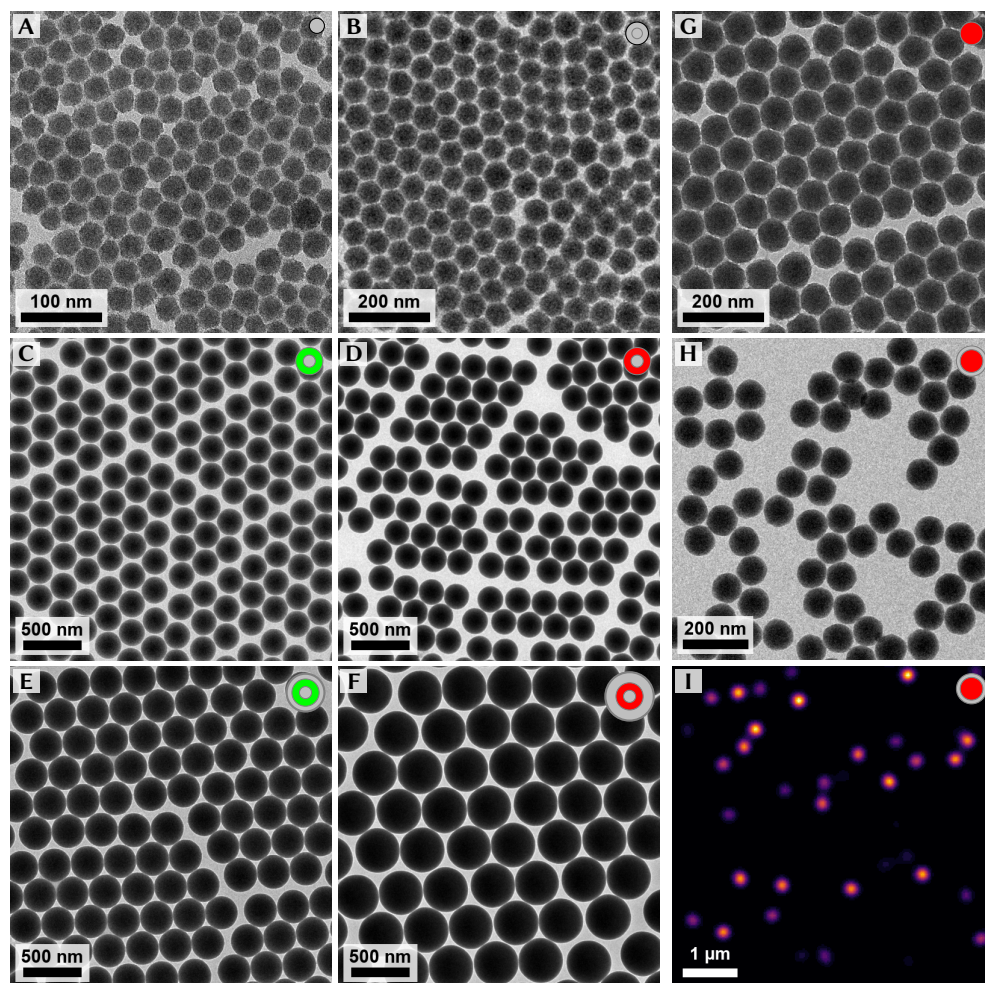


Figure 3.21: AACS as seed particles in seeded AACS and Stöber silica growth. **A:** TEM micrographs of the initial AACS particles with a size of 30.1 ± 2.3 nm (7.7%). **B:** after an AACS seeded growth step of the particles in A, the particles had a size of 68.1 ± 3.1 nm (4.6%). **C,D:** fluorescent Stöber shell growth on AACS with FITC (green) & RITC (red), the particles were 240.8 ± 3.7 nm (1.6%) and 239.3 ± 3.6 nm (1.5%) respectively. **E,F:** final particles after growth of a non-fluorescent shell around the particles in C–D, the sizes were 294.3 ± 3.6 nm (1.2%) and 391.7 ± 3.4 nm (<1%) respectively. **G:** fluorescent AACS after two seeded growth steps, the particles had a size of 84.6 ± 3.6 nm (4.2%). **H:** final silica NPs after growth of a Stöber stabilisation shell on the particles in G, the final size was 97 ± 3 nm (3%). **I:** (false coloured) CLSM optical ‘slice’ of a sample containing the particles in H, showing that the ~ 80 nm fluorescent cores were sufficiently large to obtain a high signal-to-noise ratio.

to the silica using the AACS method and without stabilisation shell the dye can leak out of the particles over time due to the more porous structure of AACS. The growth of the final shell also assured the surface properties were consistent with pure Stöber silica particles, of which the surface structure and interactions are more widely studied and understood.

3.4 Poly(methyl methacrylate) colloids

The final colloidal model system used in this thesis is that of microparticles made of the polymer poly(methyl methacrylate) (PMMA*). Like silica μ Ps, PMMA μ Ps can be fluorescently labelled and refractive index matched with common solvents to enable in-situ imaging in 3D using confocal laser scanning microscopy (CLSM). This is further aided by the low diffusion constant and large fluorescent signal as a result of the size on the upper end of the colloidal domain. Unlike μ Ps made of silica and most other materials however, PMMA μ Ps have a low enough density that they may be density matched with common solvents, meaning that sedimentation of these particles is negligible on a time scale of hours. Lastly, PMMA offers flexibility when it comes to inter-particle interactions. When dispersed in low polar solvents (dielectric constant $\epsilon_r = 5-6$) the the particles' surface are charged, which due to the typically extremely low ion concentrations in low-polar solvents can result in long ranged repulsive interactions up to tens of micrometers. The addition of organic salts can be use to precisely tune the interaction range all the way to nearly hard sphere-like behaviour.^[417] Because of all of these factors, PMMA particles have been widely used as colloidal model system for investigating interactions and colloidal crystallisation;^[88,163,213,418] moreover it has also already be demonstrated that thick layers of PHSA stabilized PMMA (up to 100's of nm) can be grown onto silica cores if they are coated first with a methacrylate based silane coupling agent.^[419]

The particles used in this work were synthesised previously in our group by Johan Stiefelhagen, therefore, we do not discuss the synthesis in detail nor do we provide detailed experimental methods. Instead, we kindly refer anyone interested in the synthesis of PMMA particles to the references provided. We do however consider this an important model system and as such chose to include some words on it in this chapter. Very briefly, PMMA μ Ps were synthesised using a dispersion polymerisation method, and were stabilised with a layer of comb-graft poly(12-hydroxystearic acid) grafted onto a PMMA backbone which acted as steric stabilisation layer.^[44,418,420-422] The particles were fluorescently labelled with 4-chloro-7-nitrobenzo-2-oxa-1,3-diazol (NBD) or (rhodamine isothiocyanate)-aminostyrene (RAS).^[418] The particle size was typically between 1 μ m to 3 μ m and polydispersities were all below 3 %, the particle size and polydispersity of PMMA particles were determined using static light scattering (SLS). The particles were dispersed in a mixture of 68 vol.% bromocyclohexane (CHB) and 32 vol.% *cis*-decalin which could simultaneously density and (nearly) refractive index match PMMA. An example of a three-dimensional image stack obtained with (high-speed) confocal microscopy is shown in **Figure 3.22**.

3.5 Concluding remarks

As we have seen and discussed several synthesis methods, it remains clear that particle synthesis can be somewhat of an art as well as a science. Reproducing established methods is certainly not guaranteed to work on a first try, even when methods are widely used

* commonly known as acrylic, Plexiglass or Perspex

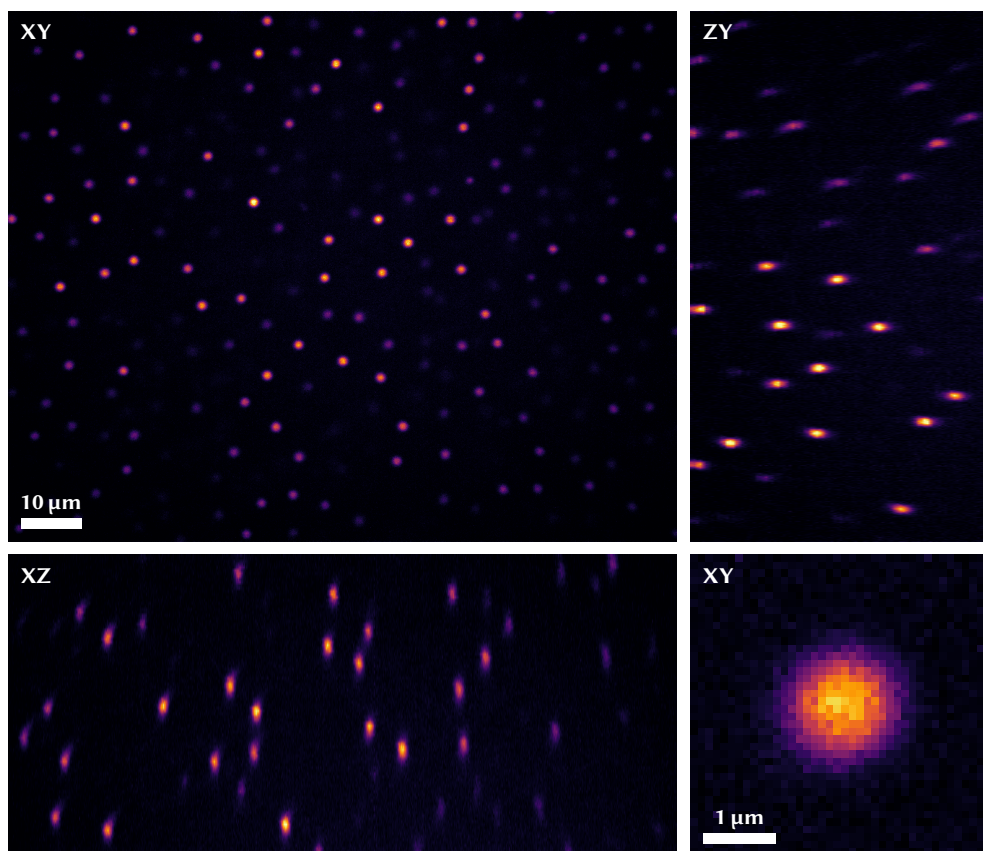


Figure 3.22: Fluorescent PMMA colloids. Three (false coloured) cross-sections of 3D image stack obtained with CLSM are shown, a zoom-in of a particle in the XY (image) plane is given in the bottom right panel. The particles had a diameter of $1.73\ \mu\text{m}$ and demonstrated long-range repulsive interactions. The image was recorded at a 2D frame rate of 200 frames/s using a $63\times / \text{NA}1.3$ glycerol immersion objective, the z -step size was $0.5\ \mu\text{m}$.

and considered ‘reproducible’. Despite this, nano- and microparticles with good utility in interaction measurements and other experiments were obtained for all reported methods. This was demonstrated in part by a number of other works in which the particles synthesised here were used, and a number of the other particle systems will feature heavily later in this thesis.

3.6 Acknowledgements

Da Wang, Katherine Elbert and Christopher Murray are acknowledged for useful discussions with regards to synthesis of the AuNPs@OIAm. Relinde van Dijk - Moes and Elleke van Harten are thanked for protocols for the AACS & growth and for useful discussions with regards to silica colloid synthesis in general. Niels van de Poll is acknowledged for synthesising the 97 nm RITC-AACS@Stöber silica nanoparticles. Roy Hoitink and Xufeng

Xu are acknowledged for contributing to the Stöber shell growth on AACS-seed particles. Johan Stiefelham is acknowledged for synthesis of all PMMA particles used in this thesis. Hans Meeldijk and Chris Schneidberg are thanked for technical support with electron microscopy.

3.7 Experimental methods

3.7.1 Chemicals

The following chemicals were all used as received: **gold(III) chloride trihydrate** ($\text{HAuCl}_4 \cdot 3 \text{H}_2\text{O}$, $\geq 99.9\%$ trace metals basis, *Sigma-Aldrich* no. 520918, stored at 4°C); **tert-butylamine borane (TBAB)**, 97%, *Sigma-Aldrich* no. 180211, stored under N_2 atmosphere); **oleylamine tech.** (OlAm tech., 70% technical grade, *Sigma-Aldrich* no. O7805); **oleylamine** (OlAm, 80–90% C_{18} content, *Thermo Scientific Acros* no. 129540010); **1,2,3,4-tetrahydronaphthalene (tetralin)**, $\geq 98\%$, *Thermo Scientific Acros* no. 146730010); **hydrochloric acid** 37 wt.% aqueous solution (ACS reagent grade, *Sigma-Aldrich* no. 258148); **nitric acid** 65 wt.% aqueous solution (analysis grade, *Thermo Scientific Acros* no. 124660025); **n-hexane** (GC grade, *Honeywell* no. 34493); **hexane tech.** (mixed isomers, $\geq 98.0\%$, *Thermo Scientific* no. L13233); **n-octane** ($\geq 99.0\%$ *Honeywell* no. 74821); **1-octadecene** (90% technical grade, *Thermo Scientific Acros* no. 129310010); **sodium citrate tribasic dihydrate** ($\geq 99\%$, *Sigma-Aldrich* no. C8532); **sodium hydroxide (NaOH)**, $\geq 97.0\%$, *Sigma-Aldrich* no. 221465); **polyvinylpyrrolidone (PVP)**, M_w 10 kDa, *Sigma-Aldrich* no. PVP10); α -**methoxy- ω -mercapto polyethylene glycol (mPEG2k-SH)**, M_w 2 kDa, *Rapp Polymere* no. 122000-40, stored at -23°C); α -**methoxy- ω -mercapto polyethylene glycol (mPEG5k-SH)**, M_w 5 kDa, *Rapp Polymere* no. 125000-40, stored at -23°C); α -**methoxy- ω -mercapto polyethylene glycol (mPEG10k-SH)**, M_w 10 kDa, *Rapp Polymere* no. 1210000-40, stored at -23°C); α -**mercapto- ω -amino polyethylene glycol hydrochloride (HS-PEG5k-NH₂·HCl)**, M_w 5 kDa, *Rapp Polymere* no. 135000-40-20, stored at -23°C); α -**mercapto- ω -carboxy polyethylene glycol (HS-PEG5k-COOH)**, M_w 5 kDa, *Rapp Polymere* no. 135000-4-32, stored at -23°C); α -**sec-butyl- ω -isopropylthiol polystyrene (PS880-SH)**, M_w 0.88 kDa ($\text{Đ} = 1.1$, where $\text{Đ} = M_w/M_n$ denotes the dispersity), *Polymer Source* no. P4431-SSH, stored at -23°C); α -**sec-butyl- ω -ethylthiol polystyrene (PS2.3k-SH)**, M_w 2.3 kDa ($\text{Đ} = 1.15$), *Polymer Source* no. P4431-SSH, stored at -23°C); α -**sec-butyl- ω -ethylthiol polystyrene (PS5.3k-SH)**, M_w 5.3 kDa ($\text{Đ} = 1.4$), *Polymer Source* no. P10826-SSH, stored at -23°C); α -**sec-butyl- ω -ethylthiol polystyrene (PS5.8k-SH)**, M_w 5.8 kDa ($\text{Đ} = 1.10$), *Polymer Source* no. P4430-SSH, stored at -23°C); **Hexadecyltrimethylammonium chloride** 25 wt.% solution in H_2O (**CTAC**, $\geq 98.0\%$, *Sigma-Aldrich* no. 292737); **sodium borohydride (NaBH₄)**, 99%, *Sigma-Aldrich* no. 213462); **ascorbic acid** ($\geq 99\%$, *Sigma-Aldrich* no. A5960); **Sodium hypochlorite** 11–15 wt.% active chlorine in H_2O (NaOCl, bleach, *Fisher Scientific* no. 15429019, stored at 5°C and used at most 2 months after opening); **L-arginine** (reagent grade, *Sigma-Aldrich* no. A5006); **ammonium hydroxide** 28.0–30.0 wt.% aqueous solution (ammonia, ACS reagent grade, *Sigma-Aldrich* no. 221228); **rhodamine B isothiocyanate mixed isomer (RITC)**, *Sigma-Aldrich* no. 283924); **fluorescein isothiocyanate isomer I (FITC)**, *Sigma-Aldrich* no. F7250); **(3-aminopropyl)triethoxysilane (APTES)**, 99%, *Sigma-Aldrich* no. 440140); **tetraethyl orthosilicate (TEOS)**, $\geq 99.9\%$, *Sigma-Aldrich* no. 800658); **ethanol** (100%, *VWR Chemicals* no. 85651.360); **abs. ethanol** (anhydrous reagent grade, *Fischer Scientific* no. 15436115); **acetone** ($\geq 99\%$, *VWR Chemicals* no. 20063.365P).

TEOS was replaced after the bottle had been opened at most 10 times or if more than 3 months had passed since first opening the bottle in order to prevent pre-hydrolysis due to exposure to ambient moisture. Ultrapure (type 1) H_2O was produced by a *Direct-Q3* Milli-Q water purification system (*Merck Millipore* no. ZRQS0P300), and had a resistivity of $\geq 18.2 \text{ M}\Omega \text{ cm}$. Single use glass scintillation vials and eppendorf tubes were used as received without additional cleaning.

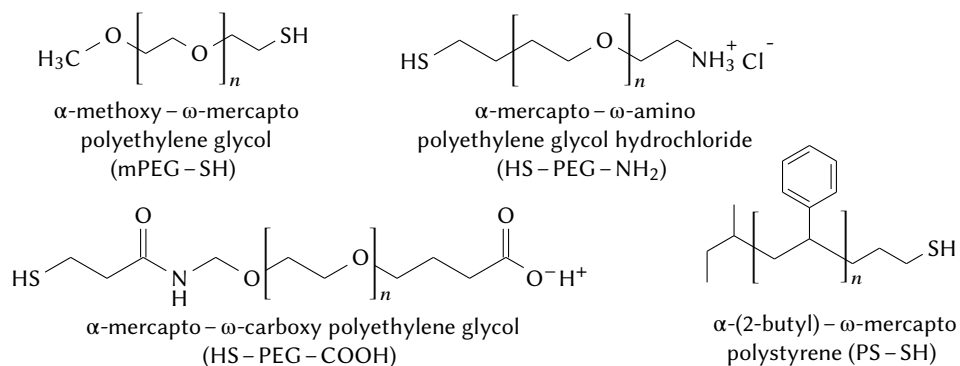


Figure 3.23: molecular structure of thiolated PEG and PS ligands used for AuNPs.

3.7.2 Synthesis of 17 nm AuNPs@citrate

Citrate stabilized spherical AuNPs were synthesised using the sodium citrate reduction method.^[353,356] A 250 mL two-neck flask with a magnetic stirring bar was cleaned with *aqua regia* (a 3:1 V:V mixture of concentrated hydrochloric and nitric acid), rinsed with copious amounts of water and dried prior to use. 100 mL H₂O and 1.00 mL of an aqueous solution containing 25 mM (10.0 g/L) HAuCl₄ · 3 H₂O were added to the flask and a reflux condenser and glass stopper were added. The flask was placed in an 130 °C oil bath and heated until boiling vigorously. Then, 3.00 mL of an aqueous solution containing 34 mM (10.0 g/L) sodium citrate tribasic dihydrate was rapidly added under vigorous stirring (1200 rpm) and the mixture was left refluxing and stirring for 15 min during which a colour change from yellow to dark blue to pink and finally deep red was observed. Stirring was slowed down to 400 rpm, the oil bath was removed and the mixture was allowed to cool down to room temperature. The particles could be stored without further purification for up to 3 months.

3.7.3 Ligand exchange of AuNPs@citrate

The molecular structure of the PEG-SH ligands is shown in **Figure 3.23**. In a typical ligand exchange, 10 mL of as synthesised AuNPs@citrate were transferred to a glass vial. The particle concentration was ~2.2 nM AuNPs based on the UV-Vis extinction at 450 nm and an extinction coefficient of $2.43 \cdot 10^8 \text{ M}^{-1} \text{ cm}^{-1}$.^[SI of 423] Then, 0.500 mL of a 2.0 mM solution of one of the PEG-SHs was added (corresponding to ca. 60 molecules/nm² of Au⁰ surface, a 10–100× excess w.r.t. the expected maximum grafting density depending on the M_W of the ligand), followed after 1 min by 0.250 mL of a 0.10 M aqueous NaOH solution in order to increase the activity of the SH-bond, giving a solution pH of ~8–9. The vial was closed and placed on a roller overnight, after which the particles were washed 3 times by collecting the particles using centrifugation (15000 relative centrifugal force –RCF, relative to earths gravitational acceleration g – for 30 min in 5 mL Eppendorf tubes) and redispersion of the sediment in 10.0 mL H₂O.

3.7.4 Silica coating of AuNPs@citrate

A fluorescent or non-fluorescent silica shell could be grown around the AuNP@citrate particles using a PVP-mediated Stöber shell growth procedure.^[348,366] 240 μL 10 wt.% PVP in H₂O was added to 10 mL of the as synthesized AuNP solution (60 PVP molecules per nm² of gold surface) and stirred (300 rpm) for 24 h. The PVP-coated particles were collected by means of centrifugation (15000 g, 30 min in 5 mL Eppendorf tubes), redispersed in 10 mL ethanol and added to a 20 mL glass vial. Then, the stirring rate was increased to 1200 rpm and 1 mL ammonium hydroxide solution was added followed by one or multiple additions of a 10 vol.% TEOS in ethanol mixture. The volume of the first TEOS addition was

typically between 10 and 50 μL of the 10% TEOS solution per 10 mL of AuNP solution. To grow larger shells, additional TEOS additions could be performed, doubling the volume of added TEOS solution each time. The mixture was left to react for 90 min between each TEOS addition to ensure complete conversion of TEOS to silica and to prevent nucleation of additional silica particles occurring (secondary nucleation). Small (20 μL) samples were taken 90 min after each addition step to prepare TEM samples in order to determine intermediate particle sizes. A typical series of additions consisted of the following additions: 10, 20, 40, 80 and 160 μL , giving mean (intermediate) particle diameters of 48.9, 57.0, 70.1, 68.8 and 113 nm respectively.

To grow a fluorescently labelled silica shell, RITC dye could be incorporated during the shell growth process. For this typically 10 mg (0.019 mmol) of RITC was mixed with 1.00 mL absolute ethanol in a 2 mL glass vial. Then, 8.73 μL APTES was added (0.037 mmol, a 2:1 mole ratio w.r.t. RITC) which turned the turbid suspension to clear dark purple. The vial was wrapped in aluminium foil to minimize exposure of the dye to light and placed on a roller for at least one hour to completely dissolve and react. The dye solution was always freshly prepared up to at most 24 hours prior to the fluorescent shell growth procedure. The shell growth procedure could be performed as described above, but ~ 1 min after each addition of the TEOS solution an equal volume of the RITC-APTES solution was added, except for the very first addition, which was needed to form a first silica layer to stabilise the particles against aggregation since the positively charged RITC dye decreases the surface charge of the particles (potentially leading to a loss of colloidal stability). For the same reason it was necessary to always grow a final undyed 'stabilization layer'. The best result was obtained when a single washing step was performed by means of centrifugation and redispersion in 10 mL ethanol and 1 mL ammonium hydroxide solution in order to remove any unincorporated dye prior to growth of the final unlabelled shell. However, small silica particles (<100 nm) are insufficiently stable and may form clusters and dumbbells upon centrifugation. Therefore, smaller particles were washed by means of dialysis against a $\sim 10\times$ excess of 10 to 1 (V/V) ethanol/ammonia mixture in a closed vessel (to prevent reaction of ammonia with atmospheric CO_2) for 1 week after which the excess ethanol/ammonia was replaced and the dialysis was left to continue for another week.

3.7.5 Synthesis of 30–150 nm AuNPs@CTAC

AuNPs@CTAC were prepared in three steps as follows:^[378]

Preparation of seed solution:

5.00 mL of a 0.10 M aqueous CTAC solution and 50.0 μL of a 50 mM aqueous $\text{HAuCl}_4 \cdot 3 \text{H}_2\text{O}$ solution were added to a 20 mL glass vial with a magnetic stirring bar and stirred at 1200 rpm. Then, 200 μL of a freshly prepared 20 mM solution of NaBH_4 in ice water was rapidly added to the vial. After three minutes, 400 μL was taken out and added to 3.60 mL of an aqueous 0.10 M CTAC solution to obtain a diluted pre-seed solution. Next, 40 μL of an aqueous 0.10 M ascorbic acid solution and 900 μL of the diluted pre-seed solution were added to a 20 mL glass vial containing a stirring bar and 10.0 mL of a 25 mM aqueous CTAC solution. The mixture was stirred at 1200 rpm and 50.0 μL of a 50 mM aqueous HAuCl_4 solution was rapidly added after which the mixture turned light pink within seconds, followed by a change to dark pinkish red over the course of two minutes indicating the formation of the AuNP seeds. The mixture was left for 10 min to assure the reaction had completed after which stirring was stopped and the mixture was stored without further purification up to 1 month.

Seeded growth:

A growth solution was prepared by mixing 10.0 mL of a 25 mM aqueous CTAC solution, 40.0 μL of a 0.10 M aqueous AA solution and a certain volume of the seed solution (V_{seed}) in a 20 mL glass vial with stirring bar. The growth solution was stirred at 1200 rpm and 50.0 μL of an aqueous 50 mM HAuCl_4 solution was rapidly added. After 2 h, the reaction was complete. The resulting particles were analyzed using UV-VIS spectroscopy and TEM imaging and could be stored or used directly etched without further purification. The seeded growth could be scaled up to larger volumes V_{growth} by performing the reaction in a suitable size Erlenmeyer flask and scaling all volumes accordingly, where for convenience

V_{growth} is taken as the volume of the CTAC solution which makes up the majority of the growth solution.

Etching-based reshaping:

To a glass vial containing 10 mL of the as-prepared AuNP solution and while stirring at 1200 rpm, 10.0 μL of a dilute aqueous NaOCl solution (1.0–1.5 wt.% active chlorine) was added, followed after ~ 2 min by a certain volume of an aqueous 50 mM HAuCl_4 solution, $V_{\text{Au}^{3+}}$. After ~ 2 min stirring was turned down to 500 rpm and the mixture was left to react until the reshaping was completed, which increased with increasing particle size (typically taking ~ 2 h for 100 nm particles) and could be followed by periodically taking UV-VIS extinction spectra: when the spectrum was no longer changing the reaction was assumed to be completed. No adverse effects were observed when the etching was left to continue overnight. Like the growth step, the etching could be scaled up to larger volumes by adjusting the volumes of all reactants accordingly. After etching was completed the particles were collected by means of centrifugation (500–10 000 RCF depending on particle size), redispersed in an equal volume of H_2O , centrifuged and finally redispersed in a 5 mM CTAC in water solution at a gold concentration of ~ 1 mg/mL.

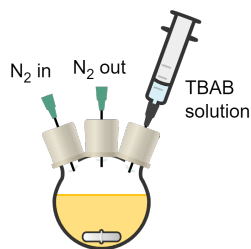
3.7.6 Ligand exchange of AuNPs@CTAC

To functionalize the surface with thiol-terminated poly(ethylene glycol) molecules (PEG-SH), CTAC-stabilised particles were collected from a batch of 400 mL unwashed as synthesised 80 nm AuNPs@CTAC by means of centrifugation (1000 RCF for 30 min in 50 mL centrifuge tubes). The particles were re-dispersed in 40 mL of an aqueous solution containing 0.50 g/L mPEG5k-SH and left to adsorb overnight. To ensure full removal of the CTAC ligands, the functionalisation procedure was repeated by collecting the particles using centrifugation and re-dispersing the particles in 40 mL of a fresh 0.50 g/L mPEG5k-SH solution. The particles were then collected by centrifugation and redispersed in 40 mL clean water three times to ensure full removal of any PEG molecules that were not bound to the AuNPs.

3.7.7 Synthesis of 2–5 nm AuNPs@OlAm

Small apolar AuNPs@OlAm were prepared as follows:^[383,388] A 50 mL three-neck flask with a magnetic stirring bar were cleaned with *aqua regia* (a 3:1 V:V mixture of concentrated hydrochloric and nitric acid), rinsed with copious amounts of water and dried prior to use. 197 mg $\text{HAuCl}_4 \cdot 3 \text{H}_2\text{O}$ (0.500 mmol) was dissolved in 10.0 mL OlAm and 10.0 mL tetralin in a glass 20 mL scintillation vial using vortex mixing, degassed using a sonication bath, and transferred to the three-neck flask and sealed off air-tight with rubber septa. The solution was placed under nitrogen atmosphere by flowing N_2 into the flask via a needle (40 mm \times \varnothing 0.9 mm) through the septum in the central neck, a second needle was added through one of the other septa acting as outlet for the N_2 flow. The solution was left stirring at 400 rpm under N_2 flow for at least 15 min prior to continuing the reaction. When performing the reaction at reduced or elevated temperature, the flask was placed in a thermostatted water or water/ice bath during this step and kept at a controlled temperature throughout the remainder of the reaction. Meanwhile, 87 mg TBAB (1.0 mmol) was dissolved in 1.00 mL OlAm and 1.00 mL tetralin using sonication for 2 min. The stirring rate of the flask was turned up to 1200 rpm and using a 2 mL syringe with a needle (40 mm \times \varnothing 1.2 mm) the TBAB solution was injected rapidly directly into the gold solution in the flask, during which the reaction mixture rapidly turned to a dark brown/black colour. The reaction was left to proceed for 2 hours, during which the colour changed to a strong dark red due to the localised surface plasmon resonance of the particle.

To remove excess OlAm, tetralin and unwanted reaction products the particles were washed using antisolvent precipitation and centrifugation. The reaction mixture was transferred to four 50 mL polypropylene centrifuge tubes using 2–5 mL of hexane and acetone was added until the particles precipitated at which point scattering could be observed and the reddish hue turned purple, this typically took between 120 and 150 mL of acetone depending on the particle size (larger particles precipitate sooner). The tubes were centrifuged at 5000 RCF for 5 min after which the supernatant was


Figure 3.24: AuNPs@citrate reaction setup

Figure 3.25: AuNPs@OIAM reaction setup

mostly clear and was discarded. The particles were redispersed in 10 mL hexane and collected in one centrifuge tube, to which ethanol was added until the particles precipitated, typically 10–15 mL ethanol was needed. The particles were then again collected using centrifugation, and finally redispersed in 5 mL hexane. To aid in long term stability of the particles, a small excess OIAM ligands was added to the particle dispersion of 5 μL OIAM per 1 mL of hexane.

3.7.8 Seeded growth of AuNPs@OIAM

For a seeded growth step on AuNPs@OIAM, a 50 mL three-neck flask with a magnetic stirring bar were cleaned with *aqua regia* (a 3:1 V:V mixture of concentrated hydrochloric and nitric acid), rinsed with copious amounts of water and dried prior to use. 100 mg $\text{HAuCl}_4 \cdot 3 \text{H}_2\text{O}$ was dissolved in 20.0 mL 1-octadecene and 1.00 mL OIAM and placed in the under nitrogen flow as described in Section 3.7.7 and stirred at 200 rpm. Meanwhile, an oil bath was pre-heated to 60 °C. After 10 min, stirring was turned to 1200 rpm and 3.00 mL of 10 mg/mL dispersion of AuNPs as prepared in Section 3.7.7 was injected into the reaction mixture using a syringe with needle (40 mm \times \varnothing 1.2 mm). After 30 s the flask was placed in the oil bath and left to react under N_2 flow and at 60 °C for 2 h after which heating was removed and the mixture was left to cool to room temperature.

To remove excess OIAM, octadecene and unwanted reaction products, the particles were washed using antisolvent precipitation and centrifugation. The particles were washed once with acetone and once with ethanol as described in Section 3.7.7. The reaction mixture was transferred to 2 50 mL polypropylene centrifuge tubes using 2–5 mL of hexane and acetone was added until the particles precipitated at which point scattering could be observed and the reddish hue turned purple, this typically took between 120 and 150 mL of acetone depending on the particle size (larger particles precipitate sooner). The tubes were centrifuged at 5000 RCF for 5 min after which the supernatant was mostly clear and was discarded. The particles were redispersed in 10 mL hexane and collected in one centrifuge tube, to which ethanol was added until the particles precipitated, typically 10–15 mL ethanol was needed. The particles were then again collected using centrifugation, and finally redispersed in 5 mL hexane. To aid in long term stability of the particles, a small excess OIAM ligands was added to the particle dispersion of 5 μL OIAM per 1 mL of hexane.

If even larger particles were desired, it was possible to use the particles from a seeded growth step as seeds in a second seeded growth procedure in the same manner as the first growth step.

3.7.9 Ligand exchange of AuNPs@OIAM

For ligand exchange, excess OIAM ligands were removed as follows: 1.00 mL of an as synthesised stock of AuNPs in hexane containing \sim 10 mg particles with excess OIAM were precipitated by adding between 0.5 and 1.5 mL ethanol, which was added until the dispersion went turbid with the required amount depending inversely on particle size, and collected with centrifugation at 5000 RCF for 5 min after which the supernatant was removed and 1.00 mL clean hexane was added. For ligand exchange with liquid thiolated ligands (e.g. 1-octanethiol, 1-dodecanethiol, 1-hexadecanethiol, ...) 20 μL of the

ligand was added directly to the cleaned particle dispersion, after which the sample was vortex mixed and left to react for at least 30 min to ensure the OLAm was fully replaced. Excess ligand was then washed away by adding 0.5–1.5 mL ethanol and centrifuging at 5000 RCF for 5 min. The particles were then re-dispersed in 1.00 mL hexane, again precipitated with ethanol and centrifuged, and finally re-dispersed in 1.00 mL hexane. For ligand exchange with thiolated polystyrene ligands, 200 μL (in case of PS880–SH and PS2.3k–SH) or 100 μL (in case of PS5.3k–SH and PS5.8k–SH) of a 1.0 μM PS-SH solution in chloroform was added to the cleaned particle dispersion. The sample was vortex mixed after which the reaction was left to proceed for at least 30 min to ensure the OLAm was fully replaced. Excess PS-SH was then washed away by adding 4 mL ethanol and centrifuging at 20 kRCF for 10 min. The particles were then re-dispersed in 200 μL clean chloroform, precipitated with 4 mL ethanol and centrifuged at 20 kRCF for 10 min, dried under nitrogen flow such that the dry particle weight could be determined, and finally re-dispersed in toluene at the desired concentration.

3.7.10 Synthesis of 200 nm non-fluorescent Stöber silica particles

Silica spheres in the size range of 150 nm to 250 nm without fluorescent labelling were synthesised as follows:^[408] an amount of ethanol, V_{EtOH} , (typically 135 mL), $V_{\text{H}_2\text{O}}$ (typically 4.50 mL) H_2O and $V_{\text{NH}_3(\text{aq})}$ (typically 12.0 mL) ammonium hydroxide solution were placed in a 250 mL round bottom flask with stirring bar (both cleaned in a saturated KOH/EtOH base-bath and rinsed several times with water and dried). Values for the reactant volumes are given in Table 3.3. The mixture was stirred 1200 rpm, and 9.00 mL TEOS was rapidly injected into the mixture. Over the course of 15 min the mixture gradually turned from transparent to a light hazy blue and eventually opaque white. After two hours, stirring was stopped and the particles were collected by means of centrifugation (100 RCF for 1 h in a 400 mL flat bottomed jug) and redispersed as a concentrated stock dispersion in in 40 mL ethanol. The volume of ethanol could be increased to obtain smaller particles or decreased for larger particles.

Table 3.3: Parameters and results of the non-fluorescent Stöber silica synthesis.

V_{TEOS}	V_{EtOH}	$V_{\text{H}_2\text{O}}$	$V_{\text{NH}_3(\text{aq})}$	diam. (nm)	PD (%)
9.00	120	4.50	12.00	219.5	6.2
9.00	120	7.50	9.00	206.0	5.3
9.00	135	4.50	12.00	182.8	4.9
9.00	150	4.50	12.00	172.9	5.3
9.00	150	7.50	9.00	168.0	5.0
9.00	180	4.50	12.00	147.7	5.4
9.00	180	7.50	9.00	155.2	4.7

3.7.11 Synthesis of micron-sized fluorescently labelled Stöber silica particles

Synthesis of 400 nm fluorescent silica Stöber cores:

Fluorescent FITC-labelled silica spheres of ca. 400 nm were produced as follows:^[404,406] 49 mg (0.13 mmol) FITC was mixed with 4.90 mL absolute ethanol in glass vial, forming a orange-green coloured turbid suspension. Then, 58.7 μL (0.25 mmol) APTES was added after which the mixture immediately turned to a strongly orange clear solution. The vial was wrapped entirely in aluminium foil to avoid exposure to light, and placed on a roller for 30 min to allow the FITC to fully dissolve and react. Then, 220 mL ethanol and 23.6 mL ammonium hydroxide solution were placed in a 500 mL round bottom flask with stirring bar which had both been cleaned in a saturated KOH/EtOH base-bath, rinsed several times with water and dried. The mixture was stirred at 700 rpm (such that the vortex ended right above the stirring bar) and 10 mL of TEOS was rapidly injected, followed immediately by the FITC-APTES mixture. Over the course of 15 min the reaction mixture turned to turbid yellow. After

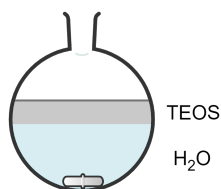


Figure 3.26: setup for AACS synthesis

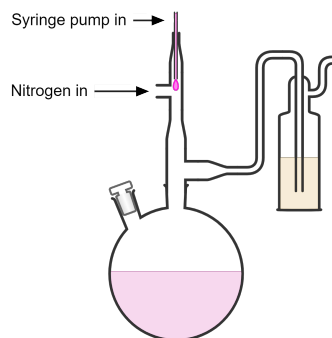


Figure 3.27: Stöber shell growth setup

2 hours, the reaction was stopped and the particles were washed to remove unincorporated dye from the mixture: the particles were collected by means of centrifugation (200 RCF for 1 h in a 400 mL flat bottomed jug), redispersed in 200 mL ethanol, centrifuged and finally redispersed in 100 mL ethanol. RITC labelled particles could be produced in a similar manner by replacing FITC with an equal weight of RITC and adjusting the APTES amount to a 2:1 molar ratio with respect to the RITC.

Fluorescent shell growth on Stöber silica cores:

Fluorescently labelled silica cores as synthesised above could be increased in size by growing a fluorescent shell as follows: 84.3 mg (0.22 mmol) FITC was mixed with 8.43 mL absolute ethanol in a glass vial, and 101 μL (0.43 mmol) APTES was added, after which the vial was wrapped entirely in aluminium foil to avoid exposure to light and placed on a roller for 30 min. Meanwhile, 256 mL ethanol, 20.0 mL of the ethanolic silica dispersion (containing 1.12 g silica by dry weight), 36.2 mL H_2O and 10.0 mL ammonium hydroxide solution were placed in a 500 mL 2-neck round bottom flask with stirring bar (both cleaned in a saturated KOH/EtOH base-bath, rinsed several times with water and dried), closed with glass stoppers and sonicated for 30 min in an ultrasonic bath. The flask was placed in a heating mantle at 35 °C and attached to a custom glass column with two connections on the sides for applying a light nitrogen flow in order to prevent ammonia vapour from reaching the top where a tube was inserted to connect to a syringe pump for controlled addition of TEOS, the setup is schematically depicted in Figure 3.27. The nitrogen was vented out through a gas wash bottle with silicone oil to avoid air intrusion and to create a very light overpressure, the nitrogen flow was controlled with a needle valve to ~1 bubble per second. 8.00 mL absolute ethanol, 8.00 mL of the FITC solution and 16.0 mL of TEOS were mixed and put in a plastic 60 mL syringe which was placed in a syringe pump and connected with teflon tubing to the top of the glass column, such that the end of the tube was above the nitrogen inlet and such that a droplet falling from the tube would fall directly into the flask below without hitting the sides of the glass. The mixture was gently stirred (400 rpm) and 29.46 mL of the TEOS/FITC mixture was added over the course of ~40 h at a rate of 0.73 mL/h. After addition was complete, the mixture was left to react for another 2 h after which heating, stirring and the nitrogen flow were removed. The particles were washed by means of centrifugation (200 RCF for 1 h in 50 mL centrifuge tubes), redispersed in 300 mL ethanol, centrifuged and finally redispersed in 100 mL ethanol.

Non-fluorescent shell growth:

The particle size was further increased by growing a non-fluorescent shell around the particles to the final desired particle size in a similar manner as the fluorescently labelled shell: 221 mL ethanol, 15.0 mL of the ethanolic dispersion of ~800 nm FITC-Silica particles, 30.0 mL H_2O and 15.0 mL ammonium hydroxide solution were sonicated and placed under nitrogen flow at 35 °C as described above. 33.95 mL

of an ethanolic 50 vol.% TEOS solution was injected using a syringe pump at a rate of initially 0.25 mL/h, after 12 hours the addition rate was increased to 0.50 mL/h, and after another 24 hours the addition rate was increased further to 1.00 mL/h and 18.0 mL ethanol, 2.00 mL H₂O and 2.00 mL ammonium hydroxide solution were added to compensate for losses through evaporation. Two hours after the addition was finished, the particles were washed by means of centrifugation (100 RCF for 20 min in 50 mL centrifuge tubes), redispersed in 80 mL ethanol, followed by 4 more sets of centrifugation and redispersion.

3.7.12 Amino-acid catalysed synthesis of silica NPs

Synthesis of 30 nm silica particles:

Amino-acid catalysed silica (AACS) seed particles were prepared as follows:^[416] a 500 mL round-bottom flask and magnetic stirring bar were cleaned in a saturated KOH in ethanol base bath, rinsed with ethanol and water and dried prior to use. 183 mg (1.05 mmol) of L-arginine and 169 g (168 mL) H₂O were added to the flask. The flask was closed off with a base-bath clean glass stopper and heated to 70 °C using a hot-plate with heating mantle and thermocouple, while stirring at 200 rpm. After 1 h to assure all arginine had dissolved, 11.2 mL TEOS was gently pipetted on top of the arginine solution such that a two-layer system was formed instead of an emulsion. The flask was closed with the stopper and wrapped in aluminium foil to keep the temperature as constant throughout the flask as possible. The reaction was left to continue at 70 °C and 200 rpm stirring overnight until the TEOS layer had fully reacted away, after which heating was removed and the particle dispersion was left to cool and stored in a glass jar without further purification.

Amino-acid catalysed seeded growth of silica NPs:

A 500 mL round-bottom flask and magnetic stirring bar were cleaned in a saturated KOH in ethanol base bath, rinsed with ethanol and water and dried prior to use. 164 mg (0.94 mmol) of L-arginine and 152 g (152 mL) H₂O were added to the flask. The flask was closed off with a base-bath clean glass stopper and heated to 65 °C using a hot-plate with heating mantle and thermocouple, while stirring at 200 rpm. After 45 min to assure all arginine had dissolved, 25.0 mL of seed particle dispersion as prepared in **Section 3.7.12** was added to the flask. After 15 min, 10.0 mL TEOS was gently pipetted on top of the arginine solution such that a two-layer system was formed instead of an emulsion. The flask was closed with the stopper and wrapped in aluminium foil to keep the temperature as constant throughout the flask as possible. The reaction was left to continue at 65 °C and 200 rpm stirring overnight until the TEOS layer had fully reacted away, after which heating was removed and the particle dispersion was left to cool and stored in a glass jar without further purification. It was possible to perform another seeded growth step to further increase the particle size to ~85 nm in an identical manner as the first growth step, except using 37 mL of the dispersion of larger cores and reducing the volume of added TEOS to 4.5 mL.

3.7.13 Shell growth on AACS silica cores

Non-fluorescent shell growth on AACS:

For growth of a thin stabilisation layer of (mostly) unlabelled Stöber silica around AACS particles, 215 mL ethanol, 8.00 mL H₂O, 11.5 mL ammonium hydroxide solution and 20 mL of unwashed 85 mL AACS particles (as obtained after two regrowth steps) were added to a 500 mL round bottom flask and stirred at 200 rpm for 10 minutes. Then, 360 µL TEOS was added, after which the mixture was left to react for 2 hours. To remove excess dye still present from the synthesis, the particles were washed using dialysis: dialysis tubing cellulose membrane (Sigma-Aldrich no D9527) was soaked in H₂O for at least 24 hours. The tubing was then rinsed with water, and subsequently with ethanol and filled with 50 mL of the particle dispersion which was placed in a closed off container containing 1 L of a 5 vol.% ammonium hydroxide solution 95 vol.% ethanol mixture for 25 days, the solvent was replaced several times during this period.

Fluorescent shell growth on AACs@Stöber:

Fluorescent RITC shells were grown on 60 nm AACs silica cores in a similar manner to fluorescent shell growth described above: 79 mg (0.15 mmol) RITC, 7.90 mL ethanol and 65.6 μL (0.28 mmol) APTES were mixed for 30 min as before, while 38 mL ethanol, 5.00 mL of unwashed aqueous 60 nm AACs particles (18.1 mg/mL dry weight), and 2.03 mL ammonium hydroxide solution were sonicated and placed under nitrogen flow at 35 °C as described in [Section 3.7.11](#). 5.75 mL RITC-APTES mixture, 5.75 mL absolute ethanol and 11.5 mL TEOS were mixed and placed in a 20 mL syringe, and added to the reaction mixture using a syringe pump at a rate of initially 0.35 mL/h, after 4 hours the addition rate was increased to 0.70 mL/h. The particles were washed once by centrifugation (200 RCF for 3.5 hours in two 50 mL centrifugation tubes) and redispersion in 80 mL.

Fluorescent FITC shells were grown on 60 nm AACs silica cores in a similar manner as the RITC shells, except that a smaller quantity of dye-APTES solution (4.00 mL instead of 7.50 mL) was used and the amount of ethanol in the initial mixture was increased to 60 mL. Otherwise, the reactant concentrations and addition rate were kept the same.

Non-fluorescent shell growth on AACs@Stöber:

The particle size of the AACs@RITC-silica core-shell particles was further increased by growing a non-fluorescent shell around the particles to the final desired particle size of 400 nm in a similar manner as before: 260 mL ethanol, 10.0 mL of the ethanolic dispersion of ~230 nm FITC-Silica particles (63.9 mg/mL dry weight), 35.0 mL H₂O and 5.0 mL ammonium hydroxide solution were sonicated and placed under nitrogen flow at 35 °C as described above. 16.4 mL of an ethanolic 50 vol.% TEOS solution was injected using a syringe pump at a rate of 0.80 mL/h. When the addition was finished, mixture was left to react for another 2 hours after which the particles were washed by means of centrifugation (200 RCF for 1 h in 400 mL plastic jugs) and redispersion in 80 mL ethanol.

The AACs@FITC-silica core-shell particles were grown to a ~300 nm by stepwise addition of TEOS: to a 20 mL vial 6.04 mL ethanol, 1.00 mL of the ethanolic particle dispersion (41.4 mg/mL dry silica weight) and 0.37 mL ammonium hydroxide solution were added, after which the vial was placed in a sonication bath for 30 min to fully disperse the particles. The vial was stirred at 1000 rpm at room temperature and 500 μL of a 10 vol.% TEOS/ethanol solution was slowly added over the course of ca. 10 s. After one hour, another 500 μL of the 10 % TEOS solution was slowly added, this was repeated once more after another hour. Finally, after another hour 508 μL of the 10 % TEOS solution was slowly added. The amount of the 10 vol.% TEOS solution added in each step could be adjusted to tune the precise final particle size to obtain a range of different sizes to precisely tune the size ratio. An overview of volumes and corresponding particle sizes is given below in [Table 3.4](#). The particles were stored without further purification.

Table 3.4: added TEOS volume and resulting particle sizes in step-wise silica shell growth on AACs@FITC-silica.

10 vol.% TEOS volume per step (μL)					diameter	PD
1	2	3	4	5	(nm)	(%)
500	500	363	0	0	290	1.5
500	500	500	175	0	294	1.2
500	500	500	338	0	299	1.2
500	500	500	508	0	303	1.0
500	500	500	500	75	334	1.3
500	500	500	500	270	330	1.2

3.7.14 Particle size analysis using transmission electron microscopy

PELCO copper 200 mesh TEM support grids coated with Formvar stabilised with 5–10 nm carbon (*Ted Pella* no. 01800) grids were purchased from *van Loenen Instruments*. The support grid was held by the copper edge in reverse (self closing) precision tweezers, 4 μL of a concentrated particle dispersion was dropcasted carefully on the carbon coated side of the support grid such that the solvent did not get pulled between the tweezer tips due to capillary action, and was left under ambient conditions for the solvent to evaporate. Using this procedure a wide variety in particle concentrations (by >1 order of magnitude) was achieved over the grid due to the coffee ring effect^[424] which eliminated the need for precise tuning of particle concentration. In case of a large background concentration of other nonvolatile species, such as excess ligand for AuNPs, a single washing step was performed by means of centrifugation and redispersion in clean solvent prior to preparing the TEM sample to remove those species.

Imaging was performed using a *FEI Tecnai 20* transmission electron microscope operated at 200 kV or a *ThermoFisher Scientific Talos 120c* transmission electron microscope operated at 120 kV. The accuracy of the spatial calibration of these microscopes was estimated to be within $\sim 1\%$ of the measured size. Micrographs were always taken at a variety of magnifications and in multiple different locations on the grid to achieve a representative sample and avoid bias due to *e.g.* size-selective drying effects or phase separation of different species. Care was taken to avoid effects of beam damage such as sintering of AuNPs due to beam-induced heating at high magnification or beam-induced shrinkage of SiO_2 colloids. For particles with extremely low polydispersities (polydispersity $\leq 2\%$ of the mean particle size) additional care was taken to avoid influence of slight variations in the measured size at different magnifications due to *e.g.* variations in the microscope calibration and pixel-biasing in the analysis by calculating the mean particle size from data at multiple different magnifications, while only using data from a single magnification level to determine the polydispersity.

Particle sizes were measured from the TEM images either by hand using ImageJ (V 1.53e),^[425] or using an automated particle-sizing algorithm described below and available on request. For all reported sizes, at least 200 particles were measured, although automated analysis allowed for several thousand particles in most cases. When using automated analysis, the results were always inspected manually and any spurious measurements were removed from the dataset. Unless otherwise mentioned, particle size is defined as the diameter of the projected image of the particle. The arithmetic mean (“average”) particle size \bar{x} and polydispersity PD_x were calculated from a list of n individual size measurements $\{x_1, x_2, \dots, x_n\}$ as follows:

$$\bar{x} = \frac{1}{n} \sum_{i=1}^n x_i \quad (3.1)$$

$$\text{PD}_x = \sqrt{\frac{1}{n-1} \sum_{i=1}^n (x_i - \bar{x})^2} \quad (3.2)$$

where the statistical error in the mean and polydispersity of n measured particles could be estimated as $\sigma_{\bar{x}} \approx \text{PD}_x / \sqrt{n}$ and $\sigma_{\text{PD}_x} \approx \text{PD}_x / \sqrt{2(n-1)}$ respectively. When reporting particle sizes in this thesis we mostly use the following notation:

$$\bar{x} \pm \text{PD}_x \text{ (RPD}_x\text{)}$$

where RPD_x is the *relative* polydispersity calculated as PD_x / \bar{x} and typically given as percentage.

A custom automated particle size analysis algorithm was implemented in the *Python* programming language (V. 3.7) and based on methods from the *Open Source Computer Vision Library* (opencv-python V. 4.4.0),^[426] and is available as importable Python library or stand-alone executable on request. It consists of a series of thresholding steps followed by a seeded watershed segmentation algorithm and ellipse-fitting of the obtained edge contours. First, median filtering with a square kernel of typically 9 pixels was used to remove noise while mostly retaining edges. An automatic intensity thresholding

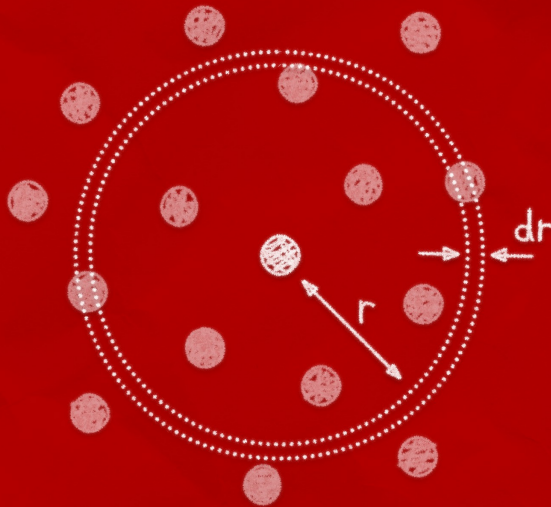
(Otsu's method) performs a rough segmentation between foreground and background. The seed regions for the particles—the foreground—is further processed to segment touching particles by performing a distance transform on the foreground regions and thresholding the resulting distance image again, resulting in a particle seed image where each particle is represented by a small region that is guaranteed to be smaller than and entirely enclosed in the area covered by the original particle. The value of this distance-threshold can be user-optimized as a too high threshold may lead to smaller particles being omitted, while a too low threshold may not segment larger touching particles from one another. The background region is obtained by performing an erosion (“shrinking”) of the background region in the original binary image with a disc kernel typically 15–20 pixels in size. This serves to assure that the background seed regions do not overlap with the particles even when the original thresholding underestimated the particle size. The kernel size is user adjustable. The particle seeds and background seeds serve to determine where there are (and are not) particles and passed to a seeded watershed segmentation which determines the optimal boundary between the seed regions. This boundary region is fitted with an ellipse, and the diameter is calculated as the diameter of a circle that has the same area as the ellipse. Additional filtering of spuriously detected regions is possible based on diameter or aspect ratio thresholds, as well as a manual point-and-click interface to remove any other spurious particles from the dataset.

3.7.15 Calculation of LSPR spectra

Optical extinction spectra for spherical gold nanoparticles were calculated with Mie theory using a custom Python implementation of the code by Demers & Hafner *et al.*^[SI of 381] (which in turn was based on Bohren & Huffman^[382, pp. 477–482]) with dielectric values from Irani & Wooten *et al.*^[427] ($\lambda \leq 500$ nm) and Johnson & Christy^[428] ($\lambda > 500$ nm); these data were chosen based on a literature comparison by Khlebtsov^[429] and interpolated with a 3rd order B-spline to allow for arbitrary choice of wavelength. The first 10 plasmon modes were included in the calculation. Theoretical extinction spectra as function of particle size were calculated by calculating the wavelength-dependent extinction cross-sections for a range of NP sizes (20 nm to 200 nm in 2.5 nm increments) in the wavelength range of 450 nm to 750 nm in 2 nm increments. The experimental data were then fitted with a weighted sum of normally distributed theoretical spectra from the binned size-dependent list, where the mean, standard deviation and area of the normal distribution—representing the mean particle size, polydispersity and total particle concentration respectively—were optimised as the fit parameters.

Part II

Interactions from Distribution Functions



CHAPTER 4

Using solvent-arresting and real-space microscopy to probe interactions in 3D

ABSTRACT

In this chapter we demonstrate that the recently proposed method of test-particle insertion may be used to determine the pairwise interaction potential between colloidal particles from 3-dimensional positional data obtained by *e.g.* confocal laser scanning microscopy or SEM-tomography, and present codes to do so in two or three dimensions and using various boundary geometries. A novel solvent-arresting procedure was utilized where the dispersing medium of the colloidal particles contained polymerisable molecules and a photoinitiator, which allowed for the samples to be arrested in-place by a rapid UV-induced polymerisation. Because arresting could be achieved on a faster time scale than the diffusion of the particles, their positions, conferring information about the interactions, were preserved as they were just before the polymerisation was induced. This arresting procedure was applied to different colloidal particle systems including nanoparticles. Finally, we show that solvent-arresting could also be used to characterise the sedimentation, real-space structure and interactions of a binary system, containing particles with two different sizes, which can form different (unary and binary) colloidal crystals upon sedimentation.

4.1 Introduction

As we have seen in **Chapter 2**, many methods for determining inter-particle interactions from microscopy data rely on the fact that colloidal particles typically follow Boltzmann statistics, which means that the likelihood of finding a particle in a certain position is directly related to the local potential energy in that position. In other words: under Boltzmann statistics and equilibrium conditions, positional probabilities and energies are directly linked. If one assumes the local potential energy only depends on interactions with other particles, these interaction energies may be extracted from measurement of the relative probabilities associated with certain inter-particle distances through measurement of a large ensemble of real-space particle coordinates. As mentioned, this probability density distribution is generally referred to as the radial distribution function, denoted $g(r)$, from which inter-particle interaction potentials may be extracted using several different methods. Here, we focus on the recently proposed iterative use of test-particle insertion to extract pair potentials,^[177,430] as it allows for arbitrary (discretised) potentials to be obtained, can be used up to comparably high particle density and relies on few assumptions about system properties.

In this chapter, we use confocal laser scanning microscopy (CLSM) in combination with a particle localisation algorithm to determine three-dimensional particle coordinates and calculate the associated distribution of particle-particle distances, such that inter-particle interactions may be extracted. As is schematically depicted in **Figure 4.1**, CLSM is a fluorescence microscopy technique which works by placing a pinhole before the detector in an optical conjugate of the real-space focal plane of the objective lens —hence “con-focal”—, such that only the light originating from a single point in the sample can reach the detector. This gives it a superior resolution to conventional wide-field microscopy techniques, most notably along the optical axis (the ‘ z direction’) such that each imaged plane represents a thin optical section, and three-dimensional imaging is possible by sequentially recording images at different heights in the sample. However, only a single spot is illuminated at a time, meaning the sample must be raster-scanned to record an image. Consequently, the time resolution of CLSM is generally orders of magnitude slower than wide-field detection with typical imaging rates of $\ll 1$ Mpx/s. This is obviously a problem in the context of interaction measurements: calculation of the $g(r)$ requires the instantaneous coordinates of a large set of particles, but the particles in colloidal dispersions are constantly moving due to Brownian motion. Although some techniques exist to achieve higher imaging rates for CLSM, as we will see for example in **Chapter 6**, these typically make compromises on resolution and signal/background and are generally not compatible with super-resolution imaging using stimulated emission depletion (STED). Instead, we propose the use a solvent-arresting procedure by which a sample of colloidal particles may be rapidly fixated such that particle positions are preserved, similar to the rapid vitrification of samples for cryogenic electron microscopy. This is achieved by replacing part of the solvent with a liquid polymerisable monomer and including a UV-sensitive radical photo-initiator, such that a short pulse of an external UV light source induces rapid cross-linking of the monomers, thereby converting the liquid solvent into a polymer gel.

First, we introduce the test-particle insertion method as an alternate means to calculate $g(r)$ in addition to the more conventional distance histogram method. Next, we discuss how these two may be combined in an iterative procedure to solve for the pairwise interaction potential from only a set of particle coordinates, and provide a practical computational

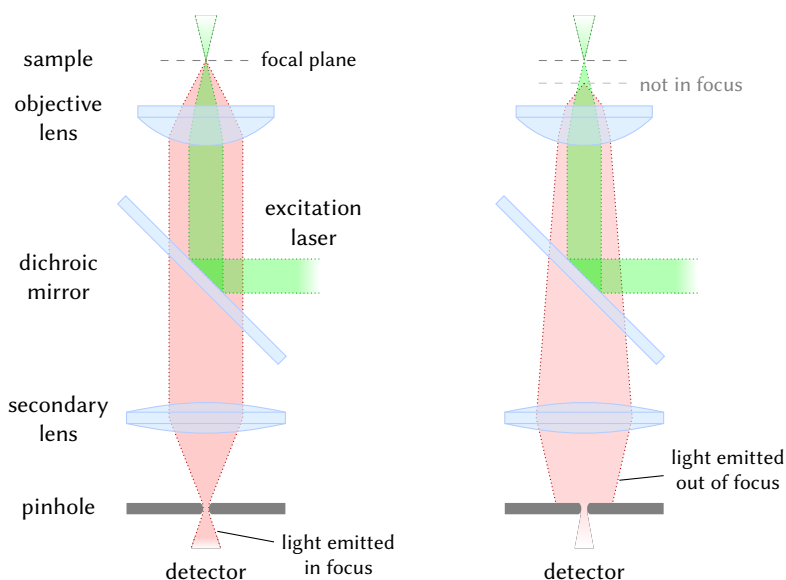


Figure 4.1: basic principles of confocal laser scanning microscopy. Even when an excitation laser is tightly focussed into a spot in the sample, fluorescence can occur in the path of the laser above and below the focal plane. By placing a pinhole in a conjugate focal plane of the objective lens and excitation laser, light originating from the focal plane is focussed on the pinhole and can thus pass through mostly unaffected (left image side), while any light originating from out-of-focus areas of the sample is *not* in focus at the pinhole and thus mostly blocked from reaching the detector (right image).

implementation to do so for simulated and experimental data in the form of a *Python* package^[431] (available on p. 115). We then introduce and benchmark the solvent-arresting procedure to ‘arrest’ colloidal dispersions for subsequent high-resolution CLSM imaging, and apply these methods to a system of silica nanoparticles and a binary system of larger silica colloids. Lastly, we show that by dispersing particles in pure monomer without any co-solvent solid samples can be prepared which are compatible with volumetric scanning electron microscopy (also known as FIB-SEM tomography), allowing for an imaging resolution on the order of single nanometers.^[262]

4.2 Theory

At its core, test-particle insertion (TPI) —also known as the Widom insertion method since it was originally proposed and derived by Widom^[174]— is not a method for determining inter-particle interactions from the radial distribution function, $g(r)$, but rather a tool to calculate $g(r)$ for a set of coordinates when the pairwise interaction potential $U(r)$ is known. It is based around the notion that the $g(r)$ may be related to the ratio of the local and global averaged probability for the (virtual/hypothetical) insertion of an additional ‘test-particle’ the system, based on the chemical potential: the change in the free energy with respect to the density. Since probability and energy are related through the Boltzmann exponent, the

insertion probability of a test particle i is given by

$$P_i = e^{-\psi_i/k_B T} \quad (4.1)$$

where ψ_i is the *insertion energy*, *i.e.* the chemical potential at the insertion position. For a system of (colloidal) particles with only pairwise interactions, the insertion energy is simply the sum of all pairwise interactions with n neighbouring particles j around the insertion point:

$$\psi_i = \sum_{j=1}^n U(r_{ij}). \quad (4.2)$$

TPI then relies on the notion that the $g(r)$ may be calculated as the ratio of $P(r)$ —the (local) insertion probability of inserting a test-particle at some distance r from a pre-existing particle—to \bar{P} , the average insertion probability of the system as a whole, *i.e.*:

$$g_{\text{TPI}}(r) = \frac{P(r)}{\bar{P}} = \frac{\langle P_i \rangle_{i \in r}}{\langle P_i \rangle_i} \quad (4.3)$$

where the angled brackets denote an ensemble average over many test-particles and subscript $i \in r$ refers to the subset of test-particles which were inserted at distance r to a pre-existing particle in the dataset. In other words, for a set of particle coordinates from *e.g.* experiments, the TPI algorithm probes a large number of positions, for each of which the energy cost of inserting a test-particle in that location is calculated as the sum of pairwise interactions with the particles in the dataset. Because the distances to all particles around the insertion location need to be calculated only once per test-particle, this requires far fewer computations than *e.g.* running a Monte Carlo simulation.^[88,432]

The choice of the insertion locations may be made in several ways. Firstly, particles may be inserted at locations which are exactly r from one of the pre-existing particles in the dataset for a discrete list of values for r . In this manner, exact distances may be probed, unlike with conventional $g(r)$ methods which rely on binning a finitely wide range of distances. This is of use for example in case of discontinuous potentials, where *e.g.* a contact value may not be accurately obtained from a bin average.^[176] However, this is an inefficient form of sampling as each insertion only contributes to a single distance even when the insertion location is within interaction range of many particles, and thus requires a large number of insertions for each r one wishes to probe. Alternatively r can be divided in bins rather than using discrete values, such that the insertion probability of every test particle may be added to all bins corresponding to the distances to nearby particles, *i.e.* a test-particle interacting with five particles contributes to up to five different bins. In this case the insertion locations may be chosen on a regular grid or using a (uniformly distributed) pseudorandom number generator.

There is of course another reason to use such binned sampling in TPI, particularly in the context of interaction measurements: it makes direct comparison possible to the $g(r)$ obtained using the more conventional distance histogram method. In interaction measurements, the $U(r)$ is *not* known *a priori* and the $g_{\text{TPI}}(r)$ cannot be calculated directly. Instead, the $g(r)$ may be calculated through the distance histogram method as

$$g_{\text{DH}}(r) = \frac{N(r, r + \delta r)}{n \rho V(r, r + \delta r)} \quad (4.4)$$

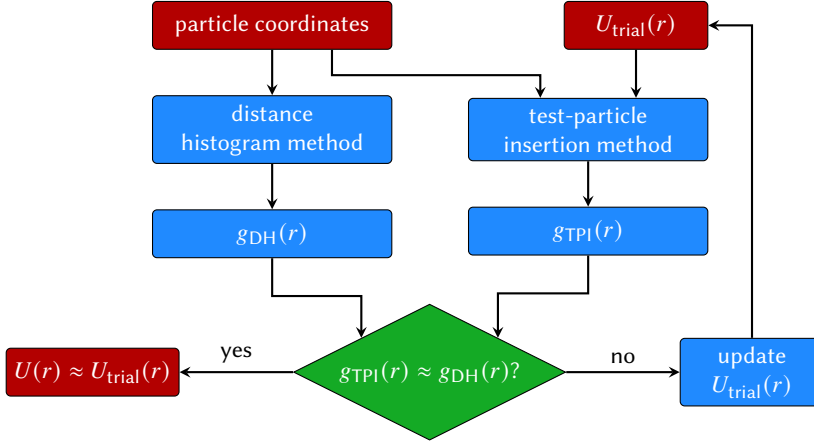


Figure 4.2: extraction of interaction potentials using iterative test-particle insertion. A set of experimental particle coordinates and an initial guess for the pair potential are used to calculate the radial distribution functions $g(r)$ using a distance histogram method (DH) and test-particle insertion (TPI). If these do not match, the difference is used to update the trial potential. This is iteratively repeated for the same set of experimental particle coordinates until a convergence criterium is met.

where $N(r, r + \delta r)$ is the number of particle pairs with a distance between r and $r + \delta r$ — i.e. the value of one bin in the histogram of all pairwise distances r —, n is the total number of particles in the system, ρ is the average number density of particles and $V(r, r + \delta r)$ is the volume of a spherical shell (in 3D) or the area of a circular ring (in 2D) with inner and outer radii of r and $r + \delta r$ respectively. Using the distance histogram method, the $g(r)$ may thus be calculated from *only* a set of particle coordinates without any knowledge of the pair potential and may be used as a reference for what is the “correct” $g(r)$. Since Henderson’s theorem (see p. 28) states that there is a unique solution for the $U(r)$ giving rise to any particular $g(r)$, if we can find a trial interaction potential $U_{\text{trial}}(r)$ which correctly reproduces the measured $g(r)$, i.e. $g_{\text{TPI}}(r) = g_{\text{DH}}(r)$, this trial potential must be identical to the ‘real’ interaction potential.

Stones & Aarts *et al.*^[177] proposed to use this in an iterative scheme as outlined in **Figure 4.2** where the trial potential is iteratively updated based on the difference between the test-particle and distance-histogram $g(r)$ ’s as follows:

$$U_{k+1}(r) = U_k(r) - k_B T \ln \left(\frac{g_{\text{DH}}(r)}{g_k(r)} \right) \quad (4.5)$$

where $U_k(r)$ and $g_k(r)$ are the trial potential and TPI result of the k^{th} iteration step respectively. Essentially, this assumes that the differences in the associated potentials of mean force are a good analogue for the differences in pairwise interaction potentials, or at least that they are similar enough such that the updated trial potential is an improvement over the previous trial potential. The procedure may be iterated until some convergence criterium is reached, such as when the error function given by the difference between the $g(r)$ ’s is smaller than some tolerance or when the change in the error between iterations reaches a threshold. In this work, we always used a pre-chosen number of iterations after which

iteration was stopped.

Unfortunately Eq. 4.5 is *not* guaranteed to converge: in some cases it can give an updated pair potential which is actually a worse predictor for the observed $g(r)$ due to differences between the potential of mean force and true pairwise interaction potential, particularly for strongly correlated systems where short-ranged interactions result in longer ranged correlations. Furthermore, the use of randomly chosen test-particle coordinates introduces a certain randomness in the result from iteration to iteration. For these reasons we employed a regulation scheme in which the updated potential is taken as a weighted average between the previous and updated trial potentials, with a gradually shifting weight such that subsequent iterations provide increasingly smaller corrections to the potential. Computational details and links to our implementation are given in Section 4.9.

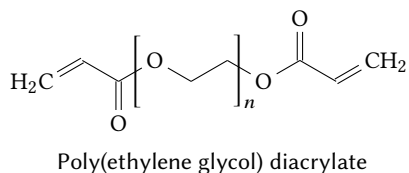
In this work, we restrict our analysis to isotropic and pairwise interactions, but show that the method may be extended to deal with multicomponent systems and measure interactions in a binary system where there are two distinct populations of particles. This still assumes all interactions to be pairwise additive, but it is worth pointing out that it is similarly possible to implement the TPI approach for a three-body or higher correlation function to assess the effects of many-body interactions from sets of multi-particle coordinates.^[178] Furthermore rather than using the fully radially averaged distribution function it would be in principle possible to use anisotropic correlations such as the cylindrical distribution function,^{[433]*} although this has not been done so to the best of our knowledge.

4.3 Solvent arresting

The use of test-particle insertion for extracting inter-particle interactions thus requires the ability to precisely determine the positions of particles in 3 dimensions at some instance in time. To enable (slow) 3-dimensional imaging such that high resolution and precise particle localisation is possible we implemented a solvent-arresting procedure based on rapid local polymerisation of monomers in the solvent, such that particle movement is stopped and particle locations from the moment the arresting was instigated are preserved. This methodology was recently introduced by our group for low-polar systems using the monomer trimethylolpropane ethoxylate triacrylate (ETPTA),^[434,435] and extended in this work to include the ability to arrest more polar systems (including water-based samples) using poly(ethylene glycol) diacrylate (PEGDA) which can have varying polarity depending on the length of the PEG backbone. Some relevant properties of different PEGDA molecules are also given in Table 4.1. To enable solvent-arresting, typically 20 vol.% of the solvent was replaced by liquid PEGDA or ETPTA monomers and 0.2 wt.% of a UV-initiated radical photo-initiator (Irgacure 2100). The arresting procedure was then initiated *in-situ* during CLSM imaging, by illuminating the region of interest with a short pulse of high-intensity UV light through a 0.9 NA condenser lens which was placed on the opposite side of the sample from the objective lens. This led to a rapid increase in viscosity and subsequent full arrest of the system as observed through the mobility of the particles.

In order for the arresting procedure to correctly preserve particle positions, and thus the information used in extracting interactions, the arresting procedure must either not affect the interactions, or occur so fast that the particles do not have time to ‘react’ to the changes in the system upon initiation of the arresting procedure. To quantify the arresting

* see also Chapter 7 for anisotropic interactions and use of the cylindrical distribution function.



M_n (g/mol)	n	ρ^{25} (g/mL)	n_D^{20}	η^{25} (mPa s)
250	3	1.11	1.463	13.4 ^[436]
575	10	1.12	1.467	58.7 ^[436]
700	13	1.12	1.496	97.6 ^[437]

Figure 4.3 & Table 4.1: structure and properties of PEGDA. The molecular structure of PEGDA contains two acrylate groups separated by a PEG backbone of varying length, each of which can form two new bonds via radical polymerization of the C=C double bond. Some physical properties of PEGDA's with different lengths are given on the right, where M_n is the average molar mass, n the average number of PEG monomer units in the backbone, ρ^{25} the density (supplier specified), n_D^{20} the refractive index (measured at 589 nm), η^{25} the viscosity (lit.) and superscripts indicate the temperature in °C at which the values were determined.

rate, we imaged the 2-dimensional diffusion of fluorescent silica marker particles during the arresting process using CLSM, and through particle localisation determined the particle's ensemble-mean squared displacements (MSD's) between sets of subsequent video frames, *i.e.* as a function of time. Defining the start of the UV-pulse as $t = 0$, the data were then fitted using a logistic (smooth step) function of the following form:

$$\frac{\text{MSD}(t)}{2d\Delta t} = D_f + \frac{D_i - D_f}{1 + e^{-k(t-t_a)}} \quad (4.6)$$

where D_i and D_f are the apparent initial and final diffusion rates at $\lim_{t \rightarrow -\infty} \text{MSD}/(2d\Delta t)$ and $\lim_{t \rightarrow \infty} \text{MSD}/(2d\Delta t)$ respectively, d is the spatial dimensionality, k determines the smoothness/steepness of the step and we define t_a as the 'arresting time', which is the point at which the MSD is exactly midway between the initial and final values. To determine the arresting time using a given solvent composition, the arresting procedure was repeated for typically three samples and in typically 6 different spots in each sample. The data for each sample were aggregated and fitted collectively with Eq. 4.6.

Some of the arresting results are shown in Figure 4.4. From the video stills it can be seen that the silica tracer particles, with a total diameter of 325 ± 11 nm (3.4%) (containing a 189 nm RITC labelled core), gave enough fluorescent and could freely diffuse around and interact in the solvent mixture.* When the UV pulse started, the movement of the particles was rapidly inhibited as the monomers formed chains and eventually a cross-linked network, with an arresting time of ~ 0.29 s. The solvent mixture in this case consisted of 60 vol.% triethylene glycol, 20 vol.% glycerol, 20 vol.% PEGDA 700 and 0.2 wt.% Irgacure 2100 photo-initiator, which was chosen because it closely matches the refractive index of silica ($n_D \approx 1.45$), has a relatively high viscosity ($\eta \approx 0.17$ Pa s[†]) thus slowing the particles down, and is non-volatile such that it could be placed in a vacuum chamber to remove dissolved oxygen, which could otherwise act as a radical inhibitor and slow the polymerisation down. However, we note that this can be partially overcome by increasing the initiator concentration. A number of different

* these particles were used instead of the silica NPs used for TPI analysis, because high-speed imaging was needed to determine the arresting rate and smaller particles did not have a strong enough fluorescent signal under those imaging conditions

† estimated using the Grunberg-Nissan mixing rule^[438]

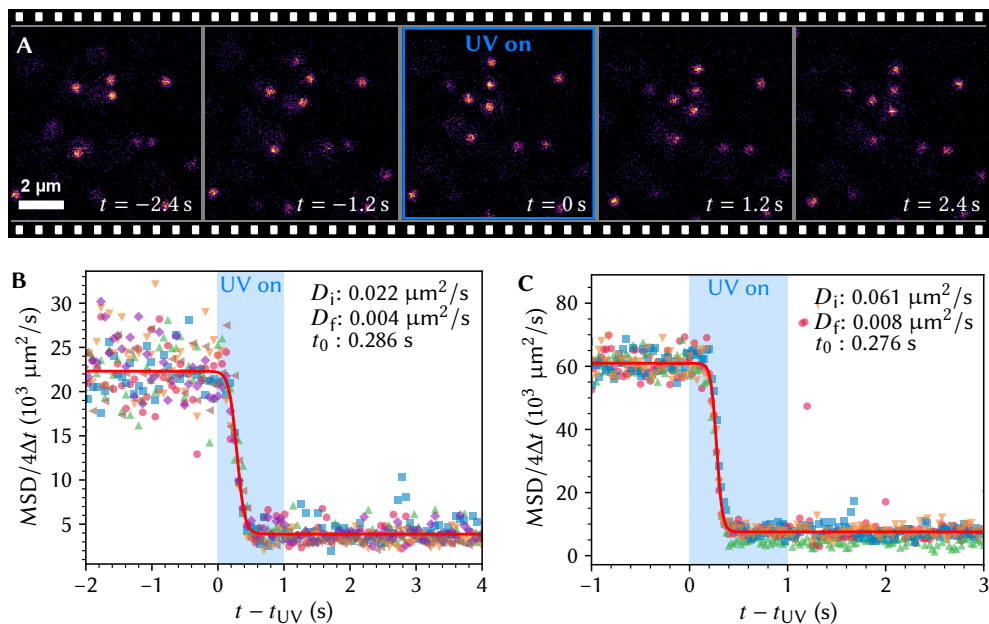


Figure 4.4: characterisation of the solvent-arresting rate. **A:** stills from a CLSM video recorded during arresting of 325 nm fluorescent silica tracer particles in a triethylene glycol / glycerol / PEGDA 700 mixture, showing that inter-particle distances are preserved from the moment the UV is turned on. **B:** MSDs during arresting of multiple such spots in the sample shown in A (different colours/markers indicating each spot/video) fitted with a smooth step function (red line), best fit parameters for the initial and final apparent diffusion coefficients and arresting time are given. **C:** Similar arresting curves for a DMSO / PEGDA 700 mixture (0.5 wt.% initiator).

solvents was found to be compatible with PEGDA including water, dimethyl sulfoxide (DMSO), ethanol, glycerol carbonate (GlyC) and dimethylformamide (DMF). For example, an arresting curve for a DMSO / PEGDA 700 mixture is shown in **Figure 4.4C**. Additionally, ETPTA may be used to arrest apolar and low-polar systems in case of solvents such as bromocyclohexane (CHB), commonly used for PMMA particles, and chlorocyclohexane (CHC), used for C_{18} -ligand functionalised silica as reported previously.^[434]

4.4 TPI analysis of arrested NP dispersions

After the arresting, the samples could be imaged in 3 dimensions using CLSM at low imaging rates to obtain large field-of-view datasets with a high signal-to-noise ratio (SNR) compared to what would be achievable without arresting. To further improve the SNR and resolution, deconvolution was applied using the *Huygens* software (v17.04, *Scientific Volume Imaging*) using a theoretical point-spread-function (PSF) based on objective type, sample and immersion medium refractive indices, glass thickness & position, pinhole size, etc. False-coloured cross-sections in the xy (imaging) and xz planes after deconvolution are shown for part of one of the z -stacks in **Figure 4.5**. The particle coordinates obtained from four of such z -stacks were used to calculate the $g_{DH}(r)$ and apply the iterative TPI procedure to extract

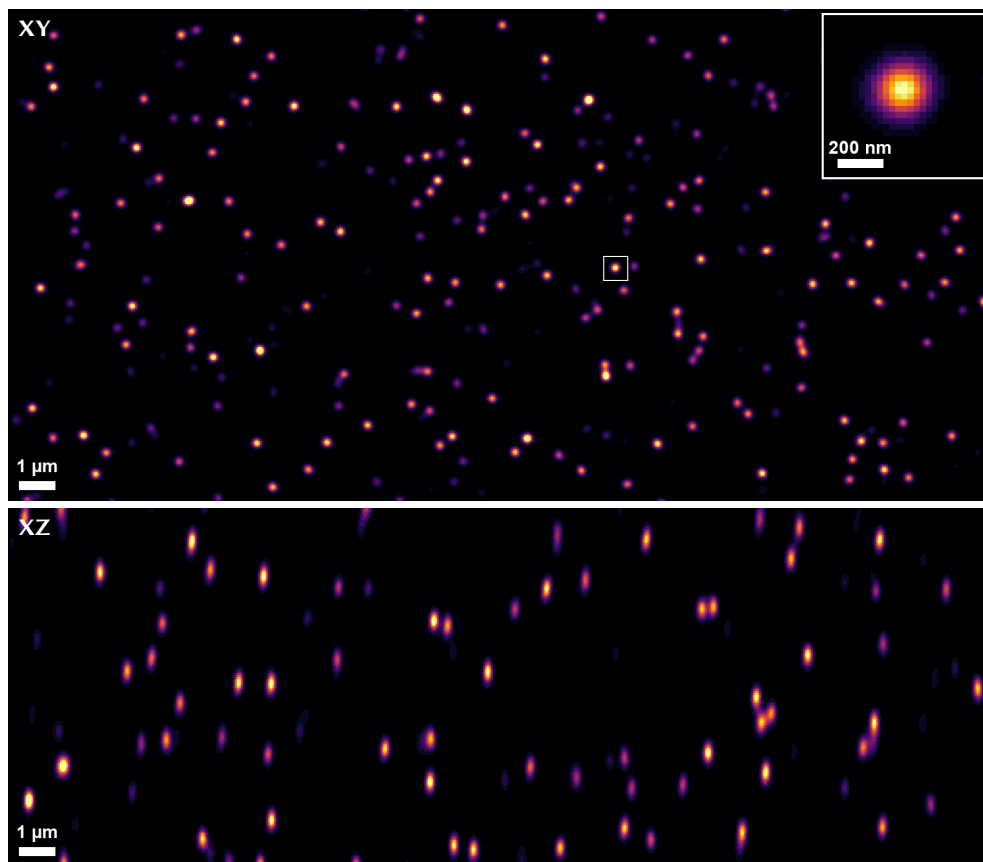


Figure 4.5: XY and XZ cross-sections of a 3D CLSM ‘z-stack’ of an arrested silica NP dispersion. Fluorescent SiO₂ NPs of 97 nm diameter dispersed in 3:1:1 (V:V) triethylene glycol/glycerol/PEGDA 700 were arrested and imaged using CLSM. A 28 μm × 14 μm × 10 μm subset of the full 56 μm × 56 μm × 10 μm dataset is shown after deconvolution was applied, the voxel size was 27 nm × 27 nm × 50 nm.

the inter-particle interactions, the results from the final iteration are shown in **Figure 4.6**. TPI was able to fit the $g(r)$ with a precision well below the uncertainty (‘noise level’) of the $g(r)$ used as input. Convergence was reached after only ~ 10 iterations as evidenced by the evolution of the mean squared deviation of the $g(r)$ and TPI result (χ^2). The corresponding interaction potential was consistent with short-ranged screened electrostatic repulsion and the data for $0.25 \mu\text{m} \leq r < 0.85 \mu\text{m}$ were fitted* with a hard core Yukawa potential of the following form:

$$U_{\text{yuk}}(r) = \frac{D\Gamma_{\text{yuk}}}{r} e^{-\kappa(r-D)} \quad (4.7)$$

where D the hard core diameter, κ^{-1} the Debye screening length and Γ_{yuk} the contact potential. The inset in **Figure 4.6B** shows a subset of the data on a log-linear plot, highlighting the

* specifically, this was done in log-space, i.e. $\ln U(r)$ was fitted with $\ln U_{\text{yuk}}$

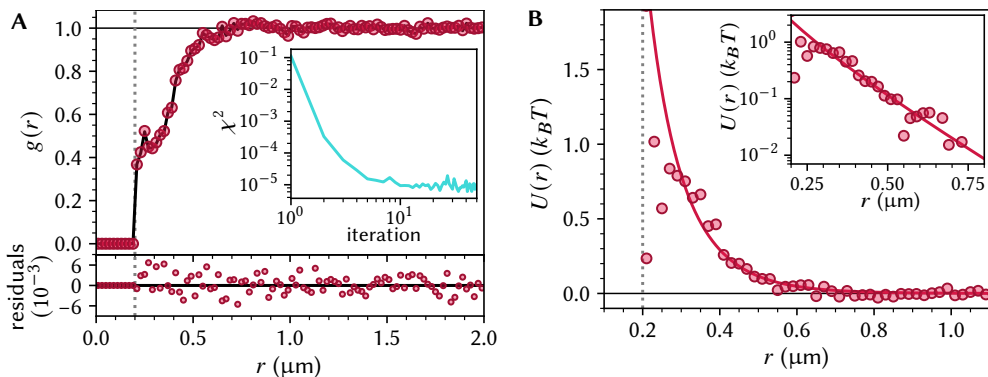


Figure 4.6: TPI of arrested silica nanoparticles. The dashed lines indicates the lower bound on inter-particle distance used in the particle localisation step, the particle diameter was 97 nm. **A:** $g_{\text{DH}}(r)$ (black line) with final $g_{\text{TPI}}(r)$ of the iterative TPI fitting routine (red circles), residuals are shown more clearly on the bottom. The inset shows evolution of the mean squared error during the iterative procedure on a log-log scale. **B:** the interaction potential used in the final iteration (circles) fitted with a Yukawa potential (red line) of $\Gamma_c = 10 k_B T$ and $\kappa^{-1} = 0.14 \mu\text{m}$. The inset shows a subset of the same data on a log-linear plot highlighting the exponential nature of the repulsion.

exponential nature of the interactions. At very short range ($\leq 0.25 \mu\text{m}$) the data deviate, which we attribute to biasing in the particle localisation due to residual signal overlap as well as the presence of some small clusters remaining after the final silica shell growth. In principle, stimulated emission depletion (STED) could be used to improve the imaging resolution and resolve closer inter-particle distances. However, when attempting this we found that in our arrested samples, the use of a significantly high intensity STED laser resulted in movement and temporary deformation of the sample during exposure, likely as a result of local heating due to the STED beam. Further optimization of the system to allow for effective STED imaging or the use of other super-resolution techniques would be highly desired to push interaction measurements using optical microscopy further into the domain of NPs and allow for measurement of more than only NPs with longer-ranged interactions as we showed here.

4.5 Sedimentation of binary colloidal systems

The ability to arrest samples for CLSM is not only useful in the context of interaction measurements, but also for the imaging of other time-dependent processes. We show that the solvent-arresting procedure could be used to characterise the microscopic structure of binary colloidal dispersions—where the two populations differed in size—at different points during sedimentation. The formation of (size) binary colloidal crystals depends sensitively on both the size ratio and the stoichiometry, as well as on the ‘usual’ parameters such as the overall particle density and inter-particle interactions. This results in a large phase space even for a given size ratio, such that it might be needed to tune the concentration and stoichiometry to obtain a certain structure.^[399,439,440] In a sedimenting sample conversely, the different sedimentation rates and gravitational heights of the differently sized species result in different sedimentation profiles of the two species, which means that both the overall

particle density and the stoichiometry continually vary along the gravitational direction. Therefore, sedimenting samples effectively probes a line through phase-space rather than a single point, thereby increasing the chance of finding binary crystals.^[441–443]

Our work was inspired by the recent work of Xu & Cölfen *et al.*,^[443] where the authors demonstrated that such binary sedimentation gradients could be probed using analytical ultracentrifugation (AUC) for a system of fluorescent 30 and 40 nm silica NPs. However, due to the small particle size it was not possible to resolve the structure of the samples throughout the sedimentation process and it was only possible to obtain structural information afterwards by drying the samples in the capillaries and imaging the dried sediments using electron microscopy. Here we performed similar experiments using fluorescent silica particles of approximately 300 and 400 nm such that CLSM could be used to image the microscopic structure. However, their much larger sedimentation rate meant that even at the minimum centrifugation rate required for our AUC, the system would be rapidly kinetically jammed.^[444] Instead, capillaries were (partially) sedimented under normal gravity and then arrested, and their sedimentation profiles were probed using CLSM. For this the particles were dispersed in a refractive-index matching mixture of 55 vol.% DMSO, 25 vol.% ethanol and 20 vol.% PEGDA 700 containing 2 mM LiCl and 0.5 wt.% photoinitiator, which was placed in capillaries which had one end internally sealed with UV-cured resin to form a ‘wall’ for the particles to sediment against. Multiple capillaries were prepared, placed vertically in the dark to sediment under normal gravity, and arrested after different sedimentation times such that the progress of the sedimentation could be followed and the sediment could be analysed at those different points in the process. The ca. 400 nm ‘large’ (L) and 300 nm ‘small’ (S) particles had theoretical gravitational heights of $\sim 12\ \mu\text{m}$ and $\sim 27\ \mu\text{m}$ respectively, not accounting for interactions and excluded volume.

Figure 4.7 shows the measurement of sedimentation profiles using CLSM on arrested samples, with high-resolution images showing the local structure in selected areas. Sedimentation profiles were determined from the fluorescence intensity of both species as a function of ‘height’, *i.e.* distance from the sealed end of the capillaries, at constant depth into the sample. For this, a series of adjacent $50\ \mu\text{m} \times 50\ \mu\text{m} \times 30\ \mu\text{m}$ low-resolution z -stacks were taken along the gravitational axis from which the fluorescence intensities were determined over the range of $2.5\ \mu\text{m}$ to $7.5\ \mu\text{m}$ from the glass–sample interface for each xz hyperplane, resulting in the height-dependent fluorescence intensities $I(h)$ of both species. These intensities were then converted to particle concentrations by correlating the particle concentration measured at some reference height from a high-resolution CLSM z -stack with the measured $I(h)$ at that height, which was typically just above the sediment (2 mm to 3 mm depending on the sample). The sedimentation profiles of samples under normal gravity, *i.e.* 1 g, show that as expected, the L particles sediment more quickly, resulting in a region of concentrated L particles on the bottom which by the 14 day mark had formed face-centred cubic (FCC) crystals, with defects and grain boundaries occupied by S particles. It was observed that the S particles were displaced upwards by the L particles during this, indicating significant mobility of the particles in the concentrated region during sedimentation. Directly above the FCC_L, above $h \approx 0.8\ \text{mm}$, was a mixed disordered (fluid-like) region with a gradually varying stoichiometry ($L/S \geq 1$), but no (binary) crystals were observed in this region in any of these samples. Further above the sediment smoothly transitioned into lower density particle gas with predominantly S particles depending on the sedimentation time, and by the 8 week mark virtually no L particles remained in the supernatant.

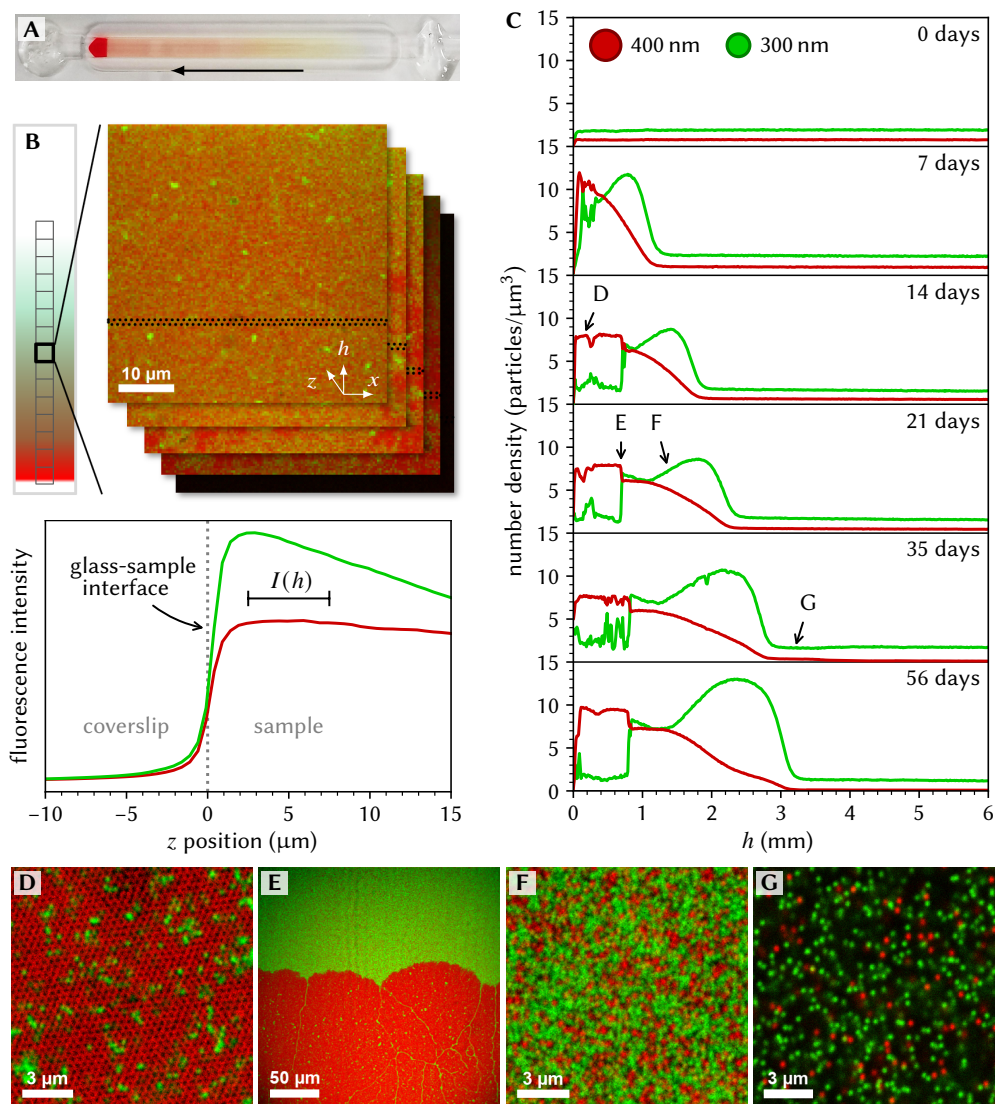


Figure 4.7: measuring binary sedimentation profiles using CLSM. **A:** photograph of one of the $0.2\text{ mm} \times 2\text{ mm}$ wide capillaries after partial sedimentation and arresting, with the arrow indicating the direction of gravity/sedimentation. **B:** schematic of the concentration gradient measurement: a tile-scan of z -stacks was recorded and the position of the glass was fitted in in each xz hyperplane (indicated with the dotted area) so that the fluorescence intensity of each species could be averaged over a fixed range above the bottom. **C:** sedimentation profiles as function of sedimentation time under normal gravity (1 g) with the positions indicated of some selected CLSM micrographs (**D–G**, where the fluorescent signals of L and S are shown in red and green respectively).

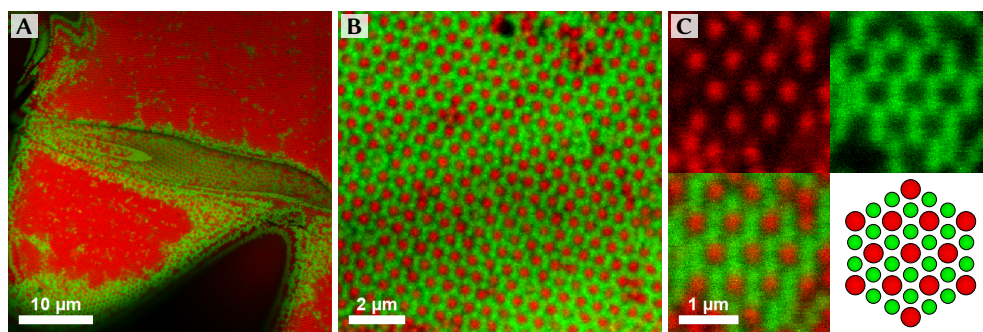


Figure 4.8: binary structures in folds of the UV glue boundary. A,B: overview and zoom-in of the bottom of a sample sedimented for 21 days at 1 g where the bottom glue boundary shows up as the dark regions. C: micrographs of individual and combined fluorescent channels of a smaller region, with a schematic of the approximate positions of particles in one image plane. Fluorescent signals of L and S are shown in red and green respectively.

The particles in our system had a size ratio of ~ 0.76 , for which the expected hard-sphere equilibrium structure at low density is coexistence of FCC crystals of the L particles with a fluid phase, and at higher density a coexistence of the so-called Laves phases (LS_2) with FCC crystals of the L particles for $S/L < 2$ or with FCC_S or a fluid for $S/L > 2$ is expected.^[399,445–447] In capillaries sedimented at 1 g only FCC_L -liquid coexistence was found, although the particles were relatively closely packed. It is possible that the system got trapped kinetically already at lower density, preventing further crystallisation. It is also of note that the formation of Laves phases is extremely sensitive to the size-ratio, and already at a size ratio of 0.74 the Laves phases are no longer expected.^[446] Slight inaccuracies in our particle size measurements are a possibility, and e.g. ionic double layers or sterically stabilising layers of PEGDA adsorbed to the particles' surfaces could also lead to different 'effective' size ratio, although neither is expected and these would generally increase the size ratio for these particles, not decrease it.

Binary structures were observed in some cases on the very bottom of the sediment, in direct contact with the UV glue boundary. As shown in **Figure 4.8**, the cured glue had a rippled/curved structure on a microscopic level. It is well known that the presence of hard surfaces can strongly affect crystallisation, where surface curvature and/or confinement effects may induce different structures than near flat surfaces or in the bulk. Another possibility is that the glue partially dissolved and locally affected inter-particle interactions. Either way, it likely does not represent the bulk equilibrium structure for these particle systems. Unfortunately we were not able to definitively assign a crystal structure to the binary structures we observed due to the fact that the small particles could not be resolved well along the z -axis and the crystallites rarely contained more than two layers of L particles, but it does not appear to be consistent with any of the $MgZn_2$ (C14), $MgCu_2$ (C15) or $MgNi_2$ (C36) Laves phases^[399] expected for this size ratio.

In addition to sedimentation under normal gravity, centrifugation was used to achieve higher sedimentation rates and thus varying density and stoichiometry gradients. When the particles were sedimented at 3 RCF (*i.e.* centrifugal forces equivalent to $3\times$ normal gravity) already after 5 days a majority of particles had sedimented, CLSM micrographs are shown

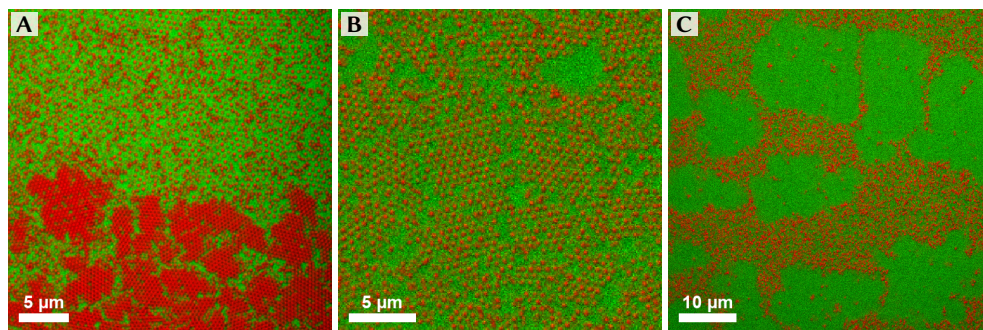


Figure 4.9: binary crystallisation during sedimentation at 3 RCF. The sample was centrifuged at 3 RCF for five days, the sediment consisted of FCC_L (A, $h \approx 1.5$ mm) transitioning into binary structures (B) and FCC_S (C, $h \approx 2$ mm). Fluorescent signals of L and S are shown in red and green respectively.

in **Figure 4.9**. At the bottom a large (~ 1.5 mm) FCC_L was present, which transitioned into a mixed region which clearly consisted of predominantly binary crystallites of the same structure found earlier, as seen from the regular spacing of L particles intermixed with S particles. However, here these spanned a considerable region of the capillary. Additionally, higher up in the sample FCC_S crystals were now observed. We emphasise however that we could only image within ~ 10 μm of the glass-sample interface in these concentrated regions due to reabsorption of the fluorescent signal, and that these structures are thus still in contact with a hard wall. Interestingly, repeating this experiment with centrifugation at 5 RCF resulted in far fewer binary crystallites intermixed with the disordered mixed state, highlighting the sensitivity of the crystal formation to the gravitational field. Finally, we prepared a similar sample where the same L particles were used but the 294 nm S particles were replaced by 315 nm particles, giving a size ratio of 0.80. Using again centrifugation at 3 RCF for 5 days, resulted in a sample with large FCC_L and FCC_S with a disordered mixed state in-between, but without any binary crystalline phase.

Of course, the formation of crystals is also highly dependent on the inter-particle interactions, with attractions in particular making it easier for the system to get stuck in a glassy state. To verify that the particles indeed had hard-sphere like behaviour, a capillary containing the same sample as in the sedimentation experiments was locally arrested in a similar manner as the silica NP system discussed previously. The codes for calculating the $g_{\text{DH}}(r)$ and for performing iterative TPI were then implemented for multicomponent systems, under the assumption that the interactions between different combinations of the different components in the system —*i.e.* LL, LS / SL and SS for a (size) binary system— were additive. Codes and implementational differences with respect to the methods for single-component systems are discussed in detail in **Section 4.9**. Results from the multi-component iterative TPI are shown in **Figure 4.10** and clearly demonstrate that no attractive interactions were present for any of the combinations. Interactions between the large particle were clearly hard-sphere like, with possibly some very minor soft (electrostatic) interactions between the S particles although we note that these had significant overlap of fluorescent signals due to the relatively thin non-fluorescent shell.

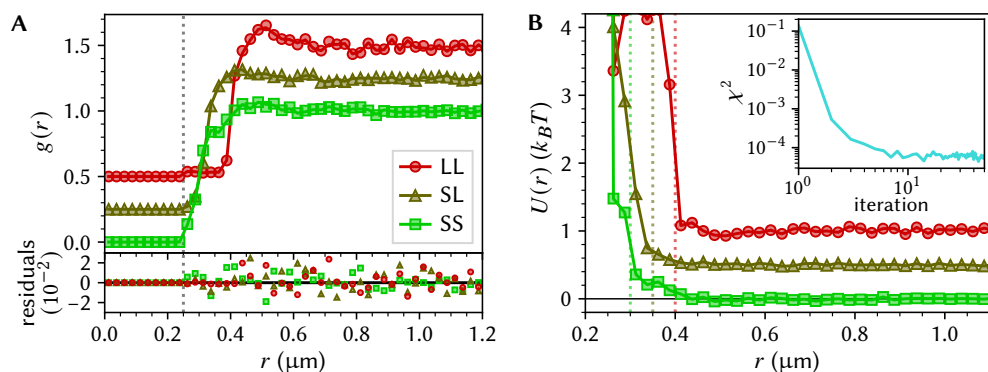


Figure 4.10: TPI of arrested binary colloidal systems. Data are vertically offset for clarity, L and S refer to the large (~ 400 nm) and small (~ 300 nm) particles respectively. **A:** $g_{\text{DH}}(r)$'s (lines) with the $g_{\text{TPI}}(r)$'s of the final iteration of the iterative TPI fitting routine (data points) for the different binary combinations, residuals are shown on the bottom. The gray dashed line indicates the lower bound on inter-particle distance used in particle localisation ($0.25 \mu\text{m}$). **B:** the $U(r)$'s used in the final iteration, with the dashed lines indicating the expected hard-core contact distance based on the particle sizes. The inset shows evolution of the mean squared error during the iterative procedure on a log-log scale.

4.6 FIB-SEM analysis of arrested samples

So far, we used PEGDA as a co-solvent with the bulk of the samples consisting of more typical solvents for colloidal dispersions. However, pure PEGDA (or ETPTA) may also be used as solvent without the presence of a majority of co-solvent, which result in much higher arresting rates and the formation of a hard plastic-like material rather than a relatively soft gel. This has previously been used to produce free-standing films of colloidal crystals.^[448] Here, we explored if such films could be characterised in 3D using scanning electron microscopy (SEM) in combination with focused ion-beam milling (FIB) where the FIB is used to repeatedly remove thin slices of material while imaging the exposed surfaces with SEM. As we have recently reported, FIB-SEM tomography can offer superior resolution in the real-space analysis of nano- and colloidal materials compared to CLSM without the stringent limitations on sample thickness found in transmission electron microscopy,^[262] and is thus a promising candidate for interaction measurements of NPs. For this, a droplet of particle dispersion was placed between two microscopy cover-glasses and arrested in a UV curing chamber such that a thin and flat film was obtained, which was coated with a 3 nm platinum layer to make the surface conductive and protect it from unwanted degradation due to the ion beam. Unfortunately we were unable to measure the arresting rate of these samples under the conditions used for arresting FIB-SEM samples (which used a UV curing chamber), but note that arresting a similar sample with pure PEGDA 700 using the UV condenser lens the arresting time was found to be $t_a \leq 35$ ms, which was the lower limit of what we could measure. Detailed experimental methods are given in [Section 4.10.5](#).

We imaged three different particle systems in 3D using FIB-SEM tomography, an overview of the FIB-milling and imaging geometry and some representative slice images are shown in [Figure 4.11](#). We found that overall the arrested PEGDA films could be milled precisely and without significant curtaining artefacts down to $>20 \mu\text{m}$ below the surface. The first particle

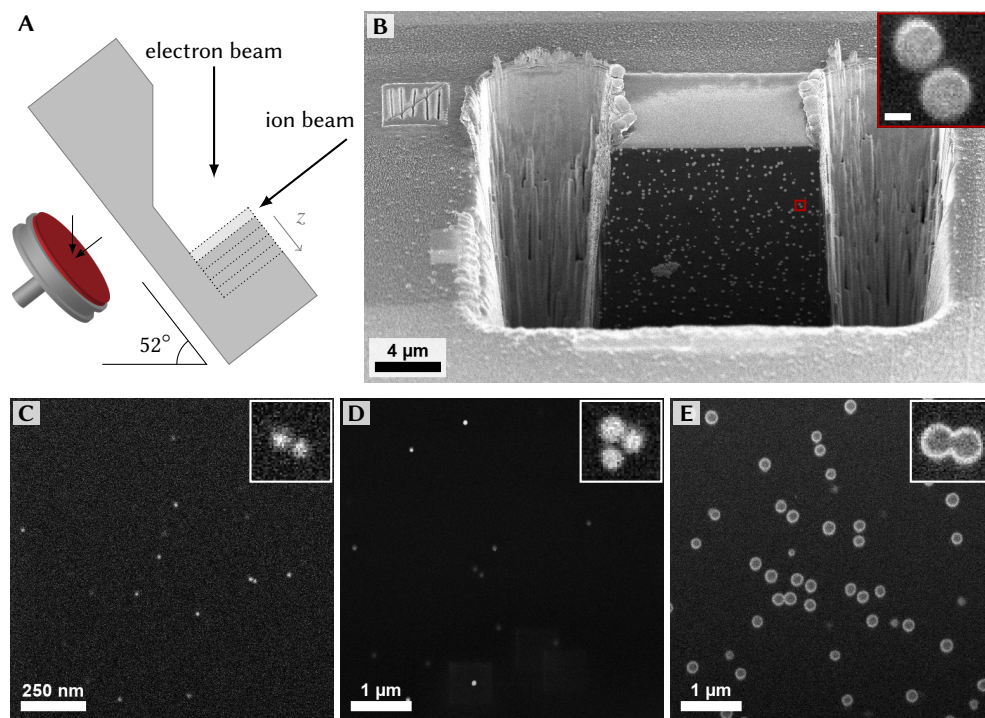


Figure 4.11: FIB-SEM tomography of arrested samples. **A:** schematic depiction of the sample, milling and imaging geometry. The sample stub with the arrested PEGDA film is tilted such that the FIB was perpendicular to the surface. **B:** low magnification overview of a region prepared for tomography, with rough-cut trenches around the region of interest. A 200 nm Pt layer was deposited locally to further protect the sample and prevent curtaining and charging artefacts. The inset shows a zoom-in of the milling surface with two particles, scale bar 100 nm). **C:** 16 nm AuNPs@mPEG5K-SH. **D:** 77 nm AuNPs@mPEG5K-SH. **E:** 176 nm silica particles.

system we investigated contained gold nanoparticles (AuNPs) of 15.5 ± 1.2 nm (8.0 %), capped with thiol-terminated poly(ethylene glycol) ligands (AuNPs@mPEG5K-SH) as introduced in [Section 3.2.1](#). We found that these particles could be dispersed directly in PEGDA 575 or PEGDA 700 after centrifugation, and imaged in FIB-SEM with sufficient resolution to resolve particles down to contact (slice thickness 3 nm), although a relatively high accumulated beam dose was needed to obtain sufficient signal ($220 \text{ e}^-/\text{nm}^2$ at 2 keV). This caused degradation and gradual shrinking of the PEGDA block (regardless of which M_w was used) over the course of the serial sectioning procedure, which resulted in strong image distortion along the z -axis (slicing axis). It was found that PEGDA 700 suffered slightly more from beam-induced shrinking than PEGDA 575, and for subsequent FIB-SEM experiments PEGDA 575 was used.

To reduce the required electron dose for an acceptable signal to noise ratio (SNR) we explored the use of much larger AuNPs@mPEG5K-SH of 76.9 ± 6.8 nm (8.8 %) in diameter, as introduced in [Section 3.2.2](#). The bigger size and much larger contrast meant that imaging of an arrested sample of these particles in pure PEGDA 575 could be done much faster than for the smaller AuNPs, resulting in a lower accumulated electron dose of $14 \text{ e}^-/\text{nm}^2$ at 2 keV.

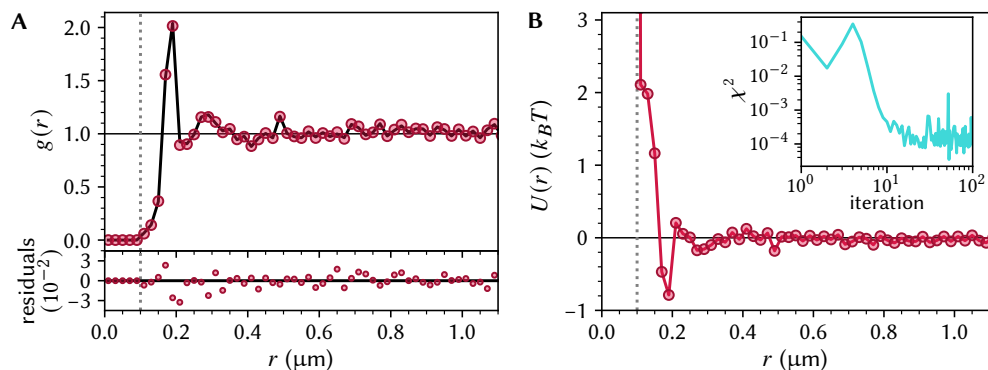


Figure 4.12: TPI analysis of AuNPs@SiO₂ in PEGDA 575. The dashed gray lines indicates the lower bound on inter-particle distance used in the particle localisation step, the particle diameter was 176 nm

Furthermore, a bigger slice thickness of 10 nm could be used, meaning that more of the most degraded material on the image surface was removed with every slice and accumulative damage over the course of the imaging series was reduced and as result no significant deformation of the sample occurred. These particles could be imaged with good image quality and resolution in all directions, although we note that particles appeared slightly asymmetrically along the z -directions in FIB-SEM as the particles could be observed slightly before they are at the imaging surface due to the beam penetrating several nm into the PEGDA. While particle localisation in these samples would be certainly feasible, the particle concentration in all of our AuNP samples was too low to determine a $g(r)$ and measure interactions.

Finally, we performed FIB-SEM analysis of arrested PEGDA 575 containing AuNPs@Stöber-SiO₂ particles with a 16 nm AuNP core and a total size of 176.0 ± 7.6 nm (4.3 %) as introduced in [Section 3.2.1](#). The rationale behind these particles was that they would behave and interact like standard Stöber-like silica particles in terms of their interactions, while the AuNP cores could be used as high contrast markers for particle localisation. In practice, we found the secondary electron contrast of silica in this size range to be excellent compared to the PEGDA, which gave a comparatively low background signal. Moreover the signal of the AuNP cores was not visible over that of the silica at the low beam energies (≤ 2 kV) we used during serial sectioning to decrease the penetration depth and improve the z -resolution, and was only observed using 15 kV or more. For future work on silica interactions using FIB-SEM we thus see no need to include a AuNP core in the particles. We performed particle localisation on a slice series which was $15.4 \mu\text{m} \times 8.7 \mu\text{m} \times 2.1 \mu\text{m}$ after alignment and data processing (slice thickness 20 nm, beam dose $14 \text{ e}^-/\text{nm}^2$) and contained ca. 1400 particles, and used these data as input for TPI, results of which are shown in [Figure 4.12](#).

The $g(r)$ firstly, shows a clear peak at just below $r = 0.2 \mu\text{m}$ corresponding well to hard-core contact for particles of this diameter, and to the qualitative observation that there was a considerable number of small clusters of two or three particles in the datasets, indicative of attractive interactions. Looking at the TPI result, we indeed see an attractive well at contact of ca. $0.8 k_B T$. These attractions could arise fully or in part from van der Waals forces which

are nearly always present, although the refractive index mismatch of the particles ($n_D \approx 1.45$) and solvent ($n_D \approx 1.47$) is fairly small and index-matching minimizes van der Waals forces. It is also possible that (some of) the attractions are the results of depletion due to partially reacted PEGDA, either prior to deliberate initiation of the polymerisation, or during the arresting procedure if it is not sufficiently fast. The latter is unlikely: while we could not directly measure arresting rates under conditions used for this sample it was likely much faster than the self-diffusion time of ~ 1.1 s. Once the photo-initiator is added to the sample, any exposure to light may initiate local reaction chain causing PEGDA oligomers to be formed in the sample in the period just before arresting, which could act as depleting agents causing attractive interactions. It is also possible that oligomers/polymers were already present in the PEGDA stock, which could be removed *e.g.* by the use of fresh reactants or distillation.

4.7 Concluding remarks

In this chapter, we have shown that solvent-arresting can be used to preserve and image large particle systems in 3D using CLSM or FIB-SEM in a way that is compatible with a wide range of particles and solvents. Secondly, we introduced the recently proposed iterative test-particle insertion method and provide a practical implementation that may be used for simulated and experimental data in a wide variety of geometries. Using these two methods, we showed that it is possible to measure (long-ranged) interactions between NPs. Iterative TPI can be a very versatile and powerful method for probing interactions in combination with high-resolution imaging and particle localisation and the results in this chapter are likely limited not by the limitations of TPI. Instead, they are more likely to be limited by the combination of the finite optical resolution of CLSM and corresponding artefacts introduced by the localisation algorithms we used here, which can significantly affect extracted potentials.^[127,204,205] This was the case in particular at short range, where there was significant signal overlap even after using deconvolution.

There may also be inaccuracies due to motion of the particles between the initiation of the reaction and the time the arrest has fully completed because the interactions are likely influenced by the ongoing polymerisation reaction, and as such any change in position after initiation likely does not represent the pre-arresting state. NPs are particularly challenging to arrest at a sufficient rate due to their higher diffusion coefficient. Arresting time, viscosity and interactions all vary from solvent to solvent, and as such there is much room but also need for optimisation. Finally, it is important to mention the somewhat obvious fact that the addition of PEGDA or a similar monomer will, to some extent, change the interactions compared to ‘pure’ solvents, and that it is thus not possible to measure the interactions as they would be without PEGDA. As we will see in the next chapter, one way around this problem is to ‘arrest’ by rapid cryogenic freezing.

Fortunately, much improvement in imaging and localisation procedures can and has been made. For example, super-resolution techniques such as STED can improve the resolution to below 100 nm and, as already discussed to some extent in **Chapter 2**, particle localisation algorithms such as PERI^[201] incorporate much more information on the physics of the imaging process than the relatively ‘naive’ assumptions underlying the faster and simpler but more limited centroiding algorithms used here, thereby achieving nanometer localisation precision. It was not feasible within the time frame of this project to additionally explore these developments in data processing, but we expect that these will be key to achieving true

nanometer scale interaction measurements using optical microscopy techniques. Secondly, we have shown that FIB-SEM analysis of arrested systems is already possible for nanoparticles and larger colloids with nanometer resolution, although further optimisation is needed to image the smallest particles without accumulating electron-beam damage over the course of the FIB serial sectioning procedure.

4.8 Acknowledgements

Adam Stones and Laura Filion are acknowledged for useful discussions on the test-particle insertion algorithm. Ernest van der Wee and Anna Nikolaenkova are thanked for their support with UV-initiated solvent arresting, in particular with ETPTA. Niels van de Poll is acknowledged for his extensive work on the characterisation of arresting rates of PEGDA with different solvents, and for synthesis, arresting and imaging of the SiO₂ NPs used in this chapter. Xufeng Xu and Roy Hoitink are acknowledged for their contributions to the project on binary sedimentation, which was performed in collaboration. Helmut Cölfen and Marjolein Dijkstra are also thanked for useful discussions on binary crystallisation and sedimentation. Matthijs de Winter and Chris Schneidenberg are thanked for training and technical support with the FIB-SEM experiments.

4.9 Computational methods



All codes used for calculating the radial distribution functions with the distance histogram and test-particle insertion methods, as well as the iterative pair-potential routines were implemented in the Python programming language (version ≥ 3.6) as importable package^[431] and are available online using the QR code on the left. Codes follow the principles outlined in [Section 4.2](#) with some additional considerations for dealing with finite (nonperiodic) boundary conditions as obtained from experimental measurements. We note that the method descriptions below pertain to 3-dimensional (volumetric) data, but are conceptually identical to the routines for 2-dimensional data when considering the 2D equivalent terms, e.g. ‘area’ instead of ‘volume’. For clarity, upright bold symbols are used throughout this section to indicate list- and array-like variables (*i.e.* analogous to vector/tensor notation) while italic variables indicate scalar values (such as individual array elements).

4.9.1 Implementation of the distance histogram method for calculating the radial distribution function

The algorithm used for calculating the radial distribution function using the distance histogram method takes an input consisting of $M \geq 1$ datasets (each taken from the same system, *e.g.* multiple time steps from a time series, multiple z-stacks from different places in an (arrested) sample, etc.) of N_m particle coordinates each. Note that these datasets are not required to share the same bounding volume and number of particles, although they must represent the same system state. A generalised description of the algorithm is as follows:

- a zero-valued list $\mathbf{g} \in \mathbb{R}^L = \{0, \dots, 0\}$ is initialised to contain pair-counts for each of the distance bins $[r, r + \delta r)$ from r_{\min} up to r_{\max} , where $L = (r_{\max} - r_{\min}) / \delta r$ is the number of distance bins
- for every set of coordinates m :
 - a zero-valued list $\mathbf{g}_m \in \mathbb{R}^L$ is initialised
 - a fast k -d tree neighbour searching algorithm from the open-source Python package *SciPy* (version 1.6.2)^[449] is used to determine the pairwise distances from all particle i in m to all neighbouring particles $j \neq i$ in m at a distance up to r_{\max} simultaneously
 - for every particle i in m :
 - * a histogram $\mathbf{g}_{m,i} \in \mathbb{R}^L$ of pairwise distances is constructed by counting the number of neighbours of i in each distance bin $[r, r + \delta r)$

- * each bin in $\mathbf{g}_{m,i}$ is divided by the *effective volume* of the spherical shell it represents, that is the intersection volume of the spherical shell around particle i with the bounding box volume
- * the values of $\mathbf{g}_{m,i}$ are added to \mathbf{g}_m
- the bin values in \mathbf{g}_m are divided by number of particles N_m to calculate the average, and added bin-wise to \mathbf{g}
- the bin values in \mathbf{g} are divided by M to determine the average over all coordinate sets
- the bin values in \mathbf{g} are divided by the overall number density of particles in the system to obtain normalised $g(r)$ values

Calculation of effective volumes (or areas in 2D) in finite boundary conditions depends on the nature and shape of the boundaries, and is discussed in more detail in [Section 4.9.3](#). In case of periodic boundary conditions, edge-correction does not need to be done on a *per particle* basis since the positions of the particle relative to the bounding box are arbitrary and can be shifted to be centred around any one reference particle i , and as such the edge correction step in the inner most (per particle i and per bin) loop is replaced with an edge correction step on a per dataset (m) and per bin basis.

For multi-component (e.g. binary) systems the $g_{\text{DH}}(r)$ is determined for each pair of components separately, including that of the component with itself, e.g. for a A/B binary system this would be AA, AB, BA and BB. This is achieved in the same manner as above, except that the k -d tree is initialised with particles from the second component in the component pair, and then queried for neighbours around the coordinates of the first component ('reference particles').

4.9.2 Implementation of the binned test-particle insertion method for calculating the radial distribution function

The algorithm used for calculating the radial distribution function using the test-particle insertion method takes an input consisting of $M \geq 1$ datasets (each taken from the same system, e.g. multiple time steps from a time series, multiple z-stacks from different places in an (arrested) sample, etc.) of N_m particle coordinates each, as well as the (pairwise) interaction potential $U(r)$ between the particles. Note that the coordinate datasets are not required to share the same bounding volume and number of particles, although they must represent the same system state. The pair potential may be any functional form, e.g. a linearly interpolated discretised potential or a model function based on physical parameters. A generalised description of the algorithm is as follows:

- a zero-valued list $\mathbf{g} \in \mathbb{R}^L$ is initialised to contain the values for each of the distance bins $[r, r+\delta r)$ from r_{\min} up to r_{\max} of the radial distribution function, where $L = (r_{\max} - r_{\min})/\delta r$ is the number of distance bins
- a zero-valued list $\mathbf{c} \in \mathbb{R}^L$ is initialised to contain the total number of pair counts in each bin
- for every set of particle coordinates m :
 - a zero-valued list $\mathbf{c}_m \in \mathbb{R}^L$ is initialised
 - a list of N_{ins} test-particle coordinates is generated within the bounding volume of dataset m using a uniformly distributed pseudorandom number generator
 - a fast k -d tree neighbour searching algorithm from the open-source Python package *SciPy* (version 1.6.2)^[449] is used to determine the pairwise distances r_{ij} from all test-particles i to all surrounding particles $j \in m$ at a distance up to r_{\max} simultaneously
 - for every test-particle i :
 - * a histogram \mathbf{c}_i of pairwise distances is constructed by counting the number of particles $j \in m$ surrounding test-particle i in each distance bin $[r, r+\delta r)$, and added bin-wise to the overall count list \mathbf{c}_m of dataset m
 - * the insertion free energy $\psi_i \in \mathbb{R}^L$ of test-particle i is calculated on a per-bin basis as the weighted histogram of pairwise distances r_{ij} where the pairwise interaction energies $U(r_{ij})$ are used as weights, i.e. ψ_i is constructed from a zero-valued list by adding each pairwise energy $U(r_{ij})$ to the matching distance bin in ψ_i for which $r \leq r_{ij} < r+\delta r$.

- * each of the bins in \mathbf{c}_i and Ψ_i are divided by the *effective volume* of the spherical shell they represent, that is the intersection volume of the spherical shell around particle i with the bounding box volume, to correct for edge effects and obtain the correct total energy and weighing assuming the volume inside the bounding box is representative for missing volume outside the boundaries
- * the insertion probability of test-particle i is calculated as $P_i = \exp(-\psi_i)$, where $\psi_i = \sum_r \Psi_i$ is the total insertion free energy of test-particle i (i.e. summed over all bins)
- the average overall insertion probability \bar{P}_m is calculated as the arithmetic mean of the insertion probabilities of all test-particles inserted in m , i.e. $\bar{P}_m = \sum_i (\psi_i) / N_{\text{ins}}$
- the average insertion probability per distance bin \mathbf{P}_m is calculated as the count weighted per-bin average over all test-particles inserted in m , i.e. $\mathbf{P}_m = \sum_i (\mathbf{c}_i \odot \mathbf{P}_i) \oslash \sum_i (\mathbf{c}_i)$, where \odot and \oslash denote the Hadamard (element-wise) product and division respectively
- the $g(r)$ of dataset m is calculated and multiplied with the total number of (uncorrected) counts as $\sum_r (\mathbf{c}_m) \odot \mathbf{P}_m / \bar{P}_m$ and added to \mathbf{g}
- the overall mean radial distribution function is calculated as $\mathbf{g} \oslash \sum_r (\mathbf{c})$, i.e. the count-weighted average over the M datasets.

For multicomponent (e.g. binary systems), the method is implemented similarly, except that separate pair potentials are used for each pair of components. For each dataset, a set single set of test-particle coordinates is used for each of the different combinations of components such that calculating, histogramming and boundary correcting the distances from the test-particles to the coordinates in the dataset needs to be done only once. In other words, the same set of test-particles is (re)used to act as reference particles for each of the different components, so that the distances to the particles in the dataset remain the same and only the interaction potential differs. The insertion free energies for each component k are calculated by summing the interactions of the test-particles with all neighbours in the dataset (i.e. all components) using the appropriate pair potential for neighbours of each component with component k . The insertion probabilities of the test-particles are then calculated as previously, and used to determine the local and ensemble insertion probabilities for each pair of components separately, to yield the $g_{\text{TP1}}(r)$ for each combination of components.

4.9.3 Calculation of missing-volume (area) correction factors

To correct for finite-volume or edge effects, the intersection volume between the bounding box—the part of the sample in which coordinates may be detected—and the spherical shells $r + \delta r$ around the (test-)particles must be known when evaluating (test-)particles closer than r_{max} to any of the edges of the bounding box in the calculation of the radial distribution function both in the conventional distance histogram method and in the test-particle insertion method. The calculation of the intersection volume is dependent on the dimensionality and geometry of the bounding box. While some of the more common cases are not unique to this work, detailed methods for $g(r)$ correction are rarely provided in full. Furthermore, the correction factors are often calculated as the effective *surface area* of a sphere r , with shell *volume* being calculated as the area multiplied with δr . This is only valid for relatively thin shells, i.e. when using small bins. The approach in this work on the other hand is to directly calculate the effective volume V_i (or *area* in case of a 2-dimensional system) of a shell $r + \delta r$, by subtracting the effective volume of the inner sphere (or circle) of radius r from the effective volume of the outer sphere (circle) of radius $r + \delta r$. For these reasons we here provide a full set of equations for the calculation of missing volume correction factors for all geometries used in this work.

Rectangular boundary conditions (2D):

Rectangular boundaries (including square boundaries) are the most common case in 2D, e.g. one video frame. To find the overlap area between a circle (with its origin inside the rectangle), the bounding rectangle is expressed in terms of the distances of the four edges to the origin of the intersecting circle, and evaluated separately for each of the four quarter-circles by looping over the four sets of adjacent boundaries. When mirrored into the positive x and y directions each ‘corner’ or quadrant represents

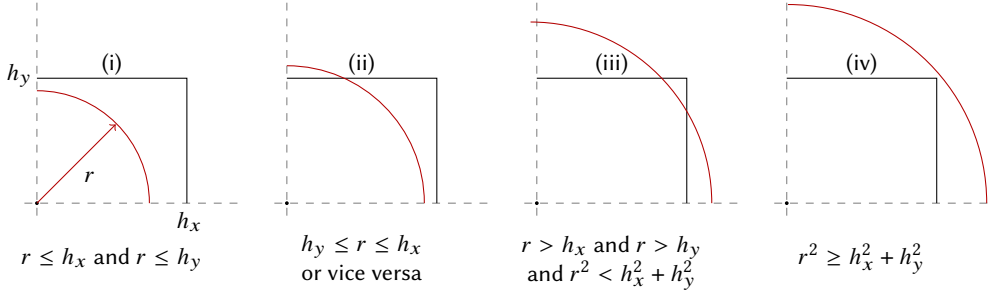


Figure 4.13: edge correction in rectangular boundary conditions. The four possible cases for the overlap area of a circle with a quadrant of the rectangular box are depicted, with r the circle radius and h_x and h_y the distances of the boundaries to the origin of the circle.

one of four possible cases outlined in **Figure 4.13**, depending on whether the box quadrant is partially or fully enclosed by the circle. The overlap area of the quarter-circle with the box quadrant in each of these cases is as follows:

$$A_{\square} = \begin{cases} \pi r^2/4 & \text{(i)} \\ \pi r^2/4 - A_{\text{cap}}(r, h_y)/2 & \text{(ii)} \\ \pi r^2/4 - A_{\text{cap}}(r, h_x)/2 - A_{\text{cap}}(r, h_y)/2 & \text{(iii)} \\ h_x h_y & \text{(iv)} \end{cases} \quad (4.8)$$

with h_x and h_y the distances of the circle's origin to the two adjacent boundaries and A_{cap} the area of a circular cap / segment given by:^[450]

$$A_{\text{cap}}(r, h) = r^2 \arccos\left(\frac{h}{r}\right) - h\sqrt{r^2 - h^2} \quad (4.9)$$

for a circular cap defined by intersecting a circle of radius r with a line at distance h from its centre. Only half the cap area is subtracted from each circle quarter in cases (ii) and (iii) since each circular cap spans two quadrants. The total overlap area is found by summing the values of the four quadrants.

Circular boundary conditions (2D):

Circular boundaries are less common but may be relevant *e.g.* when the image size is limited by the spot size of the excitation/illumination light or circular real-space aperture in optical microscopy, or due to physical boundaries in the sample such as in 2D cryo electron microscopy as discussed in **Chapter 5**. In case of circular boundary conditions, the effective area of a circle r around a particle in a circular boundary can be calculated directly as the intersection area of two circles:

$$A_{\circ} = \begin{cases} \pi r^2 & \text{if } r \leq R \text{ and } h \leq R - r \\ A_{\text{int}}(r, R, h) & \text{if } h > |R - r| \\ \pi R^2 & \text{if } R < r \text{ and } h \leq r - R \end{cases} \quad (4.10)$$

where R is the radius of the circle defining the boundary, h the distance of its origin to the particle. When the circle intersects the circular boundary, A_{int} gives the intersection area of the lens-shaped overlap area of two partially overlapping circles as:^[451]

$$A_{\text{int}}(r_1, r_2, h) = r_1^2 \arccos\left(\frac{h_1}{r_1}\right) - h_1 \sqrt{r_1^2 - h_1^2} + r_2^2 \arccos\left(\frac{h_2}{r_2}\right) - h_2 \sqrt{r_2^2 - h_2^2} \quad (4.11)$$

with partial distances h_1 and h_2 given by:

$$h_1 = \frac{r_1^2 - r_2^2 + h^2}{2h} \quad h_2 = h - h_1 = \frac{r_2^2 - r_1^2 + h^2}{2h}. \quad (4.12)$$

The other two cases are when the circle is entirely enclosed within the boundary, or when the boundary is entirely enclosed within the boundary.

Cuboidal boundary conditions (3D):

Analytical calculation of the effective shell volume in cuboidal boundary conditions (the 3-dimensional equivalent of a rectangle) is based on the equations derived by Kopera & Retsch^[452], who provide a detailed derivation and sample codes for practical implementations. Conceptually, calculation of the intersection volume between a sphere and a cuboidal box is similar to the procedure discussed for (2D) rectangular boundary conditions, now calculating the intersection volume for each of the eight octants defined by adjacent sets of three boundaries h_x , h_y and h_z by taking the volume of a sphere octant, subtracting the volume of any spherical caps where a boundary plane intersects the sphere, and adding back the double counted edge-cap area where two spherical caps overlap.

Spherical boundary conditions (3D):

The case of spherical boundary conditions is the 3D analogue to the circular boundary, with an effective volume given by:

$$V_o = \begin{cases} \frac{4}{3}\pi r^3 & \text{if } r \leq R \text{ and } h \leq R - r \\ V_{\text{int}} & \text{if } h > |R - r| \\ \frac{4}{3}\pi R^3 & \text{if } R < r \text{ and } h \leq r - R \end{cases} \quad (4.13)$$

for a sphere of radius r around a particle at distance h from the origin of the spherical boundary of radius R where

$$V_{\text{int}} = \frac{\pi}{12h} [r + R - h]^2 [h^2 + 2h(r + R) - 3(r - R)^2] \quad (4.14)$$

is the intersection volume of two partially intersecting spheres.^[453]

Periodic boundary conditions (2D/3D):

In periodic boundary conditions (PBDs), the box wraps around itself when crossing an edge so there are no interactions with particles outside of the known volume, or in other words the entire volume is known. Analogously, it can be stated that the position of the boundaries with respect to any particular particle is arbitrary and the boundary may always be shifted such that the particle is in centre, far from the boundaries. As such, there are no edge effects at a short length scale and the $g(r)$ may be calculated without edge correction for pairwise distances up to half the box dimension. At larger distances, boundary effects may still occur due to the finite volume of the periodic box. If we allow only the nearest periodic image of every neighbouring particle to be counted, fewer particles remain at large distances, and the largest possible distance at which a particle can be found is equal to the diagonal of the box. Since we can arbitrarily shift the positions of the boundaries such that a particle is exactly in the centre of the box, we do not need to care about particles individually. Instead, we can calculate correction factors for each distance bin and apply them to all particles regardless of position.

Since the shape of the boundaries does not depend on experimental limitations and may be chosen arbitrarily, we only consider the simplest shape: square (in 2D) or cubic (in 3D). The effective area of a circle r around a particle in the centre of a square box with sides of length a can be split into 3 cases, similar to (i), (iii) and (iv) in [Figure 4.13](#), given by

$$A_o = \begin{cases} \pi r^2 & \text{if } 2r \leq a \\ \pi r^2 - 4A_{\text{cap}}(r, a/2) & \text{if } a < 2r < \sqrt{2}a \\ a^2 & \text{if } 2r \geq \sqrt{2}a \end{cases} \quad (4.15)$$

where the area of a circular cap is given by Eq. 4.9. The $g(r)$ may thus be calculated up to a factor $\sqrt{2}$ further than the trivial range. In a cubic box with edge length a and periodic cubic boundary conditions there are four possible cases for the effective volume as shown by Deserno^[454]:

$$V_o = \begin{cases} \frac{4}{3}\pi r^3 & \text{if } 2r \leq a \\ -\frac{\pi}{4}(3 - 36r^2 + 32r^3) & \text{if } a < 2r \leq \sqrt{2}a \\ -\frac{\pi}{4} + 3\pi r^2 + \sqrt{4r^2 - 2} + f_1(r) + f_2(r) & \text{if } \sqrt{2}a < 2r < \sqrt{3}a \\ a^3 & \text{if } 2r \geq \sqrt{3}a \end{cases} \quad (4.16)$$

with the two functions $f_1(r)$ and $f_2(r)$ given by

$$f_1(r) = (1 - 12r^2) \arctan\left(\sqrt{4r^2 - 2}\right) \quad f_2(r) = \frac{16}{3}r^3 \arctan\left(\frac{2r(4r^2 - 3)}{(4r^2 + 1)\sqrt{4r^2 - 2}}\right). \quad (4.17)$$

We note that these correction factors merely account for the available volume in a circular or spherical shell within the periodic volume, but they do not account for other edge effects due to the finite size of the simulation volume.

Numerical approach for arbitrary boundary shape:

In addition to the geometries discussed above, our implementations for calculation of the various distribution functions allow for custom boundary correction functions to be given to enable their use for use cases with other geometries. For some boundary shapes however, analytical expressions for the intersection volume of a sphere with the boundary may be unknown or even be known not to exist. In these instances a first suitable approximation may be to calculate the intersected *area* of the sphere, and approximate the intersected shell volume as the area times the shell thickness, which is valid for small shell thickness δr . If this is not an option, a numerical approach can be used to apply a missing volume correction such as described by Larsen & Shaw^[455], or the $g(r)$ may be corrected by dividing an uncorrected $g(r)$ by the $g(r)$ of an ideal gas—simulated as uniformly distributed random coordinates—within the same bounding box. While these methods can give the correct result for sufficiently dense sampling, this is often computationally demanding compared to calculation of the correction factors through the analytical equations outlined above. An exception here is when many $g(r)$'s need to be calculated within the same set of boundaries, since the numeric correction factor needs to be calculated only once per boundary shape, while the analytical approaches given above for non-periodic boundary conditions are calculated on a per-particle basis. Numerical approaches were not used for the data presented in this thesis.

4.9.4 Implementation of iterative test-particle insertion for calculating the pair potential

The iterative test-particle insertion method to solve for a (discretised) pair interaction potential $\mathbf{u} \in \mathbb{R}^L$ from one or multiple sets of coordinate data was implemented as follows: a reference radial distribution function $\mathbf{g}_{\text{DH}} \in \mathbb{R}^L$ is first calculated using the distance histogram method described in Section 4.9.1. To avoid extreme values or division by zero, any values in \mathbf{g}_{DH} smaller than 10^{-20} were set to 10^{-20} . An initial guess for the bin values of the pair potential is then defined, in our work the initial value was typically chosen as $\mathbf{u}_1 = \{0, \dots, 0\}$ or as the potential of mean force $\mathbf{u}_1 = -k_B T \ln(\mathbf{g}_{\text{DH}})$. Next the main iterative procedure is started in which in each iteration k the trial potential is used together with the TPI algorithm described in Section 4.9.2 to calculate a trial radial distribution function \mathbf{g}_k , for which again all values $< 10^{-20}$ were clipped to that value. Then, the mean squared error $\chi_k^2 = \langle (\mathbf{g}_{\text{DH}} - \mathbf{g}_k)^2 \rangle_r$ is printed to monitor convergence. Finally, the trial potential for the next iteration is then calculated as

$$e^{-\mathbf{u}_{k+1}} = w(k)e^{-\mathbf{u}_k} \frac{\mathbf{g}_{\text{DH}}}{\mathbf{g}_k} + [1 - w(k)]e^{-\mathbf{u}_k} \quad (4.18)$$

where $0 \leq w(r) \leq 1$ a regularization parameter which aids convergence by averaging the new potential with the previous potential with a gradually decreasing emphasis on the updated potential, thereby initially allowing for large changes to the potential but avoiding noise due to the finite number of test-particles after a larger number of iterations. Any values where $e^{-u_{k+1}} < 10^{-20}$ are clipped to that

procedure is repeated until the convergence criterium is reached, in our work a predefined number of typically 50 iterations was used.

For multicomponent (e.g. binary) systems the pair potentials for each combination of components (including each component with itself) are optimized simultaneously in a single iterative loop, where the mean squared error χ^2 is taken as the average over all pairs of components. In principle, the correction factors for each combination of components are only given by the differences in those respective $g(r)$'s and do not depend on the $g(r)$'s of other combinations of components, e.g. the correction for the $U^{AB}(r)$ in an A/B binary system does not depend directly on the AA and BB $g(r)$'s. However, we note that the $U(r)$'s for the different combinations of components are interdependent through the multi-component TPI procedure, in which the total insertion free energy of the test-particles depends on the interactions with particles of all components, regardless of the type/component of the test-particle.

4.10 Experimental methods

4.10.1 Chemicals

The following chemicals were used: **poly(ethylene glycol) diacrylate** (average M_n 250 Da, **PEGDA 250**, containing 100 ppm 4-methoxyphenol (MEHQ) as inhibitor, *Sigma-Aldrich* no. 475629); **poly(ethylene glycol) diacrylate** (average M_n 575 Da, **PEGDA 575**, containing 400–600 ppm MEHQ as inhibitor, *Sigma-Aldrich* no. 437441); **poly(ethylene glycol) diacrylate** (average M_n 700 Da, **PEGDA 700**, containing 100 ppm MEHQ and 300 ppm butylated hydroxytoluene (BHT) as inhibitors, *Sigma-Aldrich* no. 455008); **trimethylolpropane ethoxylate triacrylate** (average M_n 428 Da, **ETPTA 428**, *Sigma-Aldrich* no. 409073); **MEHQ/HQ inhibitor remover** (for removing hydroquinone (HQ) and MEHQ, *Sigma-Aldrich* no. 311332); **TBC/BHT inhibitor remover** (for removing *tert*-butylcatechol (TBC) and BHT, *Sigma-Aldrich* no. 311332); **Irgacure 2100** (also known as Omnirad 2100, a liquid blend of phenyl(2,4,6-trimethylbenzoyl)phosphinate and phenyl bis(2,4,6-trimethylbenzoyl)-phosphine oxide, provided by BASF, stored in the dark); **4-(Hydroxymethyl)–1,3–dioxolan–2-one (glycerol carbonate)**, *Sigma-Aldrich* no. 455067); **glycerol** ($\geq 99\%$, *Sigma-Aldrich* no. G7893); **triethylene glycol** ($\geq 99\%$, *Acros Organics* no. 139590010); **activated alumina** (Al_2O_3 , 58 Å pore size, 205 m^2/g surface area, *Sigma-Aldrich* no. 199974); **AG 501-X8 mixed bed ion exchange resin** (*Bio-Rad* no. 1437424). All PEGDA and ETPTA monomers were stored at 4°C, Irgacure 2100 was stored in the dark and only opened in low-light conditions.

4.10.2 Measurement of the arresting rate

Sample preparation:

Fluorescent silica tracer particles of 325 ± 11 nm (3.4%) containing a 189 nm RITC labelled core were prepared using methods similar to those in [Section 3.7.11](#). These particles were used instead of e.g. the 97 nm silica particles as their larger size afforded a slower diffusion rate and much stronger fluorescent signal, such that particle localisation with reasonable precision was possible on data obtained from 2D CLSM imaging at relatively high speed, making the assumption that the presence of particles did not influence the arresting rate at the low particle concentrations used in the arresting speed determination (volume fraction $\ll 1\%$). Stock dispersions in different samples were prepared by centrifuging 0.20 mL of a ~ 40 g/L ethanolic particle stock at 500 RCF for 10 min, removing the supernatant and re-dispersing the particles in 4 mL of the desired solvent, e.g. triethylene glycol, H_2O , glycerol carbonate, DMSO, etc., and placing the sample in an ultrasonic bath for 30 min to ensure the particles were fully dispersed. The solvents were deionized over mixed bed ion exchange resin beads (in case of H_2O and glycerol carbonate) or activated alumina (all other solvents) for at least 1 week prior to use. A 10 wt.% solution

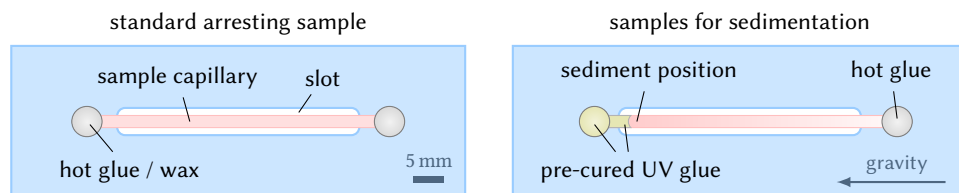


Figure 4.14: samples for solvent arresting. Borosilicate glass capillaries (200 $\mu\text{m} \times 2 \text{ mm} \times 5 \text{ mm}$ inner dimensions, 140 μm glass thickness, Vitrocom no. 3520) were filled with the sample and affixed to a modified glass microscopy slide using melted candle wax or hot-melt adhesive (hot glue). The right hand side shows a capillary as used for sedimentation experiments, prepared in the same way except that a ‘barrier’ of cured UV glue was made in one side of the capillary prior to adding the sample, such that imaging of the bottom was possible without the glue droplet getting in the way.

of Irgacure 2100 photo-initiator in ethanol was prepared and similarly deionized for at least 1 week during which it was fully wrapped in aluminium foil to prevent exposure to light. PEGDA monomers were mixed with activated alumina and the appropriate inhibitor remover(s) to deionize it and remove radical scavenging inhibitors added by the supplier to ensure a longer shelf life.

Typically 100 μL sample was prepared in a 0.5 mL Eppendorf tube by mixing the particle stock with the monomer (PEGDA or ETPTA), photo-initiator solution in the desired ratio, typically 80:20:2 by volume, and vortex mixing the tube for 1 min to ensure full homogeneity of the sample. Prior to the addition of photo-initiator, samples were either placed in a vacuum chamber for several minutes to degas (remove dissolved oxygen) or treated by bubbling nitrogen through it for several minutes in case of volatile solvents such as water. The addition of the photo-initiator and all subsequent steps were performed in rapid succession in low light conditions and out of direct line-of-sight from any windows to prevent premature (partial) polymerisation due to exposure of the sample to UV or blue light. A 100 μL volumetric pipette with an extra thin tip was used to fill the capillaries with $\sim 20 \mu\text{L}$ of the sample. The capillaries were ‘glued’ to a modified microscopy slide using two drops of melted candle (paraffin) wax or ‘hot glue’, poly(ethylene-vinyl acetate) at either end to simultaneously seal the capillary and affix it to the slide. Standard glass microscopy slides were modified by milling an elongated slot of 4 mm \times 40 mm such that the sample could be exposed from the back side without the UV light having to pass through the relatively thick (1 mm) glass slide while retaining enough space for the glue, as schematically depicted in Figure 4.14. The sample was wrapped in aluminium foil until placed onto the microscope, which was done with the room lights off.

Imaging and arresting:

A Leica no. SP8 CLSM was used to image samples through a $63\times / \text{NA}1.3$ apochromatic glycerol immersion objective (Leica no. 506194) and pure glycerol as immersion medium, the objective lens was equipped with a correction collar which was adjusted to compensate for the glass thickness of the capillary and slight differences in the refractive indices of the immersion medium and sample, thereby optimizing the z resolution. An excitation laser wavelength of 543 nm was used, which was sufficiently spectrally separated from the absorption peak of the photo-initiator that imaging did not initiate any formation of radical species. The the UV source (Thorlabs no. M365LP1-C2) had a peak wavelength of 365 nm and a total spot power of 6 mW as measured using a Thorlabs no. S175C microscope slide power meter when focused into a $\sim 1 \text{ mm}^2$ spot using a 0.9 NA condenser lens. A real-space condenser aperture was used to limit the area of exposure to a circular region of typically 0.5 mm in diameter. A variable length trigger pulse of typically 1 s was generated with an Arduino Nano microcontroller and used in combination with a Thorlabs no. LEDD1B LED driver to control the UV source. The timing of the UV pulse was detected by operating the scanning unit in 2-channel mode where one

detector channel was used for imaging the particle fluorescence (553–673 nm), and the second detector channel was set to collect light of 380–390 nm such that the detector response could be used to determine the frame during which the UV was turned on or off. Typically, a 800 px × 300 px field of view at a depth of 10 μm from the glass-liquid interface was imaged in resonant bidirectional scanning mode to achieve an imaging rate of 63 frames/s (30 ns pixel dwell time), during which the UV was turned on and arresting of the sample could be observed. Each subsequently arrested spot in the sample was taken at least 1 mm from the edge of the previous spot.

Data processing:

Particle coordinates were determined from the image frames using the open-source *Trackpy* library (v0.4.2)^[456] (implemented in the *python* programming language, v3.7.1), which is based on three steps: feature detection using the widely used intensity-weighted centroiding procedure,^[195] iterative refinement of feature coordinates for sub-pixel precision, and a linking procedure to correlate features between frames and obtain trajectories. A threshold for the integrated particle intensity was used to distinguish real particles from background noise and particles which were too far above or below the focal plane. The trajectories were corrected for sample drift by subtracting the mean displacement of all particles in each direction from each subsequent frame, which was necessary as some sample drift typically occurred upon arresting. Next, the squared displacements of particles between each set of two subsequent frames were determined and averaged over all particles to obtain the evolution of the MSD over time. The starting time of the UV pulse was determined by finding the first frame for which the mean pixel intensity in the UV-channel was more than the average of the 1st and 99th percentile of all frames, and the MSDs were stored as function of time since the start of the UV pulse. This was repeated for all arrested spots in the samples, and Eq. 4.6 was fitted to these data collectively to obtain the arresting time and initial and final apparent diffusion coefficients, where some apparent motion was present after arresting had completed due to random tracking errors as result of the large degree of shot-noise (photon counting noise) in the data.

4.10.3 Interaction potential measurement of silica NPs

Sample preparation:

For measurement of the interactions of silica NPs, deionization of solvents and removal of inhibitors from the PEGDA were done as described in Section 4.10.2. Next, 40.0 μL of an ethanolic dispersion containing 1.3 g/L fluorescent silica particles of 97.0 ± 3.1 nm (3.2 %) as prepared in Section 3.7.13 was mixed with 100 μL of a deionized mixture of 60 vol.% triethylene glycol, 20 vol.% glycerol and 20 vol.% PEGDA 700, and placed in a vacuum chamber (~1 mbar) for one hour to fully evaporate the ethanol and remove dissolved oxygen. Next, 2.0 μL of a 10 wt.% ethanolic Irgacure 2100 solution was added under low-light conditions and the sample was immediately vortex mixed for 1 min, after which a capillary was filled and affixed to a modified glass slide as described previously and shown in Figure 4.14. The sample was wrapped in aluminium foil until placed in the microscope, which was done with the room lights off.

Arresting and imaging:

Several spots in the sample of 0.5 mm diameter in the sample were arrested using a 1 s UV pulse using the methods described in Section 4.10.2. A *Leica SP8* CLSM was used to image samples through a 93× / NA1.3 apochromatic glycerol immersion STED objective (*Leica* no. 506417) using pure glycerol as immersion medium; the objective lens was equipped with a correction collar which was adjusted to compensate for the glass thickness of the capillary and slight differences in the refractive indices of the immersion medium and sample, thereby optimizing the *z* resolution. A *z*-stack consisting of 2048 × 2048 × 201 voxels at a voxel size of 27 nm × 27 nm × 50 nm starting at a height of 10 μm above the glass-liquid interface was recorded at a scan rate of 0.3 μs/px in each of the arrested regions. In total four of such *z*-stacks were recorded and used for the analysis, containing ca. $2 \cdot 10^4$ particles each (a volume fraction of 0.04 %).

Data processing:

Image data were corrected for slight xy drift during z -stack acquisition as a result of residual mechanical stress from the solvent arresting and subsequently deconvolved, both using the *Huygens Professional* software (v17.04, *Scientific Volume Imaging*). The drift correction was based on cross-correlation with sub-pixel precision using bilinear interpolation. For deconvolution, the iterative classic maximum likelihood estimation (CMLE) algorithm was used for a maximum of 20 iterations up to a SNR of 20, using theoretical point-spread-functions (PSFs) which were based on properties of the objective lens, the immersion and sample refractive indices and the position and thickness of the glass. The deconvolved datasets were split in $3\ \mu\text{m}$ subsets along the z -axis for particle localisation such that relatively thin and wide datasets were obtained. This was done to reduce the relative contribution of the z -direction to the extracted $g(r)$ and $U(r)$ as the resolution and localisation accuracy along the z -axis were poorer than in the imaging plane. Particle localisation in these datasets was done using the open-source *Trackpy* library (v0.4.2)^[456] (implemented in the *python* programming language, v3.7.1), which is based on feature detection using the widely used intensity-weighted centroiding procedure^[195] followed by iterative refinement of feature coordinates in order to achieve sub-pixel precision, which was done over an ellipsoidal region ('feature size') of $11 \times 11 \times 13$ voxels in diameter. A threshold for the integrated particle intensity over this region was used to distinguish real particles from background noise, and a threshold on the minimum separation between localised features of $0.2\ \mu\text{m}$ was used to prevent artificially high particle detections at short distance due to false-positive detections and biasing because of signal overlap from neighbouring particles. Any particles within one feature size from any of the image boundaries were removed from the dataset to prevent biasing due to partial overlap with the edges, thus effectively slightly shrinking the bounding volume. Particle coordinates were then used to calculate the $g_{\text{DH}}(r)$ as described in [Section 4.9.1](#) with $r_{\text{max}} = 2\ \mu\text{m}$ and $\delta r = 0.02\ \mu\text{m}$. This was used as input for the iterative TPI algorithm as described in [Section 4.9.4](#) to determine the $U(r)$ at the same r_{max} and δr and using 5000 test-particle insertions and 50 iterations.

4.10.4 Sedimentation experiments of binary samples

Sample preparation:

Borosilicate glass capillaries ($200\ \mu\text{m} \times 2\ \text{mm} \times 5\ \text{mm}$ inner dimensions, $140\ \mu\text{m}$ glass thickness, *Vitrocom* no. 3520) were sealed on one end by placing them in UV glue (*Norland* optical adhesive no. 68) for several minutes until ca. 5 mm of the capillary was filled, after which the capillary was attached to a modified glass microscopy slide using a droplet of UV glue on the sealed side, and subsequently placed for $>15\ \text{min}$ under a UV lamp (*UVP* no. UVGL-58, 6 W@365 nm) to ensure the glue was fully cured. Silica particle synthesis is described in detail in [Section 3.7.13](#), the resulting particles had an FITC- or RITC-labeled core and nonfluorescent shell and a total diameter of $294.3 \pm 3.6\ \text{nm}$ (1.2%) ('small particles') or $391.7 \pm 3.4\ \text{nm}$ ($<1\%$) ('large particles') respectively. In one sample, slightly larger 'small particles' were used which had a size of $315.0 \pm 5.3\ \text{nm}$ (1.7%). Each of the particle types were collected from their ethanolic stock dispersion using centrifugation (500 RCF for 20 min in 1.5 mL and redispersed in DMSO at a concentration of 140 g/L. Then, a sample was prepared by mixing 27.5 μL of the small particle stock in DMSO, 27.5 μL of the large particle stock in DMSO, 20.0 μL PEGDA 700 and 20.0 μL ethanol and 5.0 μL of a 40 mM ethanolic LiCl solution. The sample was then centrifuged for 100 RCF for 30 s in a 1.5 mL Eppendorf tube to remove any large clusters or contaminants, after which 5 μL of a 10 wt.% ethanolic solution of Irgacure 2100 was added. This gave a total concentration of 40 g/L small particles, 40 g/L large particles (number ratio $S/L \approx 2.4$), 2 mM LiCl (to screen electrostatic interactions) and 0.5 wt.% Irgacure 2100 photo-initiator. Ca. 30 μL was then used to fill the semi-sealed capillary by carefully pipetting along the inner side-wall of the capillary such that no air bubbles were included, after which the open (top) side of the capillary was sealed off using hot-melt adhesive ('hot glue'). This resulted in well-sealed samples suited for centrifugation and imaging without requiring the use of UV cured glue after filling with sample. A schematic of the sample cells is also shown in [Figure 4.14](#). The addition of the photoinitiator and any subsequent step were performed under low-light conditions to

prevent premature arresting. Samples were sedimented by placing them vertically in a dark cabinet for up to several months without leakage or premature polymerisation. Higher sedimentation rates could be achieved using centrifugation in a centrifuge equipped with a swing-out rotor in combination with custom made insets that held microscopy slides vertically in the centre of each rotor bucket, such that the centrifugal forces were aligned with the long axis of the capillaries.

Arresting and imaging:

Samples were arrested by means of direct exposure to the output of a collimated LED UV source (Thorlabs no. M365LP1-C2) with a power of 0.40 mW/mm^2 @365 nm for two times 5 s with ca. 10 second inbetween exposures, where the second exposure was to ensure all initiator had reacted away. The spot size ($\varnothing \approx 37 \text{ mm}$) allowed for the bottom $\sim 3 \text{ cm}$ of the sample to be exposed in one go, which was more than sufficient to cover the relevant part of the sediments. After exposure of the bottom, the remainder of the sample was arrested to fully stabilise the sample, but this region was never used in further analysis. After arresting, the samples could be placed horizontally in the microscope for analysis or could be stored for several weeks without observable change to the particle structure. Binary samples for binary interaction measurements were prepared at the same concentration as the sedimentation samples, but placed in a capillary without UV glue seal and arrested as discussed previously in [Section 4.10.3](#). Imaging was done for both fluorescent dyes simultaneously using laser excitation at 488 and 553 nm for FITC (small particles) and RITC (large particles) respectively, with detection ranges of 493 nm to 548 nm and 620 nm to 700 nm respectively. For characterisation of sedimentation profiles, the microscope was operated in tile-scan mode where a large area was automatically imaged in multiple adjacent tiles such that the field-of-view of the objective lens was not limiting. Tiles consisted of $128 \text{ vx} \times 128 \text{ vx} \times 61 \text{ vx}$ with a voxel size of $0.4 \mu\text{m} \times 0.4 \mu\text{m} \times 0.5 \mu\text{m}$, over a z -range of approximately $-10 \mu\text{m}$ to $20 \mu\text{m}$ with respect to the glass-sample interface to assure it was always recorded within the dataset; > 100 tiles were taken in each sample to cover at minimum up to $h = 10 \text{ mm}$. Additionally, a high-resolution z -stack of $1024 \text{ vx} \times 1024 \text{ vx} \times 71 \text{ vx}$ with a voxel size of $30 \text{ nm} \times 30 \text{ nm} \times 100 \text{ nm}$ was recorded in a region of the tile-scan measurement where the particle density was sufficiently low to allow for a particle localisation to run (typically just above the densely packed sediment), such that the particle concentration at that height could be determined.

Determination of sedimentation profiles:

Sedimentation profiles were determined from the tile-scan experiments as follows: first, each tile was corrected for inhomogeneous illumination using a correction image obtained by averaging the signal of a number of homogeneous regions in the sample. Then the corrected tile scan data were analysed as one continuous 3-dimensional (xhz) dataset and for each xh hyperplane the glass-liquid interface position was calculated by linearly interpolating the total intensity as function of depth z and taking the interface as the first z for which it was more than half the maximum value. The height-dependent fluorescence intensity $I(h)$ was then taken for each of the two species as the average over the depth range of $2.5 \mu\text{m}$ to $7.5 \mu\text{m}$ from the interface weighted by a triangular hat function around $z = 5 \mu\text{m}$. The intensities were then averaged along h over bins of $12.6 \mu\text{m}$ to obtain smoother profiles. Bleaching during the tile-scan experiments was negligible due to the low magnification and laser power and the high scan rates used. Finally, fluorescence intensities were converted to particle concentration by counting the number of particles of each species in a high-resolution z -stack in a low density region of the sample –typically just above the sediment–, and correlating that with the fluorescence intensities of the sedimentation profile measured at that height in the tile-scan.

TPI analysis of binary samples:

The same sample used for the sedimentation experiments was loaded in a capillary and arrested in the microscope using a the UV light source and high NA condenser lens as described in [Section 4.10.2](#). Then, 6 z -stacks of $1024 \text{ vx} \times 1024 \text{ vx} \times 101 \text{ vx}$ with a voxel size of $20 \text{ nm} \times 20 \text{ nm} \times 100 \text{ nm}$ were taken, and the z -stacks were corrected for drift and deconvolved as described in [Section 4.10.3](#). The stacks were split along the z -direction into 30 $2.5 \mu\text{m}$ high sub-stacks to reduce influence from the poorer z -resolution,

and particle localisation was applied as described previously (Sec. 4.10.3) for each fluorescent channel separately, with feature sizes of 0.25 and 0.6 μm in the xy plane or along the z direction respectively and a minimum separation threshold of 0.25 μm for either species with itself as well as between the two different species. Radial distribution functions and pair potentials were then determined for the large-large, small-large and small-small combinations as described in Sections 4.9.1, 4.9.2 and 4.9.4 with a bin size $\delta r = 25$ nm, cut-off $r_{\text{max}} = 2$ μm and 1000 test-particle insertions per sub-stack and 50 iterations for iterative TPI.

4.10.5 FIB-SEM analysis of arrested particle dispersions

Sample preparation:

The particles were dispersed in pure PEGDA 575 containing 0.1 wt.% Irgacure 2100. Thin and flat arrested films (~ 100 μm to 150 μm thickness) were prepared by placing a droplet of 30 μL between two standard microscopy cover glasses separated on either side of the droplet by smaller #0 coverslips which acted as spacers. The sample was then placed in a UV curing chamber (Hönle UV Technology UVACUBE 100, 100 W at 365 nm) and exposed for 5 s, after which the sample was transferred by peeling off one of the coverslips, sticking a standard 12.5 mm SEM sample stub to the sample with the use of a double sided conductive carbon sticker (PELCO Tabs no. 16084-1, and removing the other coverslip. A 3 nm layer of platinum was sputter-coated on the top surface of the sample to make it electrically conductive.

FIB-SEM imaging:

The samples were imaged using a *Fei Helios NanoLab G3 uv DualBeam* equipped with a gallium-ion beam operated at 30 kV and a needle gas injection system for local platinum deposition. A flat region of the sample (tilted to 52°) was prepared for ‘slice-and-view’ imaging by locally coating the region of interest with a 0.2 μm thick Pt layer using gas injection system in combination with the ion beam. Then, a large trench (typically 20 $\mu\text{m} \times 10$ μm) and two smaller trenches to the side (typically 5 $\mu\text{m} \times 10$ μm) were milled at an ion beam current of 2 nA to expose the inner surface and free up a block of the sample for analysis. A smaller 5 $\mu\text{m} \times 5$ $\mu\text{m} \times 0.2$ μm Pt alignment marker was prepared next to the region of interest for automatic alignment of the FIB slices. Finally, the frontal imaging surface was cleaned with the ion beam at lower current (0.43 nA) to expose the cutting surface. Serial sectioning was then done automatically using the *Fei Slice-and-View* software (v3.0) using a electron beam energy and current of 2 kV and 50 pA and a FIB current of 80 pA in case of AuNPs@PEG or 0.43 nA for AuNPs@SiOs, with slice thicknesses of 3, 10 and 20 nm and xy pixel sizes 3.4, 6.7 and 11 nm for 16 nm AuNPs@PEG, 77 nm AuNPs@PEG and 195 nm AuNPs@SiO₂ respectively. The SEM raster scanning distance was adjusted along the y -axis to correct for the offset angle between the cutting surface and the e-beam together with adaptive focussing such that the area of the surface represented by each pixel was square and in focus. Auto-focus and stigmator routines were run after every slicing operation.

Data processing:

The slice images were aligned using cross-correlation and trimmed prior to any particle tracking to exclude the first 5 slices and the top 5 μm from the PEGDA surface, where particle positions could have been affected by interactions with the sample/glass interface prior to the arresting being initiated. AuNPs could be localised directly using a conventional iterative centroiding algorithm (implementation from *Trackpy* (v0.4.2)^[456]) as discussed previously for data of CLSM of silica NPs. The silica particles in the dataset used for TPI analysis appeared with a brighter shell than in the centre, which was likely an artefact due to charging, and which was not directly compatible with centroiding. Instead, these data were ‘convolved’ by taking the FFT-based cross-correlation (implementation from *SciPy* (version 1.6.2)^[449]) of a 3D kernel representing a spherical shell of the same dimensions as the particles (with an intensity of 1 and an infill intensity of 0.5). The cross-correlation of the data with this kernel contained a strong peak in the centre of each particle which could subsequently be localised using standard centroiding without suffering from signal overlap. The particle coordinates were then used as input for iterative TPI using $\delta r = 20$ nm, $r_{\text{max}} = 1.2$ μm , $2 \cdot 10^4$ test-particle insertions and 100 iterations.

CHAPTER 5

Using cryo-TEM to measure the influence of ligand-dependent interactions on supraparticle self-assembly

ABSTRACT

In cryo-TEM, liquid samples are rapidly cryogenically vitrified such that they are preserved for high-resolution imaging using TEM. For nanoparticle dispersions, this means that particle positions can be preserved as they were before the vitrification ('freezing') commenced such that they contain information on the equilibrium interaction potential. In this chapter we show that cryo-TEM techniques may be employed in combination with the iterative test-particle insertion method presented in the previous chapter to infer interactions of colloidal nanoparticles. We use gold nanoparticles capped with ligands of varying length and study their effect on the self-assembly behaviour when the AuNPs are assembled into quasi-2D layers and 'supraparticles', which are assembled under spherical confinement in evaporating emulsion droplets, and find three qualitatively different types of self-assembly. We attempt to link these results to the interactions between the particles measured with conventional 2D cryo-TEM where the particles are confined in (almost) two-dimensional systems between interfaces. However, we show that such a conventional quasi-2D geometry is insufficient in this context due to influence of the confining interfaces on the interactions and/or due to projection errors from the non-zero sample thickness. Therefore, a novel sample preparation method for cryo-TEM based on graphene liquid cells (GLCs) is developed, which allows for the AuNP-containing emulsion droplets to be imaged directly, and for particle coordinates and interactions to be measured in three dimensions using TEM-tomography for which the spherical geometry of the droplets is ideal. Finally, we show that the use of emulsions in GLCs may also be exploited to prepare improved samples for liquid-cell TEM in general with a high density of liquid pockets of varying sizes.

5.1 Introduction

In the previous chapter we showed that the interaction potential may be extracted from a set of equilibrium particle positions in the form of coordinates from *e.g.* particle localisation of a microscopy dataset. There, we used optical- and electron microscopy in combination with a solvent-arresting procedure to determine particle positions and interactions. Here we take a conceptually similar approach where we use rapid cryogenic ‘freezing’ to arrest samples of gold nanoparticles (AuNPs) with varying ligands, and correlate their interactions with structures observed in particle assemblies prepared using established self-assembly (SA) techniques. By plunge-freezing a specially prepared sample grid for transmission electron microscopy (TEM) into a cryogen, typically liquid nitrogen or liquid ethane, cooling rates as high as 10^5 K/s may be achieved such that the samples are *vitrified*: that is the solvents cool so quickly that they transition to the solid phase without having time to crystallise. Such samples can then be stored and handled under liquid nitrogen and imaged in the vitrified state using TEM with a specialised sample holder.^[243–245,457] This process thereby thus also captures and preserves the position and structure of any particles by (almost literally) freezing the sample in time. And as was shown in the previous chapter, if the particle positions are known this gives direct insight into their interactions.

Cryo-TEM has seen enormous success in life sciences where it is used amongst others to resolve the structure of proteins and protein assemblies inside their native environment, and atomic level reconstructions are routinely achieved.^[458] Determination of coordinates of high-contrast nanoparticles in comparatively simple systems thus seems well within reason, but as discussed in **Chapter 2**, somewhat surprisingly the use of cryo-TEM for interaction measurements has seen little use in nanoparticle science. Cryo-TEM has a number of advantages compared to *e.g.* the polymerisation-based approach from the previous chapter. Firstly, the arresting can be orders of magnitude faster than the polymerisation or typical imaging rates achievable in optical microscopy, meaning that positions of even the smallest (fastest moving) NPs may be preserved and resolved as they were prior to plunge freezing commenced. Secondly, TEM can have a resolution high enough to resolve detail down to the atomic level, meaning that measurement of short-range interactions of nanometer sized particles is possible. Finally, while polymerisation-based arresting requires at least some of the solvent to be replaced with polymerisable monomers, cryogenic arresting is, at least in theory, possible for any solvent or solvent combination, provided that it is solid at cryogen temperatures and can be cooled quickly enough to prevent crystallisation. As we will discuss later this is not really the case in practice, but a wide variety of solvents and solvent mixtures may be used nonetheless, and solutes and additives are unlikely to affect the arresting rate to a degree that matters.

For our experiments, we focussed on a particle model system of 2 nm to 8 nm AuNPs with oleylamine (OAm) or thiolated polystyrene (PS-SH) ligands as introduced in **Section 3.2.3**. By tuning the particle size and the length / molecular weight of the ligands, the softness of the interactions could be tuned such that different SA behaviour may be observed.^[387,459–462] It is known for example, that for some particles the crystal structure upon SA changes from FCC to BCC with increasing ligand softness, similar to the transition in electrostatically stabilised colloids with varying interaction range.^[386,392,463] We focussed the SA experiments on the formation of supraparticles (SPs), spherical assemblies of AuNPs which in our case are between several tens of nanometers and several micrometers in diameter, but also performed some quasi-2D assembly on liquid-liquid interfaces.^[386] Next, we performed conventional

cryo-TEM imaging experiments using the AuNPs in vitrified quasi-2D toluene thin-films to measure inter-particle interactions in two dimensions via test-particle insertion as introduced in **Chapter 4**. In addition, we develop a novel procedure based on the use of graphene liquid cells (GLCs) in cryo-TEM to image the AuNPs during supraparticle-assembly directly in three dimensions using TEM tomography, for which the spherical symmetry is ideal. Finally, we found that this emulsion-based method of preparing GLCs could be used to prepare GLCs for conventional GLC-TEM experiments with an improved yield and size distribution of liquid pockets.

5.2 Self-assembly of AuNPs with varying ligands

For SA experiments, we focus on the formation of spherical assemblies of the AuNPs—so called supraparticles (SPs),^[399,464–466] the preparation of which is schematically depicted in **Figure 5.1**. These assemblies were prepared by mixing the AuNPs dispersed in toluene with water and surfactant to make an emulsion, after which the toluene was left to slowly evaporate such that the droplets gradually shrank and eventually fully evaporated, leaving the densely packed NP assemblies. To prevent too rapid shrinking of (small) droplets due to dissolution of the toluene into the water phase, the water/surfactant mixture was always saturated with toluene prior to adding the NP dispersions. Ultra-sonication was used as the emulsification method, which produced a wide range of droplet sizes such that a variety of SP sizes could be studied within a single sample. It is however equally possible to produce SPs with a narrow size range by using emulsification methods which produce more monodisperse emulsions, such as the use of a Couette rotor-stator device^[464,467] or microfluidics.^[468] TEM micrographs of SPs of AuNPs with different Au core sizes and varying ligand size are shown in **Figure 5.2**. Additionally, high-resolution SEM micrographs of some of the SPs are shown at the end of this chapter in **Figure 5.13**.

Surprisingly, AuNPs@OLAm (**Fig. 5.2A, D, G & J**) did not show evidence of crystalline ordering in the SPs made from the AuNPs with this small ligand regardless of AuNP core size, instead forming mostly what appeared to be disordered assemblies with coarser and rougher less spherical shapes. It is important to note that the high electron contrast of the particle cores and the relatively small spacing between them in case of OLAm ligands

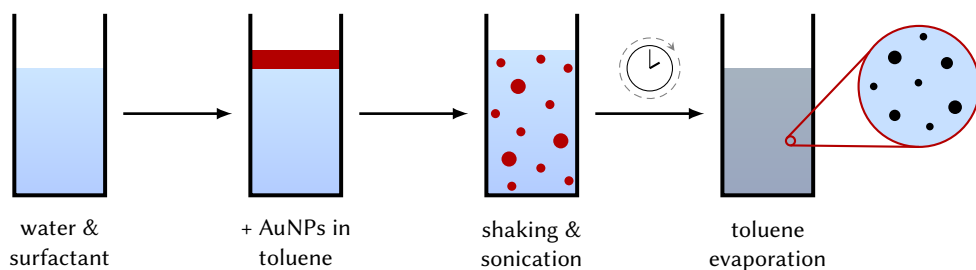


Figure 5.1: synthesis of AuNP supraparticles. Emulsion droplets of toluene containing the AuNPs were prepared by mixing the dispersion with a water/surfactant mixture, shaking the vial and placing it in an ultrasonic bath, after which the droplets were allowed to slowly evaporate, thereby slowly confining the AuNPs into spherical assemblies. The vials were covered with perforated teflon to slow and control the evaporation process.

meant that the internal structure could only be resolved for relatively small SPs (<100 nm) when using TEM. The lack of crystalline ordering in the AuNP@OLAm SPs was unexpected, since these particles readily assembled into crystalline structures during *e.g.* dropcasting the AuNP-in-toluene dispersions onto a TEM support grid directly, and earlier work in our group found icosahedral assembly of highly similar particles under comparable conditions. The disordered assembly and sometimes irregular overall shapes of the SPs are indicative of attractive interactions, as it has been previously found that even relatively small attractions may drastically lower the volume fraction at which the particles assemble,^[469] in turn resulting in polycrystalline or amorphous SPs and/or into SPs which have non-spherical shapes. The concentration of free OLAm ligand is likely a critical parameter here: too much, and the OLAm concentration in the droplets increases as toluene evaporates leading *e.g.* to depletion attractions between the particles due to OLAm micelles.^[56,58] Too little, and the loosely bound ligands can (partially) dissociate from the AuNPs surface such that they are no longer sufficiently sterically stabilised. There is some evidence for the latter in our samples as in some cases the AuNP cores had fused together in the SPs. It could be that some of the OLAm disappears from the droplets to the aqueous continuous phase, and it is known that SDS micelles can solubilise apolar molecules in the the aqueous phase.^[470] However, the sintering of AuNPs was not observed in the majority of AuNPs@OLAm SP samples and addition of a small amount of excess OLAm (0.1 vol.% w.r.t. the toluene) did not result in observable differences in the assembled structures. Another cause could be that the AuNPs@OLAm were adsorbed to the toluene-water interface and interacted through capillary interactions long before the droplets were fully dried. This could have led to buckling of the NP shell as the droplets shrank, giving an irregular ‘wrinkled’ surface. SEM imaging of the SPs of AuNPs@OLAm (see **Fig. 5.13A**) indeed revealed such surface structures for the AuNP@OLAm SPs, thus pointing towards the particles being interfacially active with attractive interactions.

The AuNPs@PS2.3k-SH SP samples (**Fig. 5.2B, E, H & K**) conversely consisted entirely of particles with clear crystalline ordering, where in many cases (depending on the orientation/viewing angle) five-fold symmetry could be seen. The overall particle shape was approximately spherical for the majority of particles with sometimes a somewhat deformed shape when multiple SPs were in contact caused by the drying forces in-between the SPs, as well as a small fraction of SPs appearing faceted with overall icosahedral shapes. To fully resolve the internal structure of the SPs, TEM tomography was performed on representative SPs (**Fig. 5.3**). From the reconstructed image volumes particle coordinates could be obtained whose local structure was analysed using average local bond order parameters (BOPs).^[471,472] Calculation of and classification based on BOPs is discussed in more detail in **Section 5.8.2**, but briefly, local BOPs describe the degree to which the local environment around a particle—typically taken as the nearest neighbour shell—conforms to different symmetries (*e.g.* 4-fold, 6-fold, etc.) and are thus sensitive to the local (crystal) structure. Using several thresholds for different orders, we classified particles as either fluid phase, FCC, HCP or BCC. It was found that the SPs possessed icosahedral ordering with 20 tetragonal FCC domains, in good agreement with previous studies which have found that the spherical confinement in SPs induces such icosahedral symmetry in the ordering of the particles.^[399,464,473–475] This structure was found for the full range of AuNP core sizes studied here, with no evidence for any dependency on the ratio of ligand to core size ratio in this range.

However, with the significantly larger PS5.3k-SH ligands (**Fig. 5.2C, F, I & L**) the majority

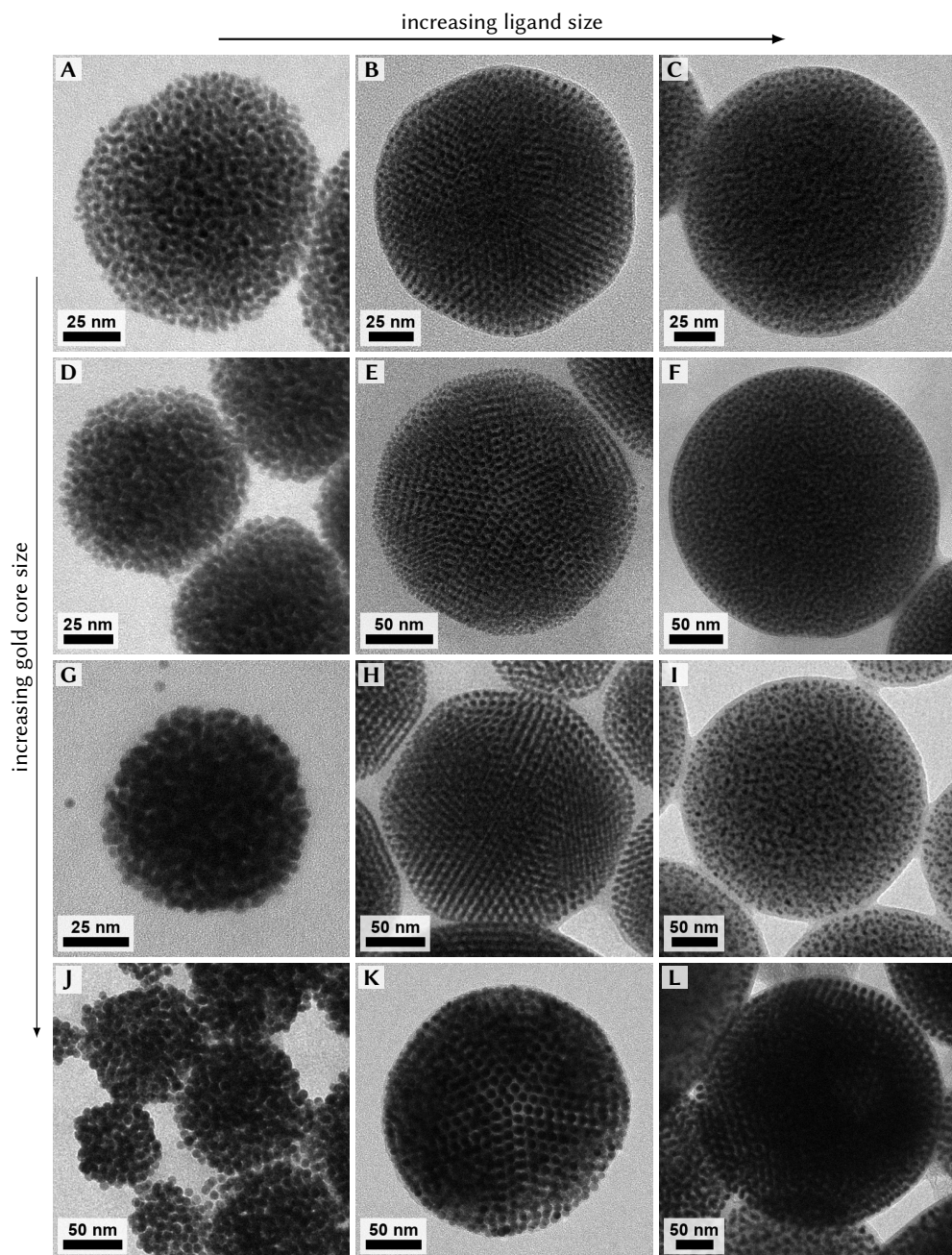


Figure 5.2: BF-TEM images of AuNP SPs with varying particle and ligand size. Particle sizes of the AuNP cores from top to bottom were 2.9 ± 0.4 nm (15 %) (A-C), 3.8 ± 0.3 nm (7 %) (D-F), 4.6 ± 0.5 nm (10 %) (G-I) and 7.8 ± 0.7 nm (10 %) (J-L). Ligands for each particle size were from left to right OIAm, PS2.3k-SH and PS5.3k-SH.

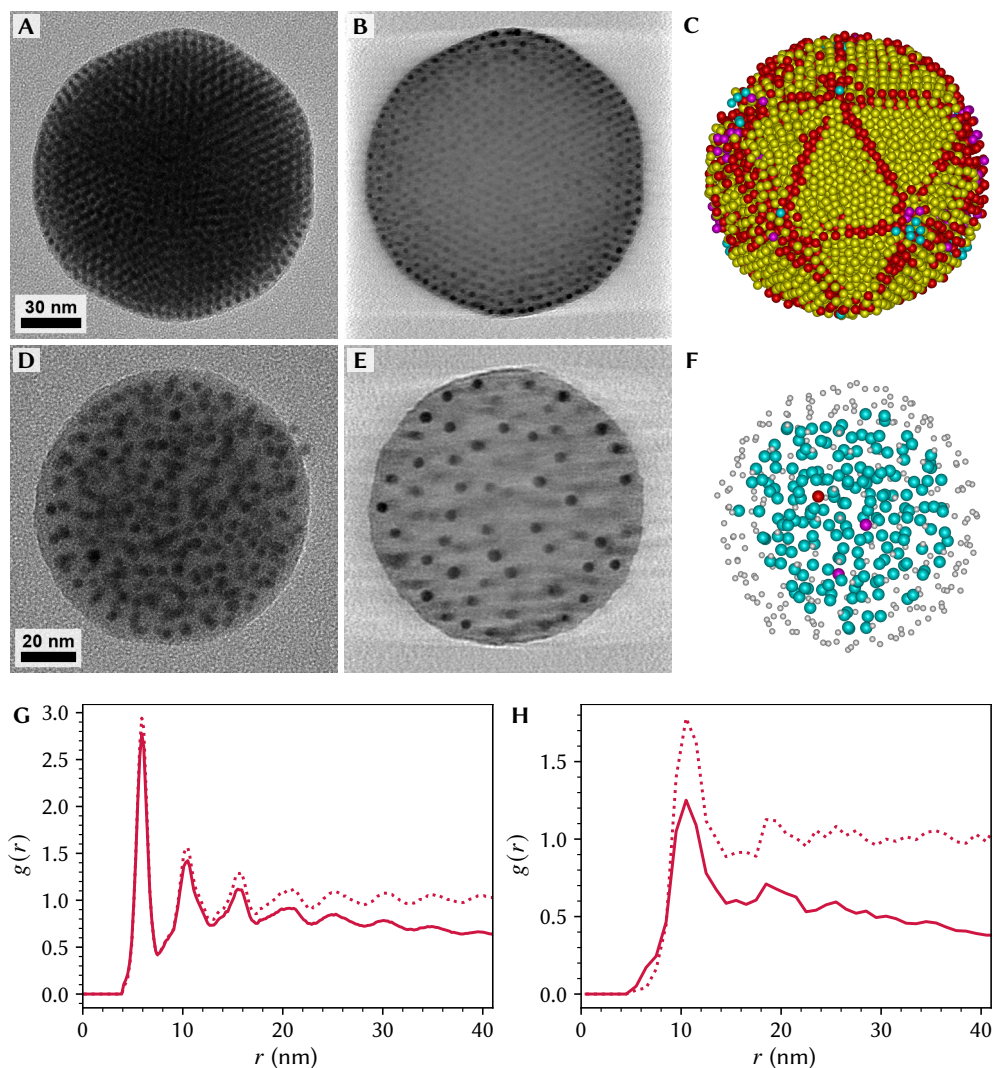


Figure 5.3: TEM tomography of supraparticles. **A–C:** 0° tilt image, xy cross-section and colour coded rendering of a SP of 2.9 nm AuNPs@PS2.3k-SH. Tomography data was recorded with a tilt range of -70° to 70° in 2° increments, the SP contained $\sim 10^4$ AuNPs. **D–F:** 0° tilt image, xy cross-section and rendering of a SP of 4.2 nm AuNPs@PS5.3k-SH. Tomography data was recorded with a tilt range of -54° to 58° in 2° increments, the SP contained 465 AuNPs. Colour coding of renderings is based on the local symmetry determined using BOP analysis, where cyan indicates liquid-like ordering, yellow FCC, red HCP and purple BCC. The outermost layer of surface particles were classified separately and are not shown (C) or depicted smaller (F) to more clearly show the internal structure of the SPs. **G,H:** $g(r)$'s of the AuNPs@PS2.3k-SH and AuNPs@PS5.3k-SH SPs respectively. The dotted lines show the $g(r)$'s when excluding the outermost layer of particles from the analysis and correcting for spherical boundary conditions.

of SPs clearly did not possess such a well-defined ordering. This was confirmed using TEM tomography and BOP analysis (Figs. 5.3D to F) which showed that the majority of AuNPs had nearest neighbour shell with liquid-like ordering, and further corroborated by the $g(r)$ which showed a relatively broad first peak and no correlations between the second peak. In contrast, the $g(r)$ of the crystalline AuNP@PS2.3-SH SPs showed strong correlations up to interparticle distances as large as the SP radius despite containing far more particles. Interestingly, for the larger AuNP core sizes (Fig. 5.2I, L) a mixture of disordered/liquid-like and crystalline SPs were observed, although the majority of SPs was still disordered. Due to time constraints, no tomography was performed on these ordered SPs, but the structure appeared in most cases qualitatively similar to that seen for the AuNP@PS2.3-SH SPs. In a few cases, in particular for the 7.8 nm cores, ‘onion-like’ ordering was observed—where the particles have local hexagonal ordering within concentric spherical shells—which has previously been found to form for hard spheres when the drying rate of the SPs is relatively high, such that lower free energy icosahedral ordering cannot be realised.^[474] The formation of this liquid-like ordering in the majority of AuNP@PS5.3k-SH SPs was surprising given the high degree of ordering when using shorter PS ligands and the fact that earlier work found crystalline structures even for high ligand to core size ratios in crystallisation experiments without spherical confinement.^[386,392,463]

In addition to the spherically symmetric SPs, we performed the more widely used SA technique of SA of NPs on liquid-air interfaces to prepare thin self-assembled layers (SALs) of the AuNPs, which are typically 1 to 10 NP layers thick and have large lateral dimensions.^[476] For this, a small amount of AuNP-in-toluene dispersion (typically containing 1 μM particles) was carefully placed on top of diethylene glycol in a small (1.5 cm \times 1.5 cm) teflon well, and mostly covered such that the toluene slowly evaporated over the course of approximately an hour. The SALs could then be scooped from the surface with a standard polymer-coated TEM support grid and dried under vacuum. TEM micrographs of SALs of AuNPs with the different ligands are shown in Figure 5.4, and tell a qualitatively similar story as the SPs. SALs of AuNPs@OAm were mostly disordered, although some locally ordered domains of typically 100 nm to 200 nm were present. The AuNPs@PS2.3k-SH assembled into crystalline structures with long-range order up to 10 μm , with predominantly the FCC crystal structure in thicker regions (see also Fig. 5.14). A variety of different thicknesses were found in the SALs, likely due to inhomogeneities in the thickness of the toluene film during the drying due to e.g. convection currents and/or air flow. Finally, the AuNPs@PS5.3k-SH showed strong local ordering, with a large spacing between the particles due to the bulky ligands, but no long ranged ordering beyond the nearest and next nearest neighbour shell.

The assembly into SPs or SALs thus painted similar pictures: AuNPs@OAm formed mostly disordered structures reminiscent of attractive interactions, AuNPs@PS2.3k-SH formed crystalline assemblies with long-range FCC ordering (in SALs) or icosahedrally arranged FCC domains (in spherical confinement), and AuNPs@PS5.3k-SH finally exhibited frozen-in local liquid-like ordering, but showed no long range ordering. The difference between the two different types of thiolated polystyrene ligands in particular was striking and prompted further experimentation with thiolated polystyrene with molecular weights of 0.88 and 5.8 kDa (PS880-SH and PS5.8k-SH). TEM micrographs of SPs of 4.6 nm AuNPs with the four different PS-SH ligands are shown at the end of this chapter in Figure 5.12. The AuNPs@PS880-SH (the shortest ligands) showed a mixture of particles, with mostly similar ordering as the AuNPs@PS2.3k-SH but with some particles with a layered ‘onion-like’

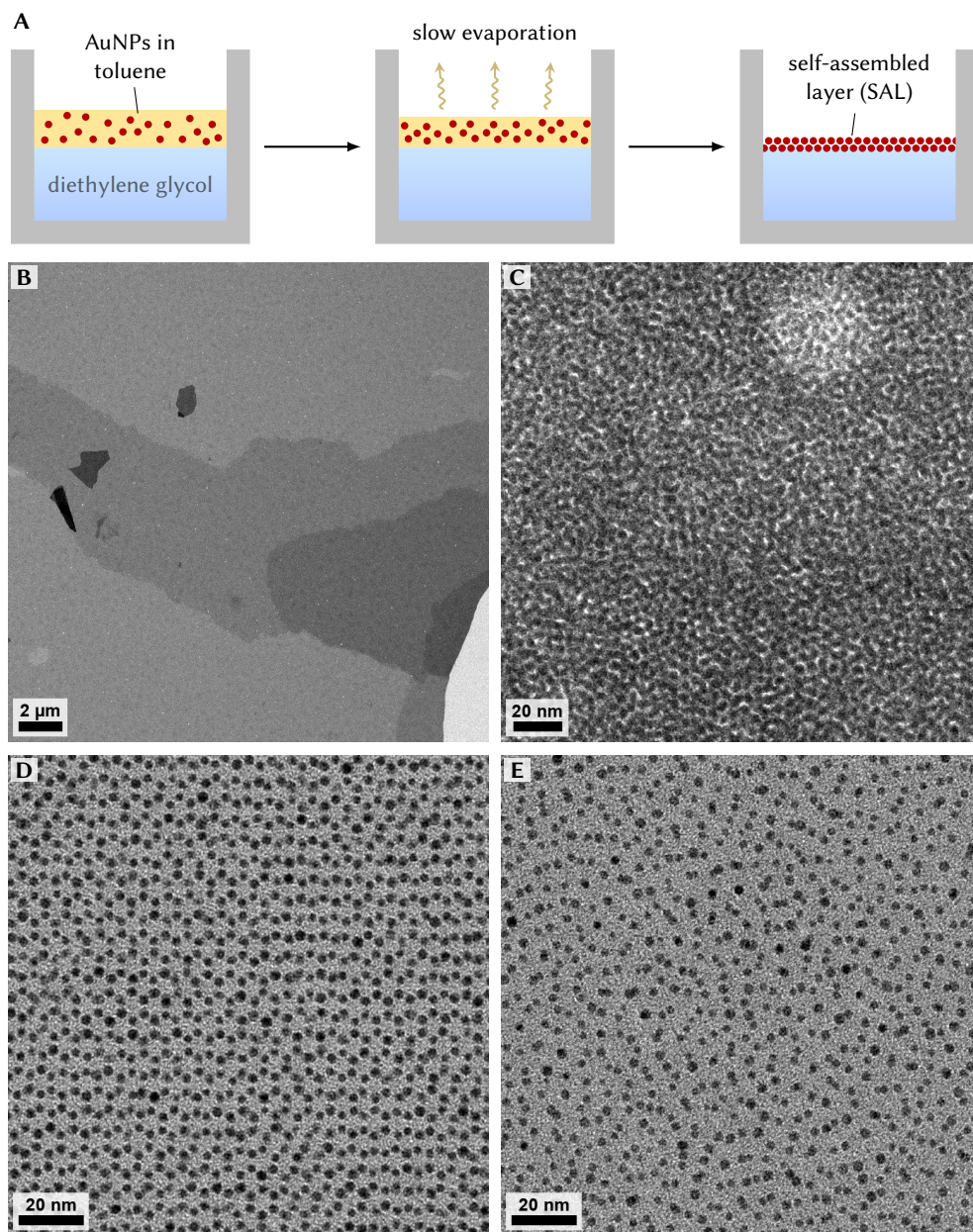


Figure 5.4: quasi-2D self-assembled layers of AuNPs. **A:** schematic depiction of the SAL synthesis. **B:** low magnification overview showing regions with consisting of AuNPs@PS2.3k-SH SALs of approximately 2, 3 or 4 monolayers thick. **C:** SAL of AuNPs@OIAM with overall disordered assembly containing some <200 nm crystalline domains. **D:** bi-layer region of a SAL of AuNPs@PS2.3k-SH showing long-ranged FCC ordering. **E:** approximately bi-layer region of a SAL of AuNPs@PS5.3k-SH showing local liquid-like ordering. The AuNP cores were 2.9 ± 0.4 nm (15 %).

ordering, wherein particles are ordered within concentric shells. On the other extreme, the AuNPs@PS5.8k-SH closely resembled the ordering seen for AuNPs@PS5.3k-SH with predominantly SPs with liquid-like ordering, and a small number of SPs with crystalline ordering.

The lack of crystalline ordering for the larger two of the ligands may be the result of a number of different processes. Firstly, it could simply be that there is a large amount of excess (unbound) ligand molecules present, meaning that during the final stages of drying the particles are effectively dispersed in a matrix of polystyrene. Even small amounts of excess ligand are known to cause changes in SA behaviour,^[477] although the final volume fraction of unbound ligand would have to be on the order of the particle volume fraction to lead to the liquid-like ordering seen here. However, several washing steps were performed after ligand exchange to remove unbound ligands and TEM samples of the particles after ligand exchange did not appear to contain a large amount of excess organic material. A second possibility is that crystallisation is frustrated by polydispersity in the individual ligands or in the ligand shells as a whole, *e.g.* when there are large variations in the number of ligands from particle to particle. While the PS5.3k-SH used in this work was rather polydisperse ($\mathcal{D} = 1.4$, or a relative PD of $\sim 63\%$ in the number of monomers, see also [Sec. 5.8.1](#)), depending on the particle size each particle likely contained at least several tens of ligand molecules. Furthermore, the same effects were observed for the larger PS5.8k-SH which was significantly less polydisperse ($\mathcal{D} = 1.1$, PD = 32%). We did not possess the means to determine the number of ligands on a per-particle basis and it is thus possible that variations in the number of ligands per particle contribute to the observed lack of crystalline ordering.

Lastly, the large ligands may have sufficient flexibility to accommodate a variety of conformations around the cores, rather than only the idealised picture of a perfectly spherical shell. While the steric interactions of longer polymeric ligands are expected to lead to soft repulsive interactions between the particles, these differ from *e.g.* screened coulomb interactions in that they are not necessarily isotropic, and the ligand shells likely interdigitate which can also lead to friction or a locally high viscosity. This is especially the case in the later stages of drying where the final structure is set, and where the interactions are unlikely to be truly pairwise additive. In other words, since individual ligand chains interact with those of their own gold core the same as with ligands of a neighbouring particle, the position of the gold cores may not be that important for the free energy of the system upon kinetic arrest. If this is true even in the purely pairwise case, we would expect to see a relatively long ranged but 'flat' tail in the $U(r)$. Since the molecular details of the ligand chains during assembly cannot be directly observed experimentally, this system would be an interesting target for further research using molecular dynamics simulations where the ligand-ligand interactions are simulated explicitly.

5.3 Cryo-TEM of quasi-2D thin films

The use of quasi 2-dimensional thin films has seen wide use in cryo-TEM experiments for two reasons: (relative) ease of sample preparation, and ease of imaging. TEM samples need to be sufficiently thin to allow enough of the electron signal to pass through the sample, which limits sample thickness to a few hundred nm at most. The in-plane field of view on the other hand may be tens or even hundreds of micrometers large, depending on the magnification and TEM thus naturally favours such a quasi-2D sample geometry. And while it is possible

to image cryogenic samples in three dimensions using TEM tomography, this is considerably more challenging and time consuming than conventional 2D transmission imaging and puts further restraints on *i.a.* sample thickness and stability under the e-beam. As discussed in **Chapter 2** such 2D cryo TEM has shown some promise in studying interactions between NPs in dispersion,^[251,255] but one must be careful in drawing general conclusions from such measurement because particles are strongly confined between or adsorbed onto liquid-air interfaces, which will affect their interactions.^[250,256] For these reasons, we investigated to what extent it was possible to measure inter-particle interactions from such quasi-2D thin films using test-particle insertion, if and how these interactions differ from those of the NPs in bulk, and to what extent these measurements can aid in understanding bulk assembly behaviour.

The vitrified thin-films of AuNPs in toluene are depicted schematically with their support in **Figure 5.5**, consisting of specialised TEM grids with 2 μm diameter holes in the polymer/carbon support film. The films were prepared by pipetting a small amount of particle dispersion onto the support grid, after which the majority of the dispersion was removed from the support by blotting for a controlled time period using blotting paper, such that only thin free-standing films remain in the support film holes. As soon as the blotting was completed, the grid was rapidly dunked into a liquid nitrogen bath (plunge-freezing) which caused the film to vitrify. We note that liquid nitrogen (LN_2) was used as cryogen instead of more commonly used liquid ethane (which allows for a higher cooling rate) because toluene is soluble in liquid ethane. The grids were stored submerged in LN_2 until placed in a LN_2 cooled cryo-holder, which was subsequently transferred to the TEM for imaging. More details on cryo-TEM sample preparation are given in **Section 5.8.4**. Example images at different magnifications are shown in **Figure 5.5**: the grid of 2 μm holes is clearly seen with some empty holes and some containing vitrified films. In most cases a single 16.8 Mpx bright-field TEM image per grid hole (such as **Fig. 5.5D**) sufficed to localise particles with a sufficient pixel density, thus giving circular boundary conditions for the region in which the particle coordinates were defined. An example image of particle localisation with the detected features and the circular boundary conditions used is also shown in **Figure 5.15**.

The 2D particle coordinates of 7.8 nm AuNPs were then used in combination with the iterative test-particle insertion method (TPI) described in **Chapter 4** to calculate $g(r)$'s and extract pairwise interaction potentials as shown in **Figure 5.6**. The $g(r)$ for the AuNPs@OLAm shows strong correlations with local near-crystalline ordering. This was not the result of an overall larger particle concentration than other samples, but rather due to the particles mostly bunching together in a single grouping per grid hole, meaning that local concentration around the particles was high enough to induce local hexagonal ordering. In this limit, the validity of the TPI approach may be called into question as the sample is at least locally nearly crystalline. Convergence of the iterative TPI was also considerably slower, as the update scheme we use (**Eq. 4.5**) alters the potential at a certain distance only based on the $g(r)$ value at that distance, while in reality long ranged correlations may be caused by short ranged forces. Nonetheless, with sufficient iterations (>1000) convergence was reached. The potential had a hard repulsive component at short range due to steric repulsion of the ligands, with a attractive potential well of $-1.4 k_B T$ at an 11 nm centre to centre (C2C) or $\sim 2.8 \pm 0.6$ nm surface to surface (S2S) distance of the nearest neighbours, which is larger than the 1.7 ± 0.4 nm S2S distance observed for dried AuNPs@OLAm in conventional TEM. The latter is not unexpected, as the presence of solvent likely swells the ligand shells and

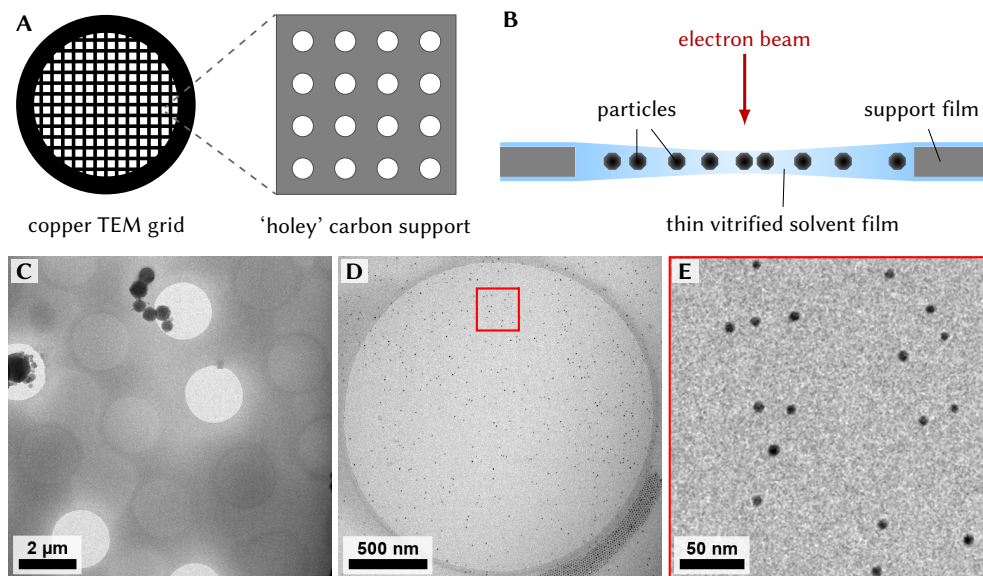


Figure 5.5: cryo-TEM of quasi-2D thin films. **A:** Quantifoil support grid with 2 μm holes. **B:** idealised schematic side view of a holes containing a vitrified ('frozen') free-standing liquid film with particles; particle size and film/support thickness are not to scale. In reality, ligands often poke through or flatten at the interface. **C:** low magnification TEM micrograph showing grid holes with and without thin films; the dark objects are water ice crystals from atmospheric moisture frozen onto the sample after vitrification. **D:** TEM micrograph of a AuNPs@PS2.3k-SH in toluene thin-film as used for particle tracking, with a zoom-in of some of the image in **E** showing the good contrast of the AuNPs over the solvent film.

reduces their interdigitation. There are also some minor secondary oscillations in the $U(r)$ at larger distance which we attribute to imperfect convergence and the effect of the suboptimal highly structured nature of the samples used, but overall the remainder of the potential tends to zero as expected.

The presence of attractions explains the bunching of the particles observed and is thus not surprising based on the cryo-TEM images, but in bulk toluene dispersion the AuNPs@OIAM were found to be long-term colloiddally stable and able to form ordered NP assemblies by simple drop-casting, both of which would not be expected in the presence of (strong) attractions in bulk. Calculations were performed to estimate the contribution of core-core van der Waals interactions to the attractions (for more info see [Sec. 5.8.6](#)), which for 7.8 nm were estimated as $-0.5 k_B T$ at 11 nm C2C, which is significant but does not explain the full magnitude of attractions observed. We note that these calculations used a bulk Hamaker constant and did not account for nano-size effects, which could increase the strength of interactions. We instead attribute the majority of attractions to interfacial interactions, as there is indirect evidence that the AuNPs@OIAM were strongly interfacially active in the cryo thin-films ([Fig. 5.16](#)). Particles were typically grouped in a single layer with consistent spacing and no overlap (which would indicate an offset along the z -axis), even in regions where the contrast of the vitrified toluene was consistent with a film thickness more than several particle

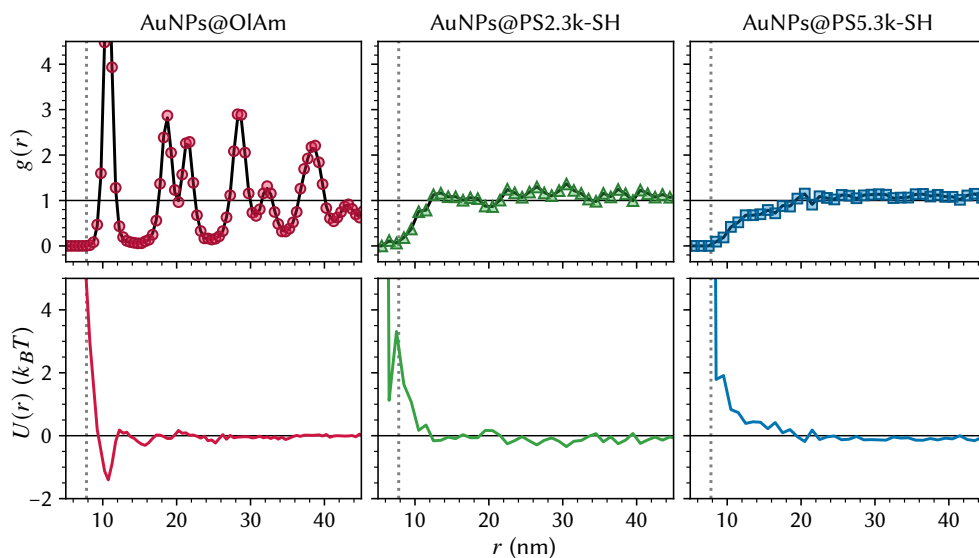


Figure 5.6: interaction potentials extracted from 2D cryo-TEM using TPI. The AuNP cores were 7.8 nm in diameter, which is indicated with the dotted gray lines.

diameters. In some cases, two separate NP layers (at the top and bottom interface) were observed (see also Fig. 5.16), where tilting the sample revealed no particles seen inbetween the two layers. This behaviour was similar to that of a different system we studied –15.7 nm AuNPs@mPEG5k-SH in water, shown in Figure 5.17– which are known to adsorb to the water-air interface.^[62,478,479] In that case, the inter-particle S2S distances of 31.9 ± 1.8 nm were also considerably larger than expected based on the ‘blob radius’ of the ligands in a good solvent ($R_0 \approx 6.6$ nm, see also Tab. 3.1), and instead more consistent with the length of (interdigitated) ligands when nearly stretched out ($L \approx 40$ nm) on the interface,^[62,479] further corroborating the fact that these particles were adsorbed on the liquid-air interface.

In contrast, samples with AuNPs@PS-SH typically showed some number of (partially) overlapping particles in thicker regions indicating a variety of z positions, while no layering or other (indirect) evidence for interfacial adsorption of the AuNPs@PS2.3k-SH was seen in the cryo-TEM experiments. To further confirm that these particles were not interfacially active, TEM-tomography was performed in a region of one of the samples where the toluene film was relatively thick at ~ 200 nm such that the height distribution of the AuNPs could be determined, similar to the work of van Rijssel & Ern e *et al.*^[250] Figure 5.7 shows an xz cross-section of the vitrified film of the dispersion together with a histogram of the particles’ positions along the z -axis. Surprisingly, the AuNPs@PS2.3k-SH showed no increased likelihood for the particles to be at the interface meaning that influence from interfacial effects on the interactions was unlikely and bulk-like behaviour could be expected. We emphasize however that interaction potentials were extracted from normal 2D TEM projection images and not from 3D coordinates of tomography reconstruction. Regions with such thick (but not *too* thick) toluene films that were stable enough and positioned favourably for tomographic imaging were rare and could not be produced reproducibly and reliably, and the stability of

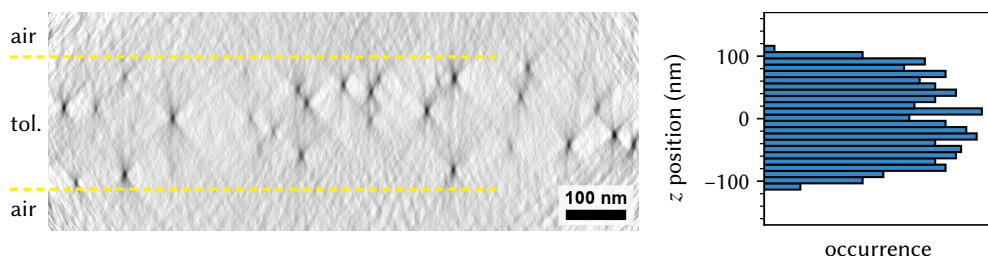


Figure 5.7: *xz* cross-section of a cryo-TEM thin film of AuNPs@PS2.3k-SH in toluene. TEM-tomography of a region where the vitrified toluene film was relatively thick shows that the particles were dispersed in the sample, and not adsorbed to the interface. Tilt angles of -50° to 40° in 5° increments and 10 SIRT iterations were used for the reconstruction; the dashed yellow lines indicate the position of the liquid-air interfaces. The histogram on the right shows the distribution of particle positions along the axis perpendicular to the plane of the toluene film.

these thicker regions under beam exposure was limited such that a relatively small number of tilt angles had to be used. Regions with a thinner solvent film were much more prevalent, but unfortunately all but the thinnest solvent films posed potential issues: even a typical film thickness of 20 nm could offer sufficient freedom for the particles along the third dimension to lead to significant projection errors, particularly at short inter-particle distances where interactions are the strongest.

Turning our attention back to the measured interaction potentials, repulsive ‘tails’ with no major attractive interactions were observed for either type of AuNPs@PS-SH. This was in line with calculations of the core-core van der Waals attractions which predicted at most weak attractive interactions of $-0.2 k_B T$ at 12 nm C2C and $-0.1 k_B T$ at 13.3 nm, at which distances the steric repulsion/stabilisation of respectively PS2.3k-SH and PS5.3k-SH ligand shells is likely already dominant. As expected, the repulsive interactions of the AuNPs@PS5.3k-SH were indeed found to be longer ranged than those of AuNPs@PS2.3k-SH. Nonetheless, for both types of particles the observed ‘hard diameter’, the point below which the $g(r)$ effectively went to zero, was close to the diameter of the AuNP cores. This was unrealistically close, as even in completely dried state the AuNPs assembled with a considerable surface-to-surface spacings of 4.1 ± 0.5 nm and 5.5 ± 0.8 nm for AuNPs@PS2.3k-SH and AuNPs@PS5.3k-SH respectively, meaning that distances below 11.0 nm and 12.5 nm respectively should be unlikely to be seen in the solvated state. Closer inspection of the cryo-TEM images revealed that in some cases partially overlapping particle signals could be seen, indicating that projection errors were the likely culprit by which the projected interparticle position in the xy plane was less than the real 3D inter-particle distance. This highlights a significant limitation of the quasi-2D approach when particles do not adsorb to the solvent-air interface, in which case tomography and 3D analysis are required to correctly analyse the system.

For most of our cryo-TEM experiments, toluene was used as solvent. This was motivated partly by the fact that it is an excellent solvent for the polystyrene ligands and that it has a solubility in water and vapour pressure which make it well-suited for SA in both SPs and thin films. Of equal importance to our experiments however was that we found toluene to be adequately suited to the cryo-TEM sample preparation and imaging pipeline. Due to differences in properties such as the evaporation and sublimation rates, the tendency to

crystallise or vitrify at temperatures and cooling rates relevant for cryogenic freezing, and the stability of vitrified films under e-beam exposure, not all solvents are equally practical when it comes to cryo-TEM imaging. Although cryo-TEM is a well-established and widely used technique in life-sciences in particular, these efforts have been focussed almost exclusively on aqueous samples. As a result, cryo-TEM sample preparation and imaging procedures for water-based samples have matured and are comparatively well-understood to the point that these can be routinely done.* In materials science conversely, a wide variety of polar and nonpolar solvents is commonly used but to the best of our knowledge no concerted effort has been made to develop and catalogue procedures for using commonly used organic solvents in cryo-TEM. Nonetheless, a number of organic solvents have been reported to be usable for cryo-TEM of nanoparticles.^[243,245,246,480,481]

In addition to toluene, we prepared cryo-TEM samples of other solvents with some example images shown in **Figure 5.18**. It was found that solvents with a high vapour pressure and/or low boiling point such as *n*-hexane and cyclohexane were poorly suited, as the thin fluid films lose significant fractions of solvent to evaporation between blotting and plunge-freezing, despite the fact that we always attempted to saturate the air in the blotting chamber with excess solvent. As a result, many of the grid holes showed large variations in particle concentration, or in many cases were mostly empty altogether. Higher boiling point / lower vapour pressure solvents such as dimethylformamide (DMF), octadecane and *cis/trans*-decalin did not suffer from these issues, but are not well suited to our solvent evaporation based self-assembly approach. Additionally, we prepared cryo-TEM samples using linear alkanes (*n*-hexane, *n*-octane, *n*-octadecane) and found these were highly unstable under the electron beam compared to cyclic molecules (decalin, toluene). It has been suggested that this is due to the strong tendency to crystallise when vitrified, which may be prevented by using alkane mixtures or branched isomers such as isooctane.^[246]

5.4 Cryo-TEM of graphene liquid cells

The direct preparation and imaging of thicker more ‘3-dimensional’ particle dispersion films for cryo-TEM remains challenging at present using the conventional blotting approach to sample preparation.^[257] This is the case even more so for organic solvents, due to *e.g.* poor control over the evaporation and wetting properties during and after the blotting phase of sample preparation, when the principle geometry of the cryo-samples are determined. By reducing the blotting time or omitting blotting entirely in processes such as for cryo-SEM (much) thicker vitrified samples may be prepared, but these cannot be imaged directly in transmission. Instead, such samples may be cut into thinner sections using microtomy or focused ion beam milling but this is often expensive and time consuming, taking many hours of preparation for each cross-section. Additionally, this still results in a flat slab-like geometry the apparent thickness of which increases with increasing tilt angle, meaning that the range of thicknesses usable for tomography remains smaller than for cylindrical or spherical geometries.

Here we propose a novel alternative strategy, which utilises recent developments in the

* this is not so much because water is particularly well-suited to cryo-TEM, but almost more to the contrary this is due to the enormous effort made in the field of life-sciences over the last four decades to develop methodology to the point that specialised devices for automated sample preparation, loading and imaging are commercially available which are developed with a focus predominantly on aqueous media. Water is actually comparatively challenging to vitrify and image due to its tendency to crystallise upon ‘slow’ cooling and/or e-beam exposure

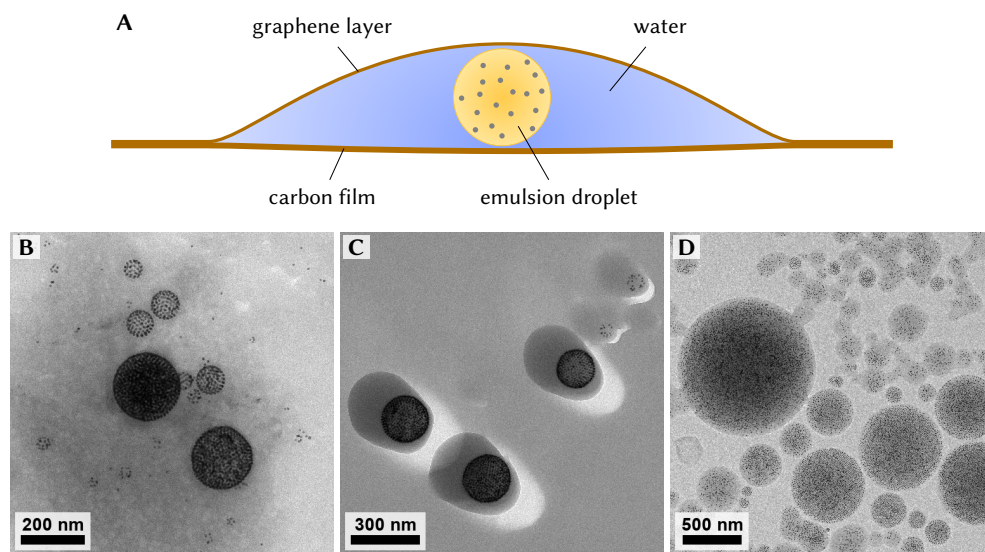


Figure 5.8: cryo-TEM of GLCs containing toluene in H₂O emulsions. **A:** approximate geometry of a GLC pocket containing an emulsion droplet. **B:** large water pocket containing multiple emulsion droplets. **C:** several pockets containing an emulsion droplet each. **D:** pockets containing only toluene and AuNPs.

preparation of graphene-based liquid cells (GLCs) for TEM,^[269,482–484] wherein we capture the dispersion of AuNPs inside of a GLC pocket, either directly or in the form of an emulsion droplet like in the SA of SPs. We used a loop-assisted transfer method wherein graphene naturally traps small pockets of sample with an air-tight seal around due to the adhesion of the top and bottom graphene sheets, such that the sample may be loaded and imaged directly in the TEM without the need for specialised LC-TEM equipment.^[485] Unlike previous LC-TEM studies however we do not use the GLCs to study NP interactions or assembly directly in the liquid phase where influence of the electron beam on the interactions is likely. Instead, we use the GLCs to controllably capture sample pockets of a desired geometry and protect them from the environment, but cryogenically freeze them prior to TEM imaging to arrest the dynamics and preserve particle positions without electron beam influence. The presence of the highly electrically and thermally conductive and strong graphene sheets also provides advantages over conventional cryo-TEM samples during imaging as it reduces charge build-up, beam-induced sublimation and other beam-damage effects.^[269,486]

The approximate geometry of a GLC pocket containing an emulsion droplet is schematically shown in **Figure 5.8** together with several example TEM micrographs of cryogenically frozen GLCs containing AuNPs in toluene in water emulsions. Here we hypothesize that some of the droplets retain their spherical shape due to their surface tension, thus essentially acting as their own spacer particle in determining the thickness of the liquid pocket. In addition to the ‘droplet in pocket’ geometry, liquid pockets were observed which contained only water, as well as pockets of a similar overall ‘wetting droplet’ pocket shape but containing only toluene with AuNPs (but no water). There were also some regions with dried AuNP assemblies which were presumably not covered by the graphene patches. The GLCs used

in this work were prepared from standard carbon support film TEM grids topped with a graphene layer, meaning that the liquid pockets were covered only on one side with graphene and had a more conventional carbon support on the other. This was done for the higher strength, lower cost and easier fabrication of the GLCs as opposed to fully graphene LCs (graphene on both sides), since the aim here was not necessarily to achieve the highest possible imaging resolution, but rather to more reliably produce liquid pockets of a more suitable geometry for analysis. However, if desired fully graphene LCs may be prepared in the same manner by using a graphene-coated holey or lacy support in place of a conventional carbon support. The sample consisted of the AuNPs@PS2.3k-SH in toluene dispersed as droplets in H₂O containing the surfactant SDS. The system was nearly identical to that used in SP synthesis, except that the droplet concentration was increased to 10 vol.% (compared to 2 vol.% in normal SP synthesis) to increase the number of droplets in the GLCs. In addition to the cryo-TEM of GLCs, some of the sample was left to evaporate the toluene completely like in the SP synthesis and imaged using conventional 'dry' TEM. After drying, crystalline SPs like those presented in [Section 5.2](#) were formed, confirming the similarity of the conditions in the toluene droplets between the cryo-TEM measurements and the SA experiments.

To determine the 3D $g(r)$ inside of the emulsion droplets, we performed cryo-TEM tomography on the GLC pockets and performed particle localisation on the reconstructed image volume. [Figure 5.9](#) shows the results of such measurements together with TPI analysis of the $g(r)$, for which we excluded the outermost layer of particles (the interface layer) and assumed an otherwise homogeneous particle distribution within the spherical boundary conditions. Unlike the interaction measurements of these particles in quasi-2D TEM experiments, attractive interactions are clearly observed with an attractive well of $0.8 k_B T$ at $r = 13$ nm. This is again larger than the $\sim 0.1 k_B T$ expected based on van der Waals calculations, although we again note that our calculations most likely underestimate the real van der Waals forces due to size-dependence of the Hamaker constant. Below this minimum, the interaction energy increases as the particles approach hard-core contact.

As can be seen from both the reconstruction images and the $g(r)$, this particular droplet was in an advanced state of drying close to the point of crystallisation. While this meant a large number of particle pairs within interaction range could be measured even from a single droplet, the surrounding medium was no longer reasonably described as just toluene, because the large number of nearby neighbours meant that particles were essentially 'swimming' in a sea of ligand. It is therefore to be expected that both steric interactions and van der Waals interactions between the ligand shells play a significant role, something which is not fully included in our core-core van der Waals calculations (where we assume the Hamaker constants of the ligand and medium to be identical) but could lead to increased attractive interactions. Furthermore the advanced state of drying and resulting high particle density made it more challenging to resolve the particles using TEM tomography and resulted in a large contrast difference between the outer layers and inside of the droplet, meaning that the accuracy of particle localisation suffered somewhat. This resulted in some 'blurring' of the interaction potential with the short range repulsions in particular likely appearing smoother than in reality, thereby effectively shifting the observed 'hard sphere' diameter (the point at which the $U(r)$ goes to effectively infinity) to lower values of r . To corroborate these results, another such dataset was recorded in a separate GLC cryo preparation of the same sample ([Fig. 5.19](#)). This sample was found to be in a similar stage of drying and its analysis yielded nearly identical results, showing the robustness of the method.

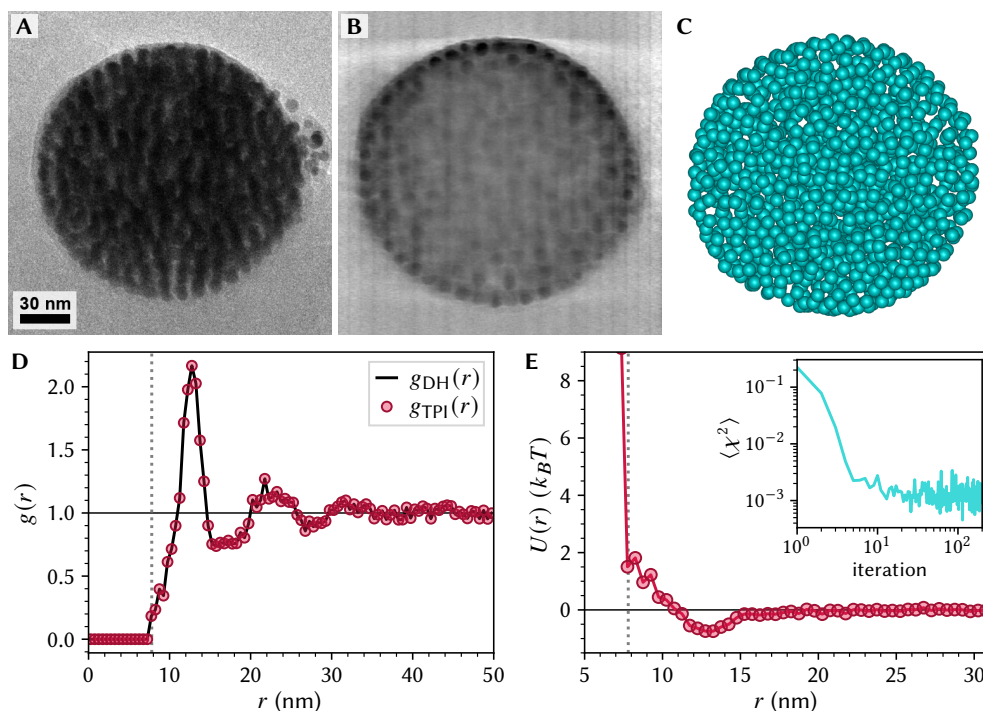


Figure 5.9: tomography and TPI of AuNPs@PS2.3k-SH in an emulsion droplet. The droplet contained 1267 AuNPs with core sizes of 7.8 ± 0.7 nm (10%) (indicated with the dotted gray lines), of which ~ 400 were located on the surface. **A–C** show the 0° tilt image, an xy cross-section of the reconstructed image volume and a rendering of the localised particle positions respectively. **D,E**: the $g(r)$ with fit and resulting $U(r)$ from TPI, 200 iterations of 10^5 test-particle insertions each were used with the inset showing evolution of the mean-squared error.

Unfortunately, the preparation of GLCs was not done in-house and the emulsions were always prepared a day prior to preparation of the GLCs, which in turn had to be kept at room temperature for at least two hours prior to cryogenic freezing. Although the emulsions were kept in a closed off vessel, partial evaporation of the droplets occurred in this time-frame which made it near impossible to precisely control the degree of drying and thereby particle concentration within the droplets. Furthermore, attachment of particles to the droplet interface made it challenging to visually assess the volume fraction inside of the droplet from a single transmission image when selecting a target for tomography, except for the extreme case when the internal volume fraction was so low that not enough data for calculating a $g(r)$ with a reasonably bin size would be possible. As such, we currently do not have data for droplets at lower volume fractions than the droplets shown here. Nonetheless, this is not a limitation of the method *per se* and we expect that better control over particle concentration in the droplets is possible when the initial volume fractions and waiting/evaporation time are controlled more precisely. Not only would this allow for interaction measurements at a variety of particle volume fractions, this would make it possible to follow self-assembly processes in droplets directly in real-space with high spatial resolution.

5.5 Using water-in-oil emulsions to prepare improved GLCs

In this work we used emulsions in GLCs to faithfully emulate the SP synthesis, with the added benefit that we expected the droplet and/or LC droplet geometry to be better suited for cryo TEM tomography. However, in addition to oil-in-water emulsions, we prepared GLCs using water-in-oil emulsions and found that the size and yield of liquid water pockets was vastly improved over conventional GLC preparation techniques. While not the focus of this thesis and chapter, we briefly discuss these results here as we believe that this may be of great use as sample preparation method for GLC-based LC-(S)TEM in general and single particle methodologies especially. This is because GLC preparation in particular has been notably challenging to achieve with a good yield. In the conventional preparation of GLCs, the number of large (>200 nm) pockets is limited as most of the water ‘escapes’ during the sealing of the graphene layers due to poor wetting. The liquid pockets generally also have complex shapes as they are predominantly defined by creases and folds in the graphene films. Some recent procedures achieve higher yields or size and shape control using specialised sample supports such as as patterned spacer layers.^[269,482,483,485] In our work conversely, we prepared the GLCs from a water-in-oil emulsion (rather than just the aqueous dispersion) using otherwise conventional preparation procedures –specifically the loop-assisted transfer method (LAT)—, without any other alterations to procedures or materials. As we will see, in doing so the discrete droplets were more likely to be trapped by the graphene sheets as liquid pockets than would be the case when using a purely aqueous sample. Specifically we used toluene as the oil phase, to which 1 wt.% SPAN80 surfactant was added to help stabilise the emulsion droplets against coalescence. Additionally, 17 nm AuNPs@mPEG5k-SH were added as ‘tracer particles’ in the aqueous phase to distinguish it from liquid pockets containing toluene, and to confirm whether particles included in the water phase would be incorporated into the liquid pockets.

Some TEM micrographs and a histogram of the number liquid pocket sizes are shown in **Figure 5.10**. We found a very high density of usable liquid (water) pockets varying from ~100 nm to tens of micrometers in size. For comparison, van Deursen & Schneider *et al.*^[485] found an overall LC density of ~85 mm⁻² for GLCs prepared with the same LAT method, with a majority of those below 250 nm in size. This means that on GLCs prepared from emulsions the LC pockets of <250 nm alone were over two orders of magnitude more prevalent than those prepared directly from just the aqueous phase, in addition to substantial numbers of much larger LC pockets. Three of these samples were prepared and all appeared qualitatively similar, but we note that our size distribution was measured from 5 grid squares on a single sample (~0.03 mm²); ideally a larger sample size of grids with measurements over a larger number of different regions of those grids would be needed to make a fair quantitative comparison. Nonetheless, it is immediately clear from our data that the density of usable LC pockets is *much* higher than the typical density of one per grid square for good samples. The success rate of grid preparation could not be ascertained from our data, but we had no failures in three samples and it can be reasonably expected that it will be similar to that for GLCs prepared with LAT in general. Finally, the vast majority of trapped liquid was in the form of pockets with an approximately circular (or for some of the larger ones elongated) ‘flattened droplet’-like shape which was much wider in the imaging plane than along the optical axis, with very few irregularly shaped pockets in folds and creases of the graphene film. The (3-dimensional) shape of some of the larger liquid pockets can also be seen in the tilt images shown in **Figure 5.20**.

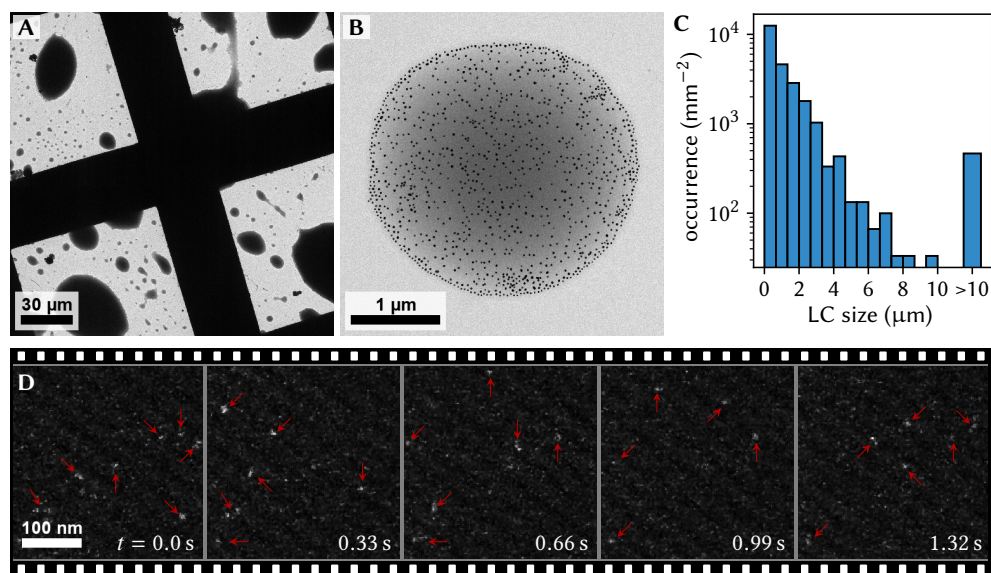


Figure 5.10: GLCs prepared from water-in-toluene emulsions. AuNPs@mPEG5k-SH of 16.7 ± 1.1 nm (6.3%) in size were added in the water phase as tracer particles. **A,B:** cryo-TEM micrographs showing the large number and variety of water pockets, the zoom-in clearly shows the tracer particles in the water droplet without any toluene remaining around it. **C:** size-distribution histogram of the LC pockets (with LC size the approximate diameter in the imaging plane). **D:** selected frames from a low dose ($\sim 20 \text{ e}^- \text{ nm}^{-2} \text{ s}^{-1}$) HAADF-STEM video showing clear motion of the AuNPs, some of the particle positions are indicated with the red arrows.

Interestingly, despite the large number of water pockets, the oil phase (which forms 90 vol.% of the original emulsion) was largely absent in our samples when imaged using room-temperature TEM. We attribute this to the good wetting of the graphene sheets by the toluene, meaning that it could leak out through gaps between the graphene sheets via the formation of a thin fluid layer between the enclosing sheets (*i.e.* a sort of capillary action) while leaving the water droplets behind. In addition to the presence of tracer particles, the pockets were confirmed to consist of water by imaging the GLCs in cryo-TEM, where the crystallisation of the water droplets under the electron beam could be clearly observed. It is also of note that in the cryogenically frozen GLCs, several regions where the water pockets were surrounded by toluene were found, meaning that some of the toluene likely did not fully evaporate in the room temperature samples until they were placed in the vacuum of the TEM. The broad distribution of liquid cell pockets ('LC sizes') is presumed to reflect that of the droplets in the emulsion it was prepared from. The emulsion had a broad range of droplet sizes due to it being prepared using ultrasonication as the emulsification method. A broad LC size distribution can be a useful feature *e.g.* when the ideal LC size is not known *a priori* or when investigation particles or assemblies of widely varying size. However, if LC pockets of specific sizes are desired and the LC size distribution reflects that of the emulsion, GLCs with monodisperse pockets may be prepared from more monodisperse emulsions made using *e.g.* shear rupturing^[467] or microfluidics.^[468]

During bright-field TEM imaging, few moving particles were observed with nearly all AuNPs in the liquid pockets being stuck to the carbon support film. This was hypothesised to be the result of the beam exposure, since these particles are known to attach to surfaces upon beam exposure.^[368] Low-dose conditions were also not employed for BF-TEM and the area illuminated by the beam typically extended far beyond the field of view (FOV) of the camera, meaning that particles could already get stuck before coming into view. To verify that particles were freely dispersed until beam exposure, we performed low-dose HAADF-STEM imaging of the AuNPs in the water pockets, where the use of STEM assured that only the FOV was illuminated and a lower accumulated electron dose could be achieved. As can be seen from the video frames in Fig. 5.10D, the majority of particles (the bright spots) were seen to rapidly diffuse, although over time an increasing number of particles were observed to get stuck to the carbon film. We stress however that this is a property of the particles, and not intrinsic to the LCs prepared in this manner. Furthermore, from tilting samples the particles appeared to attach predominantly to the carbon support film (presumably due to it accumulating charge from the beam), and not to the graphene side, meaning that particle attachment may be suppressed by using fully graphene based GLCs. Overall, the use of water-in-toluene emulsions resulted in a considerable improvement in the number and possible sizes of LC pockets, and we expect this to hold regardless of the type of particles in the aqueous phase.

5.6 Concluding remarks

Three qualitatively different types of assembly were thus observed for the different ligands used: disordered assemblies with buckled shell like shape and sometimes sintered particles in case of AuNPs@OAm, crystalline assemblies of FCC structures (in SALs) or icosahedrally ordered tetragonal FCC-like domains (SPs) for AuNPs@PS2.3k-SH, and liquid-like ordering for AuNPs@PS5.3k-SH and AuNPs@PS5.8k-SH. Using quasi-2D cryo-TEM imaging in combination with the iterative test-particle insertion method we were able to show that the AuNPs@OAm became attached to the liquid-air interface with attractive interactions of $1.4 k_B T$ between the particles, which to the best of our knowledge is one of the first uses of cryo-TEM to measure interfacial interactions between nanoparticles. Based on these measurements, it is likely that particles assembled or aggregated into disordered or polycrystalline structures at or near the droplet interface well before all toluene had evaporated, with potential buckling of a shell of particles at the interface. The exact role of the OAm concentration in this process deserves further investigation, as it is possible that the amount of OAm remaining in the particle suspension was simply insufficient to fully stabilise the particles.

The AuNPs@PS-SH on the other hand were shown *not* to adsorb to the toluene-air interface in vitrified thin films for cryo-TEM. While this meant that their interactions were likely more bulk-like during the vitrification process, it also meant in combination with the finite thickness of the thin-films that substantial variation in the z -coordinates was possible such that 2D imaging was not sufficient to accurately capture the inter-particle distances, particularly at small separation where interactions are strongest. Unlike OAm, both PS-SH ligands showed exclusively repulsive interactions in the 2D measurements, with longer ranged repulsions for the larger of the two, although the exact range and nature of the interactions could not be determined using this method due to the projection errors. While this explained the highly ordered nature of the AuNPs@PS2.3k-SH, it did not provide direct

insight into the liquid-like ordering of AuNPs@PS5.3k-SH. Instead, we pose that this could be the result of the flexibility of these largest ligand shells to deform and/or interdigitate thereby accommodating a variety of interparticle distances without significant differences in the free energy, effectively creating polydisperse interactions. This process would be complex and likely not accurately described using exclusively static, isotropic and pairwise interaction potentials. Instead of trying to measure this as a pairwise isotropic potential, we believe this to be a target of particular interest for molecular dynamics simulations with explicitly modelled ligand chains and solvent molecules through which mechanistic details behind interactions may be understood on a molecular level.

For the AuNPs with the shorter PS2.3k-SH on the other hand, we demonstrated that it is possible to measure interaction potentials directly in 3D during self-assembly using cryogenically frozen GLCs. Surprisingly we found there were attractive interactions of $\sim 0.8 k_B T$ when the system was close to the point of crystallisation, which was not expected based on *e.g.* DLVO theory and which, while small, may be enough to significantly affect assembly.^[469] These attractions may well represent direct evidence for deviations at the nanoparticle scale due to effects such as particle size dependency of the Hamaker constant. We propose that additional interaction measurements of this system at a lower volume fractions / earlier stage of drying could be used to further corroborate our preliminary findings and shed light onto the origin behind the measured interactions. We stress however that presently a major challenge with our results is that due to the vitrified/frozen nature of the samples it was not possible to observe directly which parts of the sample were “liquid” and which were dried. Instead, this could only be inferred indirectly from the density and positions of AuNPs and by comparison to conventional ‘dry TEM’ preparations of the same samples.

Finally, in using water-in-oil emulsion-based samples in GLCs we discovered that the number and sizes of liquid pockets obtained could be dramatically increased using a preparation method which relies on procedures and materials already commonly in GLC preparation, unlike most other state of the art GLC preparation methods. Furthermore, it can be reasonably expected based on these results that control over the size and number of LC pockets is possible through the composition of the original emulsion. Using low-dose imaging we were able to demonstrate that these GLCs could indeed be used to image NP dynamics in water in the electron microscope. It was beyond the scope of this work to explore GLC preparation in detail and as such we did not explore many of the parameters which may be used to tune the GLCs, but we believe that doing so may result in improvements in GLC preparation which may be of use in a far broader context than just nanoparticle science.

5.7 Acknowledgements

Tessa Vrijhoeven is acknowledged for synthesis of some of the AuNPs, SPs and SALs shown in this chapter. Hans Meeldijk is thanked for support with the preparation and imaging of 2D cryo-TEM samples. Pauline van Deursen and VitroTEM are acknowledged for support with the preparation of the GLCs and providing the required materials free of charge, and thanked for useful discussions with regards to the GLC preparation and results. Albert Grau Carbonell is thanked for support with low-dose STEM imaging of GLCs.

5.8 Methods

5.8.1 Chemicals

The following chemicals were all used as received: **oleylamine tech.** (OIAm tech., 70% technical grade, *Sigma-Aldrich* no. O7805); **oleylamine** (OIAm, 80–90% C₁₈ content, *Thermo Scientific Acros* no. 129540010); **α -methoxy- ω -mercapto polyethylene glycol (mPEG2k-SH)**, M_W 2 kDa, *Rapp Polymere* no. 122000-40, stored at –23 °C); **α -methoxy- ω -mercapto polyethylene glycol (mPEG5k-SH)**, M_W 5 kDa, *Rapp Polymere* no. 125000-40, stored at –23 °C); **α -methoxy- ω -mercapto polyethylene glycol (mPEG10k-SH)**, M_W 10 kDa, *Rapp Polymere* no. 1210000-40, stored at –23 °C); **α -mercapto- ω -amino polyethylene glycol hydrochloride (HS-PEG5k-NH₂·HCl)**, M_W 5 kDa, *Rapp Polymere* no. 135000-40-20, stored at –23 °C); **α -mercapto- ω -carboxy polyethylene glycol (HS-PEG5k-COOH)**, M_W 5 kDa, *Rapp Polymere* no. 135000-4-32, stored at –23 °C); **α -sec-butyl- ω -isopropylthiol polystyrene (PS880-SH)**, M_W 0.88 kDa ($\mathbb{D} = 1.1$, where $\mathbb{D} = M_w/M_n$ denotes the dispersity), *Polymer Source* no. P18808-SSH, stored at –23 °C); **α -sec-butyl- ω -ethylthiol polystyrene (PS2.3k-SH)**, M_W 2.3 kDa ($\mathbb{D} = 1.15$), *Polymer Source* no. P4431-SSH, stored at –23 °C); **α -sec-butyl- ω -ethylthiol polystyrene (PS5.3k-SH)**, M_W 5.3 kDa ($\mathbb{D} = 1.4$), *Polymer Source* no. P10826-SSH, stored at –23 °C); **α -sec-butyl- ω -ethylthiol polystyrene (PS5.8k-SH)**, M_W 5.8 kDa ($\mathbb{D} = 1.10$), *Polymer Source* no. P4430-SSH, stored at –23 °C); **ethanol** (100%, *VWR Chemicals* no. 85651.360); **abs. ethanol** (anhydrous reagent grade, *Fischer Scientific* no. 15436115. ***n*-hexane** (GC grade, *Honeywell* no. 34493); **hexane tech.** (mixed isomers, $\geq 98.0\%$, *Thermo Scientific* no. L13233); ***n*-octane** ($\geq 99.0\%$, *Honeywell* no. 74821); **sodium dodecyl sulfate (SDS)**, sodium lauryl sulfate, $\geq 99.0\%$, *Sigma Aldrich* no. 436143); **SPAN 80** (sorbitane monooleate, *Sigma Aldrich* no. S6760) and **diethylene glycol (DEG)**, $\geq 99.0\%$, *Merck* no. 8.03131.1000) Ultrapure (type 1) H₂O was produced by a *Direct-Q3* Milli-Q water purification system (*Merck Millipore* no. ZRQS0P300), and had a resistivity of ≥ 18.2 M Ω cm. Single use glass scintillation vials and eppendorf tubes were used as received without additional cleaning.

Some properties of oleylamine and the PS-SH ligands are given in **Section 5.8.1**, where contour lengths and root-mean-squared (RMS) end-to-end distances were calculated using the ‘equivalent freely jointed chain’ model as described in and using values from Rubinstein & Colby,^[363, pp. 53–54] and the polydispersity in the number of monomer units was calculated as $M_n \sqrt{\mathbb{D} - 1}$.^[487, p. 76] Histograms

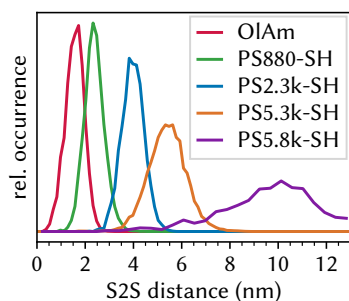


Figure 5.11 & Table 5.1: properties of thiol-terminated polystyrene ligands. M_n and M_w are the number and weight averaged molecular mass, $\mathbb{D} = M_w/M_n$ the dispersity, n the (number) averaged number of monomer units and associated polydispersity, L the (number) average contour length and R_0 the RMS end-to-end distance assuming an ideal chain (*theta*-solvent). r_{S2S} is the average surface-to-surface distance of the nearest neighbour shell measured from TEM of dried AuNP@PS-SH samples, with the full histograms of r_{S2S} shown in the figure on the left.

ligand	M_n (g/mol)	M_w (g/mol)	\mathbb{D}	n	L (nm)	R_0 (nm)	r_{S2S} (nm)
oleylamine	268	-	-	-	-	-	1.7 ± 0.4
PS880-SH	800	880	1.1	7 ± 2	1.7 ± 0.6	1.8 ± 0.3	2.4 ± 0.4
PS2.3k-SH	2000	2300	1.15	18 ± 7	4.7 ± 1.8	2.9 ± 0.6	4.1 ± 0.5
PS5.3k-SH	3800	5300	1.4	35 ± 22	9.2 ± 5.8	4.1 ± 1.4	5.5 ± 0.8
PS5.8k-SH	5300	5800	1.1	50 ± 16	12.9 ± 4.1	4.8 ± 0.8	9.9 ± 1.8

of the surface to surface (S2S) distances from dry TEM are shown in **Table 5.1**, where C2C and S2S distances were determined for each particles' 3 nearest neighbours based on the sizes and positions of each particle as obtained using the code described in **Sec. 3.7.14**, where C2C cut-off distances of resp. 8, 8, 10, 13 and 18 nm were used for the listed ligands to determine whether particles were neighbours.

5.8.2 Synthesis and characterisation of AuNP supraparticles

Synthesis:

Experimental methods for particle synthesis and ligand exchange to thiolated polystyrene ligands are given in **Sections 3.7.7** and **3.7.9**. SPs of apolar particles were synthesised as follows: 10 mL 8.0 mM aqueous SDS solution (2.3 g/L, CMC 8.2 mM at 25 °C) was mixed with 20 μ L toluene in a 20 mL glass vial to saturate the water (solubility 0.6 mL/L toluene/H₂O). Then, 200 μ L of toluene containing typically 2 g/L to 10 g/L AuNPs was added, and the vial was shaken by hand for 30 s and subsequently swirled in an ultrasonic bath (*Branson* no. 2510-DTH, 39 W/L at 40 kHz) for 1 min. The vial was then quickly covered with teflon tape, and a needle was used to poke 5 small holes in the tape to allow toluene to escape. The vial was then placed on an orbital shaker operating at 250 rpm to prevent creaming of the droplets and left shaking for typically 12 to 24 hours, after which the dispersions had gone from opaque to mostly clear, indicating full evaporation of the oil phase. The supraparticles were then collected by centrifugation at 50 RCF for 1 min followed by 250 RCF for 10 min in 5 mL Eppendorf tubes, after which the supernatants were transferred to new tubes and centrifuged for another 20 min at 1000 RCF, after which the sediments of both steps were dispersed together in 1 mL H₂O. This multi-speed procedure assured that supraparticles over a wide size range from <0.1 μ m to >10 μ m were collected without the larger SPs aggregating or breaking apart.

TEM tomography:

For tomography of SPs of AuNPs@PS2.3k-SH, 3 μ L of the washed SP dispersion was drop-casted onto a formvar/carbon 75 mesh copper tem support grid (*Ted Pella* no. 01802-F, approx. grid hole size 294 μ m) and left to dry under ambient conditions. The grid was then loaded in a single-tilt tomography holder and imaged in bright-field mode on a *ThermoFisher Scientific Talos 120c* at 120 kV and using a pixel size of 0.12 nm. Tilt series were recorded from -70° to 70° in steps of 2° with manually adjusted focus at each tilt angle. For tomography of SPs of AuNPs@PS5.3k-SH, 3 μ L of the washed SP dispersion was drop-casted onto a formvar/carbon 200 mesh copper tem support grid (*Ted Pella* no. 01801, approx. grid hole size 97 μ m) and left to dry under ambient conditions. The grid was then loaded in a single-tilt tomography holder and imaged on a *ThermoFisher Scientific Talos 120c* at 120 kV and using a pixel size of 0.12 nm. Tilt series were recorded from -54° to 58° in steps of 2° with manually adjusted focus at each tilt angle, where the maximum tilt angles were limited by shadowing of the copper grid bars. Each tilt-series were aligned coarsely using cross-correlation and subsequent fine alignment was done manually using a custom tool where the approximately spherical SPs were aligned to the centre of the field-of-view (FOV) using circular guide-lines and difference images between the previous and next tilt image. We note that manual alignment was critically important, as conventional alignment algorithms based on cross-correlation are much more sensitive to the texture of the carbon support film, resulting in the SP being significantly off-axis, while centre-of-mass based algorithms failed due to the contrast variation with varying tilt angle in BF-TEM of crystalline particles (both the individual AuNPs and the SPs as a whole). We note that more advanced algorithms are available^[488] but were not attempted, as manual alignment was faster in this case. After alignment, the tilt-images were cropped tightly to ~20 nm around the SP edges to centre it in the FOV. The tile-images were binned 2 \times 2 pixels prior to reconstruction to reduce the total number of pixels to reconstruct by a factor 8. Then, tilt-series were reconstructed using the simultaneous iterative reconstruction technique (SIRT) implemented in *Tomof* (v2.6)^[489] using 10 (for AuNPs@PS5.3k-SH) or 15 (for AuNPs@PS2.3k-SH) iterations.

Bond-order parameter analysis:

Particle coordinates were determined by particle tracking the tomography reconstructions using the open-source *Trackpy* library (v0.4.2).^[456] Classification of the particle coordinates was performed

semi-automatically based analysis of each particles' local environment using bond-orientational order parameters (BOPs).^[471,472,490,491] First, the nearest neighbour shell N_i of particle i (with N_i the number of nearest neighbours) was determined automatically using the solid angle nearest neighbour (SANN) algorithm described in van Meel & Frenkel *et al.*^[490] Then, average BOPs of order l were calculated for each particle i as

$$\bar{q}_{lm}(i) = \frac{1}{N_i + 1} \sum_{k \in \{i, N_i\}} q_{lm}(k) \quad (5.1)$$

which gives the average over all neighbours and particle i itself, and which depends on the complex quantities

$$q_{lm}(i) = \frac{1}{N_i} \sum_{j \in N_i} Y_l^m(\mathbf{r}_{ij}) \quad (5.2)$$

with $Y_l^m(\mathbf{r}_{ij})$ denoting Laplace's spherical harmonics and \mathbf{r}_{ij} the inter-particle displacement vector. Using the above, rotationally invariant BOPs $\bar{q}_1(i)$ to $\bar{q}_8(i)$ were calculated for each particle as

$$\bar{q}_l(i) = \sqrt{\frac{4\pi}{2l+1} \sum_{m=-l}^l |\bar{q}_{lm}(i)|^2}. \quad (5.3)$$

Similarly, parameters \bar{w}_l were calculated for orders $l = 2, 4, 6$ and 8 as

$$\bar{w}_l(i) = \left(\sum_{m=-l}^l |q_{lm}(i)|^2 \right)^{-3/2} \sum_{\substack{m_1, m_2, m_3 = -l \\ m_1 + m_2 + m_3 = 0}}^l [\mathcal{W}(l, m_1, m_2, m_3) q_{lm_1}(i) q_{lm_2}(i) q_{lm_3}(i)] \quad (5.4)$$

where m_1, m_2 and m_3 were summed for values from $-l$ to l as before except only for combinations adding to 0, and

$$\mathcal{W}(l, m_1, m_2, m_3) = \begin{pmatrix} l & l & l \\ m_1 & m_2 & m_3 \end{pmatrix} \quad (5.5)$$

is the Wigner $3-j$ symbol.^[472,492] Particles were then clustered into different categories using manually chosen thresholds based on parameters which were previously found to work well for simulated data of bulk colloidal systems (for which the phase was known). First, surface/interface particles – *i.e.* those on the outer surface of the SP or around void spaces – were determined as all particles for which $\bar{q}_1(i) \geq 0.1$ and removed from the dataset for further classification, as only a part of the NN shell was present which would make their classification difficult. The other particles were then classified using the following rules (in order): if $\bar{q}_6(i) < 0.2$ the particles were classified as fluid phase, otherwise if $\bar{w}_6(i) \geq 0$ the particles were classified as BCC crystal, and otherwise as FCC if $\bar{w}_4(i) < 0$ or HCP if $\bar{w}_4(i) \geq 0$.

5.8.3 Synthesis of self-assembled monolayers of AuNPs

Experimental methods for particle synthesis and ligand exchange to thiolated polystyrene ligands are given in Sections 3.7.7 and 3.7.9. A teflon block out of which a well of 1.50 cm × 1.50 cm × 1.00 cm was milled was partially filled with 1.80 mL DEG. Then, 50.0 μL of a 1 μM dispersion of AuNPs in toluene was added dropwise on top of the DEG. The top of the teflon well was partially covered with a glass microscopy slide with a small weight on top to form a hermetic seal on three sides, but leaving a 1 mm × 15 mm gap on one side to allow evaporated toluene to slowly escape. The gap size and total volume of open space above the DEG were kept constant throughout the experiments as these are known to be critical parameters in controlling the evaporation rate and thereby the resulting assemblies. The sample was left to evaporate undisturbed at room temperature in an area free of vibrations and air flow until the toluene had fully evaporated, which typically took 1 hour. Then, the sample was lifted off the surface by dipping the flat polymer coated side of a TEM support grid onto the interface with

the particles into the DEG and lifting it back out, which caused the SAL to stick to the grid. The grids were then dried overnight in a vacuum chamber to assure full evaporation of any DEG prior to transfer to a microscope for TEM imaging.

5.8.4 Cryo-TEM of free-standing thin films

Sample preparation:

Experimental methods for particle synthesis and ligand exchange to thiolated polystyrene ligands are given in [Sections 3.7.7](#) and [3.7.9](#). The particles were dispersed in toluene at a known concentration by dry mass as follows: a 2 mL glass vial was weighted and a small volume of AuNP dispersion in toluene (typically 0.5 mL) was subsequently added, after which the solvent was fully evaporated from the vial under N₂ flow at 30 °C in a *kdScientific Centrifan PE* rotary concentrator/evaporator and the dry particle mass was determined by again weighing the vial. The particles were then re-dispersed at the desired mass fraction in clean toluene. The AuNPs were dispersed at 1 μM (1.5 g/L for 3.8 nm AuNPs or 8.2 g/L for 7.8 nm AuNPs). We note that the AuNPs with all ligands rapidly dispersed immediately upon addition of solvent as evidenced by the immediate appearance of the strong dark red / brown colour typical for these dispersions and the disappearance of the metallic gold colour of the dried particle film from the walls of the vial. To ensure full dispersion, the vials were vortex mixed for several minutes. *Quantifoil* holey carbon support grids (*Ted Pella* no. 661-200-CU, orthogonal array of R 2/1, that is 2 μm diameter circular holes at 1 μm edge-to-edge hole spacing, in support film containing 10 nm carbon, total film thickness ca. 20 nm, on a 200 mesh copper grid) were used as received to prepare free-standing liquid films of fixed size in case of organic solvents. For aqueous samples the grids were glow-discharged for 90 s to make them more hydrophilic. A *FEI Vitrobot Mark IV* device was used for semi-automatic blotting and plunge freezing in a dehumidified room. Several tissues drenched in toluene were placed in the Vitrobot chamber to saturate the air and prevent evaporation of the sample as much as possible. The chamber was closed and kept at 22 °C and 3.0 μL of sample was applied to the shiny (carbon coated) side of the support grid. Immediately after this (with zero 'wait time'), the automated blotting procedure was started with 1.5 s blotting time at 'blot force' setting 2 after which the grid was immediately (zero 'drain time') shot into liquid nitrogen (LN₂). The grids were then transferred into a pre-cooled cryo grid box while submerged in LN₂ and stored under dry LN₂ for up to a week prior to imaging. Octanoic samples were prepared in similar manner. Decalin and hexadecane-based samples were prepared in a similar manner except without saturating the chamber due to their low vapour pressure and using a longer 2 s blotting time because of the higher viscosity. For aqueous samples the built-in humidifier was used to keep the relative humidity in the chamber at 100 % and liquid ethane was used as cryogen instead of LN₂.

Imaging:

Samples were transferred into a LN₂-cooled cryo-TEM holder under cold N₂ vapour in a LN₂ filled transfer station, a cooled metal shutter was placed over the sample to protect it from collecting water ice from freezing on atmospheric moisture during transfer, and then rapidly removed from the transfer station and placed in the airlock of a *FEI Talos 120c* TEM and pumped to vacuum. The TEM was operated at 120 kV/5 μA and the cryo-box was inserted, which further cools the sample and protects it from freeze-on of contaminants. The holder was left to thermally equilibrate for 30 min to decrease thermal drift, after which BF-TEM images could be recorded as normal at 'spot size' (beam intensity) 5 and magnification of 28 000× (corresponding to a pixel size of 0.51 nm) such that one 2 μm hole was entirely in the field-of-view. We note that toluene- and decalin-based samples were sufficiently stable under the beam that true low-dose imaging conditions were not required. Large variations in the thickness of the vitrified films were seen with most grids containing both completely empty squares and regions where the film was too thick for any electrons to get through. Images used for further analysis were recorded in regions where vitrified sample was seen predominantly in the holes with little sample on the surrounding support. In these regions the sample thickness was relatively constant and typically around 20 nm to 30 nm thick. For 7.8 nm AuNPs@OIAm, 2 such images containing in

total ca. $1 \cdot 10^4$ particles were recorded and used for analysis. For 7.8 nm AuNPs@PS2.3k-SH, 36 images containing in total ca. $3 \cdot 10^4$ particles were used. For 7.8 nm AuNPs@PS5.3k-SH, 36 images containing in total ca. $1 \cdot 10^4$ particles were used.

Data processing:

Particle localisation from the cryo-TEM images was done using the open-source *Trackpy* library (v0.4.2)^[456] (implemented in the *python* programming language, v3.7.1), which is based on feature detection using the widely used intensity-weighted centroiding procedure^[195] followed by iterative refinement of feature coordinates in order to achieve sub-pixel precision. A threshold for the integrated particle intensity over this region was used to distinguish real particles from background noise. A circular boundary of radius $0.95 \mu\text{m}$ was defined to restrict the set of particle coordinates to those within the support film hole and avoid any influence of the carbon support film on the results. Then, the distance histogram $g(r)$ was calculated under circular boundary conditions as described in [Section 4.9.1](#) and used as input for iterative test-particle insertion as described in [Section 4.9.4](#) to obtain interaction potentials. For 7.8 nm AuNPs@PS-SH, the $g(r)$ and TPI analysis were performed using bins of $\delta r = 1 \text{ nm}$ wide up to $r_{\text{max}} = 50 \text{ nm}$, with 50 iterations of iterative TPI of $2 \cdot 10^5$ test-particle insertions each. For 7.8 nm AuNPs@OIAm, $\delta r = 0.5 \text{ nm}$, $r_{\text{max}} = 40 \text{ nm}$ and 1000 iterations with $N_{\text{ins}} = 2 \cdot 10^4$ each were used.

5.8.5 Cryo-TEM of graphene liquid cells

Sample preparation:

Experimental methods for particle synthesis and ligand exchange to thiolated polystyrene ligands are given in [Sections 3.7.7](#) and [3.7.9](#). The particles were dispersed in toluene at a known concentration by dry mass as follows: a 2 mL glass vial was weighted and a small volume of washed $7.8 \pm 0.7 \text{ nm}$ (10 %) AuNPs@PS2.3k-SH dispersed in chloroform (typically 0.4 mL) was subsequently added, after which the solvent was fully evaporated from the vial under N_2 flow at 30°C in a *kdScientific Centrifan PE* rotary concentrator/evaporator and the dry particle mass was determined by again weighing the vial. The particles were then re-dispersed in clean toluene at a concentration of 4 g/L ($0.5 \mu\text{M}$). To prepare the emulsions, $50.0 \mu\text{M}$ of the particle dispersion were added to $500 \mu\text{L}$ of an aqueous 8.0 mM (2.3 g/L) SDS solution in a glass 2 mL vial and closed with a teflon-lined lid. The vial was shaken by hand for 30 s and subsequently swirled in an ultrasonic bath (*Branson* no. 2510-DTH, 39 W/L at 40 kHz) for 1 min to emulsify it. For water-based GLCs, the emulsions were prepared in an identical manner except that an aqueous dispersion of AuNPs@mPEG5k-SH was used as droplet phase, of which $100 \mu\text{L}$ were added to 1.00 mL of a solution of 10 g/L SPAN 80 in toluene. The vials were kept closed overnight. Emulsions were then used as sample in GLCs prepared using the loop-assisted transfer method: graphene sheets on 3.5 mm copper discs (*VitroTEM*) were placed in an aqueous copper etching solution to dissolve the copper support causing the graphene flakes to float on the interface, after which the solution was slowly replaced with clean water using a syringe. Then, $0.50 \mu\text{L}$ of emulsion was pipetted onto a carbon at 200 mesh copper TEM support grid placed on filter paper. Using a 3.5 mm metal loop, the graphene sheets were transferred from the water onto the grid with the sample, thereby displacing most of the sample into the filter paper but leaving small liquid pockets trapped between the carbon and graphene. Samples were then stored for up to a day prior to direct TEM imaging (at room temperature) or for cryogenic freezing, which was done by rapidly dipping the grids directly into liquid nitrogen using insulated tweezers. Cryo-TEM samples could be stored under liquid nitrogen for up to a week prior to imaging.

Imaging and analysis:

Cryogenically frozen GLCs were transferred to the TEM and imaged as described above for free-standing vitrified films. For the tomography datasets of emulsion droplets, a tilt range was used of -60° to 60° in steps of 4° for $-40^\circ \leq \alpha \leq 40^\circ$ and 2° for $|\alpha| > 40^\circ$. Alignment, tomographic reconstruction and particle detection were performed as described previously for SPs. The particles on the interface (the outermost layer) were removed from the data by artificially shrinking the spherical bounding box

and excluding any particles outside of it such that the internal volume could be analysed as bulk-like via the $g(r)$ and iterative TPI corrected for the apparent missing volume around the spherical boundaries. The $g(r)$ and TPI analysis were performed for each droplet separately using bins of $\delta r = 0.5$ nm wide up to $r_{\max} = 50$ nm, with 200 TPI iterations of 10^5 test-particle insertions each. Low-dose imaging of GLCs at room-temperature was performed using a *FEI Talos f200x* in HAADF-STEM mode to reduce the accumulated beam dose.

5.8.6 calculation of van der Waals interactions

The interaction of particles in a medium (rather than in a vacuum) depends not only on the interactions of the particles with each other, but also the interactions with the body of solvent the presence of a particle displaces. This medium dependent Hamaker constant, *i.e.* quantifying the van der Waals ‘contrast’, for particles of material 1 with a Hamaker constant A_{11} (against vacuum) interacting in a medium with Hamaker constant A_{22} may be estimated as follows:^[40, p. 275]

$$A_{121} \approx \left(\sqrt{A_{11}} - \sqrt{A_{22}} \right)^2 \quad (5.6)$$

where subscript 121 denotes the interaction of two bodies of material 1 in a medium of material 2. The non-retarded Hamaker constants for toluene and gold are $5.4 \cdot 10^{-20}$ J and $4.5 \cdot 10^{-19}$ J respectively,^[493] giving an approximate net Hamaker constant of $A_{\text{Au to l Au}} \approx 1.9 \cdot 10^{-19}$ J, or $\sim 48 k_B T$ at 20 °C. Neglecting van der Waals interactions between the (solvated) ligand shells due to the similarity of polystyrene (or oleylamine) and toluene (*e.g.* $A_{\text{PS}} = 6.3 \cdot 10^{-20}$ J^[494]), the interaction energy may be calculated using [Eq. 1.3](#) and is plotted for different particle sizes in [Figure 5.21](#). The Hamaker approach is of course only an approximate and at these particle sizes and interaction ranges Hamaker constants are typically size-dependent, which can lead to both an increase or decrease in the effective Hamaker constants depending on the spacing and materials involved.^[37,41,495] We note that we attempted to reproduce the results of Wijenayaka & Haes *et al.*^[495] for AuNPs in H₂O, which used methods developed by Pinchuk^[496] for silver nanoparticles, and perform similar Hamaker constant calculations for AuNPs in toluene. Unfortunately we were unable to reliably reproduce their results or known bulk Hamaker constants (in the limit of large particle size) due to the strong dependence of the calculated value on the choice of dielectric data, in particular the frequency range over which it is integrated. We did however consistently see a size-dependence with larger Hamaker constants for smaller particles, but found this effect to be much weaker for Au in toluene than for Au in H₂O, with in most cases only ~ 20 % larger values.

5.9 Supplementary figures

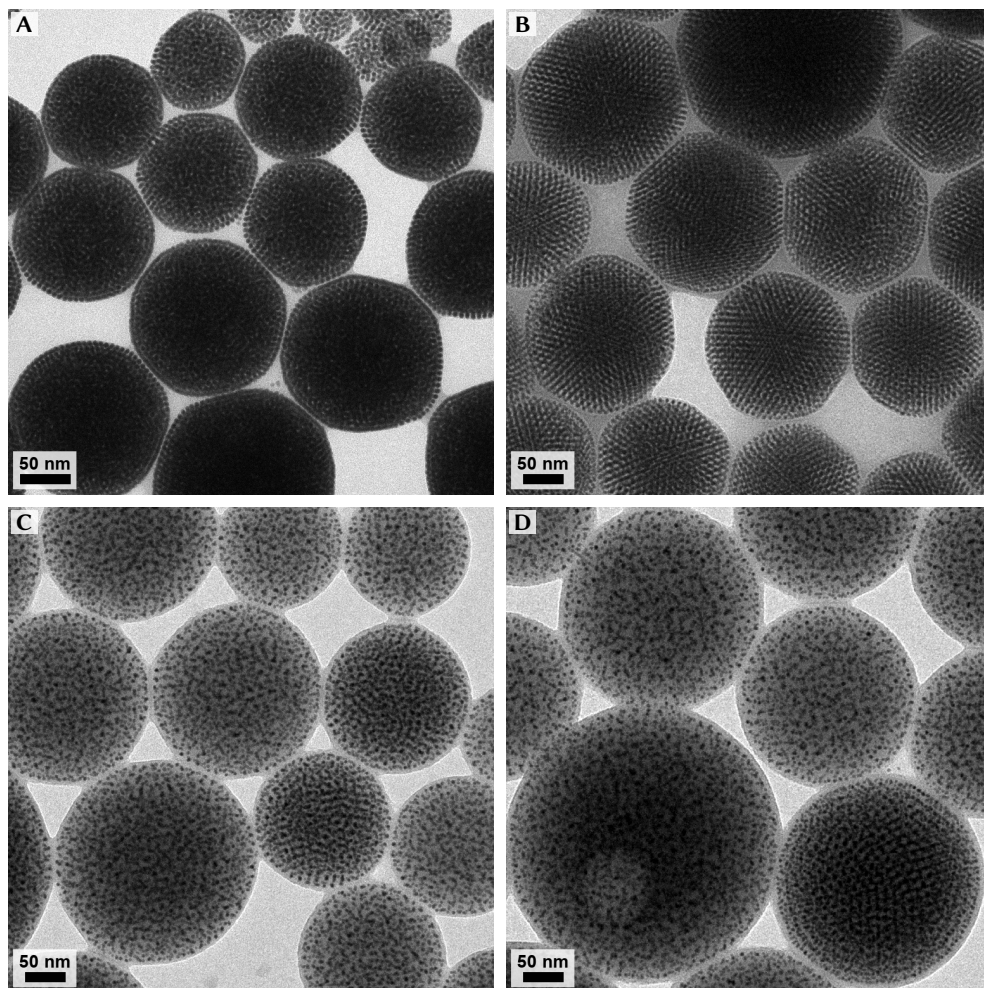


Figure 5.12: SPs prepared with additional PS-SH ligand sizes. The AuNP cores were 4.6 ± 0.5 nm (10%) in all cases. **A:** AuNPs@PS880-SH. **B:** AuNPs@PS2.3k-SH. **C:** AuNPs@PS5.3k-SH. **D:** AuNPs@PS5.8k-SH.

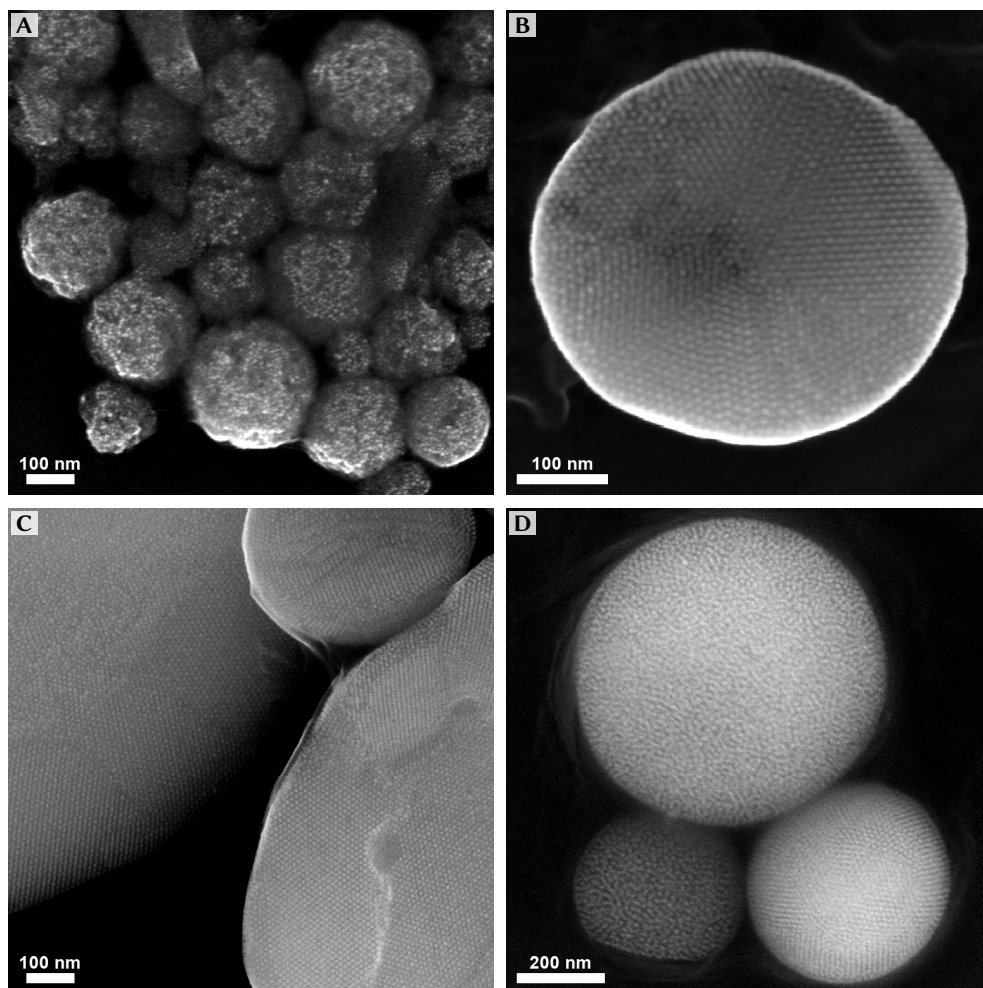


Figure 5.13: HR-SEM of AuNP supraparticles. The AuNP cores were 7.8 ± 0.7 nm (10%). All images were recorded using a beam energy of 15 kV on a immersion through-lens-detector in secondary electron detection mode. **A:** SPs of AuNPs@OIAm with a disordered buckled surface. **B,C:** interior structure of broken SPs of AuNPs@PS2.3k-SH, showing crystalline domains with 5 fold symmetry in smaller SPs or multiple larger domains in case of SPs ≥ 400 nm. **D:** SPs of AuNPs@PS5.3k-SH showing a mix of disordered/liquid-like ordered SPs and and SPs with in-plane ordered layered structures.

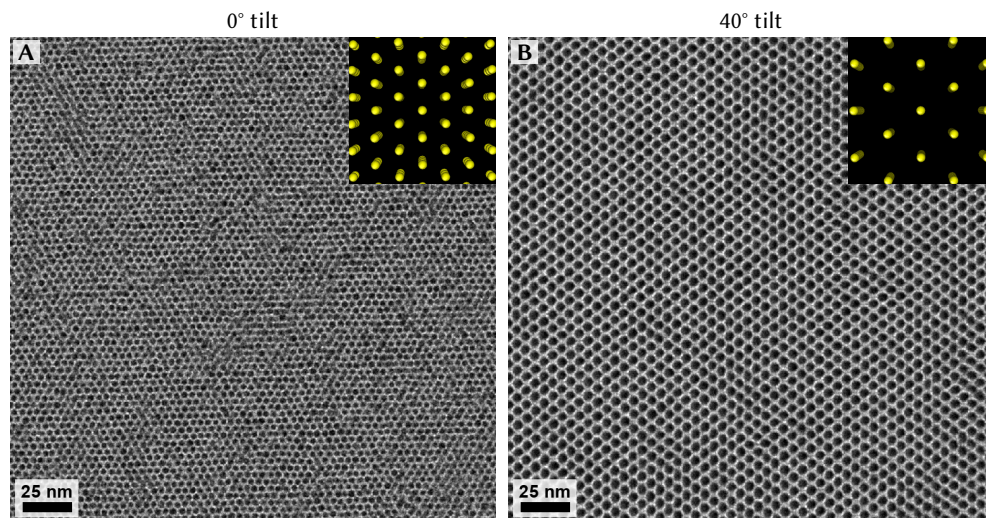


Figure 5.14: TEM micrographs of an SAL of 2.9 nm AuNPs@PS2.3k-SH. Imaged at 0° (A) and 40° (B) tilt. The imaged region contained an FCC crystal of ~ 10 particle layers thick seen along the [111] and [110] directions respectively. The insets show rendered projections along the respective FCC indices.

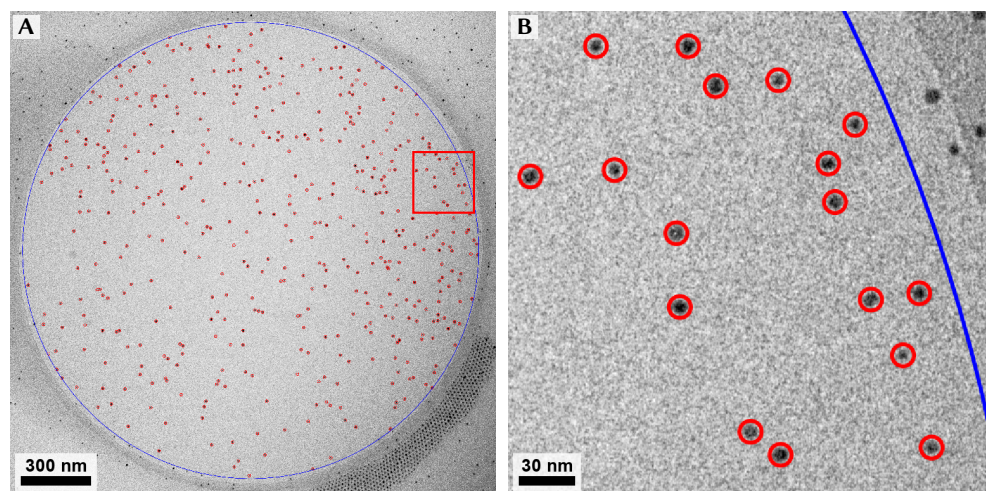


Figure 5.15: particle localisation in quasi-2D thin films. Full TEM micrograph (A) and zoom-in (B) of a vitrified toluene film containing 7.8 nm AuNPs@PS2.3-SH with particle localisation results highlighted using red circles, the large blue circle indicates the circular boundary conditions used in calculation of the $g(r)$. Any particles whose centre was outside of this region were removed from the dataset.

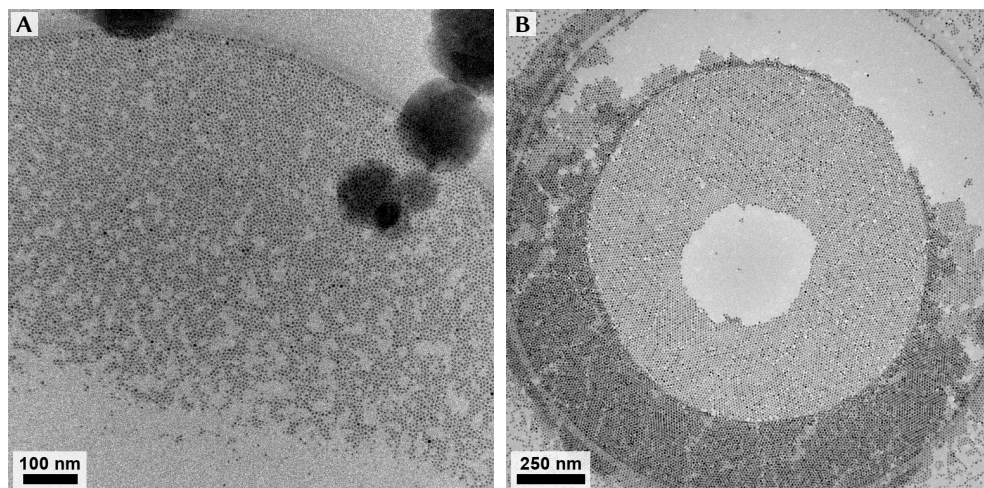


Figure 5.16: interfacial adsorption of AuNPs@OIAM. **A:** 4.2 nm AuNPs@OIAM in/on vitrified toluene thin films. **B:** 7.8 nm AuNPs@OIAM in/on vitrified toluene thin films.

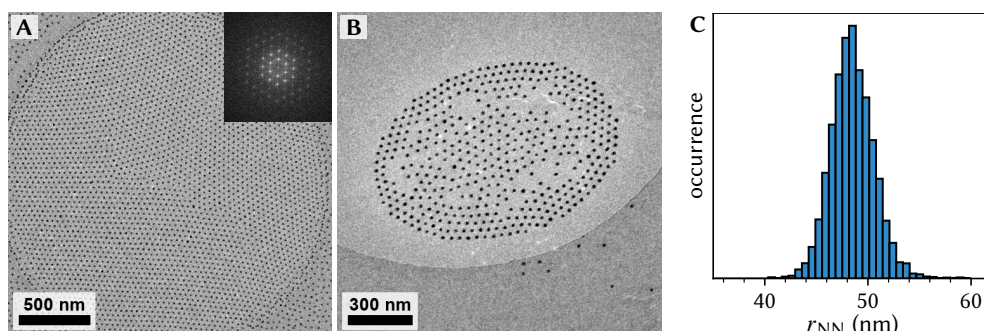


Figure 5.17: interfacial interactions of AuNPs@mPEG5k-SH on water. The AuNP cores were 15.7 ± 1.3 nm (4.8 %) and dispersed in H_2O . Cryo-TEM of these samples showed long-ranged repulsive interactions of the AuNP cores regardless of particle concentration (**A**), but a 4 \times diluted sample (**B**) revealed there were additional long-range attractive components. **C:** histogram of centre-to-centre NN distances from the sample in **B**, the mean was 48.5 ± 2.1 nm.

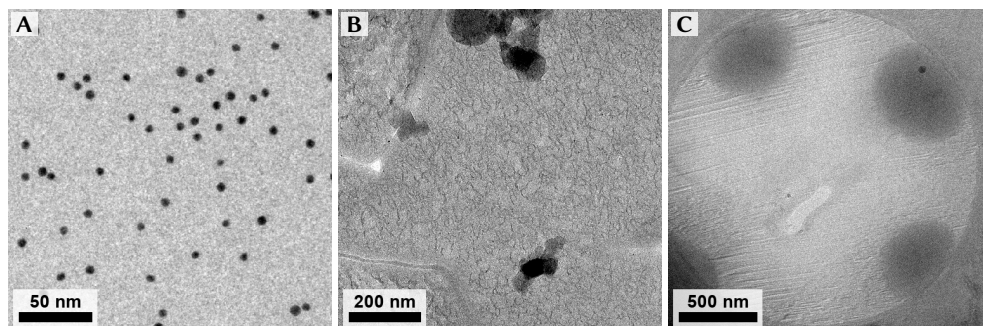


Figure 5.18: cryo-TEM of vitrified thin-films of AuNPs in different solvents. AuNPs@OIAM in various solvents. **A:** *cis*-decaline, which had similar stability as toluene. **B:** *n*-hexadecane, which formed rippled and fractured films that rapidly disintegrated under e-beam exposure. **C:** a toluene in water emulsion, where the darker regions are toluene droplets and the striping is due to diffraction contrast of water crystals.

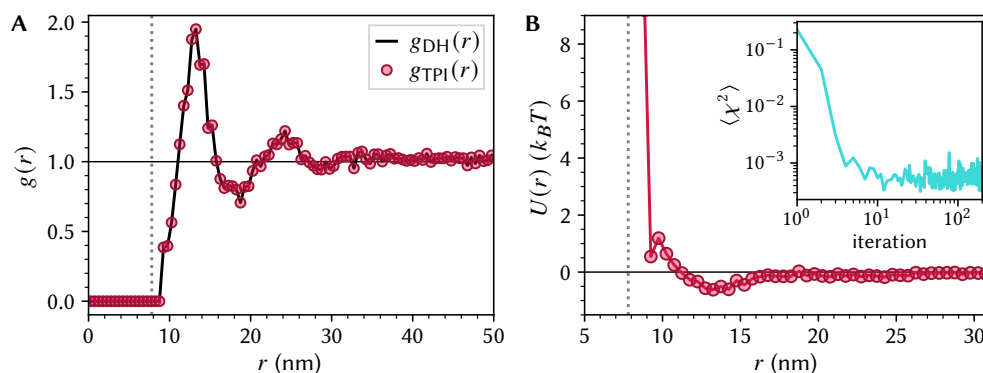


Figure 5.19: $g(r)$ and interactions through TPI of AuNPs@PS2.3k-SH in an emulsion droplet. The droplet contained 1573 AuNPs with core sizes of 7.8 ± 0.7 nm (10%) (indicated with the dotted gray lines), of which ~ 500 were located on the surface. **A,B:** the $g(r)$ with fit and resulting $U(r)$ from iterative TPI, 200 iterations of 10^5 test-particle insertions each were used with the inset showing evolution of the mean-squared error.

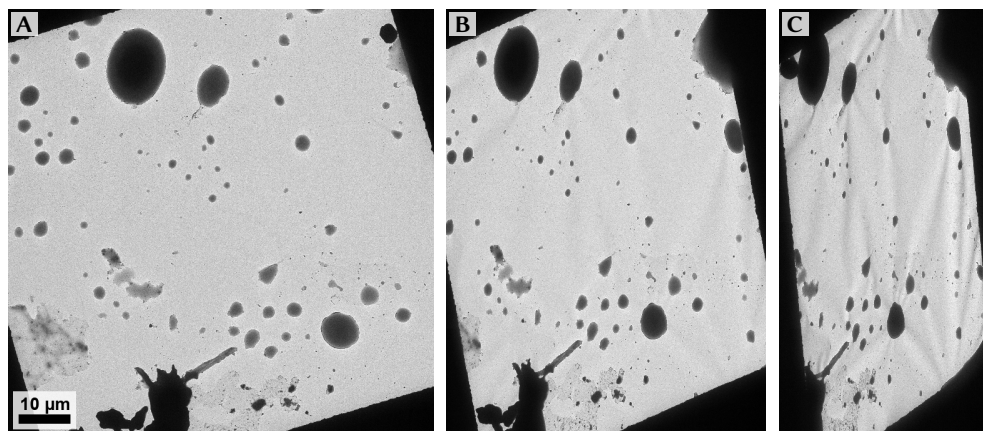


Figure 5.20: TEM micrographs of H₂O droplets in a GLC at varying tilt angle. Images A–C were recorded at tilt angles of 0°, 45° and 60° respectively, and show the flattened droplet shape of the liquid pockets.

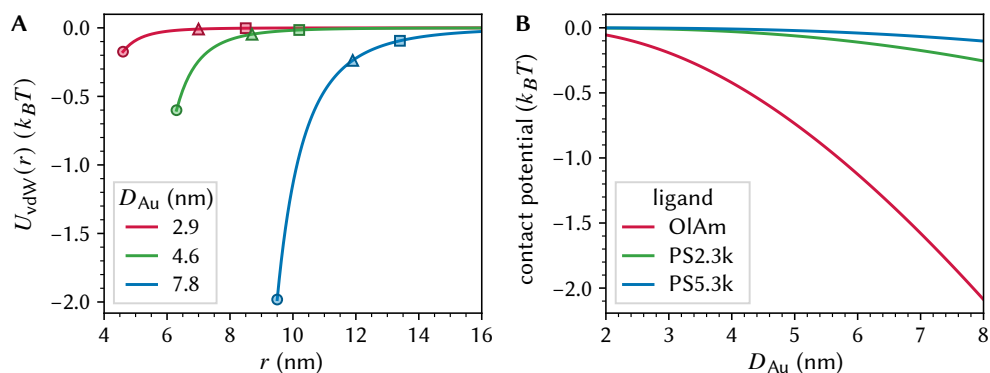


Figure 5.21: core-core van der Waals interactions of AuNPs in toluene. **A:** contribution of core-core vdW interactions to the interaction potential for various core diameters D_{Au} . Circles, triangles and squares denote approximate contact distances for OIAm, PS2.3k–SH and PS5.3k–SH ligands respectively based on dry TEM S2S spacings. **B:** contact potentials for the different ligands as function of particle size.

Part III

Interactions from Trajectories



CHAPTER 6

Measuring interaction forces from multi-particle trajectories in and out of equilibrium

ABSTRACT

The motion of colloidal particles is described by (overdamped) Brownian dynamics, where the particle velocities depend linearly on the forces acting on the particles. Therefore, the forces experienced by colloidal particles may be obtained from a set of multi-particle trajectories. If it is assumed that the forces acting on the particles are due to pairwise interactions with neighbouring particles, these pairwise interaction forces may be extracted by measurement of the total (net) forces acting on particles as a function of their local neighbourhoods. Discretisation of the pairwise interaction forces allows us to construct a system of linear equations which may be solved for the pairwise forces at all relevant inter-particle distances. Notably, this does not assume an equilibrium distribution of particles and may be used regardless of whether the system is in equilibrium or not. We first studied the robustness of this method against a variety of parameters such as the time interval between and the number of measurement points using simulated data with known interaction forces. We subsequently applied trajectory analysis to two different particle systems with tunable interactions, and demonstrated that interaction forces may be recovered from experimental data obtained using high-speed 2D and 3D fluorescence microscopy.

6.1 Introduction

The methods discussed in **Chapters 4 and 5** explicitly rely on equilibrium statistics to extract the inter-particle interactions, which means only ‘static’—that is (time)uncorrelated—sets of coordinates are required. In principle, a single snap-shot of a sufficiently large system is all that is needed to infer the interactions between the particles. While this is a valid assumption in most scenarios, there are cases where equilibrium sampling is infeasible, for example when equilibration happens over a time scale not accessible experimentally, when the sample is not stable and irreversible aggregation occurs, or when externally applied forces drive the particle distribution far out of equilibrium. Aside from this, equilibrium sampling only probes the part of the energy landscape within an energy range on the order of the thermal energy $k_B T$, while little to no statistics are obtained for features which require more energy than can be probed by thermal fluctuations, *i.e.* more than several $k_B T$, and/or for energy states which are separated by a significant energy barrier of such a height, even if the final states are close in energy. Starting from some nonequilibrium state and probing the interaction forces throughout the equilibration process would provide access to regions of the potential energy landscape inaccessible to equilibrium sampling.

Here we demonstrate it is possible to include the dynamics of the system and look at *trajectories*—the particle positions as function of time— and infer the forces on the particles *without* relying on Boltzmann statistics.^[180,182–184,497,498] As we will show in **Section 6.2**, it is possible to obtain pairwise interaction forces from the motion of colloidal particles *without* relying on equilibrium sampling based on a method proposed by Jenkins & Sinno *et al.*^[180] In short, colloidal trajectories consist of two parts: the deterministic *velocities* due to the forces experienced by the particles, and the stochastic fluctuations known as Brownian motion. The net force acting on each particle may be obtained from a velocity measurement of each particle, and subsequently a decomposition of the force into the pairwise contributions of every nearby ‘neighbour’ around the central ‘reference’ particle due to interactions. As we will see, this poses two main challenges: how can one disentangle the motion of a particle due to the interaction forces it experiences from the inherently stochastic (random) nature of Brownian motion of colloidal particles, and how can one decompose this net force experienced by a particle into the contributions of all of its neighbouring particles?

Experimentally, particle velocities may be estimated from the displacements of particles between subsequent snapshots in a microscopy series, thus providing an alternative means by which interactions may be obtained non-intrusively from microscopy data. Unlike ‘static’ measurements however this requires high imaging rates with respect to the time-scale of the motion of the particles, and this method is therefore predominantly of interest for relatively large μ Ps and those cases where equilibrium methods cannot be used. Finally, we note that a downside of not relying on equilibrium conditions is that for the analysis of the inter-particle forces the full hydrodynamic friction factors need to be known, which are a function of not only the interactions, but also the inter-particle distance and volume fraction. In principle these mobility coefficients can be included in the analysis since theoretical approximations are known and/or they can be measured experimentally, although this is not the focus of this work. In the remainder of this chapter, we neglect such hydrodynamic interactions and assume the hydrodynamic friction to be constant.

6.2 Theory

6.2.1 Forces from Brownian trajectories

First, we consider the motion of a single colloidal particle experiencing a constant force. The motion of colloidal particles in a fluid may be described as the sum of inertial, hydrodynamic, external and interaction forces, as well as a randomly fluctuating force due to collisions with solvent molecules. This force balance, known as the Langevin equation of motion, is given by:^[74]

$$\mathbf{f}_{\text{tot}}(\mathbf{r}, t) - \gamma \dot{\mathbf{r}}(t) - m \ddot{\mathbf{r}}(t) + \sqrt{2\gamma k_B T} \boldsymbol{\xi}(t) = 0 \quad (6.1)$$

where t is time, \mathbf{r} the particle position with a dot and double dot indicating the first and second derivative with respect to time respectively, $\mathbf{f}_{\text{tot}}(\mathbf{r}, t)$ is the total/net force applied to the particle (*i.e.* that counteracting those due to the solvent), γ a drag (friction) coefficient, m is the particle mass, and $\boldsymbol{\xi}(t)$ is a Gaussian distributed stochastic force with zero mean and delta-correlated time dependence, *i.e.* $\langle \boldsymbol{\xi}(t) \rangle_t = 0$ and $\langle \boldsymbol{\xi}(t) \boldsymbol{\xi}(t') \rangle_t = \delta(t - t')$. In other words, the particle experiences fluctuating 'kicks' in random directions which are uncorrelated in time and have no preferred directionality. In the simplest case the drag coefficient $\gamma = 6\pi\eta R$ for spherical particles depends only on the solvents dynamic viscosity η and the particle radius R , and is related to the diffusion coefficient as $D_0 = k_B T / \gamma$. Again, we emphasise that this is an assumption as the drag coefficient is influenced by the presence of surrounding particles even for particle displacements much less than 0.1 of the particle diameter, and also because the short-time self diffusion coefficient is influenced by interactions between the particles.^[74]

However, due to their small size colloidal particles normally exhibit *overdamped* motion with viscous forces of the solvent dominating while inertial effects may be neglected. That is to say that their Reynolds number—the ratio of inertial forces to viscous forces—is $\ll 1$ and as such $m \ddot{\mathbf{r}}(t) = 0$. In the overdamped limit, the equation of motion may then be rewritten as follows:

$$\dot{\mathbf{r}}(t) = \frac{\mathbf{f}_{\text{ext}}(\mathbf{r}, t)}{\gamma} + \sqrt{\frac{2k_B T}{\gamma}} \boldsymbol{\xi}(t). \quad (6.2)$$

for the time-dependent velocity. Measuring the velocity $\dot{\mathbf{r}}$ of a colloid at a single point in time does not directly give the force as the effects of $\boldsymbol{\xi}(t)$ are unknown, but when a time-average of many measurements of the velocity is obtained, the thermal fluctuations average out and it can be stated that

$$\mathbf{f}_{\text{ext}}(\mathbf{r}) = \gamma \langle \dot{\mathbf{r}} \rangle_t \quad (6.3)$$

with the Brownian motion acting only as noise. In other words, for a sufficient number of measurements the forces acting on a particle with overdamped dynamics may be obtained from measurements of its velocity through only an experimentally accessible coefficient γ , which in the remainder of this chapter we assume to be constant. Aside from a time-averaged velocity of a single particle, an ensemble average over many particles may be taken provided that all particles experience the same forces.

6.2.2 Linking the total force to inter-particle interaction forces

Having seen how the total or net force acting on a particle may be determined from its velocity, the next step is to follow the work of Jenkins & Sinno *et al.*^[180] and to consider a multi-particle system, for which we assume that this net force acting on each particle is only

due to the sum of all pairwise interactions with their neighbouring particles,* and that all particle pairs interact with the same distance dependent isotropic pairwise interaction force. For isotropic interactions, the force acting on a particle i along each Cartesian dimension α (i.e. α is the x , y or z dimension) due to some other particle j scales with the α -component of the displacement vector $\mathbf{r}_{ij} = \mathbf{r}_i - \mathbf{r}_j$ between the two particles. Assuming pairwise additivity to sum over many neighbouring particles j , the total force along α acting on particle i can be expressed as

$$f_i^\alpha = \sum_{\substack{j=1 \\ j \neq i}}^n \frac{r_i^\alpha - r_j^\alpha}{r_{ij}} F(r_{ij}) \quad (6.4)$$

where $F(r)$ is the pairwise interaction force, n the number of particles, $r_{ij} = \|\mathbf{r}_{ij}\|$ the centre-to-centre inter-particle distance and r_i^α and r_j^α are the α coordinates of particle i and j respectively. In principle, this may be solved for the pairwise forces, along each dimension separately or for all dimensions simultaneously, if the functional form of $F(r)$ is known. Instead, no prior knowledge of the functional form of $F(r)$ is assumed and it is approximated using a set of M constant or linear basis functions (BFs) as follows:

$$F(r_{ij}) \approx \sum_{m=0}^{M-1} g_m \phi_m(r_{ij}) \quad (6.5)$$

where ϕ_m are the basis functions and coefficients g_m give their respective magnitudes. In the simplest form, basis functions ϕ_m are ‘square wave’ (constant) basis functions, with constant value over each interval between subsequent discretisation points, given by

$$\phi_m^{\text{sq}} = \begin{cases} 1 & \text{if } r_{ij} \in m \\ 0 & \text{if } r_{ij} \notin m \end{cases} \quad (6.6)$$

Effectively, the force is discretized into M bins of width $\Delta r = r_{\text{max}}/M$ over each of which the force is constant, up to a cut-off value of r_{max} above which the pairwise force is assumed to be 0. A particle pair contributes to the m^{th} bin if $\lfloor r_{ij}/\Delta r \rfloor = m$ (with $\lfloor \dots \rfloor$ denoting the *floor* function, i.e. the value rounded down to the previous integer). In addition to square wave basis functions, linear basis functions may be used where each particle pair contributes to two partially overlapping bins with some linearly varying weight depending on the position between the bins’ centres. The linear basis functions are implemented as:

$$\phi_m^{\text{lin}} = \begin{cases} 1 + r_{ij}/\Delta r - m & \text{if } \lceil r_{ij}/\Delta r \rceil = m \\ 1 - r_{ij}/\Delta r + m & \text{if } \lfloor r_{ij}/\Delta r \rfloor = m \\ 0 & \text{otherwise} \end{cases} \quad (6.7)$$

where $\lceil \dots \rceil$ denotes the *ceiling* function (i.e. rounded up to the next integer). Note that each particle pair still has a unity ‘weight’ but spread over the two nearest bins to the left and right. The square wave and linear BFs are depicted schematically in **Figure 6.1**.

* although additional external forces due to e.g. external fields may be easily incorporated in the analysis as well, and in fact velocities due to any external spatially constant force such as gravity cancel out in the measurement of inter-particle interaction forces from multi-particle systems

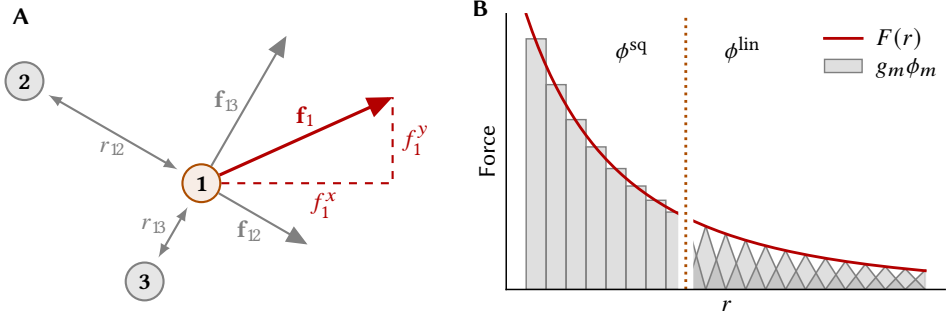


Figure 6.1: the trajectory analysis method. **A:** schematic of a three-particle system showing the relevant inter-particle distances r_{ij} and forces f_{ij} which result in a net force \mathbf{f}_i acting on particle 1. **B:** schematic depiction of the discretisation of a force profile using square wave (ϕ^{sq}) or linear (ϕ^{lin}) basis functions, with the height indicating the weight of the m^{th} bin multiplied with g_m .

Combining Eqs. 6.4 and 6.5 we obtain

$$f_i^\alpha \approx \sum_{\substack{j=1 \\ j \neq i}}^n \left[\frac{r_i^\alpha - r_j^\alpha}{r_{ij}} \sum_{m=0}^{M-1} g_m \phi_m(r_{ij}) \right] = \sum_{m=0}^{M-1} g_m C_{i,m}^\alpha \quad (6.8)$$

where the BFs and unit vectors are combined into coefficients $C_{i,m}^\alpha$, which are given by:

$$C_{i,m}^\alpha \equiv \sum_{\substack{j=1 \\ j \neq i}}^n \left[\frac{r_i^\alpha - r_j^\alpha}{r_{ij}} \phi_m \right] \quad (6.9)$$

and which, when evaluating the forces acting on many particles simultaneously, may be restated as a system of N linear equations. Here N is the number of force measurements, defined as the number of particles multiplied with the number of time intervals over which the forces are evaluated. In matrix form, this set of equations is given by

$$\begin{pmatrix} f_1^\alpha \\ f_2^\alpha \\ \vdots \\ f_N^\alpha \end{pmatrix} \approx \begin{pmatrix} C_{1,1}^\alpha & C_{1,2}^\alpha & \cdots & C_{1,M}^\alpha \\ C_{2,1}^\alpha & C_{2,2}^\alpha & \cdots & C_{2,M}^\alpha \\ \vdots & \vdots & \ddots & \vdots \\ C_{N,1}^\alpha & C_{N,2}^\alpha & \cdots & C_{N,M}^\alpha \end{pmatrix} \cdot \begin{pmatrix} g_1 \\ g_2 \\ \vdots \\ g_M \end{pmatrix} \quad (6.10)$$

or simply

$$\mathbf{f}^\alpha \approx \mathbf{C}^\alpha \cdot \mathbf{g} \quad (6.11)$$

where $\mathbf{f}^\alpha \in \mathbb{R}^N$ is a vector of the net forces along α acting on each particle in each measurement, which may be obtained from the velocity, $\mathbf{C}^\alpha \in \mathbb{R}^{N \times M}$ is the matrix of coefficients which can be determined from the particle positions, and $\mathbf{g} \in \mathbb{R}^M$ is the unknown vector of force values in the discretized pairwise force. This can be solved per dimension, or for all dimensions simultaneously as

$$\mathbf{f} \approx \mathbf{C} \cdot \mathbf{g} \quad (6.12)$$

with (in three dimensions) $\mathbf{f} \in \mathbb{R}^{3N}$ and $\mathbf{C} \in \mathbb{R}^{3N \times M}$. Provided there are more measurements than unknowns ($3N > M$), Eq. 6.12 is over-constrained and there exists a solution for the unknown pairwise force values in \mathbf{g} that minimises the difference between the measured and predicted force vectors. A linear ordinary least-squares approximation may be used to find this best solution $\bar{\mathbf{g}}$ by minimizing the squared error

$$\bar{\mathbf{g}} = \arg \min_{\mathbf{g}} \Theta(\mathbf{g}) \quad (6.13)$$

where the error function $\Theta(\mathbf{g})$ is defined as

$$\Theta(\mathbf{g}) = \|\mathbf{f} - \mathbf{C} \cdot \mathbf{g}\|^2 = (\mathbf{f} - \mathbf{C} \cdot \mathbf{g})^\top (\mathbf{f} - \mathbf{C} \cdot \mathbf{g}). \quad (6.14)$$

The minimum can be found by setting the derivative of $\Theta(\mathbf{g})$ with respect to \mathbf{g} equal to zero:

$$\frac{\partial \Theta(\mathbf{g})}{\partial \mathbf{g}} = 0 \quad (6.15)$$

which results in the following ordinary linear least squares solution:^[499]

$$\bar{\mathbf{g}} = (\mathbf{C}^\top \mathbf{C})^{-1} \mathbf{C}^\top \mathbf{f}. \quad (6.16)$$

6.2.3 Measuring velocities from discrete positional data

So far, we have assumed that the positions and velocities of the particles at some infinitesimally small time instance are known. In reality, particle trajectories as obtained from e.g. Brownian dynamics simulations or experimental data which consist of discrete time steps, and particle velocities may only be estimated from the particles' displacements over some finite time interval $t \rightarrow t + \Delta t$. The approximate velocity at time t may be estimated from two discrete sets of time steps with corresponding particle positions using a first order forward finite difference scheme (FD):^[500]

$$\dot{\mathbf{r}}_{\text{FD}}(t) = \frac{\mathbf{r}(t) - \mathbf{r}(t + \Delta t)}{\Delta t} + \mathcal{O}(\Delta t) \quad (6.17)$$

where it is assumed that the time interval is small enough that the force and thus velocity over this interval are constant. In the context of trajectory analysis for pairwise interaction forces as discussed previously, this also means there is an implicit assumption that the relative positions of neighbouring particles remain approximately constant, or that the positions at time t accurately represent the force exerted on the particle throughout the entire interval $t \rightarrow t + \Delta t$.

At first glance, it seems that the the velocity may be estimated just as well using the first order backward finite difference (BD) or central finite difference (CD) given by $\dot{\mathbf{r}}_{\text{BD}}(t) = [\mathbf{r}(t - \Delta t) - \mathbf{r}(t)]/\Delta t + \mathcal{O}(\Delta t)$ and $\dot{\mathbf{r}}_{\text{CD}}(t) = [\mathbf{r}(t - \Delta t) - \mathbf{r}(t + \Delta t)]/2\Delta t + \mathcal{O}(\Delta t^2)$,^[500] as they are very similar and based on the same assumptions as the forward difference. In fact, of the three, the central finite difference method generally provides the best estimate for the derivative of a function (up to second order $\mathcal{O}(\Delta t^2)$) as it is the sum of the forward and backward differences. However, there is a subtle but important difference due to the stochastic nature of Brownian trajectories that allows us only to use the forward difference. Considering a *forward* difference, the expected position of a particle at time $t + \Delta t$ depends

only on its position at time t , the displacement due to the force acting on the particle and the probability density distribution due to Brownian motion. However, when considering the *backward* difference we are not only considering the probability to make a certain step *towards* the current position, we must additionally account for the probability the particle was in that starting position to begin with, given by the probability distribution of particles. In other words: taking the FD is like asking “*given that a particle is here, where on average will it be next?*” while a BD is akin to asking “*if a particle is now here, where did it come from?*”

When the particles are homogeneously distributed at the start of each measurement interval the forward and backward differences give approximately the same results (provided Δt is small compared to changes in the force profile), but this is unlikely to be the case in the presence of forces acting on the particles. In reality, the influence of a potential energy landscape on the particle distribution opposes that of the effects we wish to measure for the backward difference. Consider a backward difference velocity measurement of a single particle in thermodynamic equilibrium experiencing an external force. Based on the force alone, one would expect the particle to come from the direction opposing the force —from higher energy—, such that it moved in the direction of the force. While the alternative seems unlikely, the particle would have had to get to this higher energy first which in itself is even less likely. By definition, particles in equilibrium move up in energy as much as they move down, but the fact that they spend more time at lower energy makes it more likely that they arrive to a certain energy from a lower energy (going ‘up-hill’ in the process) than that they come from even higher energy. Remarkably, it can be shown that under equilibrium conditions the forces obtained from trajectories analysed with the forward and backward difference methods differ by a factor of exactly -1 , regardless of the form of the force profile! A derivation of this result is given in [Section 6.9.1](#). For this reason, only the FD is used here for TA.

6.2.4 Forces from inertial trajectories

While the focus of this chapter is on force measurements of Brownian (overdamped) trajectories as observed for colloidal particles, it is of note to mention that interaction forces may also be obtained from fully inertial trajectories, such as in molecular dynamics. Under the assumption that trajectories are noise free ($\xi = 0$) and frictionless ($\gamma = 0$), [Eq. 6.1](#) becomes

$$\mathbf{f}(\mathbf{r}, t) = m\ddot{\mathbf{r}} \quad (6.18)$$

and forces may be estimated from the acceleration from *three* sequential snapshots using a second-order central finite difference approximation:

$$\ddot{\mathbf{r}}(t) \approx \frac{\mathbf{r}(t - \Delta t) - 2\mathbf{r}(t) + \mathbf{r}(t + \Delta t)}{\Delta t^2} + \mathcal{O}(\Delta t^2) \quad (6.19)$$

as an estimation for the acceleration at time t . The same principles as in [Section 6.2.2](#) apply and pairwise interaction forces may be applied, although in this case the data are free from Brownian ‘noise’ and averaging is only necessary to provide a reasonable estimate over the width of each bin in the discretized pairwise force. This is discussed in more detail in the original work of Jenkins & Sinno *et al.*,^[180] where it is shown that trajectory analysis is considerably more data efficient when applied to fully inertial data, *i.e.* at high Reynolds number.

6.3 Method verification

6.3.1 Test data generation

To verify the accuracy of trajectory analysis (TA), and to study the influence of properties such as measurement speed, amount of data and particle tracking noise, trajectory data were generated using Brownian dynamics (BD) simulations using a known input force. The simulated trajectory data were then analysed using TA as if the interaction force was unknown to verify its feasibility to be used on experimental data. Detailed computational methods are given in [Section 6.8.1](#) but in short, Brownian (overdamped) dynamics simulations work by calculating the force acting on particle as the sum of all pairwise interactions with other particles in the simulation ([Eq. 6.4](#)) according to the chosen pairwise force function. This is repeated for all particles in the simulation, and used it together with a normally distributed random number generator (representing ξ) to update the particles' positions for the next timestep as follows:

$$\mathbf{r}_i(t + \Delta t) = \mathbf{r}_i(t) + \frac{D_0 \Delta t}{k_B T} \mathbf{f}_i(t) + \sqrt{2D_0 \Delta t} \xi_i(t). \quad (6.20)$$

This process is repeated for many time-steps, and the coordinates $\mathbf{r}(t)$ are periodically stored for use in TA.

The force function chosen for the BD simulations was the repulsive Yukawa potential, as it is a good model for screened coulomb interactions. The Yukawa interaction is characterized by the following potential and force functions:

$$U_{\text{yuk}}(r) = \frac{\sigma \Gamma_{\text{yuk}}}{r} e^{-\kappa(r-\sigma)} \quad (6.21) \quad F_{\text{yuk}}(r) = \frac{\sigma \Gamma_{\text{yuk}}}{r} e^{-\kappa(r-\sigma)} \left(\kappa + \frac{1}{r} \right) \quad (6.22)$$

where κ is the inverse Debye screening length and Γ_{yuk} the contact value of the potential. By varying the ratio of the particle size to the screening length, $\kappa\sigma$, both harder and softer interactions may be probed. We note that this potential does not include a hard core (like most experimental systems would) in that there is no excluded volume, because infinitely steep energy barriers are not compatible with BD simulations. However by setting the contact energy sufficiently high ($\Gamma_{\text{yuk}} \geq 10k_B T$) it is unlikely for pairwise distances $\leq \sigma$ to be significantly sampled.

Keen readers might have noticed that BD simulations and TA rely on the same equations and underlying assumptions to discretize time, *i.e.* the force is assumed to be constant over the interval. Consequently, analysis with TA at the same time-step size as the simulation would give TA an 'unfair advantage' in that discretisation of time would be a perfect assumption for the simulated datasets, but not for the continuous nature of real colloidal trajectories. Therefore, it is important that the simulation time step Δt_{sim} is small enough such that the simulated trajectories appear approximately continuous at the time scale for trajectory analysis (Δt_{ta}) when using simulated data to resemble real-world trajectories. The ratio between the simulation and analysis time step was systematically varied to study up to what point the discretized nature of simulated data could affect the analysis result (not shown). It was found that the resulting force profile indeed depended on Δt_{sim} for small ratios ($\Delta t_{\text{ta}}/\Delta t_{\text{sim}} < 10$), but no significant dependency on simulation time step occurred for $\Delta t_{\text{ta}}/\Delta t_{\text{sim}} \geq 50$. These findings held regardless of Δt_{ta} . Therefore, in all further analysis was done on data simulated with Δt_{sim} at least $50\times$ smaller than the desired analysis time step.

6.3.2 Force extraction and interpretation

Simulated trajectories were analysed using trajectory analysis. To verify accuracy of the resulting force profiles, the root-mean-square deviation from the real force—the input force used in the simulations—was calculated for all M bins matching some selection criterion. It was necessary to take a subset of bins for error calculation since not all bins are (sufficiently) sampled and the range of the force which is sampled may vary between datasets, making direct comparison of RMS errors problematic. This selection criterium was normally to take all bins above some threshold distance r_{\min} , above which the bins in *all* datasets to be compared consisted of at least 10^4 particle pairs. In cases where this approach was not practical (such as when varying the length scale of the force in [Figure 6.2](#)) the error was calculated over all sampled bins. The RMS error was calculated in one of three ways:

1. the RMS deviation of the discretized force from the real force in the *centre* of each bin, r_m , calculated as $\|g_m - F(r_m)\|/\sqrt{M^*}$, with $\|\dots\|$ denoting the Euclidean norm and M^* the number of bins matching the selection criterium
2. the RMS deviation of the discretized force from the real force at the mean pairwise distance of all particle pairs contributing to each bin, $\langle r_{ij} \rangle_m$, calculated as $\|g_m \phi_m(\langle r_{ij} \rangle_m) - F(\langle r_{ij} \rangle_m)\|/\sqrt{M^*}$
3. the integrated RMS deviation of the discretized force from the real force, calculated as $\sqrt{\int_{r_{\min}}^{r_{\max}} (g_m \phi_m(r) - F(r))^2 dr / (r_{\max} - r_{\min})}$ using numerical integration with the midpoint/rectangle method and an integration step size of $dr = 10^{-3}\sigma$.

In most cases, the third method gave the most accurate representation of how well the discretized force approximated the real force since it probes all r 's, not just those which were arbitrarily chosen as bin positions. However, if for example one would want to fit a functional model to the coefficients, only the errors at the positions those coefficients are defined at are relevant. Unless mentioned otherwise, the third method was used for the calculation of RMS errors.

To verify the versatility of the method, trajectories were simulated with varying pairwise interaction forces and analysed using TA at a typical measurement time-step of $\Delta t_{\text{ta}}/\tau = 10^{-3}$ where $\tau = \sigma^2/D_0$ is the free self-diffusion time of the particles. The resulting force values g_m are plotted together with the pairwise force used in the BD simulations in [Figure 6.2](#). It can be seen that the force may be accurately recovered from Brownian trajectories for both longer- and shorter ranged forces. For finite bin width, there is a potential energy gradient over the width of the bin for any non-zero force and thus the bin is not homogeneously sampled. When this is the case, the force coefficient g_m is no longer a good approximation for the force in the centre of the bin, r_m . It was found that root-mean-square deviation of each g_m from the input force (the RMS error, inset [Fig. 6.2A](#)) was significantly reduced when the force coefficients were instead taken as approximation for the force at the mean pairwise distance of all particle pairs contributing to that bin, denoted $\langle r_{ij} \rangle_m$. As shown, the pairwise interaction *potential* may also be recovered from the pairwise force by numeric integration provided $F(r) = 0$ for $r > r_{\max}$.

Next, the methods resilience against varying particle density was tested. The volume of the (cubic) simulation box was kept constant at $(20\sigma)^3$ while the number of particles within the box was varied together with the number of time-steps such that the total number of

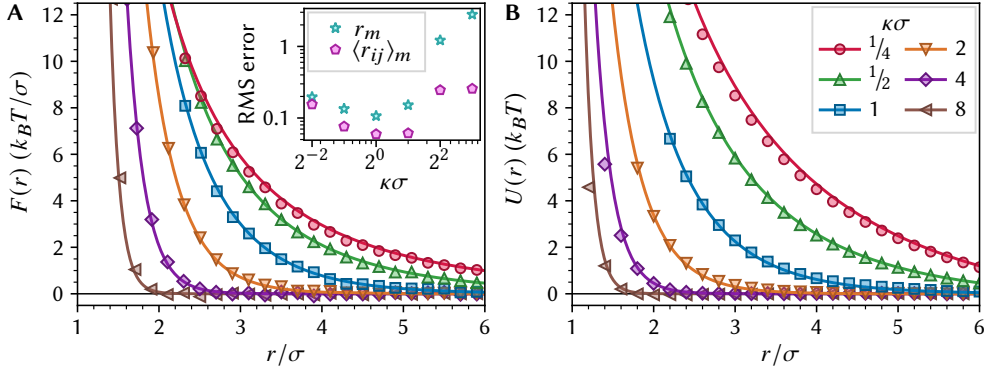


Figure 6.2: force extraction from simulated trajectories. Trajectory data were generated with BD simulations using a Yukawa force with $\Gamma_{\text{yuk}}/k_B T = 50$ and varying softness, at a density of $\varrho\sigma^3 = 0.025$ for $\kappa\sigma \leq 1$ and $\varrho\sigma^3 = 0.05$ for $\kappa\sigma > 1$. For each force profile 10^6 force measurements were evaluated at $\Delta t_{\text{ta}}/\tau = 10^{-3}$ and $r_{\text{max}}/\sigma = 8$ using 40 square wave BFs. **A:** force coefficients g_m are plotted at $\langle r_{ij} \rangle_m$ with the solid lines indicating the input force used in the simulation. Only data points to which at least 10^4 particle pairs contributed are shown. The inset shows the RMS deviation of $g_m \phi_m$ from the input force evaluated in the bin centres (r_m) and bin means ($\langle r_{ij} \rangle_m$). **B:** pairwise interaction potentials obtained by numerical integration of the force profiles in A (data points) are shown together with the pairwise potential corresponding to the pairwise force used in the simulations (solid lines).

force measurement in the analysis was kept constant. Force profiles and RMS deviations from the input force are shown in **Figures 6.3A** and **6.3B**. As the number of particle pairs within a certain r is approximately proportional to the square of the density, the available useful information per force measurement increases with increasing density while Brownian noise remains the same and as a result the RMS error decreases with increasing density. Furthermore, in the case of repulsive interactions higher energy configurations become more likely to be sampled due to the increasing pressures at higher density. On the other hand, at high density significant structuring of the colloids occurs, which may reduce the range of configurations which are sampled. In the extreme case of a (soft) colloidal crystal, the strong structural correlations make it hard for the algorithm to assign the correct pairwise components of the total force to shells of neighbours, even if the interactions are truly pairwise. As a result, deviations from the input force can occur at higher densities where significant structuring of the colloids is likely. We note that hydrodynamic interactions as function of volume fraction and distance between the particles are absent in these simulations.

The effect of the number of force measurements was studied by varying the length of the simulated trajectories used for trajectory analysis and calculating the integrated RMS deviations from the input force. In TA, Brownian motion acts as normally distributed noise on the force measurement and thus we expect the accuracy of the mean force in each bin to scale with the square root of the number of measurements contributing to each bin. As can be seen in **Figures 6.3C** and **6.3D**, the force profiles are decreasingly noisy as the number of force measurements increases and the RMS error indeed scales $\propto 1/\sqrt{N}$ for both square wave and linear BFs. However, not every force measurement is equal: while the displacement due to interaction forces scales linearly with Δt_{ta} , the displacement due to Brownian motion

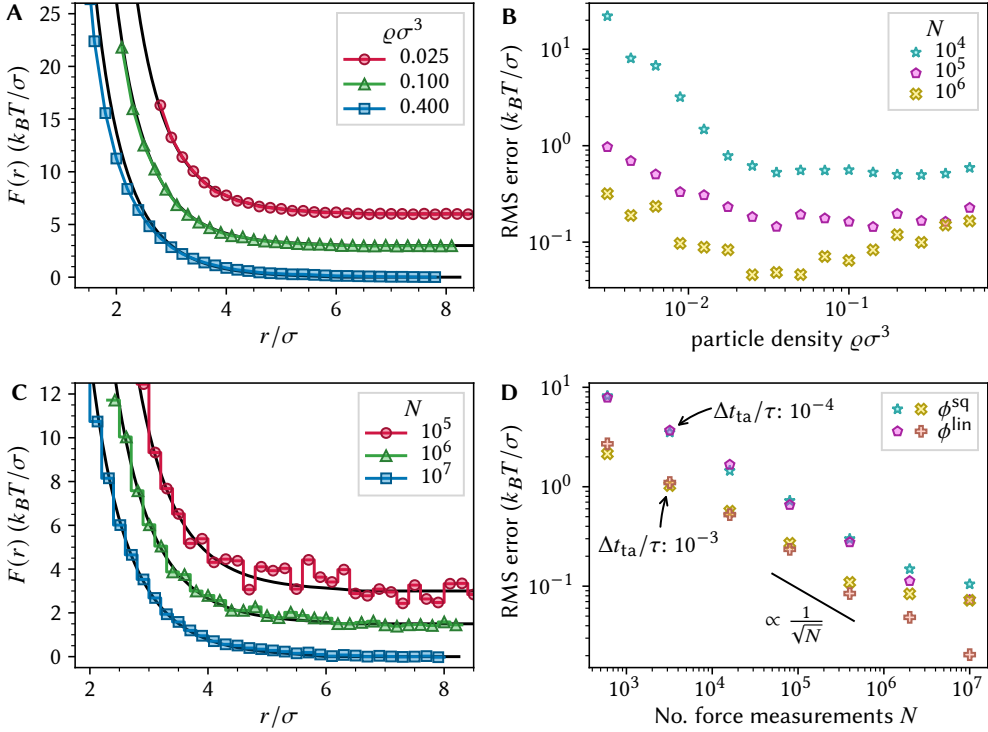


Figure 6.3: effects of particle concentration and sampling on TA. Trajectory data were generated with BD simulations using a Yukawa force ($\Gamma_{\text{yuk}}/k_B T = 50$, $\kappa\sigma = 1$) and analysed with TA ($r_{\text{max}} = 8\sigma$, $M = 40$, $\Delta t_{\text{ta}}/\tau = 10^{-4}$). **A,B:** selected force profiles and RMS errors as function of particle number density (shown for linear BFs). **C,D:** influence of the number of force measurements N at $\rho\sigma^3 = 0.025$. RMS errors in **D** were obtained with $M = 80$, the black line indicates the expected slope and is added as a guide to the eye. Force profiles in **A** and **C** were horizontally and vertically shifted for clarity, with the simulation forces in black and the data points indicating the average force and pairwise distance within each bin.

is proportional to $\sqrt{\Delta t_{\text{ta}}}$. The standard error in the force coefficients due to Brownian noise is given by:

$$\chi_F = k_B T \sqrt{\frac{2d}{N_m D_0 \Delta t_{\text{ta}}}} \quad (6.23)$$

where d is the (spatial) dimensionality of the systems motion and N_m the number of force measurements contributing to the m^{th} coefficient/bin. Consequently, the *total force measurement time*—the number of force measurements multiplied with the analysis time step size—is a better metric. In other words: one force measurement at $\Delta t_{\text{ta}}/\tau = 10^{-3}$ gives the same ‘force-to-noise’ ratio as ten force measurements at $\Delta t_{\text{ta}}/\tau = 10^{-4}$, although changing the measurement frequency can matter in other ways as we will see later. We also note that these results represent the worst case of all force measurements corresponding to a single run of subsequent time-steps, thus sampling a relatively limited range of configurations. This is especially pronounced for small time-steps and number of force measurements, as the

particles' relative positions barely change over the course of the dataset. In practice, using multiple shorter trajectories with uncorrelated starting positions can provide a wider sampling of possible configurations. Ultimately, there are diminishing returns when increasing N as deviations due to such other effects become the dominant cause for error. This can be seen in **Figure 6.3D** for square wave BFs, where errors due to the discretized nature of the method become dominant over the errors due to Brownian noise.

Let us therefore turn our attention to the choice of the type and number of basis functions. Even with perfect values for the coefficients there will be discretisation errors: a finite number of BFs cannot perfectly represent any continuously varying force. Naturally, the discretized force becomes a more and more accurate representation as the number of BFs M is increased. At the same time, increasing M will *decrease* the amount of data available for each bin, thereby decreasing the signal to noise ratio (SNR). **Figure 6.4A** depicts both of these limits for square wave BFs: with a large number of bins there is considerable fluctuations around the true force from bin to bin; with a small number of BFs the force profile accurately predicts the force at the bins' average pairwise distance (data points), but the full discretized force profile (solid line) deviates significantly near the edges of the bins. **Figure 6.4B** shows the RMS error calculated in the bins' average positions ($\langle\phi\rangle_m$) as well as the integrated error of the force profile as a whole ($\langle\phi\rangle_r$, see **p. 173** for error calculation). While square wave BFs provide a slightly better result than linear BFs near the centres of the bins, particularly at low SNR, they suffer from severe discretisation errors at small M . Linear BFs on the other hand actually provide the best approximation in-between the bin centres, reflected by the fact that $\langle\phi^{\text{lin}}\rangle_r < \langle\phi^{\text{lin}}\rangle_m$, and suffer much less from discretisation errors.

Next, the effect of the (analysis) time step size was studied: trajectory data from BD simulations were analysed with varying trajectory-analysis time step Δt_{ta} . Based on the assumptions made in TA, one would expect that 'faster is better': the longer the time interval over which the force is measured, the more the particles' positions will have changed during the interval and the less accurate it is to describe a particles local neighbourhood with only the positions at the start. If the force is assumed to remain constant over the measurement interval, then so must the relative positions of the particles and any significant relative movements lead to an effective 'blurring' of the force along r . Force profiles from TA at different time-steps and their relative error are shown in **Figures 6.4C** and **6.4D** and indeed significant artefacts can be seen at Δt_{ta} 's approaching the self-diffusion time τ of the particles. This effect is particularly pronounced where the force is steep, as a small change in r has a strong effect on the measured force. As we have already seen however, decreasing the analysis time step size also increases the relative magnitude of Brownian noise and thus more and more force measurements are needed as Δt_{ta} decreases. The effects of noise on the one hand and the inaccuracies introduced at large analysis time on the other compete, leading to an ideal measurement speed at which the error is minimized for some given system. The position of this minimum is non-trivial to predict *a priori* as it depends on the number of particle pairs measured—which in itself depends on the number of force measurements and the particle density—as well as the shape/steepness of the pairwise force and up to which inter-particle distance one wishes to measure.

6.3.3 effect of measurement noise

The analysis so far has focused on inherent limitations to TA, using what were effectively perfect trajectory data. In the experimental context, trajectory data may be obtained from

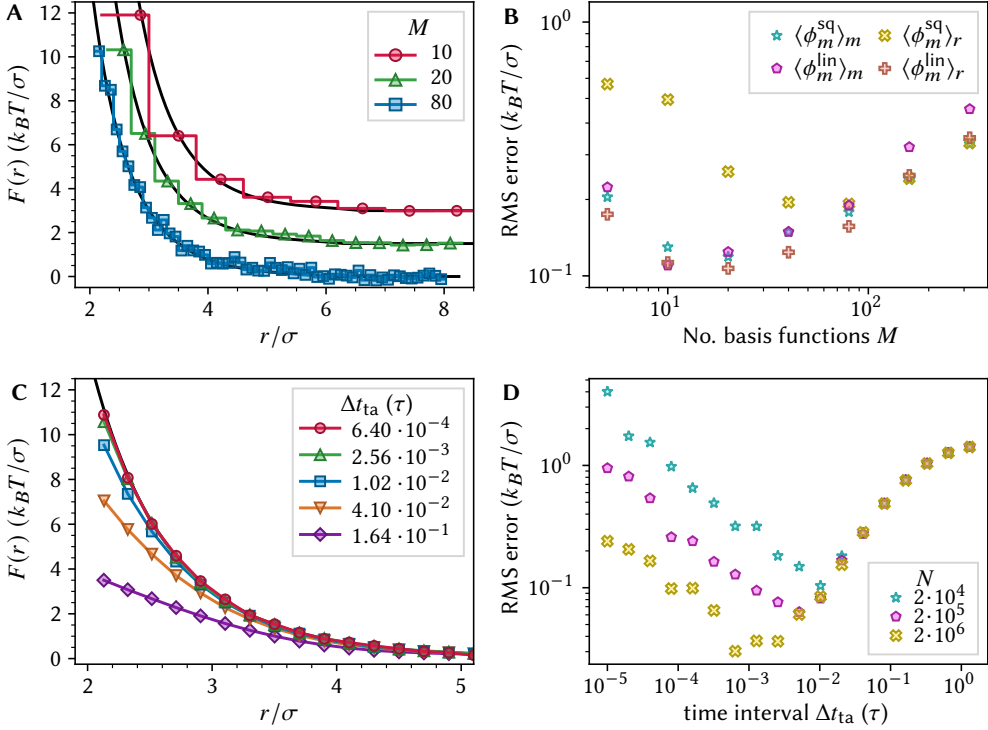


Figure 6.4: effects of basis functions and measurement interval on TA. Trajectory data were generated with BD simulations using a Yukawa force ($\Gamma_{\text{yuk}}/k_B T = 50$, $\kappa\sigma = 1$, $\varrho\sigma^3 = 0.025$, $n = 200$) and analysed with TA ($r_{\text{max}}/\sigma = 8$, $M = 40$, $\Delta t_{\text{ta}}/\tau = 10^{-4}$). **A,B:** force profiles (ϕ^{sq} and $N = 10^6$) and associated RMS errors (integrated and in BF centres) obtained with varying number of basis functions M . Force profiles in A were horizontally and vertically shifted for clarity, with the data points indicating the average force and pairwise distance within each bin. **C,D:** effects of the measurement time interval (using ϕ^{lin})

e.g. video microscopy with finite precision and some degree of noise/uncertainty on the coordinate data is unavoidable. In principle, like Brownian motion, additional ‘measurement noise’ on the coordinate data can make the obtained force profiles ‘noisier’, meaning that a larger number of force measurements is necessary to achieve a certain precision than for perfect Brownian trajectories. But this measurement noise differs from the Brownian noise in that it consists of perturbations of the positional data, not perturbations of the displacement vectors; measurement noise ‘resets’ every time step and the apparent change in position does not propagate to the next measurement point. While the noise itself may average to zero, its effect on the displacement vector used in the force measurement does not: with increasing noise on the start and end positions, the average distance between the two increases. Therefore, the effects of measurement noise were studied by displacing coordinates in simulated trajectories with normally distributed random vectors with zero mean and varying standard deviation χ_r .

Force profiles and associated RMS errors for TA on noisy data are shown in **Figure 6.5**.

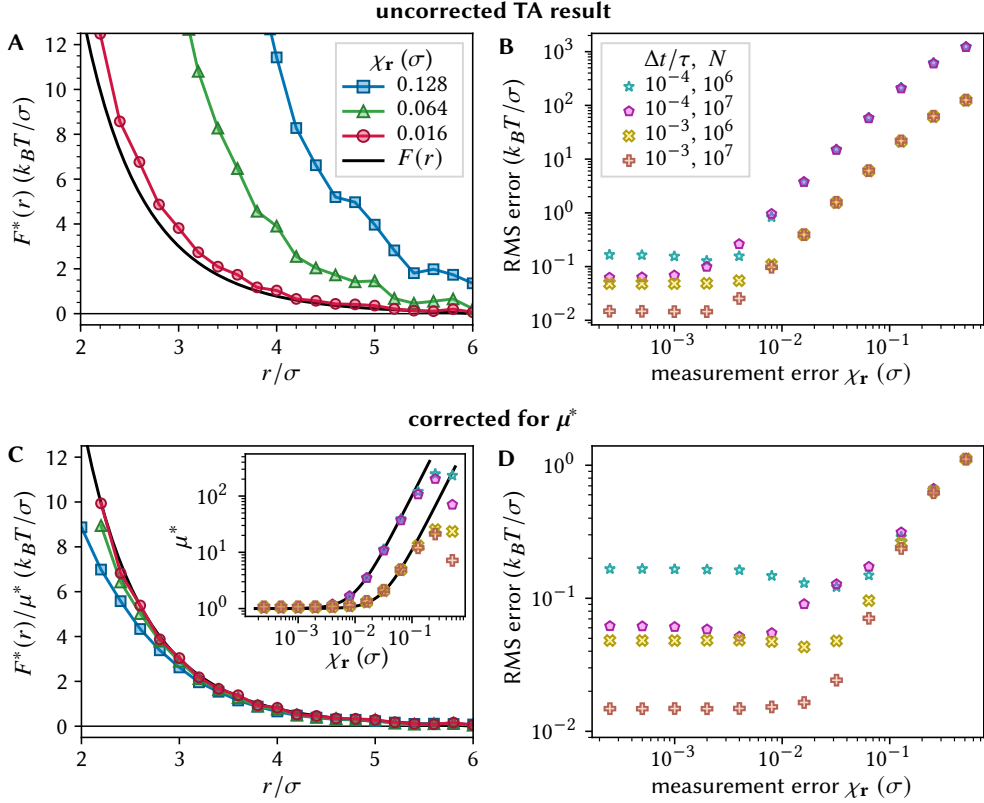


Figure 6.5: effect of measurement noise on trajectory analysis. To simulate the effect of localization errors, normally distributed random noise of varying standard deviation χ_r was added to trajectory data generated with BD simulations using a Yukawa force ($\Gamma_{\text{Yuk}}/k_B T = 50$, $\kappa\sigma = 1$, $\varrho\sigma^3 = 0.025$, $n = 200$), TA was used to recover the apparent force $F^*(r)$ ($r_{\text{max}} = 8$, $M = 40$, ϕ^{lin}). **A,B:** apparent force and associated RMS deviation from the force used in the simulations for varying measurement noise magnitude χ_r . **C,D:** the same force profiles and associated errors after correcting for μ^* . The inset shows Eq. 6.24 for $\Delta t/\tau = 10^{-4}$ and 10^{-3} (solid lines) together with the best fit for μ^* using the known input force.

In practice, the stochastic effect –the additional ‘noisiness’ from bin to bin– is negligible compared to the uncertainty introduced by Brownian noise under conditions relevant to TA, *i.e.* $\Delta t \ll \tau$ and $\chi_r \ll \sigma$. It is immediately clear from Figure 6.5A however that the systematic effect –the fact that noise on the coordinates does not average out in the displacement vector– is much more significant: the magnitude of the force appears to increase with increasing measurement noise. The apparent force $F^*(r)$ obtained using TA on noisy data was found to differ from the real force as:

$$F^*(r) = \mu^* F(r) = \left(1 + \frac{\chi_r^2}{\Delta t_{\text{ta}} D_0}\right) F(r) \quad (6.24)$$

where μ^* is a multiplication factor given as the sum of the real displacements of the particles

and the apparent displacement due to noise on the coordinate data. It is also clear that this effect disfavours the use of high imaging rates: the average displacement between frames decreases with increasing imaging rate while χ_r does not. Actually, the localization error in e.g. video microscopy typically gets worse with increasing imaging rate due to limitations in exposure time / signal collection, exacerbating influences of measurement noise on $F^*(r)$ at small Δt . Fortunately, as seen in **Figures 6.5C** and **6.5D** the correct force may be recovered in most cases when the localisation error is known and can be used to correct the apparent force for μ^* . When the magnitude of the noise is large —on the order of the discretisation step size or more— the relative positions of the particles are no longer well-defined and a blurring of the force along r starts to occur similar to the effect at low measurement speed. This leads to deviations not accounted for in **Eq. 6.24** as can be seen in the inset of **Figure 6.5C**. Additionally, experimental systems always have some non-zero polydispersity which is not accounted for here.

6.4 Experimental measurement of interaction forces in 2D

Experimental measurement of interaction forces was first demonstrated in a quasi two-dimensional system of colloidal particles confined to a planar interface. The choice for a 2D system was made based on three primary motivations: firstly, much higher imaging rates may be achieved in 2D video microscopy when compared to e.g. 3D CLSM, since 3D images consist of sequentially obtained series of 2D images. Alleviating the need for thin optical sectioning (needing a good 'z-resolution') also allows for widefield illumination and imaging, which enables much more efficient light collection and reasonable pixel dwell times even at high imaging rate because raster-scanning is not necessary. Secondly, 2D-imaging is more data efficient and allows for collection of bigger time series as well as faster (image) data processing and particle tracking. Lastly, in a quasi-2D system it is possible to achieve tunable repulsive interactions through the use of an external electric field. When confining particles to a 2D layer and applying an alternating current (AC) electric field perpendicular to the imaging plane containing the particles, the particles obtain an in-plane isotropic repulsive potential due to induced dipole moments in the particles along the field direction.* As the interaction strength depends directly on the field strength, this allows for a range of inter-particle interaction strengths to be measured within a single sample.

6.4.1 Sample preparation

To obtain a two-dimensional layer of particles, silica particles were sedimented to a glass-liquid interface. To minimize effects of particle excursions along the third (z) direction, we chose the criterium that at any given time, no more than 0.1 % of particles may be separated/elevated by more than one particle diameter away from the interface. Based on calculation of the gravitational height this required a particle size of at minimum 1.53 μm assuming silica particles in water,[†] the calculations are given in **Section 6.9.2**. Fluorescent silica particles were synthesised with a total diameter of 1.57 μm and a polydispersity of <1 %, containing a $\sim 0.8 \mu\text{m}$ fluorescent core. The particle synthesis is described in more detail in **Section 3.3.2**, with detailed experimental methods in **Section 3.7.11**. The particles

* using such induced dipolar potentials in a fully three-dimensional system is also possible as will be shown in **Chapter 7**, but considerably more complex due to the anisotropic nature of the dipolar potential outside of the plane perpendicular to the field

[†] in the experiments we use an ethanol/glycerol mixture, but the effect of different solvents on gravitational effects (through the difference in density between the solvent and particles) is very minor

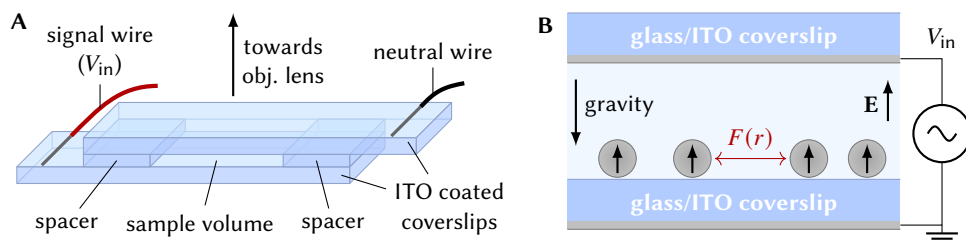


Figure 6.6: sample cells for 2D dipolar interactions. ITO-coated cover-slips (#1.5 thickness) were used as optically transparent planar electrodes, separated by a thin sample volume (typically $\sim 160 \mu\text{m}$). **A:** overview of cell construction, we note that the cell is depicted upside down compared to when it is placed in an inverted microscope (with the objective lens below the sample) in order to show the wire connections. **B:** schematic side-view of the sample cell as oriented during a measurement, with the particles sedimented to the glass-liquid interface and ITO electrodes depicted in gray. The thicknesses of cover-slips and spacers and particle-sizes are not drawn to scale.

were further purified using centrifugation to remove any small clusters and/or secondary nuclei, see [Sec. 6.8.4](#) for more details on the washing procedure.

Special sample cells were constructed which made it possible to apply an alternating current (AC) electric field using planar electrodes, thereby inducing dipolar interactions between the particles with the field (and dipole) direction perpendicular to the imaging plane. The sample cell is schematically shown in [Figure 6.6](#) and was made using cover-slips which were coated on one side with indium tin oxide (ITO), which is an optically transparent and electrically conductive coating. The ITO-coated side on the bottom cover-slip was oriented to the outside of the electric cell (towards the objective lens) and grounded, such that the interface to which the particles were confined by sedimentation was the uncoated side of the glass. This was done to prevent influence of the ITO coating on the particle motion and interactions,^[501,502] and to avoid current flow via direct electric contact through the sample. The top ITO-coated cover-slip was oriented with the conductive side facing the *inside* of the electric cell to decrease the spacing between the ITO layers such that higher field strengths could be achieved. The electric cells were filled with a dilute dispersion of the silica particles in a mixture of 30 wt.% glycerol in ethanol containing 2 mM LiCl salt, and closed off with glue. The addition of glycerol was motivated by the fact that higher relative* imaging rates could be achieved at higher viscosity; the viscosity η of the solvent was 4.46 mPa s.^[503] Ethanol was used instead of *e.g.* water because of its lower dielectric constant. This allowed for higher field strength at a given input potential and decreased losses of the electric field due to capacitance, which could have occurred if the sample acted as capacitor-resistor circuit, thereby damping high-frequency AC-fields. Determination of the field strength within the sample (*i.e.* at the location of the particles) is discussed in more detail in [Section 6.9.3](#). The ITO electrodes were connected to a signal generator and amplifier to apply a sinusoidal AC electric field with a variable amplitude and a frequency of 1 MHz. At this frequency the field switched faster than the relaxation rate of the ions clouds around the particles, meaning that the double layer was not changed by the electric field and electrophoretic effects of the particles or ions were negligible. Essentially, the particles experienced only the ‘average’

* relative to the self diffusion time $\tau = \sigma^2/D_0$

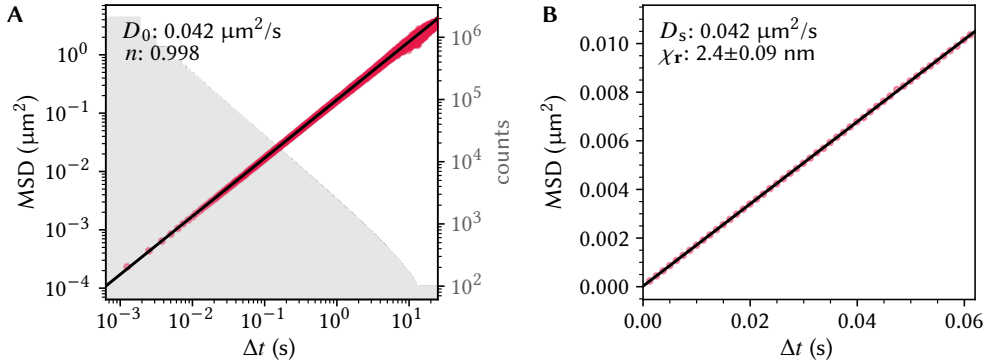


Figure 6.7: 2D mean squared displacements of sedimented silica particles. MSDs as function of time interval with no external field ($E=0$ V_{RMS}/mm) **A**: MSDs (red circles) fitted with a power-law (black line) on a log-log scale, the best fit diffusion coefficient and power-law exponent n are given in the top left. Gray bars indicate the number of particle displacements contributing to each bin. **B**: linear regression of the short-time (up to $10^{-3}\tau$) MSD to determine the self-diffusion coefficient D_s and particle tracking error χ_r .

field.^[504] An additional transformer was used to assure no DC field component was present and the input potential was measured with an oscilloscope directly at the wire connections to the sample cell.

6.4.2 Interaction forces at constant electric fields

Firstly, the interaction forces were measured at constant electric field strength. Full experimental and computational methods are given in [Section 6.8.5](#), but briefly: a certain potential was applied to the electric cell, given as the root-mean-squared (RMS) average of the sinusoidal potential, resulting in an electric field E in the sample. Using wide-field fluorescence microscopy in combination with particle tracking, trajectory data were recorded, and this was then repeated for a range of electric field strengths within the same sample. The data were then corrected for sample drift, and spurious trajectories were detected based on the single-particle mean-squared-displacements such that these trajectories could be excluded from the force evaluation in TA. The friction factor γ and particle detection error χ_r were determined from measurement of the ensemble mean squared displacements (EMSD) in the same datasets which were used for TA. The EMSDs at zero electric field are shown in [Figure 6.7](#), a diffusion coefficient D_0 of $0.042 \mu\text{m}^2/\text{s}$ was found, where we emphasise that this pertains to 2D diffusion close to a the glass substrate, and not the free (3D) diffusion coefficient of dilute particles in the bulk which was estimated to be $\sim 50\%$ higher based on the Stokes-Einstein equation. Here, the EMSD were determined up to a maximum lag time of $\sim 0.4\tau$, corresponding to displacements up as large as the typical nearest neighbour distance. To exclude effects from interactions and the finite particle concentration, and because hydrodynamic effects can be significant even at timescales as small as 0.1τ ,^[505] the self-diffusion coefficient D_s was also determined for only very short timescales (up to $10^{-3}\tau$, corresponding to displacements \ll than the typical nearest neighbour distance), but excellent agreement was found with the EMSD. From the extrapolation of the short-time MSD to zero lag time a typical particle localisation precision of ~ 3 nm was found. D_s and χ_r

were found to not differ significantly with increasing field strength, and the values obtained at zero field (no interactions beyond the hard core) were used for all datasets.

Experimental pairwise force profiles were extracted from the coordinate data using the trajectory analysis method, and compared to theoretical interaction forces for which the particles were treated as permanent point-dipoles. The in-plane interaction of point-dipoles—that is the inter-particle force between two particles in the plane perpendicular to the direction of the field—is given by the following potential and force functions:^[506]

$$U_{\text{dip}}(r) = \frac{\Gamma_{\text{dip}}}{2} \left(\frac{\sigma}{r} \right)^3 \quad (6.25)$$

$$F_{\text{dip}}(r) = \frac{3\Gamma_{\text{dip}}}{2r} \left(\frac{\sigma}{r} \right)^3. \quad (6.26)$$

The dipole strength Γ_{dip} (giving the ‘contact’ potential $\Gamma_{\text{dip}}/2$ at $r = \sigma$) depends on the induced dipole moments of the particles, which in turn depend on the *local* electric fields experienced by the particles. Here, we neglect local perturbations of the electric field due to nearby dipoles (*i.e.* $E_{\text{loc}} = E_{\text{ext}}$) and assume every particle has the same dipole moment, such that:

$$\Gamma_{\text{dip}} = \frac{\pi}{8} \varepsilon_s \varepsilon_0 \sigma^3 \alpha^2 E_{\text{ext}}^2 \quad (6.27)$$

with α the polarisability of the particles given as

$$\alpha = \frac{\varepsilon_p - \varepsilon_s}{\varepsilon_p + 2\varepsilon_s}. \quad (6.28)$$

where ε_0 is the vacuum permittivity and ε_p and ε_s are the dielectric constants of the particles and solvent respectively.

The experimental data were corrected for noise using Eq. 6.24 and are shown together with calculated interaction forces in Figure 6.8. It is clear that the interaction forces from the experimental data are consistently underestimated when compared to the theoretical interaction forces, although we note that this is by the same constant factor for all field strengths and over the majority of the interaction range, with an observed dipole strength which is $\sim 80\%$ of the theoretical value. When the data are plotted on a log-log scale (Fig. 6.8C), the correct slope corresponding to the $F(r) \propto r^{-4}$ scaling of dipolar forces is also obtained for most of the interaction range; only at large pairwise distance ($r > 5 \mu\text{m}$) the experimental data are dominated by noise, resulting in plateauing of the force profiles. While there is considerable scatter in the data, the observed standard deviation of $\sim 0.1 k_B T / \sigma$ (determined for $r \geq 8$) is in good agreement with Eq. 6.23 for the typically 10^6 to 10^7 particle pairs which were evaluated in TA at those distances. For the short distance and high field strength regime, where the forces profile is the steepest and the highest forces are found, the experimental forces also deviate qualitatively from Eq. 6.26 with a slope smaller than $\propto r^{-4}$.

The fact that the measured force is consistently lower than the theoretical force can mean that either the TA underestimates the real force, or that the calculated force profiles are not representative for our experimental system. At the very least, the results from TA seem self-consistent at first glance given that for most of the force profile the experimental and theoretical interaction forces differ only by a constant factor, and follow the correct scaling with distance and field strength. As discussed however, deviations can occur in TA due to a

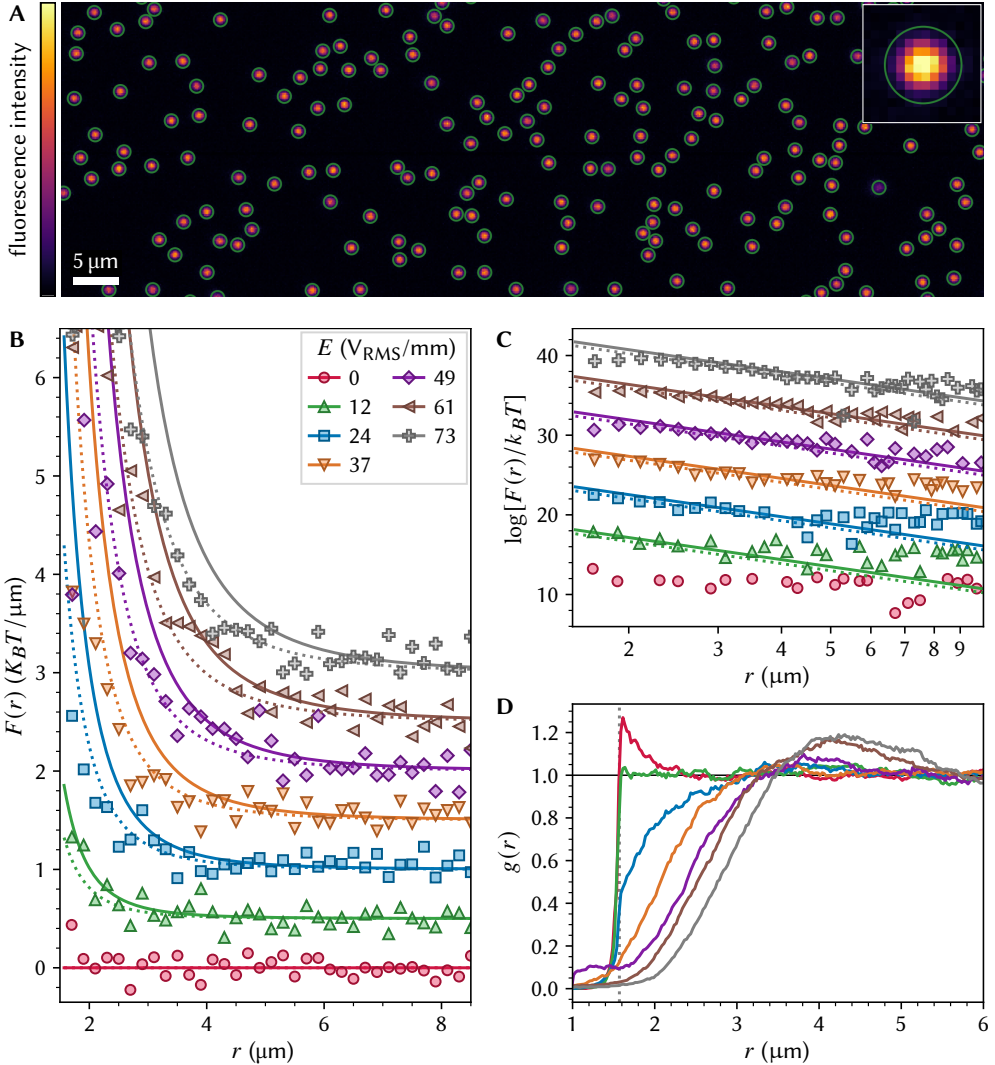


Figure 6.8: trajectory analysis of 2D dipolar interaction forces. **A:** part of a fluorescence micrograph recorded at 800 frames/s ($\Delta t_{\text{ta}}/\tau = 2 \cdot 10^{-5}$, 2048 px \times 256 px at 163 nm/px), with green circles indicating the results from particle localisation. The inset shows a zoom-in of a single particle. **B:** force profiles extracted from experimental trajectories (data points) together with theoretical interaction forces (solid lines). The dotted lines show the interaction force with dipole strength 20% lower than the theoretical value. The data are vertically offset for clarity. **C:** experimental and theoretical force profiles on a log-log scale, showing that the slope follows the expected proportionality of $F(r) \propto r^{-4}$ for intermediate forces. Data are vertically offset for clarity. **D:** radial distribution functions calculated from the trajectory data. For each field strength $N \approx 10^7$ force measurements were recorded at $\varrho\sigma^2 \approx 0.12$, and $r_{\text{max}} = 10 \mu\text{m}$ and $M = 50$ square wave BFs were used in the trajectory analysis.

number of different effects, notably for (too) large time step, at high particle concentration or in for high localisation error (after correction for μ^*). However, the localisation error is nearly 3 orders of magnitude smaller than the particle size, and the concentration relatively low at $\rho\sigma^2 = 0.12$ which is also consistent with the at most 1 peak in the $g(r)$. With a relative analysis time step of $\Delta t_{\text{ta}}/\tau = 2 \cdot 10^{-5}$ the analysis time step is considerably smaller than would be needed to cause errors of the observed magnitude, and thus not a likely cause. The influence of Δt_{ta} was studied further to verify this by performing the TA on a subset of the experimental data taken at varying intervals, shown in **Figure 6.9A**. It was found that, after correcting for the effect of χ_r via μ^* , $F(r)$ did not depend on Δt_{ta} for values up to well over an order of magnitude larger.

Surprisingly, the imaging rate —and with it other properties such as the pixel integration time, field of view, pixel readout time, etc.— did affect the magnitude of the interaction force obtained with TA. For example, when the system was imaged at 200 frames/s, a considerably lower force was obtained than the same system imaged at 800 frames/s but analysed at $1/4^{\text{th}}$ the imaging rate (*i.e.* using only every fourth time step in the analysis, resulting in the same $\Delta t_{\text{ta}} = 1/200$ s). This is likely because the particle coordinates are obtained from the integrated intensity of the particle over the exposure time and thus give a time-averaged position (assuming a constant fluorescence emission rate), analogous to motion blur in photography. While the time-averaged position can be determined very accurately, the time-average is only an approximate for the position ‘at the start of the measurement interval’, which in itself becomes more poorly defined as the image integration time increases. Motion blur has been known to affect statistical properties obtained through particle tracking in *e.g.* microrheology,^[206,507] and, in the context of TA, likely has a similar blurring effect as the use of a similarly large analysis time step. Such an effect would be particularly pronounced at short distances and/or high interaction forces, and may affect the results even at the high imaging rates used here. When the data recorded at 800 frames/s were *averaged* per set of 4 frames (rather than skipping 3 out of every 4 frames) to simulate the effect of motion blur, the results from TA *were* very similar to those recorded at 200 frames/s. This confirmed that motion blurring due to the relatively long exposure time was the likely culprit for the observed dependency of the results on Δt_{im} .

The ‘motion-blurring’ effect at longer integration time may also affect the result through sample mechanical vibrations. Although an additional displacement applied to all particles cancels (or averages) out in TA and is actually corrected for in the sample pre-processing regardless, there are slight differences in the readout time of different pixels of the camera, meaning that not all particles in a frame are recorded at the same time.* As a result, when there is non-constant drift of the sample as a whole (due to periodic mechanical vibrations), different particles may be recorded at slightly different parts of the drift cycle such that not all particles in frame obtain the same apparent drift velocity.† To check if this was the case, we performed sub-frame analysis and drift correction on data-sets recorded at different imaging rates to determine if drift velocity varied with the pixel readout phase. While small vibrations were found to be present, sub-frame analysis and drift correction on a sub-frame basis did not significantly affect the results and are thus unlikely to cause the pairwise force to be underestimated.

Finally, the trajectories of the particles are likely subject to hydrodynamic effects in a

* although the total integration time and the time interval *between* readouts are the same for all pixels

† this is essentially what is known in photography as the ‘rolling shutter effect’

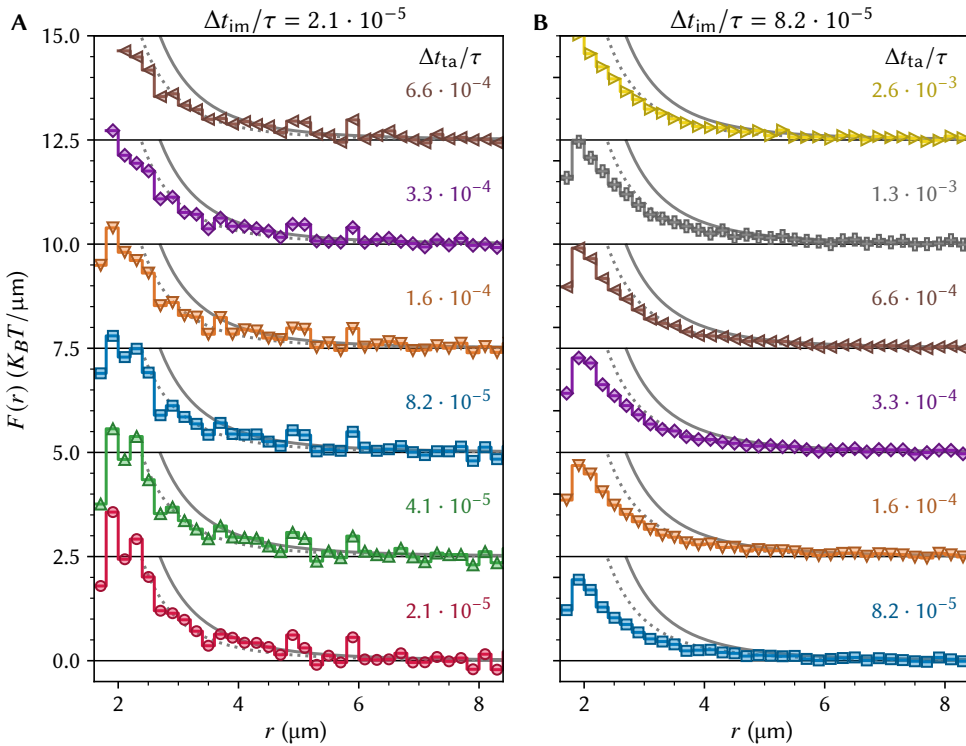


Figure 6.9: effect of the imaging and analysis time step in TA of experimental data. Data were recorded at imaging rates of 800 frames/s and 200 frames/s in the same system of quasi 2D dipolar silica particles at $E = 49 \text{ V}_{\text{RMS}}/\text{mm}$, and analysed at different rates by using only every n^{th} time step. **A:** 10^7 force measurements recorded at $\Delta t_{\text{im}} = 1.25 \text{ ms}$. **B:** $4 \cdot 10^7$ force measurements recorded at $\Delta t_{\text{im}} = 5.00 \text{ ms}$. Data are vertically offset for clarity, the solid grey line shows the theoretical interaction force and the dotted line the force using a 20% lower dipole force.

manner which is not pair-wise additive and thus not accounted for in the analysis. Even hard particles at short time-scales ($< 0.1\tau$) experience a local solvent friction which differs from free diffusion due to hydrodynamic coupling between the particles.^[223,508] Our present implementation of the TA does not account for these effects, although this is, in principle, possible to include the effects of flow fields by calculating the local mobility of each particle based on its environment such that hydrodynamic coupling is accounted for and the ‘pure’ interaction forces may be obtained.^[180] However, in such an implementation the exact calculation would have to be tailored to the dimensionality (2D or 3D) and geometry of the system (in our case the presence of a flat wall near the particles).

Although it cannot be definitively ruled out that TA consistently underestimates the real interaction forces, in reality the ‘real’ force in these experiments is unknown, and we just assume that the theoretical interaction force accurately represents the experiments. But as mentioned before, it could be that the TA does recover the correct interaction forces and that the mismatch with the calculated interactions occurs because Eq. 6.26 consistently overestimates the interaction forces in our system. For a start, the calculations assume that

the particles are surrounded by a medium of homogeneous dielectric constant (that of the solvent), which is certainly untrue due to the fact that the particles are close to a glass-liquid interface, and at least part of the dipole-field around the particles will be distorted compared to dipolar particles with isotropic surroundings. Furthermore, we have assumed that the local field strength near the particles is unaffected by the dipole fields of other particles, which is only true at low particle concentration, and that the geometry of the sample cell is that of a perfect (series) multi-layer parallel plate capacitor, which is untrue since the presence of glass spacers between the electrodes to some extent affects the effective field within the sample for a given electrode potential. For more realistic calculations of the interaction forces in the system *e.g.* finite-element modelling could be used, or the theoretical dipole-dipole interaction could be extended to account for the presence of a dielectric interface, but such calculations were deemed outside the present scope of this work. Finally, it should be mentioned that exact predictions of particle polarisabilities are frequently off compared to experimentally determined values by much more than the deviations we find here.^[509] As such, a deviation of $\sim 80\%$ should perhaps not come as a surprise.

6.4.3 Interaction forces out of equilibrium using switching electric fields

Next, we demonstrate the ability to measure interactions in a non-equilibrium system. This was achieved by using the same quasi two-dimensional system of silica particles with field-induced dipolar interactions as described above. Rather than keeping the external electric field constant however, here the trajectories were analysed in the time period just after the electric field strength—and thereby the interaction potential—was changed, such that the initial configurations at the switching point did not represent an equilibrium state for the new interaction potential. To obtain enough data of the relatively short period after the change in electric field strength where the system was far out of equilibrium, we performed the experiments by periodically switching the electric field on or off while imaging, and running TA for the trajectories aggregated for all the ‘on’ or ‘off’ periods of the field separately. By setting the rate of field switching faster than the equilibration time, the system was continually prevented from equilibrating thereby allowing for a sufficient amount of data to be collected for non-equilibrium states.

Figure 6.10 shows the results from TA on the same system used in **Section 6.4.2** but using a switching electric field that alternated between 0 and $61 \text{ V}_{\text{RMS}}/\text{mm}$, as well as the evolution of the $g(r)$ after switching the field on or off. From the evolution of the $g(r)$, which was recorded with a relatively slow switching rate of $\sim 0.1 \text{ Hz}$, it is clear that the repulsive interactions when the field was turned on caused structuring of the particles within a few seconds. However, after switching the field off the system, relying only on passive Brownian motion, equilibrated significantly slower. For this reason, we chose to perform measurements for TA with an ‘off’ time which was 4 times longer than the ‘on’ time and at a relatively high switching rate such that the system remained in an intermediate state between the two equilibrium states. The TA results are similar to those obtained using a constant field strength, showing that the analysis does not rely on the equilibrium state of the system. Furthermore, the force data with the electric field on were sampled more homogeneously using switching fields than when the field was constantly on: for the switching electric field (**Fig. 6.10**) the number of particle pairs contributing to the force at short range, *e.g.* the basis function at $F(2.0 \leq r < 2.2 \mu\text{m})$, was 19% that of the number of pairs contributing to a basis function at longer range at $F(8.0 \leq r < 8.2 \mu\text{m})$. For the equilibrium data (**Fig. 6.8**) on

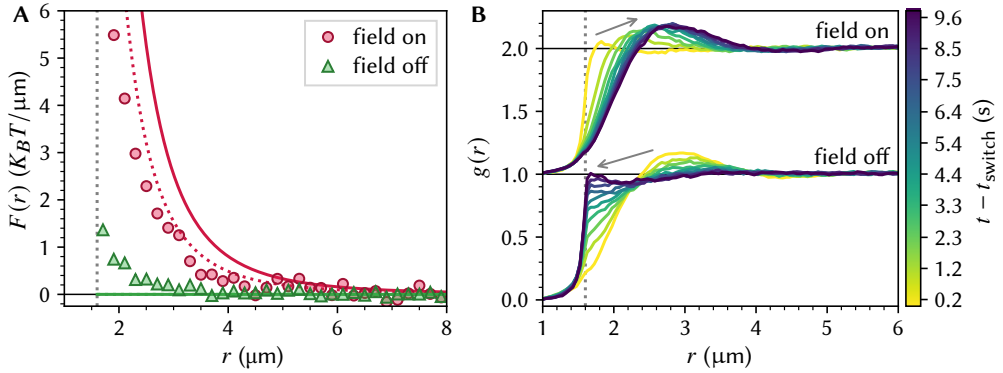


Figure 6.10: interaction forces of 2D dipolar particles in switching electric fields. **A:** force profiles from TA during the field on and off periods separately, data were recorded with $\Delta t_{\text{ta}} = 1.25$ ms with an electric field that was switched between $E = 61 \text{ V}_{\text{RMS}}/\text{mm}$ ('field on') and $0 \text{ V}_{\text{RMS}}/\text{mm}$ ('field off'), where each 'on'-period lasted for 400 frames (0.5 s) and each 'off' period 1200 frames (1.5 s) for a total number of force measurements of $\sim 3 \cdot 10^7$ and $\sim 10^8$ respectively. Solid and dotted lines represent the theoretical interaction forces and interaction forces at 20% lower dipole strength respectively. **B:** evolution of the $g(r)$ after switching the field on or off at 0.1 Hz shows that the system does not reach equilibrium within the switching time of the measurements in A.

the other hand this ratio was only 5%, meaning that in equilibrium four times more data would be required to obtain a similar precision for the short-range forces than when using switching fields.

Here, the goal of using switching electric fields was merely to demonstrate out-of-equilibrium interaction measurements, but such a scheme has a number of other use cases where interaction measurement in equilibrium would be infeasible. If the interactions can be changed or switched 'off' during the measurement, be that through the use of external electric or magnetic fields, temperature changes, or *e.g.* light-initiated chemical reactions, this can be used to extend the measurement time in cases where equilibration of the system would lead to a state not conducive to interaction measurement, such as when the equilibrium state is a crystal—in which only a small subset of configurations is sampled—, when strong ($\gg k_B T$) attractive interactions would lead for instance to complete aggregation or to string and/or sheet formation that cannot because of kinetic reasons equilibrate.^{[510]*} As we have seen, repeated 'initialisation' of the system in a non-equilibrium state can also be used to achieve more homogeneous sampling of the energy landscape. In particular this could be of use when attempting to sample unstable features of the potential energy landscape, *e.g.* when determining the exact position and height of an energy barrier, as this would be an extremely unlikely point to sample under (Boltzmann) equilibrium conditions.

* such attractions are *e.g.* present in some of the experiments in Chapter 7, where the formation of strings due to attraction of dipolar particles along the field direction is prevented by only keeping the electric field on for a short periods at a time

6.5 Experimental measurement of interaction forces in 3D

Although the quasi two-dimensional particle system discussed thus far in this chapter had some key advantages in the context of dynamic interaction measurements, in the real world colloidal particle systems tend to be three-dimensional. To perform 2D measurements therefore, it is almost invariably required to either introduce interfaces to confine particles to a 2D layer, or to perform a ‘2D’ analysis on a system where particles can also move along the third dimension. These methods can affect the measurement and the measured interaction forces in many ways that range from subtle to severe, and while these 2D experiments are generally easier to perform at the required spatial and temporal resolutions, interpretation of the results is more complicated and less generalisable than for a fully 3D system where particles are far from any interfaces. Therefore, we performed trajectory analysis on three-dimensional multi-particle trajectories obtained using high-speed laser scanning confocal microscopy.

6.5.1 Sample preparation and high-speed volumetric confocal microscopy imaging

For 3D trajectory measurements, a system of charge- and sterically-stabilised PHSA-PMMA particles in a mixture of the solvents CHB and *cis*-decaline was used as described in [Section 3.4](#), which is a widely used colloidal μP model system as it allows the interactions between the particles to be tuned from nearly hard-sphere like to extremely soft through control over the ion concentration through de-ionization or the addition of an organic salt.^[417] By tuning the ratio of CHB to decalin, the system could be simultaneously density-matched and nearly refractive-index-matched, meaning that sedimentation/creaming of the particles was negligible over a time-scale of hours even for micron-sized particles and that imaging was optimised by minimising scattering of the excitation laser by the particles. Refractive-index-matching also had the benefit of minimising van der Waals forces between the particles to significantly lower than the thermal energy. Samples were prepared with varying concentrations of the organic salt tetrabutylammonium bromide (TBABr) to produce particle batches with differently ranged interaction forces. More details on the sample preparation and imaging are given in [Section 6.8.6](#).

The systems were then imaged using an array-scanning confocal microscope designed specifically for high speed confocal imaging, which works by using an array of micro-lenses and an adjustable pinhole array to scan many hundreds of points in the sample simultaneously, such that relatively few pixels need to be scanned by each pinhole.* This minimises the time needed to record enough signal (or maximises the pixel integration time for a given imaging rate) while maintaining the capability thin optical sectioning along the optical axis (the z -axis), although there is a higher background signal due to some cross-talk between the pin-holes. To further increase the imaging rate, custom driver software was used, which among other optimisations minimised mechanical vibrations induced when z -scanning the objective lens at several Hz. Acceleration/deceleration of the z -stage and not *e.g.* the 2D imaging rate or fluorescent signal intensity were the predominant imaging rate limiting factor in our system. Time series of z -stacks were recorded for each sample, and particle trajectories were then extracted using a particle localisation algorithm, corrected for sample drift and filtered for spurious trajectories as previously. More details on imaging and data processing are given in [Section 6.8.6](#).

* this is similar to and based on so-called Nipkow spinning disc confocal microscopes,^[511] which use a spinning disc with pinholes rather than a mirror galvanometer resonantly scanning a static pinhole array over the sample

Finally, the trajectories obtained from high-speed confocal imaging were when analysed using trajectory analysis and corrected for localisation errors. The cut-off distance for the force r_{\max} (above which $F(r)$ was assumed to be 0) was varied to maximize the available data at each salt concentration, since a large cut-off means that the effective measurement volume—the region in which particles must reside for their full neighbourhood to be within the image boundaries—is reduced. We note that the localisation error was anisotropic, with a slightly larger error along the optical axis due to the lower optical resolution and larger voxel size along this direction, but this effect was found to be negligible after correcting for μ^* by comparing force profiles obtained by solving Eq. 6.11 for each dimension separately with the results from the normal ‘isotropic’ analysis. Timing differences along the optical axis within one z -stack due to the sequential slice-by-slice nature of the recording were also assumed to be negligible, which is valid when the length scale of the interactions is small compared to the z distance over which the 2D frame acquisition time varies significantly in comparison to the interval Δt_{im} between subsequent z -stacks.

6.5.2 Theoretical interaction forces

The interaction force profiles were fitted using a hard-core repulsive Yukawa (coulomb) force as formulated in Eq. 6.22, which is characterised by the contact potential Γ_{yuk} and the Debye screening length κ^{-1} . For a monovalent salt the inverse Debye length was calculated as:

$$\kappa = \sqrt{4\pi\lambda_B c_s} \quad (6.29)$$

where c_s is the number concentration of monovalent ions (*i.e.* ions per m^3) and λ_B is the Bjerrum length, the distance at which the electrostatic energy between two monovalent ions is equal to the thermal energy $k_B T$, given by:

$$\lambda_B = \frac{e^2}{4\pi\epsilon_r\epsilon_0 k_B T} \quad (6.30)$$

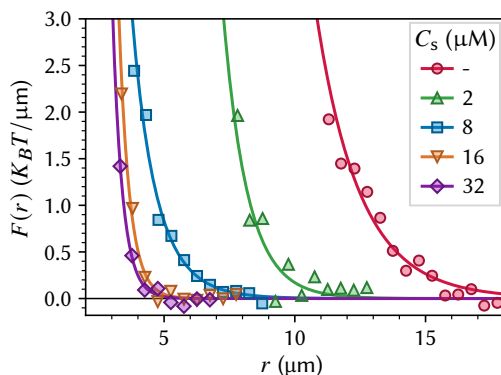
with e the elementary charge, ϵ_r the relative dielectric constant of the solvent and ϵ_0 the vacuum permittivity. For the CHB/decalin mixture used here, $\lambda_B \approx 10$ nm. In such low polar solvents ($\epsilon_r \approx 5.6$ ^[439]), salts do not necessarily dissociate fully leading to an ion concentration which is lower than expected based on the amount of added salt. The degree of dissociation of TBABr in the CHB/decalin mixture in this concentration range was previously found to be relatively low, around $\sim 0.5\%$,^[417,512] such that extremely long ranged charge interactions (many micrometers) are possible. Added salt concentrations were always corrected for this concentration-dependent degree of dissociation when calculating κ^{-1} . Finally, the contact potential depends on the size and charge density of the particles as:

$$\Gamma_{\text{yuk}} = \frac{Z^2\lambda_B}{\sigma(1 + \kappa\sigma/2)^2} \quad (6.31)$$

where Z is the net total number of elementary charges on the particle.

6.5.3 Results

The resulting pairwise force profiles for samples with different amounts of added salt are shown in Figure 6.11, with the best-fit parameters, particle charge and calculated Debye screening lengths given in Table 6.1. As expected, the interaction range decreased with increasing salt concentration, where the sample with no added salt (indicated with a dash)



c_s (μM)	κ^{-1} cal. (μm)	κ^{-1} (μm)	Γ_{yuk} ($k_B T$)	Z
-	-	2.01	$2.98 \cdot 10^3$	1030
2	0.82	1.08	$2.01 \cdot 10^3$	1065
8	0.41	1.29	$3.13 \cdot 10^1$	123
16	0.29	0.47	$6.29 \cdot 10^1$	298
32	0.20	0.44	$4.03 \cdot 10^1$	249

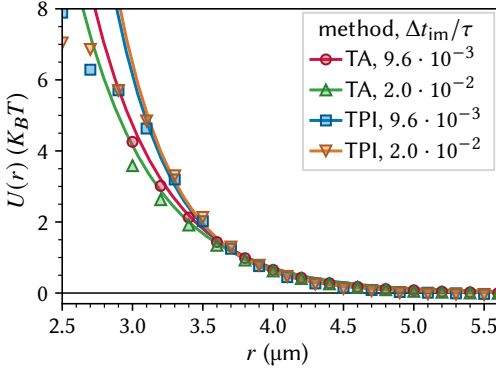
Figure 6.11 & Table 6.1: interaction forces of PMMA colloids at varying ionic strength.

Experimental interaction forces (data points) were obtained from 400 z -stacks of $1080 \times 856 \times 100$ voxels ($112 \mu\text{m} \times 90 \mu\text{m} \times 50 \mu\text{m}$) at a 3D imaging rate of 1.75 frames/s and fitted (solid lines) to obtain values for the contact potential Γ_{yuk} and κ^{-1} at different concentrations c_s of TBABr. Theoretical values for κ^{-1} , fit parameters, and values for Z (calculated from the fit parameters) are given on the right. The particle volume fractions were 0.10 % for the batches with 0 and 2 μM TBABr and 0.24 % for the batches with 8 μM to 32 μM TBABr respectively.

had the longest interaction range, limited only by the low concentration of ions always present in the solvent due to slow decomposition of CHB.^[512,513] Based on the fitted κ^{-1} , the ion concentration was ~ 3 nM, and the ionic strength was assumed to be negligibly small compared to the effect of the added TBABr in the other samples. We found that the experimental force profiles consistently overestimated the softness of the interactions when compared to the calculated values. This likely the result of the relatively large Δt_{ta} , which lead to a blurring (softening) of the force profiles.

The surface charge of these particles is known to decrease with increasing TBABr concentration, and eventually even switch go from positively to negatively charges at TBABr concentrations of several 10's to 100's of μM s depending on the particle batch.^[439] As such it is not unexpected to see lower values for Z at the higher salt concentrations, however, our results do not show a consistently declining trend. Furthermore, the charge at low salt concentration is $\sim 4 \times$ higher than previously reported measurements for very similar particles in pure CHB, whereas, if anything, the presence of decalin would be expected to lower the degree of charging.^[417,418] It is also known that the surface charge may be altered by the use of electric fields, but this mostly occurs for lower frequency fields and is expected to be negligible at the MHz frequency used here.^[514] Really, the contact potentials, and by extension the charges, are co-dependent with the fitted κ^{-1} 's and extrapolated to $r = \sigma$ from data which are noisy, subject to artefacts from the large time step and mostly sampled at $r \gg \sigma$. As such, we would not attempt or advise to draw quantitative conclusions from these results without also performing electrophoresis measurements under similar conditions.^[418,515]

To further elucidate the effects of the imaging rates, we performed TA on two datasets obtained with two different imaging rates within the same sample. Additionally, interaction potentials were obtained directly using the test-particle insertion (TPI) method discussed



TA / TPI	$\Delta t_{\text{im}}/\tau$	Γ_{yuk} ($k_B T$)	κ^{-1} (μm)	Z
TA	$9.6 \cdot 10^{-3}$	$6.37 \cdot 10^1$	0.62	252
TA	$2.0 \cdot 10^{-2}$	$4.86 \cdot 10^1$	0.66	212
TPI	$9.6 \cdot 10^{-3}$	$1.40 \cdot 10^2$	0.49	431
TPI	$2.0 \cdot 10^{-2}$	$1.57 \cdot 10^2$	0.48	463

Figure 6.12 & Table 6.2: interaction potentials from TA and TPI at varying imaging rate.

Interaction potentials were obtained for PMMA colloids from numerical integration of force profiles from TA or directly from test-particle insertion (TPI) for data recorded at 3.43 or 1.69 frames/s, with 800 z -stacks of $112 \mu\text{m} \times 60 \mu\text{m} \times 30 \mu\text{m}$ or 400 z -stacks of $112 \mu\text{m} \times 90 \mu\text{m} \times 50 \mu\text{m}$ respectively. The sample contained $6 \mu\text{m}$ TBABr (κ^{-1} calc. $\approx 0.47 \mu\text{m}$) and the particle volume fraction was 1.2%. Experimental values for Γ_{yuk} and κ^{-1} determined from fitting the force profiles (TA) or potentials (TPI) are given on the right.

in [Chapter 4](#) and compared to fits of the force profiles and potential data obtained through numerical integration of the force profiles. Interaction potentials from TA and TPI at two different imaging rates are shown in [Figure 6.12](#) with parameters obtained through fitting the force profiles and potentials respectively given in [Table 6.2](#). Again, the values for κ^{-1} obtained from TA were larger than the calculated value of $\kappa^{-1} \approx 0.47 \mu\text{m}$ based on the ion concentration due to added TBABr, and we indeed observed a larger apparent double layer thickness with larger Δt_{ta} (and associated lower value of Γ_{yuk}).

The results from test-particle insertion conversely did not depend significantly on imaging rate, although a different number of configurations was sampled due to differences in size and number of stacks. Moreover, excellent agreement was found between the screening lengths from TPI and based on calculations, and values obtained for Z are well within the range expected based on literature. Largely similar results could also be obtained using only a fraction of the data: if stacks were recorded at intervals of several seconds, only several tens of z -stacks of similar size were required to sample a similarly large configuration space. The fact that the results from TPI agreed well with our calculations but not with the TA results, provided further evidence that TA was not able to correctly recover the interaction forces for a system at these imaging rates. We can therefore only conclude that for this particle system under these imaging conditions, TPI is a more suitable approach to measure interactions.

6.6 Concluding remarks

In this chapter we have shown that it is possible to extract pairwise interaction forces from sets of multi-particle trajectories, by decomposing the net force experienced by particles, measured through the particle velocities, into the pairwise contributions of all nearby neighbouring particles. More so, we provide a practically applicable computational implementation in the form of a Python package to perform this ‘trajectory analysis’ on both simulated data with *e.g.* periodic boundary conditions, as well as real-world experimental data, all while

making no assumptions on the functional form of the interaction potential. Using simulated datasets (with known interactions) we assessed the robustness of the TA method to various parameters such as measurement rate, number of measurements, choice and number of basis functions and the effects of experimental limitations such as localisation errors.

While it is, in principle, possible to extract the pairwise interaction forces, the complicated and co-dependent interplay of the various parameters on the results and the stringent requirements on imaging/analysis rate and the amount of data required were found to make this method extremely challenging to use in practice, even for particle systems specifically chosen to optimise the measurements for TA. For some context, the data in **Figure 6.8B** alone represents well over 1.5 *terabytes* of raw imaging data, and a considerable amount of time and effort went into making it possible to record, process and store such large datasets, although we considered these procedural details beyond the scope of this thesis to discuss in detail. Of course, continuing technological improvements in computing power and high-speed imaging procedures are expected to alleviate these challenges to some extent. It is also possible, in principle, to solve a system of non-linear equations for parameters of a functional model potential, such that the number of unknowns is greatly reduced (*e.g.* only κ^{-1} and Γ_{yuk} in case of the Yukawa force), although this would require some *a priori* knowledge of at least the form of the potential, or to use *e.g.* a machine-learning approach to increase data efficiency.^[184] But perhaps more pressingly, the best choice of imaging parameters such as imaging rate and duration, depends in part on the shape and magnitude of the pairwise interaction forces, which is the very property the TA method is trying to determine. Calling this an ‘inconvenience’ would be understating the problem.

Nonetheless, using high-speed 2D fluorescence microscopy we were able to experimentally measure dipolar interaction forces with reasonable agreement to a theoretical model, where in experiments a dipole strength of circa 80 % of the theoretical model was found, which is likely the result of a combination of hydrodynamic effects and an altered dipole-dipole interaction due to the presence of the glass-liquid interface. As mentioned, theoretical predictions of the particle polarisability also frequently deviate from experimental values,^[509] potentially contributing to the discrepancies here. Notably, we have demonstrated that this reasonable agreement could be achieved even in systems which were demonstrably out of equilibrium. Using high-speed confocal microscopy interaction forces due to electrostatic repulsion were measured in 3D, although practical limitations on the achievable 3D imaging rate meant that these results quantitatively differed from predicted interactions, based on the ionic strength and literature values, as well as from our own experimentally determined interaction potentials obtained through analysis of the $g(r)$ using test-particle insertion.

At present we do *not* recommend the use of TA over other methods such as TPI whenever equilibrium analysis is possible. When it is not, a combination of velocity analysis and optical tweezers may be used to reduce the dimensionality of the imaging, or other techniques such as colloidal-probe AFM may be considered. That being said, there are presently some niche use cases, such as our work in **Chapter 7**, where TA is uniquely suitable to assess interaction forces. For such cases, we hope this work provides a useful starting point to build upon. We also expect that continuing improvements in equipment and procedures,^[185,516] as well as the use of 3D imaging techniques more suited to high-speed measurement such as holographic imaging^[190] and light-sheet microscopy,^[192] may be able to alleviate some of these challenges.

6.7 Acknowledgements

Talid Sinno is thanked for providing the data and codes for the original implementation of the TA^[180] as well as for useful discussions on TA. Siddharth Paliwal is thanked for help with Brownian dynamics simulations. Paul Moses and Dinja Sanders are thanked for their work on benchmarking TA with simulated results and for useful discussions on interpretation and comparison of their results and the results presented here. Dinja Sanders is also acknowledged for several improvements to the TA to enable analysis of larger datasets. Frank Smalenburg is thanked for his help with the derivation in Sec. 6.9.1. Gerhard Blab is thanked for many useful discussions on particle localisation, microscopy, and their effect on TA. Anna Nikolaenkova is thanked for help with the PMMA particle system and preparation of electric sample cells for microscopy. Johan Stiefelhagen is acknowledged for synthesis of the PMMA particles. Peter Helfferich is thanked for his support with fast confocal microscopy and writing drivers for fast z -scanning. Laura Fillion is thanked for many useful discussions over the years on nearly all aspects of this chapter, and for stepping in as a *de facto* co-supervisor for the work that resulted in this chapter.

6.8 Methods

6.8.1 Brownian Dynamics simulations

Brownian dynamics simulations, used to generate test-data with known interaction forces, were implemented by numerically integrating the overdamped Langevin equation (Eq. 6.2) for a system of colloidal particles. For convenience, in the simulation all parameters where appropriate were scaled with respect to the particle diameter σ , diffusion time $\tau = \sigma^2/D_0$ and/or thermal energy $k_B T$; *i.e.* these parameters were set to 1. The simulations were initialized by generating n uniformly distributed random coordinates in a cubic simulation box with periodic boundary conditions, checking for any overlapping particles ($r < \sigma$) and replacing them with newly generated coordinates until no overlapping particles were present. The simulation was then run as a loop where at each simulation step t the force vector acting on each particle was calculated as the sum of all pairwise interactions with neighbours according to Eq. 6.4, and used to calculate the particles next position with Eq. 6.20, where a new ξ was taken from a normally distributed random number generator with zero mean and unity standard deviation for each particle at each iteration. To speed up the computation, the forces were only calculated up to some threshold distance (typically $r_{\max}/\sigma = 8$) above which the force was set to 0. To avoid introducing a discontinuity in the force function, the force was linearly transitioned to 0 in the region from $(r_{\max} - 0.5)/\sigma$ to r_{\max}/σ . For inter-particle distances, the ‘nearest image’ convention was used for the periodic boundary conditions, which means that only the shortest possible distance through the periodic volume between two particles was counted. The simulation step size was always chosen sufficiently small to provide realistic motion (at most $\Delta t_{\text{sim}}/\tau = 10^{-4}$). The simulation was run for 10^4 iterations without storing data, after which snapshots were periodically stored for later analysis with the TA method while the simulation was iterated for the duration needed to acquire the desired number of force measurements. To avoid bias in the TA results due to the discretized nature of the simulated data, Δt_{sim} was always at least $50\times$ smaller than the trajectory analysis time step size Δt_{ta} .

6.8.2 Computational implementation of the trajectory analysis



The trajectory analysis method was implemented in the Python programming language as importable package^[517] and is available online using the QR code on the left. The implementation closely follows the theoretical description provided in Section 6.2 with some additional considerations to deal with both simulated and experimental datasets, and is implemented as follows: particle coordinates and associated time stamps are imported as one or more sets of consecutive time steps

from e.g. one or multiple microscopy videos, where each particle is tagged with a unique identifier such that particles are linked between time steps. The pairwise force is approximated as M BFs in the form of a list of M values where each value represents a constant force over the interval $r \rightarrow r + \Delta r$ up to r_{\max} in case of square wave BFs (Eq. 6.6), or similarly where the force is given by linear interpolation of the force values in the bin centre positions in case of linear BFs (Eq. 6.7). Here, r_{\max} is a cut-off for the maximum interaction range beyond which particles are assumed not to exert any force. The coefficient matrix \mathbf{C} scales linearly in the number of particles and time steps, which may be prohibitively memory-intensive when large datasets are analysed. Rather than storing the coefficients and forces directly, the intermediate dot products $\mathbf{X} = \mathbf{C}^T \mathbf{C}$ and $\mathbf{y} = \mathbf{C}^T \mathbf{f}$ are used to store the data for the ordinary linear least squares calculation according to Eq. 6.16. For this a zero-valued matrix $\mathbf{X} \in \mathbb{R}^{M \times M}$ and vector $\mathbf{y} \in \mathbb{R}^M$ are initialized, to which the results can be added element-wise on a per time step basis. Secondly, two zero-valued vectors of length M are initialized to keep track of the number of particle pairs contributing to each bin and the mean inter-particle distance of all particle pairs within each bin. Mean pairwise distances are recorded since the bins are generally not homogeneously sampled due to pairwise distances towards the lower-energy side of the bin being more prevalent (under Boltzmann statistics). The data are processed in a loop over all sets of two consecutive time steps as $\{\{t_0, t_1\}, \{t_1, t_2\}, \dots, \{t_{n_t-1}, t_{n_t}\}\}$ where n_t is the total number of time steps, in case of multiple such series the data of subsequent series are appended. In experimental data, particles may not be present for the entire dataset as particles may e.g. leave or enter the field of view, or be erroneously assigned a new particle identifier in the trajectory-linking phase of the particle localisation procedure. Only particles present in both coordinate sets of the time interval are considered for force evaluation. Furthermore, in non-periodic boundary conditions, particles near the boundaries may experience forces due to interaction with particles *outside* of the measurement volume whose positions are unknown. Therefore, forces are only evaluated for particles which are at least r_{\max} away from *any* of the boundaries to avoid errors due to boundary effects. In case of periodic boundary conditions for simulated trajectories, no boundary effects are expected as long as the box size is larger than $2r_{\max}$, and all particles can be considered for force calculation. Lastly, particles may be excluded from force evaluation based on other (separately determined) criteria. Forces are calculated for each of ‘selected’ particles and each dimension separately using Eqs. 6.3 and 6.17 and stored as vector $\{f_{1,x}, f_{1,y}, f_{1,z}, f_{2,x}, \dots, f_{n,y}, f_{n,z}\}$ where n is the number of particles considered in the force calculation. The coefficient matrix is calculated for the first of the two coordinate sets defining the interval, such that the particle positions at the start of the interval are evaluated according to a forward finite difference scheme (Eq. 6.17). The coefficient matrix is constructed with rows for only the subset of selected particles considered in the force calculation, however, *all* particles, so including those omitted from force evaluation, are included in calculation of their coefficients such that the complete neighbourhood of radius r_{\max} is considered. That is, for each of the selected particles all neighbours up to r_{\max} are determined, converted to coefficients $C_{i,m}^\alpha$ and added to the appropriate bin m for each dimension α . A k -d tree neighbour searching algorithm from the open-source Python package *SciPy* (version 1.6.2) is used for improved computational performance.^[449] The counter is incremented for the number of particles contributing to each bin. Then, the dot products $\mathbf{C}^T \mathbf{C}$ and $\mathbf{C}^T \mathbf{f}$ are calculated for the entire time-interval, and added element-wise to \mathbf{X} and \mathbf{y} respectively. Finally, after all time intervals are processed in the loop, the least squares solution for the discretized pairwise force is calculated as $\bar{\mathbf{g}} = \mathbf{X}^{-1} \mathbf{y}$. In our analysis, any bins to which at fewer than 10^4 particle pairs contributed were considered insufficiently sampled and omitted from plotted results to avoid effects of limited statistics at small r .

6.8.3 Chemicals

The following chemicals were used: **ethanol** (100 %, VWR Chemicals no. 85651.360); **glycerol** (≥ 99.5 %, Sigma-Aldrich no. G7893); **LiCl** (ACS reagent grade, Supelco no. 105679); **bromocyclohexane** (Cyclohexyl bromide, CHB, 98 %, Sigma-Aldrich no. 135194); **cis/trans decahydronaphthalene (decalin, mix-**

ture of cis/trans isomers, synthesis grade, *Sigma-Aldrich* no. 803101); **cis-decahydronaphthalene (cis-decalin)**, 99 %, *Sigma-Aldrich* no. 110469); **tetrabutylammonium bromide (TBABr)**, ≥ 98.0 %, *Sigma-Aldrich* no. 426288).

6.8.4 Silica particle purification

After synthesis (see [Secs. 3.3.2](#) and [3.7.11](#)), a small number (~ 1 %) of dumbbells, clusters and secondary nuclei remained in the sample. These were removed by repeated centrifugation steps. A concentrated stock dispersion was diluted to ~ 1 vol.% silica in ethanol and placed in 14 mL centrifuge tubes (which are relatively tall/narrow with $\varnothing \approx 1$ cm). The time it took for the sample to fully sediment was determined by centrifuging and pausing the centrifuge at regular intervals to check progress; it was found to take ca. 15 min at 100 RCF using a swing-out rotor for the particles to fully sediment. Since the (rotationally averaged) sedimentation coefficient of a dumbbell is between 1.3 and $1.5\times$ that of a single sphere,^[411] the samples were re-dispersed and centrifuged for 10 min (*i.e.* two-thirds of the time it took to fully sediment) at which point nearly all dumbbells should have been sedimented (but not all single particles). The top 5 mL of each tube was almost entirely clear and was carefully removed and discarded to remove any smaller particles. The next 8 mL containing only spherical particles of the main population was carefully removed from the top and set aside. The remaining sample and sediments, containing nearly all the clusters and dumbbells, still consisted for >99 % (by number) of single particles and were diluted back to 14 mL per tube to repeat the procedure and extract more particles. This was repeated once more. Next, the extracted middle fractions were combined and the purification was repeated on the purified batch twice more, each time discarding the (clear) top 5 mL and keeping the remaining top 8 mL from each centrifuge tube. This resulted in a sample with virtually no clusters or secondary nuclei, and a sphere/dumbbell ratio of $\gg 10^3$. Finally, the particles were collected using centrifugation (100 RCF for 15 min in 14 mL centrifuge tubes using a fixed-angle rotor centrifuge) and redispersed in ethanol as a concentrated stock dispersion.

6.8.5 Experimental measurement of 2D dipolar interactions

Electric cell fabrication:

ITO-coated cover-slips (#1.5 thickness, resistivity: 30–60 Ω /sq.) were purchased from *Diamond Coatings* and used as the top and bottom electrodes in electric cells, for a schematic diagram see also [Figure 6.6](#). An ITO coated cover-slip was glued with the non-conductive side onto a standard glass microscopy slide (which acted as support) using UV glue (*Norland* optical adhesive no. 68). Two thin strips of standard #0 glass cover-slip, acting as spacers, were glued onto the ITO cover-slip separated by about ~ 1 cm, and a second ITO cover-slip was glued with the non-conductive side onto the spacers. Next, electrical wires were attached to the ITO using a few drops of electrically conductive silver paint (*SPI*), forming a conductive connection, and fixed firmly in place with UV glue. One side of the sample slit was closed with UV glue, and the whole stack was cured for at least 15 minutes under UV light (*UVP* no. UVGL-58, 6 W@365 nm) to assure full curing of the glue. Next, a sample was prepared by adding 15 μ L of the concentrated ethanolic particle stock and 5 μ L of an 0.20 M ethanolic LiCl solution to 480 μ L of a 31/69 wt.% glycerol/ethanol mixture. The sample was homogenised using a vortex mixer for 2 min after which the the sample cavity of the electric cell was filled with ca. 30 μ L of the particle dispersion, where care was taken that no air pockets remained. The open side was then closed with UV glue which was cured for several minutes during which the part of the cell containing the sample was covered with aluminium foil to prevent excess bleaching of the particles, after which the cell was checked for short-circuits between the electrodes.

Fluorescence microscopy measurements:

Electric cells were placed on an inverted microscope for at least 30 min. prior to the measurement to assure that the particles were fully sedimented. The system was imaged through a $40\times$ / NA1.25 oil immersion objective in widefield fluorescence mode onto a *Hamamatsu* C11440-22CU scientific CMOS camera (2048 by 2048 pixels, 6.5 μ m physical pixel size) operated in synchronous readout mode.

A sinusoidal 1 MHz AC electric field was generated using a *Agilent* 33120A signal generator, amplified with a *Krohn-Hite* 7602M wideband power amplifier in AC coupling mode and applied to the sample with the neutral (ground) connected to the outside facing electrode to prevent current leaking or capacitive load towards the objective lens through the immersion liquid. The applied voltage was measured directly at the wire connections using a *Tektronix* TDS3052 oscilloscope. For constant field measurements, the electric field was switched on at a certain RMS field strength E , and after ca. 1 minute equilibration time two 25 s image series were recorded in two different regions of the sample, the field being kept constant throughout. The field was then switched off for at least 5 min, after which the measurement was repeated at a different field strength. In case of automatic field switching, the signal generator was operated in gated output mode, where the output was switched on or off based on a gating signal generated using an *Arduino Nano* microcontroller, which switched the gating signal state on/off every $n_{\text{on}}/n_{\text{off}}$ frames based on counting the camera's timing output signal. Again, the sample was equilibrated at zero field for at least 5 min prior to the start of the measurement.

Data processing and particle localisation:

Particle coordinates were determined using the open-source *Trackpy* library (v0.4.2)^[456] (implemented in the *Python* programming language, v3.7.1), which is based on three steps: feature detection using the widely used intensity-weighted centroiding procedure,^[195] iterative refinement of feature coordinates for sub-pixel precision, and a linking procedure to correlate features between frames and obtain trajectories. A threshold for the integrated particle intensity was used to distinguish real particles from background noise. The coordinate boundaries were then reduced by one 'feature size' along all edges, to exclude any particles from the datasets which partially overlapped with the image boundaries. Sample drift due to *e.g.* vibration or solvent flow were determined as the ensemble mean displacement vector of all particles between subsequent frames, and subtracted from the particle coordinates in subsequent time steps such that the mean displacement over the series was zero. We note that this operation should not affect TA, since an additional unidirectional displacement on all particles cancels out exactly in the apparent force two particles in a pair exert on one another (although the estimated least-squared error in the force coefficients may be incorrect in case of non-zero sample drift). Cancellation of sample drift does not hold exactly for non-periodic boundary conditions since some particle pairs near the image boundaries will see only one of the two particles included in the force evaluation, but this effect still averages out with sufficient sampling provided that particles are equally likely to be near any of the boundaries. However, determination and correction for sample drift was necessary for determination of the diffusion coefficient (see below), and provided insight into the presence and magnitude of mechanical vibrations, thermally induced drifts, solvent flow due to field- or current-induced effects or due to leakage of the sample cell. Next, MSDs were determined for all particles separately, and a lower and upper bound of 0.12 and $1 \mu\text{m}^2/\text{s}$ were used to filter spurious trajectories (*e.g.* particles stuck to the glass and dumbbells/clusters), and particles outside of these bounds were not considered for force evaluation during the TA (although they *were* considered as part of the local environment in the force evaluation of other nearby particles). Any particles present in fewer than 10 consecutive time-steps were also excluded from force evaluation. Then, the TA as described in [Section 6.8.2](#) was used to analyse the trajectories. All experimental force profiles were computed with square wave BFs and typically $r_{\text{max}} = 10 \mu\text{m}$ and $M = 50$ were used.

Determination of the diffusion coefficient:

The friction factor $\gamma = k_B T / D_0$ was determined from measurement of D_0 from the same data used for TA, by calculating the ensemble mean squared displacement (EMSD) of a subset of 100 particles per image series. To verify that the motion of the particles was consistent with Brownian diffusion, the EMSD as a function of lag time Δt was fitted to power-law behaviour of the form

$$\text{MSD} = 2dD_0\Delta t^n \quad (6.32)$$

where d is the number of spatial dimensions ($d = 2$ in the case of sedimented silica particles) and n the power law exponent, which has a value of 1 for free Brownian diffusion, < 1 for sub-diffusive behaviour and $n > 1$ for super-diffusive behaviour. This was done by performing linear regression on the logarithms of the data, *i.e.* fitting $\ln \text{MSD} = a + n \ln \Delta t$, such that the slope gives the power-law exponent and the axis intercept $a = \ln 2dD_0$ the diffusion coefficient. The MSD values were weighted by the square root of the number of observations at each lag time since considerably more short lag time data was available. Experimental EMSDs of the silica particles at $E = 0 \text{ V}_{\text{RMS}}/\text{mm}$ together with the fitted parameters are shown in **Figure 6.7A**, a diffusion coefficient of $0.042 \mu\text{m}^2/\text{s}$ was found. The presence of a nearby wall is expected to increase hydrodynamic drag on the particles, and indeed the observed D_0 is lower than the theoretical value of $D_0 \approx 0.062 \mu\text{m}^2/\text{s}$ using the Stokes-Einstein equation $D_0 = k_B T / \gamma$. The diffusion parallel to a nearby interface is typically estimated using the work of Faxen^[518] where $D^{\parallel} = \lambda^{\parallel}(h)D_0$ with λ^{\parallel} given by

$$1 - \frac{9}{16} \left(\frac{\sigma}{2h + \sigma} \right)^2 + \frac{1}{8} \left(\frac{\sigma}{2h + \sigma} \right)^3 - \frac{45}{256} \left(\frac{\sigma}{2h + \sigma} \right)^4 - \frac{1}{16} \left(\frac{\sigma}{2h + \sigma} \right)^5 \quad (6.33)$$

where h is the gap spacing, *i.e.* the distance between the wall and the particle surface. However, this is valid only for $h/\sigma \geq 1$ while salt is added to screen the charges in the system used here, such that the particles are likely close to the glass surface. For gap sizes which are small compared to the particle size ($h \ll \sigma$) Goldman & Brenner *et al.*^[519] found the following asymptotic solution:

$$\lambda^{\parallel} = - \frac{2\Lambda(h) - 1.9086}{\Lambda(h)^2 - 4.325\Lambda(h) + 1.591} \quad (6.34)$$

where $\Lambda(h) = \ln(2h/\sigma)$, meaning that the diffusion coefficient may be as low as 25% of that in the bulk, assuming a gap spacing of $h \approx 10 \text{ nm}$. In our experiments the free (bulk) diffusion coefficient was not determined, and it is possible that it was higher than the calculated value due to *e.g.* a lower than estimated viscosity. To verify that the observed value was not affected by the finite particle concentration through interactions at longer time-scales,^[505] the measured value was compared to that obtained from fitting only short-time MSDs and excellent agreement was found (see below).

Determination of the particle localisation error:

The (squared) mean particle localisation error was obtained from the y-axis intercept (value at zero lag-time) of a least-squares linear fit of the short-time MSD (up to a maximum lag time of 0.06 s , $10^{-3} \tau$) as:^[507]

$$\text{MSD} = 2d \left(D_0 \Delta t + \chi_{\text{r}}^2 \right) \quad (6.35)$$

where $d = 2$ is the number of spatial dimensions. MSD values were weighted by the square root of the number of observations at each lag time. The localisation error was determined at zero electric field to avoid influence from *e.g.* interactions and field-induced solvent flows, but image quality were independent of field strength such that similar localisation errors are expected for all field strengths recorded at the same imaging parameters.

6.8.6 Experimental measurement of 3D electrostatic interactions

Sample preparation:

Prior to use, CHB was deionized to remove ions present due to photodegradation of the solvent (predominantly H^+ and Br^- ^[432]) by bringing ca. 35 mL of the solvent into contact with ca. 2 g of activated alumina (Al_2O_3 , 58 Å pore size, 205 m^2/g surface area, *Sigma-Aldrich* no. 199974) for at least 1 week in a vial wrapped in aluminium foil to prevent exposure to light, after which the alumina was replaced and the procedure was repeated twice more, resulting in a typical solvent conductivity of $< 20 \text{ pS/cm}$ (*Scientifica* no. 627 conductivity meter). CHB was then mixed with *cis*-decalin to form a 68/32 vol.% CHB/decalin mixture which matched the density and (nearly) the refractive index of the PMMA colloids. Some properties of the solvents and particles are given in **Table 6.3**. The mixture and

excess cleaned CHB were stored in the dark over molecular sieves (3 Å, *Sigma-Aldrich* no. 208582) to prevent a build-up of ions due to photodegradation of the solvent. Next, concentrated particle stock dispersion was prepared by dispersing 100 mg of PMMA colloids ($D = 1.73 \mu\text{m}$, polydispersity = 3 %, measured with static light scattering) in 500 μL of the CHB/decalin mixture and vortex mixing for at least 30 min to ensure the particles were fully dispersed. Samples for microscopy were then prepared with varying salt concentration (Fig. 6.11) by mixing 5.0 μL of the particle dispersion with 0, 2, 8, 16 or 32 μL of a 0.20 mM TBABr in CHB/decalin solution and 195, 193, 187, 179 or 163 μL clean CHB/decalin respectively to obtain a total volume of 200 μL for each sample with TBABr concentrations of 0, 2, 8, 16 and 32 μM respectively. For comparison of TA and test-particle insertion (TPI, Fig. 6.12), a more concentrated sample was prepared by mixing 184 μL clean CHB/decalin with 10 μL of the 200 g/L particle stock and 6 μL of the 0.20 mM TBABr in CHB/decalin solution. The samples were vortex mixed for 5 min directly prior to preparation of the microscopy cells. For each sample a microscopy cell was made by filling a flat glass capillary (50 mm \times 2.0 mm \times 0.20 mm \times $y \times z$ inner size, *VitroCom* no. 3520), gluing it to a standard microscopy slide while sealing both ends using UV glue (*Norland* optical adhesive no. 68) and curing it for 5 min under UV light (*UVP* no. UVGL-58, 6 W@365 nm) during which all but the ends of the capillary was covered with aluminium foil to prevent UV exposure of the sample.

Table 6.3: some properties of CHB, *cis*-decalin and PMMA. Here, ρ is the density, η the dynamic viscosity, n_D the refractive index at 589 nm, ϵ_r the relative dielectric constant, and superscripts refer to the temperature in $^\circ\text{C}$.

solvent	ρ^{25} (g/mL)	η^{25} (mPa s)	n_D^{25}	ϵ_r^{25}	refs.
CHB	1.326	1.4052	1.4935	7.92	[520,521]
<i>cis</i> -decalin	0.893	3.3011	1.4776	2.2	[44,522]
68 vol.% CHB/dec.	1.19	2.217*†	1.4876*	5.6	[439,523]
PMMA μPs	1.19	-	1.492	2.6	[44,512]

* determined for a 64 vol.% CHB/dec. mixture; † determined at 20 $^\circ\text{C}$

High-speed confocal microscopy:

High-speed volumetric imaging was achieved using a *VisiTech Infinity*³ pinhole array confocal scanning unit equipped with 488 nm and 532 nm laser lines and a *Hamamatsu* C11440-22CU scientific CMOS camera (2048 by 2048 pixels, 6.5 μm physical pixel size) and an inverted microscope body (*Leica DMI 8*) with a 63 \times / NA1.30 glycerol immersion objective with correction collar, placed in a *PI* piezo z -stage for fast z -axis scanning of the objective lens. The microscope was operated using custom drivers to allow for faster sustained 3D imaging whereby the scanner timing was used as master timing signal for both the camera and the z -stage. During volumetric imaging, the z -stage was moved up with a constant speed while continually acquiring 2D frames, rather than using the internal feedback loop to iteratively find the target height and subsequently recording one frame before moving to the next height as is more common in traditional confocal microscopy. To prevent overshooting of the objective when rapidly moving back to the starting position of the next frame, the objective was moved down using a smooth s -curve over the course of typically 30 2D frames prior to starting the next z -stack. By reducing vibrations and overshoot due to the inertia of the objective lens this allowed for faster over-all sustained 3D imaging rates. Data were recorded as multiple independent series of typically 200 z -stacks to reduce the effects of bleaching and to obtain a more representative dataset. Image stack size varied, but a typical size would be 1080 \times 856 \times 100 voxels (112 $\mu\text{m} \times 90 \mu\text{m} \times 50 \mu\text{m}$) at a 3D imaging rate of 1.75 frames/s (223 frames/s 2D). We note that faster imaging rates were in principle possible, for example using a higher 2D imaging rate (500 frames/s) and smaller stack size (1080 \times 336 \times 60 voxels)

allowed for sustained 3D imaging rates of more than 5 frames/s, but with the relatively long-ranged interactions used here this would have resulted in an infeasibly small effective sample volume in which particles could be considered for force evaluation.

Data processing and particle localisation:

To correct for inhomogeneous illumination —where the overall fluorescence intensity was up to ~50 % higher in the centre of the frame than at the edges, depending on the sample and imaging conditions— the 2D frames were divided by a maximum-normalised correction image, obtained by averaging the frames of the first z -stack and processing it with a triangular low-pass FFT filter with a width of 5 cycles per image width. Particle localisation, drift correction, removal of spurious trajectories (MSD < 0.15 or $> 1 \mu\text{m}^2/\text{s}$) and trajectory analysis were then all performed as described for the 2D experiments. The diffusion coefficient was determined as $0.099 \mu\text{m}^2/\text{s}$ (for $\Delta t < 5$ s), typical particle localisation errors were 0.43 and 0.83 nm for 2D imaging rates of ~200 frames/s and ~300 frames/s respectively, but varied slightly with each experiment due to variations in glass thickness and flatness of the capillaries and laser alignment, and were determined on a per-dataset basis as described previously.

6.9 Supplementary info

6.9.1 Finite difference analysis of forces from Brownian trajectories

In the trajectory analysis, we effectively probe what step a particle takes over some small but finite time interval Δt , and take the mean of many such steps. To describe this theoretically for 1-dimensional motion, one can find an expression for the probability density distribution of the particle positions at time $t + \Delta t$ due to the displacement over that interval, and calculate the first moment around its position at time t :

$$\langle \dot{x} \rangle(x_t, \Delta t) = \int_{-\infty}^{\infty} (x_{t+\Delta t} - x_t) P(x_t \rightarrow x_{t+\Delta t}) dx_{t+\Delta t} \quad (6.36)$$

where x_t the starting position at time t , $P(x_t \rightarrow x_{t+\Delta t})$ is the normalized probability density distribution to make a step from x_t to a new position $x_{t+\Delta t}$, and $\langle \dot{x}_{\text{FD}} \rangle = \langle x_{t+\Delta t} \rangle - x_t$ is the expectation value for the measured mean velocity when using a forward difference scheme. Calculation of the first moment is nothing more than determining a probability-weighted mean of the displacements to all possible final positions.

The probability distribution of making a certain ‘step’ depends on the time interval and system parameters such as the diffusion coefficient and forces acting on the particles. In the simplest case, we consider a particle with no external force. With no force term, the equation of motion (Eq. 6.2) consists only of Brownian motion with a well known solution to the Fokker-Planck equation given by

$$P(x_t \rightarrow x_{t+\Delta t}) = \frac{1}{\sqrt{4\pi D_0 \Delta t}} \exp\left(-\frac{(x_{t+\Delta t} - x_t)^2}{4D_0 \Delta t}\right) \quad (6.37)$$

with an expectation value for the average displacement being equal to 0.^[524,525] This result makes sense, since Brownian motion pushes the particles equally in all direction and thus positive and negative displacements cancel out during averaging (although the *second* moment famously gives a mean squared displacement of $2D_0 \Delta t$). Solving the Fokker-Planck equation for Brownian motion in the presence of an external force $F(x_t)$ is non-trivial for all but the simplest forces. However, if we again assume that Δt is sufficiently small such that the force remains constant over the entire time interval — $F(x_t) \approx F(x_{t+\Delta t})$ —, the displacement due to the force is constant and independent of the effect of Brownian motion and we can simply shift the probability density distribution by the expected displacement due to the force. Combining Eq. 6.38 with $F(x_t)\Delta t/\gamma$, we obtain

$$P_{\text{FD}}(x_t \rightarrow x_{t+\Delta t}) = \frac{1}{\sqrt{4\pi D \Delta t}} \exp\left(-\frac{(x_{t+\Delta t} - x_t - F(x_t)\Delta t/\gamma)^2}{4D \Delta t}\right) \quad (6.38)$$

for the probability density function of a forward step. Calculating the first moment using Eq. 6.36, we obtain the expectation value

$$\langle \dot{x}_{\text{FD}} \rangle(x_t, \Delta t) \approx \frac{F(x_t)\Delta t}{\gamma}, \quad (6.39)$$

demonstrating that the force may be correctly recovered using the trajectory analysis method in combination with a forward finite difference scheme.

Let us now take a similar approach for the backward finite difference. The probability density function for a particle to have been in a position $x_{t-\Delta t}$ some time Δt before arriving at reference position x_t is given by:

$$P_{\text{BD}}(x_{t-\Delta t} \rightarrow x_t) = \frac{Q(x_{t-\Delta t})P_{\text{FD}}(x_{t-\Delta t} \rightarrow x_t)}{\int_{-\infty}^{\infty} Q(x_{t-\Delta t})P_{\text{FD}}(x_{t-\Delta t} \rightarrow x_t) dx_{t-\Delta t}} \quad (6.40)$$

where the probability to make the step is equal to Eq. 6.38 with adjusted starting and ending positions, and $Q(x_{t-\Delta t})$ is the probability for a particle to have been at the starting position $x_{t-\Delta t}$, and the integral in the denominator assures the probability density function is normalised. In equilibrium conditions the particles follow Boltzmann statistics and it can be stated that

$$Q(x_{t-\Delta t}) \propto \exp\left(-\frac{\Delta U(x_{t-\Delta t} \rightarrow x_t)}{k_B T}\right) \quad (6.41)$$

where $\Delta U(x_{t-\Delta t} \rightarrow x_t)$ is the difference in potential energy between the previous and current position of the particle. Again assuming a constant force over the time interval, we can state that the energy difference is linear in the force as $\Delta U(x_{t-\Delta t} \rightarrow x_t) = (x_t - x_{t-\Delta t})F(x_t)$. Again calculating the expectation value for the displacement, we find that

$$\begin{aligned} \langle \dot{x}_{\text{BD}} \rangle(x_t, \Delta t) &= \int_{-\infty}^{\infty} (x_t - x_{t-\Delta t}) P_{\text{BD}}(x_{t-\Delta t} \rightarrow x_t) dx_{t-\Delta t} \\ &\approx -\frac{F(x_t)\Delta t}{\gamma} \end{aligned} \quad (6.42)$$

which is exactly equal to $-\langle \dot{x}_{\text{FD}} \rangle$. In other words, in equilibrium and for a sufficiently small time step, the expected position of a particle in the previous time step is the same as the expected position in the next time step, regardless of the force and current position. Due to this, a central finite difference scheme cannot be used: its result always averages to zero.

6.9.2 Particle size and gravitational height

To assure the two-dimensional nature of particles sedimented to the glass-liquid interface, we determined the minimum particle size for which >99.9% of particles are within one particle diameter from the interface. The equilibrium gravitational profile—the particle concentration as function of height—can be estimated as

$$c(h) = c_0 e^{-h/L_g} \quad (6.43)$$

where L_g is the gravitational height given by

$$L_g = \frac{k_B T}{m_b g} \quad (6.44)$$

with g the gravitational acceleration and m_b the buoyant mass, *i.e.* the difference in mass between the particle and the volume of solvent it displaces. Since this equilibrium profile never truly goes to zero, there is always some finite probability a particle makes an excursion into the third dimension. The

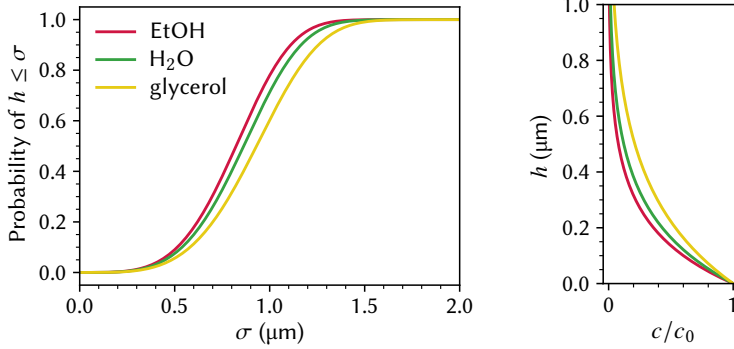


Figure 6.13: calculated sedimentation of silica colloids in some common solvents. A silica density of 2 g/mL , $g = 9.81\text{ m/s}^2$ and $T = 293\text{ K}$ were used. **A:** probability to find a particle within one diameter from the bottom as function of particle size. **B:** gravitational profile for a particle with $\sigma = 1.5\text{ }\mu\text{m}$ showing nearly all particles reside within $1\text{ }\mu\text{m}$ from the bottom.

probability of a particle having a height $h \leq h_{\max}$ can be found by normalizing Eq. 6.43 and integrating from 0 to z :

$$P_{h \leq h_{\max}}(h_{\max}) = \frac{1}{L_g c_0} \int_0^{h_{\max}} c(h) dh = 1 - e^{-h_{\max}/L_g}. \quad (6.45)$$

This probability can be interpreted as the fraction time a particle spends at most a distance h_{\max} from the bottom surface at any given time, or as the fraction of particles doing so at any given point in time. Note that these calculations do *not* account particle-particle or particle-glass interactions, nor the effect finite particle concentration has on the effective buoyant mass, and thus likely break down at high particle concentration where excluded-volume effects become significant.^[526] Eqs. 6.43 and 6.45 are plotted in Figure 6.13 for silica colloids to estimate the particle size needed for obtaining a reliably two-dimensional particle layer. A transition can be seen for a particle size of around $\sim 1\text{ }\mu\text{m}$, below which diffusion dominates and the gravitational height is large compared to the particle size, and above which gravity dominates and the gravitational height is small compared to the particle size. Indeed, plotting the predicted height distribution of $1.5\text{ }\mu\text{m}$ μPs shows that nearly all particles are within $1\text{ }\mu\text{m}$ from the bottom with only minor differences for different solvents (whose densities affect the buoyant mass). Taking as criterium for two-dimensionality that at any given time fewer than 1 in 1000 particles may exceed a height of 1σ , we find a minimum particle diameter of $1.53\text{ }\mu\text{m}$ (assuming water as dispersing medium).

6.9.3 Field strength determination

The field strength in the sample depends on several factors: the applied potential, the spacing between the electrodes, the dielectric structure of the stack and losses due to *e.g.* capacitive load. The spacing between electrodes was measured using conventional confocal laser scanning microscopy in reflection mode, where the reflection signal peaks at dielectric interfaces. The thickness of the bottom cover-slip was found to be consistently in agreement of the supplier specified thickness of $170 \pm 5\text{ }\mu\text{m}$, the sample volume was typically $160\text{ }\mu\text{m}$ thick. Because there are two different dielectric media between the electrodes (the sample and the glass cover-slip), the field strength is divided unequally over the two materials, and the field strength in the sample itself is given by:

$$E_s = V_{\text{in}} \frac{\epsilon_g}{\epsilon_s d_g + \epsilon_g d_s} \quad (6.46)$$

with V_{in} the potential difference between the electrodes. Taking the relative dielectric constants of the glass and sample as $\epsilon_g = 6.7$ ^[527] and $\epsilon_s = 26$,^[528] this results in a field strength within the sample of $\sim 1.2 V_{\text{in}}/\text{mm}$ (expressed as function of the applied input potential V_{in}). Note that the magnitude of the dipolar potential (through Γ_{dip}) is proportional to the square of the electric field, so to obtain the time-averaged interaction strength one must thus time-average the AC input potential *squared*, i.e. take the root-mean-square (RMS) voltage, and not the average absolute voltage (which differs by a factor $2\sqrt{2}/\pi$).

Electrical resistance in the wire-connections, the ITO layer and due to the reorganisation of the double layer on the dielectric surfaces in the sample combined with parasitic capacitance in the sample cell can act as a long-pass frequency filter (with typical charging time of RC , where R is the resistance and C the capacitance) and dampen out the applied AC field.^[529] Since the measurement of V_{in} occurs prior to the resistive connections, this dampening effect is not measured by the oscilloscope and the real cell potential may thus be lower than the measured value. A schematic diagram of the sample cell as RC circuit is given in **Figure 6.14C**. The capacitance of a finite parallel plate capacitor with two stacked different dielectric media (essentially two capacitors in series) is given as:^[530]

$$C = A\epsilon_0 \frac{\epsilon_s \epsilon_g}{\epsilon_s d_g + \epsilon_g d_s} \quad (6.47)$$

with A the plate area, ϵ_0 the vacuum permittivity and ϵ_s , ϵ_g the relative dielectric constants and d_s , d_g the thicknesses of the solvent/sample and glass respectively. In principle the areas of ITO over the glass spacers (which act in parallel to the main glass/sample stack) also contribute to the capacitance, however, due to the small area and lower dielectric constant of glass this had a negligible effect on overall capacitance. Assuming a typical overlap area of 4 cm^2 and resistance of $\sim 100 \Omega$ per wire connection this results in an estimated capacitance of $\sim 0.1 \text{ nF}$ and cut-off frequency $f_c = 1/(2\pi RC) \approx 7 \text{ MHz}$, which give negligible damping of $<1\%$ at 1 MHz . However, care should be taken because the damping factor scales highly nonlinearly with increasing RC time near the cutoff frequency and the calculated f_c is not that far from the field frequency. To illustrate this with an example, flipping the bottom coverslip with the conductive side to the inside of the cell would result in higher field strength (due to the smaller electrode spacing), but losses due to capacitive damping of nearly 20% of the field strength. Using a solvent with a higher dielectric constant such as water would exacerbate the problem further, giving capacitive losses of almost 60% at the electrodes when compared to the measured input potential. To experimentally verify that capacitive losses could be neglected in our samples, a special test sample cell was constructed in mostly the same way as the normal samples (same coverslips, same overlap area, same sample), except that it featured an additional set of connections on the ITO, providing an independent measurement point of the electrode potential (see **Fig. 6.14**). Applying a $1 \text{ MHz } 60.1 \pm 0.1 V_{\text{RMS}}$ input potential resulted in a measured cell potential of $59.8 \pm 0.1 V_{\text{RMS}}$ ($\sim 0.5\%$ loss) and no measurable phase shift, showing that capacitive losses can be neglected in these samples.

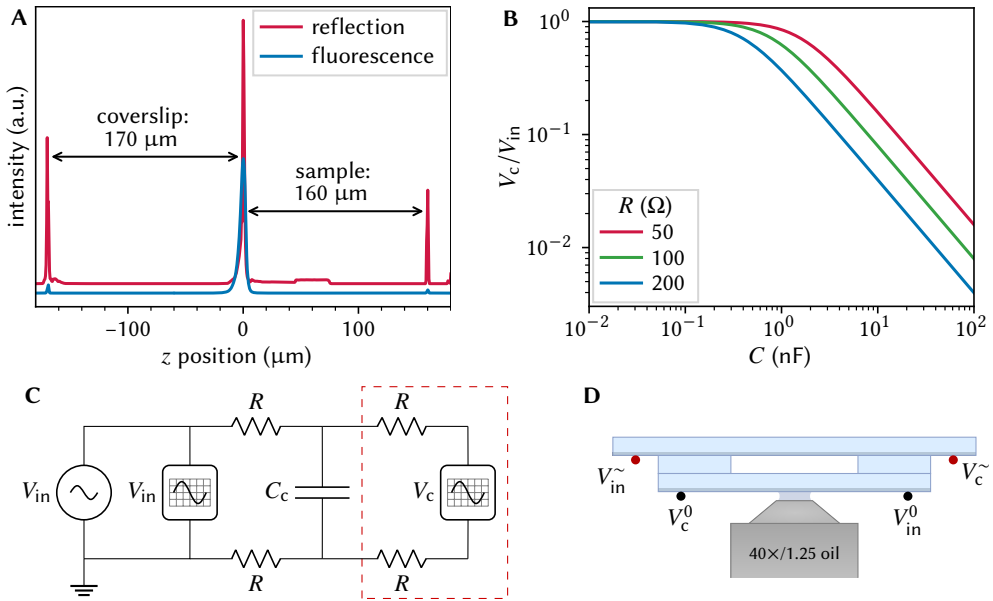


Figure 6.14: field measurement in electric cells. **A:** electrode spacing measurement with LSCM in reflection mode, with the fluorescence signal indicating position of the particles. **B:** damping factor at 1 MHz as function of cell capacitance C and connection resistance R . **C:** electric diagram of the sample cells. The area with the red dashed line is only present in the special test-cell with additional connections to measure the true cell potential. V_{in} and V_c are the RMS input and cell voltages measured with an oscilloscope. The resistance R of all wire-glass connections is assumed to be equal and was typically $\sim 100 \Omega$. The parallel ITO plates confining the (dielectric) sample are represented by the cell capacitance C_c . **D:** schematic of the test-cell, where superscripts \sim and 0 refer to the signal and neutral connections respectively.

CHAPTER 7

Measuring anisotropic interaction forces from multi-particle trajectories

ABSTRACT

While most particle systems possess approximately radially symmetric inter-particle interactions, particles with anisotropic interactions have been a subject of increasing interest due to the unique opportunities in self-assembly these systems present. However, few measurements of anisotropic interactions have been reported as we have seen in Chapter 2. In this chapter we show that the trajectory analysis method may be adapted to solve for anisotropic interaction forces, and apply this to multi-particle trajectory data of electrostatically stabilised colloids with externally applied AC electric field induced dipolar interactions. Using trajectory data from Brownian dynamics simulations we show that the correct anisotropic interaction forces may be recovered, although strong artefacts can occur when significant structural correlations are present due to the ordering of particles into string-like structures. Finally, we attempt to apply this method to a system of sterically and electrostatically stabilised micron-sized PMMA particles in an index- and density-matching solvent mixture, where dipolar interactions are induced using switching AC electric fields. By using a timed on-off switching cycle for the electric field the system may be driven out of equilibrium and thereby prevented from obtaining a large degree of structuring along the field direction. We show that anisotropic interaction forces may in principle be recovered in such a manner, although experimental limitations to the achievable 3D imaging rate in our set-up resulted in deviations in the observed forces.

7.1 Introduction

The vast majority of papers on interactions between colloidal particles have focused on spherical particles with isotropic—that is radially symmetric—interactions. There are several good reasons for this: many colloidal particle systems naturally tend towards approximately spherical particles because it minimises the surface area for a given volume and as a result, spherical particles are ubiquitous in natural as well as synthetic systems. And since most of the commonly encountered interaction types discussed in the introduction are not intrinsically directional beyond effects of the geometry of the surface, radially symmetric particles generally possess radially symmetric inter-particle interactions. In the context of measuring interactions, this has the major advantage that the interaction potential depends only on the inter-particle distance, and radially averaged distribution functions such as the $g(r)$ suffice to capture the relevant statistics and self-assembly behaviour of the system. In a more practical context, this also means that the orientation of the particles, which is typically much harder to determine than their positions, does not need to be known.

But ‘many’ does not mean ‘all’, and anisotropic particles and interactions have long been a subject of increasing interest since self-assembly of such particles can result in a whole host of structural phases not formed by isotropic particles.^[329,531] Arguably the most notable of these structures are colloid-based liquid crystals, which possess unique optical properties due to the anisotropy in their structure, and whose molecular cousins are widely used in *e.g.* display technology.^[532] But even spherical particles can possess anisotropy in their interactions due to *e.g.* magnetic or electric dipoles, or as a result of anisotropic surface chemistry such as in so-called ‘Janus particles’ and ‘patchy particles’. These anisotropic interaction forces are characterised not just by their inter-particle distance as $F(r)$, but depending on the degree of anisotropy in the system as $\mathbf{F}(\mathbf{r}_{ij}, \mathbf{u}_i, \mathbf{u}_j)$ where \mathbf{r}_{ij} is the displacement vector between the particles and \mathbf{u}_i and \mathbf{u}_j are the unit vectors giving their respective orientations.^[329]

In this chapter, we show that it is possible to extend the trajectory analysis (TA) method introduced in **Chapter 6** to solve for anisotropic interactions. We note that this possibility is not unique to the TA method and that it is, in principle, also possible to extend $g(r)$ based methods such as test-particle insertion to use the fully anisotropic $g(\mathbf{r}_{ij}, \mathbf{u}_i, \mathbf{u}_j)$. But regardless of which method is used, analysis of the fully anisotropic interactions would require enormously more data as there is a much larger parameter space to solve for: the data must be ‘divided’ over far more bins. Fortunately, the dimensionality of the problem may often be reduced since many particles only possess anisotropy along some of the axes, or may be considered as such with reasonable accuracy. For *e.g.* rod-like particles the interactions are generally expressed in terms of only the pairwise distance and the relative angle between the long axes of the particles. In the simulations and experiments here we consider particles with external field induced dipolar interactions. These may be achieved *e.g.* using magnetizable colloidal particles in an external magnetic field, or as we show here through the use of (AC) electric fields to induce dipole moments in dielectric colloidal particles, where the dipole moments are thus aligned along the field direction.^[533,534] This is similar to the quasi-2D system of dipolar interactions used in **Chapter 6**, except we now consider the full 3D interactions instead of only the isotropic plane perpendicular to the dipole axis. Again, AC electric fields with a frequency of 1 MHz are used so that the ions in the ionic double layer cannot follow the field while the electrons in the dielectrics can, thereby polarising the dielectric particles (but not the double layer) and preventing electrophoresis of the particles.

The advantage of using aligned dipolar interactions (as opposed to *e.g.* rotating permanent dipoles) in the context of this work is thus that all particles have the same ‘orientation’ (which we define as the orientation of the dipole axis, since the particles are otherwise isotropic) and therefore that only the particle positions need to be known to assess the particles’ relative orientations to one another, simplifying data collection. However, particles with induced dipolar interactions have also received wide interest because of their electro-rheology, where the rapid formation of string-like structures of colloids along the field direction can drive drastic changes in the rheological properties.^[509] Adding to this, the field-induced interactions give rise to interesting and rich phase behaviour: for example, the equilibrium structure for dipolar spheres (with a hard core) at high field and packing fraction was found to be a body centred tetragonal (BCT) phase rather than the FCC structure encountered for purely hard spheres, while at lower packing fraction so-called string fluids are observed, where the particles align in strings along the field direction which have fluid-like ordering in the plane perpendicular to the field, as well as a number of nonequilibrium phases.^[501,535] The particles used in this work (and indeed many colloidal systems) actually have significant soft electrostatic repulsions in addition to the field induced dipolar interactions, which results in so called *soft* dipolar interactions. Such systems have phase behaviour with even more complexity (including new crystal structures such as a body centered orthorhombic phase) depending on the balance of dipole strength, size of the electrostatic double layer, surface charge and volume fraction^[417,506,512,536]

7.2 Soft dipolar interaction forces

First, we introduce the soft dipolar interactions and how they can be theoretically modelled in more detail. These interactions are given by the sum of (isotropic) electrostatic interactions and (anisotropic) dipolar interactions due to dipole moments induced by external electric fields:

$$U(\mathbf{r}_{ij}) = U_{\text{es}}(\mathbf{r}_{ij}) + U_{\text{dip}}(\mathbf{r}_{ij}) \quad (7.1)$$

where $\mathbf{r}_{ij} = \mathbf{r}_j - \mathbf{r}_i$ is the displacement vector between the particles’ centres, *i.e.* the difference in their x , y and z positions. For our purposes the electrostatic interactions (U_{es}) were purely repulsive, while the dipolar interactions (U_{dip}) had both attractive and repulsive components depending on the relative orientations of the particles. The electrostatic interactions were modelled using a Yukawa potential, given in Eq. 6.21. The dipolar interactions were modelled using the following potential:^[506,536]

$$U_{\text{dip}}(\mathbf{r}_{ij}) = \frac{\Gamma_{\text{dip}}}{2} \left(\frac{\sigma}{r_{ij}} \right)^3 (1 - 3 \cos^2(\theta_{ij})) \quad (7.2)$$

where σ is the particle diameter, $r_{ij} = \|\mathbf{r}_{ij}\|$ is the pairwise distance, θ_{ij} is the angle between \mathbf{r}_{ij} and the direction of the dipole axes, and Γ_{dip} is the dipole strength (giving ‘contact’ potentials of $-\Gamma_{\text{dip}}$ and $\Gamma_{\text{dip}}/2$ at $r = \sigma$ along and perpendicular to the field direction respectively). For dipolar interactions induced by a high-frequency AC external electric field, Γ_{dip} may be calculated as:

$$\Gamma_{\text{dip}} = \frac{\boldsymbol{\mu}_i \cdot \boldsymbol{\mu}_j}{2\pi\epsilon_s\epsilon_0\sigma^3} \quad (7.3)$$

where $\boldsymbol{\mu}_i$ is the induced dipole moment of particle i depending on the local electric field \mathbf{E}_{loc} , which arises from the external field and the field of nearby dipolar particles ($\mathbf{E}_{\text{loc}} = \mathbf{E}_{\text{ext}} + \mathbf{E}_{\text{dip}}$).

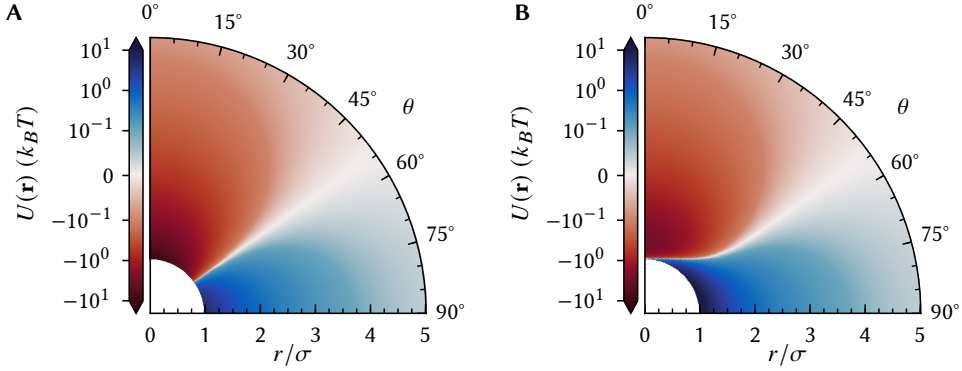


Figure 7.1: hard and soft dipolar potentials. **A:** interaction potential for two aligned dipolar particles with $\theta = 0^\circ$ the dipole axis, and a dipole strength of $\Gamma_{\text{dip}}/k_B T = 10$. **B:** the dipolar potential in **A** with electrostatic repulsion added using $\Gamma_{\text{yuk}}/k_B T = 10$ and $\kappa\sigma = 5$.

Here, we neglect perturbations of the local field due to nearby dipoles ($\mathbf{E}_{\text{loc}} \approx \mathbf{E}_{\text{ext}}$ ^[533,537]) and assume every particle has the same dipole moment $\boldsymbol{\mu}$ given by:

$$\boldsymbol{\mu} = \frac{\pi}{2} \varepsilon_s \varepsilon_0 \alpha \sigma^3 \mathbf{E}_{\text{ext}} \quad (7.4)$$

where α is the polarisability of the particles given as:

$$\alpha = \frac{\varepsilon_p - \varepsilon_s}{\varepsilon_p + 2\varepsilon_s}, \quad (7.5)$$

ε_0 is the vacuum permittivity and ε_p and ε_s are the dielectric constants of the particles and solvent respectively (assuming that at 1 MHz these are approximately the same as at zero frequency). Example plots of the dipolar and soft dipolar potential energy landscape as a function of r_{ij} and θ_{ij} are shown in **Figure 7.1**.

While the interaction potential is a scalar value, the force has both a magnitude and a direction and may instead be described by its magnitude along two perpendicular components:

$$\mathbf{F}(\mathbf{r}) = \mathbf{F}_{\text{es}}(\mathbf{r}) + \mathbf{F}_{\text{dip}}(\mathbf{r}) = F_{\text{es}}^{\parallel}(\mathbf{r}) + F_{\text{es}}^{\perp}(\mathbf{r}) + F_{\text{dip}}^{\parallel}(\mathbf{r}) + F_{\text{dip}}^{\perp}(\mathbf{r}). \quad (7.6)$$

where all displacement vectors are still pairwise but we have omitted the subscripts ij for brevity. Here we chose the directions parallel and perpendicular to \mathbf{r} , denoted F^{\parallel} and F^{\perp} respectively, such that the isotropic part $F^{\parallel}(\mathbf{r})$ dictates whether the particles experience an attractive (negative) or repulsive (positive) force with respect to each other, while the anisotropic part $F^{\perp}(\mathbf{r})$ dictates the torquing force the particle pair as a whole experiences towards (for negative forces) or away from (for positive forces) alignment with the dipole axis. For dipolar interactions, these force functions are given by:

$$F_{\text{dip}}^{\parallel}(\mathbf{r}) = -\frac{\partial U_{\text{dip}}(\mathbf{r})}{\partial r} = \frac{3\Gamma_{\text{dip}}}{2} \left(\frac{\sigma}{r}\right)^3 \frac{1 - 3\cos^2(\theta)}{r} \quad (7.7)$$

and

$$F_{\text{dip}}^{\perp}(\mathbf{r}) = -\frac{1}{r} \frac{\partial U_{\text{dip}}(\mathbf{r})}{\partial \theta} = -\frac{3\Gamma_{\text{dip}}}{2} \left(\frac{\sigma}{r}\right)^3 \frac{\sin(2\theta)}{r}. \quad (7.8)$$

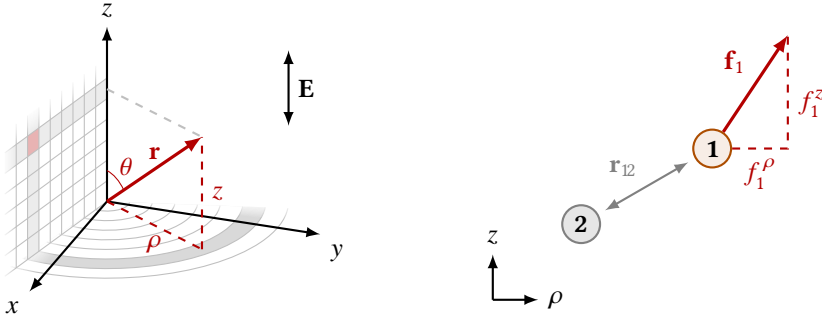


Figure 7.2: cylindrical coordinates used for anisotropic trajectory analysis. On the left, the discretisation/binning of inter-particle displacement vector \mathbf{r} into in-plane and axial distances ρ and z is schematically shown in with respect to the Cartesian xyz coordinates as obtained from particle localisation. The right shows the force experienced by a particle 1 as a result of some neighbouring particle 2 in this reduced 2D (ρ, z) plane.

Since the electrostatic repulsion is assumed to be isotropic, these forces only act along the displacement vector between the particles such that

$$F_{\text{es}}^{\parallel}(\mathbf{r}) = \frac{\sigma\Gamma_{\text{yuk}}}{r} e^{-\kappa(r-\sigma)} \left(\kappa + \frac{1}{r} \right) \quad (7.9)$$

while

$$F_{\text{es}}^{\perp}(\mathbf{r}) = 0 \quad (7.10)$$

and the anisotropic part of the force thus only depends on the dipole-dipole interactions.

7.3 Anisotropic trajectory analysis

Much of the underlying principles of trajectory analysis (TA) remain the same as introduced in [Section 6.2 of Chapter 6](#), in particular that the net forces along the different degrees of freedom in the system (typically along the x , y , and z axis) are extracted from the velocities of the particles. But where we previously only considered the inter-particle distances, now additional degrees of freedom must be introduced in the discretisation of the force depending on the dimensionality and symmetry of the system. However, the number of unknowns/bins—and with it the number of force measurements required for a certain precision— goes up with the power of the number of degrees of freedom. The system of aligned dipolar interactions we chose here has cylindrical symmetry, meaning that the anisotropy can be fully captured using only two dimensions. As shown in [Figure 7.2](#) these are the in-plane radial distance ρ and axial ‘height’ z , where the z direction is defined as the direction of the main dipole axis. In other words, like the isotropic case in the previous chapter the interaction forces are radially averaged, but only in the (2D) xy plane and not along the third (z) dimension.

In much the same way as in [Eq. 6.5](#) this allows for a discretised version of the pairwise force to be defined, except now the basis functions and coefficients depend on two parameters

(ρ and z) as follows:

$$\mathbf{F}(\mathbf{r}) \approx \sum_{m^\rho=0}^{M^\rho-1} \sum_{m^z=0}^{M^z-1} \mathbf{g}_{m^\rho, m^z} \phi_{m^\rho, m^z}(\mathbf{r}) \quad (7.11)$$

where M^ρ and M^z are the number of discretisation steps along the planar (ρ) and axial (z) directions, \mathbf{g}_{m^ρ, m^z} are the unknown coefficients and ϕ_{m^ρ, m^z} are the basis functions (BFs). For convenience, this may be rewritten as a single list of $M = M^\rho M^z$ bins as follows:

$$\mathbf{F}(\mathbf{r}) \approx \sum_{m=0}^{M-1} \mathbf{g}_m \phi_m(\mathbf{r}) \quad (7.12)$$

with $m \equiv M^z m^\rho + m^z$. As discussed however, the force is a vector quantity and can be expressed either by its magnitude and direction or by its magnitudes along two perpendicular components. Here, we consider the forces along the perpendicular axes of the cylindrical coordinate system, denoted as the force components F^ρ and F^z . In the same way, coefficients and basis functions in Eq. 7.11 may be split into g_m^ρ and g_m^z , and ϕ_m^ρ and ϕ_m^z . To further reduce the number of unknowns we make use of the symmetry of the soft dipolar interactions used here, namely:

$$F^\rho(\rho, -z) = F^\rho(\rho, z) \quad (7.13)$$

$$F^z(\rho, -z) = -F^z(\rho, z) \quad (7.14)$$

so that all data may be reflected into the half-space with positive z . We note that while we measure the interaction forces in terms of the ρ and z components, these can be trivially converted to the previously discussed parallel and perpendicular components (with respect to \mathbf{r}) through calculation of the magnitude $\|\mathbf{F}(\mathbf{r})\|$ and direction θ_F of the force. Examples of the interaction forces expressed in terms of these different components are also shown over the full z range in Figure 7.3 to show their symmetry. Using the symmetry above, ‘square wave’ BFs along both directions can be defined as:

$$\phi_m^{\rho, \text{sq}} = \begin{cases} 1 & \text{if } \lfloor \frac{\rho}{\Delta\rho} \rfloor = m^\rho \text{ and } \lfloor \frac{|z|}{\Delta z} \rfloor = m^z \\ 0 & \text{otherwise} \end{cases} \quad (7.15)$$

and

$$\phi_m^{z, \text{sq}} = \begin{cases} 1 & \text{if } \lfloor \frac{\rho}{\Delta\rho} \rfloor = m^\rho \text{ and } \lfloor \frac{z}{\Delta z} \rfloor = m^z \\ -1 & \text{if } \lfloor \frac{\rho}{\Delta\rho} \rfloor = m^\rho \text{ and } -\lfloor \frac{z}{\Delta z} \rfloor = m^z \\ 0 & \text{otherwise} \end{cases} \quad (7.16)$$

where $\Delta\rho = r_{\text{max}}/M^\rho$ and $\Delta z = r_{\text{max}}/M^z$ are discretisation step sizes (*i.e.* ‘bin widths’) and $\lfloor \dots \rfloor$ denotes the *floor* function. In this case the cut-off range for the force is implemented as an upper limit to the inter-particle distance (r_{max}) beyond which the force is assumed to be zero, although it would also be possible to use different cut-off values for ρ and z . Like

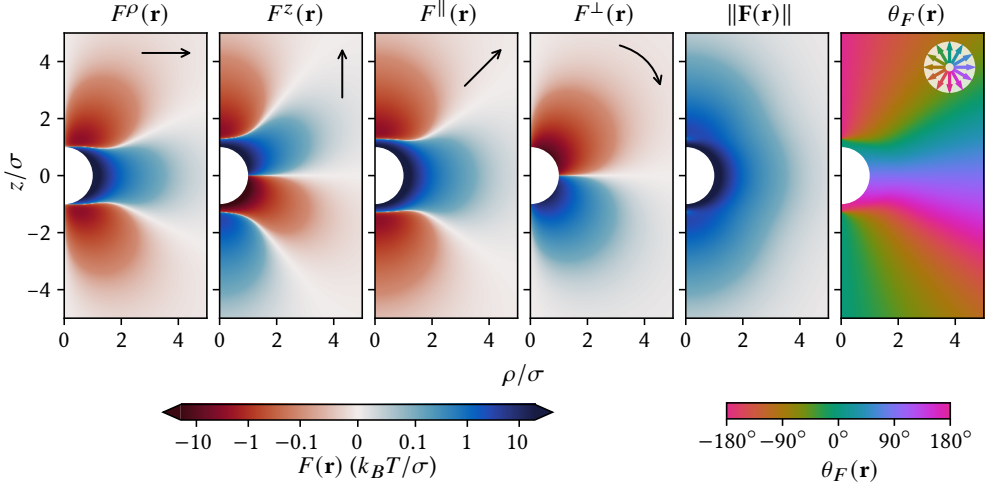


Figure 7.3: different representations of soft dipolar forces. Forces are shown along the axes of the cylindrical coordinate system (F^ρ & F^z), along or perpendicular to the particle-particle displacement vector (F^\parallel & F^\perp), and as the magnitude and direction/angle with respect to the dipole axis ($\|\mathbf{F}\|$ & θ_F), where $\Gamma_{\text{dip}}/k_B T = 10$, $\Gamma_{\text{yuk}}/k_B T = 10$ and $\kappa\sigma = 5$. Arrows indicate the direction of the (positive) force. It is clear that soft dipolar forces are symmetric in the plane at $z=0$, i.e. that $F^\rho(\rho, -z) = F^\rho(\rho, z)$ and $F^z(\rho, -z) = -F^z(\rho, z)$.

the isotropic case, it is also possible to define linear BFs as follows:

$$\phi_m^{\rho, \text{lin}} = \begin{cases} \left(m^\rho - \frac{\rho}{\Delta\rho} + 1 \right) \left(m^z - \frac{|z|}{\Delta z} + 1 \right) & \text{if } \lfloor \frac{\rho}{\Delta\rho} \rfloor = m^\rho \text{ and } \lfloor \frac{|z|}{\Delta z} \rfloor = m^z \\ \left(\frac{\rho}{\Delta\rho} - m^\rho \right) \left(m^z - \frac{|z|}{\Delta z} + 1 \right) & \text{if } \lceil \frac{\rho}{\Delta\rho} \rceil = m^\rho \text{ and } \lfloor \frac{|z|}{\Delta z} \rfloor = m^z \\ \left(m^\rho - \frac{\rho}{\Delta\rho} + 1 \right) \left(\frac{|z|}{\Delta z} - m^z \right) & \text{if } \lfloor \frac{\rho}{\Delta\rho} \rfloor = m^\rho \text{ and } \lceil \frac{|z|}{\Delta z} \rceil = m^z \\ \left(\frac{\rho}{\Delta\rho} - m^\rho \right) \left(\frac{|z|}{\Delta z} - m^z \right) & \text{if } \lceil \frac{\rho}{\Delta\rho} \rceil = m^\rho \text{ and } \lceil \frac{|z|}{\Delta z} \rceil = m^z \\ 0 & \text{otherwise} \end{cases} \quad (7.17)$$

and

$$\phi_m^{z, \text{lin}} = \begin{cases} \phi_m^{\rho, \text{lin}} & \text{if } z \geq 0 \\ -\phi_m^{\rho, \text{lin}} & \text{if } z < 0 \end{cases} \quad (7.18)$$

with $\lceil \dots \rceil$ denoting the *ceiling* function, and where we have expressed $\phi_m^{z, \text{lin}}$ in terms of $\phi_m^{\rho, \text{lin}}$ for brevity. We note that since each pair contributes to the nearest lower *and* higher bin positions along ρ and z , an extra row and column of bins at $\rho = r_{\text{max}}$ and $z = r_{\text{max}}$ are required to fully cover the $[0, r_{\text{max}})$ range when compared to square wave BFs.

To extract \mathbf{f}_i , the net force experienced by a particle i in a system of n particles, we again state that it is given as the sum of all pairwise interactions with neighbouring particles j :

$$\mathbf{f}_i = \sum_{\substack{j=1 \\ j \neq i}}^n \mathbf{F}(\mathbf{r}_{ij}). \quad (7.19)$$

This may then be combined with Eq. 7.12 to construct a system of linear equations which link the net forces experienced by the particles, as measured from the velocities, to the pairwise contributions in the form of F^ρ and F^z . The in-plane component F^ρ is extracted from the velocity components in the xy plane. The force experienced by a particle i along the x or y directions is given by:

$$f_i^\alpha \approx \sum_{\substack{j=1 \\ j \neq i}}^n \left[\frac{r_i^\alpha - r_j^\alpha}{r_{ij}} \sum_{m=0}^{M-1} g_m^\rho \phi_m^\rho(\mathbf{r}_{ij}) \right] = \sum_{m=0}^{M-1} g_m^\rho C_{i,m}^\alpha \quad (7.20)$$

where α denotes the x or y direction and r^α is the α component of the inter-particle displacement vector \mathbf{r}_{ij} , and we have defined coefficients $C_{i,m}^\alpha$ as

$$C_{i,m}^\alpha \equiv \sum_{\substack{j=1 \\ j \neq i}}^n \left[\frac{r_i^\alpha - r_j^\alpha}{r_{ij}} \phi_m^\rho(\mathbf{r}_{ij}) \right]. \quad (7.21)$$

When performing N force measurements, where we define a force measurement as the evaluation of the net force acting on one particle over one time interval, the above may then be written for both dimensions simultaneously as

$$\begin{pmatrix} f_1^x \\ f_1^y \\ f_2^x \\ \vdots \\ f_N^y \end{pmatrix} \approx \begin{pmatrix} C_{1,1}^x & C_{1,2}^x & \cdots & C_{1,M}^x \\ C_{1,1}^y & C_{1,2}^y & \cdots & C_{1,M}^y \\ C_{2,1}^x & C_{2,2}^x & \cdots & C_{2,M}^x \\ \vdots & \vdots & \ddots & \vdots \\ C_{N,1}^y & C_{N,2}^y & \cdots & C_{N,M}^y \end{pmatrix} \cdot \begin{pmatrix} g_1 \\ g_2 \\ \vdots \\ g_M \end{pmatrix} \quad (7.22)$$

or simply

$$\mathbf{f}^\rho \approx \mathbf{C}^\rho \cdot \mathbf{g}^\rho \quad (7.23)$$

where $\mathbf{f}^\rho \in \mathbb{R}^{2N}$ is a vector of the net forces acting along each direction on each particle in each measurement, $\mathbf{C}^\rho \in \mathbb{R}^{2N \times M}$ the matrix of coefficients which can be determined from the particle positions, and $\mathbf{g}^\rho \in \mathbb{R}^M$ is the unknown vector of force values in the ρ component of discretized pairwise force. The force along the z axis conversely depends only on the z components of the net force and displacement vectors, and may be written directly as

$$f_i^z \approx \sum_{\substack{j=1 \\ j \neq i}}^n \left[\sum_{m=0}^{M-1} g_m^z \phi_m^z(\mathbf{r}_{ij}) \right] \quad (7.24)$$

or shorter as

$$\mathbf{f}^z \approx \mathbf{C}^z \cdot \mathbf{g}^z \quad (7.25)$$

where the coefficients $C_{i,m}^z$ are defined as

$$C_{i,m}^z \equiv \sum_{\substack{j=1 \\ j \neq i}}^n \phi_m^z(\mathbf{r}_{ij}). \quad (7.26)$$

and $\mathbf{f}^z \in \mathbb{R}^N$, $\mathbf{C}^z \in \mathbb{R}^{N \times M}$ and $\mathbf{g}^z \in \mathbb{R}^M$. Finally, ‘best fit’ values for the unknown force coefficients g_m^ρ and g_m^z can then be determined as ordinary linear least squares solutions of Eqs. 7.23 and 7.25 in the same way as in the isotropic case.

7.4 Trajectory analysis of simulated data

The performance of anisotropic TA was evaluated by analysis of trajectories with known soft dipolar interaction forces, generated using Brownian dynamics simulations. Like in the previous chapter the simulation time step size Δt_{sim} was always set 50× smaller than the analysis time step Δt_{ta} to assure the (itself discrete) simulations accurately represented continuous trajectories. First, we simulated a fluid-like system of $n = 256$ soft dipolar particles with $\Gamma_{\text{dip}}/k_B T = 10$, $\Gamma_{\text{yuk}}/k_B T = 10$ and $\kappa\sigma = 5$ at a number density of $\varrho\sigma^3 = 0.07$ as a single simulation run of $4 \cdot 10^7$ simulation steps of $\Delta t_{\text{sim}}/\tau = 2 \cdot 10^{-5}$, where $\tau = \sigma^2/D_0$ is the free self-diffusion time of the particles. The trajectory data were then analysed using TA at a measurement interval of $\Delta t_{\text{ta}}/\tau = 10^{-3}$, giving a total number of force measurements of $N \approx 2 \cdot 10^8$. This was a much larger number of force measurements than was typically used for isotropic TA, given that due to the 2-dimensional parameter space the number of unknowns in the anisotropic case (the number of bins, typically $M = 45^2$) was the square of the equivalent number of unknowns in isotropic TA for any given precision. The interaction forces used as input for the simulations are shown together with the forces extracted using anisotropic TA in **Figure 7.4** for both square wave and linear BFs, simulation snapshots showing the fluid-like structure are also shown at the end of this chapter in **Figure 7.12**. It is clear that for most of the parameter space, both the magnitude and direction of the interaction forces are correctly recovered. When looking at the difference between the measured forces and the known input forces (**Figs. 7.4M to P**), the magnitude of the interaction forces is slightly underestimated at inter-particle distances close to contact for both types of BFs. This is where the forces are the largest and have the steepest gradients, which is comparable to where the TA results of isotropic data showed deviations from the input forces. Similarly, the magnitude of $F_{\text{sq}}^{\parallel}(\mathbf{r})$ is underestimated by up to $\sim 0.5 k_B T/\sigma$ around the energy minimum at $z/\sigma \approx 1.2$ and $\rho/\sigma < 1.5$ where the gradient of the force is steep due to the interplay between attractive dipolar and repulsive electrostatic interactions.

Curiously, a similar region is present roughly one particle diameter further along the z direction, where the magnitude of the attractive forces is underestimated even though the force gradient is comparatively low, being similar to other regions of the parameter space where such artefacts are *not* observed. This shows that deviations are not exclusively related to the interplay of the force gradient with the finite measurement interval. Instead, this ‘secondary peak’ in the error for $F_{\text{sq}}^{\parallel}(\mathbf{r})$ is likely related to structural correlations, as can be seen in the cylindrical distribution function $g(\mathbf{r})$ (**Fig. 7.4D**).^{*} While the particle density and interaction strength of this system mean that it is still in a fluid-like state, there is significant structuring with a peak value of over 10 in the $g(\mathbf{r})$ due to particles forming dimers and trimers which align along the z axis. Analysis with linear BFs conversely appears less sensitive to these correlations, with the error not exceeding $0.1 k_B T$ for $r/\sigma > 1.2$. Nonetheless, even the deviations observed using square wave BFs were small compared

^{*} the cylindrical distribution function $g(\mathbf{r})$ or $g(\rho, z)$ is simply the first anisotropic equivalent of the (isotropic) radial distribution function $g(r)$ (which was discussed extensively e.g. in **Chapter 4**), and gives the probability of finding a particle pair with a certain radial and axial offset (ρ, z) , normalised to this probability in an uncorrelated system at equal density. Calculation of the $g(\mathbf{r})$ is described in more detail in **Sec. 7.8.2**.

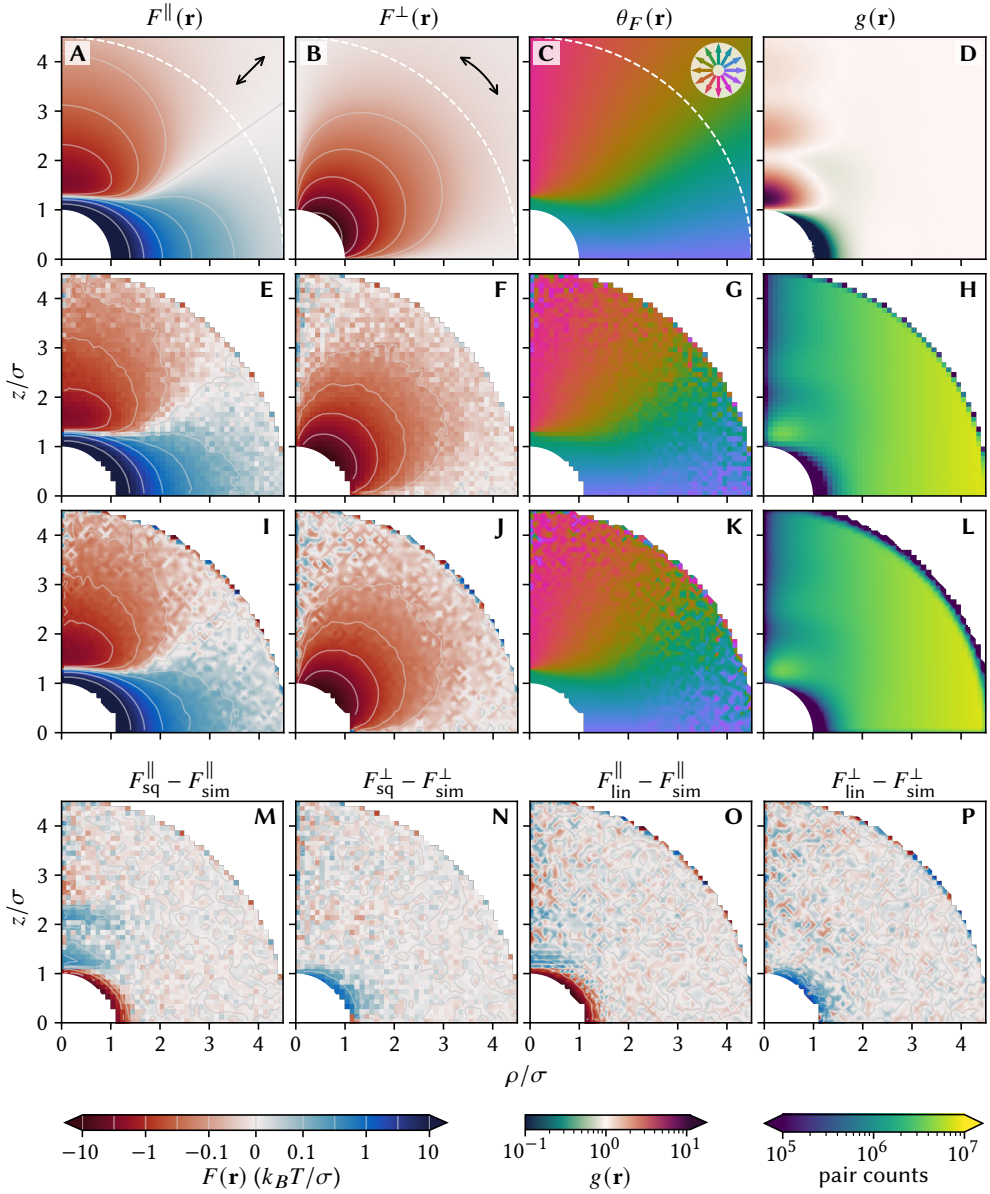


Figure 7.4: trajectory analysis of soft dipolar spheres in the fluid phase. Data were simulated using $\Gamma_{\text{dip}}/k_B T = 10$, $\Gamma_{\text{yuk}}/k_B T = 10$, $\kappa\sigma = 5$ at $\rho\sigma^3 = 0.07$, with **A–C** showing the interaction forces which were used as input for the simulations. TA was performed using $\Delta t_{\text{ta}}/\tau = 10^{-3}$, $r_{\text{max}}/\sigma = 4.5$, and $M^z = M^P = 45$. **D**: the cylindrical distribution function $g(\mathbf{r})$ of the simulated dataset. **E–H**: force profiles and (unnormalised) pair counts per bin obtained from TA of the simulated data using square wave BFs. **I–L**: data obtained from TA using linear BFs. **M–P**: deviations/errors of the measured interaction forces with respect to the simulation input, for the use of square and linear BFs respectively. For force profiles, bins with fewer than 10^3 pair counts are not shown.

to the forces at those distances and overall the TA method performed well, showing that anisotropic interactions could be quantitatively recovered from trajectory data in most of the parameter space. At larger distances where the forces and force gradients are lower ($\sim r/\sigma > 2$), the errors in the forces were only the result of Brownian ‘noise’ and finite sampling intrinsic to trajectory analysis, with root-mean-squared (RMS) deviations χ_F of around $0.02 k_B T$ for each of the components and types of BFs, which was well in line with Eq. 6.23 for 10^6 to 10^7 pair counts per bin.

Next we studied the performance of TA in a system with a higher dipole strength and shorter ranged electrostatic interactions ($\Gamma_{\text{dip}}/k_B T = 30$, $\Gamma_{\text{yuk}}/k_B T = 10$, $\kappa\sigma = 15$) at otherwise the same parameters, such that the equilibrium state was a so called string fluid in which the particles aligned in strings in the direction of the external field but had only fluid-like ordering in the xy plane. Results from TA are shown in Figure 7.5 together with the interaction forces used as input for the simulations and the $g(\mathbf{r})$ of the simulation dataset, which now showed significantly more and higher peaks. Simulation snapshots are also shown in Figure 7.13. It is immediately clear that the measured interaction forces were strongly affected by the structural correlations in the sample along the dipole axis, and that TA could not recover the correct forces under these conditions using either type of BFs. Periodic/oscillating patterns are present in F^{\parallel} along the z direction at low ρ , coinciding with the direction along which strong spatial correlations were present due to the string formation. A comparison of the real and observed parallel forces using square wave BFs reveals that for separations around the primary energy minimum —*i.e.* in the position of nearest neighbours in the strings— the magnitude of the attractive force was under- or overestimated by more than $10 k_B T$ when moving around the equilibrium separation to slightly smaller or larger z separations respectively, whereas the magnitude of the attractive forces around subsequent peaks in the $g(\mathbf{r})$ got overestimated at smaller z and vice versa by around 8, 5 and $2 k_B T$ for the second, third and fourth nearest neighbours respectively. In other words, the recovered forces appear as if some of the forces due to nearer neighbours were instead assigned to particles at larger distances in the strings.

In some sense, it should not come as a surprise that the TA method could not distinguish which neighbour was ‘responsible’ for a certain fraction of the force, since the parameter space was sampled extremely inhomogeneously. As seen in the $g(\mathbf{r})$ there were over five orders of magnitude difference in the likelihoods of finding certain pairwise distances along the string direction due to the one-dimensional nature of the ordering, a fact which was also directly reflected in the number of particle pairs sampled for each bin in the trajectory analysis. Furthermore, the sampling of certain bins is strongly codependent when particles are all part of strings, and independent values for the coefficients can thus not be expected. Nonetheless, we stress that the resulting force is the true least squares solution to the data, which in this case are exact simulated trajectories and which were not subject to measurement noise. So why are the resulting oscillating forces a better predictor for the measured velocities than the ‘real’ forces in the simulations, within the context of trajectory analysis and its assumptions/limitations?

TA relies on a number of approximations: forces are assumed to be constant over the velocity measurement interval, to be perfectly described by a discrete set of basis functions and coefficients, to be recoverable from noisy data by mean of averaging out Brownian motion and to be strictly pairwise. The latter of these can be immediately ruled out due to the simulated nature of the trajectories in this case, as the simulations only accounted for

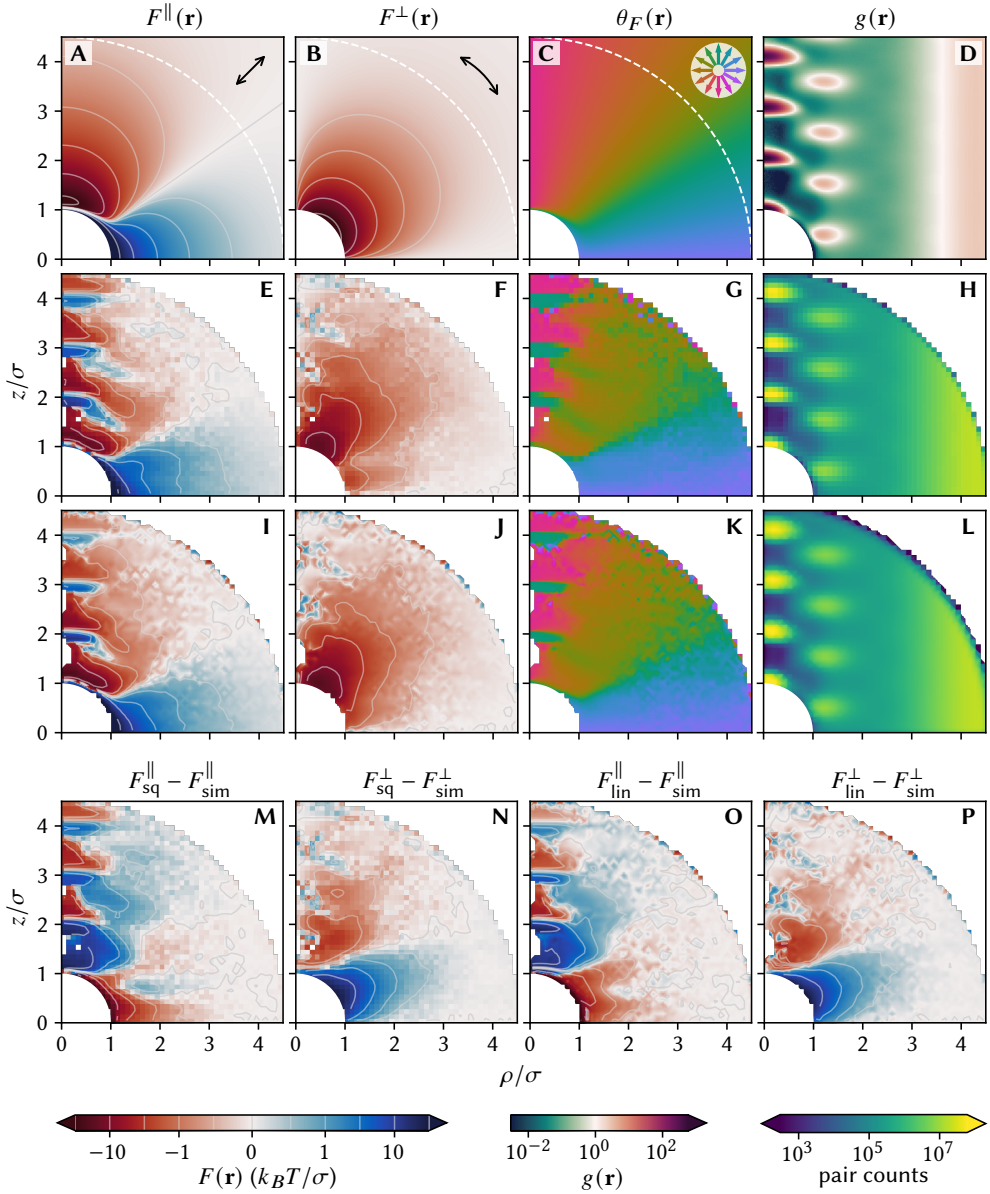


Figure 7.5: trajectory analysis of soft dipolar spheres in a string fluid. Data were simulated using $\Gamma_{\text{dip}}/k_B T = 30$, $\Gamma_{\text{yuk}}/k_B T = 10$, $\kappa\sigma = 15$ at $\varrho\sigma^3 = 0.07$, with **A–C** showing the interaction forces which were used as input for the simulations. TA was performed using $\Delta t_{\text{ta}}/\tau = 10^{-3}$, $r_{\text{max}}/\sigma = 4.5$, and $M^z = M^{\rho} = 45$. **D**: the cylindrical distribution function $g(\mathbf{r})$ of the simulated dataset with logarithmic colour scaling. **E–H**: $F(\rho, z)$ force profiles and pair counts obtained from TA of the simulated data using square wave BFs. **I–L**: data obtained from TA using linear BFs. **M–P**: deviations/errors of the measured interaction forces with respect to the simulation input, for the use of square and linear BFs respectively. For force profiles, bins with fewer than 10^3 pair counts are not shown.

pairwise interaction forces. Removing the Brownian component of the displacements used for TA* decreased the noisiness of regions of the force profiles with low sampling rates as expected, but did not significantly affect the much stronger artefacts due to correlations. Although there are always artefacts due to the finite time resolution —as discussed in more detail for isotropic TA in [Section 6.3](#)— this was also found to not be the sole reason for the deviations from the true interaction forces observed here: analysis of trajectories using a smaller time-step of $\Delta t_{\text{ta}} = 10^{-4}\tau = 50\Delta t_{\text{sim}}$ or even of ‘perfectly sampled’ data where $\Delta t_{\text{ta}} = \Delta t_{\text{sim}} = 10^{-4}\tau$ both revealed similar oscillating artefacts in the forces along the string direction ([Fig. 7.14](#)). Of note is that for these higher or even ‘perfect’ sampling rates the TA using linear BFs suffered from significantly reduced artefacts when compared to square wave BFs. This was in contrast with the lower sampling rate of $\Delta t_{\text{ta}} = 10^{-3}\tau$ where either type of BFs performed similarly poorly, hinting that both the sampling rate and the nature of the discretisation play an important role when structural correlations are present. Nonetheless, large errors were still present even at high sampling rate and when using linear BFs. To verify this premise we simulated trajectory data using a discretised version of the force profile with square wave BFs, such that its interactions could be perfectly represented by the discretised force model used in the TA, and found that the correct interactions could be recovered only when no measurement rate artefacts were present *and* when the forces could be discretised exactly ([Fig. 7.15](#)).

We suggest that square wave BFs in particular are poorly suited to data of strongly correlated particle systems: in each bin the force is assumed to be constant, but the higher the gradient of the force (the steeper the force profile) the less accurate this approximation is for the distances near the edges of the bin. Because the force gradients are highest for nearest-neighbour distances, a discretized force profile in which the force associated with the nearest neighbour is lower and the remainder of the observed net force is instead ascribed to multiple further particles can minimize this effect, leading to a lower overall least squares error.[†] Although linear BFs can better approximate the continuous force, particularly at large force gradients, the same principles apply when the true forces are not perfectly linearisable, and when the particles form highly correlated structures such as the string fluids both types of BFs ultimately suffer from the same issue in TA where the least squares solution is not a good approximate of the force. For future work it would be in principle possible to implement a non-linear version of TA where some functional form is enforced for the interaction forces and fit parameters are optimized to minimize the difference between the predicted and observed interaction forces, or even to use a machine learning based approach^[184] to solve the system of observed forces and coefficients for some finite set of parameters. Such an approach may also require solving for fewer unknowns, and thus reduce the number of force measurements required for similar precision.

Alternatively, it is of course possible to do the interaction measurements in such a way that strong structural correlations are avoided and a more homogeneous sampling of configurations is assured so that all bins have sufficient independent data available. One way to achieve this is by measuring the system in a nonequilibrium state in which strong

* to clarify: in this case Brownian motion *was* still simulated for the trajectories such that the same part of the phase diagram was sampled as before, but TA was performed only on the part of the displacements which resulted from interactions (instead of the full Brownian+interaction induced displacements)

† the least squares error here being the difference between the observed net forces and those predicted by the least squares TA result, *i.e.* $\|\mathbf{f} - \mathbf{C} \cdot \mathbf{g}\|^2$, *not* the difference between the TA result and the real interaction forces used in the simulations

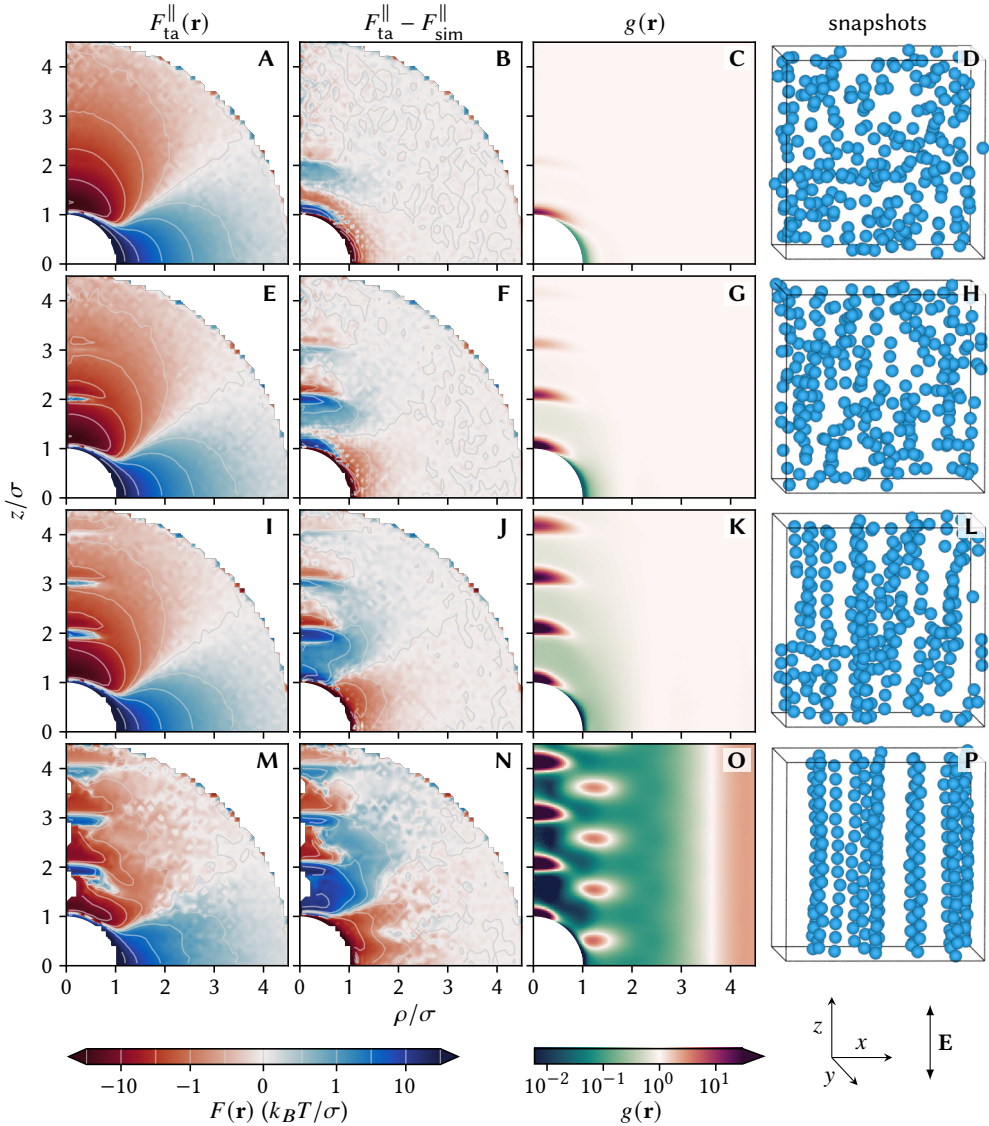


Figure 7.6: out-of-equilibrium TA during string formation. Data were simulated using $\Gamma_{\text{dip}}/k_B T = 30$, $\Gamma_{\text{yuk}}/k_B T = 10$, $\kappa\sigma = 15$ at $\varrho\sigma^3 = 0.07$, and analysed using $\Delta t_{\text{ta}}/\tau = 10^{-3}$, $r_{\text{max}}/\sigma = 4.5$ and linear BFs with $M^z = M^p = 45$. Data were simulated in a number of separate simulation runs of length 0.01τ (A–D), 0.05τ (E–H) or 0.25τ (I–L) such that the total number of force measurements was $2 \cdot 10^8$ in each case. Particle coordinates were initialised with a pseudorandom non-overlapping uniform distribution at the start of each run. Snapshots on the right show the structure at the end of a representative simulation run for each case. For comparison the results for a continuous simulation run (length $7.8 \cdot 10^2\tau$) are shown again in M–P.

correlations are not (yet) present. In our case, this was possible by performing analysis on data that had not yet equilibrated by initialising/equilibrating the system without an electric field present (and thus without the dipolar part of the interactions), and performing TA only on the trajectories right after the dipolar interactions were switched on in manner similar to the experimental out of equilibrium measurements in [Section 6.4.3](#) which were using switching electric fields to turn on or off the dipolar interactions. We simulated such data with a similar approach whereby the simulations were split up into many smaller simulation runs, each of which were initialised at the start as non-overlapping random coordinates, thereby giving the particle system in each simulation run less time to equilibrate and form strings than when performing simulations as one consecutive run. As shown in [Figure 7.6](#), artefacts from structural correlations were significantly reduced (although not avoided entirely) by measuring in a non-equilibrium state in which structural correlations were less severe.

7.5 Trajectory analysis of experimental data

For experimental measurement of anisotropic interactions, we again induced dipolar interactions through the use of high-frequency AC electric fields similar to the dipolar interactions in the two-dimensional trajectory measurements in [Chapter 6](#). Here however we applied electric fields to a system of charge stabilised PMMA colloids as was used for force measurements of isotropic charge-stabilised interaction forces in 3D. Again a density and refractive index matching solvent mixture of bromocyclohexane (CHB) and *cis*-decaline (70.8% CHB by volume) was used such that three-dimensional imaging using confocal microscopy was possible with negligible sedimentation and/or creaming for the duration of the measurements. This particle system could thus be used in combination with high-speed confocal laser scanning microscopy (CLSM) and particle localisation algorithms to study the anisotropic dipole-dipole interactions fully in 3D. The particles had a diameter of $\sigma = 1.675 \mu\text{m}$, and $2.65 \mu\text{M}$ of the organic salt tetrabutylammonium bromide (TBABr) was added to the dispersion to control the range of electrostatic interactions such that the dipole-dipole interactions were not completely obscured by long range electrostatic interactions. The sample was placed in a sample cell constructed from glass coverslips which on one side had a conductive coating of ITO and were separated with glass spacers, such that an electric field could be applied perpendicular to the imaging plane (along the optical axis, which we defined as the z axis). The construction and geometry of the electric cells are also shown schematically in [Figure 7.7](#) together with some example xz images from CLSM imaging, which show that the particles started to form strings when the field was kept on. To prevent string formation in the experiments for TA, a time-gated electric field was used, where the field alternated between ‘field off’ and ‘field on’ periods of respectively five and three time-steps long, with a field strength of $196 \text{ V}_{\text{RMS}}/\text{mm}$ @ 1 MHz during the ‘field on’ phases. The sample was imaged using high-speed CLSM as time-series of xyz stacks at an imaging rate of 1.77 stacks/s ($\Delta t/\tau = 2.1 \cdot 10^{-2}$). In total ~ 9000 stacks were recorded as multiple separate time-series of typically 500 time-steps long, containing typically 1000 particles each. Full experimental details on the sample preparation, imaging and data processing are given in [Section 7.8.5](#).

Analysis of the mean squared displacements (MSDs) from the trajectory data was used to estimate the friction factor as $\gamma = 9.6 k_B T \text{ s}/\mu\text{m}^2$ through fitting of the (short time) self-diffusion coefficient. Extrapolation of the MSD to zero lag time was also used to determine the localisation errors in the ρ and z directions separately, giving values of $\chi_{\text{r}}^{\rho} = 42 \text{ nm}$ and $\chi_{\text{r}}^z = 148 \text{ nm}$. In addition to the trajectory measurements, conductivity measurements of

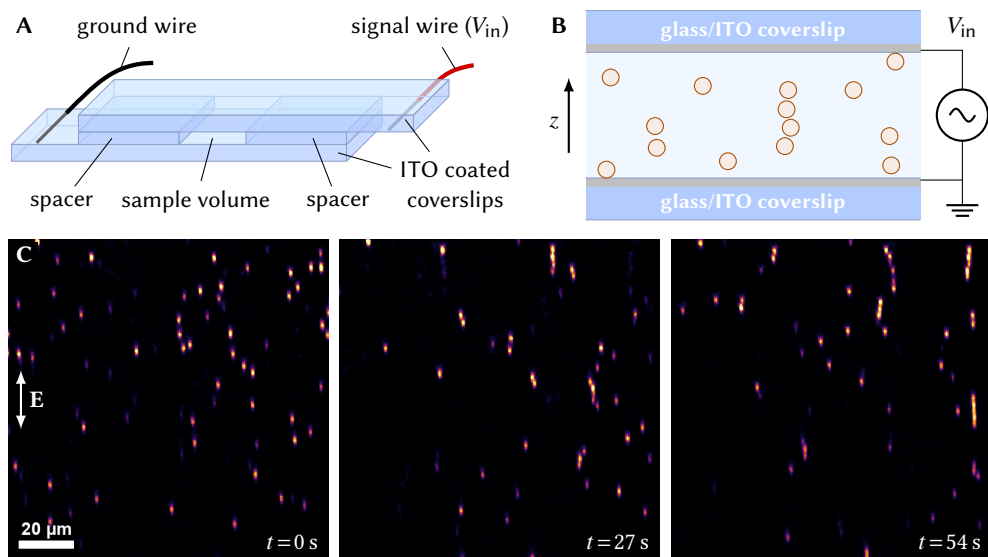


Figure 7.7: experimental samples for 3D dipolar interactions. ITO-coated cover-slips were used as optically transparent planar electrodes, separated by $\sim 130\ \mu\text{m}$ using glass spacers. **A:** overview of cell construction, where imaging was performed through the bottom (neutral) coverslip in an inverted microscope. **B:** schematic side-view of the sample cell with ITO electrodes depicted in gray. Glass thickness and particle size not drawn to scale. **C:** confocal microscopy xz sections taken during string formation of $1.68\ \mu\text{m}$ particles in a constant AC electric field of $196\ V_{\text{RMS}}/\text{mm}$ @ $1\ \text{MHz}$ along the optical (z) axis.

the solvent and micro-electrophoresis of the particle dispersion were performed to obtain an independent estimate for the interaction forces between the particles.^[515] Full details are given in **Section 7.8.6**, but briefly we used measurements of the solvent conductivity and literature values for the molar conductivity of TBABr to determine the ionic strength, thereby estimating the range of electrostatic interactions to be $\kappa^{-1} \approx 0.574\ \mu\text{m}$ ($\kappa\sigma \approx 2.91$), and used micro-electrophoresis to determine the number of surface charges as $Z \approx -135$, resulting in an electrostatic contact potential of $\Gamma_{\text{yuk}} = 17.9\ k_B T$. Finally, the strength of the dipolar interactions during the ‘field on’ phases was estimated using **Eq. 7.3** ($\epsilon_p = 2.6$, $\epsilon_s = 5.6$, $\sigma = 1.68\ \mu\text{m}$), giving an estimated contact potential of $\Gamma_{\text{dip}} = 40.9\ k_B T$.

The trajectory data were split into series of ‘field on’ phases and ‘field off’ phases which were analysed using cylindrical and isotropic trajectory analysis respectively. A representative set of particle coordinates are shown together with trajectory analysis results, the estimated interaction forces and the $g(\mathbf{r})$ in **Figure 7.8**. As shown in the snapshot and $g(\mathbf{r})$, the use of switching fields successfully enabled us to use relatively strong dipolar forces* such that the interactions were significantly anisotropic, without strong structural correlations in the form of the string formation previously described. As a sanity check we also performed cylindrical (*anisotropic*) TA on the ‘field off’ trajectories where the interactions should be isotropic as shown in **Figure 7.9**, and indeed found that $F^\perp(\mathbf{r}) \approx 0$ within the noise floor

* relative to the electrostatic interactions

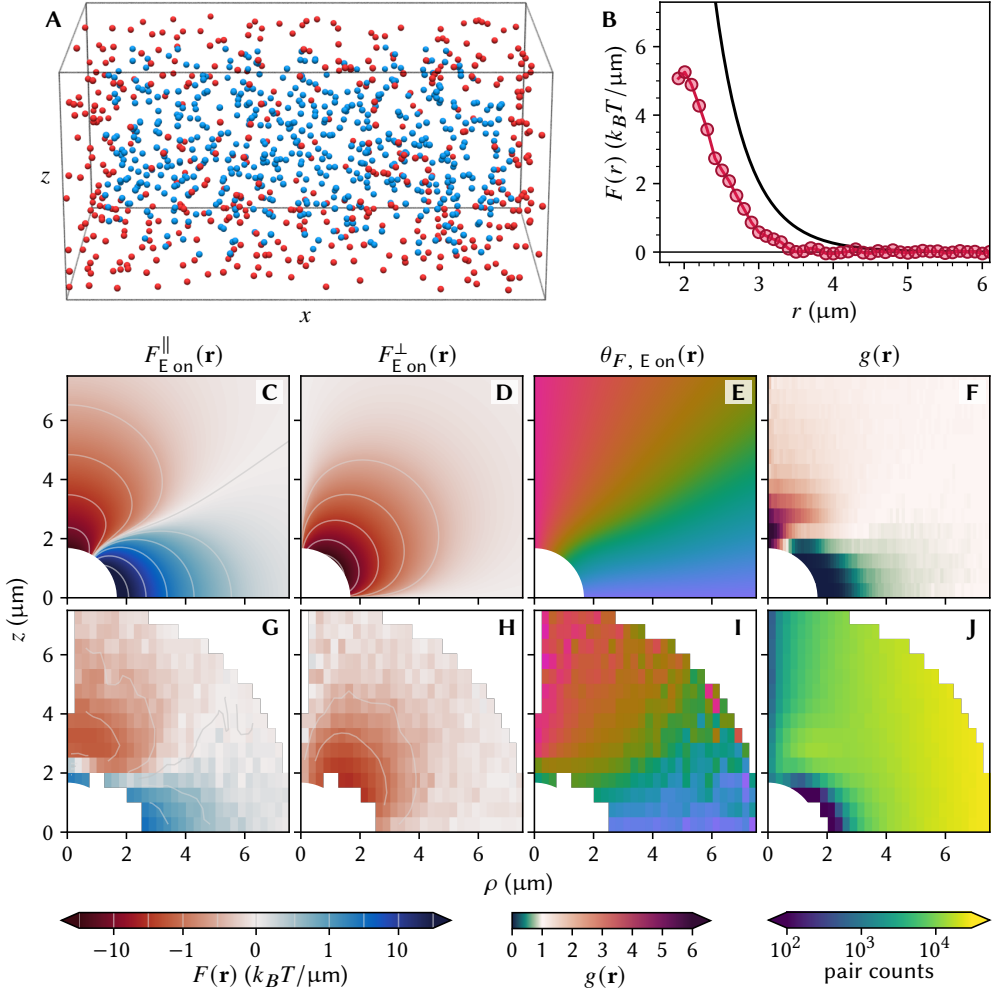


Figure 7.8: TA of 3D experimental trajectories of soft dipolar colloids. Trajectory data of $\sigma = 1.68 \mu\text{m}$ PMMA particles at $\varrho\sigma^3 = 0.009$ were recorded using high-speed CLSM at 1.77 frames/s ($\Delta t_{\text{ta}}/\tau = 0.021$) at a stack size of $1460 \times 696 \times 121$ voxels ($0.1 \mu\text{m} \times 0.1 \mu\text{m} \times 0.5 \mu\text{m}$ per voxel) with alternating ‘field off’ and ‘field on’ periods of 5 and 3 stacks respectively. **A**: rendering of a set of particle coordinates near the end of a 500 time-steps long image series ($t \approx 10\tau$), with particles used for force evaluation depicted in blue and particles closer than r_{max} from any image boundary in red. **B**: interaction force from isotropic TA of the part of the trajectory data where the electric field was off using 75 linear BFs up to $r_{\text{max}} = 7.5 \mu\text{m}$. **C–E**: estimated interaction forces during ‘field on’ phases. **F**: cylindrical distribution function during ‘field on’ phases. **G–J**: results from TA of the trajectory data during ‘field on’ phases, using $M^z = 15$ & $M^\rho = 30$ square wave BFs up to $r_{\text{max}} = 7.5 \mu\text{m}$.

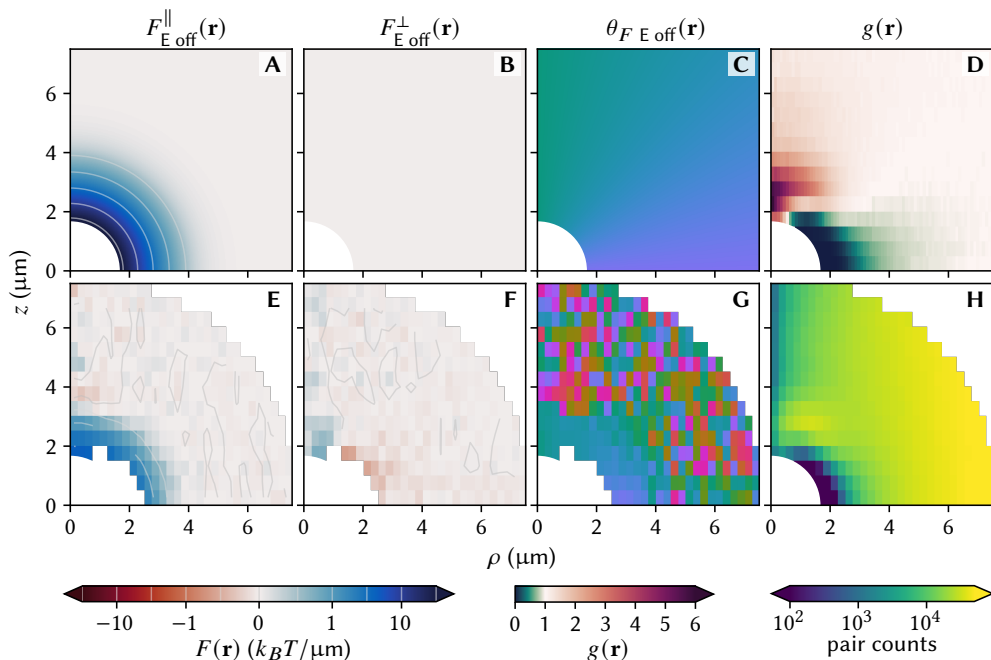


Figure 7.9: TA of 3D experimental trajectories during ‘field off’ phases. Data were from the same image series as Fig. 7.8. **A–C:** estimated electrostatic interaction forces. **D:** cylindrical distribution function during ‘field off’ phases. **E–H:** results from anisotropic (cylindrical) TA during ‘field off’ phases, using $M^z = 15$ & $M^\rho = 30$ square wave BFs up to $r_{\max} = 7.5 \mu\text{m}$.

for the entire parameter space, demonstrating that their isotropic nature could be correctly recovered and that the dipolar interactions were indeed switching on and off with the electric field. This means that if accurate not only are the results presented here—to the best of our knowledge—the first fully three-dimensional measurements of anisotropic interaction forces between colloids, they were achieved without relying on the the system being in equilibrium. Nonetheless, it is clear that the interaction forces obtained using TA do not resemble those expected based on our independent estimations of the dipole and electrostatic potentials, with an approximately fourfold difference in the magnitudes of both the isotropic and anisotropic interaction forces as well as qualitative differences in $F^\parallel(\mathbf{r})$ when the field was switched on. This throws up an important question: is there a reasonable explanation based on the work in the previous chapter for why the TA measurements resulted in such different forces, or may these results truly represent unexpectedly weaker interactions?

To get an idea of what results one could expect from TA under different conditions we simulated a dataset of the same size and density as the experimental sample using the estimated interaction forces (including switching the dipolar forces on and off), and analysed it as if it was experimental data* while accounting for different sources of errors that may be present in the experimental trajectories. The total sampling (depending on system size, ρ and N) of course affects the scatter in the data, the Brownian noise floor, but

* *i.e.* at the experimental time-step and without assuming periodic boundaries, see also Sec. 7.8.1 for details

this should not influence the shape and magnitude of the force profiles beyond that. Instead the perhaps most obvious culprit is the measurement rate, which when low can result in an underestimation of forces where the force gradient is large. Despite using equipment and methodologies specifically optimised for high-speed volumetric imaging, CLSM relies on inherently slow sequential scanning and the maximum achievable 3D imaging rate in our experiments was over an order of magnitude lower than what was probably ideal for our data. The finite speed affected the TA not only through the measurement rate itself—the time between consecutive snapshots—, but also through motion blur effects where particle positions represent a time-averaged position over some finite acquisition time, rather than a truly instantaneous positional measurement. Based on the number of 2D slice images in which a particle was typically visible, the acquisition time for a particle was estimated to be ca. 5 % of Δt_{ta} . Finally there were localisation errors, which may be corrected for to some extent using Eq. 6.24 but may still contribute further to inaccuracies in the measured forces.

Figure 7.10 shows the results from TA of data simulated to represent the experimental data with the above-mentioned artefacts. The extracted interaction forces were indeed significantly weaker than the true interaction forces as was the case for the experimental data, showing that these deviations can be largely explained by known artefacts of TA. It was found that by far the largest cause for the difference was the large time interval, with smaller but still significant reductions in the observed magnitude of the forces attributable to the presence of motion blur and localisation errors. For the latter this was particularly concentrated along the z direction due to the larger voxel size and lower resolutions, which also had the effect of slightly altering the relative magnitudes of forces in different directions. Nonetheless, the experimental data still exhibited lower interaction forces than even these ‘artefacted’ simulations. Specifically, we find an approximately 40 % lower apparent dipole strength and shorter-ranged electrostatic interactions. It is currently unclear if this is the result of unknown artefacts in the analysis, or due to inaccuracies in the estimated/calculated dipole strength. The latter is certainly a possibility since *e.g.* the dielectric contrast between the solvent and particles as well as the actual field in the sample were not measured directly, and there is some evidence for this in that the experimental $g(\mathbf{r})$ shows stronger correlations at larger z values than its simulated counterpart. Similarly, the shorter ranged electrostatic interactions may be due *e.g.* additional ions being introduced to the sample from the particle stock, the sample cell or due to decomposition of CHB. On the other hand, the presence of hydrodynamic interactions and potentially many-body effects such as perturbations of the local electric field due to the presence of nearby dipoles were all not accounted for in the analysis method and may thus introduce additional errors unaccounted for in our simulations.^[538] Ultimately though, these experiments highlight the challenging nature of the high time-sensitivity of TA in combination with the time consuming nature of 3D microscopy techniques: our results only hint at the true interactions after working backwards from an independent estimate, a procedure during which information is ultimately lost and which is thus not fully reversible.

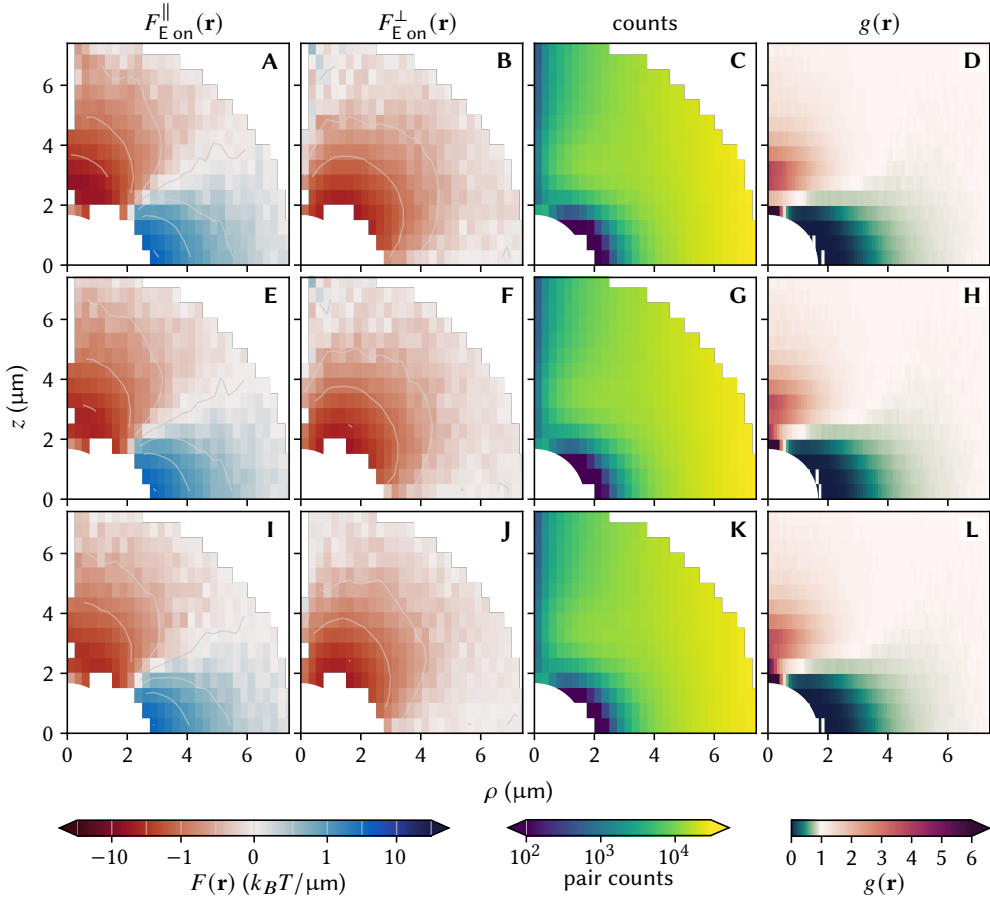


Figure 7.10: TA of simulations run using experimental parameters. Data were simulated using estimated experimental interactions and particle density and with a simulation box equal to the experimental imaging volume at $\Delta t_{sim}/\tau = 2.1 \cdot 10^{-6}$. In all cases TA was run on 10^7 force measurements without assuming periodic boundary conditions using $M^z = 15$ & $M^\rho = 30$ square wave BFs and $r_{max} = 7.5 \mu\text{m}$. **A-D**: interaction forces and $g(\mathbf{r})$ from data simulated without motion blur or localisation errors. **E-H**: interaction forces and $g(\mathbf{r})$ from data simulated with motion blur effects, for which coordinates were averaged over the first 500 steps of each 10^4 step cycle (so that $t_{ta}/\tau = 2.1 \cdot 10^{-2}$). **I-L**: interaction forces and $g(\mathbf{r})$ from data simulated with motion blur and measurement noise, which was simulated by adding normally distributed pseudorandom offsets with a standard deviation of $\chi_{\mathbf{r}}^\rho$ (to x and y coordinates) or $\chi_{\mathbf{r}}^z$ (to z coordinates).

7.6 Concluding remarks

In this chapter we have shown that analysis of interparticle trajectories as introduced in the previous chapter can be extended to account for 3D anisotropy, such that anisotropic interaction forces may be extracted from 3D trajectory data. This was demonstrated for particles with externally electric field induced soft dipolar interactions, which due to their cylindrical symmetry reduce the interaction forces to a 2D parameter space, thereby reducing the number of unknowns. Using simulated data, where interaction forces were known, we were able to show that interaction forces can be practically recovered for fluid-like systems, but found that structural correlations such as in the formation of the so-called string fluid phase can lead to severe errors in the extracted interaction forces with respect to the true pairwise forces. This was found to be due to the inexact nature of the analysis, which relies on assuming the interaction forces are exactly discretisable and remain constant over some finite time interval, neither of which is really true for experimental data. In combination with strongly co-dependent sampling of certain bins in the case of string formation, this resulted in the possibility of a lower least-squares solution where forces due to nearer neighbours were ‘attributed’ to particles further along in the strings. Neither these simulated data nor our implementation of TA however included or accounted for hydrodynamic interactions, and studying their effects on TA through simulations and/or experiments is one of our key recommendations for further research.

We then studied trajectory data of an experimental system of induced soft dipolar interactions of charge stabilised particles in an electric field, which allowed us to drive the system out of equilibrium such that string formation did not occur within the time-frame of the field-switching. Analysis of the 3D trajectories we obtained using high-speed confocal microscopy resulted in clearly anisotropic soft dipolar interaction forces, showing that it is experimentally feasible to obtain sufficient data for TA to work, but as expected the fastest practically achievable imaging rate was still at least an order of magnitude too low to obtain quantitatively accurate results. As a result, the measured interactions were over ten times weaker than what we estimated to be the ‘true’ interactions based using measurements of the field strength, surface charge and solvent conductivity. These deviations could be largely explained by the effects of the imaging rate and the relatively poor localisation accuracy, but some differences remain even then. As such it is fair to say that our results show that anisotropic interaction measurement of experimental data is possible in principle with our methodology, but that our particle system and microscopy speed were not sufficient to achieve this in practice.

Fortunately, there may be several means to mitigate the issue of measurement rate and provide more insight into the interaction forces in such anisotropic systems. Continuing improvements in methodology, (detector) technology and data analysis means that higher imaging rates for confocal microscopy than presented here should certainly be achievable, although we emphasise our measurements represent over two orders of magnitude faster imaging than is common for (conventional) 3D CLSM. Furthermore, techniques such as light-sheet microscopy structured illumination and holography can all already achieve orders of magnitude higher imaging rates than those used in our work.^[5] Since we are sensitive to the *relative* imaging rate—that is relative to the dynamics of the system—one can not only improve things by increasing the imaging rate but also by slowing down the dynamics through *e.g.* increasing the viscosity or using larger colloids. We performed preliminary experiments where highly viscous silicone oil was added in the solvent mixture in order to

increase the self-diffusion time more than tenfold, and while this was promising in terms of achievable imaging rates and extracted forces, the oil also strongly affected particle stability resulting in a large number of clusters. As a result we did not manage to obtain usable data within the time-frame of this thesis, but believe that with further optimisation this may be a feasible strategy to measure the interaction forces without such significant artefacts. We note again that it is in principle also possible to implement an anisotropic version of the iterative test-particle insertion method through *e.g.* the cylindrical distribution function and use the solvent-arresting and TPI approach discussed in [Chapter 4](#), and it would be highly interesting to compare the use of both methods for the soft dipolar interactions in this chapter and . We hope this work may be used as stepping stone to make interaction measurements of colloids with anisotropic interactions a practical reality in the near future.

7.7 Acknowledgements

This chapter was based in large parts on the work performed by Dinja Sanders for her Masters' thesis project under supervision of the author of this thesis, Laura Filion and Alfons van Blaaderen. She is acknowledged for extending TA to anisotropic systems with cylindrical symmetry using square wave BFs including memory-efficiency improvements which were vital to enable analysis of large datasets, extensive exploration of its performance on simulated data (which formed the basis for the simulation & analysis work in this chapter) and for performing the experimental work presented in this chapter as well as preliminary analysis thereof. Johan Stiefelhagen is acknowledged for synthesis of the PMMA particles. Peter Helfferich is thanked for his support with fast confocal microscopy and writing custom drivers for the microscope setup.

7.8 Methods

7.8.1 Brownian dynamics simulations

Brownian dynamics simulations, used to generate test-data with known interaction forces, were implemented as described in [Section 6.8.1](#) except using anisotropic interaction forces given along the the x and y directions by

$$F^\alpha(\mathbf{r}_{ij}) = \frac{r_i^\alpha - r_j^\alpha}{r_{ij}} F_{\text{yuk}}(r_{ij}) + \frac{r_i^\alpha - r_j^\alpha}{\rho_{ij}} F_{\text{dip}}^\rho(\mathbf{r}_{ij}) \quad (7.27)$$

where α denotes the x or y component respectively, $r_{ij} = \|\mathbf{r}_{ij}\|$, F_{yuk} was the Yukawa force given by [Eq. 6.22](#) and where the in-plane component of the dipolar force was calculated as:

$$F_{\text{dip}}^\rho(\mathbf{r}_{ij}) = -\frac{\partial U_{\text{dip}}(\mathbf{r}_{ij})}{\partial \rho} = \frac{3\Gamma_{\text{dip}}}{2} \left(\frac{\sigma}{r_{ij}}\right)^3 \frac{\rho_{ij}(\rho_{ij}^2 - 4z_{ij}^2)}{r_{ij}^4} \quad (7.28)$$

with ρ_{ij} and z_{ij} the ρ and z components of the inter-particle distance. The force along the z direction was calculated as

$$F^z(\mathbf{r}_{ij}) = \frac{z_{ij}}{r_{ij}} F_{\text{yuk}}(r_{ij}) + F_{\text{dip}}^z(\mathbf{r}_{ij}) \quad (7.29)$$

with the axial component of the dipolar force given as:

$$F_{\text{dip}}^z(\mathbf{r}_{ij}) = -\frac{\partial U_{\text{dip}}(\mathbf{r}_{ij})}{\partial \rho} = \frac{3\Gamma_{\text{dip}}}{2} \left(\frac{\sigma}{r_{ij}}\right)^3 \frac{z_{ij}(3\rho_{ij}^2 - 2z_{ij}^2)}{r_{ij}^4}. \quad (7.30)$$

The simulations were always run at a step size $50\times$ smaller than the time-step used in trajectory analysis and using 256 particles at a number density of $0.07\sigma^{-3}$ except when mentioned otherwise. Starting coordinates were initialised as a uniformly distributed pseudorandom coordinates where any overlapping particles ($r < \sigma$) were rejected and re-initialised until no overlaps were present.

7.8.2 Calculation of the cylindrical distribution function

The implementation for the cylindrical distribution function $g(\rho, z)$ largely follows the same principles as calculation of the isotropic radial distribution function $g(r)$ as described in [Section 4.9.1](#). A 2-dimensional histogram of particle pairs up to cut-off distances ρ_{\max} and z_{\max} is calculated in each time step for bins of ρ to $\rho + \delta\rho$ and z to $z + \delta z$, with bin widths $\delta\rho$ and δz . The number of counts in each histogram bin $H(\rho, z, \delta\rho, \delta z)$ is then normalised as follows:

$$g(\rho, z) = \frac{H(\rho, z, \delta\rho, \delta z)}{N\varrho V(\rho, z, \delta\rho, \delta z)} \quad (7.31)$$

where N is the total number of particles (*i.e.* particles per timestep times the number of timesteps), ϱ the number density, and $V(\rho, z, \delta\rho, \delta z)$ is the effective volume of the cylindrical shell inside the bounding box of the coordinates. For periodic boundary conditions up to a r_{\max} no larger than half the smallest box dimension the entire shell fits within the boundaries and is given simply by:

$$V(\rho, z, \delta\rho, \delta z) = \pi \left(\delta\rho^2 + 2\rho\delta\rho \right) \delta z. \quad (7.32)$$

For non-periodic cuboidal boundaries shell volumes are calculated on a per-particle basis as

$$V(\rho, z, \delta\rho, \delta z) = A_{\text{ring}}(\rho, \delta\rho)d(z, \delta z) \quad (7.33)$$

with A_{ring} the effective area of the circular ring in the ρ plane calculated as described for rectangular (2D) boundary conditions in [Sec. 4.9.3](#), and $d(z, \delta z)$ the thickness of the cylindrical ring along the z axis, given as

$$d(z, \delta z) = \sum_{h=\{h_{\min}, h_{\max}\}} \begin{cases} \delta z & \text{if } h - z \geq \delta z \\ h - z & \text{if } 0 < h - z < \delta z \\ 0 & \text{if } z \geq h \end{cases} \quad (7.34)$$

where h_{\min} and h_{\max} are the (absolute) distances of the particle to the lower and upper z boundaries respectively.

7.8.3 Implementation of trajectory analysis with cylindrical symmetry

Trajectory analysis with cylindrical symmetry was implemented in the *Python* programming language following largely the same methods as outlined for the isotropic case in [Section 6.8.2](#) with alterations as specified in [Section 7.3](#), *e.g.* using basis functions defined for the 2D (ρ, z) parameter space and the construction of separate matrices and lists for the ρ and z components of the force, $\mathbf{X}^\rho = (\mathbf{C}^\rho)^\top \mathbf{C}^\rho$, $\mathbf{X}^z = (\mathbf{C}^z)^\top \mathbf{C}^z$, $\mathbf{y}^\rho = (\mathbf{C}^\rho)^\top \mathbf{f}^\rho$ and $\mathbf{y}^z = (\mathbf{C}^z)^\top \mathbf{f}^z$, which have least squares solutions $\tilde{\mathbf{g}}^\rho = (\mathbf{X}^\rho)^{-1} \mathbf{y}^\rho$ and $\tilde{\mathbf{g}}^z = (\mathbf{X}^z)^{-1} \mathbf{y}^z$. The full code is available through the QR code provided on [page 193](#). For simulated data, forces were evaluated for all particles, and particle pairs were determined taking the periodic boundary conditions into account. For experimental data forces were evaluated only for those particles which were at least r_{\max} away from all image boundaries, taking their full neighbour shells (including particles near boundaries) into account in the calculation of the coefficient matrix. In case of linear BFs, an extra row and column of bins at ρ_{\max} and z_{\max} were used (*i.e.* $M = (M_\rho + 1)(M_z + 1)$) to correctly sample the final intervals, since each interval $(\rho, z) \rightarrow (\rho + \Delta\rho, z + \Delta z)$ is defined by the value of the coefficients at each of the four corners (see [Eq. 7.17](#)), as opposed to square wave BFs for which each interval is only defined by the lower left corner (through floor division in [Eqs. 7.15](#) and [7.16](#)).

7.8.4 Chemicals

The following chemicals were used: **bromocyclohexane** (Cyclohexyl bromide, **CHB**, 98 %, *Sigma-Aldrich* no. 135194); **cis-decahydronaphthalene** (**cis-decalin**, 99 %, *Sigma-Aldrich* no. 110469); **tetra-butylammonium bromide** (**TBABr**, ≥ 98.0 %, *Sigma-Aldrich* no. 426288).

7.8.5 Experimental measurement of 3D trajectories

Sample preparation:

Prior to use, CHB was deionized to remove ions present due to photodegradation of the solvent (predominantly H^+ and Br^- [432]) by bringing ca. 35 mL of the solvent into contact with ca. 2 g of activated alumina (Al_2O_3 , 58 Å pore size, 205 m^2/g surface area, *Sigma-Aldrich* no. 199974) for at least 1 week in a vial wrapped in aluminium foil to prevent exposure to light, after which the alumina was replaced and the procedure was repeated twice more, resulting in a typical solvent conductivity of < 20 pS/cm (*Scientifica* no. 627 conductivity meter). CHB was then mixed with *cis*-decalin to form a 70.8/29.2 vol.% CHB/decalin mixture (74.5/25.5 wt.%), which was stored in the dark over molecular sieves (3 Å, *Sigma-Aldrich* no. 208582). Next, a concentrated particle stock dispersion was prepared by dispersing 100 mg of PMMA colloids in 1.00 mL of the CHB/decalin mixture using 1 min of sonication followed by ca. 24 h of vortex mixing to ensure the particles were fully dispersed. The PMMA colloids were synthesised as described in van der Linden & van Blaaderen *et al.* [418] (see also Section 3.4) and had a diameter of $\sigma = 1.675$ μm and a polydispersity of 4 % as determined using static light scattering in hexane, and were fluorescently labelled with (rhodamine isothiocyanate)-aminostyrene (RAS) and not 'locked'. [418] A diluted sample was prepared from the CHB/decalin mixture, the PMMA stock dispersion and a 0.20 mM solution of TBABr in CHB, containing 6.5 mg/mL PMMA and 2.65 μM TBABr. The diluted sample was vortex mixed for 10 min to ensure it was fully homogenised and the particles were fully dispersed. An electric cell for microscopy was prepared by glueing two 22 mm \times 26 mm #1.5 thickness ITO-coated coverslips (30–60 Ω/sq ., *Diamond Coatings*) to two strips of #0 coverslip (~ 100 μm thickness) acting as spacers using UV glue (*Norland* optical adhesive no. 68), with the ITO-coated coverslips oriented with the conductive ITO coated sides facing the inside of the electric cell, *i.e.* in contact with the sample. Electrically conductive metal wires were attached to the ITO electrodes on opposite sides using a few drops of electrically conductive silver paint (*SPI*), forming a conductive connection, and fixed firmly in place with UV glue. The cell was then filled with the diluted sample and the open side was closed with UV-glue which was cured for 5 min under UV light, during which the sample volume was covered with aluminium foil to prevent excessive bleaching of the particles. The concentration of 'free' particles (*i.e.* not stuck to the glass) in the final samples was ca. $1.9 \cdot 10^{-3}$ μm^{-3} (volume fraction: 0.5 %).

High-speed confocal microscopy:

A sinusoidal 1 MHz AC electric field was generated using a *Agilent* 33120A signal generator, amplified with a *Krohn-Hite* 7602M wideband power amplifier in AC coupling mode. The signal generator was operated in gated output mode, where the output was switched on or off based on a gating signal generated using an *Arduino Nano* microcontroller, which continuously switched the gating signal state off for 5 z -stacks and then on for 3 z -stacks based on counting the camera's timing output signal and the number of 2D frames required for each z -stack. The applied voltage was measured directly at the wire connections using a *Tektronix* TDS3052 oscilloscope and was 0 V_{RMS} during the 'off'-state and 26.9 V_{RMS} during the 'on'-state (196 V/mm). As discussed in Section 6.9.3, capacitance of the parallel ITO electrodes in combination with resistance in the wire connections and ITO layers may have resulted in a reduced amplitude of the AC field within the sample when compared the measured potential. The combined capacitance of the sample and spacers was estimated to be ~ 0.2 nF giving a field loss due to capacitive damping of ~ 3 %, meaning the effect of parasitic capacitance on the dipole strength was likely negligible. High-speed volumetric imaging was achieved using a *VisiTech Infinity*³ pinhole array confocal scanning unit equipped with 488 nm and 532 nm laser lines and a *Hamamatsu* C11440-22CU scientific CMOS camera (2048 by 2048 pixels, 6.5 μm physical pixel size) and an inverted microscope

body (*Leica DMI 8*) with a *Leica 63× / NA1.30 APO CS2* glycerol immersion objective with correction collar, placed in a *PI* piezo z -stage for fast z -axis scanning of the objective lens. The microscope was operated using custom drivers to allow for faster sustained 3D imaging whereby the scanner timing was used as master timing signal for the camera, the z -stage and the signal generated used to apply the electric field. During volumetric imaging, the z -stage was moved up with a constant speed while continually acquiring 2D frames, rather than stopping at each height. To prevent overshooting of the objective when rapidly moving back to the starting position of the next frame, the objective was moved down using a smooth s -curve over the course of 30 2D frames prior to starting the next z -stack. To reduce the effects of bleaching and to obtain a more representative dataset the data were recorded as multiple independent series in of typically 500 z -stacks in different areas of the sample, for a total of ~ 9000 z -stacks of $1460 \times 696 \times 121$ voxels ($x \times y \times z$) at a voxel size of $0.1 \mu\text{m} \times 0.1 \mu\text{m} \times 0.5 \mu\text{m}$ (imaging volume: $152 \mu\text{m} \times 72 \mu\text{m} \times 60 \mu\text{m}$) using a 3D imaging rate of 1.77 frames/s (279 frames/s 2D, $\Delta t_{\text{ta}} = 0.565$ s, $\Delta t_{\text{ta}}/\tau = 0.021$). The electrode spacing was measured as $137 \mu\text{m}$ using a *Leica SP8* confocal microscope operated in reflection mode such that the glass-liquid interface could be seen.

Data processing and particle localisation:

To correct for inhomogeneous illumination –where the overall fluorescence intensity was up to $\sim 50\%$ higher in the centre of the frame than at the edges, depending on the sample and imaging conditions– the 2D frames were divided by a maximum-normalised correction image, obtained by averaging the frames of the first z -stack and processing it with a triangular low-pass FFT filter with a width of 5 cycles per image width. Particle coordinates were determined using the open-source *Trackpy* library (v0.4.2)^[456] (implemented in the *Python* programming language, v3.7.1), which is based on three steps: feature detection using the widely used intensity-weighted centroiding procedure,^[195] iterative refinement of feature coordinates for sub-pixel precision, and a linking procedure to correlate features between frames and obtain trajectories. A threshold for the integrated particle intensity was used to distinguish real particles from background noise. The coordinate boundaries were then reduced by one ‘feature size’ along all edges, to exclude any particles from the datasets which partially overlapped with the image boundaries. Sample drift due to *e.g.* vibration or solvent flow were determined as the ensemble mean displacement vector of all particles between subsequent frames, and subtracted from the particle coordinates in subsequent time steps such that the mean displacement over the series was zero. For trajectory analysis, each of the time-series were split into a large number of 3 time-step long ‘field on’ phases and 5 time-step long ‘field off’ phases, which were analysed separately.

Determination of the diffusion coefficient and localisation error:

The friction factor $\gamma = k_B T / D_s$ was determined from measurement of the (short time) diffusion coefficient D_s from the same data used for TA, by calculating the ensemble mean squared displacement (MSD) of a subset of 200 particles per image series. To verify that the motion of the particles was consistent with Brownian diffusion, the MSD as a function of lag time Δt was fitted along the z axis and in the ρ plane separately to power-law behaviour of the form

$$\text{MSD} = 2dD_0\Delta t^n \tag{7.35}$$

D_0 is the (long time) diffusion coefficient, d the dimensionality of the diffusion ($d = 2$ in case of D_0^ρ and $d = 1$ for D_0^z) and n the power law exponent, which has a value of 1 for free Brownian diffusion, < 1 for sub-diffusive behaviour and $n > 1$ for super-diffusive behaviour. Fitting was done by performing linear regression on the logarithms of the data, *i.e.* fitting $\ln(\text{MSD}) = a + n \ln(\Delta t)$, such that the slope gave the power-law exponent n and the axis intercept $a = \ln(2dD_0)$ the diffusion coefficient. The MSD values were weighted by the square root of the number of observations at each lag time since considerably more short lag time data was available. Values for ρ and z were determined separately since the lower optical resolution and larger pixel size along the z axis as well as field-induced flows could affect the measured value, however D_0 is in principle expected to be the same in along all spatial dimensions. As shown in **Figure 7.11A**, good agreement between both values was found with slightly sub-diffusive

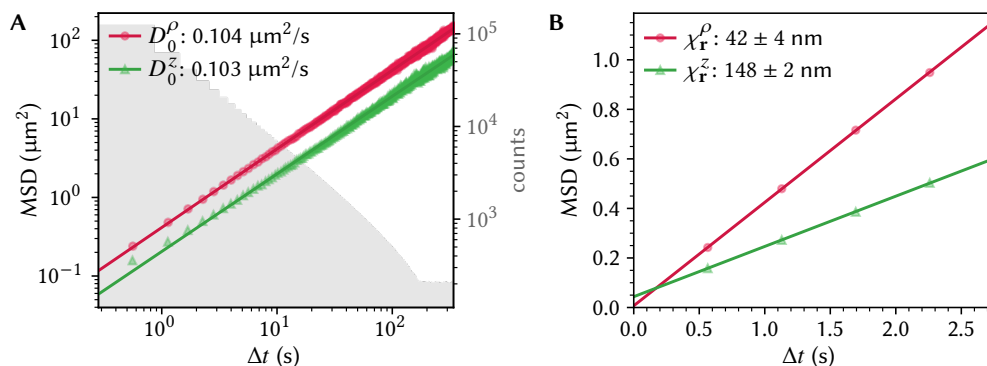


Figure 7.11: determination of diffusion coefficients and localisation errors. **A:** (ensemble) mean squared displacement (MSD, circles and triangles) plotted against lag time Δt on a log-log scale and fitted with a power-law function (lines), where the best fit parameters for the diffusion coefficients and power law exponents were $D_0^\rho = 0.104 \pm 0.001 \mu\text{m}^2/\text{s}$, $n^\rho = 1.000 \pm 0.001$, $D_0^z = 0.103 \pm 0.004 \mu\text{m}^2/\text{s}$ and $n^z = 0.988 \pm 0.002$. **B:** linear regression of short-time MSDs vs Δt to determine localisation errors ($\Delta t_{\max} = 10^{-1} \tau$), with best fit parameters of $\chi_r^\rho = 42 \pm 4 \text{ nm}$, $D_s^\rho = 0.104 \pm 0.000 \mu\text{m}^2/\text{s}$, $\chi_r^z = 148 \pm 2 \text{ nm}$ and $D_s^z = 0.102 \pm 0.000 \mu\text{m}^2/\text{s}$.

apparent behaviour for D_0^z due to the larger particle tracking error. The values were also in reasonable agreement with the theoretical value of $D_0 = 0.115 \mu\text{m}^2/\text{s}$ (using $\eta^{20} = 2.22 \text{ mPa s}$ ^[523] for the solvent viscosity). Particle localisation errors χ_r and estimates for the short-time diffusion coefficients D_s were determined from linear regression of the ensemble MSD at small lag times ($\Delta t < 0.1\tau$) using:^[507]

$$\text{MSD} = 2d \left(D_s \Delta t + \chi_r^2 \right), \quad (7.36)$$

as shown in **Figure 7.11B**, and where MSD values were again weighted by the square root of the number of samples in each bin. In principle, D_s is more appropriate for the TA as D_0 may be affected by the finite particle concentration through interactions at longer time-scales,^[505] but we note that the time-step here was not small enough to truly measure the single-particle short-time self-diffusion coefficient. Since we did not see significant difference between the overall diffusion coefficients and those at small lag times only, effects from the finite particle concentration are likely small. Because the z diffusion appeared slightly sub-diffusive, the value of $D_s^\rho = 0.104 \mu\text{m}^2/\text{s}$ was used to determine γ for TA and gave a self-diffusion time of $\tau = \sigma^2/D_0 = 27.0 \text{ s}$.

7.8.6 estimation of the screening length and surface charge

The concentration c_s of fully dissociated monovalent salt in the sample was estimated from measurement of the electric conductivity ζ of the sample as $\zeta = c_s \Lambda^0$, where Λ^0 is the limiting molar conductance of the electrolyte in a particular sample. Here, $\Lambda^0 = 19.4 \text{ cm}^2 \text{ S/mol}$ for TBA⁺Br⁻ in the CHB/decalin solvent mixture was estimated using Waldens rule, which states that the product of Λ^0 and the solvent viscosity η is the same for different solvents,^[539] i.e.

$$\Lambda_1^0 \eta_1 = \Lambda_2^0 \eta_2, \quad (7.37)$$

together with the fact that $\Lambda_{\text{TBA}^+\text{Br}^-}^0 = \Lambda_{\text{TBA}^+}^0 + \Lambda_{\text{Br}^-}^0$ and using literature values for the molar conductivities and viscosities given in the following table.

species	solvent	Λ^0 (cm ² S/mol)	η^{25} (mPa s)	ref.
HBr	ethanol	88.9	1.078	[540]
H ⁺	ethanol	64.5	1.078	[540]
TBA ⁺	water	19.4	0.890	[541]
TBABr	CHB/dec	19.7	2.217	[523]

The conductivity was measured to be $\zeta = 394$ pS/cm using a *Scientifica* no. 627 conductivity meter, giving a salt concentration of $c_s \approx 2.01 \cdot 10^{-5}$ mol/m³ and a double layer thickness of $\kappa^{-1} = 0.574$ μ m ($\kappa\sigma = 2.91$).

The surface charge Z was determined from the zeta-potential ζ through the following empirical relationship:[542,543]

$$Z = 2\pi\epsilon_0\epsilon_s \frac{k_B T}{q_e} \kappa\sigma^2 \left[\sinh\left(\frac{\tilde{\zeta}}{2}\right) + \frac{4}{\kappa\sigma} \tanh\left(\frac{\tilde{\zeta}}{4}\right) \right] \quad (7.38)$$

where $\tilde{\zeta} = \zeta q_e / (k_B T)$ and q_e is the elementary charge. The zeta-potential may be obtained from electrophoresis and depends on the the electrophoretic mobility μ_e of the colloids as follows:[544]

$$\zeta = \frac{3\eta\mu_e}{2\epsilon_0\epsilon_s f_1(\kappa\sigma)} \quad (7.39)$$

where $f_1(\kappa\sigma)$ is the so-called Henry's function which may be approximated as

$$f_1(\kappa\sigma) \approx \frac{16 + 9\kappa\sigma + 3(\kappa\sigma/2)^2}{16 + 9\kappa\sigma + (\kappa\sigma/2)^2}. \quad (7.40)$$

The electrophoretic mobility was determined at the stationary points of a parabolic electro-osmotic flow profile as described in the work of Vissers & van Blaaderen *et al.*[515] using a *Vitrocom* 0.1 μ m \times 2 μ m glass capillary with electrodes spaced 8.7 mm apart and a field strength of 7.3 V/mm. A electrophoretic mobility of $\mu_e = -260$ μ m² V⁻¹ s⁻¹ was found, resulting in $\zeta = -16.7$ mV and $Z = -135$ q_e and thereby giving an estimated contact potential of $\Gamma_{\text{yuk}} = 17.9$ $k_B T$.

7.8.7 Brownian dynamics simulations using experimental parameters

To simulate data closely representing the experimental trajectories, the methods described in [Section 7.8.1](#) were largely followed except with some additional considerations. Simulations were run using 1000 particles in a simulation box with periodic boundary conditions of 120 μ m \times 70.4 μ m \times 57.5 μ m at a step size of $\Delta t_{\text{sim}}/\tau = 2.1 \cdot 10^{-6}$ and using the estimated experimental interactions under switching field conditions: $\sigma = 1.68$ μ m, $\Gamma_{\text{yuk}} = 17.9$ $k_B T$, $\kappa^{-1} = 0.57$ μ m, $\gamma = 9.6$ $k_B T$ s/ μ m² and repeatedly $\Gamma_{\text{dip}} = 0$ $k_B T$ for $5 \cdot 10^4$ simulation steps followed by $\Gamma_{\text{dip}} = 40.9$ $k_B T$ for $3 \cdot 10^4$ simulation steps. Particle coordinates were stored at an interval of 10^4 simulation steps such that $\Delta t_{\text{ta}}/\tau = 2.1 \cdot 10^{-2}$ like in the experiments. To simulate the effects of motion blur/finite acquisition time, the particle positions averaged over the first 500 simulation steps of each 10^4 step cycle were stored instead of each 10^4 th step. A total of 10^4 consecutive coordinate sets were stored for analysis. To simulate finite particle localisation accuracy, a normally distributed random offset with a standard deviation of 0.042 μ m (for x and y) or 0.148 μ m (for z) was added to the coordinates prior to trajectory analysis.

7.9 Supplementary figures

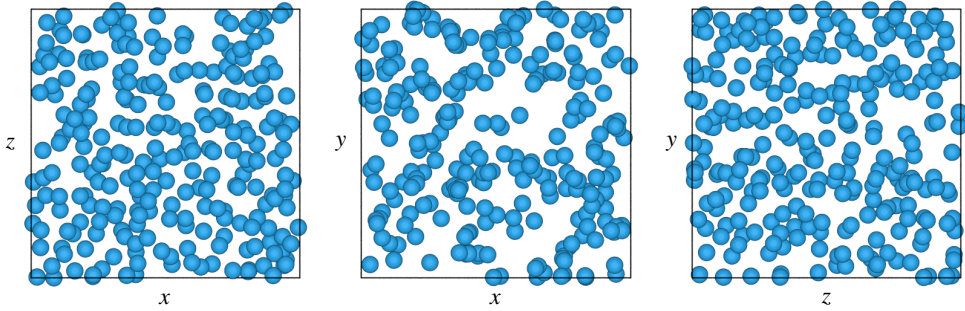


Figure 7.12: simulation snapshot of soft dipolar spheres in the fluid phase. A system of $n = 256$ particles with $\Gamma_{\text{dip}}/k_B T = 10$, $\Gamma_{\text{yuk}}/k_B T = 10$ and $\kappa\sigma = 5$ at density $\rho\sigma^3 = 0.07$ was simulated for $\sim 4 \cdot 10^8$ steps of $\Delta t_{\text{sim}}/\tau = 2 \cdot 10^{-5}$, see also [Figure 7.4](#). Front-, top- and side-view renderings of the simulation box are shown for a snapshot near the end of the simulation run.

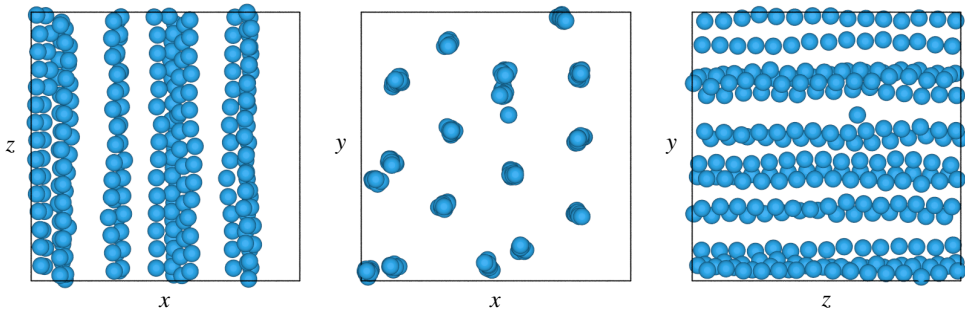


Figure 7.13: simulation snapshot of soft dipolar spheres in a string fluid. A system of $n = 256$ particles with $\Gamma_{\text{dip}}/k_B T = 30$, $\Gamma_{\text{yuk}}/k_B T = 10$ and $\kappa\sigma = 15$ at density $\rho\sigma^3 = 0.07$ was simulated for $\sim 4 \cdot 10^8$ steps of $\Delta t_{\text{sim}}/\tau = 2 \cdot 10^{-5}$, see also [Figure 7.5](#). Front-, top- and side-view renderings of the simulation box are shown for a snapshot near the end of the simulation run.

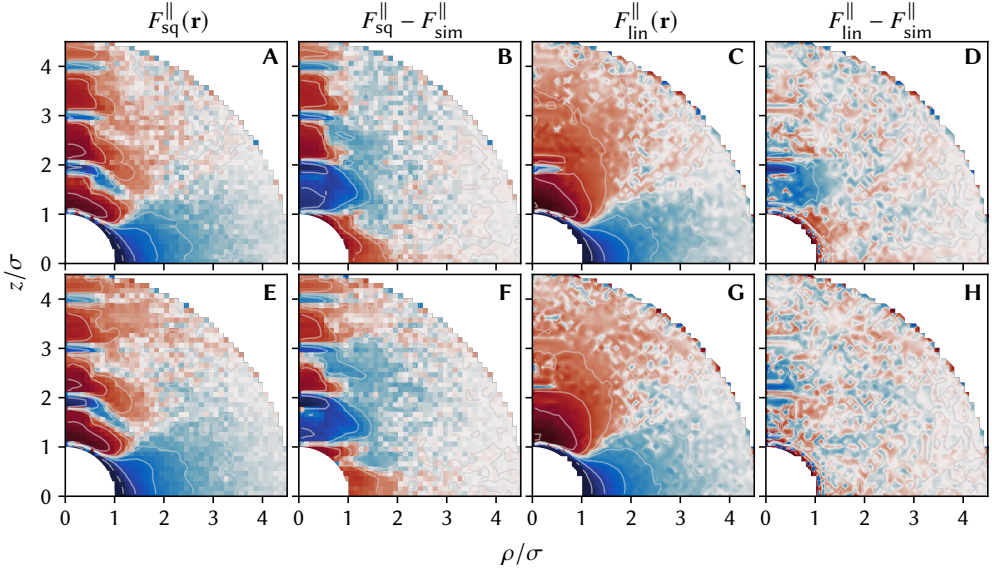


Figure 7.14: effect of sampling rate on TA of a string fluid. Analysis was performed at $\Delta t_{\text{ta}}\tau = 10^{-4}$ for data simulated at $\Delta t_{\text{sim}}\tau = 2 \cdot 10^{-6}$, *i.e.* $\Delta t_{\text{ta}}/\Delta t_{\text{sim}} = 50$, (A–D) or for data simulated at $\Delta t_{\text{sim}}/\tau = \Delta t_{\text{ta}}/\tau = 10^{-4}$ such that no sampling-rate dependent errors are present (E–H). $\Gamma_{\text{dip}}/k_B T = 30$, $\Gamma_{\text{yuk}}/k_B T = 10$, $\kappa\sigma = 15$, $\varrho\sigma^3 = 0.07$, $N = 2 \cdot 10^8$, $r_{\text{max}}/\sigma = 4.5$ and $M^z = M^\rho = 45$. For the colour scaling see Fig. 7.15.

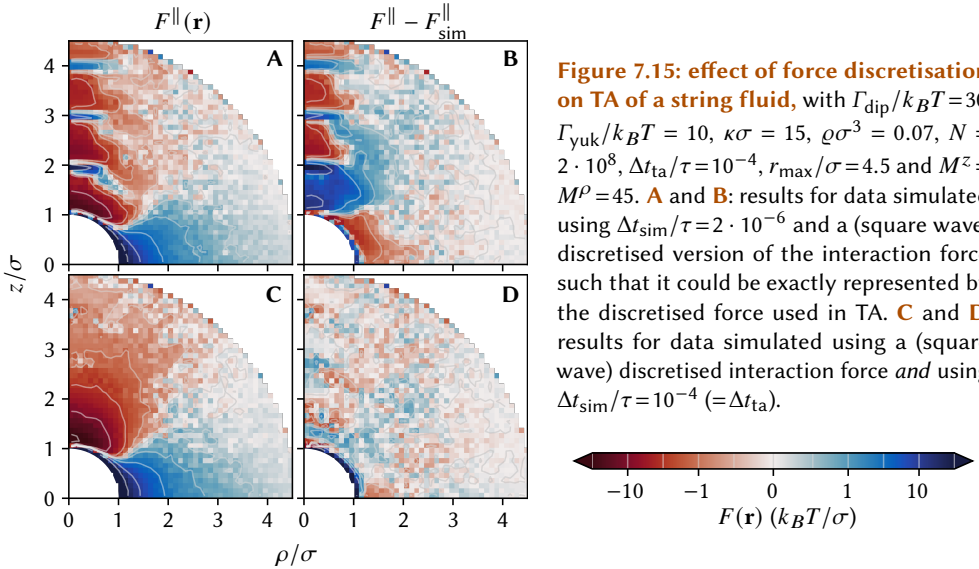


Figure 7.15: effect of force discretisation on TA of a string fluid, with $\Gamma_{\text{dip}}/k_B T = 30$, $\Gamma_{\text{yuk}}/k_B T = 10$, $\kappa\sigma = 15$, $\varrho\sigma^3 = 0.07$, $N = 2 \cdot 10^8$, $\Delta t_{\text{ta}}/\tau = 10^{-4}$, $r_{\text{max}}/\sigma = 4.5$ and $M^z = M^\rho = 45$. **A** and **B**: results for data simulated using $\Delta t_{\text{sim}}/\tau = 2 \cdot 10^{-6}$ and a (square wave) discretised version of the interaction force such that it could be exactly represented by the discretised force used in TA. **C** and **D**: results for data simulated using a (square wave) discretised interaction force *and* using $\Delta t_{\text{sim}}/\tau = 10^{-4}$ ($=\Delta t_{\text{ta}}$).

CHAPTER 8

Conclusions and outlook

In this PhD research we have attempted to develop methods to experimentally measure the interaction forces between colloidal particles, and colloidal *nanoparticles* in particular, through the statistical analysis of their distribution and motion in the surrounding fluid as observable using microscopy. Firstly however, this was placed in the context of the existing work in the field of colloid science. In addition to the development of theoretical descriptions for a wide variety of different types of nanoscale surface interaction forces, over the past several decades a wide variety of techniques have been developed and used to measure such forces between colloidal particles and other surfaces. In **Chapter 2** an extensive overview of this work was given, discussing the different experimental techniques as well as the theory behind their analysis and interpretation and the major advantages and disadvantages of each. This was done with a particular focus on pushing these measurements towards measurements of interactions between nanoparticles, whilst highlighting a number of interesting examples to show how the authors were able to overcome the particular challenges faced with when pushing towards nanoscale particles and/or interaction ranges. Nonetheless, ‘complete’ measurements of interactions between nanoparticles which meet our ‘wish-list’—that is interaction potentials measured in real-space and in 3D, at time- and energy scales relevant to self-assembly and without being affected by the measurement or nearby interfaces—, remain elusive.

Established protocols from the literature were also used to reproduce the synthesis of a variety of colloidal model systems of gold, silica and PMMA for use in the experiments in this work as well as several others in **Chapter 3**. Additionally, the ability to fine-tune interactions through the addition/exchange of a wide variety of ligands/coatings was explored as an example of the rich diversity of interactions and properties achievable through colloidal synthesis. The aim of this work was not to develop or study synthesis methods in detail, but nonetheless allowed us to make some observations on ease and reproducibility with respect to our own experiments as well as to results in the literature. While we could obtain ‘monodisperse’ particles using all of the procedures—that is to the extent one could expect for each method based on published results—, reproducibility varied significantly between methods and often a decent degree of fine-tuning was necessary even for procedures which are well understood and widely used in the literature. A good example of this was the synthesis of AuNPs@OAm where there were huge batch-to-batch differences in our experiments and often large inconsistencies with respect to results published by others, although it was possible to obtain comparable results through *e.g.* repeated attempts or size-selective precipitation. For these reasons, we encourage the inclusion of complete and fair synthesis procedures in any future work which makes use of ‘bespoke’ nanoparticles, even if that work is based on methods already published elsewhere, particularly with respect to any challenges that were encountered or ‘tweaks’ that had to be made.

Next, it was demonstrated that the interaction potential for an ensemble of colloidal (nano)particles could be obtained using real-space microscopy through analysis of the radial distribution function via test-particle insertion (TPI). We presented the first complete and practical implementation of this algorithm for a number of 2D and 3D geometries with fully analytical corrections for finite (nonperiodic) image boundaries such as encountered in experimental data. In **Chapter 4** a variation on a novel solvent-arresting procedure was presented which enabled the ‘arresting’ of a system of particles through rapid polymerisation of the solvent such that the particle positions were preserved and could be determined using 3D microscopy. Using solvent-arresting and CLSM it was possible to measure the interaction

potentials for silica nanoparticles, which were found to interact through weak long-ranged repulsive electrostatic interactions, as well as to determine binary sedimentation profiles and interaction potentials in a two-component system of ‘large’ (400 nm) and ‘small’ (300 nm) silica colloids with only hard-sphere interactions, although in both cases the short-range data were limited by biases in the particle localisation algorithm in combination with the limited optical resolution. Although the use of more advanced localisation procedures could be used to reduce these effects, we conclude that optical microscopy provides a viable approach to interaction potentials mainly for relatively large (>400 nm) colloids, as well as for smaller particles when their interactions are repulsive over a comparably long range such that their signals are optically well separated.

For smaller particles and separations, electron microscopy can be used for high resolution imaging instead. Our results demonstrated for example that 3D coordinates may be obtained through FIB-SEM analysis of arrested particle systems, although this was limited to systems with pure monomer as solvent and affected by beam-induced shrinking in our experiments. For future work we would therefore suggest FIB-SEM imaging of cryogenically vitrified samples, which allows for much higher resolution than optical microscopy while allowing relatively large volumes to be analysed compared to *e.g.* (cryo-)TEM tomography. On the other hand, TEM offers the highest possible resolution which is of particular interest for nanoparticles smaller than 10 nm, where nanoscale effects on interaction potentials are most likely. In **Chapter 5** it was shown that conventional cryo-TEM procedures for quasi-2D thin films may be combined with TPI to measure interaction potentials with nanometer resolution in 2D for a particle system with tunable interactions and varied self-assembly. However, it can also be concluded that such a quasi-2D approach introduces strong limitations due to the nature of the confining liquid-air interfaces: either the measured interactions were affected by the presence of interfaces, or the lack of interfacial interaction provided enough freedom of movement along the optical axis to introduce severe projection errors. Therefore we consider this method well-suited to measuring (interfacial) interactions for particles strongly adsorbed to the liquid-air interface, but caution should be taken in drawing conclusions that apply to particles in the bulk of the liquid. Here, a novel sample preparation approach was developed to overcome these limitations. This was based on graphene liquid cells (GLCs) and the emulsion droplet based supraparticle self-assembly method to capture, cryogenically freeze and image droplets of solvent containing self-assembling NPs. This allowed for the measurement of interaction potentials between NPs of only several nm in three dimensions and under the same conditions used for self-assembly. Additionally, it was found that the use of emulsion droplets in GLCs could lead to yields and sizes of the liquid pockets which were orders of magnitude larger than achieved using conventional GLC preparation procedures, with a likely pathway towards control over the pocket size. While not the original aim of this work, we believe this finding could have far reaching consequences for in-situ EM in both materials and biological research, and encourage further research into emulsion-based GLC preparation.

Finally, new avenues were explored for measuring interaction forces between ‘large’ micron-sized colloids based on analysis of colloidal trajectories, rather than static sets of coordinates. In **Chapter 6** we reported the first (to the best of our knowledge) experimental measurement of pairwise interaction forces from ensemble trajectory data for both a quasi-2D system of sedimented colloids on, where high-speed imaging using wide-field fluorescence microscopy was possible and interactions forces close to their theoretical value were mea-

sured, as well as in 3D using confocal microscopy for a system of density-matched colloids where the measured forces were strongly affected by artefacts due to practical limitations on the imaging speed. A particularly interesting property of this TA method is that it does not rely on thermodynamic equilibrium, and it was possible to experimentally measure interaction forces in a system of colloids which was continually driven out of equilibrium by switching repulsive interaction forces on and off through the use of external electric fields. In addition, we were able to expand on this approach in **Chapter 7** and show that measurement of *anisotropic* interaction forces in or out of equilibrium is also in principle possible using TA, although again practical limitations on the sampling rate meant that our experimental measurements suffered from significant artefacts. In principle faster measurements can alleviate most of these limitations as we have shown in 2D, and are possible using *e.g.* faster cameras and a *z*-stage with less inertia of using different techniques entirely such as light-sheet microscopy or holography. This could also be achieved by slowing the particle's motion by increasing the viscosity, although this of course places further limitations on the scope of particle systems and interactions that can be measured. Finally, there are certainly improvements possible to the way trajectory analysis is implemented. The current implementation does not account for hydrodynamic effects although these are likely significant both in and out of equilibrium due to relying on dynamics, but this could (and should) be included at least within the context of the Oseen approximation. As the TA relies on relatively crude discretization of force profiles and requires a large amount of data due to the large number of unknowns, particularly for anisotropic interactions, and here a nonlinear 'fitting' approach to a model function or using machine learning could be employed to reduce the number of unknown variables and/or represent continuous interaction forces more accurately. Nonetheless, we do not expect this approach to be feasible for the vast majority of nanoparticle systems in the (near) future as their diffusion is much faster and their imaging considerably more challenging. Instead we conclude that trajectory analysis opens up some unique possibilities for larger colloids but that, when possible, the analysis of equilibrium distributions such as in iterative TPI is preferable for interaction measurements as it is generally easier and more accurate.

In conclusion, a number of different pathways were explored that allowed for interactions between colloidal (nano)particles to be obtained from microscopy data with a variety of different advantages and limitations. The analysis of static coordinates using our implementation of iterative test-particle insertion proved versatile, efficient and accurate in a range of different conditions and geometries, significantly expanding the scope of systems that may be analysed compared to direct inversion of the $g(r)$ as is still frequently employed. We believe that for NPs, whose interaction forces are so far less well-understood than those of μ Ps, 3D electron microscopy techniques like on (cryo) FIB-SEM and/or (cryo) TEM tomography in combination with TPI currently provide the best approach towards direct measurement of (equilibrium) interaction potential measurements. Here a powerful combined approach is possible, frequently employed for life science research, where FIB-milling is employed to carve a lamella out of a vitrified sample which can then be transferred to a TEM and imaged at high resolution 2D or in 3D using tomography. While such an experiment was not possible within the scope of this work, we believe this to provide one of the most flexible and precise pathways to directly measuring 3D equilibrium interactions between particles down to the bottom end of the colloidal size range. For slightly larger nanoparticles (>20 nm) the use of cryo FIB-SEM directly for 3D imaging likely provides the best balance between complexity of

the measurement, resolution and the total volume / number of particles that can be analysed. Nonetheless, even for comparatively large colloids there are still opportunities to be explored when it comes to experimental determination of interaction forces, as we have shown for *e.g.* nonequilibrium systems and in case of anisotropy using trajectory analysis. It is of note that in principle the test-particle insertion method may be similarly adapted to extract anisotropic interaction potentials through *e.g.* the cylindrical distribution function, and it would be interesting to compare the performance of the two methods more directly. In addition, going beyond 'simple' pairwise interaction and studying many-body effects or hydrodynamic interactions would be of interest using TPI and trajectory analysis respectively. For such research topics we expect optical microscopy to continue playing a major role thanks to its ability to study colloidal systems in real-space and real-time. Our research thus shows that despite over a century of theoretical and experimental research on colloids there are still questions to be answered and experiments to be done, and we hope to have made progress in this pursuit. To this end we ultimately believe that direct measurements of interactions in combination with *e.g.* (atomistic) simulations can help deeper understand the complex interactions that govern colloidal stability and self-assembly, thereby aiding in their adoption into a large number of proposed applications.

References

- [1] R. P. Feynman (1960), “Plenty of Room at the Bottom,” *Engineering and Science Magazine*, 13 (5).
- [2] D. H. Everett, *Basic Principles of Colloid Science*. Ser. Royal Society of Chemistry Paperbacks. Royal Society of Chemistry, 1988.
- [3] J. Perrin, *Les atomes*. Paris: Librairie Félix Alcan, 1913.
- [4] R. Cerbino (2018), “Quantitative optical microscopy of colloids: The legacy of Jean Perrin,” *Current Opinion in Colloid & Interface Science*, 34, 47–58.
- [5] B. D. Leahy, N. Y. Lin, and I. Cohen (2018), “Quantitative light microscopy of dense suspensions: Colloid science at the next decimal place,” *Current Opinion in Colloid & Interface Science*, 34, 32–46.
- [6] G. M. Whitesides and B. Grzybowski (2002), “Self-Assembly at All Scales,” *Science*, 295 (5564), 2418–2421.
- [7] D. Velegol (2007), “Assembling colloidal devices by controlling interparticle forces,” *Journal of Nanophotonics*, 1 (1), 012502.
- [8] J. Hühn, C. Carrillo-Carrion, M. G. Soliman, *et al.* (2017), “Selected Standard Protocols for the Synthesis, Phase Transfer, and Characterization of Inorganic Colloidal Nanoparticles,” *Chemistry of Materials*, 29 (1), 399–461.
- [9] Z. Cheng, *Colloidal Crystallization*, in *Fluids, Colloids and Soft Materials: An Introduction to Soft Matter Physics*, 1898, John Wiley & Sons, Inc, 2016, pp. 203–248.
- [10] M. J. Solomon (2018), “Tools and Functions of Reconfigurable Colloidal Assembly,” *Langmuir*, 34 (38), 11205–11219.
- [11] K. Zhao and T. G. Mason (2018), “Assembly of colloidal particles in solution,” *Reports on Progress in Physics*, 81 (12), 126601.
- [12] O. Kruglova, P.-J. Demeyer, K. Zhong, Y. Zhou, and K. Clays (2013), “Wonders of colloidal assembly,” *Soft Matter*, 9 (38), 9072.
- [13] Z. Cai, Z. Li, S. Ravaine, M. He, Y. Song, Y. Yin, H. Zheng, J. Teng, and A. Zhang, *From colloidal particles to photonic crystals: Advances in self-assembly and their emerging applications*, 2021.
- [14] Y. Min, M. Akbulut, K. Kristiansen, Y. Golan, and J. Israelachvili (2008), “The role of interparticle and external forces in nanoparticle assembly,” *Nature Materials*, 7 (7), 527–538.
- [15] Z. Nie, A. Petukhova, and E. Kumacheva (2010), “Properties and emerging applications of self-assembled structures made from inorganic nanoparticles,” *Nature Nanotechnology*, 5 (1), 15–25.
- [16] M. A. Boles, M. Engel, and D. V. Talapin (2016), “Self-Assembly of Colloidal Nanocrystals: From Intricate Structures to Functional Materials,” *Chemical Reviews*, 116 (18), 11220–11289.
- [17] X. Li, X. Liu, and X. Liu (2021), “Self-assembly of colloidal inorganic nanocrystals: nanoscale forces, emergent properties and applications,” *Chemical Society Reviews*, 50 (3), 2074–2101.
- [18] K. J. M. Bishop, C. E. Wilmer, S. Soh, and B. A. Grzybowski (2009), “Nanoscale Forces and Their Uses in Self-Assembly,” *Small*, 5 (14), 1600–1630.
- [19] C. A. Silvera Batista, R. G. Larson, and N. A. Kotov (2015), “Nonadditivity of nanoparticle interactions,” *Science*, 350 (6257), 124277.
- [20] S. C. Endres, L. C. Ciacchi, and L. Mädler (2021), “A review of contact force models between nanoparticles in agglomerates, aggregates, and films,” *Journal of Aerosol Science*, 153, 105719.
- [21] D. Leckband and J. Israelachvili (2001), “Intermolecular forces in biology,” *Quarterly Reviews of Biophysics*, 34 (2), 105–267.

- [22] C. N. Likos (2001), “Effective interactions in soft condensed matter physics,” *Physics Reports*, 348 (4-5), 267–439.
- [23] Y. Liang, N. Hilal, P. Langston, and V. Starov (2007), “Interaction forces between colloidal particles in liquid: Theory and experiment,” *Advances in Colloid and Interface Science*, 134-135, 151–166.
- [24] D. Luo, C. Yan, and T. Wang (2015), “Interparticle Forces Underlying Nanoparticle Self-Assemblies,” *Small*, 11 (45), 5984–6008.
- [25] R. López-Esparza, M. A. Balderas Altamirano, E. Pérez, and A. Gama Goicochea (2015), “Importance of Molecular Interactions in Colloidal Dispersions,” *Advances in Condensed Matter Physics*, 2015, 1–8.
- [26] N. Kovalchuk, D. Johnson, V. Sobolev, N. Hilal, and V. Starov (2019), “Interactions between nanoparticles in nanosuspension,” *Advances in Colloid and Interface Science*, 272, 102020.
- [27] M. Dijkstra, R. van Roij, R. Roth, and A. Fortini (2006), “Effect of many-body interactions on the bulk and interfacial phase behavior of a model colloid-polymer mixture,” *Physical Review E*, 73 (4), 041404.
- [28] W. Albers and J. T. G. Overbeek (1959), “Stability of emulsions of water in oil. II. Charge as a factor of stabilization against flocculation,” *Journal of Colloid Science*, 14 (5), 510–518.
- [29] W. Albers and J. T. G. Overbeek (1959), “Stability of emulsions of water in oil. I. The correlation between electrokinetic potential and stability,” *Journal of Colloid Science*, 14 (5), 501–509.
- [30] D. Reinke, H. Stark, H.-H. von Grünberg, A. B. Schofield, G. Maret, and U. Gasser (2007), “Non-central Forces in Crystals of Charged Colloids,” *Physical Review Letters*, 98 (3), 038301.
- [31] S. D. Finlayson and P. Bartlett (2016), “Non-additivity of pair interactions in charged colloids,” *The Journal of Chemical Physics*, 145 (3).
- [32] E. Fayen, M. Impéror-Clerc, L. Filion, G. Foffi, and F. Smallenburg (2022), “Self-assembly of dodecagonal and octagonal quasicrystals in hard spheres on a plane.” Preprint: [arXiv:2202.12726](https://arxiv.org/abs/2202.12726).
- [33] B. Derjaguin and L. Landau (1941), “Theory of the stability of strongly charged lyophobic sols and of the adhesion of strongly charged particles in solutions of electrolytes,” *Acta Physicochim: USSR*, 14, 633–622.
- [34] E. Verwey and J. Overbeek, *Theory of the stability of lyophobic colloids*. Amsterdam: Elsevier Publishing Company Inc., 1948.
- [35] B. W. Ninham (1999), “On progress in forces since the DLVO theory,” *Advances in Colloid and Interface Science*, 83, 1–17.
- [36] V. A. Parsegian, *Van der Waals Forces*. Cambridge: Cambridge University Press, 2005.
- [37] M. W. Cole, D. Velegol, H.-Y. Kim, and A. A. Lucas (2009), “Nanoscale van der Waals interactions,” *Molecular Simulation*, 35 (10-11), 849–866.
- [38] I. Dzyaloshinskii, E. Lifshitz, and L. Pitaevskii (1961), “The general theory of van der Waals forces,” *Advances in Physics*, 10 (38), 165–209.
- [39] H. Hamaker (1937), “The London–van der Waals attraction between spherical particles,” *Physica*, 4 (10), 1058–1072.
- [40] J. Israelachvili, *Intermolecular and Surface Forces*, 3rd ed. Academic Press, 2011.
- [41] R. Esquivel-Sirvent and G. C. Schatz (2012), “Spatial Nonlocality in the Calculation of Hamaker Coefficients,” *The Journal of Physical Chemistry C*, 116 (1), 420–424.
- [42] R. A. Distasio, V. V. Gobre, and A. Tkatchenko (2014), “Many-body van der Waals interactions in molecules and condensed matter,” *Journal of Physics: Condensed Matter*, 26 (21), 213202.
- [43] J. Hermann, R. A. DiStasio, and A. Tkatchenko (2017), “First-Principles Models for van der Waals Interactions in Molecules and Materials: Concepts, Theory, and Applications,” *Chemical Reviews*, 117 (6), 4714–4758.
- [44] M. van der Linden, *Long-range repulsive charged colloids in and out of equilibrium*, PhD thesis, Utrecht University, 2013.
- [45] J. E. Sader, S. L. Carnie, and D. Y. Chan (1995), “Accurate Analytic Formulas for the Double-Layer Interaction between Spheres,” *Journal of Colloid and Interface Science*, 171 (1), 46–54.
- [46] D. Napper (1977), “Steric stabilization,” *Journal of Colloid and Interface Science*, 58 (2), 390–407.
- [47] D. H. Napper, *Polymeric stabilization of colloidal dispersions*. Academic Press, 1983.
- [48] H. N. Lekkerkerker and R. Tuinier, *Colloids and the Depletion Interaction*, ser. Lecture Notes in Physics. Dordrecht: Springer Netherlands, 2011, vol. 833.
- [49] Y. Mao, M. E. Cates, and H. N. W. Lekkerkerker (1995), “Depletion Stabilization by Semidilute Rods,” *Physical Review Letters*, 75 (24), 4548–4551.
- [50] J. C. Crocker, J. A. Matteo, A. D. Dinsmore, and A. G. Yodh (1999), “Entropic Attraction and Repulsion in Binary Colloids Probed with a Line

- Optical Tweezer,” *Physical Review Letters*, 82 (21), 4352–4355.
- [51] S. Asakura and F. Oosawa (1954), “On Interaction between Two Bodies Immersed in a Solution of Macromolecules,” *The Journal of Chemical Physics*, 22 (7), 1255–1256.
- [52] A. Vrij (1976), “Polymers at Interfaces and the Interactions in Colloidal Dispersions,” *Pure and Applied Chemistry*, 48 (4), 471–483.
- [53] S. Ji and J. Y. Walz (2013), “Interaction potentials between two colloidal particles surrounded by an extremely bidisperse particle suspension,” *Journal of Colloid and Interface Science*, 394 (1), 611–618.
- [54] J. Y. Walz and A. Sharma (1994), “Effect of Long Range Interactions on the Depletion Force between Colloidal Particles,” *Journal of Colloid and Interface Science*, 168 (2), 485–496.
- [55] D. Kleshchanok, R. Tuinier, and P. R. Lang (2008), “Direct measurements of polymer-induced forces,” *Journal of Physics: Condensed Matter*, 20 (7), 073101.
- [56] T. D. Edwards and M. A. Bevan (2012), “Depletion-Mediated Potentials and Phase Behavior for Micelles, Macromolecules, Nanoparticles, and Hydrogel Particles,” *Langmuir*, 28 (39), 13816–13823.
- [57] J. Ruiz-Franco and E. Zaccarelli (2021), “On the Role of Competing Interactions in Charged Colloids with Short-Range Attraction,” *Annual Review of Condensed Matter Physics*, 12, 51–70.
- [58] D. Baranov, A. Fiore, M. Van Huis, C. Giannini, A. Falqui, U. Lafont, H. Zandbergen, M. Zanella, R. Cingolani, and L. Manna (2010), “Assembly of colloidal semiconductor nanorods in solution by depletion attraction,” *Nano Letters*, 10 (2), 743–749.
- [59] H.-J. Butt and M. Kappl (2009), “Normal capillary forces,” *Advances in Colloid and Interface Science*, 146 (1-2), 48–60.
- [60] A. Maestro and E. Guzmán (2019), “Colloids at Fluid Interfaces,” *Processes*, 7 (12), 942.
- [61] V. Garbin, J. C. Crocker, and K. J. Stebe (2012), “Nanoparticles at fluid interfaces: Exploiting capping ligands to control adsorption, stability and dynamics,” *Journal of Colloid and Interface Science*, 387 (1), 1–11.
- [62] V. Garbin, I. Jenkins, T. Sinno, J. C. Crocker, and K. J. Stebe (2015), “Interactions and stress relaxation in monolayers of soft nanoparticles at fluid-fluid interfaces,” *Physical Review Letters*, 114 (10), 108301.
- [63] V. Parsegian and T. Zemb (2011), “Hydration forces: Observations, explanations, expectations, questions,” *Current Opinion in Colloid & Interface Science*, 16 (6), 618–624.
- [64] M. Ludwig and R. von Klitzing (2020), “Recent progress in measurements of oscillatory forces and liquid properties under confinement,” *Current Opinion in Colloid & Interface Science*, 47, 137–152.
- [65] M. Manciu and E. Ruckenstein (2001), “Role of the Hydration Force in the Stability of Colloids at High Ionic Strengths,” *Langmuir*, 17 (22), 7061–7070.
- [66] U. Anand, J. Lu, D. Loh, Z. Aabdin, and U. Mirsaidov (2016), “Hydration Layer-Mediated Pairwise Interaction of Nanoparticles,” *Nano Letters*, 16 (1), 786–790.
- [67] S. K. Verma, A. K. Mukherjee, and I. Sinha (2013), “Simulating interactions between nanoparticles in Lennard-Jones liquids,” *Chemical Physics Letters*, 572, 85–89.
- [68] A. E. Nel, L. Mädler, D. Velegol, T. Xia, E. M. Hoek, P. Somasundaran, F. Klaessig, V. Castranova, and M. Thompson (2009), “Understanding biophysicochemical interactions at the nano-bio interface,” *Nature Materials*, 8 (7), 543–557.
- [69] S. Pujals, N. Feiner-Gracia, P. Delcanale, I. Voets, and L. Albertazzi (2019), “Super-resolution microscopy as a powerful tool to study complex synthetic materials,” *Nature Reviews Chemistry*, 3 (2), 68–84.
- [70] A. Stradner and P. Schurtenberger (2020), “Potential and limits of a colloid approach to protein solutions,” *Soft Matter*, 16 (2), 307–323.
- [71] C. M. Niemeyer and U. Simon (2005), “DNA-Based Assembly of Metal Nanoparticles,” *European Journal of Inorganic Chemistry*, 2005 (18), 3641–3655.
- [72] W. B. Rogers and J. C. Crocker (2011), “Direct measurements of DNA-mediated colloidal interactions and their quantitative modeling,” *Proceedings of the National Academy of Sciences of the United States of America*, 108 (38), 15687–15692.
- [73] S. Loescher, S. Groer, and A. Walther (2018), “3D DNA Origami Nanoparticles: From Basic Design Principles to Emerging Applications in Soft Matter and (Bio-)Nanosciences,” *Angewandte Chemie International Edition*, 57 (33), 10436–10448.
- [74] J. K. G. Dhont, *An Introduction to Dynamics of Colloids*. Elsevier, 1996.
- [75] D. C. Prieve (1999), “Measurement of colloidal forces with TRM,” *Advances in Colloid and Interface Science*, 82 (1), 93–125.
- [76] B. Liebchen and A. K. Mukhopadhyay (2022), “Interactions in active colloids,” *Journal of Physics: Condensed Matter*, 34 (8), 083002.

- [77] D. S. Bolintineanu, G. S. Grest, J. B. Lechman, F. Pierce, S. J. Plimpton, and P. R. Schunk (2014), "Particle dynamics modeling methods for colloid suspensions," *Computational Particle Mechanics*, 1 (3), 321–356.
- [78] Y. Marcus (1988), "Ionic radii in aqueous solutions," *Chemical Reviews*, 88 (8), 1475–1498.
- [79] B. Kang, H. Tang, Z. Zhao, and S. Song (2020), "Hofmeister Series: Insights of Ion Specificity from Amphiphilic Assembly and Interface Property," *ACS Omega*, 5 (12), 6229–6239.
- [80] T. Kister, D. Monego, P. Mulvaney, A. Widmer-Cooper, and T. Kraus (2018), "Colloidal Stability of Apolar Nanoparticles: The Role of Particle Size and Ligand Shell Structure," *ACS Nano*, 12 (6), 5969–5977.
- [81] M. Klokkenburg, A. J. Houtepen, R. Koole, J. W. J. de Folter, B. H. Ern , E. van Faassen, and D. Vanmaekelbergh (2007), "Dipolar Structures in Colloidal Dispersions of PbSe and CdSe Quantum Dots," *Nano Letters*, 7 (9), 2931–2936.
- [82] J. Brijitta and P. Schurtenberger (2019), "Responsive hydrogel colloids: Structure, interactions, phase behavior, and equilibrium and nonequilibrium transitions of microgel dispersions," *Current Opinion in Colloid & Interface Science*, 40, 87–103.
- [83] M. Green (2010), "The nature of quantum dot capping ligands," *Journal of Materials Chemistry*, 20 (28), 5797.
- [84] L. M. Rossi, J. L. Fiorio, M. A. Garcia, and C. P. Ferraz (2018), "The role and fate of capping ligands in colloiddally prepared metal nanoparticle catalysts," *Dalton Transactions*, 47 (17), 5889–5915.
- [85] A. Heuer-Jungemann, N. Feliu, I. Bakaimi, *et al.* (2019), "The Role of Ligands in the Chemical Synthesis and Applications of Inorganic Nanoparticles," *Chemical Reviews*, 119 (8), 4819–4880.
- [86] B. T. Diroll, K. M. Weigandt, D. Jishkariani, M. Cargnello, R. J. Murphy, L. A. Hough, C. B. Murray, and B. Donnio (2015), "Quantifying "Softness" of Organic Coatings on Gold Nanoparticles Using Correlated Small-Angle X-ray and Neutron Scattering," *Nano Letters*, 15 (12), 8008–8012.
- [87] K. Vondermassen, J. Bongers, A. Mueller, and H. Versmold (1994), "Brownian Motion: A Tool To Determine the Pair Potential between Colloid Particles," *Langmuir*, 10 (5), 1351–1353.
- [88] C. P. Royall, M. E. Leunissen, and A. van Blaaderen (2003), "A new colloidal model system to study long-range interactions quantitatively in real space," *Journal of Physics: Condensed Matter*, 15 (48), S3581–S3596.
- [89] D. Tabor and R. Winterton (1969), "The direct measurement of normal and retarded van der Waals forces," *Proceedings of the Royal Society of London. A. Mathematical and Physical Sciences*, 312 (1511), 435–450.
- [90] J. N. Israelachvili and G. E. Adams (1976), "Direct measurement of long range forces between two mica surfaces in aqueous KNO₃ solutions," *Nature*, 262 (5571), 774–776.
- [91] J. N. Israelachvili and G. E. Adams (1978), "Measurement of forces between two mica surfaces in aqueous electrolyte solutions in the range 0–100 nm," *Journal of the Chemical Society, Faraday Transactions 1: Physical Chemistry in Condensed Phases*, 74, 975.
- [92] J. Overbeek and M. Sparnaay (1952), "Experiments on long-range attractive forces between macroscopic objects," *Journal of Colloid Science*, 7 (3), 343–345.
- [93] B. V. Derjaguin, I. I. Abrikosova, and E. M. Lifshitz (1956), "Direct measurement of molecular attraction between solids separated by a narrow gap," *Quarterly Reviews, Chemical Society*, 10 (3), 295.
- [94] J. Israelachvili, Y. Min, M. Akbulut, A. Alig, G. Carver, W. Greene, K. Kristiansen, E. Meyer, N. Pesika, K. Rosenberg, and H. Zeng (2010), "Recent advances in the surface forces apparatus (SFA) technique," *Reports on Progress in Physics*, 73 (3), 036601.
- [95] B. Derjaguin (1934), "Untersuchungen  ber die Reibung und Adh sion, IV," *Kolloid-Zeitschrift* 1934 69:2, 69 (2), 155–164.
- [96] M. Borkovec, I. Szilagy , I. Popa, M. Finessi, P. Sinha, P. Maroni, and G. Papastavrou (2012), "Investigating forces between charged particles in the presence of oppositely charged polyelectrolytes with the multi-particle colloidal probe technique," *Advances in Colloid and Interface Science*, 179–182, 85–98.
- [97] R. G. Horn and J. N. Israelachvili (1981), "Direct measurement of structural forces between two surfaces in a nonpolar liquid," *The Journal of Chemical Physics*, 75 (3), 1400–1411.
- [98] Y. Qin and K. A. Fichtorn (2006), "Solvation forces between colloidal nanoparticles: Directed alignment," *Physical Review E*, 73 (2), 020401.
- [99] H.-J. Butt, B. Cappella, and M. Kappl (2005), "Force measurements with the atomic force microscope: Technique, interpretation and applications," *Surface Science Reports*, 59 (1–6), 1–152.
- [100] H.-J. Butt, R. Berger, E. Bonaccorso, Y. Chen, and J. Wang (2007), "Impact of atomic force microscopy

- on interface and colloid science," *Advances in Colloid and Interface Science*, 133 (2), 91–104.
- [101] A. Mark, N. Helfricht, A. Rauh, M. Karg, and G. Papastavrou (2019), "The Next Generation of Colloidal Probes: A Universal Approach for Soft and Ultra-Small Particles," *Small*, 15 (43), 1902976.
- [102] H. J. Butt (1991), "Measuring electrostatic, van der Waals, and hydration forces in electrolyte solutions with an atomic force microscope," *Biophysical Journal*, 60 (6), 1438–1444.
- [103] W. A. Ducker, T. J. Senden, and R. M. Pashley (1991), "Direct measurement of colloidal forces using an atomic force microscope," *Nature*, 353 (6341), 239–241.
- [104] Y. Gan (2007), "Invited Review Article: A review of techniques for attaching micro- and nanoparticles to a probe's tip for surface force and near-field optical measurements," *Review of Scientific Instruments*, 78 (8), 081101.
- [105] C. T. McKee and J. Y. Walz (2012), "Interaction forces between colloidal particles in a solution of like-charged, adsorbing nanoparticles," *Journal of Colloid and Interface Science*, 365 (1), 72–80.
- [106] P. Sinha, I. Szilagy, F. J. Montes Ruiz-Cabello, P. Maroni, and M. Borkovec (2013), "Attractive Forces between Charged Colloidal Particles Induced by Multivalent Ions Revealed by Confronting Aggregation and Direct Force Measurements," *The Journal of Physical Chemistry Letters*, 4 (4), 648–652.
- [107] M. Elzbiaciak-Wodka, M. N. Popescu, F. J. M. Ruiz-Cabello, G. Trefalt, P. Maroni, and M. Borkovec (2014), "Measurements of dispersion forces between colloidal latex particles with the atomic force microscope and comparison with Lifshitz theory," *The Journal of Chemical Physics*, 140 (10), 104906.
- [108] D. Herman and J. Y. Walz (2015), "Forces and force-scaling in systems of adsorbing nanoparticles as measured using colloidal probe atomic force microscopy," *Colloids and Surfaces A: Physicochemical and Engineering Aspects*, 482, 165–176.
- [109] G. Trefalt, T. Palberg, and M. Borkovec (2017), "Forces between colloidal particles in aqueous solutions containing monovalent and multivalent ions," *Current Opinion in Colloid & Interface Science*, 27, 9–17.
- [110] N. Arai, S. Watanabe, and M. T. Miyahara (2019), "On the Convective Self-Assembly of Colloidal Particles in Nanofluid Based on In Situ Measurements of Interaction Forces," *Langmuir*, 35 (35), 11533–11541.
- [111] C. C. Yuan, D. Zhang, and Y. Gan (2017), "Invited Review Article: Tip modification methods for tip-enhanced Raman spectroscopy (TERS) and colloidal probe technique: A 10 year update (2006–2016) review," *Review of Scientific Instruments*, 88 (3), 031101.
- [112] P. Dörig, D. Ossola, A. M. Truong, M. Graf, F. Stauffer, J. Vörös, and T. Zambelli (2013), "Exchangeable Colloidal AFM Probes for the Quantification of Irreversible and Long-Term Interactions," *Biophysical Journal*, 105 (2), 463–472.
- [113] N. Helfricht, A. Mark, L. Dorwling-Carter, T. Zambelli, G. Papastavrou, Nicolas Helfricht, Andreas Mark, Livie Dorwling-Carter, Tomaso Zambelli, and Georg Papastavrou (2017), "Extending the limits of direct force measurements: colloidal probes from sub-micron particles," *Nanoscale*, 9 (27), 9491–9501.
- [114] O. Sqalli, M.-P. Bernal, P. Hoffmann, and F. Marquis-Weible (2000), "Improved tip performance for scanning near-field optical microscopy by the attachment of a single gold nanoparticle," *Applied Physics Letters*, 76 (15), 2134–2136.
- [115] I. U. Vakarelski and K. Higashitani (2006), "Single-Nanoparticle-Terminated Tips for Scanning Probe Microscopy," *Langmuir*, 22 (7), 2931–2934.
- [116] T. Kim, S. Myung, T. H. Kim, and S. Hong (2008), "Robust Single-Nanoparticle Probe for Contact-Mode Analysis and Dip-Pen Nanolithography," *Small*, 4 (8), 1072–1075.
- [117] X. Liu (2018), "Interactions of Silver Nanoparticles Formed in Situ on AFM Tips with Supported Lipid Bilayers," *Langmuir*, 34 (36), 10774–10781.
- [118] T. Kalkbrenner, M. Ramstein, J. Mlynek, and V. Sandoghdar (2001), "A single gold particle as a probe for apertureless scanning near-field optical microscopy," *Journal of Microscopy*, 202 (1), 72–76.
- [119] C. Leiterer, E. Wünsche, P. Singh, J. Albert, J. M. Köhler, V. Deckert, and W. Fritzsche (2016), "High precision attachment of silver nanoparticles on AFM tips by dielectrophoresis," *Analytical and Bioanalytical Chemistry*, 408 (13), 3625–3631.
- [120] T. Okamoto and I. Yamaguchi (2001), "Photocatalytic deposition of a gold nanoparticle onto the top of a SiN cantilever tip," *Journal of Microscopy*, 202 (1), 100–103.
- [121] O. Sqalli, I. Utke, P. Hoffmann, and F. Marquis-Weible (2002), "Gold elliptical nanoantennas as probes for near field optical microscopy," *Journal of Applied Physics*, 92 (2), 1078–1083.
- [122] A. Sanders, L. Zhang, R. W. Bowman, L. O. Hermann, and J. J. Baumberg (2015), "Facile Fabrication of Spherical Nanoparticle-Tipped AFM

- Probes for Plasmonic Applications,” *Particle & Particle Systems Characterization*, 32 (2), 182–187.
- [123] Q. K. Ong and I. Sokolov (2007), “Attachment of nanoparticles to the AFM tips for direct measurements of interaction between a single nanoparticle and surfaces,” *Journal of Colloid and Interface Science*, 310 (2), 385–390.
- [124] S. Salameh, J. Schneider, J. Laube, A. Alessandrini, P. Facci, J. W. Seo, L. C. Ciacchi, and L. Mädler (2012), “Adhesion Mechanisms of the Contact Interface of TiO₂ Nanoparticles in Films and Aggregates,” *Langmuir*, 28 (31), 11457–11464.
- [125] E. R. Weeks, *Microscopy of Soft Materials*, in *Experimental and Computational Methods in Soft Condensed Matter*, J. Olafsen, Ed., Cambridge University Press, 2010, ch. 1, pp. 1–24.
- [126] A. Aloï and I. K. Voets (2018), “Soft matter nanoscopy,” *Current Opinion in Colloid & Interface Science*, 34, 59–73.
- [127] K. A. Rose, M. Molaei, M. J. Boyle, D. Lee, J. C. Crocker, and R. J. Composto (2020), “Particle tracking of nanoparticles in soft matter,” *Journal of Applied Physics*, 127 (19), 191101.
- [128] M. A. Bevan and S. L. Eichmann (2011), “Optical microscopy measurements of kT-scale colloidal interactions,” *Current Opinion in Colloid & Interface Science*, 16 (2), 149–157.
- [129] D. C. Prieve, F. Luo, and F. Lanni (1987), “Brownian Motion of a Hydrosol Particle in a Colloidal Force Field,” *Faraday Discuss. Chem. SOC*, 83, 297–307.
- [130] S. G. Bike (2000), “Measuring colloidal forces using evanescent wave scattering,” *Current Opinion in Colloid & Interface Science*, 5 (1-2), 144–150.
- [131] X. Gong, Z. Wang, and T. Ngai (2014), “Direct measurements of particle–surface interactions in aqueous solutions with total internal reflection microscopy,” *Chemical Communications*, 50 (50), 6556–6570.
- [132] H.-J. Wu and M. A. Bevan (2005), “Direct Measurement of Single and Ensemble Average Particle-Surface Potential Energy Profiles,” *Langmuir*, 21 (4), 1244–1254.
- [133] H.-J. Wu, T. O. Pangburn, R. E. Beckham, and M. A. Bevan (2005), “Measurement and Interpretation of Particle-Particle and Particle-Wall Interactions in Levitated Colloidal Ensembles,” *Langmuir*, 21 (22), 9879–9888.
- [134] A. Sharma and J. Y. Walz (1996), “Direct measurement of the depletion interaction in a charged colloidal dispersion,” *Journal of the Chemical Society, Faraday Transactions*, 92 (24), 4997.
- [135] T. D. Iracki, D. J. Beltran-Villegas, S. L. Eichmann, and M. A. Bevan (2010), “Charged micelle depletion attraction and interfacial colloidal phase behavior,” *Langmuir*, 26 (24), 18710–18717.
- [136] D. Kleshchanok and P. R. Lang (2007), “Steric Repulsion by Adsorbed Polymer Layers Studied with Total Internal Reflection Microscopy,” *Langmuir*, 23 (8), 4332–4339.
- [137] V. Blickle, D. Babič, and C. Bechinger (2005), “Evanescent light scattering with magnetic colloids,” *Applied Physics Letters*, 87 (10), 101102.
- [138] M. G. Petroff, E. A. Garcia, M. Herrera-Alonso, and M. A. Bevan (2019), “Ionic Strength-Dependent Interactions and Dimensions of Adsorbed Zwitterionic Copolymers,” *Langmuir*, 35 (14), 4976–4985.
- [139] H. Najafi, H. A. Jerri, V. Valmacco, M. G. Petroff, C. Hansen, D. Benczédi, and M. A. Bevan (2020), “Synergistic Polymer–Surfactant-Complex Mediated Colloidal Interactions and Deposition,” *ACS Applied Materials & Interfaces*, 12 (12), 14518–14530.
- [140] C. Hertlein, L. Helden, A. Gambassi, S. Dietrich, and C. Bechinger (2008), “Direct measurement of critical Casimir forces,” *Nature*, 451 (7175), 172–175.
- [141] L. Helden, K. Dietrich, and C. Bechinger (2016), “Interactions of Colloidal Particles and Droplets with Water–Oil Interfaces Measured by Total Internal Reflection Microscopy,” *Langmuir*, 32 (51), 13752–13758.
- [142] S. L. Eichmann, S. G. Anekal, and M. A. Bevan (2008), “Electrostatically Confined Nanoparticle Interactions and Dynamics,” *Langmuir*, 24 (3), 714–721.
- [143] S. L. Eichmann and M. A. Bevan (2010), “Direct measurements of protein-stabilized gold nanoparticle interactions,” *Langmuir*, 26 (18), 14409–14413.
- [144] S. L. Eichmann, B. Smith, G. Meric, D. H. Fairbrother, and M. A. Bevan (2011), “Imaging Carbon Nanotube Interactions, Diffusion, and Stability in Nanopores,” *ACS Nano*, 5 (7), 5909–5919.
- [145] P. Schein, C. K. Ashcroft, D. O’Dell, I. S. Adam, B. DiPaolo, M. Sabharwal, C. Shi, R. Hart, C. Earhart, and D. Erickson (2015), “Near-Field Light Scattering Techniques for Measuring Nanoparticle-Surface Interaction Energies and Forces,” *Journal of Lightwave Technology*, 33 (16), 3494–3502.
- [146] P. Schein, P. Kang, D. O’Dell, and D. Erickson (2015), “Nanophotonic Force Microscopy: Characterizing Particle–Surface Interactions Using Near-Field Photonics,” *Nano Letters*, 15 (2), 1414–1420.

- [147] A. Lundgren, B. Agnarsson, R. Zirbs, V. P. Zhdanov, E. Reimhult, and F. Höök (2016), “Nonspecific Colloidal-Type Interaction Explains Size-Dependent Specific Binding of Membrane-Targeted Nanoparticles,” *ACS Nano*, 10 (11), 9974–9982.
- [148] D. Andrén, N. Odebo Länk, H. Šipová-Jungová, S. Jones, P. Johansson, and M. Käll (2019), “Surface Interactions of Gold Nanoparticles Optically Trapped against an Interface,” *The Journal of Physical Chemistry C*, 123 (26), 16406–16414.
- [149] F. Cui, S. Marbach, J. A. Zheng, M. Holmes-Cerfon, and D. J. Pine (2022), “Comprehensive view of microscopic interactions between DNA-coated colloids,” *Nature Communications*, 13 (1), 2304.
- [150] F. Cui and D. J. Pine (2022), “Effect of photon counting shot noise on total internal reflection microscopy,” *Soft Matter*, 18 (1), 162–171.
- [151] D. O’Dell, P. Schein, and D. Erickson (2016), “Simultaneous Characterization of Nanoparticle Size and Particle-Surface Interactions with Three-Dimensional Nanophotonic Force Microscopy,” *Physical Review Applied*, 6 (3), 034010.
- [152] D. R. Hristov, D. Ye, J. M. de Araújo, C. Ashcroft, B. DiPaolo, R. Hart, C. Earhart, H. Lopez, and K. A. Dawson (2017), “Using single nanoparticle tracking obtained by nanophotonic force microscopy to simultaneously characterize nanoparticle size distribution and nanoparticle–surface interactions,” *Nanoscale*, 9 (13), 4524–4535.
- [153] B. Agnarsson, A. Lundgren, A. Gunnarsson, M. Rabe, A. Kunze, M. Mapar, L. Simonsson, M. Bally, V. P. Zhdanov, and F. Höök (2015), “Evanescent Light-Scattering Microscopy for Label-Free Interfacial Imaging: From Single Sub-100 nm Vesicles to Live Cells,” *ACS Nano*, 9 (12), 11849–11862.
- [154] J. Bongers, H. Manteufel, K. Vondermaßen, and H. Versmold (1998), “Video microscopy: investigations of the structure and dynamics of colloidal dispersions,” *Colloids and Surfaces A: Physicochemical and Engineering Aspects*, 142 (2-3), 381–385.
- [155] G. M. Kepler and S. Fraden (1994), “Video Microscopy Study of the Potential Energy of a Colloidal Particle Confined between Two Plates,” *Langmuir*, 10 (8), 2501–2506.
- [156] R. L. Henderson (1974), “A uniqueness theorem for fluid pair correlation functions,” *Physics Letters A*, 49 (3), 197–198.
- [157] F. Frommer, M. Hanke, and S. Jansen (2019), “A note on the uniqueness result for the inverse Henderson problem,” *Journal of Mathematical Physics*, 60 (9), 093303.
- [158] R. Potestio (2013), “Is Henderson’s theorem practically useful?” *Journal of Unsolved Questions*, 3 (1), 13–15.
- [159] H. Wang, F. H. Stillinger, and S. Torquato (2020), “Sensitivity of pair statistics on pair potentials in many-body systems,” *The Journal of Chemical Physics*, 153 (12), 124106.
- [160] D. Chandler, *Introduction to Modern Statistical Mechanics*. Oxford University Press, 1987.
- [161] G. M. Kepler and S. Fraden (1994), “Attractive potential between confined colloids at low ionic strength,” *Physical Review Letters*, 73 (2), 356–359.
- [162] J. C. Crocker and D. G. Grier (1994), “Microscopic measurement of the pair interaction potential of charge-stabilized colloid,” *Physical Review Letters*, 73 (2), 352–355.
- [163] C. R. Iacovella, R. E. Rogers, S. C. Glotzer, and M. J. Solomon (2010), “Pair interaction potentials of colloids by extrapolation of confocal microscopy measurements of collective suspension structure,” *The Journal of Chemical Physics*, 133 (16), 164903.
- [164] A. Soper (1996), “Empirical potential Monte Carlo simulation of fluid structure,” *Chemical Physics*, 202 (2-3), 295–306.
- [165] D. Reith, M. Pütz, and F. Müller-Plathe (2003), “Deriving effective mesoscale potentials from atomistic simulations,” *Journal of Computational Chemistry*, 24 (13), 1624–1636.
- [166] W. Schommers (1973), “A pair potential for liquid rubidium from the pair correlation function,” *Physics Letters A*, 43 (2), 157–158.
- [167] D. Levesque, J. J. Weis, and L. Reatto (1985), “Pair Interaction from Structural Data for Dense Classical Liquids,” *Physical Review Letters*, 54 (5), 451–454.
- [168] T. O. Pangburn and M. A. Bevan (2006), “Anomalous potentials from inverse analyses of interfacial polydisperse attractive colloidal fluids,” *The Journal of Chemical Physics*, 124 (5), 054712.
- [169] J. J. Juárez, B. G. Liu, J. Q. Cui, and M. A. Bevan (2011), “KT-scale colloidal interactions in high-frequency inhomogeneous AC electric fields. II. Concentrated ensembles,” *Langmuir*, 27 (15), 9219–9226.
- [170] R. S. Hendley, I. Torres-Díaz, and M. A. Bevan (2021), “Anisotropic colloidal interactions & assembly in AC electric fields,” *Soft Matter*, 17 (40), 9066–9077.
- [171] L. Ornstein and F. Zernike (1914), “Accidental deviations of density and opalescence at the critical point of a single substance,” *Proc. Akad. Sci.*, XVII (September), 793–806.

- [172] J.-P. Hansen and I. R. McDonald, *Theory of Simple Liquids, Second Edition 3rd Edition*. Academic Press, 2006.
- [173] S. H. Behrens and D. G. Grier (2001), "Pair interaction of charged colloidal spheres near a charged wall," *Physical Review E*, 64 (5), 050401.
- [174] B. Widom (1963), "Some Topics in the Theory of Fluids," *The Journal of Chemical Physics*, 39 (11), 2808–2812.
- [175] B. M. Mladek and D. Frenkel (2011), "Pair interactions between complex mesoscopic particles from Widom's particle-insertion method," *Soft Matter*, 7 (4), 1450–1455.
- [176] A. E. Stones, R. P. A. Dullens, and D. G. A. L. Aarts (2018), "Contact values of pair distribution functions in colloidal hard disks by test-particle insertion," *The Journal of Chemical Physics*, 148 (24), 241102.
- [177] A. E. Stones, R. P. Dullens, and D. G. Aarts (2019), "Model-Free Measurement of the Pair Potential in Colloidal Fluids Using Optical Microscopy," *Physical Review Letters*, 123 (9), 098002.
- [178] A. E. Stones and D. G. A. L. Aarts (2023), "Measuring many-body distribution functions in fluids using test-particle insertion," *The Journal of Chemical Physics*, 159 (19), 194502.
- [179] S. K. Sainis, V. Germain, and E. R. Dufresne (2007), "Statistics of Particle Trajectories at Short Time Intervals Reveal n -Scale Colloidal Forces," *Physical Review Letters*, 99 (1), 018303.
- [180] I. C. Jenkins, J. C. Crocker, and T. Sinno (2015), "Interaction potentials from arbitrary multi-particle trajectory data," *Soft Matter*, 11 (35), 6948–6956.
- [181] A. C. H. Coughlan and M. A. Bevan (2017), "Effective colloidal interactions in rotating magnetic fields," *The Journal of Chemical Physics*, 147 (7), 074903.
- [182] L. Pérez García, J. Donlucas Pérez, G. Volpe, A. V. Arzola, and G. Volpe (2018), "High-performance reconstruction of microscopic force fields from Brownian trajectories," *Nature Communications*, 9 (1), 5166.
- [183] A. Frishman and P. Ronceray (2020), "Learning force fields from stochastic trajectories," *Physical Review X*, 10 (2), 021009.
- [184] M. Ruiz-Garcia, C. M. B. Gutierrez, L. C. Alexander, D. G. A. L. Aarts, L. Ghiringhelli, and C. Valeriani (2022), "Discovering dynamic laws from observations: the case of self-propelled, interacting colloids." Preprint: [arXiv:2203.14846](https://arxiv.org/abs/2203.14846).
- [185] A. Huhle, D. Klaue, H. Brutzer, P. Daldrop, S. Joo, O. Otto, U. F. Keyser, and R. Seidel (2015), "Camera-based three-dimensional real-time particle tracking at kHz rates and Ångström accuracy," *Nature Communications*, 6 (1), 5885.
- [186] K. Srinivasa Rao and R. Rajagopalan (1998), "Interaction forces in quasi-two-dimensional charged dispersions," *Physical Review E*, 57 (3), 3227.
- [187] M. Polin, D. G. Grier, and Y. Han (2007), "Colloidal electrostatic interactions near a conducting surface," *Physical Review E*, 76 (4), 041406.
- [188] C. P. Royall, A. A. Louis, and H. Tanaka (2007), "Measuring colloidal interactions with confocal microscopy," *The Journal of Chemical Physics*, 127 (4).
- [189] M. Jenkins and S. Egelhaaf (2008), "Confocal microscopy of colloidal particles: Towards reliable, optimum coordinates," *Advances in Colloid and Interface Science*, 136 (1-2), 65–92.
- [190] S.-H. Lee, Y. Roichman, G.-R. Yi, S.-H. Kim, S.-M. Yang, A. van Blaaderen, P. van Oostrum, and D. G. Grier (2007), "Characterizing and tracking single colloidal particles with video holographic microscopy," *Optics Express*, 15 (26), 18275.
- [191] M. D. Hannel, A. Abdulali, M. O'Brien, and D. G. Grier (2018), "Machine-learning techniques for fast and accurate feature localization in holograms of colloidal particles," *Optics Express*, 26 (12), 15221.
- [192] M. B. Bouchard, V. Voleti, C. S. Mendes, C. Laceyfield, W. B. Grueber, R. S. Mann, R. M. Bruno, and E. M. C. Hillman (2015), "Swept confocally-aligned planar excitation (SCAPE) microscopy for high-speed volumetric imaging of behaving organisms," *Nature Photonics*, 9 (2), 113–119.
- [193] M. J. Bergman, N. Gnan, M. Obiols-Rabasa, J.-M. Meijer, L. Rovigatti, E. Zaccarelli, and P. Schurtenberger (2018), "A new look at effective interactions between microgel particles," *Nature Communications*, 9 (1), 5039.
- [194] M. J. Bergman, S. Nöjd, P. S. Mohanty, N. Boon, J. N. Immink, J. J. E. Maris, J. Stenhammar, and P. Schurtenberger (2021), "On the role of softness in ionic microgel interactions," *Soft Matter*, 17 (44), 10063–10072.
- [195] J. C. Crocker and D. G. Grier (1996), "Methods of Digital Video Microscopy for Colloidal Studies," *Journal of Colloid and Interface Science*, 179 (1), 298–310.
- [196] R. Parthasarathy (2012), "Rapid, accurate particle tracking by calculation of radial symmetry centers," *Nature Methods*, 9 (7), 724–726.
- [197] R. Kurita, D. B. Ruffner, and E. R. Weeks (2012), "Measuring the size of individual particles from

- three-dimensional imaging experiments," *Nature Communications*, 3 (1), 1127.
- [198] M. Leocmach and H. Tanaka (2013), "A novel particle tracking method with individual particle size measurement and its application to ordering in glassy hard sphere colloids," *Soft Matter*, 9 (5), 1447–1457.
- [199] Y. Gao and M. E. Helgeson (2014), "Texture analysis microscopy: quantifying structure in low-fidelity images of dense fluids," *Optics Express*, 22 (8), 10046.
- [200] K. E. Jensen and N. Nakamura (2016), "Note: An iterative algorithm to improve colloidal particle locating," *Review of Scientific Instruments*, 87 (6), 066103.
- [201] M. Bierbaum, B. D. Leahy, A. A. Alemi, I. Cohen, and J. P. Sethna (2017), "Light Microscopy at Maximal Precision," *Physical Review X*, 7 (4), 041007.
- [202] C. van der Wel and D. J. Kraft (2017), "Automated tracking of colloidal clusters with sub-pixel accuracy and precision," *Journal of Physics: Condensed Matter*, 29 (4), 044001.
- [203] J. Baumgartl and C. Bechinger (2005), "On the limits of digital video microscopy," *Europhysics Letters (EPL)*, 71 (3), 487–493.
- [204] M. J. Bogdan and T. Savin (2018), "Errors in Energy Landscapes Measured with Particle Tracking," *Biophysical Journal*, 115 (1), 139–149.
- [205] B. D. Leahy, M. Bierbaum, J. Sethna, and I. Cohen (2018), "Biases in particle localization algorithms." Preprint: *arXiv:1801.03581*.
- [206] T. Savin and P. S. Doyle (2005), "Static and dynamic errors in particle tracking microrheology," *Biophysical Journal*, 88 (1), 623–638.
- [207] N. Chenouard, I. Smal, F. De Chaumont, *et al.* (2014), "Objective comparison of particle tracking methods," *Nature Methods*, 11 (3), 281–289.
- [208] G. M. De Luca, R. M. Breedijk, R. A. Brandt, C. H. Zeelenberg, B. E. de Jong, W. Timmermans, L. N. Azar, R. A. Hoebe, S. Stallinga, and E. M. Manders (2013), "Re-scan confocal microscopy: scanning twice for better resolution," *Biomedical Optics Express*, 4 (11), 2644.
- [209] M. A. Lauterbach, C. K. Ullal, V. Westphal, and S. W. Hell (2010), "Dynamic Imaging of Colloidal-Crystal Nanostructures at 200 Frames per Second," *Langmuir*, 26 (18), 14400–14404.
- [210] G. Pesce, P. H. Jones, O. M. Maragò, and G. Volpe (2020), "Optical tweezers: theory and practice," *The European Physical Journal Plus*, 135 (12), 949.
- [211] J. Gieseler, J. R. Gomez-Solano, A. Magazzù, I. Pérez Castillo, L. Pérez Garcia, M. Gironella-Torrent, X. Viader-Godoy, F. Ritort, G. Pesce, A. V. Arzola, K. Volke-Sepúlveda, and G. Volpe (2021), "Optical tweezers — from calibration to applications: a tutorial," *Advances in Optics and Photonics*, 13 (1), 74.
- [212] A. Rohrbach, C. Tischer, D. Neumayer, E.-L. Florin, and E. H. K. Stelzer (2004), "Trapping and tracking a local probe with a photonic force microscope," *Review of Scientific Instruments*, 75 (6), 2197–2210.
- [213] D. El Masri, P. van Oostrum, F. Smalenburg, T. Vissers, A. Imhof, M. Dijkstra, and A. van Blaaderen (2011), "Measuring colloidal forces from particle position deviations inside an optical trap," *Soft Matter*, 7 (7), 3462.
- [214] B. J. Park, B. Lee, and T. Yu (2014), "Pairwise interactions of colloids in two-dimensional geometric confinement," *Soft Matter*, 10 (48), 9675–9680.
- [215] D. W. Kang, K. H. Choi, S. J. Lee, and B. J. Park (2019), "Mapping Anisotropic and Heterogeneous Colloidal Interactions via Optical Laser Tweezers," *The Journal of Physical Chemistry Letters*, 10 (8), 1691–1697.
- [216] G. Volpe, G. Volpe, and D. Petrov (2007), "Brownian motion in a nonhomogeneous force field and photonic force microscope," *Physical Review E*, 76 (6), 061118.
- [217] Y. Roichman, B. Sun, A. Stolarski, and D. G. Grier (2008), "Influence of Nonconservative Optical Forces on the Dynamics of Optically Trapped Colloidal Spheres: The Fountain of Probability," *Physical Review Letters*, 101 (12), 128301.
- [218] Y. Roichman, B. Sun, Y. Roichman, J. Amato-Grill, and D. G. Grier (2008), "Optical Forces Arising from Phase Gradients," *Physical Review Letters*, 100 (1), 013602.
- [219] P. Wu, R. Huang, C. Tischer, A. Jonas, and E.-L. Florin (2009), "Direct Measurement of the Nonconservative Force Field Generated by Optical Tweezers," *Physical Review Letters*, 103 (10), 108101.
- [220] K. Sasaki, M. Koshioka, H. Misawa, N. Kitamura, and H. Masuhara (1991), "Pattern formation and flow control of fine particles by laser-scanning micromanipulation," *Optics Letters*, 16 (19), 1463.
- [221] P. L. Biancaniello and J. C. Crocker (2006), "Line optical tweezers instrument for measuring nanoscale interactions and kinetics," *Review of Scientific Instruments*, 77 (11), 113702.
- [222] W. B. Rogers and J. C. Crocker (2014), "A tunable line optical tweezers instrument with nanometer spatial resolution," *Review of Scientific Instruments*, 85 (4), 043704.

- [223] J. C. Crocker (1997), "Measurement of the hydrodynamic corrections to the Brownian motion of two colloidal spheres," *The Journal of Chemical Physics*, 106 (7), 2837–2840.
- [224] S. K. Sainis, V. Germain, C. O. Mejean, and E. R. Dufresne (2008), "Electrostatic Interactions of Colloidal Particles in Nonpolar Solvents: Role of Surface Chemistry and Charge Control Agents," *Langmuir*, 24 (4), 1160–1164.
- [225] I. Muntz, F. Waggett, M. Hunter, A. B. Schofield, P. Bartlett, D. Marenduzzo, and J. H. J. Thijssen (2020), "Interaction between nearly hard colloidal spheres at an oil-water interface," *Physical Review Research*, 2 (2), 023388.
- [226] M. Brunner, J. Dobnikar, H.-H. von Grünberg, and C. Bechinger (2004), "Direct Measurement of Three-Body Interactions amongst Charged Colloids," *Physical Review Letters*, 92 (7), 078301.
- [227] J. Dobnikar, M. Brunner, H.-H. von Grünberg, and C. Bechinger (2004), "Three-body interactions in colloidal systems," *Physical Review E*, 69 (3), 031402.
- [228] J. W. Merrill, S. K. Sainis, and E. R. Dufresne (2009), "Many-Body Electrostatic Forces between Colloidal Particles at Vanishing Ionic Strength," *Physical Review Letters*, 103 (13), 138301.
- [229] J. W. Merrill, S. K. Sainis, J. Bławdziewicz, and E. R. Dufresne (2010), "Many-body force and mobility measurements in colloidal systems," *Soft Matter*, 6 (10), 2187.
- [230] A. A. Al Balushi, A. Kotnala, S. Wheaton, R. M. Gelfand, Y. Rajashekara, and R. Gordon (2015), "Label-free free-solution nanoaperture optical tweezers for single molecule protein studies," *The Analyst*, 140 (14), 4760–4778.
- [231] O. M. Maragò, P. H. Jones, P. G. Gucciardi, G. Volpe, and A. C. Ferrari (2013), "Optical trapping and manipulation of nanostructures," *Nature Nanotechnology*, 8 (11), 807–819.
- [232] A. Lehmuskero, P. Johansson, H. Rubinsztein-Dunlop, L. Tong, and M. Käll (2015), "Laser Trapping of Colloidal Metal Nanoparticles," *ACS Nano*, 9 (4), 3453–3469.
- [233] F. Hajizadeh and S. S. Reihani (2010), "Optimized optical trapping of gold nanoparticles," *Optics Express*, 18 (2), 551.
- [234] R. A. Nome, M. J. Guffey, N. F. Scherer, and S. K. Gray (2009), "Plasmonic Interactions and Optical Forces between Au Bipyramidal Nanoparticle Dimers," *The Journal of Physical Chemistry A*, 113 (16), 4408–4415.
- [235] V. D. Miljković, T. Pakizeh, B. Sepulveda, P. Johansson, and M. Käll (2010), "Optical forces in plasmonic nanoparticle dimers," *Journal of Physical Chemistry C*, 114 (16), 7472–7479.
- [236] L. Tong, V. D. Miljković, P. Johansson, and M. Käll (2011), "Plasmon hybridization reveals the interaction between individual colloidal gold nanoparticles confined in an optical potential well," *Nano Letters*, 11 (11), 4505–4508.
- [237] M. Blattmann and A. Rohrbach (2015), "Plasmonic Coupling Dynamics of Silver Nanoparticles in an Optical Trap," *Nano Letters*, 15 (12), 7816–7821.
- [238] L. Lin, M. Wang, X. Peng, E. N. Lissek, Z. Mao, L. Scarabelli, E. Adkins, S. Coskun, H. E. Unalan, B. A. Korgel, L. M. Liz-Marzán, E.-L. Florin, and Y. Zheng (2018), "Opto-thermoelectric nanotweezers," *Nature Photonics*, 12 (4), 195–201.
- [239] R. Egerton and M. Watanabe (2022), "Spatial resolution in transmission electron microscopy," *Micron*, 160, 103304.
- [240] M. L. Taheri, E. A. Stach, I. Arslan, P. Crozier, B. C. Kabius, T. LaGrange, A. M. Minor, S. Takeda, M. Tanase, J. B. Wagner, and R. Sharma (2016), "Current status and future directions for in situ transmission electron microscopy," *Ultramicroscopy*, 170, 86–95.
- [241] D. Siegel, W. Green, and Y. Talmon (1994), "The mechanism of lamellar-to-inverted hexagonal phase transitions: a study using temperature-jump cryo-electron microscopy," *Biophysical Journal*, 66 (2), 402–414.
- [242] R. F. Thompson, M. Walker, C. A. Siebert, S. P. Muench, and N. A. Ranson (2016), "An introduction to sample preparation and imaging by cryo-electron microscopy for structural biology," *Methods*, 100, 3–15.
- [243] microscopy and P. L.-e. cryo-electron tomography of nanoparticles Stewart (2017), "Cryo-electron microscopy and cryo-electron tomography of nanoparticles," *Wiley Interdisciplinary Reviews: Nanomedicine and Nanobiotechnology*, 9 (2), 1–16.
- [244] J. Watt, D. L. Huber, and P. L. Stewart (2019), "Soft matter and nanomaterials characterization by cryogenic transmission electron microscopy," *MRS Bulletin*, 44 (12), 942–948.
- [245] Y. Li, W. Huang, Y. Li, W. Chiu, and Y. Cui (2020), "Opportunities for Cryogenic Electron Microscopy in Materials Science and Nanoscience," *ACS Nano*, 14 (8), 9263–9276.
- [246] A. Matatyaho Ya'akobi and Y. Talmon (2021), "Extending Cryo-EM to Nonaqueous Liquid Systems," *Accounts of chemical research*, 54 (9), 2100–2109.
- [247] D. Danino, R. Gupta, J. Satyavolu, and Y. Talmon (2002), "Direct Cryogenic-Temperature Transmis-

- sion Electron Microscopy Imaging of Phospholipid Aggregates in Soybean Oil,” *Journal of Colloid and Interface Science*, 249 (1), 180–186.
- [248] W. Umrath (1974), “Cooling bath for rapid freezing in electron microscopy,” *Journal of Microscopy*, 101 (1), 103–105.
- [249] M. F. Hayles and D. A. de Winter (2021), “An introduction to cryo-FIB-SEM cross-sectioning of frozen, hydrated Life Science samples,” *Journal of Microscopy*, 281 (2), 138–156.
- [250] J. van Rijssel, M. van der Linden, J. D. Meeldijk, R. J. A. van Dijk-Moes, A. P. Philipse, and B. H. Ern e (2013), “Spatial Distribution of Nanocrystals Imaged at the Liquid-Air Interface,” *Physical Review Letters*, 111 (10), 108302.
- [251] J. van Rijssel, V. F. D. Peters, J. D. Meeldijk, R. J. Kortschot, R. J. A. van Dijk-Moes, A. V. Petukhov, B. H. Ern e, and A. P. Philipse (2014), “Size-Dependent Second Virial Coefficients of Quantum Dots from Quantitative Cryogenic Electron Microscopy,” *The Journal of Physical Chemistry B*, 118 (37), 11000–11005.
- [252] K. Butter, P. H. Bomans, P. M. Frederik, G. J. Vroege, and A. P. Philipse (2003), “Direct observation of dipolar chains in iron ferrofluids by cryogenic electron microscopy,” *Nature Materials*, 2 (2), 88–91.
- [253] O. Balmes, J.-O. Malm, G. Karlsson, and J.-O. Bovin (2004), “Cryo-TEM observation of 3-dimensionally ordered aggregates of 5-nm gold particles in organic solvents,” *Journal of Nanoparticle Research*, 6 (6), 569–576.
- [254] M. Klokkenburg, R. P. Dullens, W. K. Kegel, B. H. Ern e, and A. P. Philipse (2006), “Quantitative real-space analysis of self-assembled structures of magnetic dipolar colloids,” *Physical Review Letters*, 96 (3), 037203.
- [255] J. Van Rijssel, B. H. Ern e, J. D. Meeldijk, M. Casavola, D. Vanmaekelbergh, A. Meijerink, and A. P. Philipse (2011), “Enthalpy and entropy of nanoparticle association from temperature-dependent cryo-TEM,” *Physical Chemistry Chemical Physics*, 13 (28), 12770–12774.
- [256] R. M. Glaeser (2018), “Proteins, interfaces, and cryo-EM grids,” *Current Opinion in Colloid & Interface Science*, 34, 1–8.
- [257] M.-H. Kang, J. Park, S. Kang, *et al.* (2021), “Graphene Oxide-Supported Microwell Grids for Preparing Cryo-EM Samples with Controlled Ice Thickness,” *Advanced Materials*, 33 (43), 2102991.
- [258] B. Kuei, M. P. Aplan, J. H. Litofsky, and E. D. Gomez (2020), “New opportunities in transmission electron microscopy of polymers,” *Materials Science and Engineering: R: Reports*, 139, 100516.
- [259] A. Rigort and J. M. Plitzko (2015), “Cryo-focused-ion-beam applications in structural biology,” *Archives of Biochemistry and Biophysics*, 581, 122–130.
- [260] C. D. Parmenter and Z. A. Nizamudeen (2021), “Cryo-FIB-lift-out: practically impossible to practical reality,” *Journal of Microscopy*, 281 (2), 157–174.
- [261] H. R. Vutukuri, S. Badaire, D. A. M. de Winter, A. Imhof, and A. van Blaaderen (2015), “Directed Self-Assembly of Micron-Sized Gold Nanoplatelets into Oriented Flexible Stacks with Tunable Interplate Distance,” *Nano Letters*, 15 (8), 5617–5623.
- [262] J. E. S. van der Hoeven, E. B. van der Wee, D. A. M. de Winter, M. Hermes, Y. Liu, J. Fokkema, M. Bransen, M. A. van Huis, H. C. Gerritsen, P. E. de Jongh, and A. van Blaaderen (2019), “Bridging the gap: 3D real-space characterization of colloidal assemblies via FIB-SEM tomography,” *Nanoscale*, 11 (12), 5304–5316.
- [263] F. M. Ross (2015), “Opportunities and challenges in liquid cell electron microscopy,” *Science*, 350 (6267).
- [264] H.-G. Liao and H. Zheng (2016), “Liquid Cell Transmission Electron Microscopy,” *Annual Review of Physical Chemistry*, 67 (1), 719–747.
- [265] B. H. Kim, J. Yang, D. Lee, B. K. Choi, T. Hyeon, and J. Park (2018), “Liquid-Phase Transmission Electron Microscopy for Studying Colloidal Inorganic Nanoparticles,” *Advanced Materials*, 30 (4), 1703316.
- [266] S. Pu, C. Gong, and A. W. Robertson (2020), “Liquid cell transmission electron microscopy and its applications,” *Royal Society Open Science*, 7 (1), 191204.
- [267] S. F. Tan, S. W. Chee, G. Lin, and U. Mirsaidov (2017), “Direct Observation of Interactions between Nanoparticles and Nanoparticle Self-Assembly in Solution,” *Accounts of Chemical Research*, 50 (6), 1303–1312.
- [268] B. Luo, J. W. Smith, Z. Ou, and Q. Chen (2017), “Quantifying the Self-Assembly Behavior of Anisotropic Nanoparticles Using Liquid-Phase Transmission Electron Microscopy,” *Accounts of Chemical Research*, 50 (5), 1125–1133.
- [269] J. Park, K. Koo, N. Noh, J. H. Chang, J. Y. Cheong, K. S. Dae, J. S. Park, S. Ji, I.-D. Kim, and J. M. Yuk (2021), “Graphene Liquid Cell Electron Microscopy: Progress, Applications, and Perspectives,” *ACS Nano*, 15 (1), 288–308.

- [270] W. J. Dearnaley, B. Schlepner, A. C. Varano, N. A. Alden, F. Gonzalez, M. A. Casasanta, B. E. Scharf, M. J. Dukes, and D. F. Kelly (2019), "Liquid-Cell Electron Tomography of Biological Systems," *Nano Letters*, 19 (10), 6734–6741.
- [271] J. Park, H. Elmlund, P. Ercius, J. M. Yuk, D. T. Limmer, Q. Chen, K. Kim, S. H. Han, D. A. Weitz, A. Zettl, and A. P. Alivisatos (2015), "3D structure of individual nanocrystals in solution by electron microscopy," *Science*, 349 (6245), 290–295.
- [272] T. A. J. Welling, S. Sadighikia, K. Watanabe, A. Grau-Carbonell, M. Bransen, D. Nagao, A. van Blaaderen, and M. A. van Huis (2020), "Observation of Undamped 3D Brownian Motion of Nanoparticles Using Liquid-Cell Scanning Transmission Electron Microscopy," *Particle & Particle Systems Characterization*, 37 (6), 2000003.
- [273] S. Gao, P. Wang, F. Zhang, G. T. Martinez, P. D. Nellist, X. Pan, and A. I. Kirkland (2017), "Electron ptychographic microscopy for three-dimensional imaging," *Nature Communications*, 8 (1), 163.
- [274] J. Lu, Z. Aabdin, N. D. Loh, D. Bhattacharya, and U. Mirsaidov (2014), "Nanoparticle Dynamics in a Nanodroplet," *Nano Letters*, 14 (4), 2111–2115.
- [275] T. J. Woehl and T. Prozorov (2015), "The Mechanisms for Nanoparticle Surface Diffusion and Chain Self-Assembly Determined from Real-Time Nanoscale Kinetics in Liquid," *The Journal of Physical Chemistry C*, 119 (36), 21261–21269.
- [276] A. Verch, M. Pfaff, and N. de Jonge (2015), "Exceptionally Slow Movement of Gold Nanoparticles at a Solid/Liquid Interface Investigated by Scanning Transmission Electron Microscopy," *Langmuir*, 31 (25), 6956–6964.
- [277] S. W. Chee, Z. Baraissov, N. D. Loh, P. T. Matsudaira, and U. Mirsaidov (2016), "Desorption-Mediated Motion of Nanoparticles at the Liquid-Solid Interface," *The Journal of Physical Chemistry C*, 120 (36), 20462–20470.
- [278] J. M. Howe (2004), "Effects of heat and electron irradiation on the melting behavior of Al-Si alloy particles and motion of the Al nanosphere within," *Journal of Electron Microscopy*, 53 (2), 107–114.
- [279] J. M. Grogan, N. M. Schneider, F. M. Ross, and H. H. Bau (2014), "Bubble and Pattern Formation in Liquid Induced by an Electron Beam," *Nano Letters*, 14 (1), 359–364.
- [280] H. Zheng, S. A. Claridge, A. M. Minor, A. P. Alivisatos, and U. Dahmen (2009), "Nanocrystal Diffusion in a Liquid Thin Film Observed by in Situ Transmission Electron Microscopy," *Nano Letters*, 9 (6), 2460–2465.
- [281] N. M. Schneider, M. M. Norton, B. J. Mendel, J. M. Grogan, F. M. Ross, and H. H. Bau (2014), "Electron–Water Interactions and Implications for Liquid Cell Electron Microscopy," *The Journal of Physical Chemistry C*, 118 (38), 22373–22382.
- [282] X. Ye, M. R. Jones, L. B. Frechette, Q. Chen, A. S. Powers, P. Ercius, G. Dunn, G. M. Rotskoff, S. C. Nguyen, V. P. Adiga, A. Zettl, E. Rabani, P. L. Geissler, and A. P. Alivisatos (2016), "Single-particle mapping of nonequilibrium nanocrystal transformations," *Science*, 354 (6314), 874–877.
- [283] A. Grau-Carbonell, S. Sadighikia, T. A. J. Welling, R. J. A. van Dijk-Moes, R. Kotni, M. Bransen, A. van Blaaderen, and M. A. van Huis (2021), "In Situ Study of the Wet Chemical Etching of SiO₂ and Nanoparticle@SiO₂ Core–Shell Nanospheres," *ACS Applied Nano Materials*, 4 (2), 1136–1148.
- [284] T. H. Moser, H. Mehta, C. Park, R. T. Kelly, T. Shokuhfar, and J. E. Evans (2018), "The role of electron irradiation history in liquid cell transmission electron microscopy," *Science Advances*, 4 (4).
- [285] Y. Liu, X.-M. Lin, Y. Sun, and T. Rajh (2013), "In Situ Visualization of Self-Assembly of Charged Gold Nanoparticles," *Journal of the American Chemical Society*, 135 (10), 3764–3767.
- [286] L. R. Parent, E. Bakalis, M. Proetto, Y. Li, C. Park, F. Zerbetto, and N. C. Gianneschi (2018), "Tackling the Challenges of Dynamic Experiments Using Liquid-Cell Transmission Electron Microscopy," *Accounts of Chemical Research*, 51 (1), 3–11.
- [287] M. N. Yesibolati, K. I. Mortensen, H. Sun, A. Broström, S. Tidemand-Lichtenberg, and K. Mølhave (2020), "Unhindered Brownian Motion of Individual Nanoparticles in Liquid-Phase Scanning Transmission Electron Microscopy," *Nano Letters*, 20 (10), 7108–7115.
- [288] Q. Chen, H. Cho, K. Manthiram, M. Yoshida, X. Ye, and A. P. Alivisatos (2015), "Interaction Potentials of Anisotropic Nanocrystals from the Trajectory Sampling of Particle Motion using in Situ Liquid Phase Transmission Electron Microscopy," *ACS Central Science*, 1 (1), 33–39.
- [289] D. A. Welch, T. J. Woehl, C. Park, R. Faller, J. E. Evans, and N. D. Browning (2016), "Understanding the Role of Solvation Forces on the Preferential Attachment of Nanoparticles in Liquid," *ACS Nano*, 10 (1), 181–187.
- [290] J. Kim, M. R. Jones, Z. Ou, and Q. Chen (2016), "In Situ Electron Microscopy Imaging and Quantitative Structural Modulation of Nanoparticle Superlattices," *ACS Nano*, 10 (11), 9801–9808.

- [291] S. F. Tan, U. Anand, and U. Mirsaidov (2017), "Interactions and Attachment Pathways between Functionalized Gold Nanorods," *ACS Nano*, 11 (2), 1633–1640.
- [292] J. Kim, Z. Ou, M. R. Jones, X. Song, and Q. Chen (2017), "Imaging the polymerization of multivalent nanoparticles in solution," *Nature Communications*, 8 (1), 761.
- [293] A. S. Powers, H.-G. Liao, S. N. Raja, N. D. Bronstein, A. P. Alivisatos, and H. Zheng (2017), "Tracking Nanoparticle Diffusion and Interaction during Self-Assembly in a Liquid Cell," *Nano Letters*, 17 (1), 15–20.
- [294] H. Cho, I. A. Moreno-Hernandez, V. Jamali, M. H. Oh, and A. P. Alivisatos (2021), "In Situ Quantification of Interactions between Charged Nanorods in a Predefined Potential Energy Landscape," *Nano Letters*, 21 (1), 628–633.
- [295] T. A. J. Welling, K. Watanabe, A. Grau-Carbonell, J. de Graaf, D. Nagao, A. Imhof, M. A. van Huis, and A. van Blaaderen (2021), "Tunability of Interactions between the Core and Shell in Rattle-Type Particles Studied with Liquid-Cell Electron Microscopy," *ACS Nano*, 15 (7), 11137–11149.
- [296] C. Zhu, S. Liang, E. Song, Y. Zhou, W. Wang, F. Shan, Y. Shi, C. Hao, K. Yin, T. Zhang, J. Liu, H. Zheng, and L. Sun (2018), "In-situ liquid cell transmission electron microscopy investigation on oriented attachment of gold nanoparticles," *Nature Communications*, 9 (1), 421.
- [297] F. Novotný, P. Wandrol, J. Proška, and M. Šlouf (2014), "In Situ WetSTEM Observation of Gold Nanorod Self-Assembly Dynamics in a Drying Colloidal Droplet," *Microscopy and Microanalysis*, 20 (2), 385–393.
- [298] D. Grzelak, P. Szustakiewicz, C. Tollan, S. Raj, P. Král, W. Lewandowski, and L. M. Liz-Marzán (2020), "In Situ Tracking of Colloidally Stable and Ordered Assemblies of Gold Nanorods," *Journal of the American Chemical Society*, 142 (44), 18814–18825.
- [299] T. Uematsu, M. Baba, Y. Oshima, T. Tsuda, T. Torimoto, and S. Kuwabata (2014), "Atomic Resolution Imaging of Gold Nanoparticle Generation and Growth in Ionic Liquids," *Journal of the American Chemical Society*, 136 (39), 13789–13797.
- [300] P. Y. Kim, Y. Gao, Y. Chai, P. D. Ashby, A. E. Ribbe, D. A. Hoagland, and T. P. Russell (2019), "Assessing Pair Interaction Potentials of Nanoparticles on Liquid Interfaces," *ACS Nano*, 13 (3), 3075–3082.
- [301] C. G. Bischak, J. G. Raybin, J. W. Kruppe, and N. S. Ginsberg (2020), "Charging-driven coarsening and melting of a colloidal nanoparticle monolayer at an ionic liquid–vacuum interface," *Soft Matter*, 16 (41), 9578–9589.
- [302] T. Tsuda and S. Kuwabata (2020), "Electron microscopy using ionic liquids for life and materials sciences," *Microscopy*, 69 (4), 183–195.
- [303] G. D. Vo and C. Park (2018), "Robust regression for image binarization under heavy noise and nonuniform background," *Pattern Recognition*, 81, 224–239.
- [304] L. Yao, Z. Ou, B. Luo, C. Xu, and Q. Chen (2020), "Machine Learning to Reveal Nanoparticle Dynamics from Liquid-Phase TEM Videos," *ACS Central Science*, 6 (8), 1421–1430.
- [305] F. k. Achter and L. Meyer (1969), "X-Ray scattering from liquid helium," *Physical Review*, 188 (1), 291–300.
- [306] R. Rajagopalan and C. Hirtzel (1987), "Effective interaction potentials in colloidal dispersions from structure data," *Journal of colloid and interface science*, 118 (2), 422–430.
- [307] M. L. Gee, P. Tong, J. N. Israelachvili, and T. A. Witten (1990), "Comparison of light scattering of colloidal dispersions with direct force measurements between analogous macroscopic surfaces," *The Journal of Chemical Physics*, 93 (8), 6057–6064.
- [308] J. S. Pedersen (1997), "Analysis of small-angle scattering data from colloids and polymer solutions: modeling and least-squares fitting," *Advances in Colloid and Interface Science*, 70 (1-3), 171–210.
- [309] G. Tóth (2006), "Reverse Monte Carlo analysis of small-angle scattering data on colloids and nanoparticles," *Journal of Molecular Liquids*, 129 (1-2), 108–114.
- [310] M.-C. Chang, C.-H. Tung, S.-Y. Chang, J. M. Carrillo, Y. Wang, B. G. Sumpter, G.-R. Huang, C. Do, and W.-R. Chen (2022), "A machine learning inversion scheme for determining interaction from scattering," *Communications Physics*, 5 (1), 46.
- [311] S. Torquato and H. Wang (2022), "Precise determination of pair interactions from pair statistics of many-body systems in and out of equilibrium," *Physical Review E*, 106 (4), 044122.
- [312] H.-Y. Kim, J. O. Sofo, D. Velegol, M. W. Cole, and A. A. Lucas (2006), "van der Waals forces between nanoclusters: Importance of many-body effects," *The Journal of Chemical Physics*, 124 (7), 074504.
- [313] H.-Y. Kim, J. O. Sofo, D. Velegol, M. W. Cole, and A. A. Lucas (2007), "Van der Waals Dispersion Forces between Dielectric Nanoclusters," *Langmuir*, 23 (4), 1735–1740.

- [314] V. V. Gobre and A. Tkatchenko (2013), “Scaling laws for van der Waals interactions in nanostructured materials,” *Nature Communications*, 4 (1), 2341.
- [315] L. T. Yan and X. M. Xie (2013), “Computational modeling and simulation of nanoparticle self-assembly in polymeric systems: Structures, properties and external field effects,” *Progress in Polymer Science*, 38 (2), 369–405.
- [316] P. Schapotschnikow, R. Pool, and T. J. H. Vlugt (2008), “Molecular Simulations of Interacting Nanocrystals,” *Nano Letters*, 8 (9), 2930–2934.
- [317] P. Schapotschnikow and T. J. H. Vlugt (2009), “Understanding interactions between capped nanocrystals: Three-body and chain packing effects,” *The Journal of Chemical Physics*, 131 (12), 124705.
- [318] K. M. Salerno, A. E. Ismail, J. M. D. Lane, and G. S. Grest (2014), “Coating thickness and coverage effects on the forces between silica nanoparticles in water,” *The Journal of Chemical Physics*, 140 (19), 194904.
- [319] T. R. Underwood and I. C. Bourg (2020), “Large-Scale Molecular Dynamics Simulation of the Dehydration of a Suspension of Smectite Clay Nanoparticles,” *The Journal of Physical Chemistry C*, 124 (6), 3702–3714.
- [320] S. Y. Joshi and S. A. Deshmukh (2021), “A review of advancements in coarse-grained molecular dynamics simulations,” *Molecular Simulation*, 47 (10–11), 786–803.
- [321] X. Liu, Y. Ni, and L. He (2019), “Interaction between capped tetrahedral gold nanocrystals: dependence on effective softness,” *Soft Matter*, 15 (41), 8392–8401.
- [322] Z. Fan and M. Grünwald (2019), “Orientational Order in Self-Assembled Nanocrystal Superlattices,” *Journal of the American Chemical Society*, 141 (5), 1980–1988.
- [323] G. Bauer, N. Gribova, A. Lange, C. Holm, and J. Gross (2017), “Three-body effects in triplets of capped gold nanocrystals,” *Molecular Physics*, 115 (9–12), 1031–1040.
- [324] C. Liepold, A. Smith, B. Lin, J. De Pablo, and S. A. Rice (2019), “Pair and many-body interactions between ligated Au nanoparticles,” *Journal of Chemical Physics*, 150 (4), 044904.
- [325] A. Widmer-Cooper and P. Geissler (2014), “Orientational ordering of passivating ligands on CdS nanorods in solution generates strong rod-rod interactions,” *Nano Letters*, 14 (1), 57–65.
- [326] D. Monego, T. Kister, N. Kirkwood, P. Mulvaney, A. Widmer-Cooper, and T. Kraus (2018), “Colloidal Stability of Apolar Nanoparticles: Role of Ligand Length,” *Langmuir*, 34 (43), 12982–12989.
- [327] A. Faruqi and G. McMullan (2018), “Direct imaging detectors for electron microscopy,” *Nuclear Instruments and Methods in Physics Research Section A: Accelerators, Spectrometers, Detectors and Associated Equipment*, 878, 180–190.
- [328] M. J. Pond, J. R. Errington, and T. M. Truskett (2011), “Implications of the effective one-component analysis of pair correlations in colloidal fluids with polydispersity,” *Journal of Chemical Physics*, 135 (12), 124513.
- [329] M. J. Solomon (2011), “Directions for targeted self-assembly of anisotropic colloids from statistical thermodynamics,” *Current Opinion in Colloid & Interface Science*, 16 (2), 158–167.
- [330] C. P. Lapointe, T. G. Mason, and I. I. Smalyukh (2009), “Shape-Controlled Colloidal Interactions in Nematic Liquid Crystals,” *Science*, 326 (5956), 1083–1086.
- [331] B. Rupp, I. Torres-Díaz, X. Hua, and M. A. Bevan (2018), “Measurement of Anisotropic Particle Interactions with Nonuniform ac Electric Fields,” *Langmuir*, 34 (7), 2497–2504.
- [332] M. Kappl and H.-J. Butt (2002), “The Colloidal Probe Technique and its Application to Adhesion Force Measurements,” *Particle & Particle Systems Characterization*, 19 (3), 129.
- [333] C. Graf and A. van Blaaderen (2002), “Metallo-dielectric Colloidal Core-Shell Particles for Photonic Applications,” *Langmuir*, 18 (2), 524–534.
- [334] L. Scarabelli, A. Sánchez-Iglesias, J. Pérez-Juste, and L. M. Liz-Marzán (2015), “A ‘‘Tips and Tricks’’ Practical Guide to the Synthesis of Gold Nanorods,” *The Journal of Physical Chemistry Letters*, 6 (21), 4270–4279.
- [335] C. Louis and O. Pluchery, *Gold nanoparticles for physics, chemistry and biology*. Imperial College Press, 2012.
- [336] M. Faraday (1857), “X. The Bakerian Lecture. — Experimental relations of gold (and other metals) to light,” *Philosophical Transactions of the Royal Society of London*, 147, 145–181.
- [337] G. Mie (1908), “Beiträge zur Optik trüber Medien, speziell kolloidaler Metallösungen,” *Annalen der Physik*, 330 (3), 377–445.
- [338] C. Daruich De Souza, B. Ribeiro Nogueira, and M. E. C. Rostelato (2019), “Review of the methodologies used in the synthesis gold nanoparticles by chemical reduction,” *Journal of Alloys and Compounds*, 798, 714–740.

- [339] M. Grzelczak, J. Pérez-Juste, P. Mulvaney, and L. M. Liz-Marzán (2008), "Shape control in gold nanoparticle synthesis," *Chemical Society Reviews*, 37 (9), 1783.
- [340] M. L. Personick and C. A. Mirkin (2013), "Making Sense of the Mayhem behind Shape Control in the Synthesis of Gold Nanoparticles," *Journal of the American Chemical Society*, 135 (49), 18238–18247.
- [341] M. N. O'Brien, M. R. Jones, K. A. Brown, and C. A. Mirkin (2014), "Universal Noble Metal Nanoparticle Seeds Realized Through Iterative Reductive Growth and Oxidative Dissolution Reactions," *Journal of the American Chemical Society*, 136 (21), 7603–7606.
- [342] A. Umar, J. Kim, and S.-M. Choi (2021), "One-Pot Synthesis of Monodisperse Single-Crystalline Spherical Gold Nanoparticles for Universal Seeds," *Crystal Growth & Design*, 21 (7), 4133–4140.
- [343] R. G. Nuzzo, B. R. Zegarski, and L. H. Dubois (1987), "Fundamental studies of the chemisorption of organosulfur compounds on gold(111). Implications for molecular self-assembly on gold surfaces," *Journal of the American Chemical Society*, 109 (3), 733–740.
- [344] J. C. Love, L. A. Estroff, J. K. Kriebel, R. G. Nuzzo, and G. M. Whitesides (2005), "Self-Assembled Monolayers of Thiolates on Metals as a Form of Nanotechnology," *Chemical Reviews*, 105 (4), 1103–1170.
- [345] Y. Yang, L. A. Serrano, and S. Guldin (2018), "A Versatile AuNP Synthetic Platform for Decoupled Control of Size and Surface Composition," *Langmuir*, 34 (23), 6820–6826.
- [346] Q. Fan, H. Yang, J. Ge, S. Zhang, Z. Liu, B. Lei, T. Cheng, Y. Li, Y. Yin, and C. Gao (2020), "Customizable Ligand Exchange for Tailored Surface Property of Noble Metal Nanocrystals," *Research*, 2020, 1–12.
- [347] E. V. Poleeva, A. T. Arymbaeva, and A. I. Bulavchenko (2020), "Varying the Surface Charges of Gold Nanoparticles in Span 80, AOT, and Span 80 + AOT Micellar Systems in n-Decane," *Russian Journal of Physical Chemistry A*, 94 (11), 2291–2298.
- [348] C. Graf, D. L. J. Vossen, A. Imhof, and A. van Blaaderen (2003), "A General Method To Coat Colloidal Particles with Silica," *Langmuir*, 19 (17), 6693–6700.
- [349] J. F. Li, Y. F. Huang, Y. Ding, Z. L. Yang, S. B. Li, X. S. Zhou, F. R. Fan, W. Zhang, Z. Y. Zhou, D. Y. Wu, B. Ren, Z. L. Wang, and Z. Q. Tian (2010), "Shell-isolated nanoparticle-enhanced Raman spectroscopy," *Nature*, 464 (7287), 392–395.
- [350] R. Jiang, B. Li, C. Fang, and J. Wang (2014), "Metal/Semiconductor Hybrid Nanostructures for Plasmon-Enhanced Applications," *Advanced Materials*, 26 (31), 5274–5309.
- [351] C. Hanske, M. N. Sanz-Ortiz, and L. M. Liz-Marzán (2018), "Silica-Coated Plasmonic Metal Nanoparticles in Action," *Advanced Materials*, 30 (27), 1707003–1707031.
- [352] Y. Lv, S. Duan, and R. Wang (2020), "Structure design, controllable synthesis, and application of metal-semiconductor heterostructure nanoparticles," *Progress in Natural Science: Materials International*, 30 (1), 1–12.
- [353] J. Turkevich, P. C. Stevenson, and J. Hillier (1951), "A study of the nucleation and growth processes in the synthesis of colloidal gold," *Discussions of the Faraday Society*, 11, 55.
- [354] G. Frens (1973), "Controlled Nucleation for the Regulation of the Particle Size in Monodisperse Gold Suspensions," *Nature Physical Science*, 241 (105), 20–22.
- [355] F. Schulz, T. Homolka, N. G. Bastús, V. Puentes, H. Weller, and T. Vossmeier (2014), "Little adjustments significantly improve the Turkevich synthesis of gold nanoparticles," *Langmuir*, 30 (35), 10779–10784.
- [356] M. Wuithschick, A. Birnbaum, S. Witte, M. Sztucki, U. Vainio, N. Pinna, K. Rademann, F. Emmerling, R. Kraehnert, and J. Polte (2015), "Turkevich in New Robes: Key Questions Answered for the Most Common Gold Nanoparticle Synthesis," *ACS Nano*, 9 (7), 7052–7071.
- [357] H. Xia, Y. Xiahou, P. Zhang, W. Ding, and D. Wang (2016), "Revitalizing the Frens Method to Synthesize Uniform, Quasi-Spherical Gold Nanoparticles with Deliberately Regulated Sizes from 2 to 330 nm," *Langmuir*, 32 (23), 5870–5880.
- [358] J. W. Park and J. S. Shumaker-Parry (2015), "Strong resistance of citrate anions on metal nanoparticles to desorption under thiol functionalization," *ACS Nano*, 9 (2), 1665–1682.
- [359] X. Xia, M. Yang, Y. Wang, Y. Zheng, Q. Li, J. Chen, and Y. Xia (2012), "Quantifying the coverage density of poly(ethylene glycol) chains on the surface of gold nanostructures," *ACS Nano*, 6 (1), 512–522.
- [360] K. Rahme, L. Chen, R. G. Hobbs, M. A. Morris, C. O'Driscoll, and J. D. Holmes (2013), "PEGylated gold nanoparticles: polymer quantification as a function of PEG lengths and nanoparticle dimensions," *RSC Adv.*, 3 (17), 6085–6094.

- [361] P. del Pino, F. Yang, B. Pelaz, Q. Zhang, K. Kantner, R. Hartmann, N. Martinez de Baroja, M. Gallego, M. Möller, B. B. Manshian, S. J. Soenen, R. Riedel, N. Hampp, and W. J. Parak (2016), "Basic Physicochemical Properties of Polyethylene Glycol Coated Gold Nanoparticles that Determine Their Interaction with Cells," *Angewandte Chemie International Edition*, 55 (18), 5483–5487.
- [362] Y. Xue, H.-M. Gao, L. Yu, N.-N. Zhang, J. Kang, C.-Y. Wang, Z.-Y. Lu, A. K. Whittaker, and K. Liu (2022), "Physiosorption of Poly(ethylene glycol) on Inorganic Nanoparticles," *ACS Nano*, 16 (4), 6634–6645.
- [363] M. Rubinstein and R. H. Colby, *Polymer Physics*. Oxford University Press, 2003.
- [364] S. D. Perrault and W. C. W. Chan (2009), "Synthesis and Surface Modification of Highly Monodispersed, Spherical Gold Nanoparticles of 50–200 nm," *Journal of the American Chemical Society*, 131 (47), 17042–17043.
- [365] J. Manson, D. Kumar, B. J. Meenan, and D. Dixon (2011), "Polyethylene glycol functionalized gold nanoparticles: the influence of capping density on stability in various media," *Gold Bulletin*, 44 (2), 99–105.
- [366] J. Fokkema, J. Fermie, N. Liv, D. J. van den Heuvel, T. O. M. Konings, G. A. Blab, A. Meijerink, J. Klumperman, and H. C. Gerritsen (2018), "Fluorescently Labelled Silica Coated Gold Nanoparticles as Fiducial Markers for Correlative Light and Electron Microscopy," *Scientific Reports*, 8 (1), 13625.
- [367] E. B. van der Wee, J. Fokkema, C. L. Kennedy, M. del Pozo, D. A. M. de Winter, P. N. A. Speets, H. C. Gerritsen, and A. van Blaaderen (2021), "3D test sample for the calibration and quality control of stimulated emission depletion (STED) and confocal microscopes," *Communications Biology*, 4 (1), 909.
- [368] A. Grau-Carbonell, F. Hagemans, M. Bransen, N. A. Elbers, R. J. van Dijk-Moes, S. Sadighikia, T. A. Welling, A. van Blaaderen, and M. A. van Huis (2023), "In situ single particle characterization of the thermoresponsive and consensolvent behavior of PNIPAM microgels and silica@PNIPAM core-shell colloids," *Journal of Colloid and Interface Science*, 635, 552–561.
- [369] G. M. Conley, S. Nöjd, M. Braibanti, P. Schurtenberger, and F. Scheffold (2016), "Superresolution microscopy of the volume phase transition of pNIPAM microgels," *Colloids and Surfaces A: Physicochemical and Engineering Aspects*, 499, 18–23.
- [370] J. Rodríguez-Fernández, J. Pérez-Juste, F. J. García de Abajo, and L. M. Liz-Marzán (2006), "Seeded Growth of Submicron Au Colloids with Quadrupole Plasmon Resonance Modes," *Langmuir*, 22 (16), 7007–7010.
- [371] N. G. Bastús, J. Comenge, and V. Puntes (2011), "Kinetically controlled seeded growth synthesis of citrate-stabilized gold nanoparticles of up to 200 nm: Size focusing versus ostwald ripening," *Langmuir*, 27 (17), 11098–11105.
- [372] N. Pazos-Perez, F. J. Garcia de Abajo, A. Fery, and R. A. Alvarez-Puebla (2012), "From Nano to Micro: Synthesis and Optical Properties of Homogeneous Spheroidal Gold Particles and Their Superlattices," *Langmuir*, 28 (24), 8909–8914.
- [373] J. Niu, T. Zhu, and Z. Liu (2007), "One-step seed-mediated growth of 30–150 nm quasispherical gold nanoparticles with 2-mercaptosuccinic acid as a new reducing agent," *Nanotechnology*, 18 (32), 325607.
- [374] C. Ziegler and A. Eychmüller (2011), "Seeded growth synthesis of uniform gold nanoparticles with diameters of 15–300 nm," *Journal of Physical Chemistry C*, 115 (11), 4502–4506.
- [375] Y. Zheng, X. Zhong, Z. Li, and Y. Xia (2014), "Successive, seed-mediated growth for the synthesis of single-crystal gold nanospheres with uniform diameters controlled in the range of 5–150 nm," *Particle & Particle Systems Characterization*, 31 (2), 266–273.
- [376] Y. J. Lee, N. B. Schade, L. Sun, J. A. Fan, D. R. Bae, M. M. Mariscal, G. Lee, F. Capasso, S. Sacanna, V. N. Manoharan, and G. R. Yi (2013), "Ultra-smooth, highly spherical monocrystalline gold particles for precision plasmonics," *ACS Nano*, 7 (12), 11064–11070.
- [377] Q. Ruan, L. Shao, Y. Shu, J. Wang, and H. Wu (2014), "Growth of Monodisperse Gold Nanospheres with Diameters from 20 nm to 220 nm and Their Core/Satellite Nanostructures," *Advanced Optical Materials*, 2 (1), 65–73.
- [378] C. Hanske, G. González-Rubio, C. Hamon, P. Formentín, E. Modin, A. Chuvilin, A. Guerrero-Martínez, L. F. Marsal, and L. M. Liz-Marzán (2017), "Large-Scale Plasmonic Pyramidal Super-crystals via Templated Self-Assembly of Monodisperse Gold Nanospheres," *The Journal of Physical Chemistry C*, 121 (20), 10899–10906.
- [379] T. Zhang, X. Li, C. Li, W. Cai, and Y. Li (2021), "One-Pot Synthesis of Ultra-smooth, Precisely Shaped Gold Nanospheres via Surface Self-Polishing Etching and Regrowth," *Chemistry of Materials*, 33 (7), 2593–2603.
- [380] N. R. Jana, L. Gearheart, and C. J. Murphy (2001), "Seeding growth for size control of 5–40 nm diam-

- eter gold nanoparticles,” *Langmuir*, 17 (22), 6782–6786.
- [381] S. M. Demers, L. J. Hsieh, C. R. Shirazinejad, J. L. A. Garcia, J. R. Matthews, and J. H. Hafner (2017), “Ultraviolet Analysis of Gold Nanorod and Nanosphere Solutions,” *Journal of Physical Chemistry C*, 121 (9), 5201–5207.
- [382] C. F. Bohren and D. R. Huffman, *Absorption and Scattering of Light by Small Particles*, 1st ed. New York: Wiley, 1983.
- [383] S. Peng, Y. Lee, C. Wang, H. Yin, S. Dai, and S. Sun (2008), “A facile synthesis of monodisperse Au nanoparticles and their catalysis of CO oxidation,” *Nano Research*, 1 (3), 229–234.
- [384] N. Zheng, J. Fan, and G. D. Stucky (2006), “One-step one-phase synthesis of monodisperse noble-metallic nanoparticles and their colloidal crystals,” *Journal of the American Chemical Society*, 128 (20), 6550–6551.
- [385] B.-H. Wu, H.-Y. Yang, H.-Q. Huang, G.-X. Chen, and N.-F. Zheng (2013), “Solvent effect on the synthesis of monodisperse amine-capped Au nanoparticles,” *Chinese Chemical Letters*, 24 (6), 457–462.
- [386] X. Ye, C. Zhu, P. Ercius, S. N. Raja, B. He, M. R. Jones, M. R. Hauwiler, Y. Liu, T. Xu, and A. P. Alivisatos (2015), “Structural diversity in binary superlattices self-assembled from polymer-grafted nanocrystals,” *Nature Communications*, 6 (1), 10052.
- [387] X. Wendy Gu, X. Ye, D. M. Koshy, S. Vachhani, P. Hosemann, A. Paul Alivisatos, X. W. Gu, X. Ye, D. M. Koshy, S. Vachhani, P. Hosemann, and A. P. Alivisatos (2017), “Tolerance to structural disorder and tunable mechanical behavior in self-assembled superlattices of polymer-grafted nanocrystals,” *Proceedings of the National Academy of Sciences*, 114 (11), 2836–2841.
- [388] K. C. Elbert, D. Jishkariani, Y. Wu, J. D. Lee, B. Donnio, and C. B. Murray (2017), “Design, Self-Assembly, and Switchable Wettability in Hydrophobic, Hydrophilic, and Janus Dendritic Ligand–Gold Nanoparticle Hybrid Materials,” *Chemistry of Materials*, 29 (20), 8737–8746.
- [389] D. Jishkariani, K. C. Elbert, Y. Wu, J. D. Lee, M. Hermes, D. Wang, A. van Blaaderen, and C. B. Murray (2019), “Nanocrystal Core Size and Shape Substitutional Doping and Underlying Crystalline Order in Nanocrystal Superlattices,” *ACS Nano*, 13 (5), 5712–5719.
- [390] M. A. Boles and D. V. Talapin (2015), “Many-Body Effects in Nanocrystal Superlattices: Departure from Sphere Packing Explains Stability of Binary Phases,” *Journal of the American Chemical Society*, 137 (13), 4494–4502.
- [391] M. A. Boles and D. V. Talapin (2019), “Binary Assembly of PbS and Au Nanocrystals: Patchy PbS Surface Ligand Coverage Stabilizes the CuAu Superlattice,” *ACS Nano*, 13 (5), 5375–5384.
- [392] H. Yun, J. W. Yu, Y. J. Lee, J.-S. Kim, C. H. Park, C. Nam, J. Han, T.-Y. Heo, S.-H. Choi, D. C. Lee, W. B. Lee, G. E. Stein, and B. J. Kim (2019), “Symmetry Transitions of Polymer-Grafted Nanoparticles: Grafting Density Effect,” *Chemistry of Materials*, 31 (14), 5264–5273.
- [393] D. Baranov, M. J. Lynch, A. C. Curtis, A. R. Carollo, C. R. Douglass, A. M. Mateo-Tejada, and D. M. Jonas (2019), “Purification of Oleylamine for Materials Synthesis and Spectroscopic Diagnostics for trans Isomers,” *Chemistry of Materials*, 31 (4), 1223–1230.
- [394] E. N. Lang and S. A. Claridge (2022), “Cow-to-cow variation in nanocrystal synthesis: learning from technical-grade oleylamine,” *Nanotechnology*, 33 (8), 082501.
- [395] E. N. Lang, C. J. Pintro, and S. A. Claridge (2022), “Trans and Saturated Alkyl Impurities in Technical-Grade Oleylamine: Limited Miscibility and Impacts on Nanocrystal Growth,” *Chemistry of Materials*, 34 (11), 5273–5282.
- [396] S. Mourdikoudis and L. M. Liz-Marzán (2013), “Oleylamine in Nanoparticle Synthesis,” *Chemistry of Materials*, 25 (9), 1465–1476.
- [397] S. Mourdikoudis, M. Menelaou, N. Fiuza-Maneiro, G. Zheng, S. Wei, J. Pérez-Juste, L. Polavarapu, and Z. Sofer (2022), “Oleic acid/oleylamine ligand pair: a versatile combination in the synthesis of colloidal nanoparticles,” *Nanoscale Horizons*, 7 (9), 941–1015.
- [398] X. Ye, C. Zheng, J. Chen, Y. Gao, and C. B. Murray (2013), “Using Binary Surfactant Mixtures To Simultaneously Improve the Dimensional Tunability and Monodispersity in the Seeded Growth of Gold Nanorods,” *Nano Letters*, 13 (2), 765–771.
- [399] D. Wang, T. Dasgupta, E. B. van der Wee, D. Zanaga, T. Altantzis, Y. Wu, G. M. Coli, C. B. Murray, S. Bals, M. Dijkstra, and A. van Blaaderen (2021), “Binary icosahedral clusters of hard spheres in spherical confinement,” *Nature Physics*, 17 (1), 128–134.
- [400] B. T. Diroll, D. Jishkariani, M. Cargnello, C. B. Murray, and B. Donnio (2016), “Polycatenar Ligand Control of the Synthesis and Self-Assembly of Colloidal Nanocrystals,” *Journal of the American Chemical Society*, 138 (33), 10508–10515.

- [401] E. D. E. R. Hyde, A. Seyfaee, F. Neville, and R. Moreno-Atanasio (2016), "Colloidal Silica Particle Synthesis and Future Industrial Manufacturing Pathways: A Review," *Industrial & Engineering Chemistry Research*, 55 (33), 8891–8913.
- [402] P. P. Ghimire and M. Jaroniec (2021), "Renaissance of Stöber method for synthesis of colloidal particles: New developments and opportunities," *Journal of Colloid and Interface Science*, 584, 838–865.
- [403] W. Stöber, A. Fink, and E. Bohn (1968), "Controlled growth of monodisperse silica spheres in the micron size range," *Journal of Colloid and Interface Science*, 26 (1), 62–69.
- [404] A. van Blaaderen and A. Vrij (1992), "Synthesis and Characterization of Colloidal Dispersions of Fluorescent, Monodisperse Silica Spheres," *Langmuir*, 8 (12), 2921–2931.
- [405] A. van Blaaderen and A. Vrij (1993), "Synthesis and Characterization of Monodisperse Colloidal Organo-silica Spheres," *Journal of Colloid and Interface Science*, 156 (1), 1–18.
- [406] N. A. Verhaegh and A. van Blaaderen (1994), "Dispersions of Rhodamine-Labeled Silica Spheres: Synthesis, Characterization, and Fluorescence Confocal Scanning Laser Microscopy," *Langmuir*, 10 (5), 1427–1438.
- [407] C. L. Kennedy, *Synthesis, microscopy and manipulation of colloidal matter*, PhD thesis, Utrecht University, 2020.
- [408] W. Gao, M. Rigout, and H. Owens (2016), "Facile control of silica nanoparticles using a novel solvent varying method for the fabrication of artificial opal photonic crystals," *Journal of Nanoparticle Research*, 18 (12), 387.
- [409] A. van Blaaderen, J. van Geest, and A. Vrij (1992), "Monodisperse colloidal silica spheres from tetraalkoxysilanes: Particle formation and growth mechanism," *Journal of Colloid and Interface Science*, 154 (2), 481–501.
- [410] W. S. Vlug, *Balls, beams and blocks: In situ observation of colloidal particles in confinement and under electron irradiation*, PhD thesis, Utrecht University, 2017.
- [411] P. M. Johnson, C. M. van Kats, and A. van Blaaderen (2005), "Synthesis of Colloidal Silica Dumbbells," *Langmuir*, 21 (24), 11510–11517.
- [412] T. Yokoi, Y. Sakamoto, O. Terasaki, Y. Kubota, T. Okubo, and T. Tatsumi (2006), "Periodic Arrangement of Silica Nanospheres Assisted by Amino Acids," *Journal of the American Chemical Society*, 128 (42), 13664–13665.
- [413] R. Watanabe, T. Yokoi, E. Kobayashi, Y. Otsuba, A. Shimojima, T. Okubo, and T. Tatsumi (2011), "Extension of size of monodisperse silica nanospheres and their well-ordered assembly," *Journal of Colloid and Interface Science*, 360 (1), 1–7.
- [414] T. M. Davis, M. A. Snyder, J. E. Krohn, and M. Tsapatsis (2006), "Nanoparticles in Lysine–Silica Sols," *Chemistry of Materials*, 18 (25), 5814–5816.
- [415] M. A. Snyder, J. A. Lee, T. M. Davis, L. E. Scriven, and M. Tsapatsis (2007), "Silica Nanoparticle Crystals and Ordered Coatings Using Lys-Sil and a Novel Coating Device," *Langmuir*, 23 (20), 9924–9928.
- [416] S. Shahabi, L. Treccani, and K. Rezwan (2015), "Amino acid-catalyzed seed regrowth synthesis of photostable high fluorescent silica nanoparticles with tunable sizes for intracellular studies," *Journal of Nanoparticle Research*, 17 (6), 270.
- [417] A. Yethiraj and A. van Blaaderen (2003), "A colloidal model system with an interaction tunable from hard sphere to soft and dipolar," *Nature*, 421 (6922), 513–517.
- [418] M. N. van der Linden, J. C. P. Stiefelhagen, G. Heessels-Gürboğa, J. E. S. van der Hoeven, N. A. Elbers, M. Dijkstra, and A. van Blaaderen (2015), "Charging of Poly(methyl methacrylate) (PMMA) Colloids in Cyclohexyl Bromide: Locking, Size Dependence, and Particle Mixtures," *Langmuir*, 31 (1), 65–75.
- [419] W. K. Kegel and A. van Blaaderen (2000), "Direct Observation of Dynamical Heterogeneities in Colloidal Hard-Sphere Suspensions," *Science*, 287 (5451), 290–293.
- [420] L. Antl, J. W. Goodwin, R. D. Hill, R. H. Ottewill, S. M. Owens, S. Papworth, and J. A. Waters (1986), "The preparation of poly(methyl methacrylate) lattices in non-aqueous media," *Colloids and Surfaces*, 17 (1), 67–78.
- [421] G. Bosma, C. Pathmamanoharan, E. H. de Hoog, W. K. Kegel, A. van Blaaderen, and H. N. Lekkerkerker (2002), "Preparation of Monodisperse, Fluorescent PMMA–Latex Colloids by Dispersion Polymerization," *Journal of Colloid and Interface Science*, 245 (2), 292–300.
- [422] M. T. Elsesser and A. D. Hollingsworth (2010), "Revisiting the Synthesis of a Well-Known Comb-Graft Copolymer Stabilizer and Its Application to the Dispersion Polymerization of Poly(methyl methacrylate) in Organic Media," *Langmuir*, 26 (23), 17989–17996.
- [423] W. Haiss, N. T. K. Thanh, J. Aveyard, and D. G. Fernig (2007), "Determination of size and concen-

- tration of gold nanoparticles from UV-Vis spectra,” *Analytical Chemistry*, 79 (11), 4215–4221.
- [424] R. D. Deegan, O. Bakajin, T. F. Dupont, G. Huber, S. R. Nagel, and T. A. Witten (2000), “Contact line deposits in an evaporating drop,” *Physical Review E*, 62 (1), 756–765.
- [425] C. A. Schneider, W. S. Rasband, and K. W. Eliceiri (2012), “NIH Image to ImageJ: 25 years of image analysis,” *Nature Methods*, 9 (7), 671–675.
- [426] G. Bradski (2000), “The OpenCV Library,” *Dr. Dobb’s Journal of Software Tools*.
- [427] G. B. Irani, T. Huen, and F. Wooten (1971), “Optical Constants of Silver and Gold in the Visible and Vacuum Ultraviolet,” *Journal of the Optical Society of America*, 61 (1), 128.
- [428] P. B. Johnson and R. W. Christy (1972), “Optical Constants of the Noble Metals,” *Physical Review B*, 6 (12), 4370–4379.
- [429] N. G. Khlebtsov (2008), “Determination of Size and Concentration of Gold Nanoparticles from Extinction Spectra,” *Analytical Chemistry*, 80 (17), 6620–6625.
- [430] A. E. Stones, *Measuring Structure and Interactions in Colloidal Fluids Using Test-Particle Insertion*, PhD thesis, University of Oxford, 2020.
- [431] M. Bransen (2024), *potentials_from_particle_insertion*, v. 1.0.0, [software]. Available at: https://github.com/MaartenBransen/potentials_from_particle_insertion.
- [432] C. P. Royall, M. E. Leunissen, A.-P. Hynninen, M. Dijkstra, and A. van Blaaderen (2006), “Re-entrant melting and freezing in a model system of charged colloids,” *The Journal of Chemical Physics*, 124 (24), 244706.
- [433] R. J. Mandle (2022), “Implementation of a cylindrical distribution function for the analysis of anisotropic molecular dynamics simulations.” Preprint: *ChemRxiv*.
- [434] E. B. van der Wee, *Quantitative 3D real-space studies of arrested colloidal structures and processes*, PhD thesis, Utrecht University, 2019.
- [435] A. Nikolaenkova, E. B. van der Wee, and A. van Blaaderen, [in preparation].
- [436] D. Han, C. Yang, N. X. Fang, and H. Lee (2019), “Rapid multi-material 3D printing with projection micro-stereolithography using dynamic fluidic control,” *Additive Manufacturing*, 27, 606–615.
- [437] J. M. Vuksanović, M. L. Kijevčanin, and I. R. Radović (2018), “Poly(ethylene glycol) diacrylate as a novel chaotropic compound for design of aqueous biphasic systems,” *Journal of Molecular Liquids*, 261, 250–264.
- [438] L. Grunberg and A. H. Nissam (1949), “Mixture Law for Viscosity,” *Nature*, 164 (4175), 799–800.
- [439] M. E. Leunissen, C. G. Christova, A.-P. Hynninen, C. P. Royall, A. I. Campbell, A. Imhof, M. Dijkstra, R. van Roij, and A. van Blaaderen (2005), “Ionic colloidal crystals of oppositely charged particles,” *Nature*, 437 (7056), 235–240.
- [440] E. C. M. Vermolen, A. Kuijk, L. C. Filion, M. Hermes, J. H. J. Thijssen, M. Dijkstra, and A. van Blaaderen (2009), “Fabrication of large binary colloidal crystals with a NaCl structure,” *Proceedings of the National Academy of Sciences*, 106 (38), 16063–16067.
- [441] C. P. Royall, E. C. M. Vermolen, A. van Blaaderen, and H. Tanaka (2008), “Controlling competition between crystallization and glass formation in binary colloids with an external field,” *Journal of Physics: Condensed Matter*, 20 (40), 404225.
- [442] M. Chen, H. Cölfen, and S. Polarz (2015), “Centrifugal Field-Induced Colloidal Assembly: From Chaos to Order,” *ACS Nano*, 9 (7), 6944–6950.
- [443] X. Xu, T. Franke, K. Schilling, N. A. Sommerdijk, and H. Cölfen (2019), “Binary Colloidal Nanoparticle Concentration Gradients in a Centrifugal Field at High Concentration,” *Nano Letters*, 19 (2), 1136–1142.
- [444] A. van Blaaderen and P. Wiltzius (1995), “Real-Space Structure of Colloidal Hard-Sphere Glasses,” *Science*, 270 (5239), 1177–1179.
- [445] A.-P. Hynninen, J. H. J. Thijssen, E. C. M. Vermolen, M. Dijkstra, and A. van Blaaderen (2007), “Self-assembly route for photonic crystals with a bandgap in the visible region,” *Nature Materials*, 6 (3), 202–205.
- [446] A.-P. Hynninen, L. Filion, and M. Dijkstra (2009), “Stability of LS and LS2 crystal structures in binary mixtures of hard and charged spheres,” *The Journal of Chemical Physics*, 131 (6), 064902.
- [447] D. Wang, E. B. van der Wee, D. Zanaga, T. Altantzis, Y. Wu, T. Dasgupta, M. Dijkstra, C. B. Murray, S. Bals, and A. van Blaaderen (2021), “Quantitative 3D real-space analysis of Laves phase superparticles,” *Nature Communications*, 12 (1), 3980.
- [448] Y. L. Wu, *Control over colloidal crystallization by shear and electric fields*, PhD thesis, Universiteit Utrecht, 2007.
- [449] P. Virtanen, R. Gommers, T. E. Oliphant, *et al.* (2020), “SciPy 1.0: fundamental algorithms for scientific computing in Python,” *Nature Methods*, 17 (3), 261–272.
- [450] E. W. Weisstein (2022), *Circular Segment*. From MathWorld—A Wolfram Web Resource, [online].

- Available at: <https://mathworld.wolfram.com/CircularSegment.html> (accessed on 11/21/2022).
- [451] E. W. Weisstein (2022), *Circle–Circle Intersection*. From MathWorld—A Wolfram Web Resource, [online]. Available at: <https://mathworld.wolfram.com/Circle-CircleIntersection.html> (accessed on 11/21/2022).
- [452] B. A. F. Kopera and M. Retsch (2018), “Computing the 3D Radial Distribution Function from Particle Positions: An Advanced Analytic Approach,” *Analytical Chemistry*, 90 (23), 13909–13914.
- [453] E. W. Weisstein (2022), *Sphere–Sphere Intersection*. From MathWorld—A Wolfram Web Resource, [online]. Available at: <https://mathworld.wolfram.com/Sphere-SphereIntersection.html> (accessed on 11/21/2022).
- [454] M. Deserno, *How to calculate a three-dimensional $g(r)$ under periodic boundary conditions*, 2004.
- [455] M. L. Larsen and R. A. Shaw (2018), “A method for computing the three-dimensional radial distribution function of cloud particles from holographic images,” *Atmospheric Measurement Techniques*, 11 (7), 4261–4272.
- [456] D. B. Allan, T. Caswell, N. C. Keim, and C. M. van der Wel, *soft-matter/trackpy: Trackpy v0.4.2*, 2019.
- [457] J. P. Patterson, Y. Xu, M.-A. Moradi, N. A. J. M. Sommerdijk, and H. Friedrich (2017), “CryoTEM as an Advanced Analytical Tool for Materials Chemists.” *Accounts of chemical research*, 50 (7), 1495–1501.
- [458] R. Danev, H. Yanagisawa, and M. Kikkawa (2019), “Cryo-Electron Microscopy Methodology: Current Aspects and Future Directions,” *Trends in Biochemical Sciences*, 44 (10), 837–848.
- [459] H. Yockell-Lelièvre, J. Desbiens, and A. M. Ritcey (2007), “Two-Dimensional Self-Organization of Polystyrene-Capped Gold Nanoparticles,” *Langmuir*, 23 (5), 2843–2850.
- [460] B. W. Goodfellow, Y. Yu, C. A. Bosoy, D.-M. Smilgies, and B. A. Korgel (2015), “The Role of Ligand and Packing Frustration in Body-Centered Cubic (bcc) Superlattices of Colloidal Nanocrystals,” *The Journal of Physical Chemistry Letters*, 6 (13), 2406–2412.
- [461] H. Duan, Y. Yang, Y. Zhang, C. Yi, Z. Nie, and J. He (2020), “What is next in polymer-grafted plasmonic nanoparticles?” *Giant*, 4, 100033.
- [462] K. Bhattacharjee and B. L. V. Prasad (2023), “Surface functionalization of inorganic nanoparticles with ligands: a necessary step for their utility,” *Chemical Society Reviews*, 52 (8), 2573–2595.
- [463] H. Yun, Y. J. Lee, M. Xu, D. C. Lee, G. E. Stein, and B. J. Kim (2020), “Softness- And Size-Dependent Packing Symmetries of Polymer-Grafted Nanoparticles,” *ACS Nano*, 14 (8), 9644–9651.
- [464] B. de Nijs, S. Dussi, F. Smalenburg, J. D. Meeldijk, D. J. Groenendijk, L. Fillion, A. Imhof, A. van Blaaderen, and M. Dijkstra (2015), “Entropy-driven formation of large icosahedral colloidal clusters by spherical confinement,” *Nature Materials*, 14 (1), 56–60.
- [465] D. Wang, M. Hermes, R. Kotni, Y. Wu, N. Tasios, Y. Liu, B. de Nijs, E. B. van der Wee, C. B. Murray, M. Dijkstra, and A. van Blaaderen (2018), “Interplay between spherical confinement and particle shape on the self-assembly of rounded cubes,” *Nature Communications*, 9 (1), 2228.
- [466] S. Wintzheimer, T. Granath, M. Oppmann, T. Kister, T. Thai, T. Kraus, N. Vogel, and K. Mandel (2018), “Supraparticles: Functionality from Uniform Structural Motifs,” *ACS Nano*, 12 (6), 5093–5120.
- [467] T. G. Mason and J. Bibette (1997), “Shear rupturing of droplets in complex fluids,” *Langmuir*, 13 (17), 4600–4613.
- [468] E. Amstad, M. Chemama, M. Eggersdorfer, L. R. Arriaga, M. P. Brenner, and D. A. Weitz (2016), “Robust scalable high throughput production of monodisperse drops,” *Lab on a Chip*, 16 (21), 4163–4172.
- [469] F. Montanarella, J. J. Geuchies, T. Dasgupta, P. T. Prins, C. van Overbeek, R. Dattani, P. Baesjou, M. Dijkstra, A. V. Petukhov, A. van Blaaderen, and D. Vanmaekelbergh (2018), “Crystallization of Nanocrystals in Spherical Confinement Probed by in Situ X-ray Scattering,” *Nano Letters*, 18 (6), 3675–3681.
- [470] A. Malliaris (1987), “Solubilization of organic molecules in sds micelles studied by static fluorescence methods,” *Advances in colloid and interface science*, 27 (3-4), 153–168.
- [471] P. J. Steinhardt, D. R. Nelson, and M. Ronchetti (1983), “Bond-orientational order in liquids and glasses,” *Physical Review B*, 28 (2), 784–805.
- [472] W. Lechner and C. Dellago (2008), “Accurate determination of crystal structures based on averaged local bond order parameters,” *The Journal of Chemical Physics*, 129 (11), 114707.
- [473] J. Lacava, P. Born, and T. Kraus (2012), “Nanoparticle Clusters with Lennard-Jones Geometries,” *Nano Letters*, 12 (6), 3279–3282.
- [474] J. Wang, C. F. Mbah, T. Przybilla, B. Apeleo Zubiri, E. Spiecker, M. Engel, and N. Vogel (2018),

- "Magic number colloidal clusters as minimum free energy structures," *Nature Communications*, 9 (1), 5259.
- [475] J. Wang, C. F. Mbah, T. Przybilla, S. Englisch, E. Spiecker, M. Engel, and N. Vogel (2019), "Free Energy Landscape of Colloidal Clusters in Spherical Confinement," *ACS Nano*, 13 (8), 9005–9015.
- [476] A. Dong, J. Chen, P. M. Vora, J. M. Kikkawa, and C. B. Murray (2010), "Binary nanocrystal superlattice membranes self-assembled at the liquid–air interface," *Nature*, 466 (7305), 474–477.
- [477] S. W. Winslow, J. W. Swan, and W. A. Tisdale (2020), "The Importance of Unbound Ligand in Nanocrystal Superlattice Formation," *Journal of the American Chemical Society*, 142 (21), jacs.0c01809.
- [478] V. Garbin, J. C. Crocker, and K. J. Stebe (2012), "Forced desorption of nanoparticles from an oil-water interface," *Langmuir*, 28 (3), 1663–1667.
- [479] S. Nayak, M. Fieg, W. Wang, W. Bu, S. Malapragada, and D. Vaknin (2019), "Effect of (Poly)electrolytes on the Interfacial Assembly of Poly(ethylene glycol)-Functionalized Gold Nanoparticles," *Langmuir*, 35 (6), 2251–2260.
- [480] H. Cui, T. K. Hodgdon, E. W. Kaler, L. Abezgauz, D. Danino, M. Lubovsky, Y. Talmon, and D. J. Pochan (2007), "Elucidating the assembled structure of amphiphiles in solution via cryogenic transmission electron microscopy," *Soft Matter*, 3 (8), 945.
- [481] J. Schmitt, S. Hajiw, A. Lecchi, J. Degrouard, A. Salonen, M. Impéror-Clerc, and B. Pansu (2016), "Formation of Superlattices of Gold Nanoparticles Using Ostwald Ripening in Emulsions: Transition from fcc to bcc Structure," *Journal of Physical Chemistry B*, 120 (25), 5759–5766.
- [482] M. Textor and N. de Jonge (2018), "Strategies for Preparing Graphene Liquid Cells for Transmission Electron Microscopy," *Nano Letters*, 18 (6), 3313–3321.
- [483] S. M. Ghodsi, C. M. Megaridis, R. Shahbazian-Yassar, and T. Shokuhfar (2019), "Advances in Graphene-Based Liquid Cell Electron Microscopy: Working Principles, Opportunities, and Challenges," *Small Methods*, 3 (5), 1900026.
- [484] H. Wu, H. Friedrich, J. P. Patterson, N. A. Sommerdijk, and N. de Jonge, *Liquid-Phase Electron Microscopy for Soft Matter Science and Biology*, 2020.
- [485] P. M. G. van Deursen, R. I. Koning, V. Tudor, M.-A. Moradi, J. P. Patterson, A. Kros, N. A. J. M. Sommerdijk, A. J. Koster, and G. F. Schneider (2020), "Graphene Liquid Cells Assembled through Loop-Assisted Transfer Method and Located with Correlated Light-Electron Microscopy," *Advanced Functional Materials*, 30 (11), 1904468.
- [486] K. S. Novoselov, V. I. Fal'ko, L. Colombo, P. R. Gellert, M. G. Schwab, and K. Kim (2012), "A roadmap for graphene," *Nature*, 490 (7419), 192–200.
- [487] A. Rudin and P. Choi, *The Elements of Polymer Science and Engineering*, 3rd ed. Academic Press, 2013.
- [488] C. Sorzano, F. de Isidro-Gómez, E. Fernández-Giménez, D. Herreros, S. Marco, J. Carazo, and C. Messaoudi (2020), "Improvements on marker-free images alignment for electron tomography," *Journal of Structural Biology*: X, 4, 100037.
- [489] C. Messaoudi, T. Boudier, C. O. S. Sorzano, and S. Marco (2007), "Tomog: tomography software for three-dimensional reconstruction in transmission electron microscopy," *BMC Bioinformatics*, 8 (1), 288.
- [490] J. A. van Meel, L. Filion, C. Valeriani, and D. Frenkel (2012), "A parameter-free, solid-angle based, nearest-neighbor algorithm," *The Journal of Chemical Physics*, 136 (23), 234107.
- [491] E. Boattini, M. Dijkstra, and L. Filion (2019), "Unsupervised learning for local structure detection in colloidal systems," *Journal of Chemical Physics*, 151 (15).
- [492] E. W. Weisstein (2023), *Wigner 3j-Symbol*. From MathWorld—A Wolfram Web Resource, [online]. Available at: <https://mathworld.wolfram.com/Wigner3j-Symbol.html> (accessed on 02/13/2022).
- [493] G. Cao and Y. Wang, *Nanostructures and Nanomaterials*, 2nd ed. World Scientific, 2011.
- [494] C. J. Drummond and D. Y. C. Chan (1997), "van der Waals Interaction, Surface Free Energies, and Contact Angles: Dispersive Polymers and Liquids," *Langmuir*, 13 (14), 3890–3895.
- [495] L. A. Wijenayaka, M. R. Ivanov, C. M. Cheatum, and A. J. Haes (2015), "Improved Parametrization for Extended Derjaguin, Landau, Verwey, and Overbeek Predictions of Functionalized Gold Nanosphere Stability," *The Journal of Physical Chemistry C*, 119 (18), 10064–10075.
- [496] A. O. Pinchuk (2012), "Size-dependent hamaker constant for silver nanoparticles," *Journal of Physical Chemistry C*, 116 (37), 20099–20120.
- [497] R. Sarfati and E. R. Dufresne (2016), "Long-range attraction of particles adhered to lipid vesicles," *Physical Review E*, 94 (1), 012604.
- [498] R. Sarfati, J. Bławzdziwicz, and E. R. Dufresne (2017), "Maximum likelihood estimations of force

- and mobility from single short Brownian trajectories,” *Soft Matter*, 13 (11), 2174–2180.
- [499] B. R. Martin, *Statistics for Physical Sciences*, 1st ed. Academic Press, 2012.
- [500] P. Wilmott, S. Howison, and J. Dewynne, *The mathematics of financial derivatives : a student introduction*, 1st ed. Cambridge University Press, 1995.
- [501] U. Dassanayake, S. Fraden, and A. van Blaaderen (2000), “Structure of electrorheological fluids,” *The Journal of Chemical Physics*, 112 (8), 3851–3858.
- [502] B. W. Kwaadgras, T. H. Besseling, T. J. Coopmans, A. Kuijk, A. Imhof, A. van Blaaderen, M. Dijkstra, and R. van Roij (2014), “Orientation of a dielectric rod near a planar electrode,” *Phys. Chem. Chem. Phys.*, 16 (41), 22575–22582.
- [503] A. S. Alkindi, Y. M. Al-Wahaibi, and A. H. Mugeridge (2008), “Physical Properties (Density, Excess Molar Volume, Viscosity, Surface Tension, and Refractive Index) of Ethanol + Glycerol,” *Journal of Chemical & Engineering Data*, 53 (12), 2793–2796.
- [504] A. Yethiraj (2007), “Tunable colloids: control of colloidal phase transitions with tunable interactions,” *Soft Matter*, 3 (9), 1099.
- [505] A. van Blaaderen, J. Peetermans, G. Maret, and J. K. G. Dhont (1992), “Long-time self-diffusion of spherical colloidal particles measured with fluorescence recovery after photobleaching,” *The Journal of Chemical Physics*, 96 (6), 4591–4603.
- [506] A.-P. Hynninen and M. Dijkstra (2005), “Phase behavior of dipolar hard and soft spheres,” *Physical Review E*, 72 (5), 051402.
- [507] A. J. Berglund (2010), “Statistics of camera-based single-particle tracking,” *Physical Review E*, 82 (1), 011917.
- [508] R. Schmitz and B. Felderhof (1982), “Mobility matrix for two spherical particles with hydrodynamic interaction,” *Physica A: Statistical Mechanics and its Applications*, 116 (1-2), 163–177.
- [509] P. Sheng and W. Wen (2012), “Electrorheological Fluids: Mechanisms, Dynamics, and Microfluidics Applications,” *Annual Review of Fluid Mechanics*, 44 (1), 143–174.
- [510] A. Yethiraj and A. van Blaaderen (2002), “Monodisperse colloidal suspensions of silica and pmma spheres as model electrorheological fluids: a real-space study of structure formation,” *International Journal of Modern Physics B*, 16 (17n18), 2328–2333.
- [511] J. Oreopoulos, R. Berman, and M. Browne, *Spinning-disk confocal microscopy*, in *Methods in Cell Biology*, vol. 123, Academic Press, 2014, pp. 153–175.
- [512] M. E. Leunissen, *Manipulating colloids with charges and electric fields*, PhD thesis, Universiteit Utrecht, 2007.
- [513] M. E. Leunissen, A. van Blaaderen, A. D. Hollingsworth, M. T. Sullivan, and P. M. Chaikin (2007), “Electrostatics at the oil–water interface, stability, and order in emulsions and colloids,” *Proceedings of the National Academy of Sciences*, 104 (8), 2585–2590.
- [514] C. Schreuer, S. Vandewiele, F. Strubbe, K. Neyts, and F. Beunis (2018), “Electric field induced charging of colloidal particles in a nonpolar liquid,” *Journal of Colloid and Interface Science*, 515, 248–254.
- [515] T. Vissers, A. Imhof, F. Carrique, Á. V. Delgado, and A. van Blaaderen (2011), “Electrophoresis of concentrated colloidal dispersions in low-polar solvents,” *Journal of Colloid and Interface Science*, 361 (2), 443–455.
- [516] B. B. Straub, D. C. Lah, H. Schmidt, M. Roth, L. Gilson, H. J. Butt, and G. K. Auernhammer (2020), “Versatile high-speed confocal microscopy using a single laser beam,” *Review of Scientific Instruments*, 91 (3), 033706.
- [517] M. Bransen (2024), *trajectories_to_forces*, v. 1.0.0, [software]. Available at: https://github.com/MaartenBransen/trajectories_to_forces.
- [518] H. Faxen (1923), “Die Bewegung einer starren Kugel langs der Achse eines mit zäher Flüssigkeit gefüllten Rohres,” *Arkiv for Matematik Astronomi och Fysik*, 17, 1–28.
- [519] A. Goldman, R. Cox, and H. Brenner (1967), “Slow viscous motion of a sphere parallel to a plane wall—I Motion through a quiescent fluid,” *Chemical Engineering Science*, 22 (4), 637–651.
- [520] S. Rodríguez, C. Lafuente, J. A. Carrión, F. M. Royo, and J. S. Urieta (1996), “Excess volumes and excess viscosities of binary mixtures of some cyclic ethers + bromocyclohexane at 298.15 and 313.15 K,” *International Journal of Thermophysics*, 17 (6), 1281–1288.
- [521] W. M. Heston, E. J. Hennelly, and C. P. Smyth (1950), “Dielectric Constants, Viscosities, Densities, Refractive Indices and Dipole Moment Calculations for Some Organic Halides 1,” *Journal of the American Chemical Society*, 72 (5), 2071–2075.
- [522] H. Chi, G. Li, Y. Guo, L. Xu, and W. Fang (2013), “Excess Molar Volume along with Viscosity, Flash Point, and Refractive Index for Binary Mixtures of cis-Decalin or trans-Decalin with C9 to C11 n-

- Alkanes,” *Journal of Chemical & Engineering Data*, 58 (8), 2224–2232.
- [523] M. E. Leunissen, J. Zwanikken, R. van Roij, P. M. Chaikin, and A. van Blaaderen (2007), “Ion partitioning at the oil-water interface as a source of tunable electrostatic effects in emulsions with colloids,” *Physical Chemistry Chemical Physics*, 9 (48), 6405–6414.
- [524] A. Einstein (1905), “Über die von der molekularkinetischen Theorie der Wärme geforderte Bewegung von in ruhenden Flüssigkeiten suspendierten Teilchen,” *Annalen der Physik*, 322 (8), 549–560.
- [525] A. Einstein, *Investigations in the theory of Brownian movement*, translated by A.D. Cowper, R. Fürth, Ed. Dover Publications, Inc., 1956.
- [526] R. Piazza (2014), “Settled and unsettled issues in particle settling,” *Reports on Progress in Physics*, 77 (5), 056602.
- [527] The SCHOTT company (2022), *Schott D263M Glass Coverslips Technical data*, [online]. Available at: www.schott.com/en-gb/products/d-263-p1000318/technical-details (accessed on 08/19/2022).
- [528] U. Kaatze (2012), “Hydrogen network fluctuations: Dielectric spectra of glycerol–ethanol mixtures,” *Chemical Physics*, 403, 74–80.
- [529] E. Hayden, Z. Aljabal, and A. Yethiraj (2017), “Frequency-Dependent Solvent Impedance and Colloid Microelectrophoresis Measurements in Partially Polar Solvents,” *Langmuir*, 33 (19), 4781–4788.
- [530] J. Tatum (2022), *Capacitors: Mixed Dielectrics*, LibreTexts, [online]. Available at: phys.libretexts.org/@go/page/6022 (accessed on 08/19/2022).
- [531] K. Deng, Z. Luo, L. Tan, and Z. Quan (2020), “Self-assembly of anisotropic nanoparticles into functional superstructures,” *Chemical Society Reviews*, 49 (16), 6002–6038.
- [532] I. Dierking (2019), “From colloids in liquid crystals to colloidal liquid crystals,” *Liquid Crystals*, 46 (13–14), 2057–2074.
- [533] H. Ma, W. Wen, W. Y. Tam, and P. Sheng (2003), “Dielectric electrorheological fluids: Theory and experiment,” *Advances in Physics*, 52 (4), 343–383.
- [534] W. Wen, X. Huang, and P. Sheng (2008), “Electrorheological fluids: structures and mechanisms,” *Soft Matter*, 4 (2), 200–210.
- [535] R. Tao and J. M. Sun (1991), “Three-dimensional structure of induced electrorheological solid,” *Physical Review Letters*, 67 (3), 398–401.
- [536] A.-P. Hynninen and M. Dijkstra (2005), “Phase Diagram of Dipolar Hard and Soft Spheres: Manipulation of Colloidal Crystal Structures by an External Field,” *Physical Review Letters*, 94 (13), 138303.
- [537] B. W. Kwaadgras, R. van Roij, and M. Dijkstra (2014), “Self-consistent electric field-induced dipole interaction of colloidal spheres, cubes, rods, and dumbbells,” *The Journal of Chemical Physics*, 140 (15), 154901.
- [538] X. Wu, F. C. Meldrum, K. Skipper, Y. Yang, and C. P. Royall (2023), “Tuning Higher Order Structure in Colloidal Fluids.” Preprint: *arXiv:2303.09029*.
- [539] R. M. Fuoss (1959), “Dependence of the Walden product on the dielectric constant,” *Proceedings of the National Academy of Sciences*, 45 (6), 807–813.
- [540] G. J. Janz and S. S. Danyluk (1960), “Conductances of hydrogen halides in anhydrous polar organic solvents,” *Chemical Reviews*, 60 (2), 209–234.
- [541] R. Robinson and R. Stokes, *Electrolyte Solutions*, 2nd ed. Butterworths, 1959.
- [542] A. L. Loeb, J. T. G. Overbeek, P. H. Wiersema, and C. V. King (1961), “The Electrical Double Layer Around a Spherical Colloid Particle,” *Journal of The Electrochemical Society*, 108 (12), 269C.
- [543] R. J. Hunter, *Zeta Potential in Colloid Science: Principles and Applications*. Academic Press, 1981.
- [544] J. W. Swan and E. M. Furst (2012), “A simpler expression for Henry’s function describing the electrophoretic mobility of spherical colloids,” *Journal of Colloid and Interface Science*, 388 (1), 92–94.

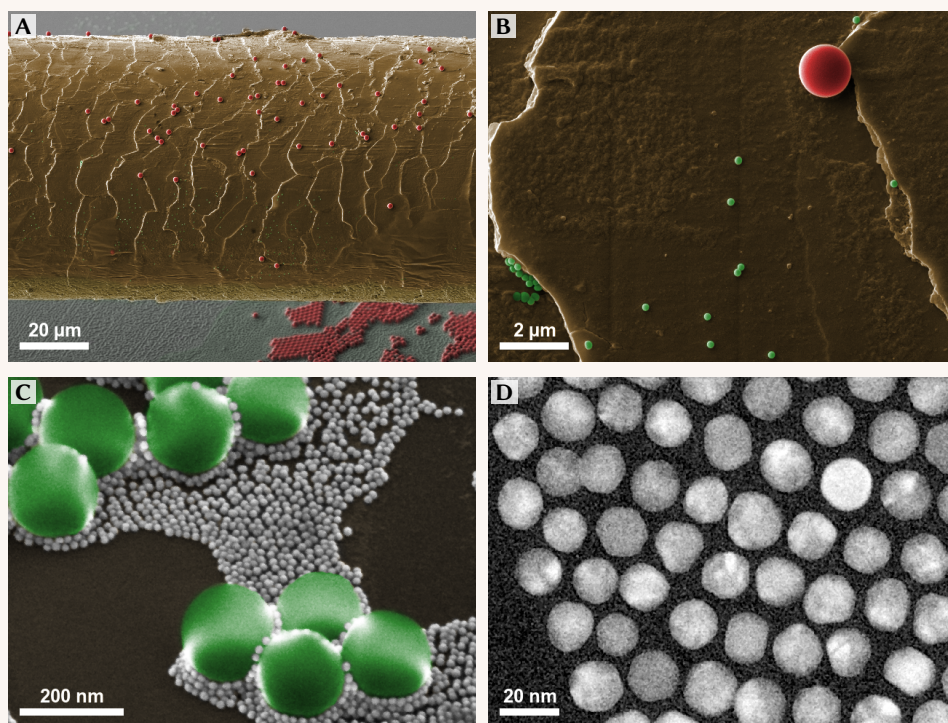
Summary for the general public

Colloids, nanoparticles and interactions. The what, how and why.

The aim of this research project was to develop experimental techniques to measure interactions between so called *colloidal particles* or *colloids*, which are microscopically small particles of between 1 nm and 10 μm in size that are finely dispersed in a liquid or gas. A particular emphasis was put on measurement of *nanoparticles*, which we define to be colloids less than 100 nm in size. To get a better idea of what these numbers and sizes mean you can look at the images in **Box 1**, which show some of the particles used in this research next to a hair. But what is it exactly that makes us interested in these particles and measuring their interactions? Colloids have a large number of interesting properties which are in many cases a direct consequence of their microscopic (or *nanoscopic*) size range and which are especially for nanoparticles often continually variable through their size and shape dependency. Like molecules, colloids constantly move in a seemingly random manner due to the collisions with the molecules around them, but unlike molecules they are large enough to be observed directly using microscopy. Their microscopic (or nanoscopic) size however also means that the individual particles are usually far too small to practically use in applications. Instead, one usually makes use of *colloidal dispersions* in which a large number of particles is stabilised in some liquid (the solvent), like the titania particles that give wall paints their white colour and the microcapsules with e-ink particles in e-reader displays. It is also possible to make use of so called *assembled materials*, where colloids are the building blocks of the material such as in naturally occurring opal gemstones. Such materials can be made via a process called *self-assembly*, wherein particles spontaneously form complex structures such as crystals under specific conditions, for example when the dispersing solvent of the particles is slowly evaporated. Self-assembly is also common in biological systems, where for example protein-protein interactions are evolved to be highly specific such that large protein complexes and materials such as keratin, the main component of hair and nails, can spontaneously form. The ability to take relatively simple ‘nano building blocks’ and prepare materials which are highly ordered over multiple length scales makes this a promising pathway for the preparation of a host of new materials. It is even possible to highly specifically tune interactions of the particles for applications, such as in the coronavirus self-tests, where gold nanoparticles with a strong red colour are coated with antigens to very specifically bind to virusparticles thereby making their presence visible.

In all of these cases the interactions between the particles –essentially how much they attract or repel each other and at what distances this occurs– are crucially important because they dictate the stability of colloidal dispersions and the structures that are formed upon self-assembly. Therefore, knowledge and understanding of the interactions between colloidal particles and how these may be affected are vital to understand the properties and self-assembly of colloidal dispersions. Fortunately, theory with which the interactions between colloids may be understood and predicted has been developed and expanded for more than a century, the most relevant of which we also discuss in **Chapter 1** of this thesis. Particularly for microparticles, colloids of more than 100 nm in size, it is often possible to accurately predict interactions based on known or measurable system properties. For nanoparticles on the other hand many of the simplifications and assumptions at the basis of these theories do not hold, as is summarised in **Fig. 1.2** on **p. 6**; nanoparticles have a complex structure which is not accurately described using approximations and averages. An important concept here is *additivity*, the idea that for microparticles we can calculate separate effects independently and then add them together in the same way that we can describe the net force on a tennis

Box 1: the size of colloids and nanoparticles



The images above were recorded using an electron microscope at magnifications of approximately $1000\times$, $10\,000\times$, $100\,000\times$ and $1\,000\,000\times$ (for A–D respectively), and show one of the authors' hairs together with colloidal particles of three different sizes: glass (silica) particles of 1.7 micrometer (depicted in red), glass particles of 170 nanometer (depicted in green) and gold nanoparticles of 17 nanometer (white). In reality electron microscopy does not record colour as it measures electrons, not light, and the smallest particles are many times smaller than the wavelength of visible light. The colours were added only to more clearly show the different particles.

ball as the sum of forces due to gravity, air resistance and the hit by the racket. On the nanometer scale however there can be coupling between different effects due to the coupling of electric fields or through structuring of solvent molecules around the particles in a way that makes them sufficiently intertwined such that they cannot be considered independently, making the prediction of nanoparticle interactions particularly complex.

Of course the development of theory is ongoing and an increasing number of interactions can be described. Nonetheless there are always cases for which theory does not exist, the information to use theory is not known or easily measurable, or where assumptions are made which do not apply in every situation, and as with any theory it is important to experimentally verify their validity in different cases. While it is possible to do this indirectly via *e.g.* particle stability, the most direct way is to compare calculations with measured interaction forces. Aside from theory, large improvements have been made with computer

simulations wherein colloidal particles and their interactions can be modelled with varying levels of detail via for example the molecular interactions of the solvent and chemical groups on the particles. The expectation is that with improved methodology and computation speed these simulations will play an increasingly important role in understanding and predicting colloid stability, but the choice of input parameters in these simulations is non-trivial and as such we expect interaction measurements to play a role in verifying and aiding these simulations such that they may be employed in cases where experimental measurements are not feasible.

What was this research based on?

As with any research project, the techniques developed and used here were based on earlier work. The first part of this thesis therefore focusses extensively on this by diving into the literature and seeing what interaction measurements have been done before, and of literature there is a lot. The last few decennia have seen the development of a number of different means by which interactions between colloids may be measured, based on an equally large number of different experimental techniques. This includes atomic force microscopy, wherein a microscopic needle attached to a cantilever can be used to ‘feel’ very small forces and determine topography with nanometer precision by scanning the needle over a surface or measure interactions by attaching a single colloid to the tip of the needle. Similarly, particles can be manipulated using ‘optical tweezers’, wherein a focused laser spot can trap and pick up particles. These can be used to measure particles by bringing them together and analysing their positions in the trap, or by releasing two particles close to one another and analysing how they move in each others vicinity after being released. However, also techniques based on light or electron microscopy without means to explicitly manipulating the particles have been used to measure interactions, through statistical analysis of their positions in a dispersion. Here, the continuous movement of the colloidal particles as a consequence of their thermal energy means they can explore their local environment and overcome small energy barriers, where the probability to find particles at certain distances from one another or to see them move in certain directions depends on the interaction forces between them. In **Chapter 2** we take a deep dive in the literature and give a comprehensive overview of these and other techniques with which interactions have been measured, the basic principles behind these measurements and their main advantages and disadvantages as summarised in **Table 2.1** on **page 51**. We do this with a particular focus on measuring interactions between nanoparticles and highlight a number of examples in which this was done, or in which interactions between microparticles were measured in new and interesting way.

How are nanoparticles made?

Colloidal particles can be prepared by milling or breaking material down until small particles with a size in the colloidal range remain, which is a so-called *top down* preparation, but in general much more control over *e.g.* size and shape can be achieved when particles are prepared from a solution of precursor materials through chemical conversion, which is called a *bottom up* preparation. An example of this is the preparation of gold nanoparticles through a reduction-oxidation reaction, where a dissolved gold-containing salt reacts with a reducing agent (an electron donor molecule) which converts the charged gold ions into uncharged metallic gold in the form of nanoparticles. Such a process often contains multiple steps which may be controlled through the concentration, reaction rate and addition of stabilising

molecules. While the development of new methods for the synthesis—that is the chemical preparation—of colloidal particles was not the focus of this research, preparation of particles with desired and well-defined properties was an integral part of the process and nearly all particles used in this research were made specifically for this work using bottom-up synthesis procedures. This is because it is necessary for the interaction measurements to precisely know things like the average particle size, and how much the individual particles' sizes vary, which we call the polydispersity. Additionally, the synthesis procedure often dictates the final properties of the surface, for example whether there are organic molecules or charges, which largely determine the interactions between the particles. In **Chapter 3** we extensively discuss the synthesis of the particles used for this work as well as several other related research projects. Here we focussed predominantly on gold nanoparticles and silica (glass) nano- and microparticles, because these materials are chemically stable, widely studied/well-understood, comparably easy to modify/coat with functional groups, and well suited to electron and optical microscopy respectively. While the synthesis procedures were based on existing work in all cases, that does not mean there was nothing new to learn. In practise, even reproducing existing protocols often yields different results, where there are sometimes small variations in size, polydispersity or stability, but it can also occur that one obtains completely different particles or no particles at all. The idea behind this chapter is thus not just to provide insight into the preparation and properties of the particles used in the experiments in other chapters, but also to provide an account of the synthesis and add more data on reproducibility of published work and how commonly occurring variations in procedures can affect the different colloidal preparation procedures.

Measuring interactions from distribution functions

In this research, we focused on microscopy-based techniques where we image a large number of particles in a colloidal dispersion and use positional data to extract interactions. In **Chapters 4** and **5** we do this through the statistical analysis of distribution functions, which describe how on average particles are positioned with respect to each other. This approach assumes that the particles are in thermodynamic equilibrium, where the average energy of all the particles does not change even though individual particles may have more or less energy as they move through the fluid. The key principle here is that the *probability* to observe a particle at a certain position is directly related to the energy it 'costs' the particle to reach that position, which for particles far from interfaces is purely a result of the interactions with other particles. Intuitively, this makes some sense: if two particles repel one another, we expect to find fewer particles close to one another than farther away, while attracting particles are *more* likely to be found at small distances. Specifically we express this as the *radial distribution function*—or $g(r)$ for short— which describes the likelihood of finding two particles at a distance r from one another relative to a completely random set of particle coordinates, which can be determined from a set of particle coordinates and which only depends on the interactions and density of the particles. The $g(r)$ is radially averaged, which means that we only look at the distance between the particles but assume the orientations of the particles don't matter, which is a valid assumption for many (but not all) colloidal particles. Additionally, we assume that interactions are pairwise additive, which means that we assume the total energy is simply the sum of all separate interactions with neighbouring particles. Although it is fairly straightforward to determine the $g(r)$ when the interactions between the particles are known using for example simulations, the opposite isn't necessarily

true under practical conditions. In this thesis we therefore explore and present a practical implementation for a recently proposed new algorithm called iterative test-particle insertion (iTPI) with which interaction potentials may be extracted under a wide variety of conditions from experimental or simulated data.

Solvent-arresting for microscopy: stopping time

While it is fairly straightforward to measure the positions of a large number of microparticles in 2D using wide-field optical microscopy, where a camera can be used to take a large image, for most colloids the effect of gravity is limited and their positions are dispersed in 3D. While fortunately 3D microscopy techniques exist, notably *confocal laser scanning microscopy* (CLSM), these work by imaging a 3D volume layer by layer, and are thus inherently slow, while the constant motion of the particles requires rather fast imaging. We solve this issue in **Chapter 4** by introducing a new solvent-arresting procedure, where we can quickly stop the motion of the particles by using dispersions containing molecules (monomers) which may be polymerised to rapidly form a gel-like structure. This fixes the particle positions in place such that they are preserved as they were before the polymerisation was initiated, which could be done in the microscope using a pulse of UV-light and a small amount of light-activated initiator molecules. Arresting samples in this way made it possible to image large sample volumes in 3D and extract their interactions through iTDI, for example for silica nanoparticles with long-ranged electrostatic interactions up to over 500 nm. We also studied a two-component system with both 300 nm and 400 nm colloids, where gravity caused sedimentation at different rates such that gradients in both the overall particle concentration and the ratio of small to large particles were obtained, meaning that a variety of different structures and crystals could be observed in a single sample. Here, solvent-arresting was used to fix sedimenting samples at different times such that the sedimentation process could be studied without disturbing it by placing the sample sideways in the microscope, as well as to measure the interactions between the small and large particles through multi-component iTDI. Ultimately however optical microscopy has a limited resolution and cannot be used to resolve inter-particle distances much smaller than half the wavelength of visible light.* For this reason we also explored solvent-arresting for electron microscopy, where resolutions down to the length scale of atoms can be achieved. By using pure monomers as solvent, dispersions of various gold and silica nanoparticles could be turned into plastic-like solid samples suitable for scanning electron microscopy, where a surface can be imaged while removing nanometer thin slices with a focused ion beam such that a 3D volume can be recorded ‘slice by slice’ with a resolution up to 100× better than optical microscopy. Of course a major downside of this method is that it has limited applicability as it allows interactions to be measured only in very specific (polymerisable) solvents.

Cryogenic transmission electron microscopy: a literal freeze-frame

In **Chapter 5** we used transmission electron microscopy (TEM) to study the self-assembly and interactions of very small gold nanoparticles of between 2 nm to 8 nm which we coated with differently sized polymers to change their interactions. Such particles are known to form different structures upon self-assembly depending on the sizes of the gold core and the polymers, which affect how ‘soft’ (gradually increasing) or ‘hard’ (like a solid surface) their interactions are. We studied the self-assembly in two geometries: within slowly evaporating

* various ‘tricks’ have been invented to circumvent this limit which are referred to as *super-resolution microscopy*, but in the context of this research distances much smaller than 300 nm were practically unresolvable

solvent droplets resulting in micron sized spherical assemblies, and within a thin evaporating solvent layer on a liquid interface resulting in large sheets/layers of only a few particles thick. TEM images of these assemblies can be seen for example in **Figures 5.2 and 5.4** on **pp. 133 and 136** respectively. Surprisingly, we found three qualitatively different types of assembly, with particles aggregating (clustering), forming structures with fivefold crystalline ordering or with only local liquid-like ordering depending on the size of the stabilising molecules. We used TEM because of its exceptionally high spatial resolution given the small size of the nanoparticles, but this requires samples of at most a micrometer in thickness and is not directly compatible with liquid samples due to the vacuum conditions needed for the electron beam. Instead, cryogenic TEM (cryo-TEM) may be employed, where a liquid sample is ‘frozen’ extremely rapidly using a cryogen, typically at $-196\text{ }^{\circ}\text{C}$ using liquid nitrogen, so that even the solvent molecules do not have time to crystallise while the sample solidifies. This literally freezes in the positions of the particles in the dispersion, similar to the solvent-arresting procedure except on a much shorter time scale, so that the frozen samples may be transferred to the microscope in a special cryo-cooled sample holder to image the structure in the frozen ‘fluid’. Conventionally this is done using thin films where particles are trapped between the interfaces so that the positions can be imaged and analysed essentially in 2D, as shown in **Figure 5.5** on **p. 139**, but we show that this is not sufficient in the context of measuring interactions between nanoparticles: either particles adsorb to the interface where their interactions are different, which happened to the particles with the smallest molecules on the surface causing them to aggregate, or the particles have sufficient ability to move within the finite thickness of the film such that the distance of the particles cannot be accurately captured in a 2D projection, which was the case for particles with the larger polymeric ligands. Therefore, we developed an entirely novel method to prepare samples suitable for cryo-TEM tomography –3D cryo-TEM–, where a sample is imaged at many different angles so that the 3D structure can be reconstructed using computer algorithms. This method was based on trapping microscopic pockets of liquid under a graphene sheet before cryogenically freezing them, as shown in **Figure 5.8** on **p. 143**. We show that with this method it is possible to trap individual solvent droplets like those used for the spherical self-assembly, and measure interactions between the particles in these droplets in 3D during self-assembly.

Measuring interaction forces from particle trajectories

Where previously we have analysed the positions of particles at one point in time under the assumption the particles were in a thermodynamic equilibrium, there are instances where this is not the case or where measurements are impractical under equilibrium conditions. Therefore we studied an alternative method to extract interaction forces from microscopy data in **Chapters 6 and 7**, based on analysis of particle *trajectories*—how their positions evolve over time— depending on the positions of neighbouring particles. This is conceptually simple: two nearby particles can be expected to move away from each other when they have repulsive interactions or move closer when they attract. However, on top of this the particles exhibit constant random motion due to the thermal energy which acts as noise on this measurement. Additionally, particle velocities can only be measured from displacements over a finite time interval, where it has to be assumed that the velocity and thus force over this interval was constant. Logically, this is only true for displacements which are small with respect to the length scale of the interactions, and this method thus requires small

time intervals. The small time intervals and displacements also mean that this method is highly sensitive to any error in the position measurements, and that the actual signal (the displacement due to the force) is small compared to the noise (the random displacements). To study the effectiveness of this trajectory analysis method we first analysed simulated trajectories, where the interaction forces were known. Here the most important conclusions were that the method works well for different interactions and particle concentrations, but as expected requires high measurement rates and large amounts of data.

Therefore, in the experiments in **Chapter 6** we first focused on a 2-dimensional system of large $1.7\ \mu\text{m}$ sedimented silica particles on a glass-liquid interface as shown schematically in **Figure 6.6**, such that high-speed fluorescence microscopy could be used to image a large number of particles with a strong signal. Here, we applied a high-frequency AC electric field perpendicular to the imaging plane which gave the particles repulsive interactions that could be controlled during the experiment through the field strength. This allowed us to record imaging series with a number of different interaction strengths within one sample, and show for the first time that such a trajectory analysis method can be used to measure interactions. Furthermore, by rapidly switching the field on and off faster than the particles could equilibrate, we could show interactions could be extracted even while the system was not in equilibrium. For some context, such a measurement at one interaction strength alone required over 20 000 images of ~ 500 particles each at a rate of 800 images per second, from which particle coordinates were determined with an average precision of 2.4 nm. We also attempted 3D measurements using CLSM on a system of particles that did not sediment, but although special equipment and methods optimized for speed resulted in imaging rates of around two 3D images per seconds, well over $100\times$ faster than conventional CLSM, these speeds were not sufficient to extract interaction forces with quantitative accuracy as was expected based on the analysis of simulated trajectories.

Finally, where we have so far only considered *isotropic* interactions—that is with radial symmetry—in **Chapter 7** we show that the trajectory analysis may be extended to account for *anisotropic* interactions, where the forces now depend both on the distance and relative angle/orientation between the particles. This was applied to particles with external electric field induced 3D dipolar interactions, where the particles attract along the field direction but have repulsive interactions perpendicular to it. In equilibrium these particles form chains along the field direction which makes interaction measurements challenging, so here the ability of trajectory analysis to measure out of equilibrium was a major advantage. Also here simulated trajectories were first used to show that it is in principle possible to accurately recover such anisotropic interaction forces, although this requires similarly high imaging rates and even larger quantities of data than for isotropic interactions, since the interaction forces are now dependent on at least two variables rather than only the distance. Next, we applied the method to experimental trajectories from 3D microscopy, where the electric field was switched on and off at regular intervals to prevent string formation. Again, as expected it was not possible to achieve the imaging rates desired to quantitatively recover the interaction forces, which were underestimated by more than tenfold when compared to theory. Nonetheless, the isotropic nature of the interactions in the electric field, and the isotropic nature of interactions when the field was off, were qualitatively corrected. This makes these results, to the best of our knowledge, the first fully 3-dimensional interaction measurements of anisotropic interaction forces between freely diffusing particles.

Conclusions and a look to the future

In this thesis we discussed why it is relevant to be able to measure interaction forces between colloidal particles experimentally, and gave a comprehensive overview of different methods by which this has been done previously. In our own experiments we chose to do this through statistical analysis of microscopy data because both optical and electron microscopy are among the most widely used analysis techniques for colloidal particles and can be used to measure the interaction forces without affecting the properties and positions of the particles, relying instead on their own thermal movements. But despite several methods having been reported that make this possible *in principle*, the actual number of studies using such measurements is small, particularly where nanoparticles are concerned. One of the reasons that we can give based on this research is that there is a big difference between ‘in principle’ and ‘in practice’. While it may be possible to measure with high resolution, with high speed or in 3D, that doesn’t mean it is trivial or even possible to measure in 3D with high speed and high resolution. To actually perform the experiments with sufficient resolution under the required conditions is often challenging, and this research is in some ways more an account of pushing boundaries by solving a million small problems than it represents radically new ideas. But while many asterisks could be placed next to most of the results we reported here, important progress has most definitely been made and we have opened new avenues to future work on interaction measurements. We have made two proposed methods for extracting interaction forces from microscopy data into a practical reality, which vastly broadened the scope of techniques, conditions and particle systems for which interaction measurements may be possible, and demonstrated this for a range of different techniques and particle systems. In this process we have not only improved and characterised the theory and implementations for these methods, but also developed new and improved procedures for microscopy sample preparation with potential application beyond just measuring interactions. Finally, in some cases our measurements directly contributed new data to open questions about interactions between particles, such as in the results from cryo-TEM where attractive interactions were unexpectedly found. And especially *because* the limitations of this work are often practical and technical in nature rather than ‘principle’ the future looks bright: equipment and procedures are always undergoing improvements that can directly enable more precise and more efficient interaction measurements. Therefore we hope that this thesis forms a basis for practical and effective interaction measurements under conditions where theory is not (yet) sufficiently able to make accurate predictions, and that the methods described here can become part of the toolbox of the researchers of tomorrow.

Samenvatting voor een breed publiek

Colloïden, nanodeeltjes en interacties. Maar waarom?

Voor het onderzoek in dit proefschrift hebben we geprobeerd om technieken te ontwikkelen om interacties te meten tussen microscopisch kleine deeltjes, zogeheten *colloïdale deeltjes* of *colloïden*. In het bijzonder is hiervoor gekeken naar het meten van de interacties tussen *nanodeeltjes*. Wat colloïden en nanodeeltjes precies zijn kun je in meer detail lezen in **Kader 1**, maar kort gezegd zijn dit deeltjes met groottes uitgedrukt in micrometers (afgekort μm) of nanometers (nm). Maar waarom zijn we eigenlijk geïnteresseerd in deze deeltjes en het meten van hun interacties? Colloïden hebben een hoop bijzondere eigenschappen die in de meeste gevallen een direct gevolg zijn van de microscopische groottes van de deeltjes, maar dat betekent ook dat individuele deeltjes over het algemeen veel te klein zijn om praktisch in toepassingen te kunnen gebruiken. In plaats daarvan maakt men voor toepassingen meestal gebruik van colloïdale dispersies waarin een grote hoeveelheid deeltjes gestabiliseerd is in een vloeistof, zoals de titaniadeeltjes die muurverf wit maken en de microcapsules met *e-ink* deeltjes in e-reader displays. Ook kan er gebruik worden gemaakt van zogeheten *geassembleerde materialen* waarin colloïden als het ware de bouwstenen van

Kader 1: Wat zijn colloïdale deeltjes en nanodeeltjes?

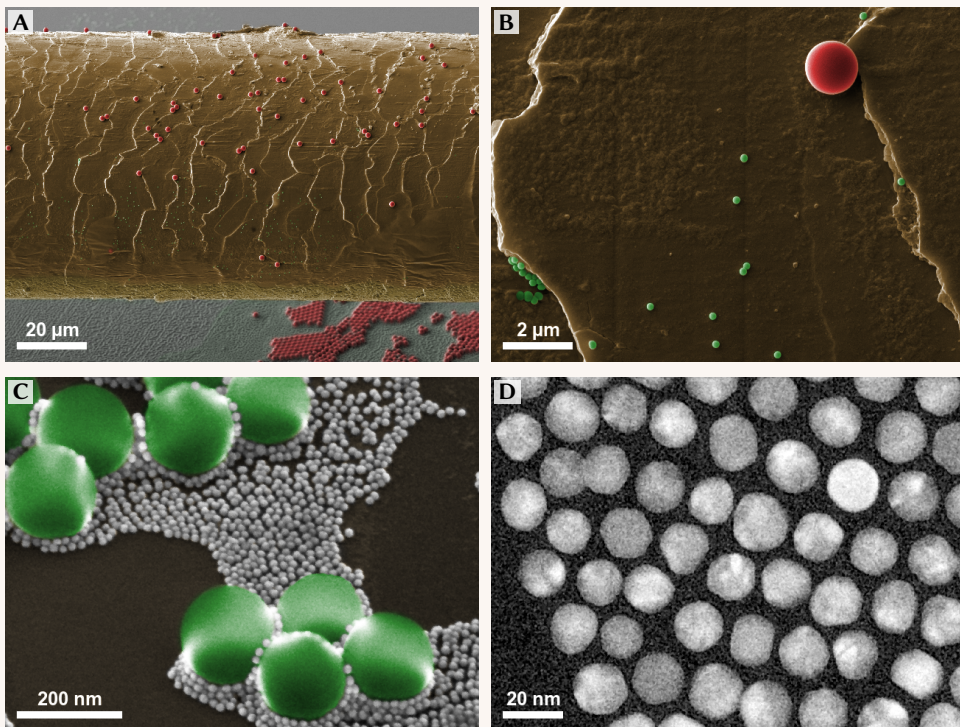
Colloïdale deeltjes, ook wel *colloïden* genaamd, zijn microscopische kleine deeltjes die gedispergeerd (fijn verdeeld) zijn in een andere stof, meestal in een gas of een vloeistof. Specifiek zeggen we dat deeltjes ‘colloïdaal’ zijn als ze een typische grootte hebben tussen één nanometer en tien micrometer: respectievelijk een miljoenste en een honderdste van een millimeter. Nanodeeltjes zijn de kleinste groep van de colloïdale deeltjes met eigenschappen die zeer sterk kunnen afhangen van de vorm en grootte van de deeltjes. In dit proefschrift noemen we colloïden nanodeeltjes als ze een diameter (grootte) hebben van minder dan honderd nanometer; colloïden van méér dan honderd nanometer noemen we ook wel *microdeeltjes*. Om een beter beeld te krijgen van deze groottes kun je ook kijken naar de afbeeldingen hiernaast en naar **Fig. 1.1** op **p. 3**. Voorbeelden van colloïden zijn de oliedruppels in melk, de pigmentdeeltjes in verf en inkt en de roetdeeltjes in rook, maar ook veel eiwitten, virussen en sommige bacteriën hebben een colloïdale grootte. In dit onderzoek kijken we met name naar colloïdale suspensies: ‘vaste’ deeltjes gedispergeerd in een vloeistof (ook wel het oplosmiddel genoemd).

Wat colloïdale deeltjes bijzonder maakt is dat ze klein genoeg zijn om in veel aspecten overeen te komen met moleculen, waarbij de deeltjesgrootte vaak bepalend is. Zo bewegen ze continu op een willekeurige manier in het rond door botsingen met de moleculen om hen heen en zijn ze vaak maar in beperkte mate beïnvloed door zwaartekracht. Tegelijkertijd zijn ze groot genoeg om hun structuur en dynamiek direct te kunnen observeren met licht- of elektronenmicroscopie, en kunnen hun eigenschappen in het geval van microdeeltjes over het algemeen goed beschreven worden met ‘klassieke’ theorieën — zonder kwantummechanica. Nanodeeltjes daarentegen zijn zodanig klein dat veel theoretische benaderingen niet meer van toepassing zijn en grenzen vervagen: zo is er geen duidelijk oppervlakte meer omdat alle atomen binnen nanometers van de omgeving zitten, zijn ze klein genoeg dat kwantummechanische effecten een belangrijke rol spelen, en is het niet meer aan te nemen dat materialen ‘continu’ zijn, wat betekent dat de groottes en aantallen van individuele atomen en moleculen een rol beginnen te spelen. Dit maakt het bestuderen van nanodeeltjes ingewikkeld maar juist ook interessant. De wisselwerking met hun omgeving —zij het chemisch, magnetisch, elektrisch, via licht of hoe dan ook— is vaak uitzonderlijk goed controleerbaar door de grootte en vorm van de deeltjes te variëren.

De volgende afbeeldingen zijn gemaakt met een elektronenmicroscop bij vergrotingen van ca. $1000\times$, $10\,000\times$, $100\,000\times$ en $1\,000\,000\times$ (resp. A–D) en tonen een hoofdhaar van de auteur met

het materiaal zijn, zoals in de natuurlijk voorkomende edelsteen opaal. Zulke materialen kunnen gemaakt worden via *zelfassemblage*, een proces waarin deeltjes onder de juiste omstandigheden spontaan complexe structuren zoals kristallen vormen, bijvoorbeeld door het oplosmiddel waarin ze gedispergeerd zijn langzaam op te drogen. Zelfassemblage komt veel voor in de biologie waar o.a. eiwit-eiwit interacties zeer specifiek afgestemd zijn zodat grote eiwitcomplexen of materialen als keratine, het hoofdbestanddeel van nagels en haar, spontaan kunnen vormen. De mogelijkheid om uit relatief simpele ‘nanobouwstenen’ materialen te creëren met een structuur die geordend is over meerdere lengteschalen maakt dit ook een veelbelovende strategie voor het prepareren van allerlei nieuwe materialen, bijvoorbeeld voor katalysatoren: stoffen of materialen die gebruikt worden om industriële chemische reacties mogelijk te maken en te versnellen. Het is zelfs mogelijk om de interacties van colloïdale deeltjes met elkaar of met hun omgeving nauwkeurig te controleren om een specifiek doel te bereiken: in een zelftest voor het coronavirus zitten bijvoorbeeld (rode) goud nanodeeltjes met een speciale coating van antigenen die heel specifiek aan virusdeeltjes binden en daarmee hun aanwezigheid in de vorm van een rood streepje zichtbaar maken.

daarop colloïden van drie verschillende groottes: glasbolletjes van 1.7 micrometer (weergegeven in rood), glasbolletjes van 170 nanometer (groen) en goud nanodeeltjes van 17 nanometer (wit). In werkelijkheid meet een elektronenmicroscop geen kleur en zijn de kleinste deeltjes vele malen kleiner dan de golflengte van zichtbaar licht, de kleuren zijn dus alleen ter verduidelijking toegevoegd.



In alle gevallen zijn de interacties tussen de deeltjes —simpel gezegd of de deeltjes elkaar afstoten of aantrekken en op welke afstand en met welke kracht dit gebeurt— van groot belang omdat ze bepalend zijn voor de stabiliteit van de colloïdale dispersie of de structuren die door de deeltjes gevormd worden in een zelfassemblageproces. Kennis en begrip over de interacties tussen de deeltjes en hoe die beïnvloed kunnen worden zijn daarom ook noodzakelijk om colloïdale dispersies en zelfassemblage te begrijpen en hun gedrag te voorspellen. Gelukkig is sinds het begin van de vorige eeuw veel theorie ontwikkeld om de stabiliteit en verschillende soorten interacties van colloïden te voorspellen, waarvan de belangrijkste principes ook kort worden beschreven in **Hoofdstuk 1** van dit proefschrift. Met name voor microdeeltjes is het in veel gevallen mogelijk om de interacties nauwkeurig te voorspellen op basis van bekende of meetbare systeemeigenschappen. Voor nanodeeltjes geldt echter dat veel van de versimpelingen en aannames in deze theorieën niet meer juist zijn, zoals wellicht het beste samengevat is in **Figuur 1.2** op p. 6; nanodeeltjes hebben een complexe structuur die niet goed uitgedrukt kan worden in benaderingen en ‘gemiddelden’. Ook is hierin het concept van *optelbaarheid* belangrijk: bij microdeeltjes kunnen we over het algemeen stellen dat de netto interactiekracht de som is van verschillende effecten die los van elkaar beschouwd kunnen worden, net zoals dat we de nettokracht op een tennisbal kunnen bepalen door de krachten door zwaartekracht, luchtweerstand en het racket los van elkaar uit te rekenen en bij elkaar op te tellen. Op de schaal van nanometers zijn er daarentegen vaak wisselwerkingen tussen de verschillende effecten die verantwoordelijk zijn voor interacties, bijvoorbeeld door koppeling van elektrische velden of structurering van de moleculen van de vloeistof om de deeltjes heen. Door deze wisselwerkingen zijn de interacties tussen nanodeeltjes vaak *niet* optelbaar, oftewel de verschillende ‘soorten’ interacties zijn onderling afhankelijk en kunnen niet meer los van elkaar beschouwd worden.

De ontwikkeling van theorie op dit gebied staat natuurlijk niet stil en er zijn theoretische beschrijvingen voor telkens meer effecten die de interacties van nanodeeltjes beïnvloeden. Toch zijn er altijd gevallen waarvoor nog geen theorie bestaat of waarin niet alle informatie bekend is om interacties te berekenen. Ook is theorie altijd gebaseerd op aannames die afhankelijk van de situatie wel of niet van toepassing kunnen zijn, en zoals bij elke theorie is het daarom belangrijk om de geldigheid in verschillende situaties experimenteel te verifiëren. Dat kan indirect, bijvoorbeeld door de stabiliteit van deeltjes onder verschillende omstandigheden te bestuderen, maar het meest directe bewijs is te verkrijgen door de voorspelde interacties te vergelijken met experimenteel bepaalde interactiekrachten. Ook zijn er grote vooruitgangen gemaakt in het gebruik van computersimulaties, en interacties van colloïdale nanodeeltjes met elkaar en hun omgeving kunnen in variërende gradaties van nauwkeurigheids gemodelleerd worden waarbij bijvoorbeeld de intermoleculaire interacties tussen het oplosmiddel en chemische groepen op de oppervlakte van de nanodeeltjes expliciet berekend worden. De verwachting is dat zulke simulaties in de toekomst een belangrijke rol zullen spelen in het begrijpen en voorspellen van het gedrag van colloïden, maar de keuze van inputparameters zoals inter-atomaire of inter-moleculaire interacties is hierin niet triviaal. Ook hier kunnen interactiemetingen dus een belangrijke rol spelen in het bepalen van de juiste parameters en het valideren van simulatiemethodes. Wanneer we weten dat deze simulaties de realiteit goed kunnen benaderen kunnen we die vervolgens ook inzetten om te voorspellen onder welke omstandigheden deeltjes de gewenste eigenschappen hebben, of om interacties te bepalen onder omstandigheden waar het niet praktisch haalbaar is om experimentele metingen te doen.

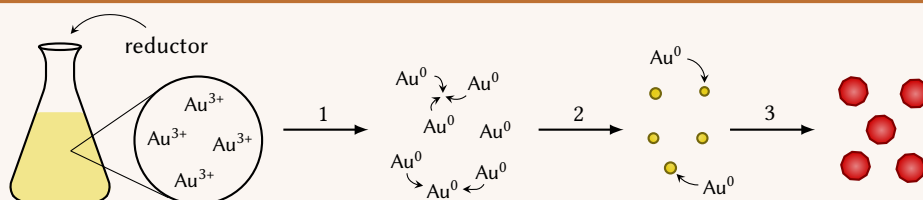
Wat was er voorafgaand aan dit onderzoek al bekend?

Zoals vrijwel ieder onderzoek zijn de technieken die we hier ontwikkeld en geëvalueerd hebben gebaseerd op eerder werk van anderen. In het eerste deel van de dit proefschrift gaan we hier in detail op in door de literatuur in te duiken op zoek naar experimentele interactiemetingen, en door een aantal gepubliceerde methodes voor het maken van colloïdale deeltjes na te werken en te vergelijken met de gepubliceerde resultaten. Er is dan ook veel literatuur over dit onderwerp: in de afgelopen paar decennia zijn diverse verschillen methodes om interacties tussen colloïden te meten ontwikkeld, gebaseerd op een groot aantal verschillende experimentele technieken waaronder licht- elektronen- en atoomkrachtmicroscopie. Die laatste werkt bijvoorbeeld door een atomair scherp naaldje aan het einde van een bladveer te bevestigen en heel nauwkeurig de afbuiging van de veer te meten terwijl de naald over een oppervlak bewogen wordt, om zo de kracht tussen de punt van de naald en het oppervlakte te meten en daarmee het reliëf in kaart te brengen. Hierbij is het ook mogelijk om een enkel colloïdaal deeltje aan de punt van de naald te bevestigen en langzaam naar een ander deeltje op de oppervlakte te bewegen, zodat bij iedere afstand de interactiekrachten tussen de twee deeltjes kunnen worden bepaald. Een andere methode is met een zogenaamde *optische pincet*: met gefocusseerde laserbundels kunnen individuele colloïden in een vloeistof ‘opgepakt’ en gemanipuleerd worden. Interactiekrachten kunnen dan gemeten worden door bijvoorbeeld twee deeltjes naar elkaar toe te brengen en te kijken hoe ze in de laserspots verschuiven, of door twee deeltjes in elkaars nabijheid te brengen, los te laten, en te kijken hoe ze bij elkaar weg bewegen. Zoals eerder genoemd is een bijzondere eigenschap van colloïden dat ze continu door hun omgeving bewegen dankzij botsingen met vloeistofmoleculen om hen heen, wat uiteindelijk een uiting is van de thermische energie – uitgedrukt in de temperatuur. Dit betekent dat deeltjes ook zonder dat we ze extern hoeven te manipuleren op een hoop verschillende afstanden van andere deeltjes kunnen worden gevonden, waarbij de waarschijnlijkheid om een bepaalde afstand tot een ander deeltje te vinden afhangt van de interactie-energie tussen deeltjes. Het is daardoor ook mogelijk om via licht- of elektronenmicroscopie een groot aantal deeltjes tegelijk te bekijken en statistische analyse toe te passen op de afstanden tussen de deeltjes of de manier waarop ze zich door de vloeistof bewegen. In **Hoofdstuk 2** geven we een uitgebreid overzicht van deze en andere methodes voor het meten van interacties tussen colloïden. Helaas zijn veel van de besproken technieken primair geschikt voor microdeeltjes en zijn metingen aan nanodeeltjes een stuk zeldzamer in de literatuur, terwijl er juist voor interacties op de schaal van nanometers nog de meeste open vragen zijn. Om die reden bespreken we voor alle technieken of en hoe deze toepasbaar zijn op nanodeeltjes in het bijzonder, waarbij we voor elke techniek de basisprincipes en de belangrijkste voor- en nadelen benoemen zoals samengevat in **Tabel 2.1** op p. 51. Daarnaast hebben we een aantal specifieke voorbeelden uitgelicht waarin interactiemetingen werden toegepast op nanodeeltjes of waarin interacties op anderszins vernieuwende manieren zijn gemeten.

Hoe worden colloïdale deeltjes gemaakt?

Colloïden kunnen worden gemaakt door materiaal fijn te malen of af te breken tot er deeltjes met een colloïdale grootte overblijven, een zogeheten *top down* preparatie, maar over het algemeen heeft men veel meer controle over o.a. de vorm en grootte van deeltjes als ze gemaakt worden door ze vanuit een oplossing van grondstoffen via chemische omzetting te groeien, ook wel een *bottom up* methode genoemd. Een voorbeeld van zo’n procedure is de

Kader 2: synthese van goud nanodeeltjes



Hierboven zie je een schematische weergave van een typische syntheseprocedure van goud nanodeeltjes van 15 nm. Hierbij beginnen we met een oplossing van een zout dat drievoudig positief geladen goudionen (Au^{3+}) bevat. Deze verhitten we tot $100\text{ }^\circ\text{C}$ waarna we een reductor (een stof die elektronen kan afstaan) toevoegen, die de ionen begint om te zetten in ongeladen goudatomen (1). Omdat deze Au^0 atomen slecht oplosbaar en reactief zijn beginnen ze snel met elkaar te reageren tot kleine clusters van atomen die het begin van deeltjes vormen, dit noemen we *nucleatie* (2). Als de concentratie van deze kerndeeltjes een bepaald niveau bereikt wordt het veel waarschijnlijker dat nog ongebonden of nieuwgevormde Au^0 atomen reageren met bestaande deeltjes dan dat ze nieuwe clusters vormen, de *groeifase* van de reactie. De deeltjes groeien nu langzaam verder tot alle goudionen zijn weggereageerd (3), waarbij de kleur van het reactiemengsel geleidelijk overgaat in een dieprode kleur door de groeiende deeltjes.

chemische omzetting van een goudoplossing tot metallisch goud in de vorm van nanodeeltjes. Je kunt hierover meer lezen in **Kader 2**. Hoewel het ontwikkelen van nieuwe methodes voor de synthese —het in het lab maken— van colloïden niet de focus van dit onderzoek is, is het prepareren van deeltjes met goed gedefinieerde en controleerbare eigenschappen een integraal onderdeel van het proces, en zijn vrijwel alle colloïden in dit proefschrift speciaal voor dit onderzoek gemaakt via zo'n 'bottom up' methode. Zo is het voor de metingen bijvoorbeeld niet alleen belangrijk om nauwkeurig te weten wat de grootte van de deeltjes is, maar ook dat alle deeltjes ongeveer dezelfde grootte hebben, de zogeheten *polydispersiteit* die beschrijft hoe groot de spreiding in deeltjesgroottes rond het gemiddelde is. Ook bepaalt de synthese wat er op het oppervlakte van de deeltjes zit, bijv. geladen groepen of organische moleculen, waarvan de eigenschappen grotendeels bepalen wat voor interacties er tussen de deeltjes zijn. In **Hoofdstuk 3** bespreken we daarom in detail de synthese van diverse soorten colloïden die gebruikt zijn voor de experimenten in de rest van dit onderzoek als ook voor een aantal andere onderzoeksprojecten. We hebben er hierbij voor gekozen om ons voor de kleinste deeltjes te richten op goud nanodeeltjes vanwege hun goede chemische stabiliteit (waardoor ze zonder speciale procedures lang houdbaar zijn), het hoge contrast in elektronenmicroscopie (belangrijk voor meting van de deeltjesgrootte en de interactiemetingen) en omdat het relatief eenvoudig is om de oppervlakte van gouddeeltjes te coaten met verschillende organische verbindingen (zoals korte polymeren) waarmee de interacties systematisch gevarieerd kunnen worden. Ook hebben dispersies van goud nanodeeltjes de bijzondere eigenschap dat hun kleur afhangt van de vorm, grootte en omgeving van de deeltjes, waardoor je al tijdens de synthese een visuele indicatie hebt of de deeltjes de juiste grootte hebben en het in één oogopslag te zien is als de deeltjes hun colloïdale stabiliteit verliezen en beginnen te *aggregeren*, oftewel samenklonteren. Daarnaast hebben we diverse groottes nano- en microdeeltjes gemaakt

van silica, het hoofdbestanddeel van zand en glas. Silicadeeltjes zijn zeer gecontroleerd te groeien waardoor een hele lage polydispersiteit kan worden behaald, waarbij het mogelijk is om verschillende kleuren fluorescente moleculen in de structuur te bouwen zodat de deeltjes kunnen worden bekeken met behulp van fluorescentiemicroscopie, wat het ook mogelijk maakt om de posities van de deeltjes te bepalen in 3D. De syntheseprocedures van deze deeltjes waren in alle gevallen gebaseerd op eerder gepubliceerde methoden, maar dat betekent niet dat er niets nieuws te leren viel. Het naverken van protocollen blijkt in de praktijk namelijk lang niet altijd te betekenen dat exact dezelfde resultaten worden behaald, waarbij soms alleen kleine verschillen in grootte, polydispersiteit of stabiliteit worden waargenomen, maar het soms ook zo kan zijn dat er helemaal geen of totaal andere deeltjes gemaakt worden. Het idee achter dit hoofdstuk is dus niet alleen dat het inzicht geeft in de eigenschappen van de deeltjes die we gebruiken, maar ook dat we meer data toevoegen over de reproduceerbaarheid van gepubliceerde syntheseprocedures en laten zien wat het effect van veelvoorkomende variaties in deze procedures kan zijn.

Interacties meten via distributiefuncties

In dit onderzoek maken we gebruik van microscopie om een groot aantal deeltjes in een colloïdale dispersie in beeld te brengen en hieruit de interacties tussen de deeltjes te meten. In **hoofdstukken 4 en 5** doen we dit door statistische analyse van zogeheten *distributiefuncties* die beschrijven hoe de deeltjes over de vloeistof verdeeld zijn en ten opzichte van elkaar gepositioneerd zitten. Deze aanpak gaat er vanuit dat de colloïdale deeltjes in *thermodynamisch evenwicht* zijn, waarbij de gemiddelde energie van een groot aantal deeltjes niet verandert maar de energie van individuele deeltjes op elk willekeurig moment behoorlijk kan variëren. In plaats van zelf de deeltjes te positioneren maken we dus gebruik van hun spontane beweging door de thermische energie om de verschillende posities (en daarmee verschillende krachten) te peilen. Een colloïdaal deeltje heeft een typische energie in de orde van $1 k_B T$ waarbij T de temperatuur is in Kelvin ($20\text{ }^\circ\text{C} \approx 293\text{ K}$) en $k_B = 1.38 \cdot 10^{-23}\text{ J/K}$ de *Boltzmannconstante* is. Het belangrijkste principe voor onze interactiemetingen is dat de waarschijnlijkheid ofwel kans om een deeltje op een bepaalde plaats te observeren direct afhangt van de energie die het een deeltje kost om die plek te bereiken. Voor de deeltjes in een homogene colloïdale dispersie ver weg van wanden en oppervlaktes zijn energiever verschillen tussen verschillende posities puur het gevolg van de interactiekrachten tussen de deeltjes. De verdeling van een groot aantal deeltjes hangt dus enkel af van de interacties die we willen meten, en dit betekent dat we ‘alleen maar’ de posities van een groep deeltjes ergens in de dispersie hoeven te bepalen om de interacties te kunnen berekenen! Simpel gezegd werkt dit als volgt: als deeltjes een repulsieve interactiekracht hebben —ze stoten elkaar af— dan kost het energie om twee deeltjes naar elkaar toe te bewegen, en zal je deeltjes gemiddeld vaker ver van elkaar weg observeren dan dicht bij elkaar. Andersom zullen deeltjes met attractieve interacties zich gemiddeld juist vaker dicht bij andere deeltjes bevinden. Door te meten hoe vaak we deeltjes op verschillende afstanden van elkaar vinden kunnen we dus indirect bepalen wat voor interacties de deeltjes hebben. We gebruiken hiervoor specifiek de *radiële distributiefunctie* —kort genoteerd als $g(r)$ — die beschrijft wat de waarschijnlijkheid is om twee deeltjes op een afstand r van elkaar te vinden relatief aan die waarschijnlijkheid in een volledig willekeurige set deeltjesposities bij dezelfde concentratie (maar zonder interacties). De $g(r)$ is radiëel gemiddeld, wat betekent dat we alleen kijken naar de afstanden tussen de deeltjes terwijl we er vanuit gaan dat de oriëntatie van de deeltjes niet uitmaakt voor

de interactiekrachten. Ook nemen we met het gebruik van de $g(r)$ aan dat alle interacties *paarsgewijs optelbaar* zijn, dus dat de interacties van een deeltje met elk van de naburige deeltjes los van elkaar beschouwd kunnen worden. Voor veel colloïden zijn dit redelijke aannames, maar zoals we later zullen zien zijn er gevallen waar dat niet het geval is. Hoewel het redelijk eenvoudig is om de $g(r)$ te voorspellen op basis van de interacties tussen de deeltjes, bijv. via computersimulaties, is het in de praktijk niet triviaal om het omgekeerde te doen en de oorspronkelijke interacties tussen de deeltjes terug te rekenen uit de $g(r)$ onder praktisch werkbare omstandigheden. We rapporteren daarom in dit proefschrift een praktische implementatie van een recent voorgesteld algoritme genaamd *iteratieve testdeeltjes-insertie* (iTDI) waarmee de interacties onder een groot scala aan omstandigheden uit experimentele en gesimuleerde data kunnen worden berekend.

Oplosmiddelfixatie voor lichtmicroscopie: stop de tijd

Om de $g(r)$ en daarmee via iTDI de interacties te kunnen berekenen hebben we dus de posities van een groot aantal deeltjes op een willekeurig moment in de tijd nodig. Dit is vrij eenvoudig in twee dimensies door met een camera door een microscoop een foto te maken en hieruit de posities te meten, maar voor de meeste colloïden heeft de zwaartekracht maar een beperkt effect en zijn de bewegingen en interacties driedimensionaal. Gelukkig bestaan er technieken om driedimensionale microscopische afbeeldingen te maken zoals *confocale laserscanmicroscopie*, maar die werken over het algemeen door een volume 'laagje voor laagje' één voor één te meten en hebben daarom een grote Achilleshiel: tijd. Diezelfde bewegingen die ervoor zorgen dat deeltjes zich verdelen naargelang de interactiekrachten zorgen ervoor dat onrealistisch snel zou moeten worden gemeten om een onbewogen 3D microscopieafbeelding te maken. In **Hoofdstuk 4** gebruiken we daarom een nieuwe methode om de beweging in een colloïdale dispersie stil te zetten waarbij de posities van de deeltjes behouden worden. Door een deel van het oplosmiddel te vervangen door polymeriseerbare moleculen (monomeren) en toevoeging van een UV-gevoelige initiator, konden we met een korte puls UV licht op het juiste moment het oplosmiddel snel in een gel veranderen waarin de deeltjes plotseling niet meer konden bewegen, waarna we zonder tijdsdruk de posities van de deeltjes konden bepalen zoals die waren op het moment dat de polymerisatiereactie werd gestart. We noemen deze methode oplosmiddelfixatie, en laten zien dat het hiermee in combinatie met iTDI bijvoorbeeld mogelijk was om silica nanodeeltjes van ca. 100 nm stil te zetten en repulsieve langeafstands-elektrostatistische interacties tot meer dan 500 nm te meten. Ook hebben we oplosmiddelfixatie toegepast op een binair (twee-component) systeem met silicabollen van zowel 300 nm als 400 nm. Doordat deze twee groottes deeltjes onder invloed van zwaartekracht met andere snelheden sedimenteerden, kon gelijktijdig een gradiënt in zowel de deeltjesconcentratie als in de verhouding tussen de aantallen grote en kleine deeltjes worden verkregen, waardoor een aantal verschillende structuren en kristallen gelijktijdig in één sample konden worden geobserveerd. Door de samples te fixeren kon de structuur bovendien na verschillende sedimentatietijden stil worden gezet en worden bekeken zonder de sedimentatiegradiënten te verstoren, en konden de interacties van zowel beide types deeltjes met zichzelf als tussen de verschillende types deeltjes gelijktijdig worden gemeten onder dezelfde omstandigheden waaronder de verschillende structuren werden gevormd. Lichtmicroscopie zoals we het hier gebruikt hebben is veelzijdig maar heeft een resolutie die uiteindelijk gelimiteerd is door de golflengte van zichtbaar licht, en op afstanden van minder dan enkele honderden nanometers zijn deeltjes niet meer van elkaar

te onderscheiden.* Voor het bestuderen van nanodeeltjes gebruikt men daarom met name elektronenmicroscopie, waar dit geen beperking is doordat de golflengte van de gebruikte elektronen vele malen kleiner is dan de typische bindingslengte tussen atomen. We hebben daarom ook onderzocht of oplosmiddelfixatie gebruikt kan worden om colloïdale dispersies te fixeren zodat ze gemeten kunnen worden in een SEM, een elektronenmicroscopietechniek waarbij met hoge resolutie de oppervlakte van materialen kan worden afgebeeld (o.a. te zien in afb. A, B en C in **Kader 1**). SEM kan worden gecombineerd met een gefocuseerde ionenbundel, waarmee gecontroleerd nanometer-dunne laagjes van het materiaal verwijderd kunnen worden, om zo laagje voor laagje een 3D structuur bloot te kunnen leggen. We laten voor verschillende silica- en goud nanodeeltjes zien dat het mogelijk is om puur monomeer als oplosmiddel te gebruiken waardoor de gefixeerde samples geschikt zijn voor FIB-SEM, waardoor een tot wel 100× betere resolutie behaald kan worden dan met conventionele lichtmicroscopie. Wel is een groot nadeel hierbij dat dit uiteraard maar beperkt toepasbaar is omdat enkel de interacties in het specifieke fixatiemiddel gemeten kunnen worden.

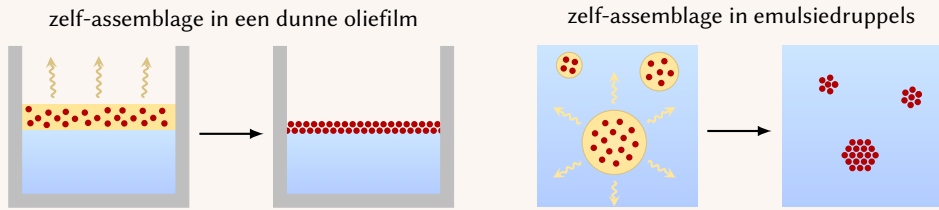
Cryogene elektronenmicroscopie: bevroren en bekijken.

In **Hoofdstuk 5** hebben we gekeken naar de zelf-assemblage en het meten van interacties tussen zeer kleine goud nanodeeltjes van tussen de 2 en 8 nm die gedispergeerd waren in het oplosmiddel toluen, waarbij de stabiliserende moleculen aan de oppervlakte konden worden vervangen door een coating van korte polymeerketens met verschillende lengtes. Het is bekend dat zulke deeltjes afhankelijk van de grootte van de polymeerlaag verschillende kristalstructuren kunnen vormen in zelf-assemblage, waarbij de hypothese was dat de polymeermoleculen afhankelijk van hun lengte meer of minder uitsteken in de vloeistof en zo in verschillende mate repulsieve interacties tussen de deeltjes veroorzaken. Die interacties zouden dan door de combinatie van de groottes van de goudkern en polymeerlaag kunnen variëren van ‘hard’ (als een biljartbal) tot relatief zacht, waarbij de repulsie geleidelijk aan toeneemt terwijl de deeltjes dichterbij elkaar komen. Ook voor dit onderzoek hebben we gekeken naar de zelf-assemblage van deze deeltjes, in twee verschillende geometrieën die beiden structuren opleverde die dun genoeg waren om met TEM te kunnen bekijken, namelijk quasi tweedimensionale lagen en in bolvormige supradeeltjes. Hierover kun je meer lezen in **Kader 3**; microscopieafbeeldingen van de gemaakte structuren zijn o.a. te zien in **figuren 5.2 en 5.4**. Hierbij vonden we drie verschillende vormen van assemblage: deeltjes zonder de polymeercoating waren niet voldoende gestabiliseerd en aggregeerden voordat het droogproces voltooid was, terwijl deeltjes met korte en middellange polymeerketens kristalstructuren vormde. Opvallend was dat deeltjes met langere polymeerketens niet kristalliseerde, maar structuren vormde met alleen ordening over korte afstanden. Om de invloed van de coating op de interacties en de invloed van de interacties op de gevormde structuren te vergelijken was het dus interessant om de interacties van deze deeltjes in toluen te meten, maar het extreem kleine formaat maakt dit een lastige opgave. Zoals genoemd is het mogelijk om met nanometer resolutie naar oppervlakten te kijken met SEM, maar verreweg de beste resolutie is mogelijk met een transmissieelektronenmicroscop (TEM) waarbij men door het materiaal heen kijkt en als het ware de ‘schaduw’ afbeeldt (bijv. afb. D), een beetje vergelijkbaar met hoe een röntgenfoto gemaakt wordt. De keerzijde hiervan is dat elektronen in tegenstelling tot fotonen (licht) sterke interacties met vrijwel

* er zijn in de afgelopen decennia diverse ‘trucs’ uitgevonden om onder deze limiet uit te komen, ook wel *superresolutiemicroscopie* genoemd, maar in de context van dit onderzoek zijn afstanden van minder dan 300 nm tussen deeltjes met lichtmicroscopie praktisch onmeetbaar.

Kader 3: zelf-assemblage van nanodeeltjes door verdamping

Hieronder zie je schematisch twee manieren die we gebruikt hebben om nanodeeltjes te laten zelf-assembleren via verdamping van het apolaire (olieachtige) en vluchtige oplosmiddel toluen. Hiervan kon een dun olielaagje gevormd worden op de oppervlakte van een polaire (met olie onmengbare) vloeistof. Door de toluen langzaam te laten verdampen bleef een laag nanodeeltjes achter op de vloeistof van enkele millimeters lang en breed maar slechts één of een paar nanodeeltjes dik, dit wordt ook wel een quasi tweedimensionale zelf-geassembleerde laag genoemd. Ook hebben we bolvormige kristallen van nanodeeltjes gemaakt, ook wel supradeeltjes genoemd, door een emulsie van toluendruppeltjes met nanodeeltjes in water te maken en de toluen langzaam uit de emulsie te laten verdampen waardoor de nanodeeltjes bij elkaar gebracht werden.



alle materie hebben, en dus al door heel weinig materiaal volledig geblokkeerd worden. Om die reden werken elektronenmicroscopen vrijwel altijd onder vacuüm en moeten de samples voor TEM extreem dun zijn, typisch minder dan een micrometer dik, wat ook betekent dat we niet zomaar een vloeistof met deeltjes in het vacuüm van de microscoop kunnen stoppen. Gelukkig bestaat hiervoor een oplossing die vooral wordt toegepast in de biochemie, waar water essentieel is voor de structuur van cellen en eiwitten: cryo-TEM. Het idee is eenvoudig: door een vloeibaar sample cryogeen te bevriezen –dat betekent extreem snel en koud, typisch in minder dan een milliseconde bij $-196\text{ }^{\circ}\text{C}$ m.b.v. vloeibare stikstof– wordt de structuur zó snel omgezet naar een vaste stof dat de posities van deeltjes en zelfs de vloeistofmoleculen geen tijd hebben om te verplaatsen in het proces, vergelijkbaar met de oplosmiddelfixatiemethode (maar zo'n duizend keer sneller). Voor water betekent dit bijvoorbeeld dat er geen ijskristallen worden gevormd maar zogeheten amorf ijs waarin de moleculen grotendeels ongeordend zijn, maar ook voor andere oplosmiddelen is dit mogelijk. Door een dispersie van nanodeeltjes cryogeen te bevriezen en in een speciale gekoelde houder in het vacuüm van de TEM te brengen is het in principe dus mogelijk om nanodeeltjes in een 'vloeistof' te bekijken, waarbij de deeltjesposities bewaard zijn zoals ze waren op het moment dat ze ingevroren werden. Dit wordt meestal gedaan in de vorm van een dunne vloeistoffilm zoals te zien in **Figuur 5.5** op p. 139, waarbij de geometrie min of meer tweedimensionaal is met de deeltjes opgesloten in de dunne film, en 2D microscopie en analyse voldoende is om de structuur te bepalen. Ons onderzoek laat echter zien dat deze geometrie niet geschikt is voor het meten van interacties. Veel nanodeeltjes hebben de neiging om aan oppervlakten te adsorberen waardoor de interacties tussen de deeltjes totaal kunnen veranderen ten opzichte van de interacties in de 'bulk' van een vloeistof, weg van oppervlaktes, zo ook onze deeltjes met de kleinste moleculen die sterk aggregaerden op de vloeistofoppervlakte. De deeltjes met de polymeercoating aan de andere kant bleken juist niet aan de vloeistofoppervlakte te gaan zitten, maar een gevolg hiervan was dat ze voldoende vrijheid in de dikte van de vloeistoflaag hadden dat de aanname van een tweedimensionale geometrie niet meer correct was. We

hebben daarom een geheel nieuwe manier ontwikkeld om cryo-TEM samples te prepareren voor die geschikt zijn voor *tomografie*, een techniek voor 3D TEM waarbij het sample onder veel verschillende hoeken bekeken wordt waaruit met computeralgoritmes de 3D structuur kan worden berekend. We laten zien dat het mogelijk is om individuele oliedruppeltjes, zoals die gebruikt voor de zelf-assemblage van supradeeltjes, te vangen onder een atomair dunne grafeenlaag en ze cryogeen in te vriezen tijdens het assemblageproces zoals te zien in **Figuur 5.8** op p. 143. Hiermee konden interacties van de deeltjes in de oliedruppels in 3D bepaald worden.

Interacties meten uit bewegingen

In de bovenstaande experimenten hebben we alleen gekeken naar de posities van deeltjes op één moment in tijd, waarbij we onder de aanname van een thermodynamisch evenwicht interacties konden bepalen. Dit is een zeer vaak gemaakte aanname, omdat een hoop theorie enorm vereenvoudigd wordt wanneer een systeem in evenwicht is, wat effectief inhoudt dat de gemiddelde energie van de deeltjes niet verandert over tijd. Maar wat als we geïnteresseerd zijn in deeltjessystemen die *niet* in evenwicht zijn, of waarbij metingen onpraktisch zijn onder evenwichtsomstandigheden? **Hoofdstukken 6 en 7** gaan daarom over een alternatieve methode om interacties te bepalen waarbij gekeken wordt naar de bewegingen (of snelheden) van de deeltjes, dus het verloop van de deeltjesposities over tijd, in plaats van alleen de posities op één tijdstip, afhankelijk van de posities van naburige deeltjes. Het idee is conceptueel vrij eenvoudig: als twee deeltjes dicht bij elkaar zitten en elkaar afstoten, is de kans groter dat ze vervolgens bij elkaar weg bewegen dan naar elkaar toe. De praktijk is echter lastiger, omdat colloïdale deeltjes naast beweging door de interacties zoals al eerder genoemd continu op een willekeurige manier bewegen door botsingen met vloeistofmoleculen. Dit zorgt er weliswaar voor dat de deeltjes veel verschillende configuraties en afstanden bezoeken, maar werkt ook als een soort ruis die onze metingen kan domineren afhankelijk van de interactiekrachten en deeltjesgrootte. Ook kan de snelheid niet instantaan gemeten worden uit één microscopieplaatje. In plaats daarvan konden we de snelheid meten als een verplaatsing over een tijdsinterval tussen twee opvolgende plaatjes, waarbij we aangenomen hebben dat de snelheid (en dus de interactiekracht) over dat tijdsinterval ongeveer constant was. Dit was uiteraard alleen het geval als het tijdsinterval, en daarmee de gemeten verplaatsing, heel klein waren ten opzichte van de grootte van de deeltjes en de lengteschaal van de interacties. Tegelijkertijd betekende zulke kleine verplaatsingen dat de methode erg gevoelig was voor hoe nauwkeurig de posities van de deeltjes bepaald konden worden. Ook maakte dit dat het signaal —de verplaatsingen door interactiekrachten— erg klein waren ten opzichte van de ruis —de willekeurige verplaatsingen door het oplosmiddel— omdat die twee effecten een verschillende tijdsafhankelijkheid hebben, waardoor meer data nodig was bij kleinere tijdsintervallen om een vergelijkbare precisie te behalen.

Om de effectiviteit van de bewegingsanalysemethode te verifiëren en de invloed van deze en andere effecten te bestuderen hebben we de methode eerst uitgebreid getest op gesimuleerde data waarbij de interactiekrachten exact bekend waren om zo een overzicht te maken van de parameters waarbij interacties nauwkeurig gemeten kunnen worden. De belangrijkste conclusies hierbij waren dat de methode in principe goed werkt voor verschillende soorten interacties en verschillende deeltjesconcentraties, maar dat afhankelijk van de precieze interactiekrachten zeer hoge meetsnelheden en grote hoeveelheden data benodigd zijn. Experimenteel hebben we daarom in **Hoofdstuk 6** eerst naar een effectief tweedimen-

sionaal deeltjessysteem gekeken, waarbij hogesnelheid fluorescentiemicroscopie gebruikt kon worden om in één keer een groot aantal deeltjes met veel signaal in beeld te brengen. Dit hebben we gedaan door relatief grote silicadeeltjes van 1.7 μm in een vloeistofmengsel met een hoge viscositeit en lage dichtheid te bekijken, zodat de deeltjes onder invloed van zwaartekracht sedimenteerden tot ze allemaal op de oppervlakte van een microscoopglasje lagen, zoals schematisch weergegeven in **Figuur 6.6** op p. 180. Door een hoogfrequent elektrisch veld aan te leggen over het sample konden we bovendien de deeltjes repulsieve elektrostatistische interacties geven, waarbij we de sterkte van de interacties tijdens de meting konden instellen via het aangebrachte voltage. Hierdoor konden we in één sample en op dezelfde deeltjes metingen doen aan verschillende sterktes interactiekrachten, en hebben we voor het eerst laten zien dat zulke metingen via de deeltjesbewegingen mogelijk zijn. Ook konden we ervoor zorgen dat de deeltjes uit thermodynamisch evenwicht waren door de interacties continu ‘aan’ en ‘uit’ te zetten via het veld, waarbij we hebben laten zien dat het ook zonder evenwicht mogelijk was om de interacties te bepalen. Om een idee te geven van de meetsnelheden en hoeveelheid data die nodig waren voor dit soort metingen: per interactiesterkte hebben we zo’n 500 deeltjes voor meer dan 20 000 tijdstappen gevolgd bij een meetsnelheid van 800 afbeeldingen per seconde, wat betekent dat meer dan een *terabyte* aan ruwe microscopiedata nodig was voor de interactiemetingen in **Figuur 6.8** op p. 183. Hieruit hebben we vervolgens de posities van de deeltjes bepaald met een gemiddelde nauwkeurigheid van 2.4 nm, minder dan 0.2 % van de deeltjesgrootte en ruim 200× kleiner dan de golflengte van het licht waarmee we meten! Omdat zulke 2D metingen niet voor alle deeltjes mogelijk of relevant zijn hebben we ook geprobeerd om deeltjessnelheden te meten in 3D via confocale microscopie. Helaas is dit een inherent langzame meettechniek en was met speciaal voor snelheid geoptimaliseerde apparatuur en methodologie de maximale meetsnelheid ca. twee 3D afbeeldingen per seconde, zo’n 100 tot 1000× keer sneller dan in conventionele confocale microscopie, wat desondanks niet snel genoeg was om kwantitatief de juiste interacties te bepalen. Wel konden we hierbij kwalitatief laten zien wat voor soort interacties de deeltjes hadden, en in combinatie met simulaties aantonen dat de metingen overeenkomen met wat we gezien de meetsnelheid verwachten, waarmee het aannemelijk is dat de bewegingsanalysemethode werkt zoals verwacht mits de meetsnelheid afdoende is.

Tot slot zijn we bij alle tot nu toe genoemde metingen zijn we uitgegaan van interacties die *isotroop* zijn, dat wil zeggen rondom symmetrisch zodat ze puur afhangen van de afstand tussen de deeltjes en niet van hun relatieve oriëntatie/hoek. In **Hoofdstuk 7** hebben we de theorie achter de bewegingsanalysemethode uitgebreid naar *anisotrope* interacties, dus interacties die *niet* symmetrisch rond het deeltje zijn. Dit hebben we toegepast op deeltjes met dipolaire interacties die we met een extern hoogfrequent elektrisch veld konden induceren, waarbij de deeltjes elkaar langs één richting aantrekken (de richting van het externe elektrische veld) terwijl ze elkaar in het vlak loodrecht daarop juist afstoten. In thermodynamisch evenwicht vormen deze deeltjes lange ketens in de richting van het veld die interactie-metingen moeilijker maken, en hier was het dus een voordeel van de bewegingsanalysemethode dat we de metingen in een niet-evenwichtstoestand konden uitvoeren waarin ketenvorming tegengegaan werd. Ook hier hebben we eerst met gesimuleerde data laten zien dat het in principe mogelijk is om zulke interacties nauwkeurig te meten, hoewel dit evengoed hoge meetsnelheden en nog veel meer data vergt dan voor isotrope interacties. Vervolgens hebben we de bewegingsanalyse toegepast op 3-dimensionale experimentele metingen met confocale microscopie waarbij we het externe elektrische veld snel aan- en

uitgezet werd om de ketenvorming tegen te gaan. Wederom was het hier niet mogelijk was om de meetsnelheid te behalen die volgens de analyse nodig was om kwantitatief correcte metingen te doen, waardoor de sterkte van de interactiekrachten met meer dan een factor tien onderschat werd door de bewegingsanalyse. Maar ondanks de te lage meetsnelheid bleek de methode wel goed in staat om de anisotrope aard van de interacties in een elektrisch veld correct te bepalen, terwijl in periodes waar het elektrische veld uitstond zoals verwacht puur isotrope interacties werden gemeten. Voor zover wij weten maakt dit onze resultaten de eerste volledig 3-dimensionale metingen van anisotrope interactiekrachten tussen vrij diffunderende colloïdale deeltjes ooit.

Conclusies en een vooruitblik

We hebben in dit proefschrift besproken waarom het belangrijk is om de interactiekrachten tussen colloïden te meten en een uitgebreid overzicht gegeven van de verschillende manieren waarop men dit tot nu toe heeft geprobeerd. In onze eigen experimenten hebben we ervoor gekozen om dit te doen door statistische analyse van microscopiedata omdat zowel licht- als elektronenmicroscopie behoren tot de meestgebruikte analysetechnieken in de colloïdchemie en deze technieken gebruikt kunnen worden zonder de posities en eigenschappen van de deeltjes te beïnvloeden. Maar ondanks dat over de afgelopen decennia diverse manieren zijn gerapporteerd waarmee zo'n analyse in principe mogelijk zou moeten zijn, is het aantal daadwerkelijk gerapporteerde metingen vrij klein, met name als we het specifiek over nanodeeltjes hebben. Eén van de redenen die we op basis van dit onderzoek kunnen geven is dat er een groot verschil is tussen 'in principe' en 'in de praktijk'. Het is prima mogelijk om met hoge resolutie te meten, om met hoge snelheid te meten of om in 3D te meten, maar dit betekent niet dat we zomaar met hoge resolutie en hoge snelheid in 3D kunnen meten. Om daadwerkelijk met voldoende nauwkeurigheid en snelheid onder de vereiste omstandigheden microscopie te doen is vaak zeer uitdagend, en dit proefschrift is dan ook in zekere zin meer een verhaal van grenzen verleggen door heel veel kleine problemen op te lossen dan van een radicaal nieuwe aanpak. Maar hoewel er nog steeds bij veel van de metingen in dit onderzoek kanttekeningen te plaatsen zijn, zijn er wel degelijk belangrijke stappen gezet en nieuwe paden geopend voor toekomstig onderzoek. We hebben van twee nieuwe manieren om interacties uit microscopiedata te halen een praktische realiteit gemaakt, waarmee de verscheidenheid aan technieken, omstandigheden en deeltjessystemen waarmee interacties gemeten kunnen worden enorm uitgebreid zijn, en dit ook voor een grote verscheidenheid aan technieken daadwerkelijk laten zien. In dit proces hebben we niet alleen de theorie en analysemethodes verbeterd en geëvalueerd, maar ook vooral nieuwe verbeterde procedures ontwikkeld voor microscopie die breder toepasbaar zijn dan enkel het meten van interacties. Tot slot dragen onze metingen in enkele gevallen ook al bij aan nieuwe inzichten over de interacties zelf, zoals bij de cryo-TEM metingen waar onverwacht attracties werden gemeten wanneer de deeltjesconcentratie hoog was. En juist omdat de limitaties van de metingen in dit onderzoek veelal praktisch van aard waren en niet 'principeel', ziet de toekomst er voor dit soort onderzoek rooskleurig uit: apparatuur en methodologie ondergaan continue verbeteringen waardoor efficiëntere en nauwkeurigere interactie-metingen mogelijk zullen worden. We hopen dan ook dat dit proefschrift de basis legt voor praktische en effectieve interactiemetingen met deeltjes en onder omstandigheden die (nog) niet zomaar theoretisch kunnen beschreven, en dat de technieken die we hier hebben ontwikkeld een onderdeel worden van de toolbox van de onderzoekers van morgen.

Acknowledgements

While a PhD is in many ways a rather personal pursuit and can, at times, feel frustrating and lonely, I am incredibly grateful for the many kind, clever, funny and generally wonderful people I've crossed paths with over the last 6(!) years. As is the temporary nature of academic research I have seen many people finish and move on to new challenges while others have started and picked up where they left off, and yet as I am writing this it still feels a little unreal that it is now my turn to finish and say goodbye.

But the only way to begin is by beginning, and no better place to start than with the one who started it all: my promotor and supervisor, Prof. **Alfons van Blaaderen**. Ik wil je bedanken dat je me aangemoedigd en de kans geboden hebt om mijn droom om wetenschapper te worden waar te maken, en dat je me altijd het vertrouwen en de vrijheid gegeven hebt om mijn eigen pad te volgen en mijn PhD vorm te geven. Ik heb in onze waarschijnlijk honderden wetenschappelijke discussies *altijd* het gevoel gehad dat je mijn ideeën respecteerde als je gelijke en ook mijn intuïtie en inschattingsvermogen vertrouwde wanneer we met een andere blik naar resultaten of plannen keken, waarbij je me altijd scherp hebt gehouden door verkeerde aannames of onlogische redeneringen er feilloos tussenuit te pikken, en waarbij de experimenten en feiten altijd het laatste woord hadden ongeacht aan wiens 'kant' van de discussie ze stonden. Je continue passie en motivatie om de wetenschap verder te pushen, of dat nou in grote 'firsts' of in incrementele praktische verbeteringen gaat, en het feit dat je van beiden het belang erkent, hebben me meer dan eens geholpen om gemotiveerd te blijven en om de 'bigger picture' te blijven zien terwijl ik het gevoel had dat ik vast zat op een dood spoor of de resultaten maar niet kwamen. Daarnaast hebben je kennis en goede geheugen voor literatuur me vaak in de goeie richting gewezen om antwoorden te vinden op vragen waarvan ik soms nog niet eens wist dat ik ze had. Bedankt voor alle jaren van samenwerking!

As the experiments in this thesis show, experimental research means pushing boundaries, and I could never have achieved this without the help of our amazing technical support staff: **Relinde van Dijk-Moes, Elleke van Harten, Peter Helfferich** and **Dave van den Heuvel**. **Relinde**, ik wil je bedanken voor al je jaren van inzet om het lab een fijne en veilige werkplek te houden, en voor je behulpzaamheid en openheid bij de talloze keren dat ik iets kwam vragen of dat ik weer eens wilde ideeën had om iets in het lab te veranderen. Daarnaast ben je natuurlijk een hartstikke gezellige kletser en hebben we over de jaren heel wat uren afgepraat aan de koffietafel, in het lab en in de gangen. **Elleke**, ook jou wil ik bedanken voor je inzet voor de labs en natuurlijk al je input over deeltjessynthese, en ik ga onze vele (soms iets te lange) lunchpauzegesprekken over politiek, maatschappij of wat dan ook missen. Ik

heb het daarnaast altijd erg fijn gevonden om met je te kunnen praten over je ervaringen en perspectieven op het doen van een PhD en werken in de wetenschap. **Peter**, zonder jouw behulpzaamheid en brede kennis over elektronica, optica en IT was de microscopie en analyse daarvan in deze thesis nooit zo ver gekomen, om nog maar te zwijgen over alle kapotte en zich misdragende spullen die ik over de jaren voor je ‘gevonden’ heb. **Dave**, zonder je eeuwige vrolijkheid en optimisme zouden de wandelgangen van het OL niet hetzelfde voelen. Je maakt je altijd met het benodigde doorzettingsvermogen hard voor de veiligheid en het welzijn van iedereen in onze groep, en ik wil je heel erg bedanken dat je mij en vele anderen daarin (vaak letterlijk) ondersteund hebt. Ook wil ik natuurlijk **Hester van der Putte**, **Mijke Heldens**, **Dianne Ickenroth** en **Mariette Kemner-van de Corput** bedanken voor hun hulp met praktische en administratieve zaken, die wellicht niet in een proefschrift staan maar daarom niet minder belangrijk zijn om dit onderzoek mogelijk te maken. **Hester**, jouw warmte en gezelligheid blijken uit elk gesprek, en ik kan me geen SCMB groep inbeelden (of herinneren) zonder dat jij daar deel van uitmaakt. Mijn dank gaat daarnaast ook uit naar **Chris Schneijdenberg**, **Hans Meeldijk** en **Eric Hellebrand** van het *Electron Microscopy Centre*. Jullie hebben niet alleen één van de beste faciliteiten voor EM in Nederland mogelijk gemaakt, maar me ook vrijwel alles wat ik weet over TEM en SEM bijgebracht en me talloze keren uit de brand hebben geholpen als iets niet werkte of als ik weer onconventionele plannen of samples had. Bedankt voor jullie altijd positieve energie en behulpzaamheid.

Much of the work in this thesis would not have existed without some excellent students: **Niels van de Poll**, **Dinja Sanders** and **Tessa Vrijhoeven**, who are respectively the best hogeschool, master and bachelor students I’ve had the pleasure of supervising. **Niels**, niet alleen was het altijd heel gezellig om met je samen te werken, je zorgvuldige en systematische werk heeft ook geresulteerd in de prachtige fluorescente silica nanodeeltjes en nauwkeurig gefinetuned procedures in Hoofdstuk 4. **Dinja**, het was gelijk duidelijk dat je ambitieus was en een goeie uitdaging niet uit de weg ging, waarbij ik me soms aardig in de materie moest verdiepen om je bij te kunnen houden, terwijl je daarnaast ook nog ‘even’ experimenten deed op de grens van wat technisch mogelijk is. Het resulteerde in Hoofdstuk 7, mijn persoonlijk favoriet in dit proefschrift. **Tessa**, je had een echt experimenteel project met de bijbehorende uitdagingen, maar je hebt in korte tijd een heel scala aan mooie deeltjes en assemblies gemaakt waarvan een groot deel te zien is in Hoofdstuk 5, in wat misschien wel de mooiste microscopische plaatjes in dit proefschrift zijn.

My gratitude also extends to all my colleagues from the UU and elsewhere who collaborated with me on research in this thesis and on other projects during my time in the group. I’d like to thank **Roy Hoitink**, **Xufeng Xu** and **Helmut Cölfen**, for the work on binary sedimentation presented in Chapter 4. I also want to thank **Laura Filion** for co-supervising Dinja’s and her involvement in the work in Chapters 6 and 7. Without her ideas and our many discussions I would not have managed to wrap my head around how all of it works. Finally, a huge thank you is in order to ‘team liquid-cell’, *i.e.* **Tom Welling**, **Sina Sadighikia**, **Albert Grau Carbonell** and **Marijn van Huis** for all the cool in-situ TEM work I got to be part of and which resulted in a number of nice articles (and figures in Chapter 3), as well as for the many fun and interesting discussions on particle diffusion, interactions, or LC-TEM, and for the countless times they’ve helped me out with all my EM questions and needs.

And then there are of course all the colleagues with whom I had many fun talks in the

hallways, at coffee and lunch breaks and at borrels, and with whom I shared more cookies and cakes than are probably good for me. Of course I want to thank all the group leaders/staff of SCMB for encouraging a fun, social and inclusive atmosphere, and for being part of this themselves. Thanks to **Chris, Stijn, Mark** and **Sander** for being fun office mates in 0.18! Thank you to the ‘old guard’, e.g. **Fabian, Da, Jessi, Ernest, Fankje, Anna**, and many others for being welcoming and making the group a nice and social place when I started. Thanks **Naud, Maaïke, Jesper** and the rest of the CMI group for all the nice talks at our shared coffeekbreaks and borrels. **Rama**, thank you for all of our nice conversations over coffee breaks and in the lab and for teaching me a bit about your culture. **Naveed**, you are without a doubt one of the nicest and funniest people I’ve ever met and I always left our conversations smiling, no matter if we were joking or ranting. **Tom**, we hebben al vanaf de master vaak samengewerkt en in die tijd heel wat gelachen en mooie resultaten behaald. Thanks voor alles wat je me over TEM hebt geleerd en het verbaast me niks dat je nu een mooie positie in Japan hebt. **Albert**, thanks for all the nice collaborations, fun chats and for all your help with TEM. **Robin**, bedankt voor al onze leuke gesprekken bij lunchpauzes, schools, en borrels. **Erik**, vanaf nog vóór de bachelor kruisten onze paden vaak, en ik ben benieuwd waar we elkaar in de toekomst nog gaan tegenkomen. Het was altijd leuk om met je te sparren over wetenschap en te kletsen over reality tv! **Harith**, it was always nice to work and chat with you, and to see you continue some of the work from my masters thesis resulting in a nice paper. **Kelly**, bedankt voor je gezelligheid en alle leuke en interessante discussies over synthese, thesissen/papers schrijven of wat dan ook. **Roy**, ik heb met niemand anders zo veel uren in het lab, achter microscopen en voor computerschermen doorgebracht als met jou. Dat was niet alleen altijd gezellig en productief, maar ook heel leerzaam dankzij jouw kritische blik en goeie suggesties. **Marjolein**, je aanstekelijke vrolijkheid maakt dat het altijd als een feestje voelt zodra je erbij bent, om nog maar te zwijgen over alle leuke activiteiten die je georganiseerd hebt, bedankt! **Rinske**, bedankt voor je humor en gezelligheid, en hoop dat we nog vaak gaan boulderen. **Caroline**, es freut mich sehr dass ich dich kennengelernt habe und ich hoffe dass wir noch oft zusammen Deutsch oder Niederländisch üben können! And of course thanks to everyone else, **Gerhard, Meike, Kanako, Geert, Ethan, Diogo, Thijs, Ivo, Willem, Tim** and many others who all contributed to the generally lovely vibes, fun times and tasty baked goods over the last few years.

To my paranymphs and best friends **Jitse** and **Daphne**, bedankt dat jullie er altijd voor me zijn en dat ik met jullie over alles kan praten. Of ik jullie nou te vaak of te weinig spreek, het voelt altijd vertrouwd en verveelt nooit, en ik ben super blij om jullie dicht bij me te hebben tijdens de verdediging. Jullie zijn *awesome* ♡.

Aan al mijn vrienden en familie, bedankt voor al jullie steun en gezelligheid de afgelopen jaren en voor alle keren dat jullie me met beide benen op de grond hebben gehouden. Zonder jullie had ik dit nooit kunnen doen.

And finally to the most important person in my life: **Sandra**, you were there with me for the entire journey from start to end, you were hyped with me when I was excited and you were there for me when I was struggling. I love you and couldn’t be more proud of you ♡. Thank you so much for the last six years and I can’t wait to see what we’ll be doing next.

List of publications

1. M. Bransen and A. van Blaaderen. “Measuring interaction forces between colloids: towards nanoparticles.” [*in preparation*]
2. A. Grau-Carbonell, F. Hagemans, M. Bransen, ..., M. A. van Huis (2023) “In situ single particle characterization of the theroresponsive and co-nonsolvent behavior of PNIPAM microgels and silica@PNIPAM core-shell colloids.” *Journal of Colloid and Interface Science*, 635, 552–561. DOI: [10.1016/j.jcis.2022.12.116](https://doi.org/10.1016/j.jcis.2022.12.116)
3. J. E. S. van der Hoeven, H. Gurunayanan, M. Bransen, D. A. M. de Winter, P. E. Jongh, A. van Blaaderen (2022), “Silica-Coated Gold Nanorod Supraparticles: A Tunable Platform for Surface Enhanced Raman Spectroscopy.” *Advanced Functional Materials*, 2200148. DOI: [10.1002/adfm.202200148](https://doi.org/10.1002/adfm.202200148)
4. A. Grau-Carbonell, S. Sadighikia, T. A. J. Welling, R. J. A. van Dijk-Moes, R. Kotni, M. Bransen, A. van Blaaderen and M. A. van Huis (2021), “In Situ Study of the Wet Chemical Etching of SiO₂ and Nanoparticle@SiO₂ Core-Shell Nanospheres.” *ACS Applied Nano Materials*, 4(2), 1136–1148. DOI: [10.1021/acsanm.0c02771](https://doi.org/10.1021/acsanm.0c02771)
5. T. A. J. Welling, S. Sadighikia, K. Watanabe, A. Grau-Carbonell, M. Bransen, D. Nagao, A. van Blaaderen, and M. A. van Huis (2020), “Observation of Undamped 3D Brownian Motion of Nanoparticles Using Liquid-Cell Scanning Transmission Electron Microscopy.” *Particle & Particle Systems Characterization*, 37(6), 2000003. DOI: [10.1002/ppsc.202000003](https://doi.org/10.1002/ppsc.202000003)
6. J. E. S. van der Hoeven, E. B. van der Wee, D. A. M. de Winter, M. Hermes, Y. Liu, J. Fokkema, M. Bransen, M. A. van Huis, H. C. Gerritsen, P. E. de Jongh and A. van Blaaderen (2019), “Bridging the gap: 3D real-space characterization of colloidal assemblies via FIB-SEM tomography.” *Nanoscale*, 11(12), 5304–5316. DOI: [10.1039/c8nr09753d](https://doi.org/10.1039/c8nr09753d)
7. M. van der Linden, A. J. van Bunningen, L. Amidani, M. Bransen, H. Elnaggar, P. Glatzel, A. Meijerink and F. M. F. de Groot (2018), “Single Au Atom Doping of Silver Nanoclusters.” *ACS Nano*, 12(12), 12751–12760. DOI: [10.1021/acs.nano.8b07807](https://doi.org/10.1021/acs.nano.8b07807)

About the author

Maarten Bransen was born on the 5th of January 1994 in De Meern, and is said to have proclaimed at a rather young age that “when I’m a grown-up, I want to be a scientist”. In 2012 he obtained his VWO Gymnasium diploma from *Leidsche Rijn College* with a focus on natural sciences and technology, and started his bachelors degree in chemistry at *Utrecht University*. During his bachelors degree he participated in an honours programme and was awarded a *Topsector Chemiebeurs*, a scholarship to promote excellence in chemistry. He graduated *cum laude* in 2015. The next step was a masters degree in Nanomaterials Science at the same university, where he performed his masters thesis project under supervision of Prof. Alfons van Blaaderen and Prof. Petra de Jongh for which he was awarded the university wide prize for best masters thesis. During the final six months of his degree he performed a research internship under supervision of Prof. David Norris at the *ETH Zürich* in Switzerland, after which he obtained his masters degree *cum laude* in 2017. In 2018 he fulfilled his long time dream of becoming a scientist (and a grown-up –although opinions on that may vary–), and started his PhD research at *Utrecht University* under supervision of Prof. Alfons van Blaaderen on measuring interactions between colloidal particles, which culminated in this thesis.



When he is not in the lab, Maarten can often be found hiking or skiing in Switzerland. Aside from that he greatly enjoys rock climbing, music, making and watching theatre, and generally having a good time with his partner and friends.

